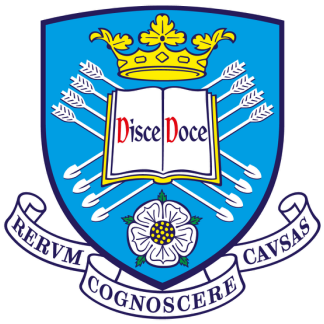

The University Of Sheffield.

Investigating the roles of the extracellular matrix in zebrafish heart morphogenesis

Christopher John Derrick

A thesis submitted in partial fulfilment of the requirement for the degree of Doctor of Philosophy

The University of Sheffield
Department of Biomedical Sciences

August 2020

Acknowledgements

Above all, I have one person to thank for the truly fantastic time I have had in the lab over the last 3 and a half years: Emily Noël. She is a truly excellent teacher, scientist and friend. I feel privileged to have been the "Guinea pig" in what is a brilliant lab to work in. To say I am sad to be leaving is a great understatement.

Other members of the rapidly growing lab have become firm friends for life, in particular Eric, Juliana, Farah, Philippa and more recently Emma. I can almost guarantee I will never have lab meetings that will be as much fun or be fuelled by so many biscuits!

In the wider community, I'd like to thank Elisabeth, Aaron, Karishma and Davide for conversations in the corridor, where so many "secret experiments" were developed and gossip (both scientific and not) was exchanged.

On the subject of secret experiments, Karen – you're a legend! Thank you for letting me use the light sheet on that Friday afternoon!

The Aquarium staff are truly an amazing bunch. I will particularly miss listening to Radio 2 with Susie, and I have Sarah Burbidge to thank for introducing me to the station in the first place.

I'm also grateful to Tanya Whitfield, Andy Grierson, Simon Johnston, Ryan MacDonald, Freek van Eeden and Marcelo Rivolta for helpful discussions on various points throughout my time in Sheffield. Of course, special mention must be made to the brilliant Tim Chico and his epic lab meetings.

A quick mention should also go to the members of Sheffield Bridge Club. I will miss you all!

I have been told on pain of death I have to mention the "help" some of my friends have provided, be it through asking truly random science questions or in trying to maintain some semblance of a work-life balance. So (in alphabetical order): Himsworth, Joshkins, Matt and Vicky – promise kept!

Finally, and most importantly, whilst none of my family have a clue what it is exactly I have been doing up here, they have been incredibly supportive and encouraging throughout. At what is a very odd time for everyone, I miss you all.

Abstract

Tissue morphogenesis requires co-ordination of changes in cell shape, gene expression and the integration of both intrinsic and extrinsic patterning cues. One such example of a complex tissue morphogenesis is the asymmetric looping of the linear heart tube during embryogenesis. Heart looping is required for the correct alignment of the chambers to facilitate septation, chamber ballooning and subsequent connection to the rest of the cardiovascular system. The necessity for robust heart morphogenesis is evident in the prevalence of congenital heart diseases which occur in around 1% of live births, and are the leading cause of birth defect-related deaths worldwide.

Most organ systems, including the heart are composed of distinct tissue types with specialised functions: during cardiac development, the heart tube comprises an outer layer of contractile myocardium surrounding a specialised endothelial cell layer known as the endocardium. During heart looping both the myocardial and endocardial tissue layers undergo distinct morphogenetic changes, and each play important roles in providing temporal and spatial signals to the other, together driving robust early cardiac morphogenesis. Separating the myocardium and endocardium is a specialised extracellular matrix (ECM) termed the cardiac jelly. Numerous studies have highlighted the importance of the cardiac jelly during later stages of heart development, however little work since its initial characterisation has investigated the mechanisms by which this ECM promotes asymmetric heart morphogenesis.

In this thesis I highlight the pivotal and previously underappreciated role of the embryonic cardiac jelly in promoting distinct aspects of cardiac morphogenesis in zebrafish. Common to all ECMs are the large, heterotrimeric Laminin complexes, secreted early during ECM deposition. I first identify and characterise the expression of multiple different Laminin subunits in the heart at the onset of heart looping and

go on to show a broad requirement for Laminins in promoting cardiac morphogenesis. Subsequently, I identify the specific Laminin isoforms which are required during heart development and uncover two distinct roles for Laminins: promoting asymmetric morphogenesis and restricting cardiac size.

Secondly, I uncover an asymmetry in the embryonic cardiac jelly, prior to the initiation of heart looping morphogenesis (which correlates with the expression of an ECM-modifying gene). I show that the cardiac ECM is rich in the Proteoglycan Hyaluronic Acid and that chamber-specific regionalisation of the ECM is required to promote heart morphogenesis.

Together, this work demonstrates that the constituents of the embryonic cardiac jelly and their regionalised expression are critical in promoting the robust, asymmetric morphogenesis of the linear heart during embryonic development.

Abbreviations Used ..... *x*

List of Figures and Tables ..... *xiv*

1. Introduction **1**

1.1 Congenital Heart Diseases and Heart Development *1*

1.1.1 The incidence of Congenital Heart Diseases 1

1.1.2 An overview of vertebrate heart development 4

1.2 Heart looping morphogenesis: the integration of intrinsic and extrinsic cues *8*

1.2.1 Embryonic left-right asymmetry and heart looping morphogenesis 9

1.2.2 Heart looping is tissue intrinsic 10

1.2.3 Biomechanical models of heart looping 11

1.2.4 The role of heart contractility and blood flow in cardiac development 14

1.3 Zebrafish as a model for vertebrate development *16*

1.3.1 Advantages of zebrafish usage 16

1.3.2 Reverse genetic approaches in zebrafish 17

1.3.3 Genetic robustness in zebrafish 21

1.4 Development of the Zebrafish Heart *25*

1.4.1 Specification of cardiac progenitors, formation of the cardiac disc (0-22hpf) 26

1.4.2 Heart jogging: the disc-to-tube transition (22-24hpf) 27

1.4.3 Heart looping and initiation of valvulogenesis (24-56hpf) 30

1.4.4 Heart maturation (56hpf onwards) 38

1.4.5 Comparison of Zebrafish and Human heart anatomy 39

1.5 An overview of the Extracellular Matrix *42*

1.5.1 Identification, characterisation and nomenclature of Laminins: non-collagenous glycoproteins 43

1.5.2 Laminins in development 48

1.5.3 Laminin receptors 51

1.5.4 The structure of Glycosaminoglycans and Proteoglycans 53

1.5.5 Functions of Glycosaminoglycans and Proteoglycans in tissue morphogenesis 56

1.6 The role of the Extracellular Matrix in cardiovascular development *58*

1.6.1 Laminins and Integrins....58
1.6.2 Proteoglycans....61
1.7 Rationale....*63*
2. Materials and Methods....65
2.1 Zebrafish husbandry....*65*
2.1.1 Zebrafish lines....65
2.1.2 Zebrafish care....66
2.1.3 Zebrafish embryo collection and staging....66
2.1.4 Micro-injection....67
2.1.5 Drug treatments....69
2.2 Molecular Techniques....*71*
2.2.1 Isolation of total RNA....71
2.2.2 Generation of cDNA....72
2.2.3 Polymerase Chain Reaction (PCR) and Sequencing....73
2.2.4 TOPO-TA Cloning....75
2.2.5 Gateway cloning: generation of middle entry vectors....76
2.2.6 Gateway cloning: generation of LR constructs....79
2.2.7 Bacterial transformation....80
2.2.8 mRNA transcription or riboprobe synthesis and cleanup for *in situ* hybridisation....81
2.3 mRNA in situ hybridisation (ISH)....*83*
2.3.1 Probes generated for this work....83
2.3.2 Probes generated for this work by others....84
2.3.3 Probes previously generated in other works....85
2.3.4 mRNA *in situ* hybridisation protocol....85
2.3.5 Imaging *in situ* hybridisations....88
2.3.6 Quantification of heart looping and heart area....88
2.3.7 Quantification of *hapln1a* expression domain....89
2.3.8 Genotyping post ISH....89
2.3.9 Statistical Analysis....90
2.4 Fluorescent in situ hybridisation (FISH)....*91*
2.5 CRISPR-Cas9 gRNA Design and Synthesis....*93*

2.5.1 gRNAs used....93
2.5.2 Ultramer-based, one-part gRNA: crRNA sequence design....94
2.5.3 Ultramer-based, one-part gRNA synthesis....94
2.5.4 sygRNA, two-part gRNA design for generating mutant lines....96
2.5.5 sygRNA, two-part gRNA design for knockdown by CRISPRi....96
2.5.6 sygRNA, two-part gRNA reconstitution and storage....97
2.5.7 Cas9 protein dilution and storage....97

2.6 Generation of Zebrafish mutant, knockdown and transgenic lines....98
2.6.1 Generation of stable mutant lines....98
2.6.2 Generation of transient CRISPR F0 mutant lines....102
2.6.3 Generation of *Tg(ubi-dCas9-poly(A), cryaa:CFP)*....103
2.6.4 Global CRISPRi....104

2.7 Light sheet imaging....105
2.7.1 Image Acquisition....105
2.7.2 ECM quantification....105

2.8 Immunohistochemistry....106
2.8.1 Immunohistochemistry protocol....106
2.8.2 Imaging....107

2.9 Semi-quantitative PCR....107
2.9.1 Collection of embryos....107
2.9.2 Polymerase Chain Reaction....108
2.9.3 Quantification and normalisation of band intensity....110
2.9.4 Statistical Analysis....111

3. Identification and characterisation of Laminin expression dynamics during early heart morphogenesis....112

3.1 Results....113
3.1.1 Identification of Laminin subunits with dynamic and tissue-specific expression during heart morphogenesis....113
3.1.2 Identification of specific integrins as potential Laminin receptors during heart morphogenesis....121
3.1.3 Laminin subunit genes display distinct mechanisms of regulation of expression 124

3.1.4 *lamc1* is required for heart morphogenesis 132

3.2 Discussion *137*

4. *lamb1b* is dispensable for heart morphogenesis 144

4.1 Results *144*

4.1.1 *lamb1b* exhibits dynamic expression during heart looping 144

4.1.2 Generation and characterisation of *lamb1b* coding sequence mutants by CRISPR-Cas9 mutagenesis 147

4.1.3 *lamb1b* coding sequence mutants display hallmarks of genetic compensation .. 155

4.1.4 *lamb1b* ATG morphants have severe cardiac defects which are likely to be due to off-target effects 162

4.1.5 Developing CRISPRi as a tool for targeted gene knockdown 170

4.1.6 Generation and characterisation of *lamb1a* coding sequence mutants by CRISPR-Cas9 mutagenesis 174

4.1.7 Deletion of the *lamb1b* promoter demonstrates that *lamb1b* is dispensable for heart development 180

4.2 Discussion *186*

5. Laminins are required to limit heart size 193

5.1 Results *193*

5.1.1 *lamb1a* coding sequence mutants display hallmarks of genetic compensation and up-regulate *lamb1b* 193

5.1.2 *lamb1b* does not compensate for loss of *lamb1a* 197

5.1.3 *lamb1a* is required to limit heart size, but is dispensable for heart looping morphogenesis 209

5.1.4 Lamb1a-Lamc1 containing Laminin isoforms are required to limit heart size 218

5.1.5 *lamb1a* mutants display mis-regulation of flow responsive genes 230

5.2 Discussion *244*

6. The cardiac jelly displays regional asymmetry during heart development 253

6.1 Results *254*

6.1.1 Light sheet microscopy identifies regional differences in ECM thickness in the developing heart 254

6.1.2 The cardiac jelly is rich in the glycosaminoglycan Hyaluronan....258
6.1.3 Previously identified proteoglycan-related genes not exhibit left-right asymmetric expression in the heart tube....260
6.1.4 Expression of *hyaluronan and proteoglycan link protein 1a* (*hapln1a*) overlaps with observed ECM expansion....264
6.1.5 Regionalised expression of *hapln1a* is required for correct cardiac morphogenesis....269
6.1.6 *hapln1a* expression is independent of embryonic left-right asymmetry....273
6.2 Discussion....*275*
7. *rhoca* and *rhocb* are dispensable for early cardiac development....284
7.1 Results....*284*
7.1.1 *rhoca* is expressed in the heart during looping morphogenesis....284
7.1.2 Generation and characterisation of *rhoca* CDS mutants....286
7.1.3 Loss of *rhoca* does not affect *rhocb* expression....293
7.1.4 Generation and characterisation of *rhocb* CDS mutants....295
7.1.5 Loss of *rhoca* does not affect cardiac size in adults....298
7.2 Discussion....*300*
8. Discussion....303
8.1 Cell-ECM signalling....*303*
8.2 ECM and biochemical interactions....*306*
8.3 Cardiac function and ECM....*308*
8.4 Regulation of ECM synthesis....*310*
8.5 The dynamic ECM as a driver of heart development....*314*
8.6 Therapeutic futures....*324*
9. References....327
10. Appendix....369

Abbreviations Used

4OHT	4-Hydroxytamoxifen
ALPM	Anterior Lateral Plate Mesoderm
AMI	Acute Myocardial Infarction
AOS	Adams-Oliver Syndrome
AVC	Atrioventricular Canal
BA	Bulbus Arteriosus
BAV	Bicuspid Aortic Valve
BM	Basement Membrane
BMP	Bone Morphogenetic Protein
CCM	Cerebral Cavernous Malformation
CDS	Coding Sequence
CHD	Congenital Heart Disease
CRISPant	Embryo subjected to CRISPRi
CRISPR	Clustered regularly interspaced short palindromic repeats
CRISPRi	CRISPR interference
crRNA	CRISPR RNA
CS	Chondroitin Sulfate
CSPG	Chondroitin Sulfate Proteoglycan
dCas9	Catalytically dead Cas9 nuclease
DDW	Double-Distilled Water/RNAse Free Water
DORV	Double Outlet Right Ventricle
dpa	days post amputation
dpf	days post fertilisation
dpi	days post injury
DWS	Dandy-Walker Syndrome
E	Embryonic Day (mouse)
ECM	Extracellular Matrix
EJC	Exon-Junction Complex
EMT	Epithelial-to-Mesenchymal Transtion

EndoMT	Endothelial-to-Mesenchymal Transition
ENU	N-ethyl-N-nitrosourea
FGF	Fibroblast Growth Factor
FISH	Fluorescent *in situ* hybridsation
FN	Fibronectin
GAG	Glycosaminoglycan
GAP	GTPase Activating Protein
GBM	Glomerular Basement Membrane
GDI	Guanine nucleotide Dissociation Inhibitor
GEF	Guanine Exchange Factors
gRNA	guide RNA (crRNA + tracrRNA)
HA	Hyaluronan/Hyaluronic Acid
HH	Hamburger-Hamilton (chick)
HOS	Holt-Oram Syndrome
hpf	hours post fertilisation (zebrafish)
HREM	High-Resolution Episcopic Microscopy
HS	Heparan Sulfate
HSPG	Heparan Sulfate Proteoglycan
IFT	Inflow Tract
IHC	Immunohistochemistry
inX	Incross (mating of identical genetic background)
ISH	*in situ* hybridisation
ISVs	Intersegmental Vessels
KD	Knockdown
KO	Knockout
KS	Keratan Sulfate
KV	Kupffer's Vesicle
L-R	Left-Right
LE	Laminin-EGF like
LG	Laminin-Globular

LHT	Linear heart tube
LLC	Large Latent Complex
LN	Laminin-N terminal
LN-XXX	Laminin- αXβXγX
LPM	Lateral Plate Mesoderm
LTBP	Latent TGF-β Binding Protein
MI	Myocardial Infarction
MMP	Matrix Metalloproteinases
MO	Morpholino oligonucleotide
Morphant	Embryo injected with morpholino
MPZ	Maternal-Paternal-Zygotic
MQ	MilliQ water
NICD	Notch-Intracellular Domain
NMD	Nonsense-Mediated Decay
OFT	Outflow tract
outX	Outcross (mating of different genetic backgrounds)
P	Postnatal day (mouse)
PAM	Protospacer Adjacent Motif
PCR	Polymerase Chain Reaction
pERK	phospho-ERK
PG	Proteoglycan
pMLC2	Phospho-Myosin Light Chain 2
PTC	Premature Termination Codon
RA	Retinoic Acid
ROI	Region Of Interest
RV	Right Ventricle
SAN	Sino-Atrial Node
Semi-qPCR	Semi-quantitative PCR
SHF	Second Heart Field
TGFβ	Transforming Growth Factor beta

tracrRNA	trans-activating crRNA
WT	Wild-type
Z	Zygotic

List of Figures and Tables

Figure 1.1. Comparison of Vertebrate Heart Looping 3

Figure 1.2. Mechanisms of targeted gene knockdown and knockout in zebrafish 18

Figure 1.3. Stages of heart development in zebrafish 25

Figure 1.4. Heart jogging re-organises left-right asymmetry to dorsal-ventral tube asymmetry 29

Figure 1.5. Second heart field addition and myocardial-endocardial cross-talk are required for looping morphogenesis 31

Figure 1.6. Early valvulogenesis in zebrafish 34

Figure 1.7. Comparison of human and zebrafish heart anatomy 41

Figure 1.8. The Extracellular Matrix 42

Figure 1.9. Structure and assembly of Laminins 46

Figure 1.10. Canonical Laminin-Integrin interactions 52

Figure 1.11. Interaction between Hyaluronan and Proteoglycans 55

Table 2.1. Zebrafish lines 65

Table 2.2. Morpholino sequences 67

Table 2.3. Morpholino dilutions 68

Table 2.4. Verso cDNA Reverse Transcription reaction 72

Table 2.5. RT-OligodT Mix 73

Table 2.6. RT-Reaction Mix 73

Table 2.7. BioMix Red PCR 74

Table 2.8. BioMix PCR Programme 74

Table 2.9. Phusion Taq Reaction 74

Table 2.10. Phusion PCR Programm 74

Table 2.11. TOPO reaction volumes 75

Table 2.12. Gateway plasmids used 76

Table 2.13. Primers for cloning of *lamb1b* 76

Table 2.14. Primers used in cloning of *pME* 77

Table 2.15. BP Reaction for *pME* 78

Table 2.16. LR Reaction 79
Table 2.17. LR constructs generated 80
Table 2.18. Colony PCR volumes 81
Table 2.19. Colony PCR Programme 81
Table 2.20. Probes generated for this work 83
Table 2.21. Probes cloned by other members of the lab 84
Table 2.22. Probes previously published 85
Table 2.23. ISH solutions 87
Table 2.24. ProteinaseK treatment timings 88
Table 2.25. FISH solutions 92
Table 2.26. CRISPR-Cas9 gRNAs used 93
Table 2.27. Primers for amplification of Ultramers 95
Table 2.28. MegaShortScript T7 Reaction 96
Table 2.29. CRISPR-Cas9 genotyping 100
Table 2.30. *lamb1b* splicing primers 101
Table 2.31. *rhoca* splicing primers 102
Table 2.32. CRISPR-Cas9 F0 genotyping 103
Table 2.33. CRISPRi genotyping 104
Table 2.34. IHC primary antibodies 106
Table 2.35. IHC secondary antibodies 106
Table 2.36. Housekeeping control semi-qPCR primers 109
Table 2.37. *lamb1a* semi-qPCR primers 109
Table 2.38. *lamb1b* semi-qPCR primers 110

Figure 3.1. Tomo-Seq identifies 5 laminin subunits expressed in the zebrafish heart at 30hpf. 114
Figure 3.2. Dynamic expression of Laminin subunit genes during heart morphogenesis 115
Figure 3.3. *lama5* and *lamb2* are expressed exclusively in the myocardium 118

Figure 3.4. *lama4* and *lamb1b* are expressed exclusively in the endocardium 119

Figure 3.5. *lamb1a* and *lamc1* are expressed in both the myocardium and endocardium 120

Figure 3.6. The Laminin-binding integrins *itga3*, *itga7* and *itgb1* are expressed in the heart during looping morphogenesis 122

Figure 3.7. Canonical Notch signalling is required for *lamb1b* expression 125

Figure 3.8. Canonical Notch signalling may be required during early heart looping 127

Figure 3.9. Expression of endocardial Laminin subunits is flow dependent 130

Figure 3.10. *lamc1* F0 mutants recapitulate the stable *sleepy* phenotype 133

Figure 3.11. *lamc1* F0 mutants exhibit a profound heart looping phenotype 135

Figure 3.12. Laminins are required for heart morphogenesis 138

Figure 4.1. *lamb1b* exhibits dynamic expression and restriction to the atrioventricular canal during heart looping 146

Figure 4.2. Generation of *lamb1b* coding sequence mutants by CRISPR-Cas9 mutagenesis 149

Figure 4.3. *lamb1b* zygotic coding sequence coding sequence mutants do not display cardiac abnormalities 150

Figure 4.4. Valve and endocardial markers are unaltered in *lamb1b* zygotic coding sequence mutants 151

Figure 4.5. *lamb1b* mutant adults do not display body size or cardiac defects 152

Figure 4.6. *lamb1b* maternal-paternal-zygotic coding sequence mutants do not display cardiac abnormalities 154

Figure 4.7. *lamb1b* mutant mRNA does not undergo alternative splicing 157

Figure 4.8. *lamb1b* coding sequence mutant mRNA transcripts appear to undergo decay 159

Figure 4.9. Expression of other Laminin beta subunits is unchanged in *lamb1b* zygotic coding sequence mutants 161

Figure 4.10. *lamb1b* ATG morphants have severe cardiac defects 163

Figure 4.11. Morpholino-mediated knockdown of *lamb1b* affects cardiac patterning 165

Figure 4.12. Morpholino-mediated knockdown of *lamb1b* results in expansion of valve markers 166

Figure 4.13. *lamb1b* coding sequence mutants are not protected against the *lamb1b* ATG morphant phenotype 169

Figure 4.14. Generation of *Tg(ubi:dCas9, cryaa:CFP*) for global CRISPRi 171

Figure 4.15. Knockdown of *lamb1b* is not observed using *Tg(ubi:dCas9, cryaa:CFP)* 173

Figure 4.16. Generation of *lamb1a* coding sequence mutants by CRISPR-Cas9 mutagenesis 175

Figure 4.17. *lamb1a* coding sequence mutants recapitulate previously published *lamb1a* alleles 176

Figure 4.18. *lamb1a* does not compensate for loss of *lamb1b* heart looping 178

Figure 4.19. Targeted deletion of the *lamb1b* promoter by CRISPR-Cas9 results in complete loss of *lamb1b* transcript 181

Figure 4.20. *lamb1b* promoter mutants do not phenocopy *lamb1b* ATG morphants 183

Figure 4.21 *lamb1b* promoter mutants do not recapitulate expansion of *notch1b* observed in *lamb1b* ATG morphants 185

Figure 5.1. *lamb1b* mutant transcripts are subject to RNA decay 194

Figure 5.2. *lamb1b* is up-regulated in *lamb1a* coding sequence mutants with allele-specific persistence 197

Figure 5.3. Titration of sub-phenotypic dosage of NMD blocking morpholino 198

Figure 5.4. Morpholino-mediated knockdown of nonsense-mediated decay machinery does not recover *lamb1a* transcript or impact heart looping morphogenesis 201

Figure 5.5. Pharmacological inhibition of nonsense-mediated decay does not recover *lamb1a* transcript levels or impact heart looping morphogenesis 204

Figure 5.6. *lamb1b* expression is abolished in *lamb1a; lamb1b* promoter double mutants **207**
Figure 5.7. *lamb1* subunits are dispensable for heart looping morphogenesis **208**
Figure 5.8. *lamb1a* is required to limit restrict heart size independent of *lamb1b* **211**
Figure 5.9. *gup^{tj299a}* mutants have larger hearts and up-regulate *lamb1b* **213**
Figure 5.10. *lamb1a* is dispensable for heart looping morphogenesis, but is required to limit heart size **215**
Figure 5.11. *lamb1a* is required to limit chamber size **217**
Figure 5.12. *lamc1* is required to restrict heart size and promote heart morphogenesis **220**
Figure 5.13. The *lamc1* cardiac phenotype is epistatic to *lamb1a* **222**
Figure 5.14. Laminins perform distinct roles during heart development **224**
Figure 5.15. *lamb2* expression is unchanged by loss of *lamb1a* and/or *lamb1b* **226**
Figure 5.16. *lamb2* is dispensable for heart looping at 55hpf **227**
Figure 5.17. *lamb2* is dispensable for early heart morphogenesis **229**
Figure 5.18. *lamb1a* mutants display mild cardiac patterning defects **231**
Figure 5.19. *lamb1a* mutants display flow-independent expression of flow-dependent genes **233**
Figure 5.20. Knockdown of *gata1a* does not rescue heart size in *lamb1a* mutants **236**
Figure 5.21. Increasing blood flow is not sufficient to increase heart size **239**
Figure 5.22. *lamb1a* mutants display an increase in pERK at 30hpf **242**
Figure 5.23. Inhibition of ERK5 activity does not rescue the *lamb1a* phenotype **243**
Figure 5.24. Laminins perform distinct functions during heart development **245**

Figure 6.1. Ventricular ECM is thin and uniformly distributed in the looped heart **255**
Figure 6.2. The atrium displays regional differences in cardiac jelly thickness following heart looping morphogenesis **256**
Figure 6.3. The cardiac jelly is asymmetrically expanded at the venous pole prior to heart looping morphogenesis **257**
Figure 6.4. Hyaluronic Acid is not asymmetrically deposited into the cardiac jelly **259**

Figure 6.5. Endocardial *has2* is not asymmetrically expressed in the heart tube **260**

Figure 6.6. Chondroitin Sulfate Proteoglycans exhibit dynamic and complementary expression patterns during early heart morphogenesis **262**

Figure 6.7. *acana* and *acanb* are expressed in the heart post-looping **263**

Figure 6.8. *hapln1a* expression asymmetrically overlaps observed ECM expansion prior to heart looping **266**

Figure 6.9. Proteoglycan components display distinct expression patterns in the cardiac cone **268**

Figure 6.10. Regionalised *hapln1a* expression is required to promote proper heart morphogenesis **271**

Figure 6.11. Expression of *hapln1a* is independent of embryonic left-right laterality **274**

Figure 6.12. Model for regionalised gene expression during zebrafish heart development **276**

Figure 7.1. *rhoca* is expressed in the heart during early morphogenesis **286**

Figure 7.2. Generation of *rhoca* coding sequence mutants by CRISPR-Cas9 mutagenesis **287**

Figure 7.3. *rhoca* zygotic mutants do not exhibit cardiac phenotypes **289**

Figure 7.4. *rhoca* maternal-paternal-zygotic mutants do not have significant morphological defects **291**

Figure 7.5. *rhocb* is expressed in the heart and expression is not altered by loss of *rhoca* **294**

Figure 7.6. Generation of *rhocb* coding sequence mutants by CRISPR-Cas9 mutagenesis **296**

Figure 7.7. *rhoca* and *rhocb* are dispensable for early heart morphogenesis **297**

Figure 7.8. Loss of *rhoca* does not impact adult heart size **299**

Table 10.1. Primer sequences used to generate mRNA ISH probes **369**

1. Introduction

1.1 Congenital Heart Diseases and Heart Development

1.1.1 The incidence of Congenital Heart Diseases

Congenital heart diseases (CHDs) are structural malformations of the heart, arising due to failures in the multi-faceted process of heart development. Globally CHD is present in approximately 1% of live births and is the most common cause of birth-defect related deaths (Bernier et al., 2010; Hoffman and Kaplan, 2002; Linde et al., 2011; Members et al., 2012). One categorisation of CHDs: severe, moderate or mild describes how whilst severe and moderate manifestations are likely to be detected either before birth or postpartum as they can be life-threatening, mild CHDs - which account for greatest prevalence - often go undiagnosed due their asymptomatic nature (Hoffman and Kaplan, 2002). Severe CHDs encompass all cyanotic heart diseases (the mixing of oxygenated and deoxygenated blood) which present major anatomical disruption to the heart (Hoffman and Kaplan, 2002) such as double outlet right ventricle (DORV) in which both the pulmonary artery and aorta are connected to the right ventricle. Mild CHDs do not exhibit such striking defects in gross heart morphology (Hoffman and Kaplan, 2002), instead encompassing more subtle abnormalities such as aortic incompetence (also known as aortic insufficiency). Moderate CHDs are in some cases almost completely asymptomatic due to their relatively minor impact on cardiac morphology, for example small ventricular septal defects (Hoffman and Kaplan, 2002). Nonetheless, all forms of CHD have a major impact on the individual's life (Saha et al., 2019).

A range of CHDs are commonly associated with syndromes such as Down, Edward, DiGeorge, Holt-Oram and Alagille (Muntean et al., 2016). Mapping of the causative element in these syndromes has identified genes or clusters of genes that play roles in the development of the heart (Muntean et al., 2016; Pierpont et al., 2000; Sifrim et al., 2016). CHDs present in non-syndromic cases are more common and have

been linked to mutations in specific genes or specific sets of genes (Muntean et al., 2016; Sifrim et al., 2016). Mapping and identification of regions associated with CHDs in both syndromic and non-syndromic patients has identified transcription factors, signalling ligands, receptors and components of the extracellular matrix (Muntean et al., 2016; Pierpont et al., 2000; Sifrim et al., 2016).

Using multiple vertebrate models, the characterisation of the expression patterns and functions of these genes has shown that many are required during very early heart development (Moon, 2008; Stainier, 2001). Furthermore, generation of mutants in genes associated with CHDs has proven fruitful in beginning to uncover the molecular mechanisms which result in both correct and improper cardiac development (Moon, 2008; Stainier, 2001). Together, this highlights how understanding development of the heart at early stages is critical to uncovering how loss of function of these and other genes results in CHDs. I will set out the main landmark events in vertebrate heart development, demonstrating their high level of conservation between model organisms. I will also provide examples of mutations in genes that promote these specific processes and in which mutations cause CHDs and how use of animal models in this context has furthered our knowledge of heart development.

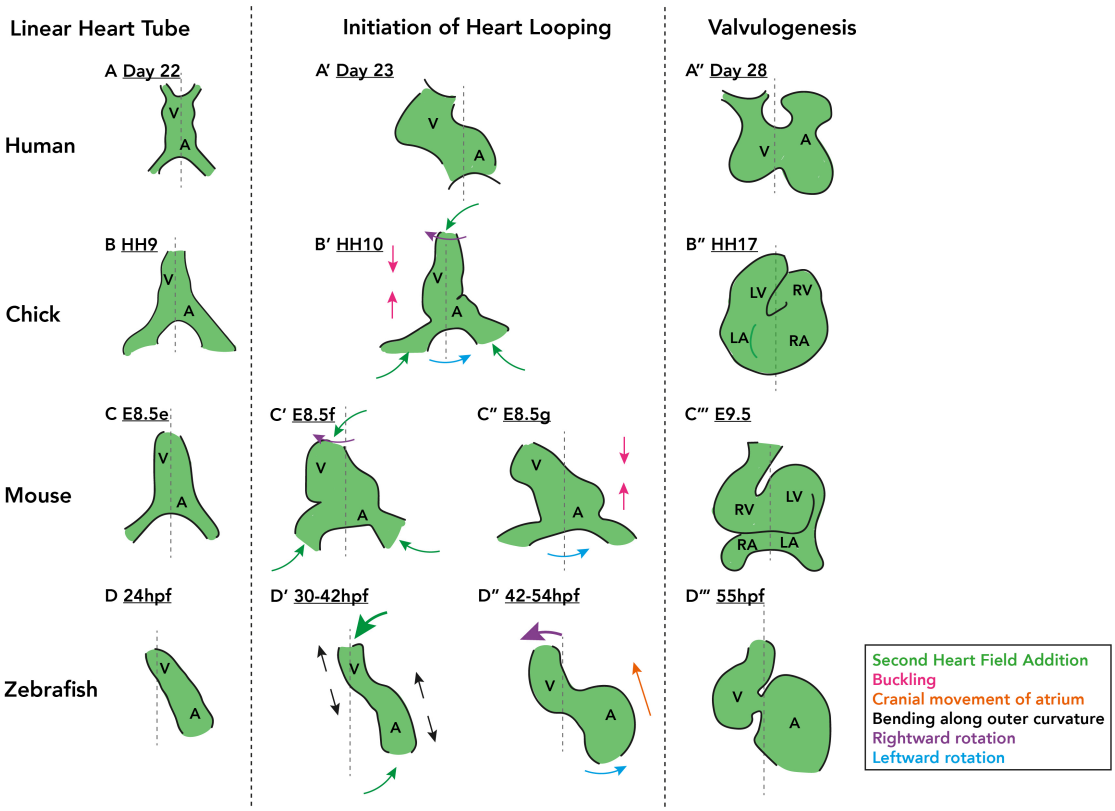

Figure 1.1. Comparison of Vertebrate Heart Looping.

Comparison of events during heart looping in morphogenesis Human, Chick, Mouse and Zebrafish. **(A-A'')** The linear heart tube forms in humans at 22 days (A), begins to undergo morphogenesis at 23 days (A') and valves start to form between chambers at 28 days (A''). **(B-B'')**. At HH9 the linear heart tube has formed in Chick. (B') Starting at HH10, the heart tube buckles/bends ventrally (magenta), the arterial pole rotates rightward (purple) followed by the leftward rotation at the venous pole (cyan). Cell number is increasing by second heart field addition (green). (B'') At HH17, valves begin to form between the chambers. **(C-C''')** The initial shaping of heart looping morphogenesis occurs rapidly in mouse during E8.5, starting at E8.5e (C). (C') At E8.5f rightward rotation at the arterial pole shifts the ventricle, whilst cell number increases through second heart field addition. (C'') E8.5g the heart buckles due to addition from second heart field and the venous pole undergoes leftward rotation forming the basic shape of the heart by E9.5 (C''') when valves begin to form. **(D-D''')** Heart looping morphogenesis in zebrafish begins at 24hpf, the linear heart tube

1.1.2 An overview of vertebrate heart development

A number of vertebrate models, together with complementary genetic analysis in non-vertebrates have been utilised to understand the complex morphogenetic process of heart development. Whilst the exact architecture of the final, mature cardiovascular system differs between mammals/birds, reptiles and teleost fish, the basic morphological processes which generate their respective four, three and two-chambered hearts is well conserved (Figure 1.1). During embryogenesis, the heart is the first organ to form and function. At day 22 in humans, embryonic day (E)8.5e (5-6 somites) in mice, Hamburger-Hamilton stage (HH)9 in chick and 24 hours post fertilisation (hpf) in zebrafish the heart is clearly identifiable as a linear tube (LHT) (Figure 1.1A, B, C, D) (Fishman and Chien, 1997; Garrec et al., 2017). Outer, contractile myocardium is separated from the endocardium, a specialised endothelial cell population, by the cardiac jelly or extracellular matrix (ECM). Although the precursor structures to the LHT differ between different model organisms, the formation of the LHT represents a highly conserved morphological

Figure 1.1 continued.

Is positioned asymmetrically under the left eye (D). (D') In early S-looping, the primary addition of cells to the heart is at the arterial pole and the chambers bend along their outer curvatures (black). (D'') During advanced S-looping the atrium moves cranially (orange) and similar to mice and chick, rotations at the poles occur, predominantly at the arterial pole. By 55hpf (D''') the heart has well defined morphological chambers with the atrioventricular valve developing at the constriction between chambers. Images and stages based on: Desgrange et al., 2019; Fishman and Chien, 1997; Garrec et al., 2017; Lombardo et al., 2019; Männer, 2009; Martin et al., 2015; Pater et al., 2009. A: atrium, V: ventricle, LA: left atrium, RA: right atrium, LV: left ventricle, RV: right ventricle. Left-right axis inverted, with midline denoted by grey line.

stage in the development of the cardiovascular system in vertebrates. At this early stage, whilst appearing morphologically uniform, the LHT already displays highly regionalised gene expression, necessary for correct function during and after gestation (Bruneau, 2008).

The first gene linked to syndromic CHD was through the autosomal dominant condition Holt-Oram syndrome (HOS). Mapping the genetic region suspected to contain the lesion, and comparing multiple familial cases of HOS identified the causative gene as *T-box transcription factor 5* (*TBX5)* (Basson et al., 1997). Timing of *Tbx5* expression in the heart is highly conserved between chick, mouse and zebrafish, with expression identified in the mouse cardiac crescent at E8, the chick bilateral cardiac primordia at HH8, the analogous stage (Bruneau et al., 1999) and in the zebrafish heart tube at 26hpf (Garrity et al., 2002). As the heart tube undergoes morphogenesis, *Tbx5* expression is maintained throughout heart development, and subsequently is excluded from the right ventricle (RV) and outflow tract (OFT) (Bruneau et al., 1999). Importantly there is a high degree of correlation between *Tbx5* expressing regions and those affected in HOS patients (Bruneau et al., 1999) and both mice and zebrafish *tbx5* mutants have cardiac phenotypes consistent with a role for *TBX5* in heart development (Bruneau et al., 2001; Garrity et al., 2002). These early studies highlight that loss of function of genes expressed throughout the heart during early development result in specific malformations of the heart.

Following heart tube formation and beginning at day 23 in humans E8.5f (6-8 somites) in mice, HH10 in chick and 30hpf in zebrafish, the linear heart tube undergoes a robust, dextral, asymmetric morphogenesis known as heart looping (Figure 1.1A', B', C', D') (Fishman and Chien, 1997; Garrec et al., 2017). The highly asymmetric nature of heart looping is crucial in positioning the chambers of the heart in correct alignment, facilitating accurate septation (division) of the chambers and valves between chambers. Ultimately, this ensures unidirectional blood flow through the heart and integration of the organ into the rest of the cardiovascular

system. The need for tightly-controlled rightward looping of the LHT during development is exemplified in the condition Situs ambiguus or Heterotaxy syndrome. This results in randomisation of the internal organs across the left-right body axis and can cause a spectrum of morphological cardiac abnormalities such as sinistral looping of the heart resulting in incorrect attachment of the great vessels to heart and life-threatening cyanotic CHDs (Kim, 2011). However, whilst this demonstrates that heart looping is a critical developmental process, in comparison to other events during heart development, relatively little is known about how it progresses and how it is regulated (see 1.2).

During heart looping, multiple processes begin to shape the organ, one of which is a dramatic increase in cell number in the myocardium, despite insufficient proliferation to account for this increase (Cruz et al., 1977; Pater et al., 2009). This increase in cell number is achieved through addition of cells to the developing heart from a pool of progenitor cells known as the second heart field (SHF), initially identified in chick and conserved in both mice and zebrafish (Figure 1.1 B', C', D'). In mice and chick, SHF addition generates the majority of cardiac tissue, giving rise to the right ventricle and atrial tissue (Cruz et al., 1977; Kelly et al., 2001; Mjaatvedt et al., 2001; Waldo et al., 2001), whilst in zebrafish the major contribution of SHF is to the single ventricle (Hami et al., 2011; Kelly et al., 2014; Pater et al., 2009). Defects in the proper patterning, placement and formation of septa between these structures of the heart, amongst other developmental abnormalities including those affecting the vestibular system are observed in DiGeorge syndrome patients, also known as 22q11.2 syndrome, and mapping of the region identified the causative gene *TBX1 (T-box transcription factor 1)* (Lindsay et al., 2001; Merscher et al., 2001). *TBX1* regulates a multitude of developmental processes necessary for SHF addition (Baldini et al., 2017; Plageman and Yutzey, 2004), one key, highly conserved role being proliferation of the progenitor pool (Chen et al., 2009; Nevis et al., 2013). In both mice and zebrafish *tbx1* mutants, addition of the SHF is affected leading to severe heart looping abnormalities in the embryo.

As heart looping morphogenesis proceeds, clear divisions begin to form between the chambers heart. In mice and chick, septa form physical barriers between each of the chambers, with valves forming to facilitate unidirectional blood flow from one chamber to another (Day 28 in humans, E9.5 in mice, HH17 in chick, 55hpf in zebrafish) (Fishman and Chien, 1997). The development of these valves is most clearly observed in the zebrafish model where a constriction forms between the atrium and ventricle, known as the atrioventricular canal (AVC), the precursor to the atrioventricular valve (discussed in more detail in 1.4.3 and 1.6.3) (Beis et al., 2005; Walsh and Stainier, 2001). Additional valves form in the Outflow Tract (OFT), where blood exits from the ventricle into the vascular bed of the respiratory system, alos conserved in zebrafish (Duchemin et al., 2019). In Alagille syndrome, the majority of patients have defects in the pulmonary valves in the heart. Mapping of the causative region identified mutations in the notch ligand *JAG1 (Jagged1)* (Li et al., 1997) and *NOTCH2 (Notch receptor 2)* (McDaniell et al., 2006). Subsequently, multiple roles have been defined for Notch in the development of valve tissue, with studies in mouse, chick and zebrafish models demonstrating that signalling ligands and downstream effectors highly conserved between species.

Concomitant with valvulogenesis is the development of the trabecular myocardium, a mechanism used to increase muscle content and surface area for oxygen uptake in the ventricle through co-ordinated myocardial proliferation (Day 30 in humans, E9.5 in mice, HH16 in chick, 60hpf in zebrafish) (Samsa et al., 2013). Trabeculation is also dependent on Notch signalling and mutations in *MIB1* (*mindbomb homolog 1*), a conserved regulator of the Notch pathway have been linked to familial cases of Left-Ventricular Non-Compaction, which results in a failure in trabeculation (Luxán et al., 2013). Chamber maturation and valve development build upon blueprint of the correctly looped heart, and both processes are dependent on the correct flow patterns of blood through the heart (see 1.4.3), which itself requires heart looping morphogenesis to proceed correctly. Therefore, the early morphogenesis of the heart is critical in building the necessary elements of both form and function to

ultimately generate the mature, functional heart (Bruneau, 2008; Harvey, 2002; Srivastava and Olson, 2000).

Together, these examples of human syndromic CHDs and the associated genetic mutations, highlight the power of vertebrate model systems in understanding how the complex process of heart development is achieved. Furthermore, the genes which regulate these processes are highly conserved between organisms separated by millions of years of evolution (Keyte et al., 2014). More generally, the severity of CHD is linked with spatiotemporal expression of genes in the linear heart tube which are required to setup the necessary pathways to promote morphogenesis and form the looped organ. This demonstrates that understanding the earlier processes of heart development, in particular heart looping, is crucial to a better understanding of the aetiology of CHDs and ultimately the development of better treatments for patients in mitigating the lifelong effects of these diseases.

1.2 Heart looping morphogenesis: the integration of intrinsic and extrinsic cues

Heart looping morphogenesis shapes the linear heart tube into the morphologically complex form of the mature heart. Yet the final form of the heart must reflect the need to integrate the rest of the cardiovascular system: zebrafish have a single circulatory loop, whilst birds and mammals have two separate systems (Keyte et al., 2014). Therefore, partitioning of the heart during looping to generate more complex four-chambered structures in the mouse, versus a simpler two-chamber heart required in the fish, necessitates different degrees of looping morphogenesis: the mouse heart undergoes a helical loop, the zebrafish undergoes a simpler S-loop (Desgrange et al., 2018). However, the basic morphological processes that drive heart looping morphogenesis are highly conserved and integrate various intrinsic and extrinsic mechanisms to shape the linear tube, which I discuss below.

1.2.1 Embryonic left-right asymmetry and heart looping morphogenesis

Heart looping is a highly asymmetric process and the earliest morphological event to break the bilateral symmetry of the vertebrate embryo. However, molecular asymmetries exist in the embryo prior to heart formation, directed by a left-right organiser: the node in mouse, Hensen's node in chick and Kupffer's vesicle in zebrafish (Grimes and Burdine, 2017). The left-right organiser is a ciliated organ, in which co-ordinated movement of the cilia result in asymmetric fluid flow towards the future left-side of the embryo, driving a signalling cascade that results in up-regulation of Nodal (a conserved signalling ligand of the Transforming growth factor beta (TGF-β) family) in the left-lateral plate mesoderm of the embryo, (E8.0 in mice, HH7 in chick, 14hpf in zebrafish) (Burdine and Schier, 2000; Levin, 2005; Long et al., 2003). Thus, the asymmetric expression of Nodal in the left-lateral plate mesoderm provides a parsimonious mechanism in driving the directionality and morphogenesis of asymmetrically shaped and positioned organs such as the heart and gut.

This basic model would therefore suggest that a loss of Nodal signalling would result in a failure of both morphogenesis and positioning of these organs. However, mutations in the zebrafish Nodal homolog *southpaw* (*spaw*), results in total randomisation of gut morphogenesis, but crucially asymmetric morphogenesis still occurs, demonstrating that in the gut, left-right asymmetry is dispensable for morphogenesis, but instructive for its directionality (Grimes et al., 2019; Noël et al., 2013). Similarly, loss of *spaw* does not result in a failure of the heart to undergo looping morphogenesis: heart looping still occurs in over 90% of embryos. Yet distinct from gut morphogenesis and genetic asymmetry in the brain, over 70% of *spaw* mutant hearts undergo dextral looping morphogenesis. This demonstrates that a strong bias towards correct looping morphogenesis persists despite the absence of Nodal signalling or indeed cilia function in the Kupffer's vesicle (Noël et al., 2013). Similarly, whilst the directionality of heart looping in mice with loss of *Nodal* display randomised heart looping, asymmetric morphogenesis still occurs

(Brennan et al., 2002) and more recently it has been elegantly demonstrated that *Nodal* is not required to initiate the process of heart looping (Desgrange et al., 2019). Together this shows that directionality of heart looping morphogenesis is only partially influenced by extrinsic left-right asymmetry in the embryo and that asymmetric morphogenesis of the heart tube is an inherent property of the tissue.

1.2.2 Heart looping is tissue intrinsic

The tissue movements required to implement the robust asymmetric movements in heart development across the vertebrates suggests that the mechanisms required to bend and shape the heart tube are partially intrinsic to the heart itself. Multiple early studies tested this through the use of explant culture of the chick heart which suggested that cells of the heart held an intrinsic programme to initiate looping morphogenesis, however the exact staging of hearts was unclear (Butler and Keith, 1952; Castro-Quezada et al., 1972; Llorca and Gil, 1967). A definitive study explanted chick hearts at the between HH8-10, (linear tube stage and early looping phase), cultured them for 24hrs *ex vivo*, and examined cardiac morphology. Under *ex vivo* conditions, all but one explant out of 36 underwent looping morphogenesis, confirming multiple previous reports that heart looping in the chick is intrinsic (Butler and Keith, 1952; Castro-Quezada et al., 1972; Llorca and Gil, 1967; Manning and McLachlan, 1990).

Whilst this identified the intrinsic nature of the heart tube to undergo morphogenesis, the directionality of looping was not fully explored. Building upon the early chick *ex vivo* studies, dissected zebrafish hearts at 28hpf cultured *ex vivo* for 24hrs also display a robust asymmetric loop, even in the absence of *Nodal* signals (Noël et al., 2013). Using lineage-labelling to orient the explanted heart tube, 79% of explanted hearts undergo a dextral loop, demonstrating that not only is the nature of heart looping tissue intrinsic, there is also a preferential direction in

which the tube will bend in the absence of external cues (Lombardo et al., 2019; Noël et al., 2013).

Further investigation of the intrinsic nature of dextral heart looping identified a requirement for the activity of the actomyosin cytoskeleton. Drug treatments with either Blebbistatin or Cytochalasin B, abrogated any tube morphogenesis in either explanted hearts or hearts *in vivo*, whilst explants treated with Nocodazole did not show any effect (Noël et al., 2013). This confirmed earlier studies in chick, which had demonstrated that microtubules were not required for the initial looping of the heart in the embryo (Icardo and Ojeda, 1984). Together, these experiments demonstrate that heart looping morphogenesis is a tissue intrinsic process, guided by external cues such as left-right asymmetry in the embryo.

1.2.3 Biomechanical models of heart looping

Heart looping requires the coordination of multiple processes to drive the complex tissue rearrangement and techniques have been developed which are being applied to begin to define these processes at a tissue level. Recently a highly detailed characterisation using high-resolution episcopic microscopy (HREM) subdivided the E8.5 stage mouse further into E8.5c to E8.5j, defining landmark changes to the tissue architecture during this time (Garrec et al., 2017). During heart looping, SHF addition and low levels of proliferation cause the length of the cardiac tube to increase between 8.5e and 8.5j, whist the distance between the poles of the heart remains constant, implicating a buckling mechanism in heart looping, a mechanism first proposed in chick (Garrec et al., 2017; Patten 1922) (Figure 1.1C'). Concomitant with buckling of the heart tube, the attachment between the heart tube and the body wall - the dorsal mesocardium - is broken down, a process also necessary for heart looping morphogenesis. Thirdly, as the heart tube buckles, two temporally separate, opposing rotations at the poles of the heart are observed. At E8.5f, the arterial pole undergoes approximately a 25-degree rotation displacing the arterial

pole to the right of the midline, whist the venous pole displays a leftward displacement at stage E8.5g (7-8 somites) (Figure 1.1C', C''). These movements, together with the buckling mechanism identified (due to growth of the heart tube) and breakdown of the dorsal mesocardium, bend the mouse heart tube (Garrec et al., 2017). Together, the use of high-resolution imaging and *in silico* modelling is beginning to uncover the relative contribution of each of these mechanisms to promote the asymmetric morphogenesis of the heart tube.

Further applications of these techniques in mice has identified that the interaction between these processes is crucial in generating the correct form of heart loop, in particular between embryonic laterality and tissue-intrinsic processes in heart morphogenesis. Upon loss of asymmetric Nodal signalling, four classes of heart looping phenotype are observed in which looping is randomised with equal incidence (Desgrange et al., 2019). Neither the breakdown of dorsal mesocardium, nor distance between the two poles is affected following loss of *Nodal*, instead the initial rotations at the poles of the heart are randomised and also less pronounced. Computer simulation of the four different possibilities of randomisation in pole rotation and dampened levels of rotation accurately recapitulated the four loss of *Nodal* function mutant classes (Desgrange et al., 2019). Together this demonstrates that Nodal signalling is dispensable for asymmetric morphogenesis of the mouse heart, but acts to generate opposing left-right asymmetric rotation of the poles of the heart, which together with Nodal-independent buckling through cell addition and the breakdown of the dorsal mesocardium generates the loop of mouse heart (Desgrange et al., 2019; Garrec et al., 2017) (Figure 1.1C'-C'').

Further, enhanced computer simulations have recently been used to consider changes in all three axes of the looping heart (dorsal-ventral, anterior-posterior and left-right) (Honda et al., 2019). EdU experiments identified a low level of cell proliferation in the first few hours of heart morphogenesis, generating the ventrally directed bulge of the heart tube (Honda et al., 2019). Application of the arterially

localised rightward displacement of the tube (Desgrange et al., 2019; Garrec et al., 2017) subsequent to the ventral bulge was then sufficient to generate the initial helical loop of the tube (Honda et al., 2019). This *in vivo* data, together with computer modelling strongly correlates with modelling of heart looping in the chick embryo. Using a physical model, the shape of the chick heart at stage HH16 could be accurately achieved through an initial ventral bending, followed by rightward rotation at the cranial pole, left-ward rotation at the venous pole and compression along the cranial-caudal axis (Männer, 2004) (Figure 1.1B').

Similar mechanical movements have been recently characterised in the zebrafish heart, separated in into early S-looping (30-42hpf, Figure 1.1D') and advanced S-looping (42-54hpf, Figure 1.1D'') (Lombardo et al., 2019). Between 30-42hpf, both chambers bend along the outer curvature, morphologically separating the two chambers (Figure 1.1D'), also during this time, another laterality-independent mechanism rotates the tube leftward (Baker et al., 2008). During advanced S-looping the atrium moves cranially, positioning the two chambers side-by-side; simultaneously both chambers expand in a process known as cardiac ballooning (Lombardo et al., 2019) (Figure 1.1D''). Using mosaic expression analysis, a similar role for torsional movement in the heart tube observed in mice has been described in zebrafish: between 48-54hpf a right angular shift occurs in the ventricle (arterial pole), whilst at the venous pole, a mild leftward rotation occurs, both rotations are most prominent at the poles of the heart (Lombardo et al., 2019) (Figure 1.1D''). Importantly, these cellular movements appear well conserved with mouse heart pole rotation (Desgrange et al., 2019; Garrec et al., 2017) and the chick physical model (Männer, 2004) (Figure 1.1B', C' C'', D', D''), however whether the presence of a similar structure to the dorsal mesocardium in mice is also remodelled during heart looping in zebrafish has not yet been shown.

In summary, this demonstrates a highly similar, intrinsic suite of cellular of behaviours that shape the linear heart into the loop that is built upon by ballooning.

Crucially, the recent work quantifying and modelling heart looping in mice upon loss of *Nodal* demonstrates that whilst these mechanisms are able to generate an intrinsic loop of the heart tube, additional extrinsic factors such as rotational asymmetries, cell addition and breakdown of surrounding tissues are necessary to refine the shape of the intrinsic loop further. These advances have only been possible until recently due limited quantification techniques, but with the advent of higher resolution imaging and 3D-rendering, the morphology of the heart and therefore the mechanisms which generate this morphology can be better understood.

1.2.4 The role of heart contractility and blood flow in cardiac development

Heart function initiates prior to heart morphogenesis and thus contractility, blood flow, and morphogenesis are tightly coupled during cardiac development. At the initial stage of looping morphogenesis, the heart tube is a linear, valve-less, pumping tube. One study suggests that under these conditions, the formation of a looped, valve-less tube is able to generate a greater pressure, proposing that even the early morphological changes of the tube improves its ability to move blood around the embryo during development (Hiermeier and Männer, 2017). Thus, form and function during heart development are highly interconnected.

Regionalised differences in cell shape and size accompany heart morphogenesis, and studies in zebrafish have shown these to be dependent on chamber contractility (Auman et al., 2007). Between 27hpf and 52hpf, cells residing in the outer curvature of the ventricle increase in size and become more elongated whilst at the inner curvature, cells do not change their shape as dramatically, both observations similar to those made in the chick (Auman et al., 2007; Manasek and Monroe, 1972). Mutations in *myh6* (*myosin, heavy chain 6, cardiac muscle, alpha* formerly *amhc*) results in loss of atrial contractility, resulting in smaller, more circular ventricular cells at 52hpf. (Auman et al., 2007). Loss of ventricular contractility (resulting from *myh7*

(*myosin heavy chain 7*, formerly *vmhc*) mutations) has the opposite impact on ventricular cell morphology, cells are large and less circular (Auman et al., 2007). Similar to the myocardium, the endocardium also undergoes regionalised cell shape changes, including increase in cell area and circularity. However, distinct from the myocardial tissue, the endocardium also undergoes proliferation during heart looping, which upon complete loss of heart contractility is abolished (Dietrich et al., 2014). Therefore, heart form influences heart function (Hiermeier and Männer, 2017) and heart function influences heart form (Auman et al., 2007; Dietrich et al., 2014; Hoog et al., 2018)

Distinct from heart contractility is the sensation of blood flow, which is also required for heart morphogenesis (Lombardo et al., 2019) (see 1.4.3 for more detail). One example is the immobilisation of blood cells through acrylamide injection in mice which results in reduced heart volume, reduction in trabeculae formation and a significant reduction in heart looping (Hoog et al., 2018). In the chick, blood flow through the OFT increases between HH13 and HH18. These haemodynamic forces at the OFT regulate the shape and size of the vessel through sensation of blood flow mediated by mechanotransductive transcription factors. Activation of these pathways result in vasodilation, leading to a reduction in the overall forces experienced by the endocardial cells, whilst supplying the increasing demand for oxygenated blood as development continues (Groenendijk et al., 2004; Midgett et al., 2015).

Together these studies highlight the importance of heart contractility and blood flow through the heart during morphogenesis and that they cannot be uncoupled. As such, a suitable model organism which allows for characterisation of form and function during heart looping morphogenesis is needed to investigate these mechanisms.

1.3 Zebrafish as a model for vertebrate development

1.3.1 Advantages of zebrafish usage

Many vertebrate models exist with which to study cardiac development, each with their own advantages. Zebrafish embryos are small, develop rapidly *ex utero* and are transparent, making them an ideal model with which to understand development of internal organs such as the heart. Their transparency also facilitates live imaging of multiple transgenic lines, which can highlight various different tissues in a single embryo.

An additional benefit to zebrafish studying cardiovascular development is that when heart function is compromised, oxygen diffusion is sufficient to sustain life, meaning that the role of blood flow can be investigated more fully than other model organisms. In particular, this allows imaging of blood flow dependent processes during development through temporarily blocking heart function and acquiring detailed, high resolution images to gain insight into the interaction between form and function during heart development (Arrenberg et al., 2010; Samsa et al., 2015; Steed et al., 2016; Vermot et al., 2009). Furthermore, the oviparity of zebrafish means that where mutations result in lethality due to a failure in implantation or placental development, this is not a factor zebrafish.

The extensive number of embryos that can be collected from a single cross and cost efficiency compared to mice has made zebrafish ideal candidates for forward genetics screens to identify mutants with defects in specific developmental processes. Commonly these mutations are functional nulls, allowing determination of the gene function by characterising development in the absence of its activity. This approach has been successful in identifying hundreds of genes with diverse roles in development that have shown to be well conserved with other vertebrates, including humans. Sequencing of the zebrafish genome and comparison with the human genome has identified 47% of human genes have a direct, one-to-one match

with a zebrafish gene. More broadly, 71.4% of human genes have at least one zebrafish gene, whilst 82% of disease-causing genes in humans has at least one zebrafish orthologue (Howe et al., 2013). The 'one-human-to-many-zebrafish' class of genes, where there are 2.28 zebrafish genes for every human gene (Howe et al., 2013) is thought to have arisen due the additional round of whole genome duplication referred to as the teleost-specific genome duplication.

1.3.2 Reverse genetic approaches in zebrafish

Whilst forward genetic screens offers an unbiased method to identify genes with important roles in biological processes, these studies require large numbers of animals, are time consuming and expensive. The sequencing of the zebrafish genome has subsequently allowed reverse genetic methodologies, an increasingly-favoured candidate-led approach to investigate the role of specific genes in development, being quicker, cheaper and using fewer animals than forward genetics. Broadly two reverse genetic approaches are commonly used in zebrafish: knockdown, reducing levels of functional protein without mutating the DNA; and knockout, abrogating gene function through mutation of the DNA (Figure 1.2).

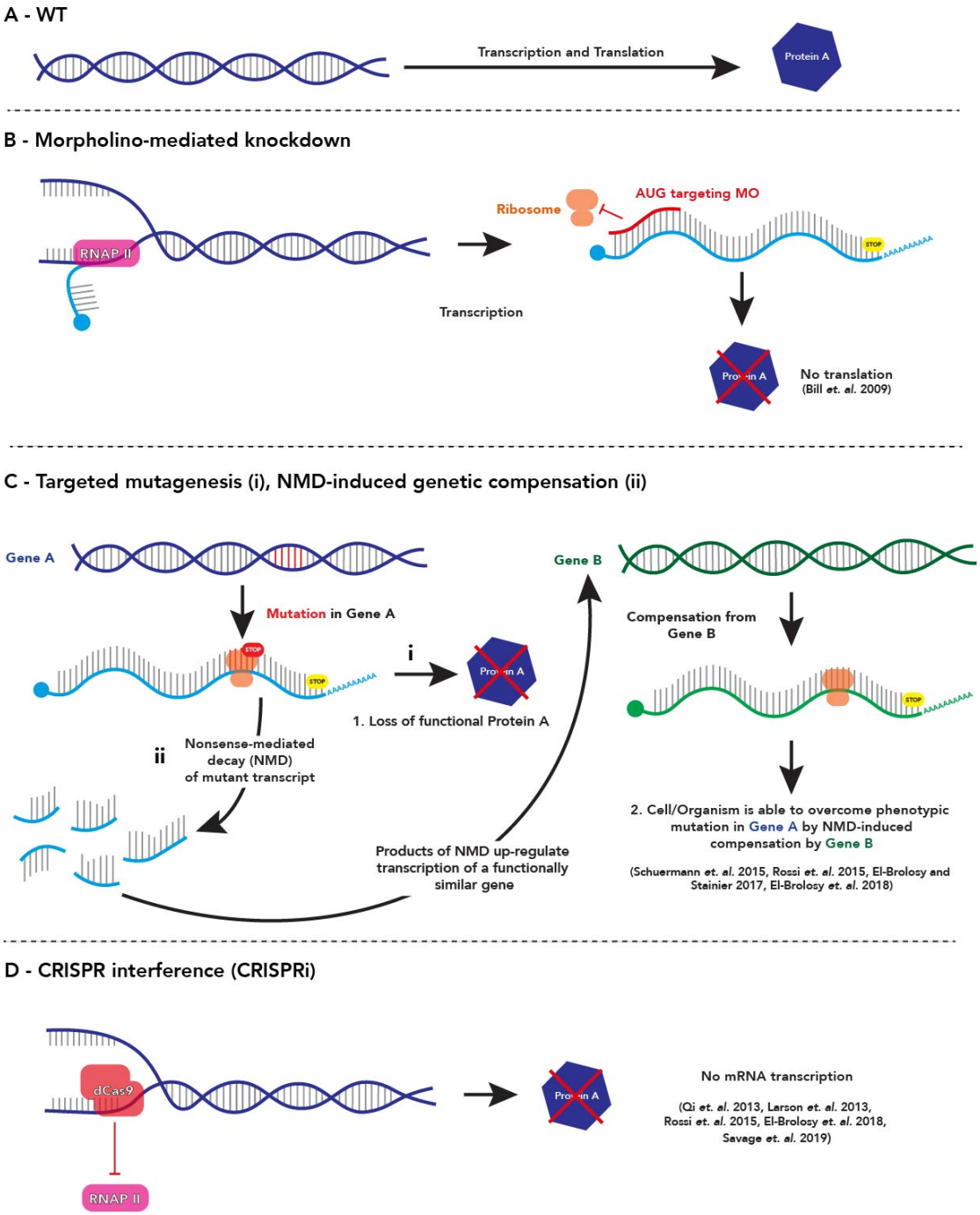

Figure 1.2. Mechanisms of targeted gene knockdown and knockout in zebrafish.

Comparison of different basic mechanisms currently available in zebrafish to target gene function. **(A)** Under WT conditions, transcription and translation of a protein coding gene generates functional protein. **(B)** Translation blocking morpholinos (red) bind the AUG initiation codon of the sense mRNA (cyan), preventing binding of the ribosome (orange), leading to absence of translation. **(C)** Targeted mutagenesis of Gene A (purple) results in a genetic lesion in the DNA (red) which is then present as

For a long time, the preferred reverse genetic approach to assess the role of a specific gene in zebrafish development was knockdown by the use of antisense morpholino oligonucleotides (MOs Figure 1.2B) (Nasevicius and Ekker, 2000). Morpholino usage in zebrafish is wide-spread, entailing injection of short DNA sequences complementary to the target gene at the 1-cell stage which are capable of either inhibiting initiation of protein translation (Figure 1.2B) or blocking correct splicing of the transcript (Bill et al., 2009). Prior to the development of targeted mutagenesis techniques, morpholino usage was commonplace in functional studies to ascribe specific functions to genes across a broad range of biological processes. Alongside mapping, MOs remain widely used as a secondary method to confirm a mutation identified in a forward genetic screen. Morpholinos are subject to decay following injection, and this limits use of morpholino knockdown to interrogation of the very early stages of development, anecdotally until approximately 3dpf. Therefore, examining larval or adult phenotypes is not possible using morpholinos.

However, use of MOs in reverse genetic approaches have proved troublesome. Injection of MOs has been reported to result in up-regulation of *tp53* (*tumor protein p53*) and induce cell death (Robu et al., 2007). Furthermore MOs may have off-target effects, interfering with the function of a separate gene (Eisen and Smith, 2008; Lai et al., 2019). Additionally, there is no standard working concentration for

Figure 1.2 continued

a premature stop codon (red), upstream of the WT stop codon (yellow) in the transcribed mRNA (cyan). Classically (i) the mutation is expected to result in loss of functional protein through loss of domains or degradation of the mRNA. More recent studies have identified that the mutation can activate nonsense-mediated decay (NMD) of the transcript (ii) and products of decay can up-regulate expression compensating Gene B (green) which prevents deleterious phenotype from emerging. **(D)** CRISPR interference uses gRNAs to target catalytically dead Cas9 (dCas9) to the promoter of the gene, sterically blocking the binding of RNA Polymerase II (pink) leading to no mRNA translation and therefore loss of protein.

MO use, or complete consensus in the design of negative control experiments, which include injection of a scrambled MO, control MO or *tp53* alone (Robu et al., 2007). Together this can make correctly interpreting morphant (embryo injected with a morpholino) phenotypes challenging.

More recently, genome-editing techniques such as Zinc Finger Nucleases, TALEN, and CRISPR facilitate the specific targeted mutagenesis of genes to generate knockouts, which revolutionised the ability to interrogate gene function (Gaj et al., 2013; Pickar-Oliver and Gersbach, 2019). The common CRISPR-Cas9 system uses sequence specific CRISPR RNA (crRNA) which anneals to the common trans-activating crRNAs (tracrRNAs) to recruit the Cas9 nuclease. The two RNA components are commonly referred to as a single guide RNA (gRNA). Target recognition by the Cas9 protein requires a protospacer adjacent motif (PAM) upstream of the crRNA-binding region in order to cleave the DNA (Gaj et al., 2013). Subsequently, in the stable lines generated, transcription of targeted genes results in mRNA with a nonsense mutation, leading to a frameshift and a premature termination codon (PTC) (Figure 1.2C).

During the pioneer round of translation, if the PTC is more than 50-55bp upstream of an exon-exon boundary marked by an exon junction complex (EJC) Upf1 and a Smg1-Smg8-Smg9 complex associate with the termination complex. Smg1 activates Upf1 through phosphorylation, resulting in repression of mRNA translation and recruitment of mRNA decay factors through an interaction between phosphorylated Upf1 and Smg7. This results in the exonucleolytic decay of the mRNA, referred to as nonsense-mediated decay (NMD) an evolutionarily conserved pathway in vertebrates and other classes (Maquat, 2005; Popp and Maquat, 2016; Wittkopp et al., 2009). Destruction of the transcript or generation of a truncated protein (which dependent on location of PTC is likely to be non-functional) leads to loss of gene function. The phenotype that results from this loss-of-function can then be studied to understand the role of the gene during development (Figure 1.2Ci).

1.3.3 Genetic robustness in zebrafish

Whilst genome-editing technologies have been rapidly adopted and have revolutionised our ability to analyse gene function in specific developmental processes, studies are reporting that the subsequent link between mutant phenotype and gene function is more complex than initially supposed. Multiple studies have reported that novel mutations generated in genes resulted in no phenotype, despite clear developmental phenotypes when the same gene was subjected to morpholino-mediated knockdown or RNA silencing (Braun et al., 2008; El-Brolosy and Stainier, 2017; Gao et al., 2015; Lin et al., 2017, 2007; Rossi et al., 2015; Savage et al., 2019; Williams et al., 2015) A large-scale study in zebrafish set out to define the roles of genes with well characterised phenotypes achieved through MO knockdown, but only three of the 24 mutant lines recapitulated the morpholino phenotype (Kok et al., 2015). This resulted in a backlash against MO usage in zebrafish (Eisen and Smith, 2008; Kok et al., 2015; Stainier et al., 2017), and also raised concerns over the requirement of many genes, which upon mutagenesis had no effect on development of the embryo. Following this, guidelines for MO usage were laid out by the zebrafish community and mainly focussed upon MO usage only following validation that the morphant and mutant phenotypes were comparable (Stainier et al., 2017).

However, one study examined more closely the disparity between the *mt2* (*metallothionein 2*) mutant and morphant phenotype (which exhibited defects in angiogenesis). Zygotic *mt2* mutants did not show any development phenotypes, but the maternal zygotic mutants of *mt2* did show a similar phenotype to the morphants (Schuermann et al., 2015). Examination of *mt2* transcript levels in two different *mt2* mutant alleles identified varying levels of *mt2* expression which correlated with phenotypic severity: the more *mt2* transcript present, the more severe the phenotype. Partial removal of two conserved NMD pathway components, *smg1* and *upf1*, in the stronger *mt2* mutant allele resulted in increase in penetrance of the *mt2*

morphant phenotype, suggesting that degradation of mutant mRNA transcript could result in differences in phenotypic severity through activation of a compensatory mechanism (Schuermann et al., 2015).

This compensatory pathway was investigated further in zebrafish *egfl7* (*EGF-like-domain, multiple 7*) mutants. Knockdown of *EGFL7* in human cells lines, zebrafish and frog results in a severe vascular defect (Charpentier et al., 2013; Huang et al., 2014; Parker et al., 2004), however a mouse *Egfl7* knockout has no reported phenotype (Kuhnert et al., 2008; Schmidt et al., 2007) and a zebrafish *egfl7* null mutant does not have a developmental phenotype and survives to adulthood (Rossi et al., 2015). RNA-profiling and mass spectrometry of mutant, morphant and wild-type *egfl7* zebrafish embryos revealed significant up-regulation of *emilin2a*, *emilin3a* and *emilin3b* in *egfl7* mutants, which were shown to be able to compensate for loss of *egfl7* (Rossi et al., 2015). Interestingly, there was no up-regulation of compensating *emilins* in a 3bp deletion *egfl7* mutant, which maintains the reading frame and shows no reduction of transcript (Rossi et al., 2015). Together this suggested that mutations that result in a reduction of mutant transcript levels could up-regulate compensatory genes, whilst embryos subject to knockdown of the same gene by MO were unable activate compensation (Figure 1.2C). This could explain the basis for absence of phenotypes associated with genetic knockout where the associated knockdown exhibits severe phenotypes.

Supporting this, a recent study has begun to identify the mechanisms by which increased degradation of mutant transcripts is able to up-regulate compensatory genes. Where mutant mRNA is directed for NMD, up-regulation of compensating genes can be abolished through the inhibition of NMD either by pharmacological inhibition of NMD, or through mutation of *upf1*, a critical factor for activation of NMD (El-Brolosy et al., 2019; Wittkopp et al., 2009). This led to the suggestion that mutagenesis approaches should be designed to overcome the NMD-induced genetic compensation, for example by targeting the gene promoter for deletion or

deleting the entire gene rather than introducing PTCs in the coding sequence (El-Brolosy et al., 2019). Using this methodology, deletion of the entire *egfl7* locus recapitulated the original *egfl7* morphant phenotype, in striking contrast to the previously published *egfl7* mutants (El-Brolosy et al., 2019; Rossi et al., 2015). Crucially, genetic compensation does not appear to be a zebrafish-specific consideration: genetic compensation has been reported in *C. elegans*, mouse and human cell and tissue lines (Dawlaty et al., 2011; Freudenberg et al., 2011; Jackson and Pereira-Smith, 2006; Mulligan et al., 1998; Raj et al., 2010) and a similar approach to targeted promoter deletion in cell lines appears sufficient to overcome this phenomenon.

Whilst analysis of mutant lines is suitable for assessing the impact of loss of function of a gene throughout the embryo, there remains a requirement for spatiotemporal knockdown, not widely available in zebrafish. One promising possibility is CRISPR interference (CRISPRi) where the CRISPR-Cas9 technique has been modified for knockdown, rather than knockout. CRISPRi employs a catalytically dead Cas9 (dCas9, which cannot cleave DNA) which is recruited by gRNAs to act as a "roadblock" preventing either initiation or elongation of transcription of a target gene (Larson et al., 2013; Qi et al., 2013) (Figure 1.2D). Using an mRFP reporter in *E. coli*, Qi et al. (2013) demonstrated that CRISPRi can carry out highly effective and specific gene silencing by preventing transcription. CRISPRi was applied to investigate the role of *egfl7* in zebrafish by knocking down transcription using two gRNAs targeting the non-template strand (Rossi et al., 2015). CRISPants (embryos subject to knockdown by CRISPRi) of *egfl7* recapitulate the MO phenotype and similarly to *egfl7* morphants, did not show an up-regulation of *emilin* genes observed in the nonsense deletion *egfl7* mutant (Rossi et al., 2015). A similar result has been described for *tmem33* (*transmembrane protein 33*), a gene for which the mutant has no phenotype, but morphants and CRISPants show a severe delay in angiogenesis (Savage et al., 2019) Together these results demonstrate that CRISPRi-mediated knockdowns appear able to perturb gene function sufficiently to

interrogate the role of a gene in development without activating genetic compensation mechanisms (Rossi et al., 2015; Savage et al., 2019).

Altogether, this demonstrates the variety of tools available for genetic manipulation of the zebrafish and thus its suitability with which to investigate the mechanisms which drive cardiac development. The next section will outline in greater detail the development of the zebrafish heart, with particular focus on the stages involved in heart looping morphogenesis.

1.4 Development of the Zebrafish Heart

The zebrafish heart develops rapidly in the first few days of embryonic development, with the LHT visible at 24hpf (Figure 1.3B) undergoing looping morphogenesis by 30hpf (Figure 1.3C). By 2dpf (Figure 1.3D) the heart has completed initial morphogenesis and begins to mature, morphologically appearing to compact in size (Figure 1.3E).

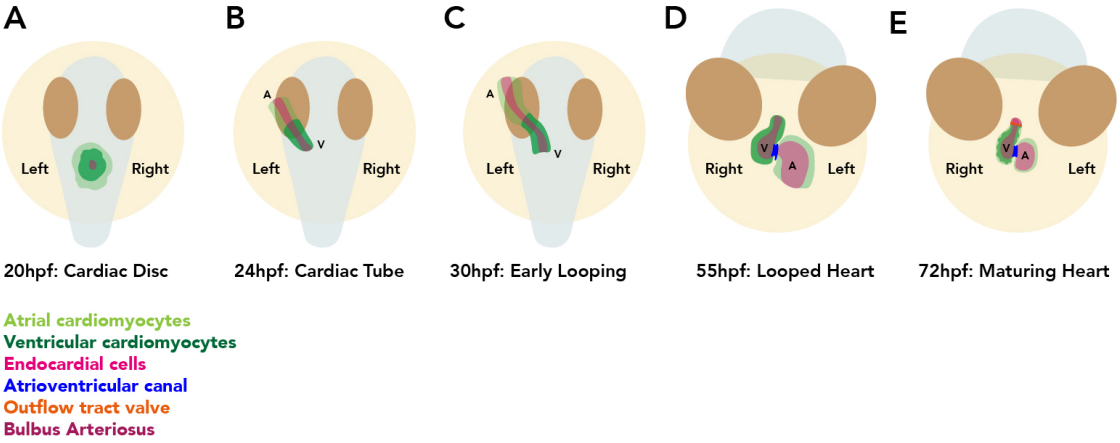

Figure 1.3. Stages of heart development in zebrafish.

Schematic of key stages of zebrafish heart development. **(A)** The precursor structure to the linear heart tube at 20hpf is the cardiac disc. At the centre are endocardial cells (magenta), surrounded by ventricular cardiomyocytes (dark green) and further surrounded by atrial cardiomyocytes (light green). **(B)** The heart tube forms by jogging, in which the heart becomes asymmetrically positioned under the left eye, with the atrium positioned more anteriorly than the ventricle and the endocardium encompassed by the myocardium. **(C)** By 30hpf the heart has begun looping morphogenesis, with the heart descending over the yolk and chambers taking on more distinct shapes at their outer curvatures. **(D)** At 55hpf, the heart has undergone the main morphogenetic movements of looping and is positioned over the yolk with a constriction visible between the single atrium and ventricle where the atrioventricular canal (blue) is forming. **(E)** At 3dpf, the morphology of the heart changes, with the chambers becoming more compacted and closer to one another. The development of the outflow tract valve (orange) has commenced. A-C: dorsal views, D-E: ventral views. A: atrium, V: ventricle.

1.4.1 Specification of cardiac progenitors, formation of the cardiac disc (0-22hpf)

Classic lineage tracing identified that atrial and ventricular myocardial cells are segregated as early as 5hpf (Stainier et al., 1993). Following gastrulation, these cardiomyocytes are located bilaterally in the anterior lateral plate mesoderm (ALPM), with atrial precursors residing more laterally than the ventricular precursors (Bakkers, 2011; Brown et al., 2016). Live cell tracking shows that the endocardium is also derived from the ALPM developing from a pool of cells residing anterior to the cardiomyocytes that also gives rise to the head vasculature, aortic arches and primitive myeloid progenitors (Bussmann et al., 2007).

Between 16hpf and 19hpf, the bilateral, linearly arranged cardiomyocytes migrate toward the midline of the embryo, with cells at the extreme poles of each population migrating towards their more centrally located neighbours, and fuse at the midline to form the cardiac disc (Holtzman et al., 2007) (Figure 1.3A). However, at 16hpf, endothelial cells reside more anterior than myocardial cells and the two bilateral endocardial populations have already met at the midline of the embryo, highlighting that endocardial migration begins slightly before myocardial migration (Bussmann et al., 2007). Interestingly, proper cardiomyocyte migration requires the presence of the endothelium, as in *cloche* mutants, which lack endothelial cells, despite cardiomyocyte convergence towards the midline, no angular cell movements take place to form the cardiac disc (Holtzman et al., 2007).

Furthermore, a reciprocal interaction is necessary for correct specification of the endocardium as the heart disc forms. In *hand2* (*heart and neural crest derivatives expressed 2*) mutants, where myocardial progenitors are absent (Yelon et al., 1999) at 22hpf, no *nfat1c* (*nuclear factor of activated T cells 1*, a marker for the endocardium) (Pompa et al., 1998) positive endocardial cells are present in the disc (Palencia-Desai et al., 2015). Studies at these early timepoints demonstrate that

even before tube formation, the interaction between the two cell layers of the future heart tube is critical for heart development.

1.4.2 Heart jogging: the disc-to-tube transition (22-24hpf)

At 20hpf the zebrafish cardiac disc is positioned in the middle of the ALPM (Figure 1.3A, 1.4A), where endocardial cells are surrounded first by a ring of ventricular cardiomyocytes, and at the periphery a ring of atrial cardiomyocytes (Bakkers, 2011; Brown et al., 2016). Concomitant with heart disc formation, the zebrafish embryo exhibits genetic left-right asymmetries, as a result of Kupffer's vesicle (KV) activity and subsequent asymmetric Nodal signalling. Downstream targets of Nodal signaling in the heart disc include *bmp4* (*bone morphogenetic protein 4*), *has2* (*hyaluronan synthase 2*) and *lft2* (*lefty2*), whose expression is either elevated on, or restricted to, the left side of the disc (Chen et al., 1997; Chocron et al., 2007; Lenhart et al., 2013; Smith et al., 2008). *has2* displays a more distinct left-side restriction which is dependent on *southpaw,* as *southpaw* morphants have bilateral *has2* expression (Smith et al., 2008; Veerkamp et al., 2013).

Asymmetric expression of *has2* on the left side of the cardiac disc results in a reduction of BMP (Bone Morphogenetic Protein) activity on the left side of the heart disc (Veerkamp et al., 2013). Expression of a non-muscle myosin is positively regulated by BMP and restricted by *spaw* (Veerkamp et al., 2013) resulting in an up-regulation of phospho-myosin light chain 2 (pMLC2) on the right side of the disc, where BMP is more active (Veerkamp et al., 2013). These genetic asymmetries in the heart disc correlate with regional differences in migration patterns of cells within the four quadrants of the cardiac disc as the heart tube forms between 22-24hpf (Campos-Baptista et al., 2008; Lenhart et al., 2013; Smith et al., 2008; Veerkamp et al., 2013). The major contribution to the changes in migration speed comes from a significantly slower migration rate of anterior cardiac cells of the disc, but more

broadly, cells of the right cardiac disc migrate slower (Campos-Baptista et al., 2008; Lenhart et al., 2013; Smith et al., 2008; Veerkamp et al., 2013).

At the same time as regionalised cell migration, the heart disc also undergoes a rotation and involution event resulting in a complex rearrangement of cardiac tissue as the heart transitions from disc to tube (a process known as heart jogging) (Rohr et al., 2008; Smith et al., 2008) (Figure 1.4A). This rotation and migration of cells results in redistribution of cardiac cells, positioning the initially left-sided, Nodal-responsive *lft2*-positive cells from the cardiac disc on the dorsal face of the linear heart tube (Baker et al., 2008; Smith et al., 2008) (Figure 1.4B), whilst those initially in the posterior of the disc reside on the left side of the heart (Guerra et al., 2018). Heart jogging positions the linear heart tube under the left eye of the embryo (Figure 1.3B, 1,4B), where the arterial pole remains at the midline and the venous pole is displaced left (Chen et al., 1997). Mutants in the Nodal pathway, for example *southpaw*, or the Nodal-responsive transcription factor *foxH1* (*forkhead box H1*), present with a heart tube positioned down the midline of the embryo (Lenhart et al., 2013; Noël et al., 2013). In these mutants, loss of *southpaw* activity results in a failure of *has2* restriction to the left side of the disc, and a uniform dampening of BMP activity. This results in a loss of asymmetric migration directionality during heart disc rotation and generally slower migration speeds (Campos-Baptista et al., 2008; Lenhart et al., 2013; Veerkamp et al., 2013), leading to a failure of disc rotation and extension of the heart tube down the midline of the embryo, demonstrating the tight link between embryonic asymmetry and heart lateralisation.

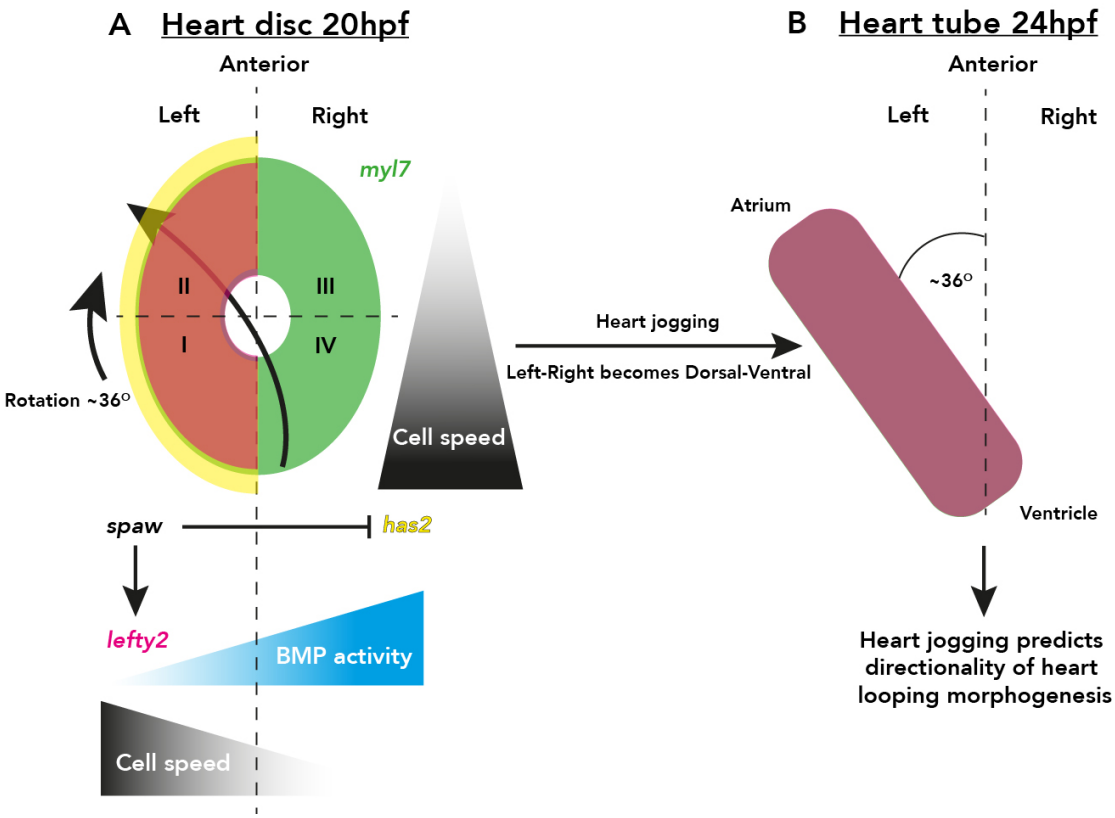

Figure 1.4. Heart jogging re-organises left-right disc asymmetry to dorsal-ventral tube asymmetry.

Current model of heart jogging, which generates the linear heart tube from the cardiac disc. **(A)** The heart disc (*myl7*, green) displays left-right asymmetry, dependent on the expression of the Nodal signaling pathway (*spaw*). L-R asymmetry cues are required to promote expression of *lefty2* (magenta) and restrict the *hyaluronan synthase 2* (*has2*, yellow) to the left side. The asymmetric expression of *has2* results in dampening of responsiveness to BMP ligands, resulting in increased BMP activity on the right of the disc (blue triangle), which promotes cell adhesion over motility through non-muscle myosins. The asymmetries in the heart disc result in increased migration speed on the left of the disc and in the posterior of this disc (black triangles). This results in an asymmetric, left-directed migration and right-ward rotation of the heart disc (jogging). **(B)** Heart jogging positions the linear heart tube asymmetrically under the left eye, with ventricle/arterial pole remaining at the midline (dotted line) and the

1.4.3 Heart looping and initiation of valvulogenesis (24-56hpf)

Following heart tube formation, repositioning of the chambers begins as the heart tube loops (Figure 1.3C). The directionality of cardiac looping is accurately predicted by the direction of heart jogging. In all cases where the heart jogs to the left, hearts loop to the right, and under conditions where the heart jogs to the right, the heart loops to the left (Chen et al., 1997; Grimes et al., 2019) (Figure 1.4B). The re-organisation of left-right asymmetry in the heart disc to dorsal-ventral asymmetry in the heart tube (Baker et al., 2008; Smith et al., 2008), supports the model of a Nodal-independent mechanism regulating heart looping morphogenesis due to spatial disconnection of laterality of the tube and whole embryo (Lombardo et al., 2019; Noël et al., 2013). There is however an interaction between Nodal and the actomyosin cytoskeleton which is required to promote asymmetric morphogenesis. Sub-phenotypic treatment with Cytochalasin B of *southpaw* mutants is able to significantly reduce the proportion of right-ward looped hearts and increase the incidence of non-looped hearts (Noël et al., 2013).

Conserved with mice and chick, during zebrafish heart looping, myocardial cell number increases predominantly through addition of new cardiomyocytes into the heart tube from the second heart field (Pater et al., 2009), a pool of cardiac precursors in the adjacent mesoderm. Between 24hpf-48hpf cells are first added to

Continued from Figure 1.4.

atrium/venous pole displaced to the left. The asymmetric movements of the heart disc lead to a reorganisation of the left-right patterning of the disc to the dorsal-ventral polarity of the heart tube, leading to *lefty2* positive cells being positioned on the dorsal surface of the heart (magenta). Dorsal views. Model based on: Baker et al., 2008; Campos-Baptista et al., 2008; Lenhart et al., 2013; Rohr et al., 2008; Smith et al., 2008; Veerkamp et al., 2013.

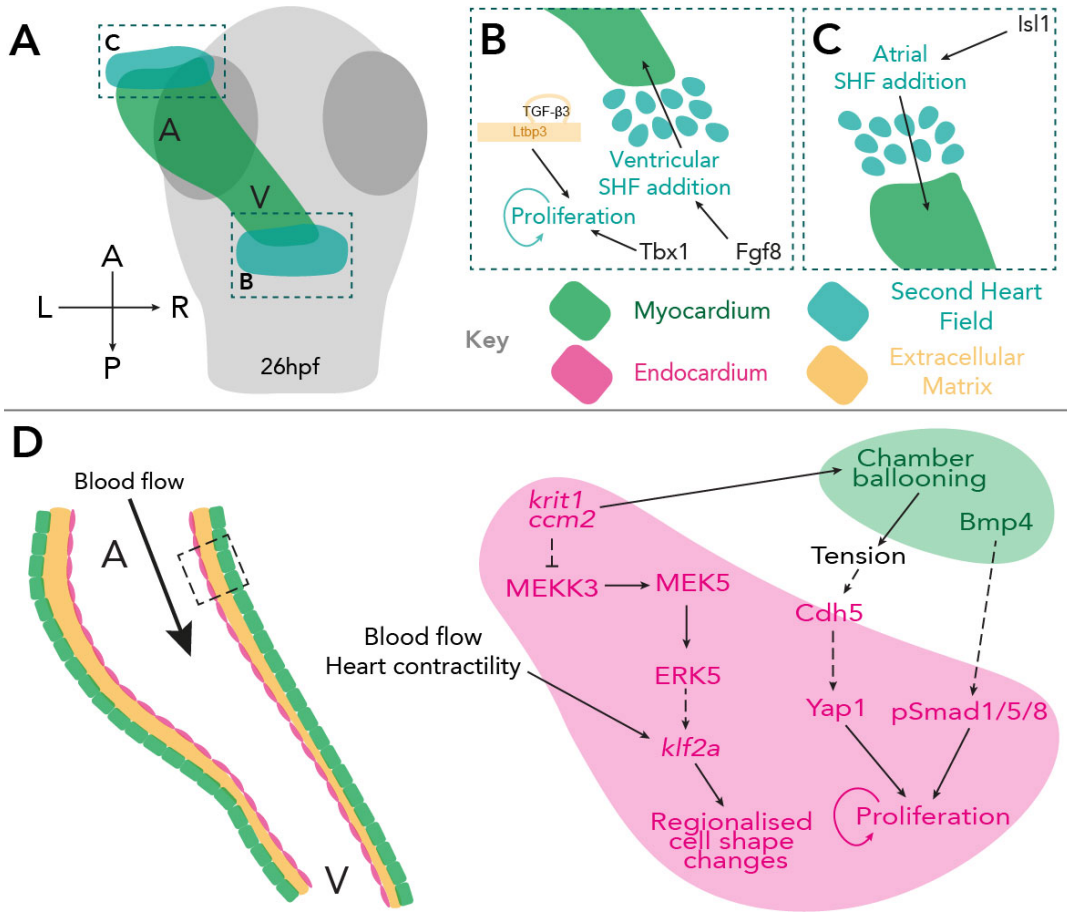

Figure 1.5. Second heart field addition and myocardial-endocardial cross-talk are required for looping morphogenesis.

(A) Dorsal view of 26hpf zebrafish embryo. The linear heart tube (green) is positioned under the left eye with pools of cardiac progenitors (SHF, turquoise) present at both poles. **(B)** At the arterial pole, TGF-β3 localised to extracellular matrix by Ltbp3 is required for SHF proliferation. Fgf8 signalling and the transcription factor Tbx1 are required for addition of the SHF to the ventricle. **(C)** At the venous pole Isl1 is required for SHF addition. **(D)** Cross-talk between the myocardium (green) and endocardium (magenta), together with blood flow regulate changes to endocardial cell shape and proliferation. Functional endocardial CCM signalling limits *klf2a* expression and promotes myocardial chamber ballooning. Based on: Bornhorst et al., 2019; Dietrich et al., 2014; Hami et al., 2011; Nevis et al, 2013; Pater et al., 2009; Zhou et al., 2011; Zhou et al., 2015. A: atrium, V: ventricle.

the arterial pole of the heart, in a mechanism dependent upon Fibroblast growth factor 8 (Fgf8) signalling, whilst the later addition at the venous pole is dependent upon the function of the transcription factor Islet1 (Isl1) (Hami et al., 2011; Pater et al., 2009) (Figure 1.5A-C). Similar to mice, loss of FGF signalling or mutations in the key transcriptional regulator of SHF addition *tbx1* leads to loss of arterial structures and defects in heart looping morphogenesis (Felker et al., 2018; Hami et al., 2011; Lazic and Scott, 2011; Nevis et al., 2013; Reifers et al., 2000). TGF-β signalling is also required at the arterial pole for correct SHF addition to maintain SHF proliferation (Zhou et al., 2011). This is achieved by Ltbp3 (Latent transforming growth factor beta binding protein 3) which anchors TGF-β3 in the ECM (Figure 1.5B). In summary, timely and controlled cell addition together with maintenance of this progenitor pool during cardiac development is critical to generate the correct shape of the heart.

During cardiac morphogenesis the chambers of the heart contribute to looping by elaboration of their outer curvatures, characterised by the expression of *natriuretic peptide A* (*nppa*, *ANF* in mice) (Habets et al., 2002) where it is excluded from the inner curvature and non-working myocardium at the atrioventricular canal (Auman et al., 2007). *nppa* is closely linked to *natriuretic peptide B* (*nppb*), a gene which displays a much tighter restriction to the outer curvatures of the heart (Grassini et al., 2018) (Figure 1.6A-C). Loss of both *nppa* and *nppb* result in a spectrum of cardiac phenotypes, broadly impacting on heart morphology and the formation of the atrioventricular valve. Interestingly, cardiac contractility is important the regulation of *nppa* expression during heart development as loss of *myh7* results in failure of restriction of *nppa*, whilst loss of *myh6* results in a reduction of *nppa* expression in the ventricle (Auman et al., 2007). Together this identifies a link between heart contractility, heart looping and chamber ballooning during cardiac morphogenesis.

Whilst chamber ballooning is predominantly observed to be myocardial, co-ordination of growth and cell shape change between the myocardium and

endocardium is required to maintain cardiac shape and function. Under experimental conditions which result in overgrowth of the atrium through increased Wnt signalling, endocardial tissue tension increases, transmitted through Cadherin5 (Cdh5) (Bornhorst et al., 2019) (Figure 1.5D). This increased tension in the endocardium correlates with increased Yap (Yes1 associated transcriptional regulator) activity, resulting in increased atrial endocardial proliferation to co-ordinate chamber morphogenesis of both tissues (Bornhorst et al., 2019). Another identified cross-talk between the myocardium and endocardium regulates the ballooning of the endocardium through regionalised changes in cell shape and size, thought to be dependent on myocardial-derived BMP signals and the sensation of blood flow (Dietrich et al., 2014) (Figure 1.5E).

Another conserved signalling pathway required for heart looping and correct chamber ballooning is the cerebral cavernous malformation (CCM) pathway. Mutations in components of the CCM pathway results in enlarged chambers of the heart due to uncontrolled chamber ballooning associated with a profound looping phenotype, but not through a mechanism of increased cell number (Mably et al., 2006, 2003). CCM pathway components are expressed in endothelial and endocardial cells (Mably et al., 2006, 2003), where they regulate multiple different signalling pathways including the MEKK3-ERK5 axis (Otten et al., 2018; Zhou et al., 2015), however the most obvious effect on the heart following loss of CCM activity is in the myocardium (Mably et al., 2006, 2003) (Figure 1.5E). Thus, heart looping and chamber ballooning require intricate cross-talk between the two tissues layers during heart development and these two processes are tightly coupled during morphogenesis and orchestrated by both biochemical and biomechanical signals.

Concomitant with heart looping morphogenesis is the onset of valvulogenesis at the AVC, and these processes are tightly linked. The cellular mechanisms of valve formation are well conserved between zebrafish, mice and chick and require the co-

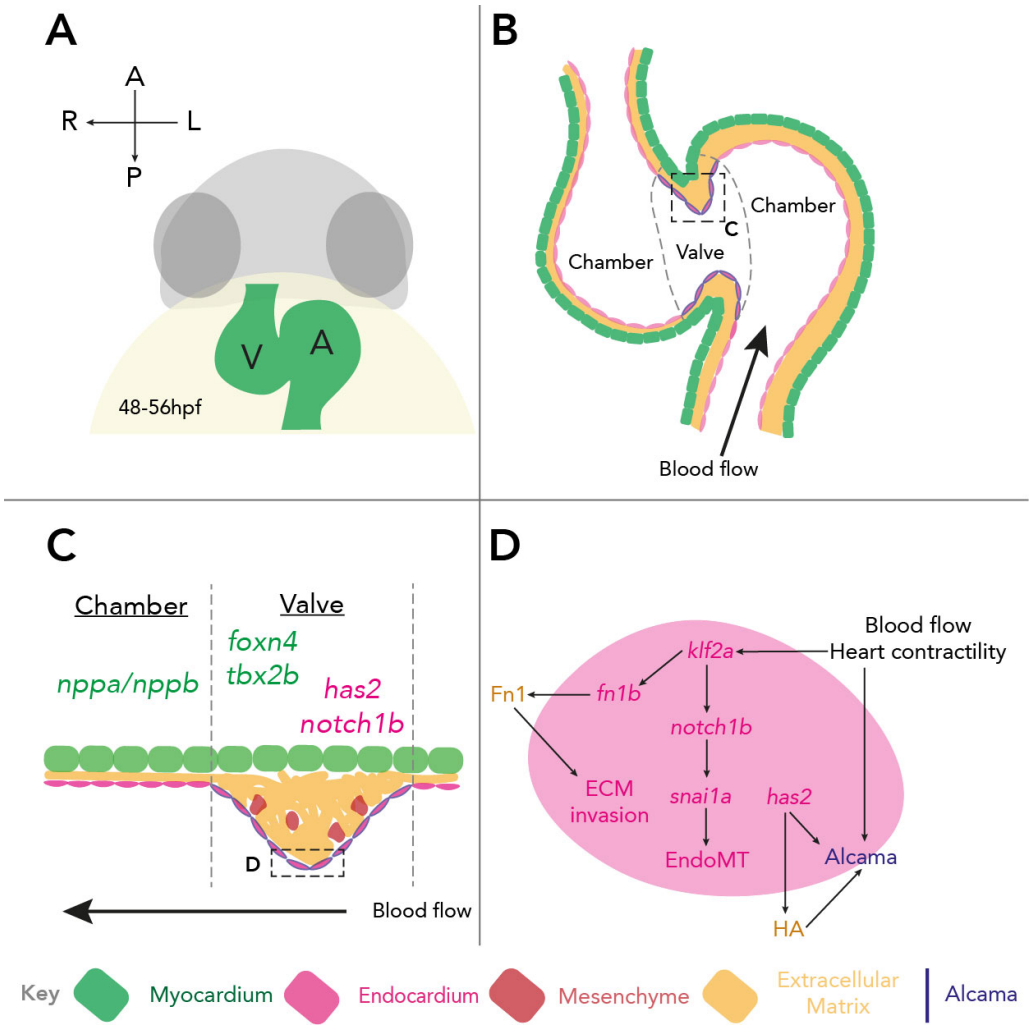

Figure 1.6. Early valvulogenesis in zebrafish.

(A-B) Ventral view of zebrafish embryo between 48-56hpf, the heart has undergone initial stages of morphogenesis and the chambers are morphologically distinct separated by the developing atrioventricular valve where localised ECM deposition drives formation of the endocardial cushions. (C) Morphological differences are correlate with transcriptional differences between the chambers and the AVC. Chamber myocardium (green) is marked by expression of *nppa/nppb* whist valve myocardium expresses *foxn4* and *tbx2b*. Valve endocardium (magenta) expresses key, conserved markers of valvulogenesis *has2* and *notch1b*. (D) Endocardial cells of the AVC respond to reversing flow through up-regulation of *klf2a* which maintains expression of *notch1b* to regulate EndoMT and drives expression of fn1b which is required for ECM invasion. Has2 expression is required for locaslied HA deposition which leads to expression of the cell adhesion molecule Alcama. Based on: Auman

ordination of myocardial and endocardial interactions. At 36hpf, endocardial cells at the interface between the ventricle and atrium change their morphology from squamous to cuboidal and up-regulate Alcama (activated leukocyte cell adhesion molecule a) (Beis et al., 2005). These cellular rearrangements are dependent on the transcription factor Foxn4 (Forkhead box N4) and its interactions with Tbx5: mutations in *foxn4* result in loss of *notch1b* (*notch receptor 1b*) restriction and absence of the transcription factor *tbx2b* (*t-box transcription factor 2b*), which regulates valve development (Chi et al., 2008).

This correlates with the tightly regulated expression of *has2* expression at the atrioventricular canal which is required for the presence of Alcama-positive cells in the endocardium (Lagendijk et al., 2011) (Figure 1.6C, D)and localised increase in cardiac jelly at this region, termed the atrioventricular cushions (Peal et al., 2011). At 48hpf, protrusions from endocardial cells are observed interacting with the cardiac jelly, and endocardial cells invade the cardiac jelly at the AVC by 56hpf (Steed et al., 2016).

This migration of endocardial cells into the cardiac jelly represent a highly specialised form of Epithelial to Mesenchymal transition (EMT) known as EndoMT (Endothelial-to-Mesenchymal transition) (Gunawan et al., 2019; Pestel et al., 2016). EndoMT is promoted by Notch signalling - over-activation of Notch signalling leads to abnormally large atrioventricular valves and an up-regulation of the pro-EMT factor *snai1a* (*snail family zinc finger 1a*), whilst inhibition of Notch activity results in under-developed valves (Timmerman et al., 2004) (Figure 1.6D).

Figure 1.6 continued.

et al., 2007; Grassini et al, 2018; Heckel et al., 2015 Lagendijk et al., 2011; Pestel et al., 2016; Steed et al, 2016; Vermot et al., 2009

These morphological and transcriptional changes associated with valve development are almost exclusively dependent on heart contractility. This is most clearly demonstrated by a mutant in *cardiac troponin, type T2a* (*tnnt2a*, formerly *silent heart*, *sih*) isolated from a forward genetic screen, where mutants exhibit a loss of heart contractility, expression of *notch1b* and Notch reporter activity in the endocardium is abolished (Samsa et al., 2015). In *tnnt2a* mutants, endocardial cells at the presumptive AVC retain their squamous morphology, do not converge towards the valve (Boselli et al., 2017; Steed et al., 2016) and do not initiate Alcama expression (Beis et al., 2005). Heart contractility is also critical for the correct development of the valve through regulation of *has2* expression (Lagendijk et. al. 2011).

While loss of contractility in models such as *tnnt2a* mutants/morphants implies a requirement for cardiac function in distinct aspects of heart development, dissecting the mechanical roles of contractility compared to blood flow and its sensation in these specific processes can be challenging upon straight-forward loss of contractility. Further complicating analysis of contractility mutants, *tnnt2a* loss-of-function models also display pericardial oedema as early as 30hpf, and this increase in fluid surrounding the heart is also likely to impact upon morphogenesis independent of any requirement for blood flow in shaping the cells of the heart (Auman et al., 2007; Sehnert et al., 2002).

Heart contractility and blood flow orchestrate atrioventricular valve development through multiple mechanisms, one of which is through sensation of blood flow shear stress in endocardial cells through the oscillatory flow-responsive transcription factor *kruppel-like factor 2a* (*klf2a*) (Heckel et al., 2015; Vermot et al., 2009). Reduction in blood viscosity through morpholino-mediated knockdown of either *gata1a* (*GATA binding protein 1a, formerly gata1*) or *gata2a* (*GATA binding protein 2a, formerly gata2*), both master regulators of erythropoiesis (Brownlie and Zon, 1999) results in differing effects on *klf2a* expression and opposing defects in valvulogenesis (Heckel

et al., 2015; Vermot et al., 2009). *gata1a* morphants result in subtle changes to *klf2a* expression but a dramatic decrease in shear stress (Heckel et al., 2015; Hsu et al., 2019; Vermot et al., 2009) whilst *gata2a* morphants display a significant reduction in *klf2a* expression. Knockdown of *klf2a* results valve morphogenesis defects, together with a reduction in *bmp4* and clear loss of *notch1b* expression, both key signalling molecules in valve development (Vermot et al., 2009). As well as setting up the necessary signalling pathways at the valve, *klf2a* also regulates localised ECM synthesis necessary for the development of the atrioventricular cushions. Between 48hpf to 56hpf, the expression of *fibronectin 1b* (*fn1b*) increases 3-fold, is highly restricted to the AVC and is dependent on *klf2a* function. Knockdown of *fn1b* leads to a failure of EndoMT into the cardiac jelly, a crucial step in valvulogenesis (Steed et al., 2016). Together this places *klf2a* as a major integrating transcription factor in the development of the atrioventricular valve. *klf2a* also plays a role in the development of the endocardium during ballooning, where sensation of blood flow through *klf2a* is required for endocardial proliferation (Dietrich et al., 2014).

A close reciprocal relationship exists between blood flow patterns through the heart and the looping morphogenesis as one ultimately causes a perturbation on the other. In line with the link between form and function of the heart, the sensation of blood flow is proposed to be required for proper cardiac morphogenesis more generally, with altering of blood viscosity by knockdown of either *gata1a* and *gata2a* resulting in a failure of heart looping (Lombardo et al., 2019). Interestingly, knockdown of either or both *gata1a* and *gata2a* results in a less severe looping defect than observed in *tnnt2a* morphants (Lombardo et al., 2019), potentially confirming two distinct requirements for blood flow and heart contractility in promoting heart looping (Auman et al., 2007).

1.4.4 Heart maturation (56hpf onwards)

As development progresses, specialisation between the two chambers becomes more apparent. During ventricular maturation, myocardial cells begin to delaminate and invade into the ventricular cardiac jelly in a process known as trabeculation. Similar to valve development, trabeculation is dependent upon heart contractility as *tnnt2a* morphants display a complete lack of trabeculae (Samsa et al., 2015). Blood flow during trabeculation also regulates Notch signalling, although recovery of Notch activity in *tnnt2a* morphants, is not sufficient to recover the loss of trabeculae phenotype, suggesting multiple pathways are active during this process (Samsa et al., 2015).

Specialisation of the atrium is mainly characterised by the emergence of the Sino-Atrial node (SAN) or pacemaker at the base of the inner curvature of the atrium (Pater et al., 2009). These cells are some of the last to be added to the heart and express the transcription factor Isl1 and loss of *isl1* function results in pacing defects (Pater et al., 2009). Although specified during earlier morphogenesis (prior to 56hpf) (Burkhard and Bakkers, 2018), mutations affecting the function of the SAN are more pronounced at 3dpf than 2dpf (Tessadori et al., 2012), suggesting a key requirement for function from 3dpf onwards. Distinct to that of ventricular trabeculation, between 7dpf-14dpf, the atrial wall undergoes a significant morphological change. Referred to as "webbing", individual cells of the atrium make sparse contacts with one another. Additionally, and similar to the adult ventricular myocardium, the atrial myocardium is derived from clonal expansion of the embryonic myocardium (Foglia et al., 2016; Gupta and Poss, 2012).

Between 3-4dpf, the atrioventricular valve continues to develop and increase in efficiency (Scherz et al., 2008). By 80hpf the atrioventricular valve is a multi-layered mass of originally endocardial cells expressing high levels of *klf2a* with low levels of cell proliferation (Steed et al., 2016). By 102hpf, the morphology of the

atrioventricular valve is similar to valve present in the adult (Scherz et al., 2008). At the outflow tract of the heart a second valve forms between the ventricle and the bulbus arteriosis (BA) from 56hpf onwards, and functions to regulate blood flow into the aortic arches. This has recently been shown to regulated by a similar, yet distinct set of cellular behaviours to that of the development of the AVC, including the Klf2a-Notch1b pathway (Duchemin 2019, Hsu 2019).

Initiating around 72hpf, the pro-epicardium begins to cover the surface of the maturing heart generating the third cardiac tissue layer of the heart: the epicardium (Bakkers, 2011). The epicardium is important in supporting the function of the myocardium, containing the precursors necessary to generate the coronary vasculature and other cell types (Ruiz-Villalba and Pérez-Pomares, 2012). Development of the epicardial layer is dependent on heart contractility, as movement of the pro-epicardium onto the heart is compromised in *tnnt2a* morphants (Peralta et al., 2013), further demonstrating the coupling of form and function during heart development.

Finally, as the larva begins to develop into the juvenile stage, a third rotation of the heart (terminal rotation) occurs between 84hpf and 120hpf. This rotation dramatically alters the arrangement of the chambers, such that the ventricle moves from the right to ventral and the atrium moves from left to dorsal and it is this position that the heart retains throughout life (Singleman and Holtzman, 2012).

1.4.5 Comparison of Zebrafish and Human heart anatomy

The final form of the zebrafish heart is distinctly different from that of the human heart (Figure 1.7), reflecting the key differences in the nature of oxygen exchange. The 4-chambered mammalian/avian heart is a closed double circulatory loop, collecting deoxygenated blood from the soma and moving it to the lungs where it is oxygenated, returns to the heart is then returned to the rest of the body (Figure

1.7A). Instead, the two-chambered zebrafish heart only delivers deoxygenated blood to the gills in a single circulatory loop (Figure 1.7B). Importantly despite these differences, the fundamentals of cardiac function are highly conserved with pacing of the heart regulated by the sinoatrial node located at the base of the atrium which fills with deoxygenated blood (Figure 1.7) and valves present at homologous positions between chambers and the major vessels which are integrated into the heart.

Ultimately, the final form of the heart is not critical to elucidating how the organ takes shape during embryonic development. Instead, it is the conservation of mechanisms both at a genetic and cellular level (1.1.2, 1.2 and 1.4.3), and integration of biomechanical cues that is important. The co-ordination of these processes is necessary to generate the correct form of the heart, which is necessary for its function.

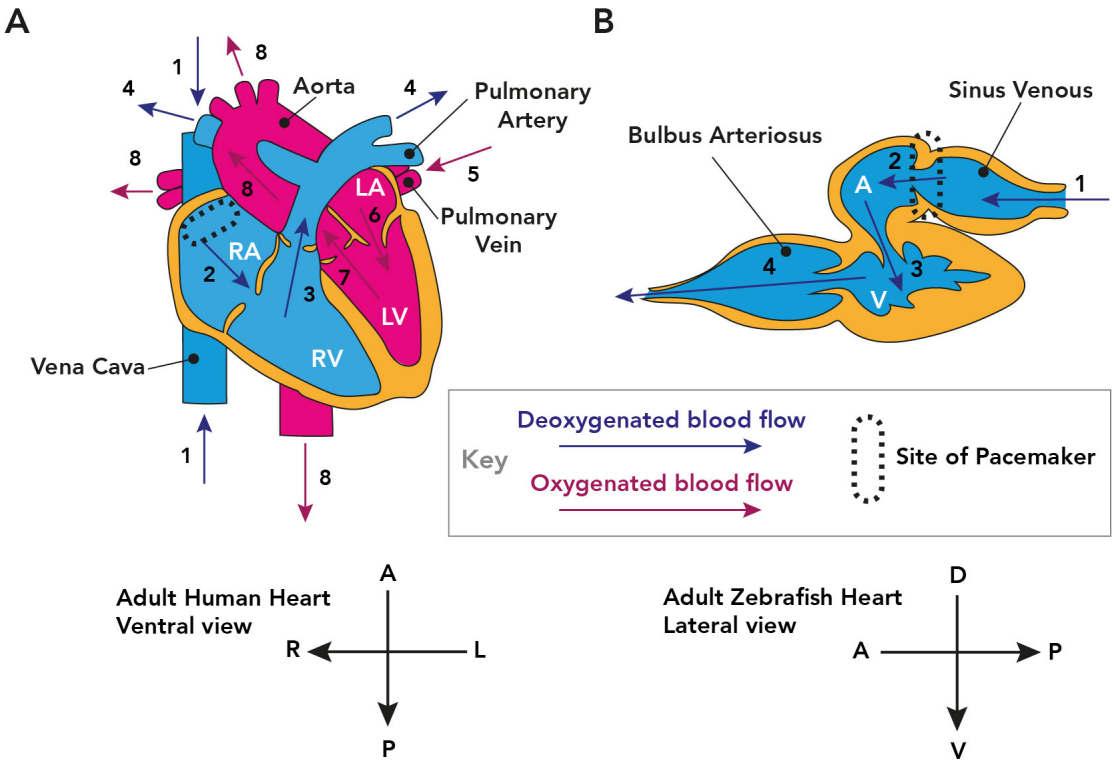

Figure 1.7. Comparison of human and zebrafish heart anatomy

(A) The Human heart (ventral view) is a closed, double circulatory loop, where the blood passes through the heart twice per circuit. Deoxygenated blood (blue) returns to the heart through the Vena Cava (1) into the right atrium (2) through the tricuspid valve into right ventricle (3), exiting the heart by the Pulmonary Artery (4) to the lungs. Oxygenated blood (red) returns to the heart through the Pulmonary Vein (5) into the left atrium (6) through the mitral valve into the left ventricle (7) and exits the heart through the Aorta (8). **(B)** The Zebrafish heart (lateral view) is a closed, single circulatory loop, which delivers deoxygenated blood to the gills. Blood enters the heart through the Sinus Venous (1) into the single atrium (2) through the atrioventricular valve into the ventricle (3) and exiting the heart via the outflow tract valve into the Bulbus Arteriosus (4) and into the vascular bed of the gills. In both hearts, the pacemaker is positioned sinoatrially (Burkhard et al., 2017; Tessadori et al., 2012). RA: right atrium, RV: right ventricle, LA: left atrium, LV: left ventricle, A: atrium, V ventricle.

1.5 An overview of the Extracellular Matrix

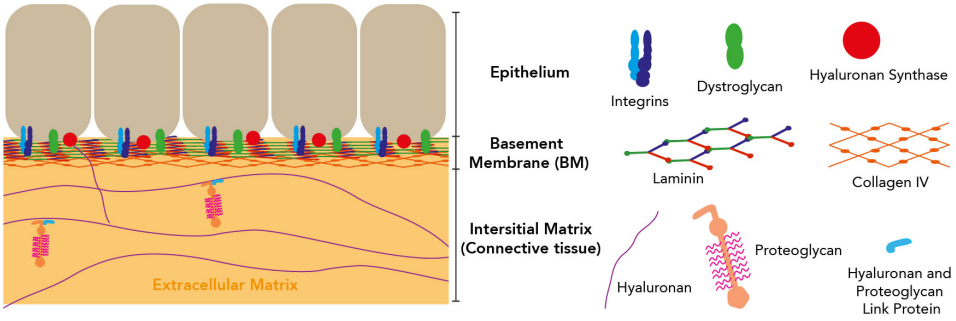

Figure 1.8. The Extracellular Matrix.

Basic structure of the extracellular matrix surrounding an epithelium. The Basement Membrane provides physical support to the cells via direct attachment, most frequently through Integrins and/or Dystroglycan. Underneath the Basement membrane, the Interstitial Matrix provides a structural scaffold for tissues. The Basement Membrane commonly contains Laminins and Collagen IV, together with Nidogen (not shown) and Perlecan (not shown) whilst the Interstitial Matrix classically contains Hyaluronan (purple) synthesised by cell surface Synthases (red), Proteoglycans, Fibronectin (not shown) and other Collagens such as Collagen I (not shown).

Tissue morphogenesis, such as heart looping, requires co-ordination of changes in cell shape, gene expression and the integration of intrinsic and extrinsic patterning cues often across multiple, distinct tissue types. Whilst many studies focus on the interactions between cells in a tissue such as the sending and receiving of intercellular signaling molecules, membrane-membrane interactions through junctional complexes, and at an intracellular level on the changes in transcription factors, the interaction between the cells in a tissue undergoing morphogenesis and the extracellular environment is often under-appreciated. The ECM contains a milieu of different molecules, but can be broadly divided into glycoproteins (including Proteoglycans and Laminins, discussed in detail below) and fibrous proteins such as Collagen (Bonnans et al., 2014; Mouw et al., 2014). The ECM can be separated into

two levels: the basement membrane (BM) which provides direct, physical support connections and the underlying connective tissue or interstitial matrix (Figure 1.8). The specific composition of the ECM, and a cells ability to interact with any of these constituents will influence its attachment and migration, provide different biomechanical cues to the cell, and facilitate or prevent receipt of biochemical signals (Bonnans et al., 2014; Mouw et al., 2014). This range of potential interactions between the cell and the ECM is highly diverse and represented in the wide range of developmental abnormalities and lethal phenotypes observed upon loss of ECM components (Chew and Lennon, 2018; Miner et al., 2004; Rozario and DeSimone, 2009), however, the precise mechanisms linking the ECM to distinct cellular processes which go on to shape the tissue is only beginning to be elucidated. During heart looping, the heart tube contains a specialised ECM separating the outer layer of contractile myocardium from the inner endocardium. This cardiac jelly has been proposed to play a variety of roles during heart development (Barry, 1948; Davis, 1924; Nakamura and Manasek, 1981) and therefore understanding the interactions between the cardiac jelly, and the cells of the heart during asymmetric morphogenesis may provide insight into how this process is achieved. I will first focus on specific classes of ECM molecules and subsequently the roles these families have been linked to cardiovascular development and function.

1.5.1 Identification, characterisation and nomenclature of Laminins: non-collagenous glycoproteins

Laminin was initially isolated from a mouse tumour-synthesised basement membrane, and described as a high molecular weight non-collagenous protein distinct from Fibronectin (Chung et al., 1979; Timpl, 1989). Two years later, electron microscopy revealed the structure of the isolated Laminin as a "rigid asymmetric cross" (Engel et al., 1981), the components of which broadly resolved to be three polypeptide chains which assembled into the trimer with equimolar amounts (Hogan et al., 1980; Howe and Dietzschold, 1983). An initial nomenclature system defined

the originally isolated Laminin as being composed of α1, β1 and γ1, as all isolated Laminins were found to contain three genetically distinct subunits, with the original Laminin (α1β1γ1) designated Laminin-1 (Burgeson et al., 1994). A further refinement came in 2005, with the composition of each trimer naming the Laminin instead, meaning that Laminin-1 was to be referred to as Laminin-111 (comprising α1, β1 and γ1 respectively) (Aumailley et al., 2005).

Since its initial identification, 5 alpha chains, 4 beta chains and 3 gamma chains have been described in vertebrates with a high degree of evolutionary and functional conservation in zebrafish. Based on microsynteny, zebrafish share ten out of the twelve mammalian Laminin subunits, having no *laminin, beta 3* (*lamb3*) or *laminin, gamma 2* (*lamc2*) orthologs (Sztal et al., 2011). As well as the 10 mammalian orthologs, two duplicated β subunits are present in zebrafish: *laminin, beta 2-like (lamb2l)* a pseudogene of *laminin, beta 2* (*lamb2*) (conserved in mammals) (Jacoby et al., 2009) and *laminin, beta 1b* (*lamb1b*) a paralogous gene to *laminin, beta 1a* (*lamb1a*) (human *LAMB1*) (Sztal et al., 2011). *lamb1b* is not present in humans or mice however, phylogenetic analysis suggests that two copies of Laminin β1 may have been the ancestral state and that humans and mice have subsequently lost functional *lamb1b* genes (Sztal et al., 2011). The high level of conservation of Laminin subunits show that zebrafish represent a suitable model to understand the role of multiple Laminin subunits during development.

Whilst Laminin trimers are highly diverse, all Laminin subunits share a common protein structure with both globular and rod-like domains, which associate by their coiled-coil domains (Figure 1.6A). All alpha chains possess a much larger C-terminal domain consisting of 5 LG (Laminin Globular) domains which undergo varying levels of cleavage, and mediate the interaction between Laminin and the cell membrane (Domogatskaya et al., 2012) (Figure 1.6). These LG domains in the alpha subunit are C-terminal to the coiled-coil domain, which is conserved in the β and γ coiled-coil domains and mediates the interactions between the subunits required for trimer

formation (Domogatskaya et al., 2012) (Figure 1.6A, B). N-terminal to the coiled-coil domains are frequently referred to as the short arms which are required for isoforms to polymerise (Bruch et al., 1989). Short arms of Laminin subunits vary in length between α, β and γ chains, but also within each subfamily, due to differing numbers of LE (Laminin Epidermal Growth Factor like) repeats the most striking being *lama3* (*laminin, alpha 3*) and *lama4* (*alminin, alpha 4*). (Domogatskaya et al., 2012) (Figure 1.6A) Other than *lama3*, *lama4* and *lamc2* all Laminins possess an N terminal Laminin domain (LN) (Figure 1.6A) which are important for polymerisation of the Laminin network (Domogatskaya et al., 2012) (Figure 1.6C).

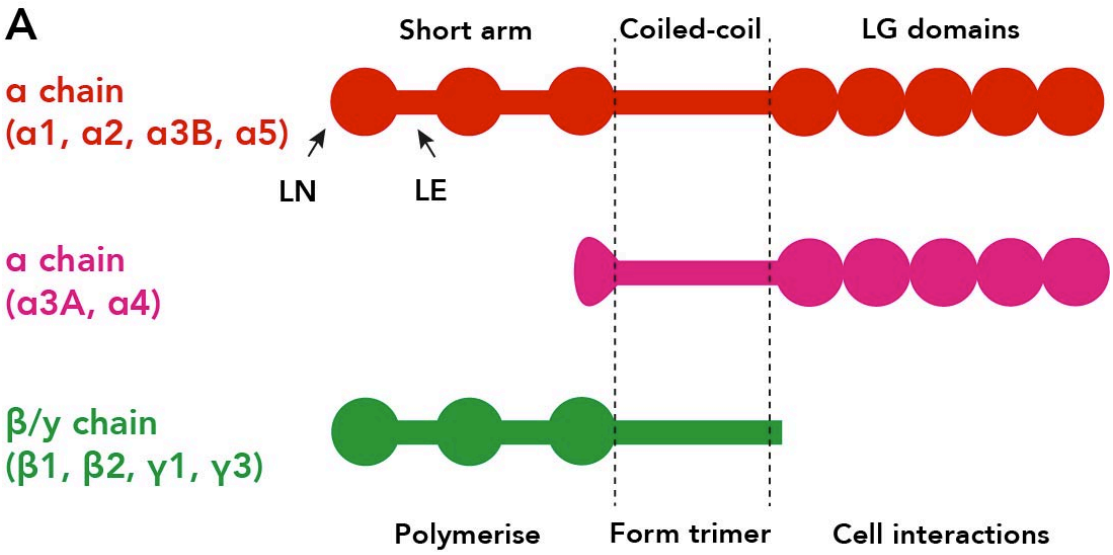

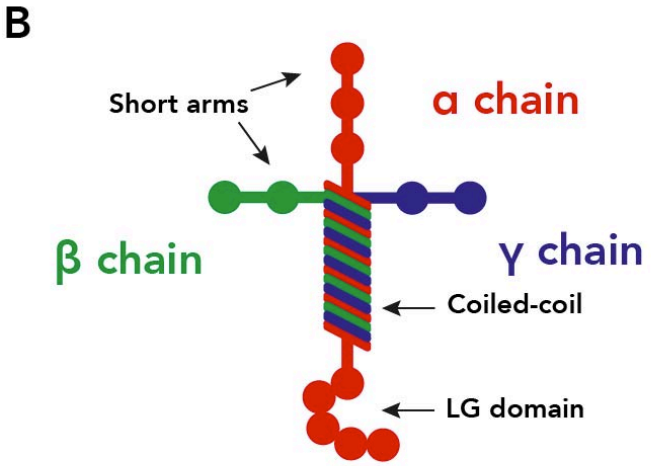

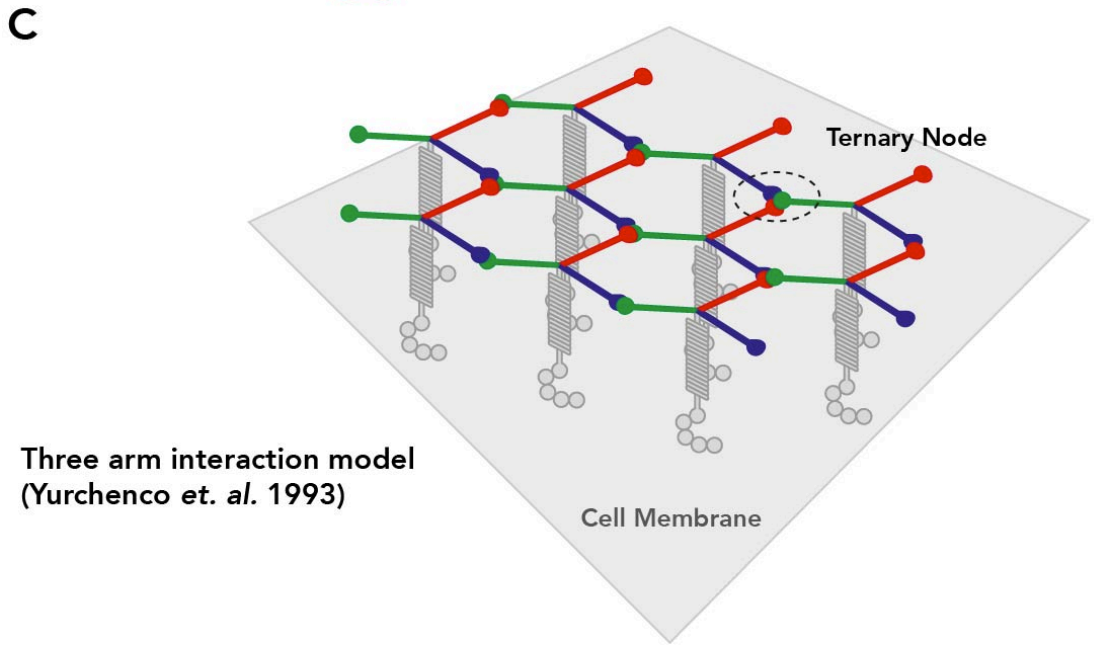

Three arm interaction model
(Yurchenco *et. al.* 1993)

Combinatorial transfection studies in HEK293 cells showed that the α1 chain could be secreted singularly or together with the β1γ1 complex, suggesting that alpha chains may act to drive Laminin trimer secretions (Yurchenco et al., 1997). Biochemical and electron microscopy analysis of various fragments of Laminin trimers developed the "Three arm interaction model" (Yurchenco and Cheng, 1993). This proposes that each short, N-terminal arm of a subunit would preferentially form a ternary node with one another, generating a hexagonal lattice-like structure of Laminin short arms in the basement membrane where the LG domains at the C-terminal end of the trimer interacting with the cell membrane (Figure 1.6C). The highly modular nature of Laminin subunits and their combinatorial nature allows tissue-specific expression of different subunits to drive regionalised deposition of distinct Laminin isoforms, encoding specificity to the Laminin-component of the ECM in different developmental contexts.

Figure 1.9. Structure and assembly of Laminins.

Structure and assembly of Laminins. **(A)** Classically, Laminin alpha chains have 3 distinct domains (red): the short arm (alternating Laminin N-terminal (LN) repeats and Laminin EGF-like (LE) repeats), coiled-coil and LG (Laminin Globular) domains. 3 alpha chains (α3A and α4) do not posses a short arm (magenta). β/γ chains (except γ2) all possess the short arm and coiled-coil domains, but do not have an LG domains. **(B)** Typical Laminin trimer, containing 1 α, 1 β and 1 γ subunit, associating through their coiled-coil domains, with the LG domain and each subunits short arm accessible. **(C)** The three arm interaction model of Laminin assembly. Each short arm of the Laminin trimer associates with two others, forming a ternary node, assembling into a hexagonal lattice. The LG domains of the alpha chains are free to interacti with the cell membranes, anchoring cells to the Laminin-containing basement membrane. Schematics based on: Domogatskaya et al., 2012; Yurchenco and Cheng, 1993.

1.5.2 Laminins in development

Laminins are one of the first ECM components to be generated during embryonic development with *Lamb1 (laminin B1)* and *Lamc1 (laminin, gamma 1)* expressed from as early as the 4-cell stage of the mouse embryo and production of the complete trimer detectable from the 16-cell stage (Cooper and MacQueen, 1983). Laminins play a role in one of the earliest processes in development, implantation of the embryo. *Lamc1* null mice result in post-implantation lethality by E6.0 (Smyth et al., 1999), due to a failure to generate any embryonic membrane or the basement membrane which forms during early placental development (Reichert's membrane) (Smyth et al., 1999). *Lamb1* null embryos have a similar spectrum of phenotypes, suggesting that Lamb1-Lamc1-containing trimers are crucial for embryo implantation (Miner et al., 2004).

Two Lamb1-Lamc1 containing Laminin trimers are present at implantation stages: Laminin-111 and Laminin-511 (Miner et al., 2004). As *Lamb1* and *Lamc1* are common to both, the precise role of each trimer could be identified through examination of *Lama1* (*Laminin, alpha 1*) and *Lama5* (*Laminin, alpha 5*) mutations. *Lama1* mutant embryos survive for a day longer that *Lamb1* or *Lamc1* mutants although Reichert's membrane is absent (Miner et al., 2004). However, *Lama5* mutant embryos survive until E17, much longer than either *Lama1*, *Lamb1* or *Lamc1* mutants (Miner et al., 1998). To explain this discrepancy, it was suggested that LN-111 could compensate for the absence of LN-511 and that Lama5-containing BM could compensate for a short time in *Lama1* mutants (Miner et al., 2004). Overexpression of *Lama5* in *Lama1* mutant mice resulted in a mild rescue, where *Lama1* mutant/*Lama5* overexpression mice were larger and more developed at E6.5 (when *Lama1* mutants die) but were still smaller than their control littermates (Miner et al., 2004). These early studies highlight that some broad functions of Laminin alpha chains are conserved in development, and that alpha chains are the key Laminin subunit in providing functional specificity of a trimer. However, whilst there

is a partial rescue by LN-511 in *Lama1* mutant mice, LN-511 is not able to fully rescue, suggesting that other ECM components, which interact solely with LN-111, cannot be organised properly by LN-511.

In zebrafish, the role of specific Laminin subunits and their associated trimers have been highlighted through forward genetic screens from which three mutants - *bashful* (*laminin, alpha 1*, *lama1*), *grumpy* (*laminin, beta 1a, lamb1a*) and *sleepy* (*laminin, gamma 1, lamc1*) - were identified that display notochord, brain and eye defects (Eeden et al., 1996; Karlstrom et al., 1996; Odenthal et al., 1996; Pollard et al., 2006; Schier et al., 1996; Stemple et al., 1996). As zebrafish development is aplacental, the requirement for *lamb1a* and *lamc1* in the embryo could be characterised further than in the mice models. The *grumpy* and *sleepy* lesions result in an indistinguishable phenotype with shortened body axes due to a failure in proper differentiation of the notochord, demonstrating a role for *lamb1a* and *lamc1* in the development of the notochord basement membrane (Parsons et al., 2002).

A second forward genetic screen identified a further role for *lamb1a* in establishing the laterality of the zebrafish digestive system (Hochgreb-Hägele et al., 2013). At 30hpf in *lamb1a* mutants, the gut fails to loop asymmetrically to the left, instead remaining at the midline (Hochgreb-Hägele et al., 2013). Further characterisation identified multiple roles for *lamb1a*: first in the KV and notochord for establishing L-R asymmetry and subsequently the asymmetric migration of the LPM during gut looping (Hochgreb-Hägele et al., 2013).

The strongest *bashful* (*lama1*) allele only affects the development of anterior regions of the notochord (Pollard et al., 2006; Stemple et al., 1996). Similar to mice, a high degree of redundancy between *lama1*, *lama4* and *lama5* exists in the development of the notochord in zebrafish. Morpholino-mediated knockdown of *lama5* or *lama4* in *lama1* mutants resulted in a more severe notochord phenotype although neither loss of both *lama1-lama4* nor *lama1-lama5* was able to totally recapture either the

lamb1a or *lamc1* axis phenotype (Parsons et al., 2002; Pollard et al., 2006). This suggested that LN-111, LN-411 and LN-511 function with partial redundancy together to regulate notochord development, and that the most severe phenotype in *lamb1a* or *lamc1* mutants is observed due to loss of all three complexes.

One of the most well characterised basement membranes is the glomerular basement membrane (GBM) of the nephron, required to support the ultrafiltration of the blood in the kidney. Two major cells types line the GBM, endothelial cells on the inner face and podocytes on the outer face, both of which generate their own ECM which later combine to form the GBM (Miner and Li, 2000). Characterised in mice, initially both cell types express *Lama1* and *Lamb1*, but as development progresses, expression of *Lama1* is replaced quickly by *Lama5*, and subsequently, over a longer time course *Lamb1* to *Lamb2*, resulting in a maturation of the Laminin component of the GBM from LN-111, to 511 and finally to the postnatal LN-521 (John and Abrahamson, 2001; Miner and Sanes, 1994).

As a result of this isoform switching, different glomerular phenotypes are observed in mutants for different Laminin chains (Abrass et al., 2009, 2006; Kikkawa and Miner, 2006; Miner et al., 2004; Shannon et al., 2006), in particular, mutations in *Lamb2* results in proteinuria postnatally following isoform switching (Noakes et al., 1995). Although appearing normal, *Lamb2* mutant mice die between Postnatal day (P)15 and P30, with apparently normal glomeruli morphology, however, Lamb1 remains a major component of the GBM, failing to show loss of expression in these postnatal kidneys suggesting either a failure to down-regulate or a compensatory mechanism (Noakes et al., 1995). Although no kidney phenotype has been examined zebrafish *lamb2* mutants display relatively subtle phenotypes, similar to mice models. Zebrafish *lamb2* mutant muscle degeneration is similar to other dystrophic mutants such as *lama2* and *dystrophin*, although distinct from the other mutants, the phenotype recovers and adults display no clear morphological or behavioural phenotype (Jacoby et al., 2009).

Mutations in *LAMA2* (*Laminin, alpha 2*) are the most common cause of Congenital Muscle Dystrophy Type 1A, which leads to death early in childhood (Helbling-Leclerc et al., 1995). *Lama2* is contained in the trimer LN-211 which is crucial for muscle development and function, and postnatally is almost the only Laminin isoform in muscle (Domogatskaya et al., 2012). Loss of LN-211 ultimately results in uncoupling of the muscle from the ECM, resulting in poor co-ordination of muscle contraction that results in damage to tissue. In a further example of redundancy between Laminins, over-expression of *Lama1* in skeletal muscle in a *Lama2* mutant background could reduce features of Congenital Muscular Dystrophy in a mouse model (Gawlik et al., 2004).

In summary, Laminins perform, multiple, crucial roles during development and exhibit a high level of functional redundancy, particularly between alpha chains. Often, multiple Laminin isoforms are expressed in one tissue, where each isoform performs a distinct role and can be subsequently be replaced by other trimers as the basement membrane matures over the course of morphogenesis.

1.5.3 Laminin receptors

The major cell surface receptors that bind to the ECM are the integrin family, a heterodimer consisting of one of 18 α chains and one of 8 β chains, both of which are important in providing the ligand-binding specificity. Broadly integrins bind four different classes of ECM molecule, but α3β1, α6β1, α6β4 and α7β1 dimers all bind to Laminins (Nishiuchi et al., 2006).

Similar to Laminins, integrins are required early in embryogenesis. *Itgb1* null mice embryos die shortly after implantation, likely due to *Itgb1* being a key constituent of half of the known 24 integrin heterodimers (Anderson et al., 2013). One well-defined pathway involving *Itgb1* is in differentiation of the mammary gland epithelium. Responsiveness to the hormone Prolactin is only achieved upon simultaneous

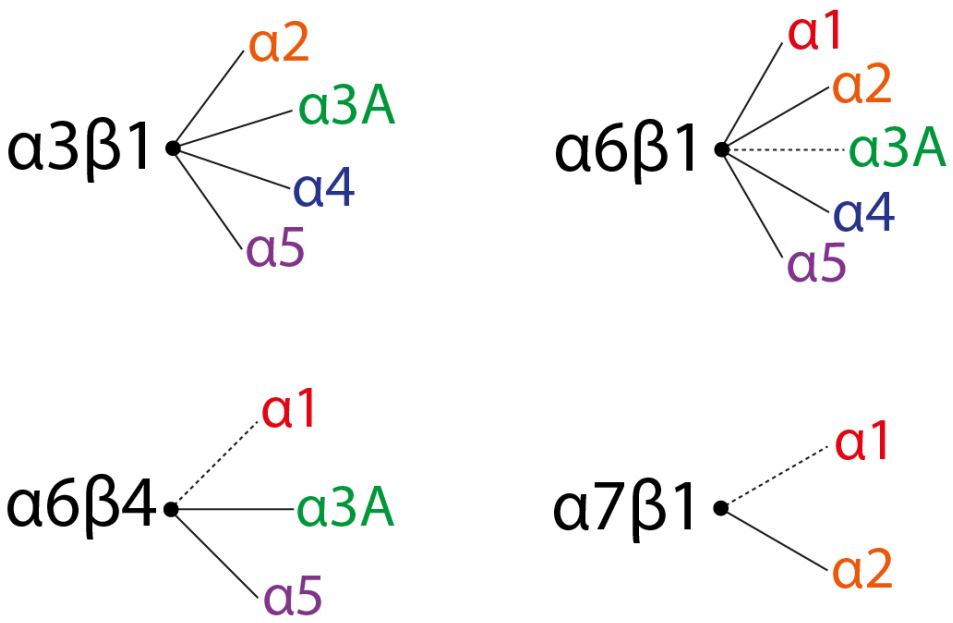

Figure 1.10. Canonical Laminin-Integrin interactions.

Summary of the 4 classical Laminin binding integrin heterodimers interactions with Laminin alpha chains. Based on: Knoll et al, 2007; Miner and Yurchenco 2004; Nishiuchi et al., 2006.

binding of β1 integrin to the Laminin-111 of the basement membrane and together, these two active receptors facilitate intercellular signalling and expression of milk genes (Naylor et al., 2005; Taddei et al., 2008, 2003). Integrin signalling from the basolateral surface is also key in setting up epithelial cell polarity, activating the small GTPase Rac1 and leading to orientation of the apical pole of MDCK cells in culture (O'Brien et al., 2001). Therefore, the characterisation of integrin expression may help to inform function of Laminin isoforms in a basement membrane. Furthermore, within the integrin family, α3β1, α6β1, α6β4 and α7β1 dimers bind to Laminins each with distinct dissociation constants (Nishiuchi et al., 2006) (Figure 1.10).

The other main Laminin receptor, Dystroglycan is heterodimeric glycoprotein derived from post-translational cleavage of a single gene product *Dag1* (Moore and Winder, 2010). α-Dystroglycan interacts with ECM components which contain LG domains such as those present on Laminin (Figure 1.9A) and through binding to β-

Dystroglycan to the actin cytoskeleton. Dystroglycan is a ubiquitous cell adhesion molecule, and similar to a requirement for laminins in early development, loss of *Dag1* in mice results in disruption of Reichert's membrane, changes to Laminin and Collagen IV localisation and developmental defects from E6.5 onwards (Williamson et al., 1997). Dystroglycan and different integrin heterodimers are expressed on the same cells where they are able to interact to regulate intracellular cell signalling for example, integrin α6β1 and Dystroglycan have pro- and anti-ERK regulatory mechanisms respectively (Ferletta et al. 2003).

Whilst integrins listed in Figure 1.10 and the Dystroglycan complex are the more canonical laminin binding partners, other complexes such as the Lutheran blood group specifically binds Lama5 LG domains. Furthermore, other interactions between integrins α1β1, α2β1 with the LN domains of Lama1 and Lama2 or αvβ3 with the IVa domain of Lama5 (Miner and Yurchenco 2004). Together this suggests that characterising the composition of both Laminin and their receptors may help to define which Laminins are required and how they may function during heart development .

1.5.4 The structure of Glycosaminoglycans and Proteoglycans

Whilst Laminins and Collagens form the basis of the ECM, Proteoglycans (PGs) are involved in more complex ECM structures. Proteoglycans are composed of a core protein (such as Aggrecan, Versican, Neurocan) covalently linked to Glycosaminoglycans (GAGs), long hydrophilic disaccharide moieties, the most common being Heparan Sulfate (HS), Chondroitin Sulfate (CS) or Keratan Sulfate (KS) (Figure 1.11B) (Esko., 2017; Lindahl et al., 2017). Distinct from the other Glycosaminoglycans, Hyaluronic Acid (Hyaluronan, HA) is not modified any further (Esko., 2017). Whilst some aspects of Proteoglycan synthesis and function are conserved in evolution, *C. elegans* and *D. melanogaster* do not possess the enzymes required to generate HA, but can synthesise HSPG (Esko., 2017). PGs, by

nature of the negatively charged GAGs are able to draw water into the extracellular environment and as such provide compressive resistance to the ECM, as well as functioning to limit the diffusion of signalling ligands in a GAG-specific manner.

Broadly, Proteoglycans are classed as Chondroitin Sulfate Proteoglycans (CSPGs) or Heparan Sulfate Proteoglycans (HSPGs), based on the GAG linked to the core protein. Typically, CSPGs are secreted into the ECM containing Aggrecan, Neurocan or Versican, HSPGs can be localised to either the cell surface, where the core proteins are commonly Syndecans or Glypicans or in the ECM where the core proteins are Agrin or Perlecan (Pomin and Mulloy, 2018).

All Glycosaminoglycans are composed of a repeating disaccharide motif where each specific GAG has a different pair of sugars (Lindahl et al., 2017). All GAGs except KS require Uronic acid, synthesised by the highly conserved enzyme *UDP-glucose dehydrogenase* (*jekyll* in zebrafish, *sugarless* in *Drosophila*) (Lin et al., 1999; Lindahl et al., 2017; Walsh and Stainier, 2001). HA is synthesised of an indefinite length by the Hyaluronan Synthase (Has) class of enzymes which are present in vertebrates and bacteria. Whilst the synthesis of CS, HS or KS is coupled with core protein translation at the Golgi, synthesis of HA occurs at the cell membrane where Has' are localised and is synthesised directly into the ECM (Esko., 2017).

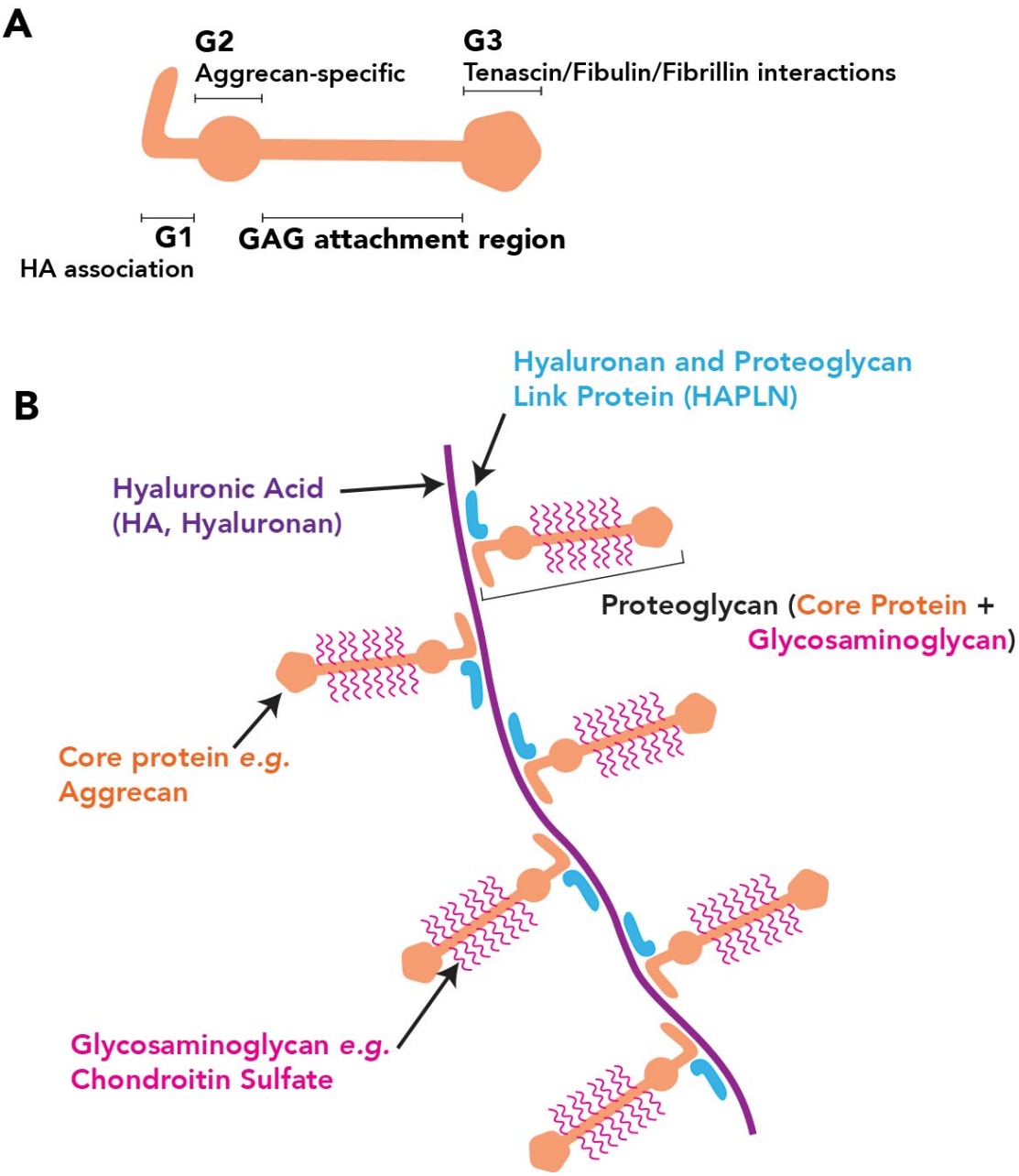

Figure 1.11. Interaction between Hyaluronan and Proteoglycans.

Structure and assembly of Hyaluronan and Proteoglycans. (A) Domain structure of the Lectican core protein Aggrecan. The G1 domain associates with Hyaluronan and is common to all Lectican core proteins. The G2 domain is unique to Aggrecan, with no known function but is highly conserved between species. The G3 domain is able to link the Proteoglycan aggregates with other components of the ECM such as Tenascin, Fibulin and Fibrillin. Glycosaminoglycans are covalently attached to Aggrecan between the G2 and G3 domain (or G1, G3 domains in other Lecticans).

Aggrecan is by far the best studied core protein with a critical role in cartilage, the ECM synthesised by Chondrocytes, where it is covalently attached to Chondroitin Sulfate GAGs (Roughley and Mort, 2014). The negative charge of the CS generates a large osmotic pressure through water attraction, critical for the load bearing properties which cartilage requires. Systematic analysis of the Aggrecan protein defined its structure consisting of three globular domains, with the region between G2 and G3 the site of CS or KS addition (Figure 1.11A). This modular nature of core proteins is a conserved feature however the G2 domain is specific only to Aggrecan, whilst G1 and G3 are highly conserved with Versican (Aspberg, 2012; Kiani et al., 2002). PGs can further associate with HA (Hardingham and Muir, 1972), and studies of Aggrecan interactions with HA suggest that non-covalent PG interactions with HA require the G1 domain (Aspberg, 2012; Kiani et al., 2002) the stability of which is dependent on the family of Hyaluronan and Proteoglycan binding Link Protein (Hapln) (Spicer et al., 2003) (Figure 1.11B)

1.5.5 Functions of Glycosaminoglycans and Proteoglycans in tissue morphogenesis

Similar to the manner in which specific Laminin isoform composition dictates specific spatiotemporal roles within development, the specific core proteins component of the PG can have distinct effects during development. Implantation of Aggrecan near to migrating streams of neural crest results in diversion from the normal migration pattern away from the implant, suggesting that Aggrecan plays an inhibitory role neural crest migration (Perissinotto et al., 2000). Contrastingly, when Versican coated micro-membranes were inserted in the migratory pathway, cells direct their

Figure 1.11 continued.

(B) Proteoglycans (orange core protein, decorated by magenta Glycosaminoglycans) can associate with Hyaluronan (purple) and is stabilised, non-covalently by the family of Hyaluronan and Proteogylcan Link Proteins (HAPLNs, cyan). Schematics based on: Aspberg, 2012; Faltz et al., 1979.

migration towards the exogenous Versican sources, suggesting Versican acts more as an attractant (Perissinotto et al., 2000). These reciprocal roles of Aggrecan and Versican tally well with their complementary expression patterns, where Versican expression is localised to permissive areas of neural crest migration, whilst Aggrecan expression is present in non-permissive areas (Perissinotto et al., 2000). In addition to the functional studies demonstrating the role of core proteins in a variety of developmental processes, mouse loss-of-function models for key biosynthetic enzymes for Heparan Sulfate, *Ext1* (*Exostosin glycosyltrasnferase 1*) and *Ext2* (*Exostosin glycosyltrasnferase 2*), are embryonic lethal exhibiting gastrulation defects, however maternal deposition of *ext2* in zebrafish allows development to proceed further (Poulain and Yost, 2015). Loss *Ext1* function in neural stem cells results in a complete loss of neurons, astrocytes and oligodendrocytes (Poulain and Yost, 2015). Together this shows that, similar to Laminins, the modular nature of PGs in the extracellular matrix through expression of specific core proteins, linked with particular GAGs is able to dictate specific, developmental outcomes.

In cell culture, expression of the BMP antagonist Noggin at the cell surface is dependent on functional HS production (Paine-Saunders et al., 2001). Furthermore, membrane-localised Noggin attached to HSPG is able to bind BMP4, preventing uptake/signalling in the target cell and dampening BMP signalling in an ECM context-dependent manner (Paine-Saunders et al., 2001). In zebrafish, absence of HS results in ectopic BMP activation affecting myotome development (Dolez et al., 2010). Interestingly, this absence of HS is due to a loss of *lamc1* (Dolez et al., 2010), suggesting complex interactions between different components of the ECM during development in regulating biochemical signalling, further to providing structural support.

1.6 The role of the Extracellular Matrix in cardiovascular development

Most organ systems, including the heart are composed of distinct tissue types with specialised functions. During cardiac development the heart tube comprises an outer layer of contractile myocardium surrounding the endocardium, and separated by a layer of ECM termed the cardiac jelly, coined by Davis in 1924. Numerous studies have highlighted the importance of the cardiac jelly during heart maturation; however, little is known about the role of the embryonic cardiac ECM during earlier stages of heart morphogenesis. Below I detail what is currently understood about the role of Laminins and Proteoglycans in cardiovascular development across vertebrate models. In particular for Laminins, whilst very little is known about their role in heart development, I highlight important lessons that can be learned from their roles in vascular development.

1.6.1 Laminins and Integrins

In its simplest form, the vascular system composes of the single endothelial cell layer in contact with blood on one side and the BM on the other (Hallmann et al., 2005). The main Laminin components of the vascular basement membrane are LN-411 and LN-511, where *Lama4* is expressed during early development (E8.5 onwards), and *Lama5* is only detectable after 3 weeks of postnatal expressed in predominantly larger vessels (Hallmann et al., 2005).

A well-characterised model of sprouting angiogenesis is the development of the intersegmental vessels (ISVs) in zebrafish, where endothelial cells delaminate from the dorsal aorta and migrate anteriorly between the somites (Gore et al., 2012). *lama4* is expressed in the dorsal aorta, and together with *lama1*, Laminin-111 and -411 function redundantly in promoting the migration of ISVs (Pollard et al., 2006).

Lama4 is also expressed in the endothelial cells of the heart, the blood vessel basement membrane and peripheral sarcolemma of cardiomyocytes in mice (Iivanainen et al., 1997; Wang et al., 2005). Loss of *Lama4* results in enlarged hearts and significantly larger cardiomyocytes compared to wild-type (WT) (Wang et al., 2005). *Lama4* mutant mice survive postpartum but are haemorrhagic, with haemorrhage typically occurring in regions with smaller blood vessels. This phenotype seems to be associated with physical stress during birth as E18.5 embryos displayed milder haemorrhages than newborn pups at sites of greater physical stress (Thyboll et al., 2002). At 16-20 weeks, *Lama4* mutant hearts have a significant increase in markers of hypoxia, and further characterisation supports a mechanism of sustained hypoxia, likely resulting from a compromised basement membrane, resulting in cardiomyopathy (Wang et al., 2005). Functional studies show that whilst loss of *Lama4* does not affect heart rate, there were multiple cases of cardiac dysfunction including arrhythmia and reduced left ventricular end diastolic diameter at 36-40 weeks old (Wang et al., 2005). Mutants also displayed increased frequency of sudden death (Thyboll et al., 2002). In line with the requirement for all three subunits of the trimer being required for secretion, Lamb1 and Lamc1 protein levels were almost absent in *Lama4* mutants. Additionally, whilst northern blot analysis had previously shown no differences in the level of *Lama5* mRNA (Thyboll et al., 2002), an up-regulation of Lama5 protein was observed in *Lama4* mutant mice at 4 weeks old (Wang et al., 2005), further demonstrating the complex, redundant and compensatory genetic interactions between Laminin subunits.

Using a cornea angiogenesis assay, *Lama4* mutant mice display irregular, unco-ordinated branching of distorted, haemorhhagic vessels (Thyboll et al., 2002). One potential mechanism which may could explain this phenotype is the interaction between *Lama4*, tip cells of sprouting angiogenic vessels and Notch signalling (Stenzel et al., 2011). *Lama4* expression is most concentrated in the tip cell in the postnatal mouse retina and loss of *Lama4* results in a reduction of Notch signal in endothelial cells (Stenzel et al., 2011), consistent with the hypersprouting phenotype

previously identified and a link between Laminins and Notch signalling (Thyboll et al., 2002). This again identifies interactions between the ECM and signalling ligands in regulating the structure of a tissue.

Comparison of patients with dilated cardiomyopathy to control populations revealed two deleterious mutations in *LAMA4* not present in control populations, both of which significantly impact the structure of the *LAMA4* protein and its ability to interact with integrins (Knoll et al., 2007). In cell culture, fewer endothelial cells adhere to the mutant forms of *LAMA4*-containing substrate compared to WT *LAMA4*, due to a reduction in the affinity of integrin α3β1 for the mutant *LAMA4* substrate (Knoll et al., 2007). Morpholino-mediated knockdown of zebrafish *lama4* results in a low penetrance of cardiac dysfunction. Furthermore, injection at a lower, sub-phenotypic dose into heterozygous *integrin-linked kinase* (*ilk*) mutants results in a low penetrance cardiac dysfunction and haemorrhage, suggesting a potential interaction between *lama4*, *ilk* and integrins in the heart to promote tissue integrity (Knoll et al., 2007).

Further supporting a conserved role for Laminins in cardiac development, Laminin has recently been shown to be present in the chick heart at HH28, surrounding the outer epicardial layer of the heart and deeper in the myocardial tissue closer to the trabecular myocardium (Jallerat and Feinberg, 2020). However, the exact isoform structure was not examined.

An additional link between Laminins and heart development is exemplified by Dandy-Walker Syndrome (DWS) (Darbro et al., 2013; Haddadi et al., 2018), a rare brain malformation which is linked to mutations in *LAMC1* and the Laminin interacting protein *NID1 (Nidogen-1*). Interestingly, 26-38% of patients with Dandy-Walker Syndrome also present with CHDs, supporting a role for Laminins in heart development. It is not clear what the link between Laminins and the pathology is because no model for Dandy-Walker syndrome exists, potentially due to the early

lethality of *Lamc1* mice and the need for complex cell-ECM interactions which cannot yet be accurately recapitulated *in vitro*.

1.6.2 Proteoglycans

Proteoglycans have been shown to play major roles in the development of the heart. *Has2* (the major enzyme producing Hyaluronic Acid in the heart) mutant mice have severe cardiac defects and die at E9.5-10, with a near total absence of cardiac jelly, despite presence of other ECM components such as Laminins (Camenisch et al., 2000), implying that the cardiac jelly of the mouse embryo at these early development stages contains HA. More definitive characterisation of the localisation of HA in the cardiac jelly has been achieved in zebrafish. Previously stains for HA, and now the recent development of a live HA sensor, has demonstrated that the cardiac jelly is rich in HA from at least 48hpf, a comparable stage to when *Has2* mutant mice arrest in development (Grassini et al., 2018; Hernandez et al., 2019; Lagendijk et al., 2011; Smith et al., 2011). The expression of *Has2* and *Versican* correlate strongly in the heart at E9.5 and *Versican* mutant mice display the same severe cardiac abnormalities as loss of *Has2*, strongly suggesting that Versican is the core protein interacting with HA in the cardiac jelly (Mjaatvedt et al., 1998; Yamamura et al., 1997). Whilst a role for HA in dampening BMP signalling in formation of the zebrafish heart tube from the disc is well described in 1.4.2, little work has examined the role of HA and associated PGs in promoting heart looping morphogenesis, instead the main focus of the role of PGs in heart development has been in the formation of the AVC (Butcher and Markwald, 2007; Camenisch et al., 2002, 2000; Lagendijk et al., 2013; Patra et al., 2011).

Multiple other PG components are associated with the correct development of the atrioventricular canal and other structures of the heart. Using the AVC explant method, *Has2* mutant AVC explants fail to migrate, but addition of exogenous HA to the explant culture or transformation of the cells with *Has2* cDNA could restore

migration of the explants (Camenisch et al., 2002, 2000). Thus, the composition of the AV cushions is important for regulating the EndoMT process. Supporting a conserved role for PGs in heart development in zebrafish, loss of a key synthetic enzyme required for the generation of HA, HS and CS (*UDP-glucose 6-dehydrogenase*, *ugdh*, *jekyll*) results in a failure heart looping and formation of the constriction at the AVC (Walsh and Stainier, 2001). Further supporting the possibility that CSPG are required during heart development is the requirement for Chondroitin Sulfate synthesis by the enzyme *chsy1* (*chondroitin sulfate synthase 1*) in zebrafish (Peal et al., 2009). CS is localised to the cardiac jelly surrounding the atrioventricular canal at 36hpf, and loss of CS appears likely to affect the process of EndoMT in the zebrafish AVC (Peal et al., 2009). The core protein Aggrecan has been linked to cardiac defects and been shown to be expressed in the developing heart in both zebrafish and chick at post-looping stages (Rambeau et al., 2017; Zanin et al., 1999). Interestingly, Aggrecan is expressed 16-times less in human Biscuspid Aortic Valve (BAV) patients (Rambeau et al., 2017). Another class of HA interacting proteins previously shown to be important is the link protein Hapln1 (*Hyaluronan and proteoglycan link protein 1*), expressed at the developing valves of the heart, overlapping HA and Versican (Wirrig et al., 2007). Mutagenesis of *Hapln1* in mouse results in cardiac abnormalities in pups at E13.6 consistent with a role for *Hapln1* in valve development and therefore interaction with HA and Versican, further supported by reduction in levels of Versican protein in *Hapln1* mutant mice (Wirrig et al., 2007). Together this demonstrates a broad requirement for different PG components during development with Versican Chondroitin Sulfate Proteoglycans and HA predicted to be key players in regulating this process.

As well as a structural role, the cardiac jelly acts a mediator of intracellular signalling during heart development. During SHF addition in mice, FGF-FGFR interactions are dependent on the production of HSPGs by *Ext1*, which is required for maintenance of progenitor population (Zhang et al, 2015). Additionally, cells of the SHF residing in the splanchnic mesoderm require an Itga5-Fn axis to be sensitised to the FGF8

(Mittal et al, 2010). Another class of proteins, Latent TGF-β-binding proteins (LTBPs), anchor TGF-β ligands in the ECM; cells must then interact and cleave these complexes to receive ligand. In zebrafish *ltbp3* is required to maintain SHF proliferation (Zhou et al., 2011), whilst *Ltbp1L* (*Latent transforming growth factor beta binding protein 1, long form*) is required for multiple processes in the development of valves and OFT in mice (Todorovic et al, 2011, 2007). Together, these studies demonstrate how the cardiac jelly is a key component facilitating cell-cell communication either through corralling of receptors and ligands or anchoring specific signalling ligands in the ECM.

The interaction between the myocardium and endocardium during heart looping is important for setting up the expression of genes such as *has2* for correct valvulogenesis (Patra et al., 2011). Knockdown of the ECM molecule *npnta* (*nephronectin a*), leads to increased *has2* in the ventricular endocardium resulting in increased HA deposition. This endocardial expansion can be recovered through inhibition of BMP, a signalling ligand expressed in the myocardium (Patra et al., 2011). This again demonstrates the necessity for co-ordinated interactions between myocardial and endocardial tissue layers in the generation of the correct ECM environment during looping morphogenesis. Altogether, this highlights the importance of Proteoglycans in cardiac development. However, whilst the roles for tube formation in zebrafish and valve development in mice, zebrafish and chick have been well characterised, despite identification of HA in the cardiac jelly in the looping heart, what role HA and its interacting partners play a role in promoting heart looping morphogenesis is unclear.

1.7 Rationale

Together, multiple lines of evidence suggest that the constituents of the ECM are required for the correct development of the heart, but characterisation of the roles of these components is lacking. In particular many studies have identified that

Laminin is present in the heart during later stages (W. C. W. Chen et al., 2016; Jallerat and Feinberg, 2020; Notari et al., 2018; Thyboll et al., 2002; Wang et al., 2005) and some studies have highlighted that loss of specific Laminin subunits leads to developmental abnormalities in the heart at later stages. The impact of loss of specific Laminin subunits on the morphogenesis of the heart tube has never been examined extensively. Similarly, whilst roles have been implied for HA and associated PGs in promoting heart looping, no comprehensive investigation of components related to PG synthesis expression during this critical developmental transition exists.

In light of these open questions I set out to investigate the role of the ECM in promoting heart looping morphogenesis. Zebrafish represent an excellent model system for this approach, displaying high levels of conservation not only in the processes which shape the linear heart tube, but also in genes related to ECM biology. Furthermore, the variety of transgenic lines and optical clarity facilitate live imaging to draw pertinent, *in vivo* conclusions about cardiac development.

I establish a suite of Laminin subunit genes with dynamic and tissue-specific expression in the heart at the onset of looping morphogenesis and identify two distinct roles for Laminin complexes during heart development. Harnessing the ability to live image the developing zebrafish heart *in vivo* with numerous transgenic lines, I discover the HA-rich cardiac jelly is asymmetrically expanded prior to heart looping and go on to investigate the mechanism by which this regionalised ECM expansion is required to promote heart looping. Finally, I characterise the role of a small Rho GTPase, a potential link between the cardiac jelly and the cells of the heart. In summary this work begins to define the ECM as a key regulator of the asymmetric morphogenesis of the heart tube during development.

2. Materials and Methods

2.1 Zebrafish husbandry

2.1.1 Zebrafish lines

The following zebrafish lines were used in this work:

Table 2.1 Zebrafish lines

Line	Reference
Wildtype (AB)	-
Wildtype (TL)	
Tg(myl7:eGFP)	Huang et. al. 2003
Tg(myl7:lifeActGFP)	Reischauer et. al. 2014
Tg(fli1a:AC-tagRFP)^{sh511}	Savage et. al. 2019
spaw^{t30973}	Noël et. al. 2013
gup^{tj2998a}	van Eeden et. al. 1996, Odenthal et. al. 1996, Karlstrom et. al. 1996
Tg(lft2:GalFF; UAS:RFP)	Derrick et. al. 2019
lamb1b$^{\Delta 2}$	Generated in this study
lamb1b$^{\Delta 25}$	
lamb1a$^{\Delta 19}$ (*lamb1a^{sh589}*)	
lamb1a$^{\Delta 25}$ (*lamb1a^{sh590}*)	
lamb1b$^{\Delta 56}$	
lamb1b$^{\Delta 183}$ (*lamb1b^{sh587}*)	
lamb1b$^{\Delta 428}$ (*lamb1b^{sh588}*)	
rhoca$^{\Delta ATG}$ (*rhoca^{sh592}*)	
rhoca^{ins10}	
rhocb$^{\Delta 20}$ (*rhocb^{sh593}*)	
rhocb$^{\Delta 38}$ (*rhocb^{sh594}*)	
Tg(Ubi:dCas9-poly(A), cryaa:CFP)^{sh595}	
Tg(Ubi:dCas9-poly(A), cryaa:CFP)^{sh596}	

2.1.2 Zebrafish care

Adult zebrafish were maintained in circulating water at a temperature of 28.5^{O}C with a 14hr. day, 10hr. night cycle.

2.1.3 Zebrafish embryo collection and staging

Following collection of embryos by pair-mating, fertilised embryos were maintained in E3 medium (5mM NaCl, 0.17mM KCl, 0.33mM $CaCl_2$, 0.33mM $MgSO_4$) at 28.5^{O}C. Embryos were staged according to Kimmel et. al. (1995). When required, development of WT embryos was slowed by incubating at 23-24^{O}C and subsequently restaged according to Kimmel et. al. (1995). Embryos older than 24hpf for use in light-sheet microscopy, *in situ* hybridisation, fluorescent *in situ* hybridisation or immunohistochemistry were transferred into E3 medium containing 0.003% 1-phenyl 2-thiourea (PTU, Sigma P7629) to inhibit pigment formation and aid imaging.

Prior to fixation, embryos were dechorionated by hand using Jewellers forceps (Dumont no. 5). Embryos older than 48hpf were incubated in 0.2M KCl in E3 medium containing 0.0003% PTU for 30 minutes at 28.5^{O}C prior to fixation, arresting the heart to standardise contraction phase of the heart for subsequent imaging.

Embryos were fixed overnight in 4% paraformaldehyde (PFA, Cell Signalling Technology #12606), washed 3 times in PBST for 5 minutes at room temperature and then serially washed into 100% MeOH for long term storage at -20^{O}C.

2.1.4 Micro-injection

Glass injection needles were prepared using a P-1000 Flaming/Brown Micropipette Puller with Borosilicate Glass Capillaries from Word Precision Instruments. Needles were loaded using micro loader tips, and attached to a PV820 Pneumatic PicoPump (World Precision Instruments). The needle tip was broken under a dissecting microscope using Jewellers forceps and the tip immersed in Mineral Oil (Sigma M5904) placed on a Stage Micrometer (Agar Scientific L4201). Droplet size was adjusted to 0.5nL as measured by a Micrometer.

Embryos were collected from pair-mated adult zebrafish and loaded onto a 1.5% Agarose gel mould (made with E3 medium) and covered with E3. Embryos were injected as described below and subsequently transferred into fresh E3. At approximately 1hour old, embryos negative for Phenol Red (Sigma P0290) or embryos that appeared unfertilised or dead were discarded.

2.1.4.1 DNA morpholino oligonucleotide injections

The following morpholinos were used in this study:

Table 2.2 Morpholino sequences

Gene target	Sequence	Reference
tp53	GCGCCATTGCTTTGCAAGAATTG	(Langheinrich et. al. 2002) (ZFin *tp53-MO4*)
tnnt2a	CATGTTTGCTCTGATCTGACACGCA	(Sehnert et. al. 2002) (ZFin *tnnt2a-MO1*)
lamb1b ATG	ACGATGAGGCTTTTCCACACTACAG	This study
smg1	AACCATTGGTTTGTTACCTGGTGCA	Witkopp et. al. 2009 (ZFin *smg1-MO2*)
upf1	TTTTGGGAGTTTATACCTGGTTGTC	Witkopp et. al. 2009 (ZFin *upf1-MO2*)
gata1a	CTGCAAGTGTAGTATTGAAGATGTC	Galloway et. al. 2005 (ZFin *gata1a-MO1*)

Morpholinos (Table 2.2) were ordered from GeneTools (www.gene-tools.com, except *gata1a*, a gift from J. Serbanovic-Canic) at 300nM for target of interest or 100nM for *tp53*. Morpholinos were reconstituted to 1mM working stock in MilliQ water (MQ). Resuspended morpholinos were heated at 60^{O}C for 10 minutes to ensure the morpholino was in solution and left to cool to room temperate before use.

Morpholinos were stored at -20^{O}C. Prior to each use the morpholino was first defrosted at room temperature, then heated at 60^{O}C for 10 minutes to ensure the morpholino was in solution.

The following concentrations of morpholinos were used:

Table 2.3 Morpholino dilutions

Gene target	Concentration	Dilution factor
tp53	0.25mM	1 in 4
tnnt2a	0.125mM	1 in 8
lamb1b ATG	0.5mM	1 in 2
smg1	0.5mM	1 in 2
upf1	100µM	1 in 10
	50µM	1 in 50
	12.5µM	1 in 80
	10µM	1 in 100
gata1a	1423.7ng	1 in 5

2.1.4.2 RNA injections

For live imaging of the Hyaluronan sensor ssNcan-GFP (Grassini et al., 2018) a 1nL injection volume containing *ssNcan-GFP* mRNA (186pg) and Phenol Red (25%) was injected into the yolk of one-cell stage embryos.

To increase blood viscosity, *epoa* mRNA was injected. A plasmid containing the *epoa-203* (danRer10/GRCz10) coding sequence (Paffett-Lugassy et al., 2007), was linearised with NotI and transcribed with SP6 (see 2.2.8). A 1nL injection into the yolk of the single-cell stage embryo containing: *epoa* mRNA (20pg) (Paffett-Lugassy et al., 2007) and Phenol Red (25%) was carried out. Sham injection controls replaced *epoa* mRNA with MQ water, maintaining Phenol Red at 25%.

2.1.5 Drug treatments

2.1.5.1 DAPT. (N-[N-(3,5-Difluorophenacetyl)-L-alanyl]-S-phenylglycine t-butyl ester)

DAPT powder (Merck D5942-5MG) was dissolved in 231µL 100% DMSO (Sigma 276855) to give a stock concentration of 50mM (5mg/231µl). Prior to treatment, embryos were manually dechorionated and 20 embryos were placed in each well of a 6-well plate. Stock DAPT was diluted 1:500 in E3-PTU to give a final concentration of 100µM DAPT (in 0.2% DMSO), and 3mL was added to treatment wells. In addition, two control groups were included: 3mL of E3-PTU, E3-PTU with 0.2% DMSO (vehicle control). Embryos were incubated in DAPT or control medium from 22hpf to 55hpf, at which point the drug was removed by briefly rinsing embryos in E3 medium, and embryos were subsequently fixed in 4% PFA overnight at 4^{O}C.

2.1.5.2 NMDi14. 4,5-Dimethyl-2-[[2-(1,2,3,4-tetrahydro-6,7-dimethyl-3-oxo-2-quinoxalinyl)acetyl]amino]-3-thiophenecarboxylic acid ethyl ester, Ethyl 2-{[(6,7–dimethyl–3-oxo-1,2,3,4-tetrahydro-2-quinoxalinyl)acetyl]amino}-4,5-dimethyl-3-thiophenecarboxylate

NMDi14 (henceforth NMDi) powder (Merck 530838) was dissolved in 4810µL 100% DMSO to give a stock concentration of 5mM (10mg/4810µL). Prior to treatment, embryo chorions were opened to improve access of the drug during development. 20 embryos obtained from a *lamb1a*$^{\Delta 25}$/+ incross were placed in each well of a 6-well plate. Stock NMDi was diluted 1:500 in E3-PTU to give a final concentration of 10µM, or diluted 1:250 in E3-PTU to give a final concentration of 20µM. Both drug treatments had a final concentration of 1% DMSO. Two control groups for each concentration of NMDi were included: E3-PTU and E3-PTU with 1% DMSO (vehicle control). Embryos were incubated in 3mL of NMDi or control medium from 8hpf to 55hpf, when the drug was removed by briefly rinsing embryos in E3 medium, and embryos were subsequently fixed in 4% PFA overnight at 4^{O}C. During treatment embryos were covered due to the light sensitive properties of the drug.

2.1.5.3 XMD17-109 (ERK5i). 11-Cyclopentyl-2-((2-ethoxy-4-(4-(4-methylpiperazin-1-yl)piperidine-1-carbonyl)-phenyl)amino)-5-methyl-5H-benzo[e]pyrimido[5,4-b][1,4]diazepin-6(11H)-one

A stock of 10mM XMD17-109 (henceforth ERK5i) was a gift from S. Johnston. Prior to treatment, embryos were manually dechorionated and 20 embryos (10 *lamb1a*$^{\Delta 25}$ mutants and 10 siblings) were placed in each well of a 6-well plate. Stock ERK5i was diluted 1:10,000 in E3 to give a final concentration of 1µM and the final concentration of DMSO was 1%. The two control groups were: E3, and E3 with 1% DMSO (vehicle control). Embryos were incubated in 3mL of ERK5i or control medium from 24hpf to 55hpf, at which point the drug was removed by briefly rinsing embryos three times in E3 medium. Embryos were left to develop until 72hpf and subsequently fixed in 4% PFA overnight at 4^{O}C. During treatment embryos were covered due to the light sensitive properties of the drug.

2.2 Molecular Techniques

2.2.1 Isolation of total RNA

At the appropriate stage 50 dechorionated embryos of the relevant genotype were placed into an Eppendorf with TriReagent (Invitrogen AM9738) and homogenised, followed by addition of one-fifth volume of chloroform and well mixed. Following a 5 minute incubation at room temperature the two liquid phases were separated by ultra-centrifugation at 15000rpm for 15 minutes at 4^{O}C. The aqueous phase was removed to a new Eppendorf where an equal volume of Propan-2-ol (Isopropanol) was added, mixed and incubated at room temperature for 15 minutes. RNA was pelleted by ultra-centrifugation at 15000rpm for 15 minutes at 4^{O}C, the resulting pellet was washed twice in 75% Ethanol and then left to air dry at room temperature. RNA was resuspended in 30µL DDW (Double distilled water/RNAse free water) and subsequently diluted to 500ng/µL.

2.2.2 Generation of cDNA

2.2.2.1 Verso

cDNA generated by Reverse Transcription using Verso cDNA synthesis kit (Invitrogen AB-1453/A) with 500ng of RNA template. A 20µL reaction was assembled at room temperature (Table 2.4) and incubated at 42^{O}C for 20 minutes, 2 minutes at 95^{O}C and then diluted 1:2 with MQ.

Table 2.4 Verso cDNA Reverse Transcription reaction

Reagent	Volume (µL)
5X cDNA synthesis buffer	4
dNTP mix	2
Oligo dTs	1
RT enhancer	1
Verso	1
500ng RNA	X
DDW	11-X

2.2.2.2 Superscript IV

cDNA generated by Reverse Transcription using Superscript IV Reverse Transcriptase (ThermoFisher 18090010) with 2µg of RNA template. OligodT primers (Invitrogen 12577-011) were annealed to the RNA template at 65^{O}C for 5 minutes (Table 2.5). The reverse transcription reaction mix (Table 2.6) was added to the annealed RNA-OligodT, incubated at 42^{O}C for 2 minutes before adding 2µL Superscript RT IV enzyme and incubated for 50 minutes at 42^{O}C, followed by 15 minutes at 70^{O}C. 2µL of RNAseH (Thermo EN0201) was added to degrade the RNA template and incubated at 37^{O}C for 20 minutes. cDNA was diluted with 40µL DDW and the concentration measured by NanoDrop to control for variability in cDNA synthesis for subsequent PCR.

Table 2.5 RT-OligodT Mix

Reagent	Volume (µL)
2µg RNA	X
10mM dNTPs	2
Oligo dTs (500ng/µL)	2
MQ	12-X

Table 2.6 RT-Reaction Mix

Reagent	Volume (µL)
5X First Strand Buffer	8
25mM $MgCl_2$	8
0.1mM DTT	4
RNAse Out	2

2.2.3 Polymerase Chain Reaction (PCR) and Sequencing

2.2.3.1 Primer design

Primers were designed using Primer3 (http://primer3.ut.ee/) or manually. Primers were ordered from Integrated DNA Technologies (IDT), reconstituted at 100µM in MQ and stored at -20^{O}C.

2.2.3.3 BioMix Red

Standard PCRs were 10µL BioMix Red (BiolineBIO25006) as detailed in Table 2.7 and the programme carried out in a BioRad Thermocycler (Table 2.8).

Table 2.7 BioMix Red PCR

Reagent	Volume (µL)
cDNA/gDNA	1
Forward Primer (10µM)	0.2
Reverse Primer (10µM)	0.2
BioMix Red	5
MQ	3.7

Table 2.8 BioMix PCR Programme

Step	Temperature	Time
1	95^{O}C	3min.
2	95^{O}C	30s
3	Annealing Temp. (55^{O}C-58^{O}C)	30s/kb
4	72^{O}C	1min.
5	Repeat steps 2-4 n times (typically 30)	
6	72^{O}C	5min.
7	5^{O}C	5min.

2.2.3.4 Phusion Taq

PCR products of full-length coding sequences were generated using Phusion-Taq Polymerase (NEB M0530S) in a 50µL reaction detailed in Table 2.9 and the programme carried out in a BioRad Thermocycler (Table 2.10)

Table 2.9 Phusion Taq Reaction

Reagent	Volume (µL)
MQ	35
5X High Fidelity Buffer	10
10mM dNTPs	1
Forward Primer (10µM)	1
Reverse Primer (10µM)	1
cDNA	1
Phusion-Taq	1

Table 2.10 Phusion PCR Programme

Step	Temperature	Time
1	98^{O}C	3min.
2	98^{O}C	30s
3	Annealing Temp. (55^{O}C-58^{O}C)	30s/kb
4	72^{O}C	1min.
5	Repeat steps 2-4 40 times	
6	72^{O}C	10min.
7	5^{O}C	5min.

2.2.3.5 Sequencing

Where PCR products were required to be sequenced, a 60µL BioMix Red reaction was carried out and purified using a QIAGEN PCR Purification kit (QIAGEN 28016). Purified PCR products were sequenced by Sanger at the Sheffield University Genomics Core Facility.

2.2.4 TOPO-TA Cloning

The DNA sequence to be ligated was amplified from 55hpf cDNA obtained from WT embryos in a 10µL BioMix Red PCR, using sequence specific primers (See relevant sections or appendix). 5µL of the resulting PCR product was resolved by 1% TAE gel electrophoresis to determine efficiency of reaction and the remaining 5µL was diluted accordingly with MQ prior to cloning.

The PCR product was blunt end ligated into either pCRII-TOPO (ThermoFisher 450640) or pCR4-TOPO (ThermoFisher 450071) at room temperature for 5 minutes (Table 2.11) and kept at 4^{O}C before 1µL was used for transformation into either TOP10 cells (ThermoFisher C404003) or DH5α sub-cloning efficiency cells (ThermoFisher 18265017) (See 2.2.7).

Table 2.11 TOPO reaction volumes

Reagent	Volume (µL)
(Diluted) BioMix PCR product	1
Salt solution	0.5
pCR4-TOPO/pCRII-TOPO	0.5
MQ	1

2.2.5 Gateway cloning: generation of middle entry vectors

The following Gateway plasmids were used in this work (Table 2.12):

Table 2.12 Gateway plasmids used

Construct	Reference
p5E-myl7	Palencia-Desai et. al. 2015
p5E-Ubi	Mossiman et. al. 2011
p5E-hsp70	Kwan et. al. 2007
p5E-fli1a	Villefranc et. al. 2007
pME-rhoca	Generated in this study
pME-lamb1b	
pME-hapln1a	
pME-dCas9	Savage et. al. 2019
p3E-poly(A)	Kwan et. al. 2007
pDestTol2pA3	Bakkers lab
pDestTol2pA2-cryaa:CFP	Savage et. al. 2019

2.2.5.1 Primers used for cloning of middle entry vectors

The following primers were used to clone *lamb1b* into pCR4-TOPO (Table 2.13):

Table 2.13 Primers for cloning of *lamb1b*

	Sequence	Short Name
lamb1b ORF-F	AACACTGCTGGAGAACAAGC	CD22
lamb1b ORF-R	TTAAGCGCAGGTGCTGTAGA	EN111

The following primers were used to isolate relevant coding sequences flanked by attB sites (Table 2.14):

Table 2.14 Primers used in cloning of pME

	Sequence (att sites, *Kozak*, Sequence Specific)
lamb1b-F	GGGGACAAGTTTGTACAAAAAAGCAGGCTT*GCCGCCACC*ATGAGGCTTTTCCAC ACTACAG
lamb1b-R	GGGGACCACTTTGTACAAGAAAGCTGGGTTTAAGCGCAGGTGCTGTAGA
rhoca-F	GGGGACAAGTTTGTACAAAAAAGCAGGCTT*GCCGCCACC*ATGGCGGCTATCAGG AAAAAG
rhoca-R	GGGGACCACTTTGTACAAGAAAGCTGGGTTCACAACAGTGAGCACCCGC
hapln1a-F	GGGGACAAGTTTGTACAAAAAAGCAGGCTTC*GCCGCCACC*ATGATTGCTCTGTTT TCTGT
hapln1a-R	GGGGACCACTTTGTACAAGAAAGCTGGGTTTTACTGCTGGGCTTTGTAGCAATA

The Kozak sequence (Table 2.14, red) was used to increase the efficiency of transcription (Kozak, 1987).

2.2.5.2 Generation of *pME-rhoca/pME-hapln1a*

The coding sequence of *rhoca* or *hapln1a* was amplified from 24hpf cDNA using Phusion-Taq polymerase (Table 2.9 (NEB M0530S)), resolved by gel electrophoresis and subsequently purified by QIAGEN Gel Extraction kit (QIA 28704) into 30µL MQ. The concentration and purity of the PCR product was determined by NanoDrop. The PCR product was subsequently ligated into pDONR221 using BP Clonase II (ThermoFIsher 11789020) overnight at 25^{O}C (Table 2.15). Following recombination, 1µL of ProteinaseK (supplied with the kit) was added to the reaction for 10 minutes at 37^{O}C. Constructs were stored at 4^{O}C until transformation into TOP10 cells (see 2.2.7) and grown on LB Agar plates with Kanamycin (50µg/mL). Single colonies were assayed for presence of pME by Colony PCR (see 2.2.7) using the primers used to generate original PCR product (Table 2.14). A single positive bacterial colony was used to inoculate 50mL LB midi cultures, which were grown overnight at 37^{O}C.

Plasmid DNA was recovered using QIAGEN Midi-Prep kit (QIA 12143) and resuspended in 100µL MQ, followed by Sanger sequencing to confirm correct recombination had occurred and no point mutations had been introduced by the PCR.

Table 2.15 BP Reaction for pME

Reagent	Volume (µL)
TE (pH8.0)	8-X-Y
90ng attB1-gene-attB2	X
150ng pDONR221	Y
BP Clonase II Plus	2

2.2.5.3 Generation of *pME-lamb1b*

The *lamb1b* coding sequence was isolated by PCR with Phusion Taq from 24hpf cDNA and blunt-end ligated into the pCR4-TOPO-Seq vector (See 2.2.4). Successful integration of the insert was confirmed by colony PCR and Sanger sequencing as described above (See 2.2.7). The resulting *pCR4-lamb1b* plasmid (50ng) was used as a PCR template to generate a *lamb1b* PCR product with attB sites. Gateway cloning and all subsequent steps to generate *pME-lamb1b* were performed as described above (2.2.5.2).

2.2.6 Gateway cloning: generation of LR constructs

Generation of final Gateway constructs was carried out by incubating 20fM of p5ME, pME, p3E and pDest together with LR Clonase II (Table 2.16 (ThermoFisher 12538120) overnight at 25^{O}C (see Table 2.17 for relevant cassettes). Following recombination, 1µL of ProteinaseK (supplied with the kit) was added to the reaction for 10 minutes at 37^{O}C. Constructs were stored at 4^{O}C until transformation into TOP10 cells (See 2.2.7) and were grown overnight at 37^{O}C on LB Agar plates with Ampicillin (100µg/mL). Colonies were picked from agar plates and used to inoculate 3mL LB Broth with Ampicillin (100µg/mL) and grown at 37^{O}C overnight in a shaking incubator (New Brunswick Scientific, innova 44). Plasmid DNA was isolated by QIAGEN Mini-Prep (QIA 27106) and diagnostic restriction digests were carried out to confirm correct orientation and recombination order of all cassettes in the final plasmid. A single colony containing the correct final plasmid was grown overnight at 37^{O}C in 50mL LB with Ampicillin. Plasmid DNA was recovered by QIAGEN Midi-Prep and eluted into 100µL MQ, followed by Sanger sequencing to confirm correct recombination had occurred.

Table 2.16 LR Reaction

Reagent	Volume (µL)
TE (pH8.0)	4
20fM p5E	1
20fM pME	1
20fM p3E	1
20fM pDest	1
LR Clonase II Plus	2

Table 2.17 LR constructs generated

Construct	*p5E*	*pME*	*p3E*	*pDest*
fli1a:lamb1b-poly(A)	*fli1a*	*lamb1b*	*poly(A)*	*pDestTol2pA3*
fli1a:rhoca-poly(A)	*fli1a*	*rhoca*		
hsp70:lamb1b-poly(A)	*hsp70*	*lamb1b*		
hsp70:rhoca-poly(A)	*hsp70*	*rhoca*		
ubi:dCas9-poly(A)	*ubi*	*dCas9*		*pDestTol2pA2-cryaa:CFP*
myl7:hapln1a-poly(A)	*myl7*	*hapln1a*		*pDestTol2pA3*

2.2.7 Bacterial transformation

Chemically competent cells were thawed on ice. 1µL of ligation reaction was added to the competent cells (typically 50µL), gently mixed and incubated on ice for 30 minutes. For TOP10 transformation, cells were heat-shocked at 42^{O}C for 30 seconds, and DH5α sub-cloning cells were heat-shocked at 42^{O}C for 20 seconds. Following heat shock, cells were incubated on ice for 2 minutes, before addition of 250µL of SOC medium (Sigma S1797). Cells were then placed horizontally in a shaking incubator at 225rpm for 90 minutes at 37^{O}C.

Transformed cells were pelleted at 3000rpm for 5 minutes at room temperature and the pellet resuspended in 30µL of the SOC supernatant. Cells were plated on LB agar (Sigma L7025) containing either Kanamycin (Sigma K1377. 50µg/mL) or Ampicillin (Sigma A0166. 100µg/mL) together with IPTG (0.1M Merck I6758) and X-Gal (20mg/mL. Thermo-Fisher R0404) for blue-white selection where appropriate and incubated at 37^{O}C overnight.

To identify colonies positive for the plasmid with successful ligation of PCR product, up to 8 white colonies were resuspended individually in 10µL MQ. 5µL of colony resuspension was used as a template for colony PCR (Tables 2.18 and 2.19), using primers that were originally used to clone the fragment. 10µL of the PCR was resolved by 1% TAE gel electrophoresis and the remaining 5µL of MQ that

contained a positive colony was grown in 50mL of LB (Sigma L72275) with relevant antibiotic overnight at 37^{O}C with agitation. The plasmid containing the inserted DNA sequence was isolated using a QIAGEN Midi-Prep kit. Sanger sequencing using M13F and M13R primers (Sheffield Core Genomics Facility) was used to identify the orientation of the insert in the vector for transcription of the anti-sense mRNA probe.

Table 2.18 Colony PCR volumes

Reagent	Volume (µL)
Colony in MQ	5
Forward Primer (10µM)	0.4
Reverse Primer (10µM)	0.4
BioMix Red	10
MQ	4.2

Table 2.19 Colony PCR Programme

Step	Temperature	Time
1	94^{O}C	2min.
2	94^{O}C	20s
3	60^{O}C (drops 1^{O}C per cycle)	20s
4	72^{O}C	45s
5	Repeat steps 2-4 9 times	
6	94^{O}C	20s
7	50^{O}C	20s
8	72^{O}C	45s
9	Repeat steps 6-8 14 times	
10	72^{O}C	3min.
11	10^{O}C	5min.

2.2.8 mRNA transcription or riboprobe synthesis and cleanup for *in situ* hybridisation

To generate the template for mRNA transcription, 15µg of relevant plasmid DNA was digested overnight in a 50µL reaction (Restriction enzymes from New England BioLabs, Tables 2.20, 2.21 and 2.22). Following linearisation, the template was purified using a QIAGEN PCR Purification kit and eluted into 30µL MQ. A 1:5 dilution of digested plasmid DNA together with a 1:10 dilution of undigested plasmid was resolved by gel electrophoresis to confirm linearisation, and the concentration of the linaearised template was assayed by NanoDrop.

Following linearisation, a transcription reaction using 1µg of linearised template in the presence of either digoxigenin-UTP (Roche 11277073910) or fluorescein-UTP (Roche 11685619910) to label the RNA probe was incubated at 37^{O}C for 2hrs (Tables 2.20, 2.21 and 2.22). Subsequently 3µL of TURBO DNAase (Invitrogen AM2238) was added to the transcription reaction for 30 minutes at 37^{O}C to remove the DNA template. The RNA probe was recovered using an Ammonium Acetate precipitation and ultracentrifugation at 15000rpm for 15 minutes at 4^{O}C.

The resulting RNA pellet was reuspended in 10-20µL DDW depending on size a 1:5 dilution of the RNA was resolved by gel electrophoresis to confirm integrity of RNA.

Where RNA was to be used for mRNA *in situ* hybridsation (2.4, 2.4), Hyb- or Formamide (See Table 2.23) or was added to the RNA probe, which was stored at -20^{O}C.

Where mRNA was to be injected (2.1.4.2), a 1:10 dilution was used to assay concentration and purity and then subsequently diluted to the necessary concentration. A working concentration was stored at -20^{O}C and the stock mRNA was stored at -80^{O}C.

2.3 mRNA *in situ* hybridisation (ISH)

2.3.1 Probes generated for this work

Table 2.20 Probes generated for this work

Probe target	Vector	Linearisation	Transcription	Plasmid number
lamb1a	pCR4-TOPO	NotI	T3	pCD10
has2	pCR4-TOPO	NotI	T3	53
rhocb	pCR4-TOPO	SpeI	T7	pCD11
lamb2l	pCRII-TOPO	NotI	SP6	pCD13
lamb4	pCRII-TOPO	NotI	SP6	pCD14
tbx2b	pCRII-TOPO	NotI	SP6	82
itga6a	pCRII-TOPO	NotI	SP6	pCD18
itga6b	pCRII-TOPO	NotI	SP6	pCD19
itgb4	pCRII-TOPO	NotI	SP6	pCD20
tbx5a	pCRII-TOPO	NotI	SP6	83
rhoca	pCRII-TOPO	NotI	SP6	pCD27
itga7	pCRII-TOPO	NotI	SP6	pCD23
acana	pCRII-TOPO	NotI	SP6	pCD25
acanb	pCRII-TOPO	NotI	SP6	pCD26
dCas9	pCRII-TOPO	NotI	SP6	132
chsy1	pCRII-TOPO	BamHI	T7	105

See Appendix for primer sequences

2.3.2 Probes generated for this work by others

Table 2.21 Probes cloned by other members of the lab

Probe target	Made by	Linearisation	Transcription	Plasmid number
lama4	E. Pollitt	NotI	T3	31
lama5	E. Pollitt	SpeI	T7	32
lamc1	E. Pollitt	NotI	T3	33
itga3b	E. Pollitt	SpeI	T7	35
itga5	E. Noël	NotI	T3	12
itgb1a	E. Pollitt	NotI	T3	34
lamb2	A. Uruchurtu	NotI	SP6	97
hapln1a	E. Noël	SpeI	T7	11

2.3.3 Probes previously generated in other works

Table 2.22 Probes previously published

Probe target	Reference	Linearisation	Transcription	Plasmid number
myl7 (cmlc2)	Yelon et. al. 1999	NotI	T7	143
myh7l (vmhcl)	Bakkers lab	NotI	T7	81
myh6 (amhc)		PstI	T7	2
lamb1b	Sztal et. al. 2011	NcoI	SP6	4
nfatc1	Lagendijk et. al. 2011	NcoI	T7	59
nppa (anf)	Berdougo et. al. 2003	NotI	SP6	57
bmp4	Chen et al 1997	EcoRI	T7	54
notch1b	Rob Wilkinson, unpublished	HindIII	T7	142, 145
vcana (vcan)	Kang et al 2004	From T. Whitfield		
vcanb				
klf2a	Novodvorsky et. al. 2015	From. T Chico		
hbbe1.1	Quinkertz and Campos-Ortega et. al. 1999	XhoI	T3	164

2.3.4 mRNA *in situ* hybridisation protocol

Based on Thisse and Thisse (2007)

Embryos stored in MeOH were serially rehydrated into PBST (Table 2.23), washed four times in PBST and then permeabilised with Proteinase K (PK) in PBST (10µg/mL ProteinaseK in PBST), with length of incubation dependent on embryonic stage (Table 2.24). Following a rinse in PBST, embryos were refixed in 4% PFA for 20 minutes at room temperature, washed 5 times in PBST at room temperature for 5 minutes and pre-hybridised in Hyb+ (50µg/ml Heparin (Merck 2106), 500µg/mL Yeast tRNA (Invitrogen 15401-29) in Hyb- See Table 2.26) at 70^{O}C with gentle

agitation. Following a minimum of 1hr in Hyb+, Hyb+ was removed and digoxygenin- and/or fluorescein-labelled probes in Hyb+ (Tables 2.20, 2.21, 2.22, 2.23) at appropriate dilutions were added to the embryos and incubated at 70^{O}C overnight with gentle agitation. After probe removal, embryos were serially washed from Hyb- into 2xSSCT (1:10 20X SSC, 0.2% Tween-20) and then washed twice in 0.2xSSCT (1:100 20X SSC, 0.2% Tween-20) at 70^{O}C. Following this, embryos were transferred by step-wise washes into PBST at room temperate and then washed twice in PBST. Embryos were blocked in Blocking buffer (2% Serum (Sigma S3772), 2mg/mL Bovine Serum Albumin (Sigma A9418) in PBST) for a minimum of 2hrs at room temperature prior to incubation with a pre-incubated anti-DIG-AP conjugated antibody (1 in 5000 (Roche 11093274910)) or anti-Fluo-AP conjugated antibody (1 in 5000 (Roche 11426338910)) (see below) in blocking buffer overnight at 4^{O}C with gentle agitation. The antibody was removed and embryos were washed a minimum of 8 times in PBST over 2-4hrs at room temperature and then washed 3 times in AP-staining buffer (Table 2.23). Embryos were then incubated with Nitro-blue tetrazolium/5-bromo-4-chloro-3-inodyl phosphate (NBT/BCIP (Roche 11681451001)) diluted 1:50 or Iodonitrotetrazolium/5-bromo-4-chloro-3-inodyl phosphate (INT/BCIP (Roche 1168146001)) diluted 3:400 in AP-Staining Buffer and protected from the light for the remainder of the protocol. Upon visual inspection of sufficiently developed staining, embryos were rinsed 3 times in PBST, fixed in 4% PFA overnight at 4^{O}C and subsequently serially washed into 100% MeOH or 50% glycerol for long term storage at 4^{O}C. When examining levels of gene expression in embryos subjected to different interventions that could not be separated post-image acquisition (morpholino or drug treatments and their respective controls), staining was stopped at the same time across all groups.

Preincubation of the antibody was carried out by homogenising embryos of varying stages in PBST and incubating with anti-DIG or anti-Fluo antibody (1:100 dilution) for 1hr at room temperature. Embryos were sedimented by centrifugation at 15000rpm for 15mins at 4^{O}C and the supernatant containing the pre-incubated antibody removed. Sodium Azide (Sigma S8032) was added to the pre-incubated antibody at a final concentration of 0.02% and the antibody solution was stored at 4^{O}C.

Table 2.23 ISH solutions

Name	Composition				
PBST	Phosphate Buffered Saline (Oxoid BR0014G)	0.2% Tween-20 (Sigma P2287)			
20X SSC (50mL) pH 7.0	87.5g NaCl (Sigma S7653)	44.1g Sodium Citrate (VWR 27833.360)	500mL MQ		
Hyb- (50mL)	25mL Formamide (50%) (Sigma 47671)	12.5mL 20XSSC (5X SSC)	500µL 10% Tween-20 (0.1%)	460µl 1M Citric Acid (9.2mM pH 6.0)	10.54mL MQ
AP-Staining Buffer (50mL)	5mL 1M Tris-HCl pH 9.5 (10mM Tris-HCl) (Sigma T1503)	2.5mL 1M $MgCl_2$ (50mM $MgCl_2$)	1mL 5M NaCl (100mM NaCl)	500µL 10% Tween-20 (0.1% Tween-20)	41mL MQ

Table 2.24 ProteinaseK treatment timings

Time (hpf)	Length of PK-PBST treatment (minutes)
19-21	3
24	5
26	6
30	10
33	12
37	15
45-48	20
50	23
55	25
63	35
72-80	45

2.3.5 Imaging *in situ* hybridisations

Embryos stained with NBT/BCIP only were imaged in Murray's Medium (BBA. 2:1 Benzyl Benzoate (Sigma B6630): Benzoic Acid (Sigma 402834)). Embryos stained with NBT/BCIP and INT/BCIP were imaged in 80% Glycerol. Images acquired on an Olympus BX51 Microscope.

2.3.6 Quantification of heart looping and heart area

Images for quantification were blinded using the ImageJ Blind_Analysis plugin (https://github.com/quantixed/imagej-macros/blob/master/Blind_Analysis.ijm), to prevent confirmation bias. Quantification of the ratio of looped distance to linear distance was calculated for each heart in Fiji, using *myl7* expression to demarcate the morphology of the heart (Figure 3.8). Heart/chamber area was quantified by tracing the *myl7*, *myh6* or *myh7l* expression domain in Fiji.

2.3.7 Quantification of *hapln1a* expression domain

Two-colour *in situ* images were split into red, green and blue channels in Fiji and the blue channel discarded. The green channel (representing red (*myl7*), INT stain) was used to define the atrium and ventricle as two regions of interest (ROIs), and the area of each chamber was measured. The red channel (representing blue (*hapln1a*), NBT stain) was thresholded to a standardised level, the chamber ROIs applied and the area of *hapln1a* expression within each ROI measured. Percentage coverage of *hapln1a* could then be calculated for each chamber. The green channel was then processed for heart looping ratio (2.3.7, Figure 3.8)

2.3.8 Genotyping post ISH

Following imaging of individual embryos, single embryos were placed in 50µL SEL-ProteinaseK (see 2.6.1.2) for extraction of gDNA. The gDNA was subsequently diluted 1:1 with MQ, and 1µL used for the relevant genotyping PCR.

2.3.9 Statistical Analysis

Quantitative data was analysed in Prism. Heart looping ratio and *myl7* area are displayed using median and interquartile range, with non-parametric tests applied and multiple comparisons where appropriate.

Individual injected embryos or embryos obtained from mutant incrosses are displayed as individual data points and statistical tests performed based on each embryo representing an individual experimental unit, subjected to small experimental variations. A minimum of two biological repeats were performed, unless otherwise stated.

Quantitative measurements from all embryos subjected to a single drug treatment were averaged to give a single measurement per drug treatment (each drug treatment representing a single experimental unit as all embryos of one repeat are subjected to the same intervention). Each biological repeat of a drug treatment is displayed as individual data points, and statistical tests performed on the arithmetic average of three biological repeats.

2.4 Fluorescent *in situ* hybridisation (FISH)

From MacDonald et. al. (2013) and
https://wiki.zfin.org/display/prot/Triple+Fluorescent+In+Situ

Embryo fixation, dehydration, rehydration, ProteinaseK digestion, re-fixation, PBST washes and pre-hybridisation were carried out as described in the ISH protocol above (2.3.5). To detect the expression of two separate genes in a single sample, Hyb+ containing two RNA probes (one labelled with Digoxygenin and the other Fluorescein) was added to embryos and incubated at 70^{O}C overnight with gentle agitation. After probe removal, embryos were serially washed from 5X (Table 2.25) into 2xSSCT (see 2.3.5) and then 0.2xSSCT at 70^{O}C, followed by step-wise washes into PBST at room temperate washes. Embryos were then incubated in 2% H_2O_2-PBST (H_2O_2: VWR 26222.298) for 1hr with gentle agitation before being blocked in TBST (Table 2.25) for 4hrs at room temperature. TBST was removed and replaced with anti-fluorescein POD-conjugated antibody (1:625 in TBST (Roche 11426346910)) and incubated overnight at 4^{O}C with gentle agitation. Antibody solution was removed and embryos were extensively washed in TNT a minimum of 8 times over 2-3hrs at room temperature before being rinsed in Amplification buffer (Perkin Elmer FP1134) and stained with Tyr-Cy5 (1:50 in Amplification buffer) for 1hr. Following detection of the fluorescein probe, embryos were briefly washed in TNT before being incubated with 2% H_2O_2-TNT, washed in TNT and blocked in TBST for a minimum of 4hrs at room temperature. TBST was removed and replaced with anti-DIG POD-conjugated antibody (1:125 in TBST (Roche 1120773910)) and incubated overnight at 4^{O}C with gentle agitation. Antibody solution was removed and embryos were extensively washed in TNT a minimum of 8 times over 2-3hrs at room temperature before being rinsed in Amplification buffer and stained with Tyr-Cy3 (1:50 in Amplification buffer) for 1hr. Following detection of the digoxygenin probe, embryos were briefly washed in TNT before being incubated with 2% H_2O_2-TNT, washed in TNT and fixed in 4% PFA overnight. Embryos were either mounted in

VectaShield for imaging or washed in PBST and then into TNT for immunohistochemistry (2.8).

Table 2.25 FISH solutions

Name	Composition			
5X (50mL)	25mL Formamide (50%)	12.5mL 20XSSC (5X SSC)	1.25mL 10% Tween-20 (0.25% Tween-20)	11.25mL MQ
TNT (1L)	100mL 1M Tris pH 7.5 (0.1M Tris-HCl)	30mL 5M NaCl (0.15M NaCl)	50mL 10% Tween-20 (0.5% Tween-20)	820mL MQ
TBST	50mL TNT	0.25g Perkin Elmer Blocking Powder (0.5%)		

2.5 CRISPR-Cas9 gRNA Design and Synthesis

2.5.1 gRNAs used

The following gRNAs were used in this study (Table 2.26):

Table 2.26 CRISPR-Cas9 gRNAs used

	crRNA sequence (PAM)	Stable or G0 line	One-part/Two-part	Short name
lamb1b CDS	GGCAGCTGTTACCCTGCGACCGG	Stable - injected by E.Noël	One-part	EN79
lamb1a CDS	GGATCCTCAATCCTGAAGGCAGG	Stable - injected by E.Noël	One-part	EN143
lamb1b promoter 1	TTGTTAATAGCATAGTACATTGG	Stable, co-injected	Two-part	CD95
lamb1b promoter 2	GGAGAACAAGCAAAACGATGAGG		Two-part	CD96
rhoca CDS	GGCGGCTATCAGGAAAAGCTGG	Stable - injected by E.Noël	One-part	EN75
rhocb CDS	GAAGTGGACAGCAAACAGGTGGG	Stable	One-part	CD63
lamc1 F0 1	GGCTTTCAATGCGACCGTGGTGG	F0, co-injected	One-part	EJP7
lamc1 F0 2	GGCGTGCAGTCACGGAGCGATGG		One-part	EJP8
lamb2 F0 1	GGACAGTGTCCATGCCGACCTGG	F0, co-injected	One-part	CD257
lamb2 F0 2	CGAGCCGTCGACAGAAGGAGAGG		One-part	CD269
lamb2 F0 3	TGCCGGAAACTGTACCCCTGGGG		One-part	CD280
lamb2 F0 4	AGACTGTCAGGAGAACCACTGGG		One-part	CD281
lamb1b CRISPRi 1	GCGTGGTGCAGGGTTTGTAGCGG	CRISPRi, co-injected	Two-part	CD107
lamb1b CRISPRi 2	CGCACACATGTCATTGTGATCGG		Two-part	CD108

2.5.2 Ultramer-based, one-part gRNA: crRNA sequence design

One-part gRNAs are a single, RNA oligonucleotide which contains both the sequence-specific CRISPR RNA (crRNA) sequence concatenated with the Cas9 recruiting trans-activating RNA (tracrRNA).

The crRNA sequence of one-part gRNAs were designed using CHOPCHOP v2.0 (Labun et al., 2016) (recently updated to v3.0 https://chopchop.cbu.uib.no/) using danRer10/GRCz10 assembly of the zebrafish genome. Base parameters were unchanged from coding sequence targeting and NGG PAM, however 5' requirements were set to NG or GN for *in vitro* transcription (2.5.3).

Suitable crRNA sequences were selected on the basis of maximal efficiency and minimal off-target scores. For generation of *rhocb* mutants, targeting strategy was to introduce a premature stop codon into the coding sequence. For *lamc1* F0 crRNA selection, both crRNAs were selected for targeting of the start codon (E. Pollitt). For *lamb2* F0 selection, the lookup table available from (Wu et al., 2018) was used to identify 4 regions of interest and crRNAs targeting each region were selected to maximise likelihood of generating sufficient deleterious mutations for F0 analysis.

2.5.3 Ultramer-based, one-part gRNA synthesis

Following selection of suitable crRNA sequence (2.5.2) the first two nucleotides were converted from NG/GN to GG and the Protospacer Adjacent Motif (PAM) sequence (NGG) removed. The reverse complement of the resulting sequence was inserted into the Ultramer skeleton (replacing x), resulting in the placement of a T7 promoter (bold) upstream of the crRNA sequence with the tracrRNA sequence downstream, facilitating transcription of a single one-part gRNA. This DNA Ultramer was ordered from IDT at 4nM, resuspended in MQ to a final concentration of 100μM and stored at -20^{O}C for long term.

Ultramer skeleton sequence (bold denotes T7 promoter):

AAAGCACCGACTCGGTGCCACTTTTTCAAGTTGATAACGGACTAGCCTTATTTTAACTTGCT
ATTTCTAGCTCTAAAACxxxxxxxxxxxxxxxxxxxx**CTATAGTGAGTCGTATTA**CGC

The Ultramer template was amplified in a 100µL BioMix PCR (See Table 2.27 for primer sequence), purified by QIAGEN PCR Purification kit, eluted into 30µL MQ and the concentration measured using a NanoDrop. Subsequently a minimum of 30ng of amplified template was utilised as the template in a T7 MegaShortScript transcription reaction (Invitrogen AM1354 Table 2.28) and incubated for a minimum of 4hrs. at 37^{O}C. Following transcription, 1µL of TURBO DNAse was added to the reaction and incubated at 37^{O}C for 20 minutes to remove the DNA template, before Ammonium Acetate precipitation and ultracentrifugation at 15000rpm for 15 minutes at 4^{O}C. The supernatant was removed and the RNA pellet was resuspended in 10µL DDW and kept on ice. A 1 in 10 dilution of the gRNA was made in order to determine the concentration, whilst a 1 in 50 dilution was resolved by gel electrophoresis to confirm RNA integrity. The remaining gRNA was diluted to the appropriate concentration (see 2.6.1 and 2.6.2) and aliquoted for storage at -20^{O}C to reduce freeze-thaw cycles. Non-aliquoted gRNA was kept at -80^{O}C for long term storage.

Table 2.27 Primers for amplification of Ultramers

	Sequence	PCR programme
gRNA primer F	GCGTAATACGACTCACTATAG	40 cycles, 60^{O}C annealing temperature
gRNA primer R	AAAGCACCGACTCGGTGCCAC	

Table 2.28 MegaShortScript T7 Reaction

Reagent	Volume (µL)
T7 MSS buffer	2
ATP	2
CTP	2
GTP	2
UTP	2
T7 MSS enzyme	2
Amplified ultramer (minimum 30ng)	X
Nuclease Free Water	8-X

2.5.4 sygRNA, two-part gRNA design for generating mutant lines

gRNAs for targeted deletion of the annotated *lamb1b* promoter were designed using ApE (A Plasmid Editor) to encompass the annotated promoter (https://epd.epfl.ch//) and start codon based on danRer10/GRCz10 assembly of the zebrafish genome. 5nM of custom crRNAs and standardised tracrRNA were ordered from Merck/Sigma at 5nM (TRACRRNA05N-5NMOL), both with HPLC purification.

2.5.5 sygRNA, two-part gRNA design for knockdown by CRISPRi

gRNAs for targeted knockdown of *lamb1b* by CRISPRi were designed in line with strand binding considerations where gRNAs targeted to inhibit transcription initiation are not strand specific, and gRNAs designed to block elongation should target the non-template strand (Larson et al., 2013; Qi et al., 2013).

The top seven hits for regions either surrounding the *lamb1b* initiating ATG codon or *lamb1b* Exon 2 were initially defined by CHOPCHOPv2.0 to minimise off-target effects and then ranked by Sequence Scan for CRISPR (SSC: http://cistrome.org/SSC/) on the basis of efficacy for "CRISPR inhibition or

activation". To maximise likelihood of dCas9 recruitment, gRNAs targeting a TGG were discounted and then remaining gRNAs were selected to enrich for +1C and minimise +4T relative to the PAM site (Xu et al., 2015). 5nM of custom crRNAs were ordered from Merck/Sigma at 5nM with HPLC purification.

2.5.6 sygRNA, two-part gRNA reconstitution and storage

Working on ice, both 5nM crRNA and 5nM tracrRNA pellets were resuspended in 10µL DDW to give a stock solution of 500µM. 5µL was stored at -80^{O}C for long term, the remaining 5µL was diluted further by the addition of 6.7µL DDW to give a working stock of 213.5µM. 10µL of this working stock was aliquoted and stored at -20^{O}C, the remaining 1.7µL was diluted 1:10 by the addition of 15.3µL DDW, resulting in an additional working stock of 21.4µM which was aliquoted and stored at -20^{O}C.

2.5.7 Cas9 protein dilution and storage

Cas9 protein (*S. pyogenes*) was ordered from NEB (M0386T, concentration 20µM) and was diluted 1:3 with NEB Dilutent B (300mM NaCl, 10mM Tris-HCl, 1mM DTT, 0.1mM EDTA, 500µg/mL BSA, 50% Glycerol, pH7.4. B8002S), giving a stock concentration of 6.67µM which was aliquoted and stored at -20^{O}C.

2.6 Generation of Zebrafish mutant, knockdown and transgenic lines

2.6.1 Generation of stable mutant lines

2.6.1.1 Micro-injection

lamb1b promoter mutants were generated by injecting two sequence-specific crRNAs (CD95 and CD96 both at 61.2nM), together with tracRNA (122.5nM), Cas9 protein (3.9nM) and Phenol Red (14%) in a 2nL volume into the yolk of at the single-cell stage of embryos obtained from a *Tg(myl7:lifeActGFP)/+* in-cross.

rhocb mutants were generated by injecting a single, one-part ultramer-based gRNA (CD63 33.4pg), Cas9 protein (6.67nM) and Phenol Red (33%) in a 1nL volume into the yolk of at the single-cell stage of embryos obtained from a *Tg(myl7:lifeActGFP)/+* in-cross.

2.6.1.2 Identification and establishment of mutant zebrafish lines by CRISPR-Cas9 mutagenesis

Following micro-injection of gRNA and Cas9 (2.6.1.1), efficiency of mutagenesis was confirmed at 1dpf. Embryos were dechorionated and gDNA extracted in SEL buffer (50mM KCl, 2.5mM $MgCl_2$, 10mM Tris pH8.3, 0.005% NP40, 0.005% Tween-20, 0.001% Gelatine) with 100µg/mL ProteinaseK (Ambion AM2542) by incubation at 60^{O}C for 1hr then 95^{O}C for 15 mins to denature the Proteinase K. gDNA was subsequently diluted 1:1 with MQ. 1µL of gDNA was used as a template for PCR (for primers used see Table 2.29). The presence of potential PCR heteroduplexes, indicating successful targeted mutagenesis, was examined by resolving the PCR products on a 4% TBE (89mM Tris-HCl, 89mM Boric Acid, 2mM EDTA) gel.

Upon confirmation of successful mutagenesis, a subset of injected embryos were grown to adulthood (F0) and subsequently screened by outcrossing to WT adults and collecting embryos to assess transmission of a suitable germ-line mutation using the PCR heteroduplex assay described above. Sanger sequencing was used to identify the nature of the lesion, and F0 founders transmitting suitable mutations were selected to establish stable lines.

Remaining embryos were grown to adulthood (F1) and gDNA extracted from fin biopsies (fin-clips) was utilised to identify heterozygous mutant adults. Sanger sequencing at Sheffield University Core Genomics Facility was used to confirm the mutation in each case.

Table 2.29 CRISPR-Cas9 genotyping

	Sequence	Annealing Temperature and no. cycles	Genotyping
lamb1bCDS-F	AGCTATTGCTCTGCACACTTTG	58^{O}C, 31 cycles	*lamb1b*$^{\Delta 2}$: BslI digestion. Mutant allele has lost restriction site. *lamb1b*$^{\Delta 25}$: Can resolve differences in size of PCR product.
lamb1bCDS-R	TGAACAATAAAAACGAGGGCTT		
lamb1aCDS-F	CTTCTGTCTCTCATGGGCCA		Can resolve differences in size of PCR product for either allele.
lamb1aCDS-R	TGCCTTTACTTTGAATTCTGGGG		
lamb1bprom-F	TCACACTAAGACATGGGGCA		Can resolve differences in size of PCR product for either allele.
lamb1bprom-R	ACCAAGCAACCAAAACACTGA		
rhocaCDS-F	AAAGATTAGGCTGATTGGGGTT		*rhoca*$^{\Delta ATG}$: Can resolve differences in size of PCR product. *rhoca*^{ins10}: AhdI digestion. Mutant allele has introduced restriction site.
rhocaCDS-R	CTCGAACACAGTAGGCACGTA		
rhocbCDS-F	AGCTATCCGTAAGAAGCTGGTG		Can resolve differences in size of PCR product for either allele.
rhocbCDS-R	ATAAACGCACATATGCTTGCAC		

2.6.1.3 Analysis of *lamb1b* coding sequence mutations on *lamb1b* mRNA splicing

Homozygous mutant embryos for either *lamb1b*$^{\Delta 2}$ or *lamb1b*$^{\Delta 25}$ were collected by incrossing adult homozygous mutants for the respective mutations. WT embryos were collected from an incross of *Tg(myl7:eGFP)/+*. cDNA was reverse transcribed using Superscript reverse transcriptase from RNA isolated at 55hpf from each genotype as described above (2.2.2.2).

PCR primers were designed to amplify two 500bp regions at the 5' end (Table 2.30) of the *lamb1b-201* coding sequence (using danRer10/GRCz10 assembly of the zebrafish genome), using an annealing temperature of 58°C over 31 cycles. The resulting PCR products were purified and sequenced as described above (2.6.1.2).

Table 2.30 *lamb1b* splicing primers

Pair no.	Sequence	Amplicon size (bp)	Short name
Pair 1	CTCTTCTCCCACGATCCACA	450	CD191
	TTCAGCCTCCAAATCCAGCT		CD192
Pair 2	GGTGTACCGCTACTACGCTT	503	CD193
	CGTTTGTCTCTCGGCCTACT		CD194

2.6.1.4 Analysing the effect of the *rhoca*$^{\Delta ATG}$ mutation on *rhoca* mRNA splicing

rhoca$^{\Delta ATG}$ homozygous mutant embryos were obtained from an incross of *rhoca*$^{\Delta ATG}$ homozygous mutant adults. WT embryos were collected from an in-cross of *Tg(myl7:eGFP)/+*. Two regions of the *rhoca-201* coding sequence (danRer10/GRCz10 genome assembly) were amplified by PCR (primers in Table 2.31), purified and sequenced as above.

Table 2.31 *rhoca* splicing primers

Pair no.	Sequence	Amplicon size (bp)	Short name
Pair 1	TGTGTGCATGTGGATTGAGC	837	EN35
	CTCCAACTTGCCTCAACACC		EN36
Pair 2	CGGCGAGTCAGATTCCCATT	226	CD159
	CGGTCATAGTCCTCCTGTCC		CD160

2.6.2 Generation of transient CRISPR F0 mutant lines

Generation of F0 mutants was carried out according to (Wu et al., 2018). One-part, ultramer-based gRNAs were designed and synthesised as described previously (2.5.1, 2.5.2., 2.5.3).

For generation of *lamc1* F0 mutants, two *lamc1*-targeting gRNAs (*lamc1* F0 1 and *lamc1* F0 2 500pg each, Table 2.32) were injected together with Cas9 protein (1.9nM) and Phenol Red (14%) in a volume of 1nL into the yolk of embryos obtained from either WT or *lamb1a*$^{\Delta 25}$ incross.

For generation of *lamb2* F0 mutants, four *lamb2* targeting one-part gRNAs (*lamb2* F0 1, F0 2, F0 3 and F0 4 each at 214.3pg, Table 2.32) were injected together with Cas9 protein (1.9nM) and Phenol Red (14%) in a 1nL volume into the yolk of embryos obtained a *lamb1a*$^{\Delta 25}$ incross.

Injection mixtures were assembled on ice and prior to loading into micro-injection needle were incubated at 37^{O}C for 5 minutes to aid Cas9-gRNA Ribonucleoprotein complex formation for more efficient mutagenesis (Burger et al., 2016; Wu et al., 2018).

2.6.2.1 Confirmation of F0 gRNA targeting

To confirm F0 gRNA efficiency, gDNA was extracted from injected embryos and PCR amplification of targeted regions carried as described in 2.6.1.2, using primers (Table 2.32).

Table 2.32 CRISPR-Cas9 F0 genotyping

	Sequence	Short Name	Genotyping
lamc1 F0 1/2-F	ATCAAGACAGTGACGGTAGCAA	EP19	Confirm gRNA cuts, genotype *lamc1 F0*
lamc1 F0 1/2-R	TGTGGCATGATTTAGTGACTCC	EP20	
lamb2 F0 1-F	TGTGAATGCAGTTTAGAGGGCT	CD263	Confirm gRNA cuts
lamb2 F0 1-R	CAGCACACTCTCTGATTTTTGC	CD264	
lamb2 F0 2-F	CTGGCAGGTGTATCGCTACTTT	CD272	
lamb2 F0 2-R	ATCCTGATAGCAGGGTCAAGAA	CD273	
lamb2 F0 3-F	ACCTCTGCACTTTTAGACCACC	CD286	
lamb2 F0 3-R	TAACCAAATGTTCTCAGAGGGG	CD287	
lamb2 F0 4-F	CATACAGTTTACAGGCCAGTGC	CD288	Confirm gRNA cuts, genotype *lamb2 F0*
lamb2 F0 4-R	GGGAGAGAATCAAACCAGAAAA	CD289	

2.6.3 Generation of *Tg(ubi-dCas9-poly(A), cryaa:CFP)*

To generate *Tg(ubi-dCas9-poly(A), cryaa:CFP)* transgenic zebrafish the *ubi-dCas9-poly(A), cryaa:CFP* construct (50pg, 2.2.6) was injected together with *tol2* mRNA (50pg) and Phenol Red (25%) in a volume of 1nL into the yolk of 1-cell stage embryos obtained from a *Tg(myl7:eGFP)/+* in-cross. Embryos were screened at 2dpf and those with CFP+ eyes were grown to adulthood (F0).

CFP+ F0 adults were outcrossed to WT and germline transmission assessed by the presence of CFP+ eyes in the progeny at 2dpf. CFP+ and CFP- embryos from

potential founders were separated and fixed for *in situ* hybridisation (2.3) to confirm segregation of *dCas9* expression with the CFP+ transgenesis marker.

Upon confirmation of germ lime transmission of construct together with CFP as a transgenesis marker, F0 founders were outcrossed to WT (TL), and CFP+ embryos were grown to adulthood to generate a stable *Tg(ubi-dCas9-poly(A), cryaa:CFP) line*.

2.6.4 Global CRISPRi

Attempted knockdown of *lamb1b* transcription was carried out by injecting 2 crRNAs (CD107, 4.98n and CD108, 4.98nM) together with tracrRNA (9.95nM) and 7% Phenol Red in a 1nL volume into the yolk of 1-cell stage embryos obtained from a *Tg(ubi:dCas9, cryaa:CFP)*^{sh595} outcross to WT (TL). Embryos were dechorionated and fixed at 24hpf in 4% PFA overnight at 4°C.

2.6.4.1 Confirmation of CRISPRi gRNA targeting

As a proxy to confirm CRISPRi gRNAs can efficiently recruit dCas9 protein, CRISPRi gRNAs were injected together with active Cas9 protein. gDNA was extracted from injected embryos and PCR amplification of targeted regions carried as described in 2.6.1.2, using primers (Table 2.33) to confirm Cas9 is being recruited to, and cutting, the desired locus.

Table 2.33 CRISPRi genotyping

	Sequence	Short Name
lamb1b CRISPRi 1-F	CGCACCCTGAAAAATCATATCT	CD119
lamb1b CRISPRi 1-R	AGAGCTGTAGTGTGGAAAAGCC	CD120
lamb1b CRISPRi 2-F	AAGTTTCATCGTGCAACCTTTC	CD121
lamb1b CRISPRi 2-R	TTCGTTGGGCCTACCTCTAATA	CD122

2.7 Light sheet imaging

2.7.1 Image Acquisition

Initial observation of ECM asymmetry was made in embryos obtained from an incross of *Tg(myl7:lifeActGFP)/+; Tg(fli1a:AC-tagRFP)/+* double transgenic zebrafish, which were selected for brightest fluorescence intensity prior imaging at 26hpf. Quantification of left-right ECM thickness at 26hpf and 50hpf was carried out in embryos obtained from an in-cross *of Tg(myl7:lifeActGFP)/+; Tg(fli1a:AC-tagRFP)/+; Tg(lft2:GalFF)/+, Tg(UAS:RFP)/+* quadruple transgenic zebrafish, which were selected for brightest fluorescence intensity prior imaging. *ssNcan-GFP* injected embryos were obtained as described above (2.1.4.2)

Embryos were anaesthetised using Tricaine (Merck 10521) in E3 medium and embedded in 1% low melting point agarose (Sigma A9414) in Brand capillaries (Brand 701934). Embryos were imaged in a Zeiss light sheet Z.1 system using a 10X objective lens, and oriented to acquire optical cross sections through the heart for single slice time-lapse images of 2 minutes in length. Data was acquired using ZEN software (Zeiss). Hearts were imaged at the venous pole of 1dpf embryos and at venous and arterial poles in 50hpf embryos.

2.7.2 ECM quantification

Manual quantification of left and right cardiac ECM width was carried out on 5 systole and 5 diastole time points for each imaged heart. The *Tg(lft2:GalFF, UAS:RFP)* line (referred to as *lft2* line) was used to demarcate dorsal (*lft2*+) and ventral (*lft2*-) myocardium, allowing accurate orientation of the left-right axis. The distance between the myocardial signal (*myl7*+) and endocardial signal (*fli1a*+) was quantified on both left and right side of the heart tube using the line and measure features in Fiji. The left/right ratio of cardiac ECM thickness was calculated by dividing left ECM measurement by right ECM measurement, where a value of

greater than one denoted a left-sided ECM expansion. The mean ECM ratio of the 5 measurements for each contraction cycle (giving 1 diastole and 1 systole measurement per embryo) was then plotted for a total of 6 embryos at 1dpf and 5 embryos at 2dpf.

2.8 Immunohistochemistry

2.8.1 Immunohistochemistry protocol

Embryos were serially rehydrated into PBST, washed four times in PBST and then twice in PBS-Triton (0.2% Triton-X (Sigma T8787) in PBS). Embryos were blocked in IHC-Blocking buffer (10% Goat Serum (Invitrogen 10000C) in PBS-Triton) for a maximum of 30 minutes at room temperature, before IHC-blocking buffer was removed and replaced with IHC-blocking buffer containing 1% DMSO and primary antibodies at required concentrations (Table 2.34). Embryos were incubated in antibody solution overnight at 4^{O}C with gentle agitation. Following removal of primary antibodies, embryos were extensively washed in PBS-Triton before addition of IHC-Blocking buffer containing 1% DMSO and secondary antibodies at required concentrations (Table 2.35). Embryos were incubated overnight at 4^{O}C with gentle agitation and were protected from the light for the remainder of the protocol. Following removal of secondary antibodies, embryos were extensively washed in PBS-Triton at room temperature before being prepared for imaging.

Table 2.34 IHC primary antibodies

Antigen	Species	Dilution	Reference
GFP	Chicken	1:500	Aves. GFP-1010

Table 2.35 IHC secondary antibodies

Raised against	Species	Fluorophore	Reference
Chicken	Donkey	Cy2	Jackson Lab

2.8.2 Imaging

Embryos were dissected and mounted in VectaShield (Vector Laboratories) between a coverslip (Menzel-Gläser 15787582) and glass slide (VWR ROTHH870.1) prior to imaging on Nikon A1 Inverted Confocal microscope (Wolfson Light Microscopy Facility).

2.9 Semi-quantitative PCR

2.9.1 Collection of embryos

For collection of *lamb1a* homozygous mutants, *lamb1a*$^{\Delta 19}$*/+; lamb1b*$^{\Delta 2}$*/+ or lamb1a*$^{\Delta 25}$*/+; lamb1b*$^{\Delta 2}$*/+* adults were incrossed and homozygous *lamb1a* mutants were sorted from WT siblings at 1dpf by morphological differences in anteroposterior axis (Stemple et al., 1996).

Homozygous mutant embryos for either *lamb1b*$^{\Delta 2}$ or *lamb1b*$^{\Delta 25}$ were collected by in-crossing adult homozygous mutants for the respective mutations. *lamb1b*$^{\Delta 2}$ heterozygous embryos were collected from an outcross of homozygous mutant *lamb1b*$^{\Delta 2}$ males to female *Tg(myl7:eGFP)/+*, whilst *lamb1b*$^{\Delta 25}$ heterozygous embryos were collected from an outcross of homozygous mutant *lamb1b*$^{\Delta 25}$ females to male *Tg(myl7:eGFP)/+*. WT embryos were collected from an incross of *Tg(myl7:eGFP)/+*.

55hpf cDNA for each genotype was generated using Superscript IV (see 2.2.2.2), from which two separate reverse transcriptions were performed for two biological repeats. A third biological repeat carried out from RNA isolated from a separate collection of embryos at 55hpf.

2.9.2 Polymerase Chain Reaction

3 technical repeats were carried out per cDNA generated, totalling 9 technical repeats. Per technical repeat 7 PCRs were performed on the 5 generated cDNAs, consisting of 2 loading control PCRs: *gapdh* and *eefa1l1* (Table 2.36) and 5 gene specific PCRs covering the first 1kb, middle 500bp and last 1kb of the genes of interest (Tables 2.37 and 2.38).

Each 10µL PCR reaction was assembled using cDNA-BioMix and Primer-MQ master mixes to limit pipetting error, giving a final reaction concentration of cDNA of 150ng/µL and Primers of 200nM.

PCRs were carried out with an annealing temperature of 58^{O}C, however cycle numbers were reduced to enable comparison of relative levels between different cDNA group. For quantification of *lamb1a* cDNA levels, both experimental and control PCRs were subject to 23 cycles. For quantification of levels of *lamb1b* cDNA, control PCRs (*gapdh* and *eefa1l1*) were subject to 22 cycles compared to 28 cycles for experimental (*lamb1b*) due to the low levels of *lamb1b* mRNA expression compared to *gapdh* and *eefa1l1*.

8µL of resulting PCR products were resolved by gel electrophoresis using a 3% TAE (40mM Tris HCl, 20mM Acetic Acid, 1mM EDTA) gel. Gels were imaged using a BioDoc-It imaging System and care was taken to ensure no band was over-saturated when images were acquired.

Table 2.36 Housekeeping control semi-qPCR primers

Gene	Sequence	Amplicon size (bp)	Short name
gapdh	GGACACAACCAAATCAGGCA	172	CD15
	GGTGGAGTCGTACTGGAACA		CD16
eefa1l1	TGGTTATTGGCCACGTCGA	144	CD17
	CCCAGGCGTACTTGAAGGA		CD18

Table 2.37 *lamb1a* semi-qPCR primers

Pair no.	Sequence	Amplicon size (bp)	Short name
Pair 1	CTGAGCTGGGAGATGTTTGC	476	CD177
	TGGCCCATGAGAGACAGAAG		CD178
Pair 2	ACTGAGGGCGAGGTCATTTT	458	CD203
	GCTCGGTAAACTGCCATGTC		CD204
Pair 3	TCGCCATACACACTCATCGA	454	CD205
	CTCCAGCAATACACTCGCAC		CD206
Pair 4	AATGTGGAGGAGAGGGATGC	520	CD207
	TCGTTCACCATCTCTGCTGT		CD208
Pair 5	CACTCAAACAGGCCGCAG	450	CD209
	CCAGTTCATTGGCTTTGTCCT		CD210

Table 2.38 *lamb1b* semi-qPCR primers

Pair no.	Sequence	Amplicon size (bp)	Short name
Pair 1	CTCTTCTCCCACGATCCACA	450	CD191
	TTCAGCCTCCAAATCCAGCT		CD192
Pair 2	GGTGTACCGCTACTACGCTT	503	CD193
	CGTTTGTCTCTCGGCCTACT		CD194
Pair 3	AACAGTGGAAGAGGATGCCA	525	CD195
	CATCATCCTCTGCGTGTGTG		CD196
Pair 4	ATCAGAGCAAAGCACGAGTG	463	CD197
	CTCAGTTTGAATTCGGTCGCT		CD198
Pair 5	AGAGACAAGCTGAGGACACC	420	CD199
	GACCTAGAAACTGTGTCCGTT		CD200

2.9.3 Quantification and normalisation of band intensity

Following image acquisition, gel images were pre-processed by rotation to ensure all bands were parallel across the horizontal axis, cropped to region of interest for quantification, and finally the look-up table was inverted.

Quantification of band intensity was carried out using the Fiji>Analyze>Gels pipeline. The area under curve for band intensity, together with area above curve for background intensity was subtracted from 100% defined as "band percentage intensity". Band percentage intensity was then normalised to either *gapdh* or *eefa1l1* loading controls to define "relative band intensity". Relative band intensity for each experimental cDNA was then normalised to relative band intensity of WT cDNA to give "relative level normalised to WT loading control".

2.9.4 Statistical Analysis

PCR quantifications were analysed in Prism. Relative levels between mutant and either heterozygous siblings (*lamb1b*) or siblings (*lamb1a*) were compared using One-way ANOVA.

3. Identification and characterisation of Laminin expression dynamics during early heart morphogenesis

Laminins comprise one of the major classes of ECM component and their multiple different α, β, and γ chains allow for different trimers/isoforms to be secreted into the ECM. In numerous examples, specific Laminin isoforms regulate different cellular processes in a context-dependent manner during development. Despite the importance of the cardiac jelly in heart looping morphogenesis, little is known about which Laminin isoforms contribute to the cardiac jelly, or whether Laminins play a role in promoting vertebrate heart development. Furthermore, investigating the roles of selected Laminin genes during development is challenging due to lethality in mouse models as a result of implantation defects, making the zebrafish a suitable model system to begin to understand the role of Laminins in vertebrate heart development.

Here, I define the expression dynamics of six Laminin subunits during early heart morphogenesis in zebrafish, identifying groups of subunits with distinct tissue-restricted expression. I go on to investigate mechanisms which regulate the expression of these subunits during heart development, identifying specific subunits with either flow-dependent or flow-independent regulation. Finally, I describe a novel role for Lamc1-containing Laminin isoforms in promoting heart looping morphogenesis. This work begins to uncover the role of Laminins in cardiac development and potential mechanisms that control their expression during morphogenesis.

3.1 Results

3.1.1 Identification of Laminin subunits with dynamic and tissue-specific expression during heart morphogenesis

To identify Laminin subunits expressed in the heart during early cardiac morphogenesis, a spatial transcriptomics dataset (Tomo-Seq., Junker et al., 2014) mapping gene expression in the heart at 26hpf (Derrick et al., 2019) and 30hpf (E. Noël, unpublished data, Figure 3.1) was mined for candidate genes, together with an mRNA *in situ* hybridisation (ISH) screen of candidates at 30hpf and 55hpf (Figure 3.2). At 30hpf, six Laminin subunits are expressed in the zebrafish heart: two alpha chains: *laminin, alpha 4* (*lama4*, Figure 3.2A) and *laminin, alpha 5* (*lama5*, Figure 3.2B); three beta chains: *laminin, beta 1a* (*lamb1a*, Figure 3.2C), *laminin, beta 1b* (*lamb1b*, Figure 3.2D) and *laminin beta 2* (*lamb2*, Figure 1E), and a single gamma chain: *laminin, gamma 1* (*lamc1*, Figure 3.2F). Despite expression in the heart at 30hpf of *lamb1a* (Figure 3.2C), no reads were present in the Tomo-Seq datasets (Figure 3.1), this is likely due to a failure to correctly map to the locus following sequencing (E. Noël, personal communication). By 55hpf, following initial heart looping morphogenesis, expression of the majority of Laminin subunits becomes restricted to the ventricle and atrioventricular canal (Figure 3.2A', B', C', E' and F') with the exception of *lamb1b*, which is expressed only in the atrioventricular canal (Figure 3.2D'), the precursor to the atrioventricular valve.

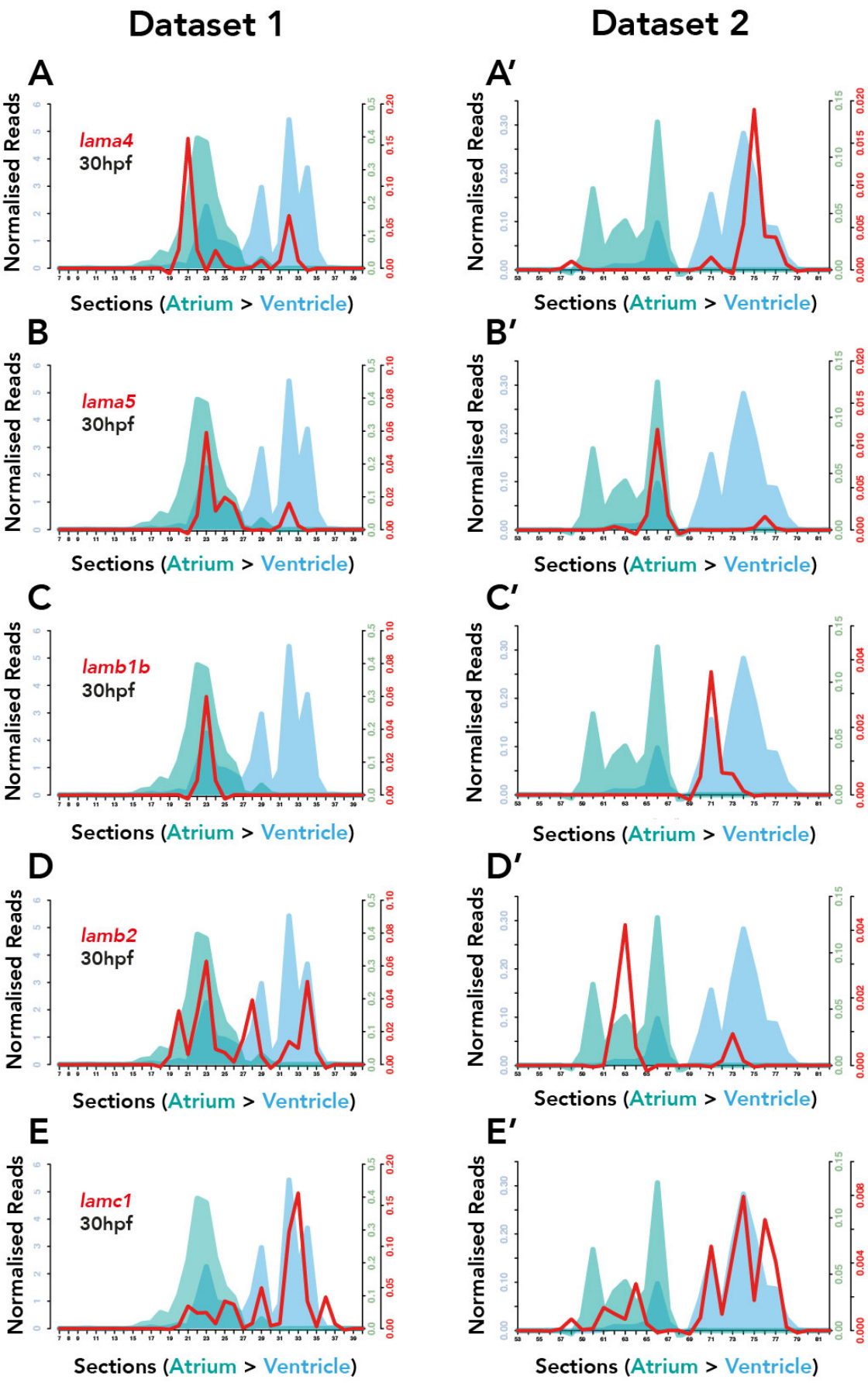
Dataset 1
Dataset 2
A
A′
lama4
30hpf
B
B′
lama5
30hpf
C
C′
lamb1b
30hpf
D
D′
lamb2
30hpf
E
E′
lamc1
30hpf
Normalised Reads
Sections (Atrium > Ventricle)

Figure 3.1. Tomo-Seq identifies 5 laminin subunits expressed in the zebrafish heart at 30hpf.

Spatially resolved transcriptomic datasets from single hearts isolated at 30hpf. Individual slices from the venous pole to the arterial pole (identified by the atrial marker *myh6* (green) and ventricular marker *myh7l* (blue)) along the x-axis, with read number normalised to spike-in RNA on the y-axis. Tomo-Seq identifies at least 5 laminin subunit genes are expressed in the heart (red) in both datasets: **(A-A')** *lama4*, **(B-B')** *lama5*, **(C-C')** *lamb1b*, **(D-D')** *lamb2* and **(E-E')** *lamc1*. Experimental procedures and data analysis performed by E. Noël.

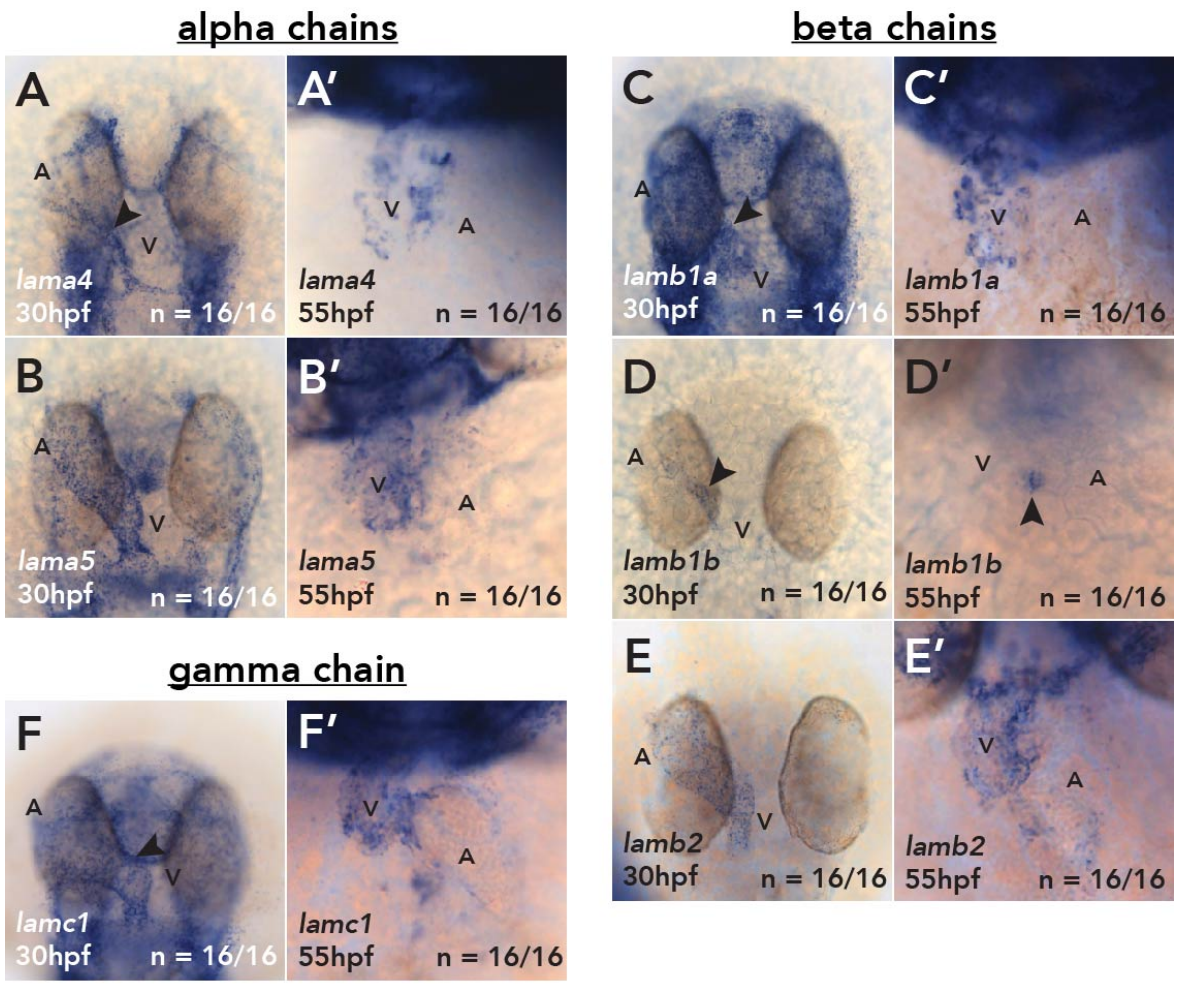

Figure 3.2. Dynamic expression of Laminin subunit genes during heart morphogenesis.

mRNA *in situ* hybridisation of Laminin subunit genes during zebrafish heart looping at 30hpf and 55hpf. **(A-A')** *laminin, alpha 4* (*lama4*) is expressed throughout the heart (A, arrowhead) and in the connecting vasculature at the arterial pole at 30hpf and is restricted to the ventricle and atrioventricular canal at 55hpf (A'). **(B-B')** *laminin, alpha 5* (*lama5*) is expressed throughout the heart at 30hpf and is restricted to the ventricle and atrioventricular canal at 55hpf (B'). **(C-C')** *laminin, beta 1a* (*lamb1a*) is expressed throughout the heart at 30hpf (C, arrowhead) and is restricted to the ventricle with a punctate expression 55hpf (C'). **(D-D')** *laminin, beta 1b* (*lamb1b*) expression is observed in the heart at 30hpf, with expression predominantly in the ventricle (D, arrowhead), by 55hpf expression is restricted to the atrioventricular canal (D', arrowhead). **(E-E')** *laminin, beta 2* (*lamb2*) expression is expressed throughout the heart at 30hpf (E) by 55hpf expression remains in the ventricle, with low levels in atrium (E'). **(F-F')** *laminin, gamma, 1* (*lamc1*) is

During early heart development, the looping heart tube compromises two tissue layers; an outer myocardial layer surrounding the endocardium, a specialised endothelium. To examine the tissue layer in which each Laminin subunit is expressed, two colour fluorescent *in situ* hybridisation (FISH) was carried out at 30hpf for each subunit gene, together with an endothelial marker *fli1a* (Palencia-Desai et al., 2015; Schumacher et al., 2013) on embryos expressing the myocardial transgene *Tg(myl7:eGFP)* (Figures 3.3, 3.4 and 3.5). This approach identified a subset of Laminin subunits expressed only in the myocardium: *lama5* and *lamb2* (Figure 3.3), subunits expressed exclusively in the endocardium: *lama4* and *lamb1b* (Figure 3.4) and two Laminin subunits which are expressed in both the myocardium and endocardium: *lamb1a* and *lamc1* (Figure 3.5). Together this demonstrates tight spatiotemporal control of specific Laminin subunit expression during early heart looping morphogenesis, and suggests that distinct endocardial or myocardial Laminin complexes may be required for this stage of heart development.

Figure 3.2 continued.

expressed widely throughout the head of the embryo with expression observed in the heart (F, arrowhead), by 55hpf, *lamc1* remains expressed in the ventricle, with lower levels of expression in the atrium (F'). A, B, C, D, E, F dorsal views. A', B', C', D', E', F' ventral views. V: ventricle. A: atrium.

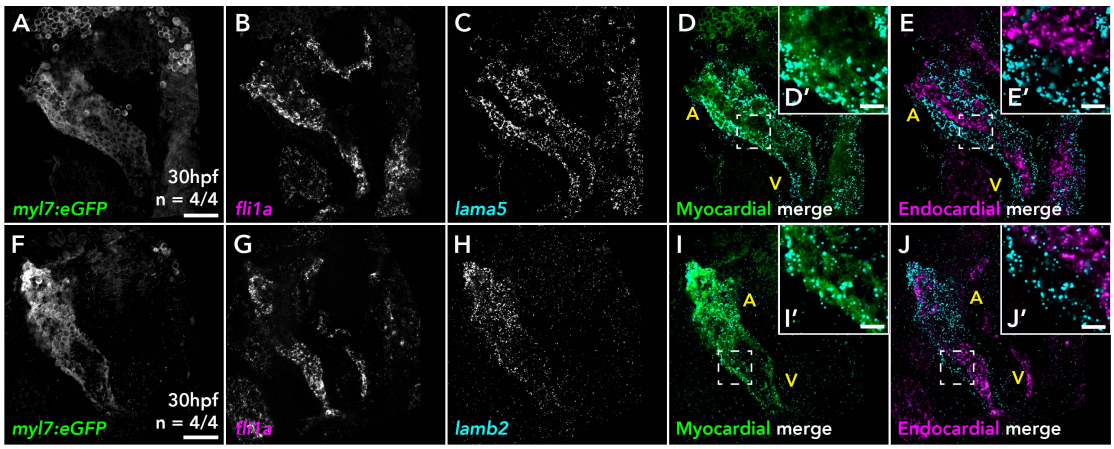

Figure 3.3. *lama5* and *lamb2* are expressed exclusively in the myocardium.

Single-plane confocal images of mRNA *in situ* hybridisation and immunohistochemistry to identify tissue of expression of *lama5* and *lamb2* at 30hpf. **(A, F)** Anti-GFP antibody highlighting the myocardial transgene *myl7:eGFP*. **(B, G)** mRNA *in situ* hybridisation of the endothelial marker fli1a. **(C)** mRNA *in situ* hybridisation of *lama5*. **(D-D')** Merge of myocardium (green) and *lama5* (cyan) expression demonstrating that *lama5* and *myl7* expression overlap (inset, D'). **(E-E')** Merge of endocardium (magenta) and *lama5* (cyan) expression demonstrating that *lama5* and *fli1a* expression do not co-localise (inset, E'). **(H)** mRNA *in situ* hybridisation of *lamb2*. **(I-I')** Merge of myocardium (green) and lamb2 (cyan) expression demonstrating that *lamb2* and *myl7* expression overlap (inset, I') **(J-J')** Merge of endocardium (magenta) and *lamb2* (cyan) expression demonstrating that *lamb2* and *fli1a* expression do not co-localise (inset, J'). Dorsal views, anterior to top. V: ventricle. A: atrium. Scale bars A, F: 50µm. D', E', I', J': 10µm.

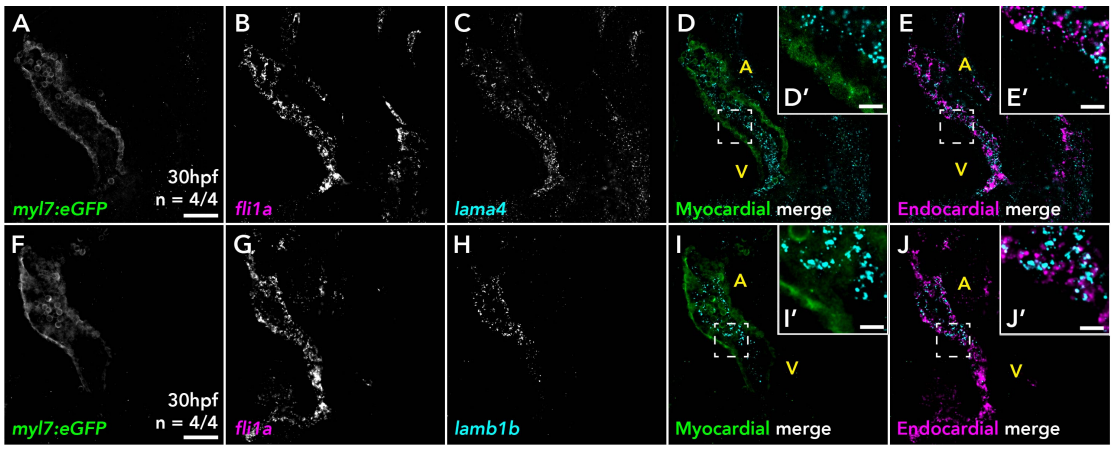

Figure 3.4. *lama4* and *lamb1b* are expressed exclusively in the endocardium.

Single-plane confocal images of mRNA *in situ* hybridisation and immunohistochemistry to identity tissue of expression of *lama4* and *lamb1b* at 30hpf. **(A, F)** Anti-GFP antibody marking the myocardial transgene *Tg(myl7:eGFP)*. **(B, G)** mRNA *in situ* hybridisation of the endothelial marker *fli1a*. **(C)** mRNA *in situ* hybridisation of *lama4*. **(D-D')** Merge of myocardium (green) and *lama4* (cyan) expression demonstrating that *lama4* and *myl7* expression do not co-localise (inset, D'). **(E-E')** Merge of endocardium (magenta) and *lama4* (cyan) expression demonstrating that *lama4* and *fli1a* expression overlap (inset, E'). **(H)** mRNA *in situ* hybridisation of *lamb1b*. **(I-I')** Merge of myocardium (green) and *lamb1b* (cyan) expression demonstrating that *lamb1b* and *myl7* expression do not co-localise (inset, I') **(J-J')** Merge of endocardium (magenta) and *lamb1b* (cyan) expression demonstrating that *lamb1b* and *fli1a* expression overlap (inset, J'). Dorsal views, anterior to top. V: ventricle. A: atrium. Scale bars A, F: 50µm. D', E', I', J': 10µm.

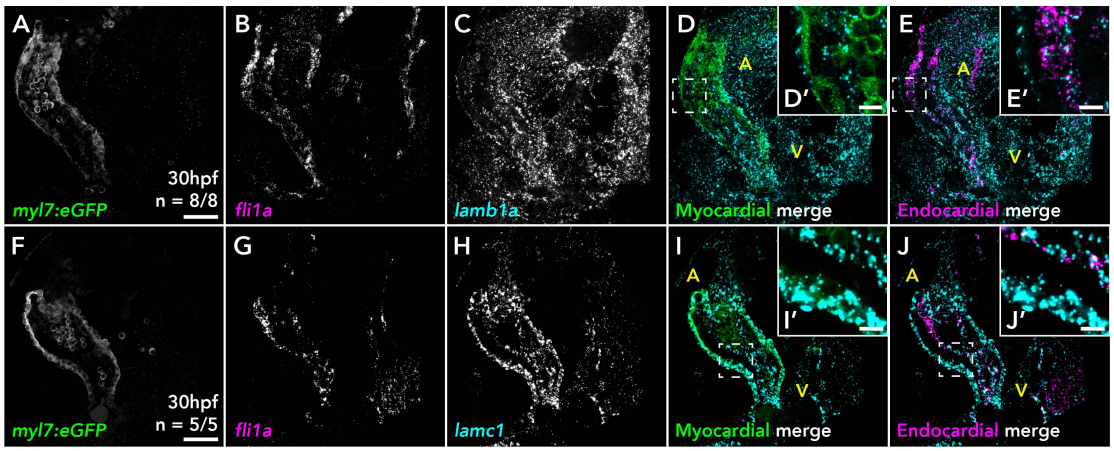

Figure 3.5. *lamb1a* and *lamc1* are expressed in both the myocardium and endocardium.

Single-plane confocal images of mRNA *in situ* hybridisation and immunohistochemistry to identity tissue of expression of *lamb1a* and *lamc1* at 30hpf. **(A, F)** Anti-GFP antibody marking the myocardial transgene *myl7:eGFP*. **(B, G)** mRNA *in situ* hybridisation of the endothelial marker *fli1a*. **(C)** mRNA *in situ* hybridisation of *lamb1a*. **(D-D')** Merge of myocardium (green) and *lamb1a* (cyan) expression demonstrating that *lamb1a* and *myl7* expression overlap (inset, D'). **(E-E')** Merge of endocardium (magenta) and *lamb1a* (cyan) expression demonstrating that *lamb1a* and *fli1a* expression overlap (inset, E'). (H) mRNA *in situ* hybridisation of *lamc1*. **(I-I')** Merge of myocardium (green) and *lamc1* (cyan) expression demonstrating that *lamc1* and *myl7* expression overlap (inset, I') **(J-J')** Merge of endocardium (magenta) and *lamc1* (cyan) expression demonstrating that *lamc1* and *fli1a* expression overlap (inset, J'). Dorsal views, anterior to top. V: ventricle. A: atrium. Scale bars A, F: 50μm. D', E', I', J': 10μm.

3.1.2 Identification of specific integrins as potential Laminin receptors during heart morphogenesis

Having identified a number of different Laminin subunit genes with cardiac expression, a further ISH screen of Laminin-binding integrins was carried out to identify possible receptors (Figure 3.6). The Laminin binding sub-family of integrins consists of α3β1, α6β1, α7β1, α6β4 (Barczyk et al., 2009; Nishiuchi et al., 2006) and zebrafish possess two paralogs of genes encoding human *ITGA3* (*Integrin subunit alpha 3*) (*itga3a*, *itga3b*), *ITGA6* (*Integrin subunit alpha 6*) (*itga6a*, *itga6b*) and a least 4 annotated paralogs of human *ITGB1 (Integrin subunit beta 1)* (*itgb1a*, *itgb1b*, *itgb1b.1*, *itgb1b.2)* (Mould et al., 2006). Only the expression of *itgb1a* and *itgb1b*, the predominantly *ITGB1* paralogs expressed in early development (Mould et al., 2006) which have previously identified expression patterns or roles in heart development in zebrafish (Renz et al., 2015; Wang et al., 2014) were examined.

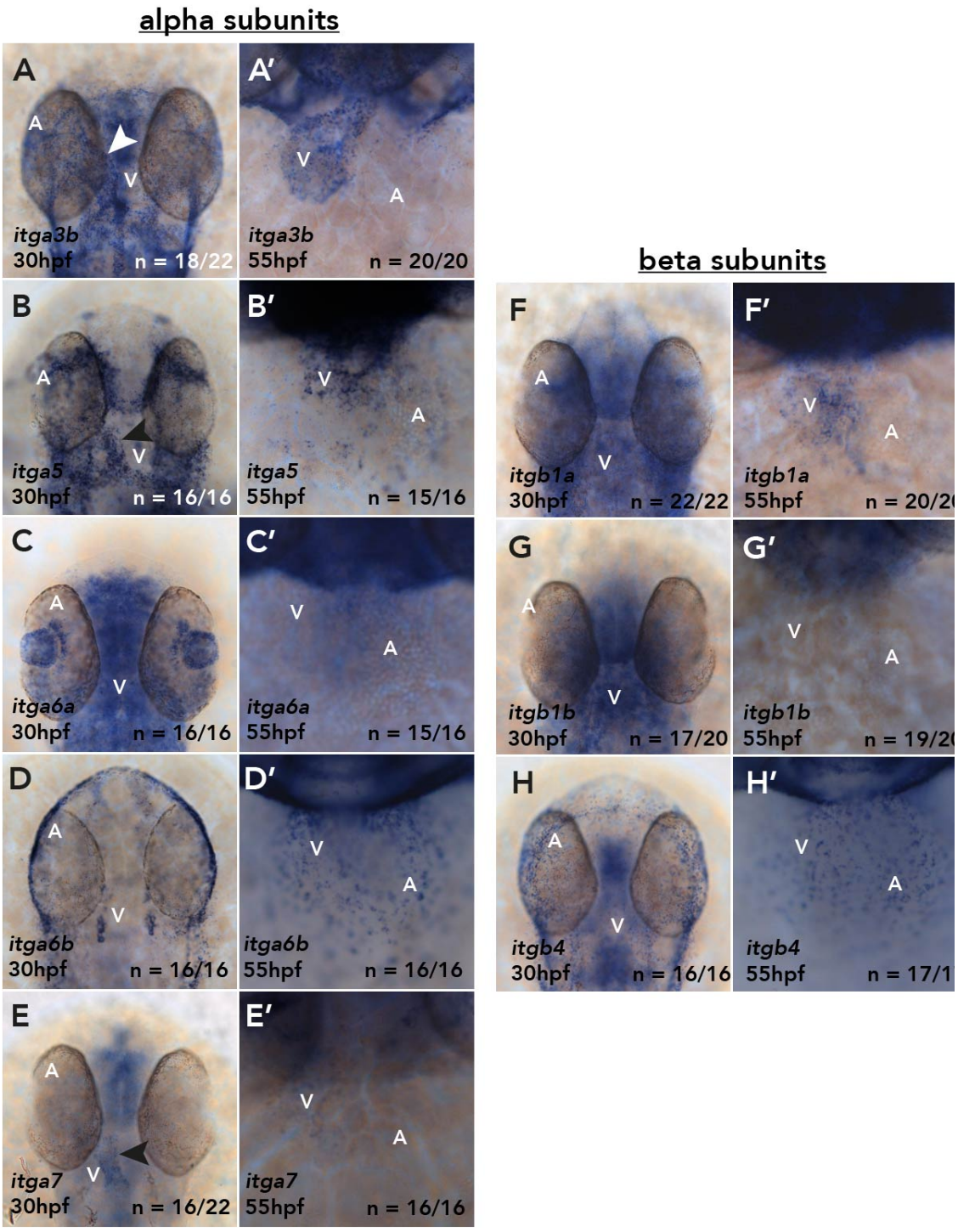

Figure 3.6. The Laminin-binding integrins *itga3*, *itga7* and *itgb1* are expressed in the heart during looping morphogenesis.

mRNA *in situ* hybridisation of integrin subunit genes during zebrafish heart looping at 30hpf and 55hpf. (A-A') *integrin alpha, 3b* (*itga3b*) is expressed throughout the heart at 30hpf (A, arrowhead) and is restricted to the ventricle at 55hpf (A'). (B-B') Expression of *integrin alpha 5* (*itga5*) is clearly visible at the arterial pole at 30hpf

At 30hpf, *itga3b* and *itga7 (integrin, alpha 7)* show clear cardiac expression, predominantly in the ventricle (Figure 3.6A, E) with expression of *itga3b* still present in the ventricle at 55hpf (Figure 3.6A') whilst *itga7* expression is absent or undetectable (Figure 3.6E'). Interestingly, *itga6a* and *itga6b* show very distinct and complementary expression patterns (Figure 3.6C-D'). *itga6a* shows little or no spatial restriction at 30hpf, with relatively uniform staining throughout the head of the embryo (Figure 3.6C) and potentially very low levels of expression in the heart following looping at 55hpf (Figure 3.6C'). Conversely *itga6b* expression appears exclusively epidermal at 30hpf (Figure 3.6D) with staining absent from cardiac tissue at 55hpf, instead expression appears to be retained in the overlying epidermis (Figure 3.6D'). Alongside *itga3b* and *itga7*, *itga5 (integrin, alpha 5)*, the integrin α

Figure 3.6 continued.

(B, arrowhead) and remains expressed in the ventricle at 55hpf, with low levels of expression in the atrium (B'). (C-C') *integrin alpha, 6a* (*itga6a*) does not show any spatial restriction at 30hpf (C) and may be weakly expressed in the heart at 55hpf (C'). (D-D') *integrin alpha, 6b* (*itga6b*) expression is localised to epidermal tissue at 30hpf, with no expression in the heart tube (D); at 55hpf punctate expression of *itga6b* suggests expression in the epidermis overlaying the heart, rather than expression in cardiac tissue (D'). (E-E') *integrin alpha, 7* (*itga7*) expression is mainly observed at the arterial pole of the heart at 30hpf (E, arrowhead) but expression is absent in the heart at 55hpf (E'). (F-F') *integrin beta, 1a* (*itgb1a*) does not show clear spatial restriction in the heart tube at 30hpf (F), but is weakly expressed in the ventricle and atrioventricular canal at 55hpf (F'). (G-G') *integrin beta, 1b* (*itgb1b*) does not show clear spatial restriction in the heart tube at 30hpf (G), and expression is absent from the heart at 55hpf (G'). (H-H') *integrin beta, 4* (*itgb4*) expression is localised to epidermal tissue at 30hpf, with no expression in the heart tube (H); at 55hpf punctate expression, similar to *itga6b* (D') suggests expression in the epidermis overlaying the heart, rather than cardiac expression (H'). A, B, C, D, E, F, G, H dorsal views. A', B', C', D', E', F', G', H' ventral views. V: ventricle. A: atrium.

chain necessary for binding Fibronectin, is also expressed in the heart from at least 30hpf onwards (Figure 3.6B-B').

Examination of the relevant integrin β subunits in the zebrafish heart identifies *itgb1a* and potentially *itgb1b* (Figure 3.6F-G') as partners of *itga3b* and/or *itga7* in binding and possibly transducing the Laminin ECM signal. *itgb1b* expression, similar to *itgb1a* is ubiquitous throughout the embryo at 30hpf (Figure 3.6G), however in some embryos, expression is observed in the heart (n = 3/20, data not shown).

In summary, this demonstrates that the genes necessary to generate integrin α3β1 and α7β1, two forms of Laminin-binding integrin complexes, are expressed in heart in the same developmental window as Laminin genes. Based on expression analysis at 30hpf and 55hpf, it would also suggest that α6β1and α6β4 integrins are unlikely to play a role in early heart morphogenesis. Together with the analysis of Laminin subunit expression, this suggests that Laminin-integrin signalling may play a role in cardiac morphogenesis.

3.1.3 Laminin subunit genes display distinct mechanisms of regulation of expression

Understanding the mechanisms by which different ECM environments are generated during development may provide insight into the role of the ECM, however the regulation of expression of distinct ECM components during development remains relatively understudied. In particular, whilst all other Laminin subunits identified appear to remain expressed in at least one chamber of the heart at 55hpf (Figure 3.1), *lamb1b* expression becomes restricted to the atrioventricular canal, between the atrium and ventricle (Figure 3.2D'). This expression pattern closely follows that of both *notch1b* and *delta-like 4 (Drosophila)* (*dll4*) (Wang et al., 2013), suggesting that *lamb1b* expression may be dependent on Notch signalling and therefore the expression of *lamb1b* at the AVC may be required for development of the AVC.

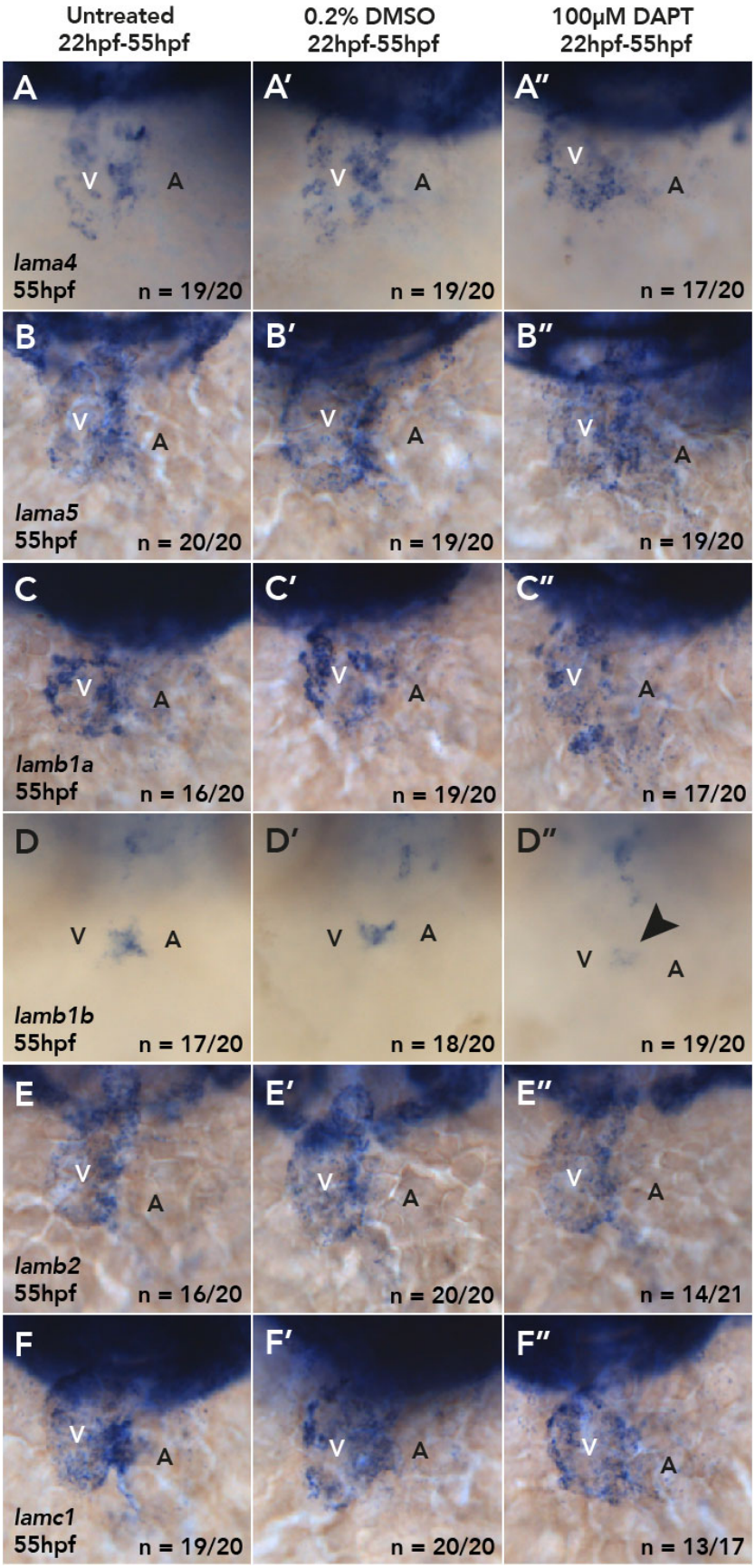
Untreated
22hpf-55hpf
0.2% DMSO
22hpf-55hpf
100µM DAPT
22hpf-55hpf
A
V
A
lama4
55hpf
n = 19/20
A′
V
A
n = 19/20
A″
V
A
n = 17/20
B
V
A
lama5
55hpf
n = 20/20
B′
V
A
n = 19/20
B″
V
A
n = 19/20
C
V
A
lamb1a
55hpf
n = 16/20
C′
V
A
n = 19/20
C″
V
A
n = 17/20
D
V
A
lamb1b
55hpf
n = 17/20
D′
V
A
n = 18/20
D″
V
A
n = 19/20
E
V
A
lamb2
55hpf
n = 16/20
E′
V
A
n = 20/20
E″
V
A
n = 14/21
F
V
A
lamc1
55hpf
n = 19/20
F′
V
A
n = 20/20
F″
V
A
n = 13/17

To investigate whether expression of *lamb1b*, or the other Laminin subunits expressed during early heart morphogenesis is dependent on Notch signalling, WT embryos were incubated with the canonical Notch inhibitor DAPT. DAPT inhibits the γ-secretase required for the cleavage (Dovey et al., 2009) and subsequent release of the Notch Intracellular Domain (NICD) which functions as a transcription factor (Bray 2016). Embryos were incubated in 100μM DAPT (a concentration known to affect heart development in zebrafish) (Timmerman et al., 2004) from 22hpf-55hpf, and expression of the six Laminin subunits examined by ISH (Figure 3.7). Embryos treated with DAPT showed a clear morphological hallmark of Notch inhibition: curvature of the body axis (data not shown) (Yang et al., 2008).

Incubation with DAPT from 22hpf-55hpf results in a clear down-regulation of *lamb1b* expression in the AVC (Figure 3.7D''), demonstrating that canonical Notch signalling is required from early heart tube stage to maintain *lamb1b* expression. However, expression of the other five Laminin subunits showed comparable levels of expression between untreated, 0.2% DMSO (vehicle control) and 100μM DAPT-treated embryos (Figure 3.7D).

Figure 3.7. Canonical Notch signalling is required for *lamb1b* expression.

mRNA *in situ* hybridisation analysis of Laminin subunit expression at 55hpf, in untreated and vehicle-only controls, and embryos incubated with the canonical Notch inhibitor DAPT between 22-55hpf. **(A-C'')** Expression of *lama4*, *lama5* and *lamb1a* is unaffected in either vehicle control (A', B', C') or DAPT treated (A'', B'', C'') embryos compared to untreated (A, B, C). **(D-D'')** *lamb1b* expression is unchanged in vehicle control (D') embryos compared to untreated (D), but inhibition of canonical Notch signalling results in a marked reduction in *lamb1b* expression (D'', arrowhead). **(E-F'')** Expression of *lamb2* and *lamc1* is unaffected in either vehicle control (E', F') or DAPT treated (E'', F'') embryos compared to untreated (E, F). Ventral views. V: ventricle. A: atrium.

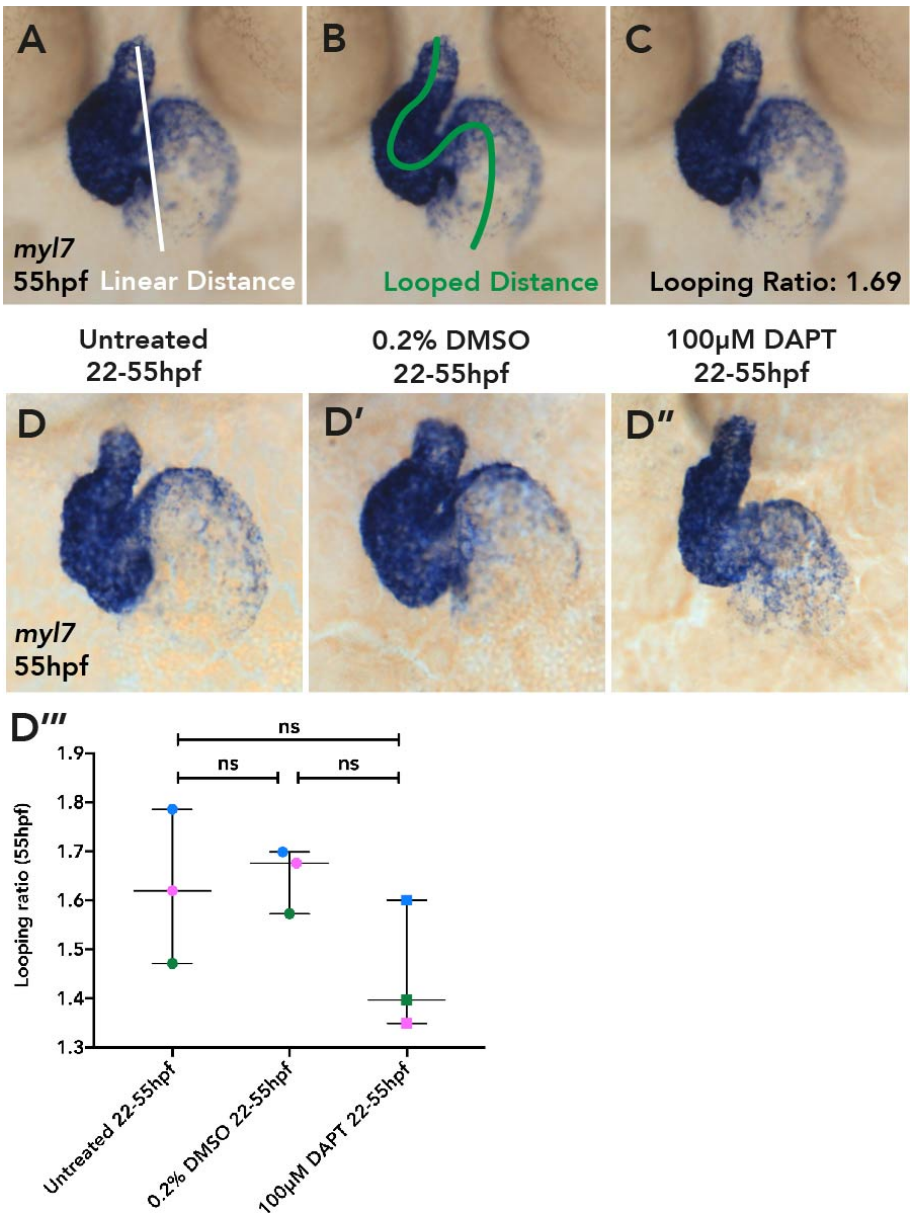

Figure 3.8. Canonical Notch signalling may be required during early heart looping.

(A-C) Representative measurements taken to quantify heart looping morphogenesis. Expression of the pan-myocardial marker *myl7* is used to outline the heart by mRNA *in situ* hybridisation. The linear distance is measured from the arterial to venous pole (A, white line). The looped distance, traversing the midline of the heart is measured (B, green line), and divided by the linear distance gives the looping ratio (C). **(D-D'')** Representative images of hearts from either untreated (D), 0.2% DMSO treated 22hpf-55hpf (D') or 100μM DAPT treated 22hpf-55hpf (D'') marked by *myl7* expression. **(D''')** Quantification of effect of inhibition of canonical Notch signalling between 22hpf-55hpf on heart looping morphogenesis at 55hpf. Each point

Whilst canonical Notch signalling has a well-defined role in both zebrafish and mouse models of valvulogenesis (MacGrogan et al. 2016; Timmerman et al. 2004), there has been no description of a potential early role in heart morphogenesis. Therefore, the effect of DAPT treatment from 22hpf-55hpf on heart looping was examined using a quantitative method to assess how robustly the heart had undergone looping morphogenesis (Figure 3.8A-C). The expression of mRNA of the pan-cardiac marker *myosin light chain 7* (*myl7*, previously *cardiac myosin light chain 2, cmlc2*) is used to identify the heart by mRNA *in situ* hybridisation (Figure 3.8A) and two measurements are taken. The linear distance (Figure 3.8A, white line) and the looped distance (Figure 3.8B, green line) from the arterial pole to the venous pole are measured and the ratio of looped to linear distance gives the looping ratio (Figure 3.8C), where a measurement closer to 1 represents a less looped heart.

Heart morphology of embryos incubated in DAPT from 22hpf-55hpf were quantified using this method and the averages of three repeats plotted (Figure 3.8D-D'''). Inhibition of canonical Notch signalling during early looping morphogenesis does not significantly reduce looping ratio when compared to controls (Figure 3.8D''').

Figure 3.8 Continued.

represents the average of an individual repeat, colour coding denotes the same repeat amongst control groups. No significant reduction is observed between DAPT treated or control groups. A, B, C, D-D'': ventral views. D'': Median with interquartile range, Kruskal-Wallis, Dunn's multiple comparisons. ns: not significant

Expression of *notch1b* in the zebrafish heart is dependent upon blood flow, mediated by the mechanotransductive transcription factor *klf2a* (Samsa et al., 2015; Vermot et al., 2009). As *lamb1b* is dependent at least partially upon Notch signalling (Figure 3.7D-D''), it is possible that *lamb1b* expression may also be dependent upon blood flow. To investigate whether *lamb1b* or other Laminin subunits are regulated by flow during cardiac development, an anti-sense morpholino oligonucleotide targeting *tnnt2a*, (previously *silent heart, sih*), a cardiac troponin required for heart contractility (Sehnert et al., 2002) was injected at the 1-cell stage to prevent cardiac contractility, and expression of Laminin subunits examined at 50hpf by mRNA *in situ* hybridisation.

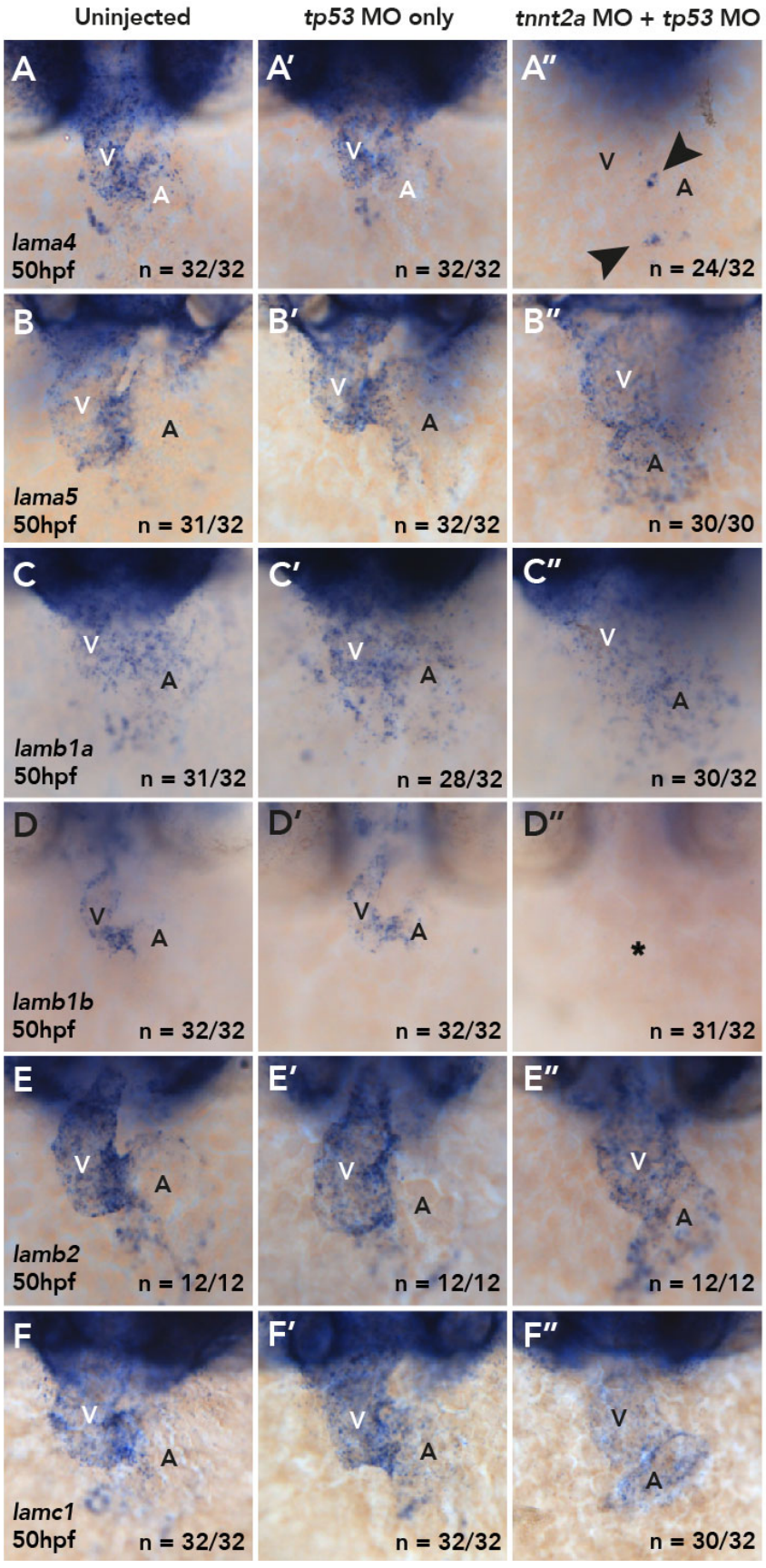
Uninjected
tp53 MO only
tnnt2a MO + tp53 MO
A
V
A
lama4
50hpf
n = 32/32
A′
V
A
n = 32/32
A″
V
A
n = 24/32
B
V
A
lama5
50hpf
n = 31/32
B′
V
A
n = 32/32
B″
V
A
n = 30/30
C
V
A
lamb1a
50hpf
n = 31/32
C′
V
A
n = 28/32
C″
V
A
n = 30/32
D
V
A
lamb1b
50hpf
n = 32/32
D′
V
A
n = 32/32
D″
*
n = 31/32
E
V
A
lamb2
50hpf
n = 12/12
E′
V
A
n = 12/12
E″
V
A
n = 12/12
F
V
A
lamc1
50hpf
n = 32/32
F′
V
A
n = 32/32
F″
V
A
n = 30/32

Strikingly, loss of blood flow results in the near total loss of *lama4* expression from the ventricular endocardium (Figure 8A''), however, a significant proportion of *tnnt2a* morphant embryos retain *lama4* expression in two puncta; the localisation of which could represent the atrioventricular canal and/or cardiac pacemaker cells (Arrenberg et al., 2010; Tessadori et al., 2012) (n = 24/32, Figure 3.9A'').

In line with regulation by canonical Notch signalling, *lamb1b* expression is absent under no flow conditions (Figure 3.9D''). Distinct from the endocardial Laminin

Figure 3.9. Expression of endocardial Laminin subunits is flow dependent.

mRNA *in situ* hybridisation analysis of Laminin subunit expression at 50hpf, in uninjected, *tp53* morphlino (MO) injected only controls, and embryos injected with *tnnt2a* and *tp53* morpholino. **(A-A'')** *lama4* expression is restricted to the ventricular endocardium in uninjected (A) and *tp53* MO only (A') but is absent in the heart apart from two puncta in embryos subject to *tnnt2a* knockdown (A'', arrowheads). **(B-B'')** *lama5* is expressed in the ventricular myocardium with low levels of expression in the atrial myocardium in uninjected (B) and *tp53* MO only (B'), and remains expressed at similar levels in embryos subject *tnnt2a* knockdown (B''). **(C-C'')** *lamb1a* is expressed in the ventricle and lower levels in the atrium in uninjected (C) and *tp53* MO only (C'), but is reduced in both chambers in embryos subject *tnnt2a* knockdown (C''). **(D-D'')** Expression of *lamb1b* is restricted to the ventricular endocardium and atrioventricular canal in uninjected (D) and *tp53* MO only (D'), but is totally absent from the hearts in embryos subject *tnnt2a* knockdown (D''). **(E-E'')** *lamb2* expression is expressed in the ventricular myocardium with low levels of expression in the atrial myocardium in uninjected (E) and *tp53* MO only (E'), and remains expressed at similar levels in embryos subject *tnnt2a* knockdown (E''). **(F-F'')** *lamc1* is expressed in the ventricle and lower levels in the atrium in uninjected (F) and *tp53* MO only (F'), but is reduced in both chambers in embryos subject *tnnt2a* knockdown (F''). Ventral views. V: ventricle. A: atrium.

subunits *lama4* and *lamb1b* (Figure 3.4), the expression of the myocardial Laminin subunits *lama5* and *lamb2* appears comparable between *tnnt2a* morphants and control embryos (Figure 3.9B-B'', E-E''). However, upon *tnnt2a* knockdown, expression of *lamb1a* and *lamc1*, the two subunits expressed in the myocardium and endocardium (Figure 3.5), show an overall reduction in expression (Figure 3.9C-C'', F-F''). One hypothesis for this may be that whilst myocardial Laminin expression is flow-independent, endocardial expression of *lamb1a* and *lamc1* could be dependent upon heart contractility and most likely blood flow.

Taken together, these data highlight that expression of the cardiac Laminin subunits is regulated by multiple, distinct mechanisms. More generally, endocardial Laminin expression is likely to be regulated by blood flow, whilst the expression of myocardial Laminins is blood flow independent. However, specific subunits may have different hierarchical regulation as endocardial *lamb1b* is at least partially dependent upon canonical Notch signalling (Figure 3.7), whilst *lama4* expression, also expressed in the endocardium is independent of Notch signalling (Figure 3.9).

3.1.4 *lamc1* is required for heart morphogenesis

The identification of multiple Laminins subunits with specific spatio-temporal regulation during early cardiac development, suggests that they may play multiple roles in heart development. To examine the broad functional role of the Laminin complexes identified, the single gamma subunit, *lamc1*, common to both the myocardium and endocardium (Figure 3.5F-J) was targeted for mutagenesis. Since removing a single subunit from a Laminin trimer is sufficient to prevent secretion from the cell and therefore act to negate the function of the complex (Libby et al., 2000; Yurchenco et al., 1997) I hypothesised that this would allow me to interrogate a broad role for Laminins in heart development. Based on the CRISPR F0

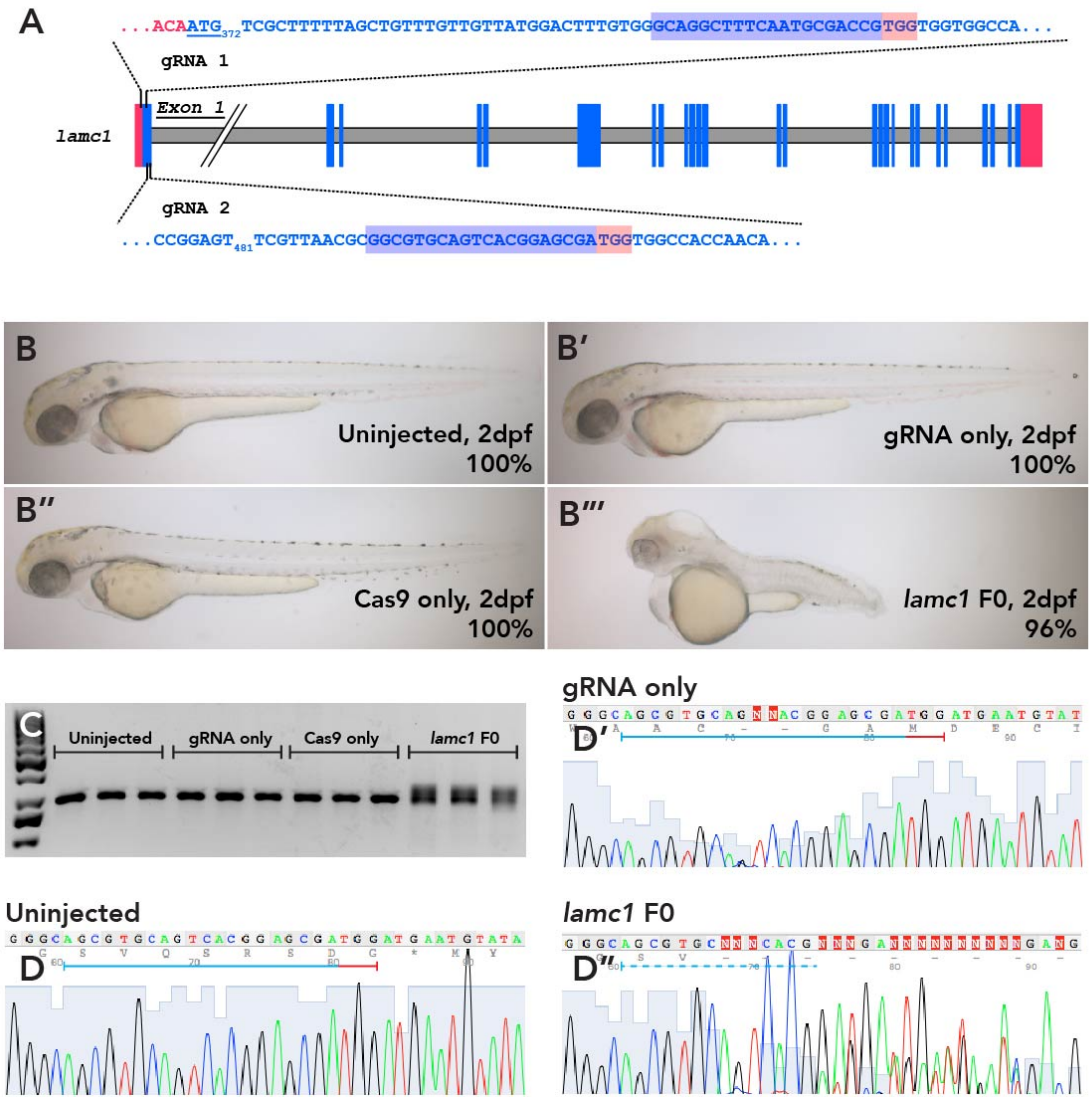

Figure 3.10. *lamc1* F0 mutants recapitulate the stable *sleepy* phenotype.

(A) Schematic showing *lamc1* genomic DNA, coding exons in blue, non-coding exons in red, based on *lamc1-201* from danRer10/GRCz10 (oblique cut line represents 50kbp). Two gRNAs (spacer highlighted in blue, PAM highlighted in red) targeting the first exon of *lamc1* downstream of the annotated initiating ATG codon (underlined) were used to generate F0 mutants by injecting together with Cas9 protein. **(B-B'')** Representative brightfield images at 2dpf of either uninjected (B), *lamc1*-targeting gRNA only (B'), Cas9 protein only (B'') or *lamc1*-targeting gRNAs together with Cas9 protein, referred to as *lamc1* F0 mutants (B'''). Only *lamc1* F0 mutants display a shortened body axis, hydrocephalus and lens defects, identical to the published stable *sleepy/lamc1* mutants. **(C)** Gel electrophoresis of PCR product

methodology (Burger et al., 2016; Wu et al., 2018) two gRNAs targeting the first exon of *lamc1* were injected together with active Cas9 protein into WT embryos at the 1-cell stage to generate F0 mutants (Figure 3.10A).

lamc1 F0 mutants recapitulate the morphological phenotype of stable *lamc1* (*sleepy*) mutants with a high level of efficacy (Figure 3.10B-B''') (Odenthal et al., 1996; Parsons et al., 2002; Stemple et al., 1996). Furthermore, *lamc1* F0 mutants can be genotyped efficiently, enabling blind analysis and correlation of phenotype with successful mutagenesis of *lamc1* (Figure 3.10C-D''). Heart looping was quantified as previously described (Figure 3.8A-C) to examine the effect of loss of *lamc1* on heart development (Figure 3.11).

Figure 3.10 continued.

amplified from region targeted by *lamc1* gRNAs (A) used to generate *lamc1* F0 mutants. Injection of *lamc1* targeting gRNAs only or Cas9 only does not result in band shifts observed in *lamc1* F0 mutants, used to confirm mutagenesis of the *lamc1* locus. **(D-D'')** Sanger sequencing as a secondary method to confirm mutagenesis of the *lamc1* gene. gRNA only injected embryos (D') do not display any change to gene sequence compared to uninjected controls (D), whilst *lamc1* F0 mutants (D'') have multiple reads in the same region, indicative of successful mutagenesis. B-B''': lateral views, anterior left.

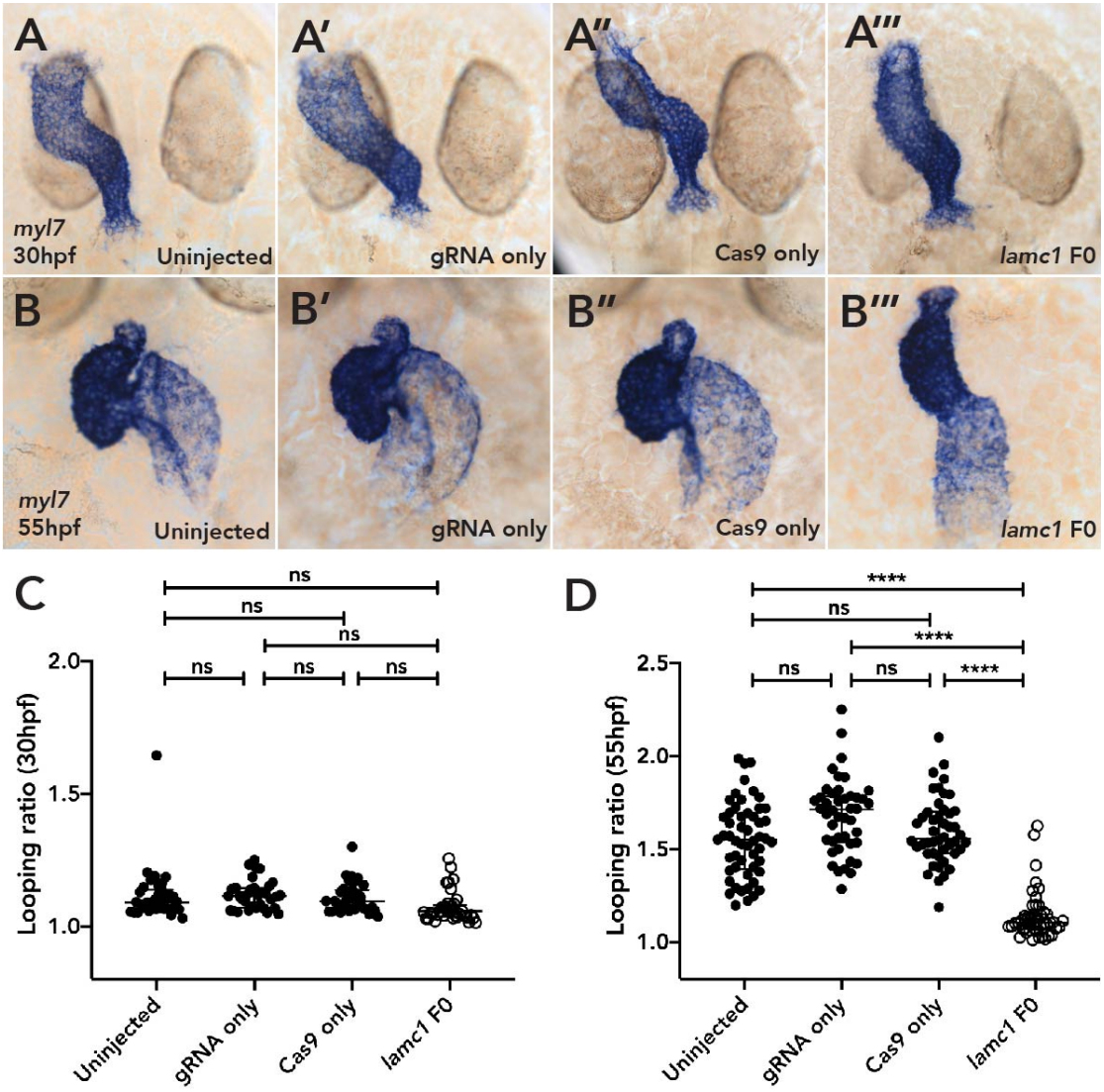

Figure 3.11. *lamc1* F0 mutants exhibit a profound heart looping phenotype.

Quantitative analysis of heart looping in *lamc1* F0 mutants at 30hpf and 55hpf. **(A-A''')** Representative images of mRNA *in situ* hybridisation analysis of *myl7* expression at 30hpf to examine heart morphology in uninjected (A), *lamc1*-targeting gRNA only (A'), Cas9 only (A'') and *lamc1* F0 mutants (A'''). No obvious cardiac phenotypes are apparent in *lamc1* F0 mutants when compared to controls. **(B-B''')** Representative images of mRNA *in situ* hybridisation analysis of *myl7* expression at 55hpf to examine heart morphology in uninjected (B), *lamc1*-targeting gRNA only (B'), Cas9 only (B'') and *lamc1* F0 mutants (B'''). *lamc1* F0 mutants at 55hpf display a severe heart looping phenotype where the atrium has failed to move cranially (B'''). **(C)** Quantification of heart looping ratio in *lamc1* F0 mutants and control groups at

At 30hpf, *lamc1* F0 heart morphology appears normal, with no reduction in heart looping ratio, when compared to either uninjected or injection control embryos (Figure 3.11A-A''', C). However, at 55hpf *lamc1* F0 mutant hearts appear almost linear (Figure 3.11B''') and exhibit a significant reduction in heart looping ratio when compared to control embryos (Figure 3.11D).

Together, this demonstrates that loss of the only Laminin gamma subunit expressed at the onset of heart looping reveals a major role for Laminin complexes in driving cardiac morphogenesis (Figure 3.12). Furthermore, since *lamc1* F0 mutant hearts are morphologically indistinguishable from control embryos at 30hpf (Figure 3.11C), this suggests the key window of Laminin function in promoting heart looping is between 30hpf and 55hpf (Figure 3.12C).

Figure 3.11 continued.

30hpf, no significant differences are measured. **(D)** Quantification of heart looping ratio in *lamc1* F0 mutants and control groups at 55hpf. No significant differences are present between uninjected, *lamc1*-targeting gRNA or Cas9 only controls, however *lamc1* F0 mutants have a significant reduction in heart looping ratio at 55hpf when compared to any control group. A-A''', B-B''': dorsal views. C, D: Median with interquartile range, Kruskal-Wallis, Dunn's multiple comparisons. ns: not significant, ****: $p<0.0001$

3.2 Discussion

Laminins are a major component of all ECMs, and *Lamb1* and *Lamc1* are expressed from as early as the 4-cell stage of mouse development (Cooper and MacQueen, 1983). Here I have identified six Laminin subunit genes expressed in the heart during early looping morphogenesis in zebrafish which are expressed in one or both of the tissue layers of the developing heart tube (Figures 3.2, 3.3, 3.4, 3.5, 3.12A).

Previously studies have described the expression of specific Laminin subunits in the developing zebrafish (Sztal et al., 2011) in which *lama3* and *laminin, gamma 3* (*lamc3*) were reported to be expressed in the heart at 72hpf and 48hpf respectively. Neither gene was enriched in the transcriptomics dataset at 26hpf or 30hpf, suggesting that expression may be required later in cardiac development, following heart looping. Additionally, expression of *lamb1a*, *lamb1b* and *lamc1* were not previously described (Sztal et al., 2011) although the study mainly focussed on myotome expression.

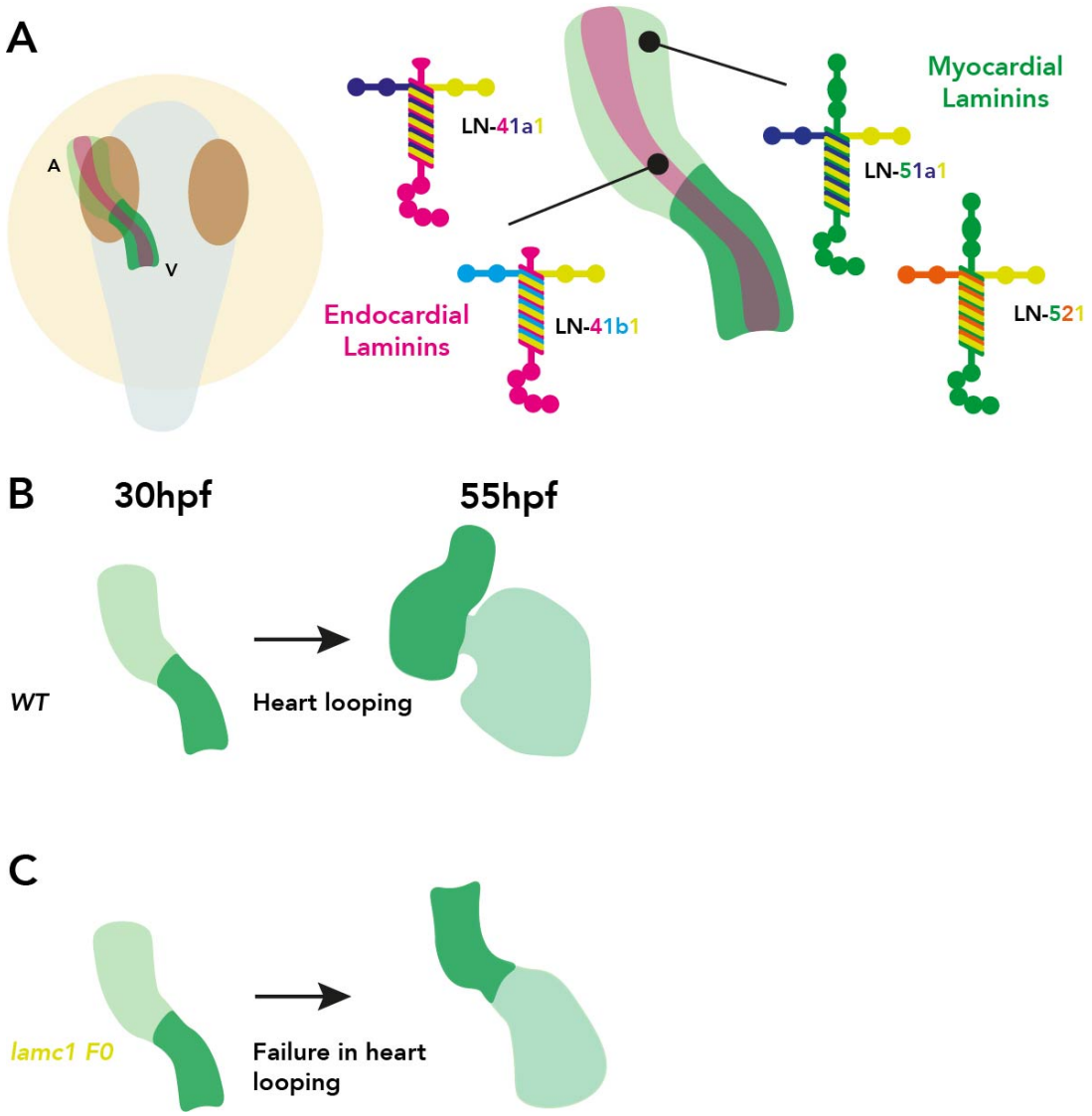

Figure 3.12. Laminins are required for heart morphogenesis.

(A) At 30hpf, six Laminin subunit genes are expressed in the zebrafish heart, suggesting that four distinct isoforms (two endocardial, magenta, two myocardial, green) may be functioning to promote heart morphogenesis. (B) In WT embryos, between 30hpf and 55hpf, the heart undergoes a robust, asymmetric dextral looping morphogenesis. (C) In *lamc1* F0 mutants, heart morphology appears normal at 30hpf, but by 55hpf, the heart has failed to loop, and the chambers have not ballooned. A: atrium, V: ventricle.

Broadly, the tissue-specific expression of Laminin subunits in the heart described here correlates with previously published expression patterns in zebrafish (Figure 3.12A) (Parsons et al., 2002; Pollard et al., 2006; Sztal et al., 2011) and mice (Frieser et al., 1997; Miner et al., 2004; Wagner et al., 2018). I have identified two potential LN-411 complexes expressed in the endocardium LN-41a1 and LN-41b1, and on a broader level within the embryo, expression of *lama4*, *lamb1a*, *lamb1b* and *lamc1* appear to overlap in the vasculature of the developing zebrafish (Parsons et al., 2002; Pollard et al., 2006; Sztal et al., 2011) data not shown) and is consistent with expression and proposed roles in mammalian vascular biology (Russo et al., 2016; Stenzel et al., 2011; Thyboll et al., 2002; Wang et al., 2005; Yousif et al., 2012). More intriguing is the expression of two Laminin complexes in the myocardium with different beta subunits (LN-51a1 and LN-521). Studies in cell culture demonstrated that inclusion of a different beta chain is sufficient to alter the behaviour of Schwann cells (Patton et al., 1998), suggesting that these two different complexes may perform distinct roles. Furthermore, whilst *lamb1a* (and *lamc1*) is expressed relatively globally throughout the embryo (Sztal et al., 2011) (data not shown), *lamb2* expression is confined only to the somites and myocardium, the two sites of contractile muscle (data not shown) (Jacoby et al., 2009). This suggests a role for *lamb2* in the assembly of basement membranes in contractile tissue. Both *LAMB1* and *LAMB2* chains are detectable in human heart samples at gestational weeks 8/9 (end of the first trimester), and are present in the ECM that surrounds the cardiomyocytes as well as the basement membrane surrounding the endocardium (Roediger et al., 2010). This conservation of gene expression and localisation strongly supports the use of zebrafish as a model for understanding the role of Laminins in heart development, and in particular how specific subunits may regulate distinct aspects of cardiac formation.

Although I have demonstrated a broad conservation of expression, a key to ECM biology is examining secretion, localisation and turnover of specific components (Matsubayashi et al. 2020). Exemplifying the need to characterise Laminin

localisation in the ECM is that in mice, despite ubiquitous translation of Lamb2 in myotubes, a short sequence present in the Lamb2 coiled-coil domain is responsible for localisation to "hot-spots" on the post-synaptic membrane (Martin et al., 1995). Therefore, developing specific antibodies against each laminin subunit that function reliably in zebrafish or tagging of relevant subunits (Keeley et al., 2020) would be necessary to examine the spatiotemporal dynamics of basement membrane assembly during heart development. Endogenous tagging is critical, as over-expression of ECM components through copy number variants has been linked to CHDs (Silversides et al., 2012; Soemedi et al., 2012).

Regulation of expression of ECM components during development is an important aspect of defining how ECM synthesis is directed to enable the precise morphogenesis of an organ. By using a pharmacological inhibitor of the canonical Notch pathway and knockdown of a cardiac troponin, I have begun to uncover at least three possible mechanisms which regulate the expression of Laminin subunits during heart development.

The finding that *lamb1b* expression is reduced but not abolished by DAPT treatment suggests that *lamb1b* expression could be only partially Notch dependent, and that another mechanism regulated by blood flow promotes *lamb1b* expression. Alternatively, inhibition of Notch signalling by DAPT may not be fully penetrant, or non-canonical Notch signalling, which DAPT does not inhibit (Andersen 2012), also regulates *lamb1b* expression. Examining *lamb1b* expression in *notch1b* mutants (Kettleborough et al., 2013) would help further establish the role of Notch in promoting transcription of ECM components.

Blood flow, sensed through *klf2a*, has previously been shown to regulate *fibronectin 1b* (*fn1b*) expression, another ECM component whose expression overlaps with *lamb1b* (Steed et al., 2016). This suggests a conserved mechanism functioning at the AVC, whereby mechanical and transcriptional pathways converge to generate a

unique ECM environment at the developing valve, potentially required for EndoMT (Steed et al., 2016). An intriguing finding is the Notch-independent, blood flow-dependent gene expression of Laminins in the endocardium as most blood flow dependent genes and processes have been shown to be regulated by Notch (Samsa et al., 2015; Vermot et al., 2009). Two candidate signalling pathways for regulating endocardial expression of *lama4*, *lamb1a* and *lamc1* are BMP signalling, as a role for *bmp4* in zebrafish has been ascribed to both myocardial and endocardial development, linked by blood flow (Dietrich et al., 2014; Patra et al., 2011) and Wnt signalling which is dependent on blood flow in both mice and fish (Goddard et al., 2017) Myocardial Laminin expression appears to be both blood-flow and Notch independent, suggesting other signalling pathways may regulate their expression.

Laminins most commonly exert a biological function through the binding and activation of integrin receptors (Anderson et al., 2013; Campbell and Humphries, 2011). I have characterised the expression of the key Laminin binding integrin subunits and identified *itga3b*, *itga7*, *itgb1a* and potentially *itga6a* expressed during the same time as Laminin expression (Figure 3.6). Furthermore, it is also likely that the Fibronectin receptor α5β1 is expressed in the heart at the same point, in line previously defined roles of Fibronectin and Integrin α5β1 in different processes during heart development (Gunawan et al., 2019; Mittal et al., 2013; Steed et al., 2016). The expression patterns of the two zebrafish *ITGA6* paralogs likely represents a division of labour, with Itga6b solely performing the role of the α6β4 receptor to anchor keratinocytes to LN-332 in the epidermis (Margadant et al., 2010), whilst Itga6a performs the remaining functions.

The class of patients with dilated cardiomyopathy which have mutations in *LAMA4* affect interaction between the α3β1 integrin receptor and the Laminin complex (Knoll et al., 2007). Additionally, sub-phenotypic doses of *lama4*-targeting morpholino injected into *integrin-linked* kinase (*ilk*) mutant zebrafish results in

cardiac dysfunction (Knoll et al., 2007), reinforcing the link between Laminins and their classical receptors in heart development.

At later stages of heart development (E15), all cells of the mouse heart express *Itgb1*, alongside both *Itga6* and *Itga7*, yet *Itga3* expression is not observed (Hierck et al., 1996). This may suggest different temporal roles for Laminin-binding integrins in heart development or potentially, *Itga3* and *Itga6* may have exchanged roles as zebrafish and mouse diverged during evolution. Further work examining expression of *itga3b*, *itga6a* and *itga7* expression throughout cardiac looping and into early trabeculation stages may provide some insight.

Mutations in *LAMC1* (*Laminin subunit gamma 1*) and *NID1* (*Nidogen 1*) are linked to Dandy-Walker Syndrome (DWS), (Darbro et al., 2013), a rare congenital brain malformation of which 26-38% of cases also present with CHDs (Haddadi et al., 2018). Targeted mutagenesis of *lamc1* in zebrafish using the F0 method (Burger et al., 2016; Wu et al., 2018) results in a morphological phenocopy of the stable *sleepy* mutant (Figure 3.10), validating the F0 methodology. Loss of *lamc1* results in a profound cardiac phenotype whereby the heart has failed to undergo looping morphogenesis by 55hpf (Figure 3.11, 3.12B-C); *lamc1* F0 mutants also display severe hydrocephalus (Figure 3.10) another trait of DWS (Haddadi et al., 2018). Deletion of the single Laminin gamma gene expressed in the heart, effectively functions as a Laminin-null for the heart, as all three subunits are required for assembly of the trimer inside the cell and subsequent secretion into the ECM (Libby et al., 2000; Yurchenco et al., 1997). Therefore, this highlights a crucial role of Lamc1-containing Laminins in zebrafish development in promoting the asymmetric morphogenesis of the heart and may also provide a model for a greater understanding of the pathology of CHDs in DWS patients. However, whilst this demonstrates that Laminins are required in the ECM for proper heart development, I have identified at least 4 distinct, potential complexes (LN-41a1, LN-41b1, LN-51a1 and LN-521, Figure 3.12A) which may perform this role, and through investigation

and comparison of cardiac phenotypes associated with loss of either Laminin alpha chains or Laminin beta chains, the role of one or more of these complexes can begin to be defined.

4. *lamb1b* is dispensable for heart morphogenesis

I have previously shown that Laminins are required for heart morphogenesis, and although the exact composition of the Laminin isoform required remains unclear, I have demonstrated that Lamc1 is a component. In this chapter, using CRISPR-Cas9-mediated mutagenesis I target the previously poorly characterised zebrafish Laminin subunit *lamb1b*, to investigate its function in heart development. I show that despite predicted loss of function, *lamb1b* coding sequence mutants are homozygous viable and non-phenotypic. However, a wealth of studies has highlighted multiple mechanisms by which an organism is able to overcome damaging mutations through genetic robustness. I go on to examine exon-skipping, genetic compensation and start to develop tools necessary to investigate gene function to avoid these mechanisms and other off-target effects. Finally, I delete the *lamb1b* promoter to definitively understand the function of *lamb1b* in heart morphogenesis. These data present multiple points for consideration in the design and characterisation of mutant lines in zebrafish for future studies.

4.1 Results

4.1.1 *lamb1b* exhibits dynamic expression during heart looping

Whilst mutagenesis of *lamc1* identified a role for Laminins in promoting heart looping, multiple alpha and beta chains are expressed in the heart which could assemble with Lamc1 to form one of four potential isoforms (Chapter 3). Therefore, to begin to identify which specific Laminin complexes containing Lamc1 promote heart looping, mutagenesis of a gene encoding a candidate beta chain was undertaken.

I have previously identified that *lamb1b* exhibits highly dynamic expression in the endocardium becoming restricted to the atrioventricular canal, and which is dependent on blood flow and canonical Notch signalling similar to other genes involved in valve specification (Heckel et al., 2015; Steed et al., 2016; Vermot et al., 2009; Wang et al., 2013) (Figure 1.7). Since the majority of CHDs manifest as structural defects which affect valve specification and function (Pierpont et al., 2000), and previous analysis of heart looping in *lamb1a* mutants suggests it is dispensable for heart development (Hochgreb-Hägele et al., 2013) this strongly supported a role for *lamb1b* in cardiac development.

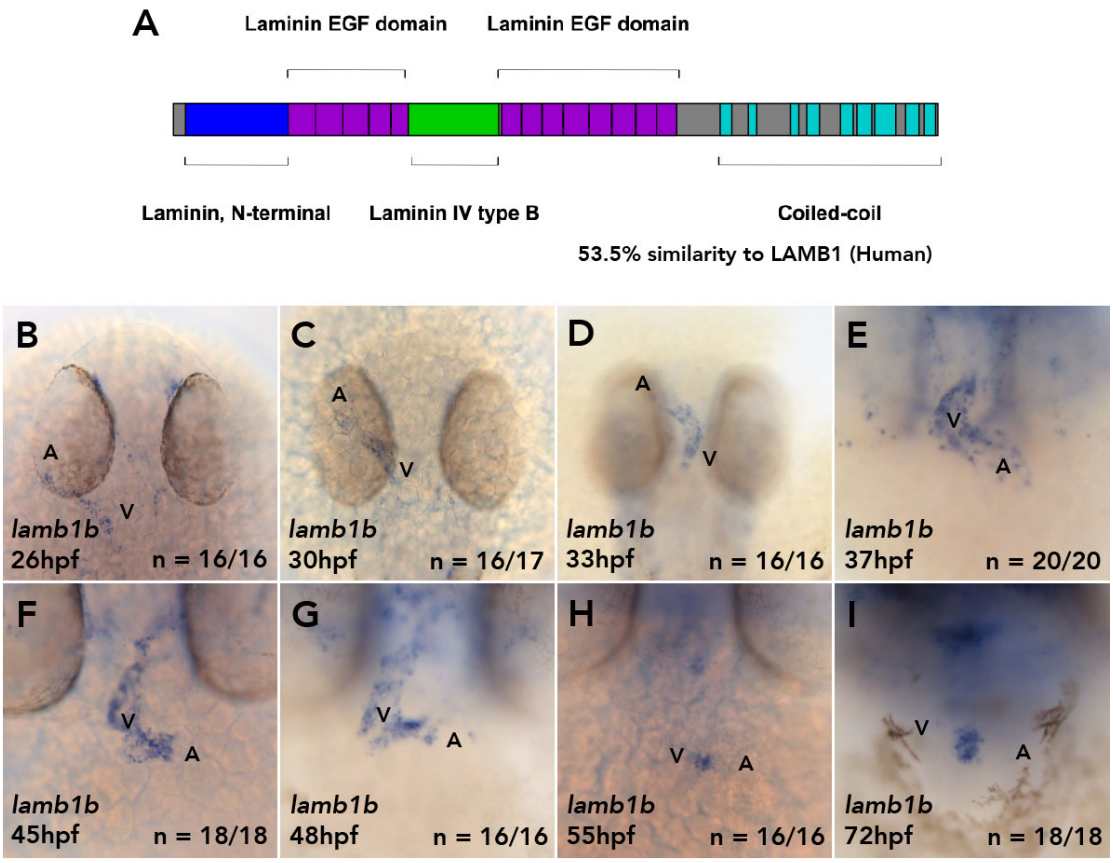

Figure 4.1. *lamb1b* exhibits dynamic expression and restriction to the atrioventricular canal during heart looping.

Characterisation of *lamb1b* expression during heart looping morphogenesis by mRNA *in situ* hybridisation. **(A)** Schematic of *lamb1b* structure based on UniProt accession number F1QE6B (Designed in IBS: Liu et al, 2015). Zebrafish Lamb1b protein shares 53.6% amino acid similarity to Human LAMB1. Blue: Laminin N-terminal domain, Purple: Laminin EGF-like repeats, Green: Laminin IV type B, Cyan: Coiled-coil domain. **(B-E)** At 26hpf, *lamb1b* is expressed throughout the endocardium of the developing heart (B), with expression gradually being lost from the atrium between 30hpf-37hpf (C-E). **(F-H)** At 45hpf, *lamb1b* expression is absent from the atrium (F), and expression in the ventricle is gradually reduced between 48hpf (G) and 55hpf, resulting in restriction of *lamb1b* expression to the atrioventricular canal at 55hpf (H). **(I)** Expression of *lamb1b* persists at the atrioventricular canal until at least 72hpf. B-D, dorsal views. E-I: ventral views. V: ventricle. A: atrium.

To examine whether *lamb1b* expression follows the dynamics of AVC markers over the course of looping a detailed time course of *lamb1b* expression by ISH was undertaken. Prior to the initiation of heart looping (26hpf), *lamb1b* is expressed throughout the endocardium of the linear heart tube (Figure 4.1B). As heart looping morphogenesis begins, *lamb1b* expression remains prominent in the ventricle, whilst expression is gradually lost in the atrium from 30hpf onwards with expression of *lamb1b* in the atrium absent by 45hpf (Figure 4.1F). At 48hpf, *lamb1b* remains expressed at the AVC, but expression is reduced in the ventricular endocardium (Figure 4.1G) By 55hpf *lamb1b* expression is only present in the presumptive endocardial cushions, the expression of which persists until at least 72hpf (Figure 4.1H-I). Therefore, *lamb1b* expression closely follows that of genes with previously-described roles in promoting valvulogenesis such as *notch1b*, *dll4*, *has2*, and *fn1b* (Lagendijk et al., 2011; Steed et al., 2016; Vermot et al., 2009; Wang et al., 2013).

4.1.2 Generation and characterisation of *lamb1b* coding sequence mutants by CRISPR-Cas9 mutagenesis

Having identified *lamb1b* as a candidate gene required to promote heart looping as part of the Lamc1-containing Laminin isoform, possibly through a role at the atrioventricular canal, CRISPR-Cas9-mediated genome editing was used to generate stable *lamb1b* mutant zebrafish lines (Figure 4.2). A gRNA targeting the second exon of *lamb1b* (Figure 4.2A) was co-injected with active Cas9 protein at the 1-cell stage (E. Noël) and F0 adults were screened for germline transmission of *lamb1b* mutations. Two F0 adult founders transmitting deletions within the *lamb1b* coding sequence were identified and outcrossed to establish the stable *lamb1b* mutant lines *lamb1b*$^{\Delta 2}$ and *lamb1b*$^{\Delta 25}$, both of which are predicted to result in premature termination codons in the Lamb1b Laminin N-terminal domain (Figure 4.2B-C).

To examine the result of the loss of *lamb1b* function, adult heterozygous *lamb1b* mutants were incrossed and heart looping ratio analysed at 55hpf (Figure 4.3).

lamb1b mutants do not display any obvious morphological defects (data not shown) and heart looping ratio is not significantly reduced when compared to WT or heterozygous siblings of either allele (Figure 4.3C, 4.3D), in contrast with the reduction in heart looping observed in *lamc1* F0 mutants (Chapter 3).

However, whilst no overt heart phenotype in either *lamb1b* coding sequence mutants was identified, the most prevalent CHDs are subtle and affect valve tissue (Loffredo, 2000; Pierpont et al., 2000), suggesting that loss of *lamb1b* could result in subtle changes to valve markers. First, to confirm endocardial specification was not affected in *lamb1b* mutants, ISH analysis of the endocardial marker *nfatc1* (Palencia-Desai et al., 2015; Pompa et al., 1998) was performed and found to be normal in both *lamb1b* mutant alleles (Figure 4.4A-A', B-B'). Secondly, the expression of two key markers of AVC development, *has2* (Lagendijk et al., 2011) and *bmp4* (Vermot et al., 2009) were examined. At 55hpf, both *has2* (Figure 4.4C-D') and *bmp4* expression (Figure 4.4E-F') are unchanged in *lamb1b* zygotic mutant alleles, further suggesting that loss of *lamb1b* does not significantly impact upon heart development.

Although no embryonic phenotype was observable in *lamb1b* mutants, developmental defects could be too subtle to be identified by ISH or may manifest in later life (Pierpont et al., 2000). To investigate whether *lamb1b* function is required past embryonic stages, homozygous mutants were grown to adulthood (Figure 4.5). *lamb1b* mutants are adult viable and fertile, with no difference in body length at approximately six months of age when compared to siblings (Figure 4.5A, B). Additionally, no difference in heart mass normalised to body mass is observed in *lamb1b* homozygous mutants when compared to heterozygous siblings at approximately 2 years old (Figure 4.5C, D).

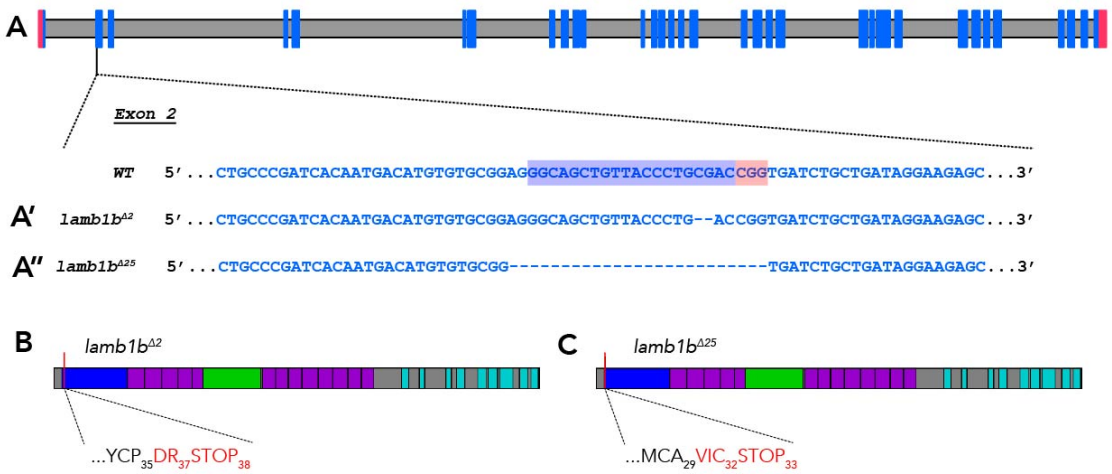

Figure 4.2. Generation of *lamb1b* coding sequence mutants by CRISPR-Cas9 mutagenesis.

Mutagenesis strategy and predicted impact on Lamb1b protein **(A)** Schematic of *lamb1b* genomic DNA based on danRer10/GRCz10, Red: non-coding DNA, Blue: coding DNA, Grey: intronic DNA. A single gRNA targeting Exon 2, spacer highlighted in blue, PAM highlighted in red, was injected and two mutations were identified. **(A')** The *lamb1b*$^{\Delta 2}$ allele results in a 2bp deletion. **(A'')** The *lamb1b*$^{\Delta 25}$allele results in a 25bp deletion. **(B)** Predicted effect of the *lamb1b*$^{\Delta 2}$ allele. The initial 35 amino acids are unaffected, followed by two altered amino acids and a premature stop codon. **(C)** Predicted effect of the *lamb1b*$^{\Delta 25}$ allele. The initial 29 amino acids are unaffected, followed by three altered amino acids and a premature stop codon.

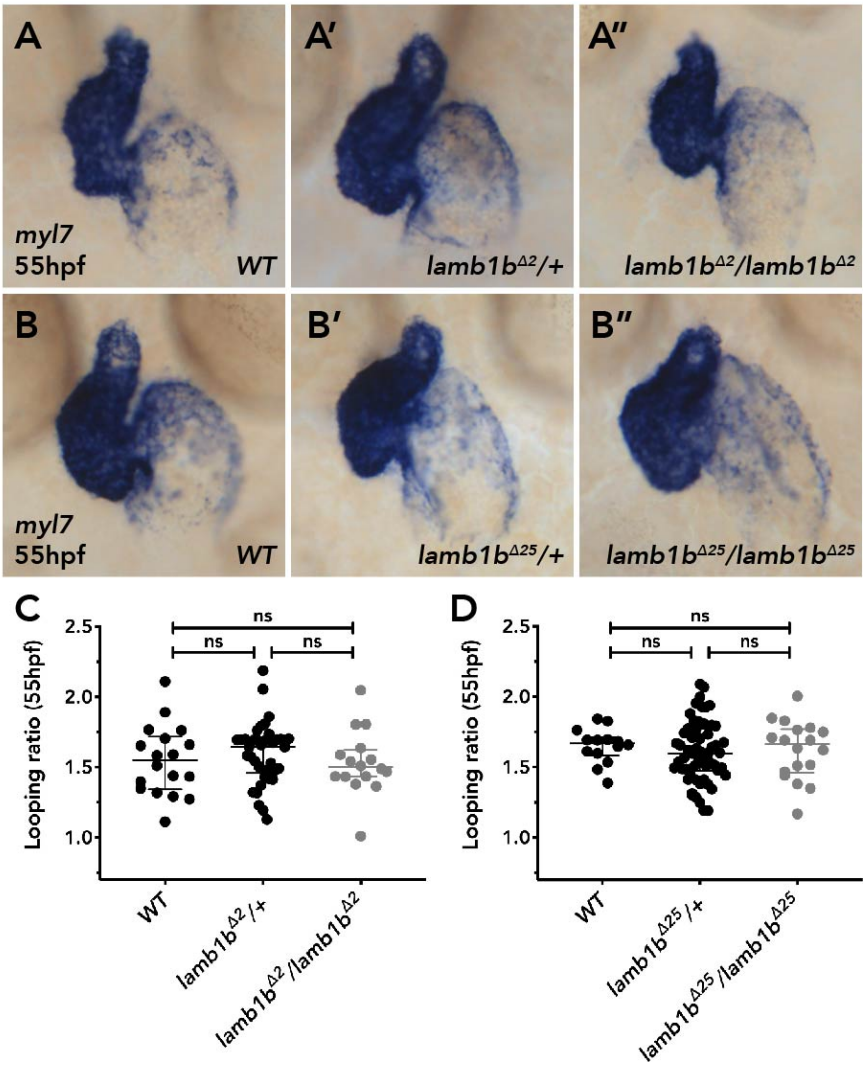

Figure 4.3. *lamb1b* zygotic coding sequence mutants do not display cardiac abnormalities.

Quantitative analysis of heart looping in *lamb1b* mutants at 55hpf **(A-A'')** Representative images of mRNA *in situ* hybridisation analysis of *myl7* expression at 55hpf to examine heart morphology in WT (A), *lamb1b*$^{\Delta 2}$ heterozygotes (A') and *lamb1b*$^{\Delta 2}$ homozygous mutants (A''). **(B-B'')** Representative images of mRNA *in situ* hybridisation analysis of *myl7* at 55hpf to examine heart morphology in WT (B), *lamb1b*$^{\Delta 25}$ heterozygotes (B') and *lamb1b*$^{\Delta 25}$ homozygous mutants (B''). **(C-D)** Quantification of heart looping ratio of *lamb1b*$^{\Delta 2}$ mutants and siblings (C) and *lamb1b*$^{\Delta 25}$ mutants and siblings (D) and 55hpf reveals no significant differences in heart looping of mutants compared to siblings. Ventral views. C, D: Median with interquartile range, Kruskal-Wallis, Dunn's multiple comparisons, ns: not significant.

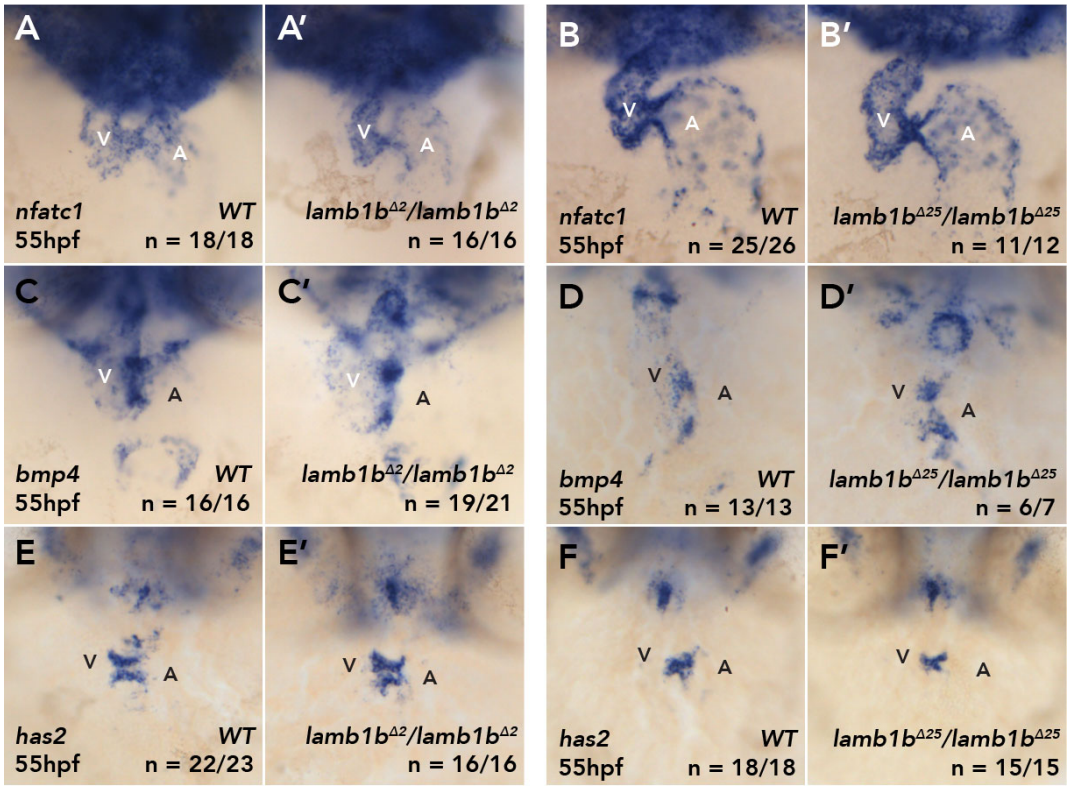

Figure 4.4. Valve and endocardial markers are unaltered in *lamb1b* zygotic coding sequence mutants.

mRNA *in situ* hybridisation analysis of *nfatc1*, *bmp4* and *has2* in *lamb1b* coding sequence and WT siblings at 55hpf. **(A-B')** The endocardial marker *nfatc1* shows no change in expression between WT siblings (A, B) and *lamb1b*$^{\Delta 2}$ or *lamb1b*$^{\Delta 25}$ homozygous mutants (A', B'). **(C-D')** *bmp4* shows no change in expression between WT siblings (C, D) and *lamb1b*$^{\Delta 2}$ or *lamb1b*$^{\Delta 25}$ homozygous mutants (C',D'). **(E-F')** The valve marker *has2* shows no change in expression between WT siblings (E, F) and *lamb1b*$^{\Delta 2}$ or *lamb1b*$^{\Delta 25}$ homozygous mutants (E',F'). Ventral views. V: ventricle. A: atrium.

Previous studies have shown that specific Laminin subunit transcripts are maternally supplied during oogenesis (Pollard et al., 2006), thus maternal deposition of *lamb1b* may mask a zygotic role for *lamb1b* in heart development. Adult *lamb1b* homozygous mutants were incrossed to generate maternal-paternal-zygotic (MPZ) *lamb1b* mutant embryos, abolishing any wild type *lamb1b* transcripts from the

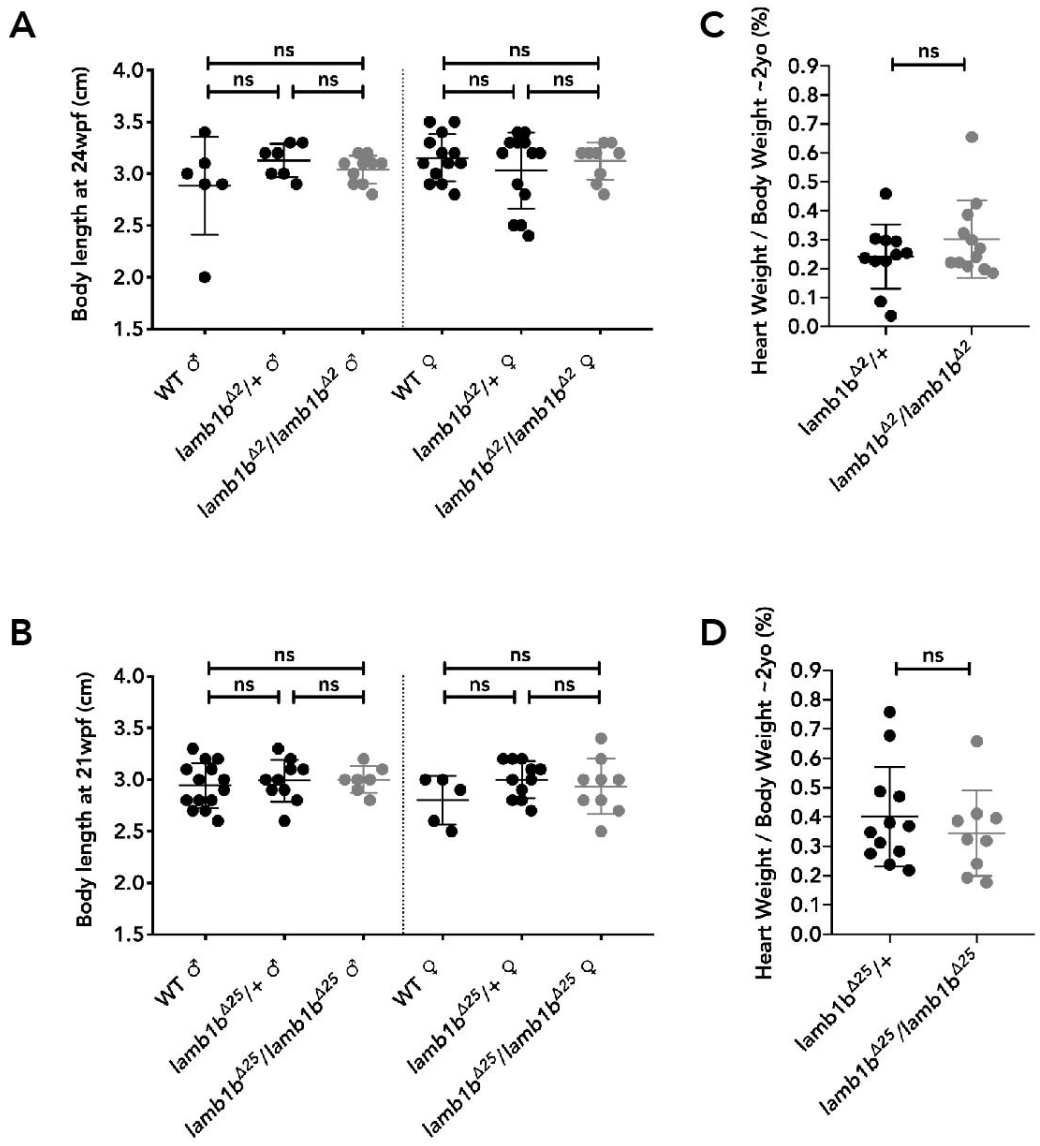

Figure 4.5. *lamb1b* mutant adults do not display body size or cardiac size defects.

(A-B) Loss of Lamb1b function does not significantly alter adult body length at 24 weeks post-fertilisation for either sex in *lamb1b*$^{\Delta 2}$ homozygous mutants compared to sibling controls (A) or at 21 weeks post-fertilisation for either sex in *lamb1b*$^{\Delta 25}$ homozygous mutants compared to sibling controls (B). **(C-D)** Comparison of heart weight expressed as a percentage of body weight in adult *lamb1b* heterozygous and homozygous mutants, both obtained from a *lamb1b* heterozygous incross at approximately 2 years old. No significant differences are present between homozygous mutants and their respective heterozygous siblings. Arithmetic Mean with Standard Deviation A, B: Ordinary one-way ANOVA with Sidak's multiple comparison test C, D: Brown-Forsythe and Welch ANOVA, ns: not significant.

developing embryo. When compared to WT or *lamb1b* zygotic mutants (WT and zygotic mutant data reproduced from Figure 4.3), neither allele of *lamb1b* MPZ mutants presented with a cardiac phenotype (Figure 4.6C, D). Together, these data suggest that as neither zygotic, nor MPZ *lamb1b* coding sequence mutants have significant defects in heart looping nor abnormalities in valve specification (Figure 4.3, 4.4, 4.6), and adult mutants are homozygous viable, fertile and do not display obvious morphological differences (Figure 4.5) that *lamb1b* may be dispensable for development.

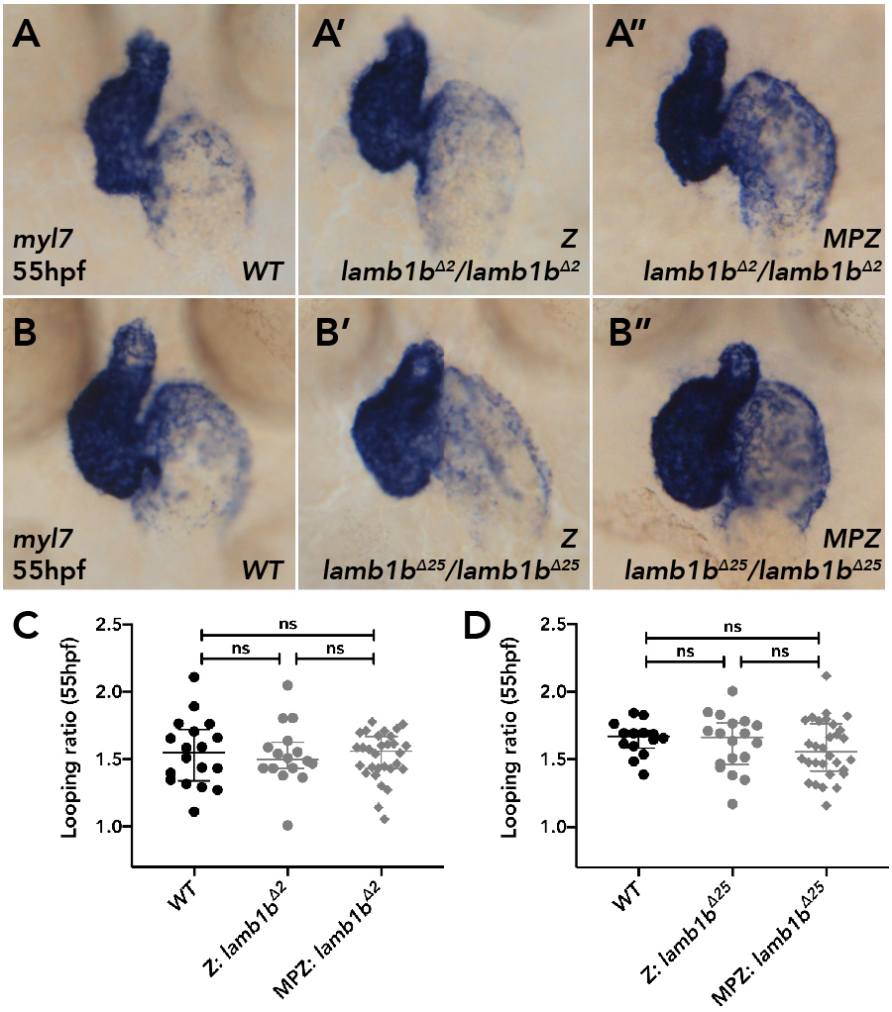

Figure 4.6. *lamb1b* maternal-paternal-zygotic coding sequence mutants do not display cardiac abnormalities.

Quantitative comparison of heart looping and heart size in *lamb1b* Zygotic (Z) and *lamb1b* Maternal-Paternal-Zygotic (MPZ) mutants at 55hpf. **(A-A'')** Representative images of mRNA *in situ* hybridisation analysis of *myl7* at 55hpf to examine heart morphology in WT (A), *lamb1b*$^{\Delta 2}$ Zygotic mutants (A') and *lamb1b*$^{\Delta 2}$ Maternal-Paternal-Zygotic mutants (A''). **(B-B'')** Representative images of mRNA in situ hybridisation analysis of *myl7* at 55hpf to examine heart morphology in WT (B), *lamb1b*$^{\Delta 25}$ Zygotic mutants (B') and *lamb1b*$^{\Delta 25}$ Maternal-Paternal-Zygotic mutants (B''). **(C-D)** Quantification of heart looping ratio of WT, zygotic and maternal-paternal-zygotic *lamb1b*$^{\Delta 2}$ (C) and *lamb1b*$^{\Delta 25}$ mutants (D) at 55hpf no significant differences are measured. Ventral views. C, D: Median with interquartile range, Kruskal-Wallis, Dunn's multiple comparisons, ns: not significant

4.1.3 *lamb1b* coding sequence mutants display hallmarks of genetic compensation

Although *lamb1b* mutants do not display any obvious phenotypes, a number of studies across plants, cell culture and animal models have demonstrated that an absence of phenotype does not categorically define a gene as having no function (El-Brolosy et al., 2019; El-Brolosy and Stainier, 2017). Highlighted by in-depth comparative analyses of zebrafish loss-of-function models, a number of different mechanisms have been identified by which an organism with a deleterious mutation is able to proceed through development, termed genetic robustness. This phenomenon can be achieved by activating mechanisms such as transcriptional adaptation: "changes in RNA levels or processing resulting from a genetic mutation and not from the loss of gene function" i.e. the gene attempts to rescue itself (El-Brolosy and Stainier, 2017) or genetic compensation: "changes in RNA or protein levels that can functionally compensate for the loss of function of another gene" i.e. the gene activates another to bring about rescue (El-Brolosy and Stainier, 2017).

One study in zebrafish study has shown that transcriptional adaption by exon skipping is in some cases able to recover the frame of a mutant transcript (Anderson et al., 2017). Of the seven mutations studied, three showed exon-skipping to maintain the frame of the transcript and did not show a reduction in transcript levels, whilst in two other mutants, the frame was not maintained and transcript levels were significantly lower (Anderson et al., 2017). Therefore, by skipping exons the genome is able to overcome some mutations, maintain the reading frame and theoretically produce functional protein, although this was not examined in the study.

To investigate the possibility that *lamb1b* mutants utilise exon-skipping to excise the genetic lesion and maintain the reading frame in mutant transcripts (Anderson et al., 2017), total RNA was isolated at 55hpf from an incross of *lamb1b* mutants (Figure 4.7, inX), an outcross of *lamb1b* mutants (Figure 4.7, outX) and WT RNA from an incross of AB adults (Figure 4.7, WT). cDNA was generated from total RNA and two

sets of PCR primers used to amplify two regions of the *lamb1b* coding sequence spanning multiple exons: either the region containing the genetic lesion in *lamb1b* mutants (Figure 4.7A, Pair 1) or a region downstream (Figure 4.7A, Pair 2) to investigate possible exon skipping in *lamb1b* mutants. Gel electrophoresis of PCR products using either primer pair from *lamb1b* MPZ mutants does not identify extra bands which would be a hallmark of exon skipping (Figure 4.7B ,C). A second band is observed in *lamb1b*$^{\Delta 25}$ heterozygous cDNA for pair 1 (Figure 4.7B), reflecting the two different sizes of PCR product due to the deletion. Sanger sequencing of PCR products from pair 1 (Figure 4.7D-D''), confirmed the deletion was still present in mRNA derived from *lamb1b* mutants, ruling out exon skipping as a possible mechanism of compensation in *lamb1b* mutants.

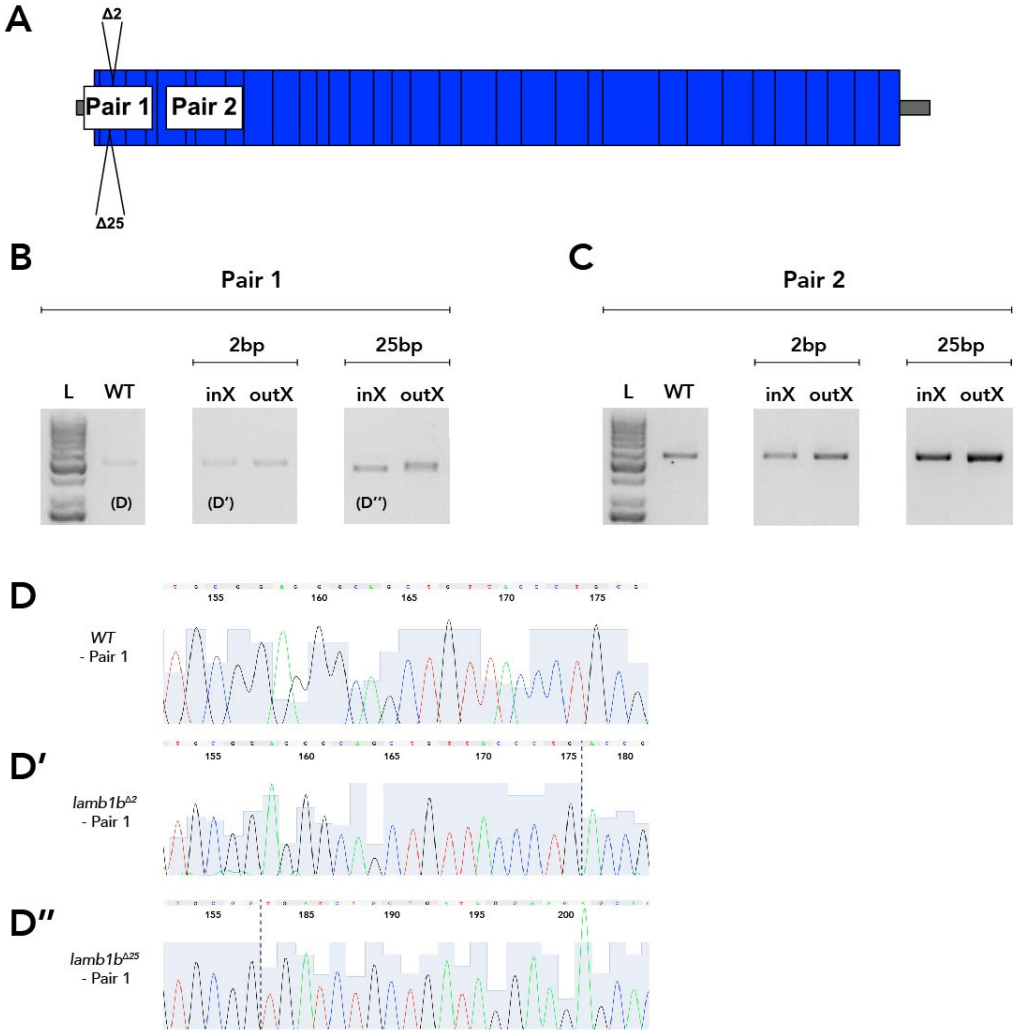

Figure 4.7. *lamb1b* mutant mRNA does not undergo alternative splicing.

(A) Schematic of *lamb1b* mRNA (blue: translated, grey: non-translated), showing region amplified by primers to examine presence of alternative splicing, Pair1 covers the two mutation sites. **(B)** Gel electrophoresis of PCR products using primer Pair 1 with WT cDNA, cDNA obtained from an incross (inX) or outcross (outX) of *lamb1b*$^{\Delta 2}$ homozygous mutants, or cDNA obtained from an incross or outcross of *lamb1b*$^{\Delta 25}$ homozygous mutants. No unexpected extra bands are observed compared to WT or outX cDNA. **(C)** Gel electrophoresis of PCR products using primer Pair 2 with WT cDNA, cDNA obtained from an inX or outX of *lamb1b*$^{\Delta 2}$ homozygous mutants, or cDNA obtained from an inX or outX of *lamb1b*$^{\Delta 25}$ homozygous mutants. No unexpected extra bands are observed compared to WT or outX cDNA. **(D-D'')** Sanger sequencing traces of PCR products from (B). Both *lamb1b*$^{\Delta 2}$ (D') and *lamb1b*$^{\Delta 25}$ (D'') homozygous mutant mRNA still contain the genetic lesion.

The second, more commonly reported mechanism that could explain absence of phenotype in *lamb1b* mutants is genetic compensation activated by NMD of mutant transcript (El-Brolosy et al., 2019; Schuermann et al., 2015). NMD is activated when premature termination codons are located more than 55bp upstream of exon-intron boundaries resulting in the mutant transcript being targeted for destruction (Maquat, 2005; Popp and Maquat, 2016; Wittkopp et al., 2009) (Figure 1.2Cii). As NMD products are able to induce genetic compensation (El-Brolosy et al., 2019; Schuermann et al., 2015) and the premature termination codon created in both *lamb1b* mutant alleles lies more than 55bp upstream of the exon2-3 boundary (Figure 4.8A, B), it is likely that these mutant transcripts may be targeted for degradation, and thus initiate genetic compensation.

To examine this possibility the expression of *lamb1b* in *lamb1b* mutants was examined. *in situ* hybridisation analysis of *lamb1b* expression in embryos at 55hpf obtained from an incross of *lamb1b* heterozygous adults demonstrates a clear reduction in *lamb1b* transcript levels at the AVC when compared to WT siblings (Figure 4.8C-C'', D-D'', brackets), suggesting that the *lamb1b* transcript is subject to decay, possibly by NMD. A secondary method, semi-qPCR examined relative levels between *lamb1b* homozygous mutants and heterozygous carriers across five different regions of the *lamb1b* transcript (Figure 8E-G'). Levels of *lamb1b*$^{\Delta 2}$ mutant transcript show a significant reduction in levels compared to *lamb1b*$^{\Delta 2}$ heterozygous transcript in the four 3'-most regions assayed (Figure 4.8E, F , F'). *lamb1b*$^{\Delta 25}$ mutants display a trend towards reduction compared to controls, when levels are normalised to either *gapdh (glyceraldehyde-3-phosphate dehydrogenase)* (Figure 4.8G) or *eef1a1l1 (eurkaryotic translation elongation factor 1 alpha, like 1)* (Figure 4.8G') in WT across almost all 5 regions of the transcript. This disparity between the ISH data and semi-qPCR for *lamb1b*$^{\Delta 25}$ allele may arise because of the sensitivity of the semi-qPCR assay, due to *lamb1b* only expressed at very low levels through the vasculature of the embryo (data not shown) or that the *lamb1b*$^{\Delta 2}$ allele is the more

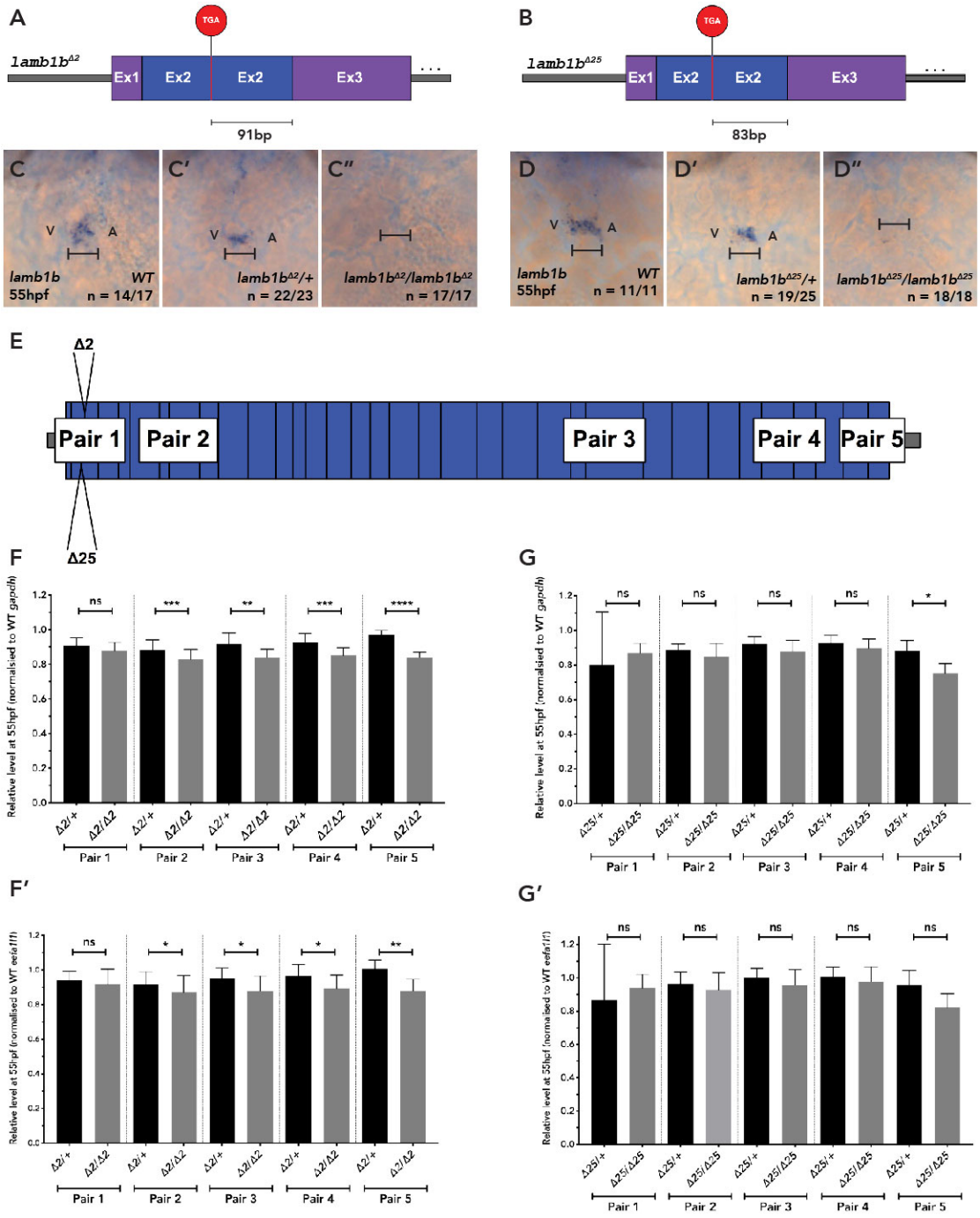

Figure 4.8 *lamb1b* coding sequence mutant mRNA transcripts appear to undergo decay.

mRNA *in situ* hybridisation analysis and semi-quantitative analysis of levels of *lamb1b* mRNA mutant transcript. **(A-B)** Schematic of *lamb1b* mRNA, demonstrating that both predicted alleles have premature stop codon (Red, TGA) greater than 50-55bp upstream of the exon2-exon3 junction. **(C-D'')** Analysis of *lamb1b* expression at the atrioventricular canal (brackets) at 55hpf in WT (C, D), *lamb1b*$^{\Delta 2}$ heterozygotes

severe allele. However, since *lamb1b* mutants display a reduction in *lamb1b* transcript assayed by ISH and a trend towards reduction of transcript levels by semi-qPCR, together with the positioning of the PTC at a location that may initiate NMD, it is possible that NMD of *lamb1b* mutant transcripts could activate genetic compensation, rescuing any phenotypes induced in *lamb1b* mutants.

Previous studies have shown that to evade damaging phenotypes upon loss of gene function, NMD-activated compensation up-regulates the expression of genes of the same family, or genes which contain similar functional domains (El-Brolosy and Stainier, 2017; Rossi et al., 2015). Therefore, the most probable candidate for up-regulation in *lamb1b* mutants is another Laminin beta subunit. ISH expression analysis of all annotated Laminin beta subunits at 55hpf (Figure 4.9) does not show any clear up-regulation of *lamb1a* or *lamb2*, subunits with previously described expression in the heart (Figure 4.9A-D'). In addition, the two remaining Laminin beta genes which are not expressed in the WT heart at 55hpf, *lamb2l* and *lamb4*

Figure 4.8 continued.

(C'), *lamb1b*$^{\Delta 25}$ heterozygotes (D'), *lamb1b*$^{\Delta 2}$ homozygous mutants (C'', D''). *lamb1b* expression is absent in *lamb1b* homozygous mutants. *lamb1b* expression is absent in *lamb1b* homozygous mutants. **(E)** Schematic of *lamb1b* mRNA (blue: translated, grey: non-translated), showing region amplified by primers used for semi-qPCR. Pair1 encompasses the two mutation sites. **(F-F')** Quantification of levels of transcript in *lamb1b*$^{\Delta 2}$ heterozygous carriers and homozygous mutants, normalised to WT *gapdh* (F) or *eefa1l1* (F') loading control. Levels of regions 2 to 5 show a significant reduction in *lamb1b*$^{\Delta 2}$ homozygous mutants. **(G-G')** Quantification of levels of transcript in *lamb1b*$^{\Delta 25}$ heterozygous carriers and homozygous mutants, normalised to WT *gapdh* (G) or *eefa1l1* (G') loading control. Region 5 shows a significant reduction in *lamb1b*$^{\Delta 25}$ homozygous mutants. C-D'': ventral views, V: ventricle. A: atrium. F-G': Arithmetic mean with standard deviation, One-way ANOVA. ns: not significant, *: p<0.05, **: p<0.01, ***: p<0.001, ****: p<0.0001

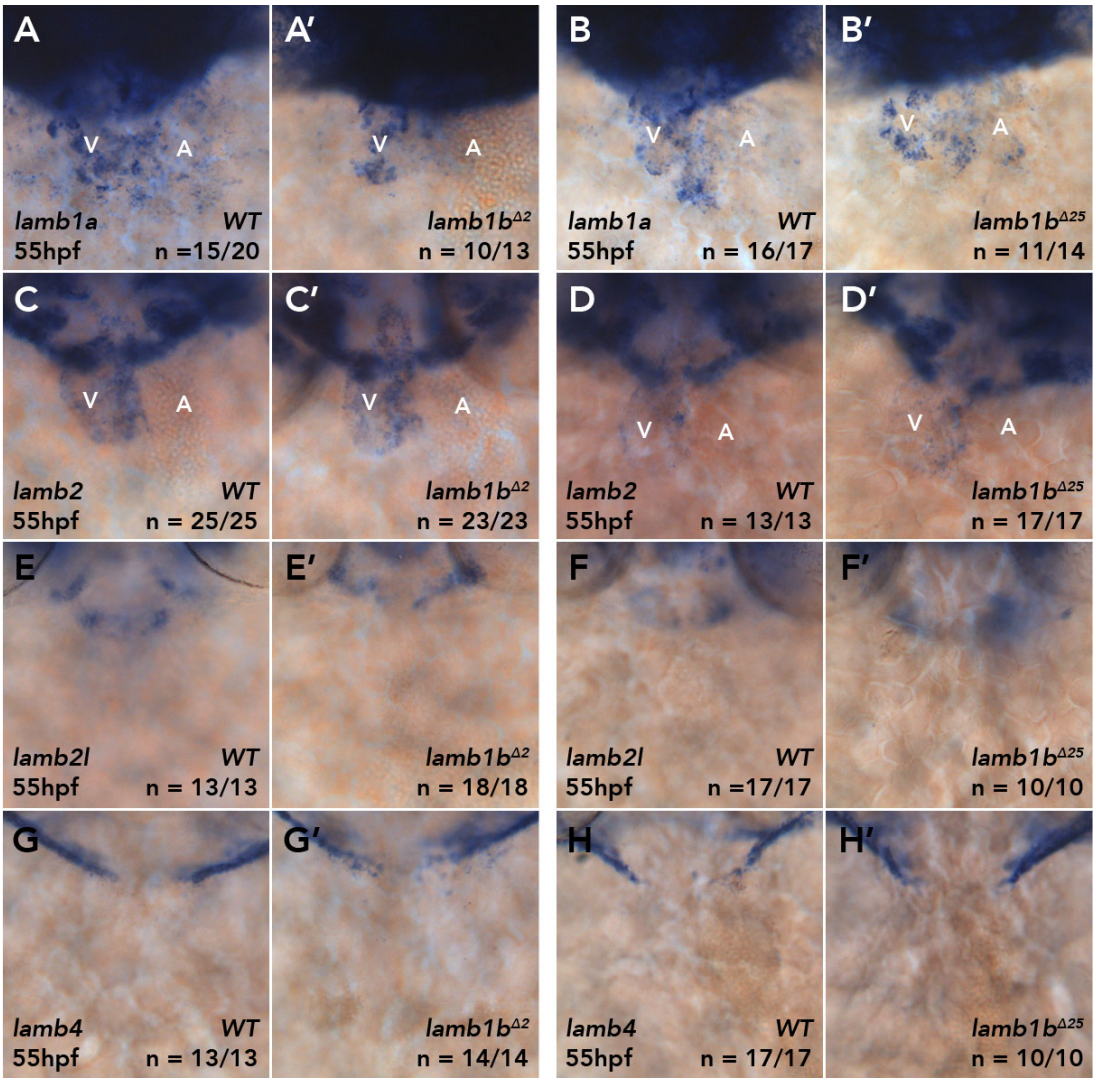

Figure 4.9. Expression of other Laminin beta subunits is unchanged in *lamb1b* zygotic coding sequence mutants.

mRNA *in situ* hybridisation analysis of all annotated Laminin beta subunits in *lamb1b* coding sequence mutants and WT siblings at 55hpf. **(A-B')** Expression of *lamb1a* in the heart shows no change between WT siblings (A) and *lamb1b*$^{\Delta 2}$ homozygous mutants (A') or in WT siblings (B) and *lamb1b*$^{\Delta 25}$ homozygous mutants (B'). **(C-D')** Expression of *lamb2* in the heart shows no change between WT siblings (C) and *lamb1b*$^{\Delta 2}$ homozygous mutants (C') or in WT siblings (D) and *lamb1b*$^{\Delta 25}$ homozygous mutants (D'). **(E-F')** At 55hpf, *lamb2l* is not expressed in the heart in either WT siblings (E, F) and *lamb1b*$^{\Delta 25}$ or *lamb1b*$^{\Delta 25}$ homozygous mutants (E',F'). **(G-H')** At 55hpf, *lamb4* is not expressed in the heart in either WT siblings (G ,H) and *lamb1b*$^{\Delta 2}$ or *lamb1b*$^{\Delta 25}$ homozygous mutants (G',H'). Ventral views. V: ventricle. A: atrium.

(*laminin, beta 4*) (Figure 4.9E-H) are not up-regulated in the hearts of *lamb1b* mutants (Figure 4.9E'-H'). Whilst *lamb1b* mutants do not display any clear up-regulation of other Laminin beta subunit genes, this does not rule out the possibility of genetic compensation being active in *lamb1b* mutants, potentially through the functional compensation of one of the other Laminin beta subunit genes which are normally expressed in the developing heart.

4.1.4 *lamb1b* ATG morphants have severe cardiac defects which are likely to be due to off-target effects

The products of NMD of mutant transcripts are proposed to activate genetic compensation (El-Brolosy et al., 2019). As morpholinos function without activating NMD but prevent generation of the functional protein (Figure 1.2), resulting in a loss-of function phenotype, this may explain the widespread disparity between phenotypes observed in embryos subject to gene knockdown and coding sequence mutants of the same gene (Kok et al., 2015). Therefore, as no obvious compensating gene is up-regulated in *lamb1b* mutants (Figure 3.10), a morpholino targeting the annotated initiating ATG of *lamb1b* (Figure 4.10A) was injected into WT embryos at the 1-cell stage to examine the role of *lamb1b* in heart looping morphogenesis.

At 55hpf, when *lamb1b* mutants display no cardiac defects (Figure 4.3, 4.6), *lamb1b* ATG morphants have a mildly dysmorphic hearts and a significant reduction in heart looping ratio when compared to uninjected or *tp53* MO only injected control embryos (Figure 4.10B-B'', E). To further characterise the effect of *lamb1b* knockdown, ISH expression analysis of individual chamber markers was carried out to analyse ventricle (*myosin heavy chain 7, like, myh7l*, formerly *vmhcl*) and atrium (*myh6*) development either singularly (Figure 4.10C-C'') or together (Figure 4.10D-D''). Analysis of chamber morphology revealed a significant reduction in both ventricular (4.10C-C'', F) and atrial circularity (4.10D-D'', G) in *lamb1b* morphants, suggesting that *lamb1b* plays a role in regulating the shape of both chambers.

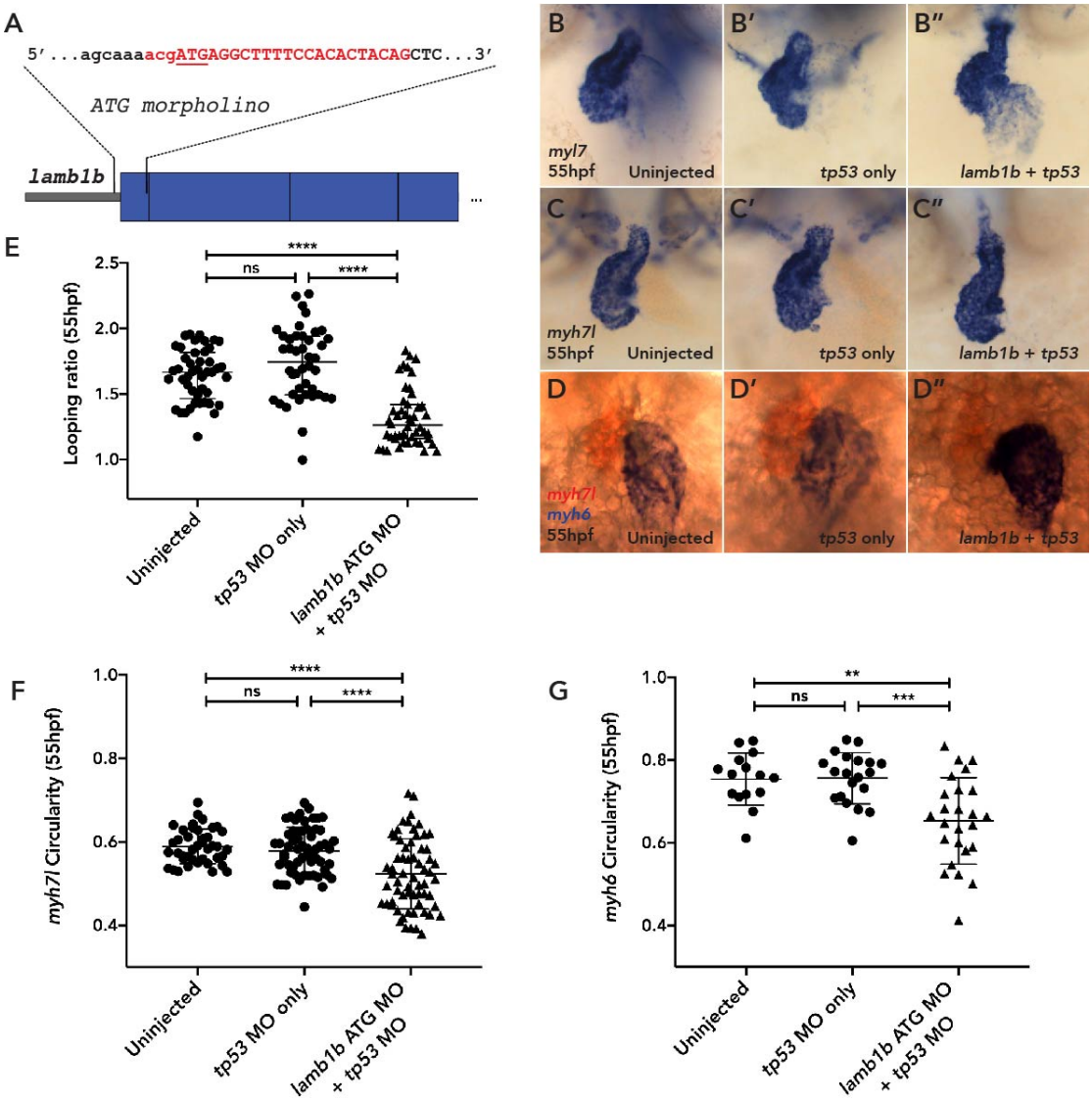

Figure 4.10. *lamb1b* ATG morphants have severe cardiac defects.

Analysis of the impact of the *lamb1b* ATG morpholino on heart looping morphogenesis and heart morphology at 55hpf using mRNA *in situ* hybridisation. **(A)** Schematic highlighting region of *lamb1b* mRNA (blue: translated, grey untranslated) bound by *lamb1b* ATG morpholino (red, ATG underlined). **(B-B'')** Representative images of mRNA *in situ* hybridisation analysis of *myl7* at 55hpf to examine heart morphology in uninjected (B), *tp53* MO only injected (B') and *lamb1b* ATG MO + *tp53* MO injected embryos (B''). **(C-C'')** Representative images of mRNA *in situ* hybridisation analysis of *myh7l* at 55hpf to examine ventricle morphology in uninjected (C), *tp53* MO only injected (C') and *lamb1b* ATG MO + *tp53* MO injected embryos (C''). **(D-D'')** Representative images of mRNA *in situ* hybridisation analysis

Figure 4.10 continued.

of *myh6* (blue) and *myh7l* (red) at 55hpf to examine heart and specific morphology in uninjected (D), *tp53* MO only injected (D') and *lamb1b* ATG MO + *tp53* MO injected embryos (D''). **(E)** Quantification of heart looping ratio in uninjected, *tp53* MO only and *lamb1b* MO + *tp53* MO embryos at 55hpf where injection of the *lamb1b* ATG MO results in a significant reduction in heart looping ratio compared to either control group. **(F-G)** Quantification of ventricular (F) and atrial (G) circularity in uninjected, *tp53* MO only and *lamb1b* MO + *tp53* MO embryos at 55hpf where injection of the *lamb1b* ATG MO results in a significant reduction in both ventricular and atrial circularity compared to either control group. B-D'': ventral views. E: Median with interquartile range, Kruskal-Wallis, Dunn's multiple comparisons. F, G: Arithmetic mean with standard deviation, Tukey's multiple comparisons. ns: not significant, **: $p<0.01$, ***: $p<0.001$, ****: $p<0.0001$

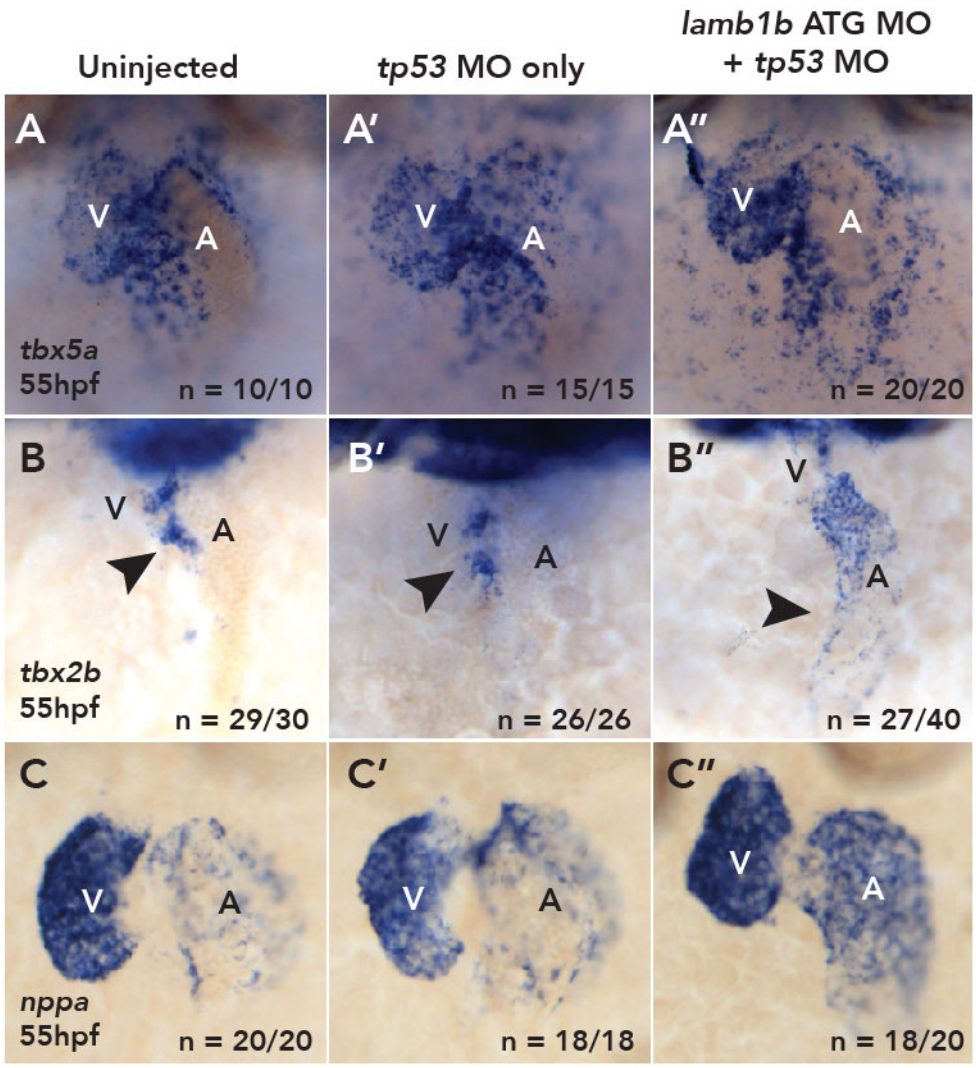

Figure 4.11. Morpholino-mediated knockdown of *lamb1b* affects cardiac patterning. mRNA *in situ* hybridisation analysis of *tbx5a*, *tbx2b* and *nppa* expression in *lamb1b* morphants at 55hpf. **(A-A'')** Expression of *tbx5a* at 55hpf is comparable between uninjected (A), *tp53* MO injected (A') and *lamb1b* ATG MO + *tp53* MO injected embryos (A''). **(B-B'')** In uninjected embryos at 55hpf (B), *tbx2b* is expressed at the atrioventricular canal (B, arrowhead), *tp53* MO injection (B') does not alter *tbx2b* expression. Injection of *lamb1b* ATG MO + *tp53* MO results expansion of *tbx2b* expression into the atrium (B'', arrowhead). **(C-C'')** Expression of *nppa* at 55hpf is comparable between uninjected (C), *tp53* MO injected (C') and *lamb1b* ATG MO + *tp53* MO injected embryos (C''). Ventral views. V: ventricle. A: atrium.

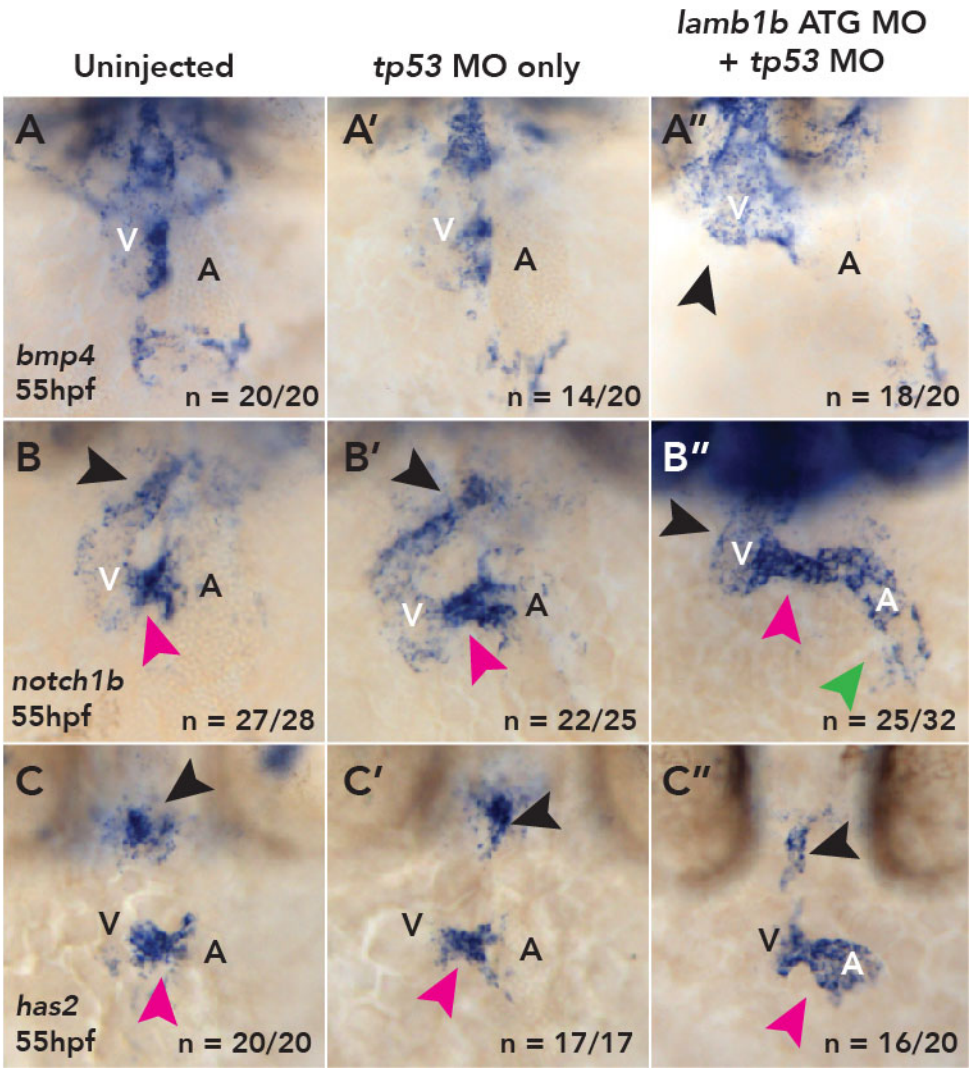

Figure 4.12. Morpholino-mediated knockdown of *lamb1b* results in expansion of valve markers.

mRNA *in situ* hybridisation analysis of valve markers *bmp4*, *notch1b* and *has2* in *lamb1b* morphants at 55hpf. **(A-A'')** *bmp4* expression at the inflow tract, atrioventricular canal and outflow tract in uninjected embryos (A) is not affected by *tp53* MO injection (A'). Injection of *lamb1b* ATG MO + *tp53* MO results in expansion of *bmp4* expression into the ventricle (A'', arrowhead). **(B-B'')** In uninjected embryos at 55hpf *notch1b* is expressed at the atrioventricular canal (B, magenta arrowhead) and outflow tract (B, black arrowhead), and *tp53* MO injection (B') does not alter *notch1b* expression. Injection of *lamb1b* ATG MO + *tp53* MO results in profound expansion of *notch1b* expression throughout the endocardium and into the atrium (B'', green arrowhead). **(C-C'')** *has2* expression in injected embryos (C) strongly

Patterning of the myocardium in *lamb1b* morphants appears unaffected as *tbx5a (T-box transcription factor 5a)* and *nppa* (*natriuretic peptide A*) expression appear normal (Figure 4.11A-A'', C-C''), however knockdown of *lamb1b* often resulted in expansion of *tbx2b* (*T-box transcription factor 2b*, a marker of non-working myocardium at the AVC) (Sedletcaia and Evans, 2011) into the atrium (Figure 4.11B''). Other markers associated with valve development, *notch1b* (Figure 4.12A-A'') (Vermot et al., 2009) and *has2* (Figure 4.12B-B'') (Lagendijk et al., 2013, 2011) are also expanded into the atrium, with *notch1b* expression also present in the ventricular endocardium, further suggesting that *lamb1b* may be required to properly restrict the valve program. Furthermore, another readout of correct cardiac patterning also involved in valve development, *bmp4*, is expanded into the ventricle at 55hpf (Figure 4.12C-C''). Together, knockdown of *lamb1b* results in a severe cardiac phenotype, characterised by a reduction in heart looping, changes to the morphology of both chambers and expansion of valve markers. This suggests that *lamb1b* coding sequences mutants may display genetic compensation, or alternatively that the phenotypes observed in *lamb1b* morphants are due to off-target effects.

To confirm that the *lamb1b* knockdown phenotype is specifically due to the loss of *lamb1b* function and not due to off-target effects, the *lamb1b* ATG morpholino was injected into 1-cell stage embryos from an in-cross of *lamb1b* heterozygotes (Figure 4.13). The current dogma suggests that should *lamb1b* mutants exhibit genetic

Figure 4.12 continued.

overlaps with *notch1b* expression at the atrioventricular canal (C, magenta arrowhead) and outflow tract (C, black arrowhead), expression is unchanged in *tp53* MO injected embryos (C'). Injection of *lamb1b* ATG MO + *tp53* MO (C'') results in mild expansion of *has2* expression into the ventricular endocardium (C'', black arrowhead) and atrial endocardium (C'', magenta arrowhead). Ventral views. V: ventricle, A: atrium.

compensation, injection of the *lamb1b* ATG morpholino into *lamb1b* mutants should not result in a phenotype as function of the compensating gene would not be affected, whilst WT or heterozygous *lamb1b* siblings would still present with the knockdown phenotype (Stainier et al., 2017). However, *lamb1b*$^{\Delta 2}$ mutants injected with the *lamb1b* ATG morpholino, have a significant reduction in looping ratio (Figure 4.13A) compared to injection controls, and appear phenotypically similar to WT siblings injected with the morpholino, demonstrating that the *lamb1b*$^{\Delta 2}$ mutants are not protected against the *lamb1b* ATG morphant phenotype. Additionally, neither coding sequence mutant allele of *lamb1b* displays protection from a significant reduction in atrial circularity (Figure 4.13B, C). In summary, this demonstrates that whilst *lamb1b* ATG morphants display a severe cardiac phenotype, this is likely to be due to off-target effects of the morpholino as *lamb1b* homozygous mutants are not protected from these morphological defects.

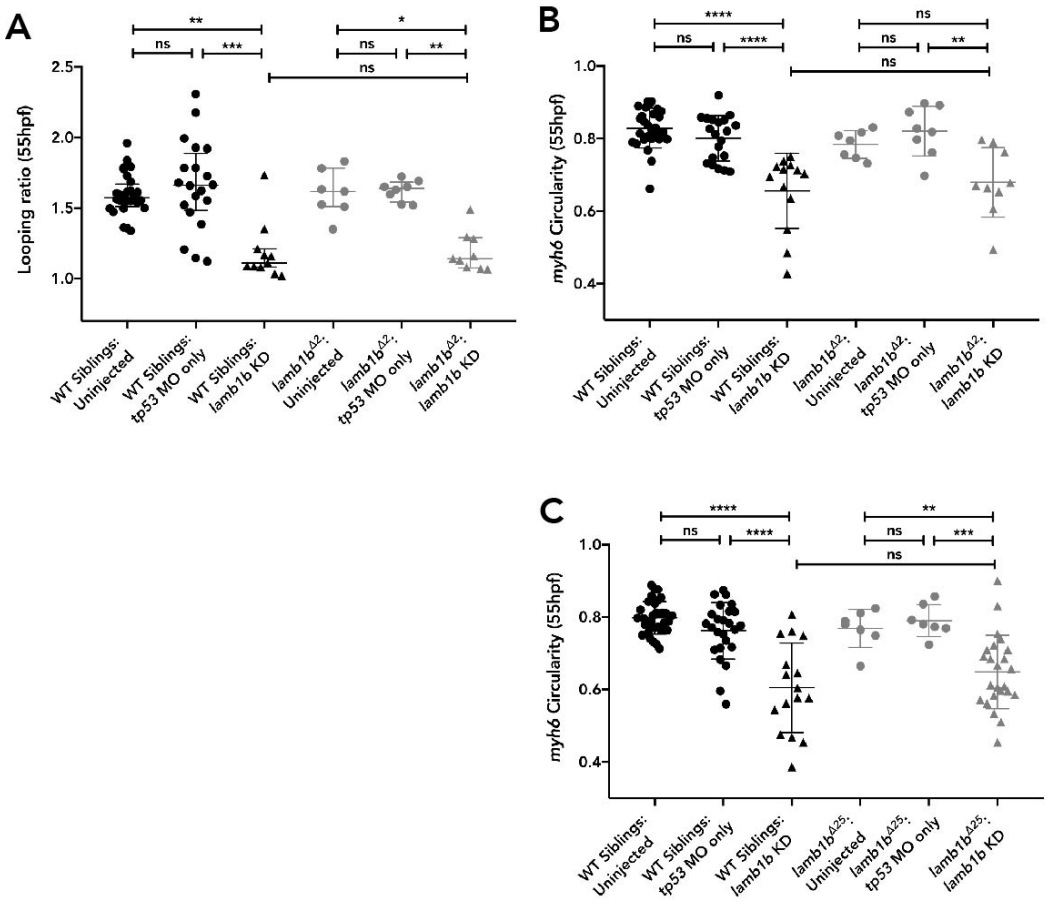

Figure 4.13. *lamb1b* coding sequence mutants are not protected against the *lamb1b* ATG morphant phenotype.

(A) Quantification of looping ratio in injection controls and *lamb1b* ATG + *tp53* MO injected embryos in a *lamb1b*$^{\Delta 2}$ heterozygous incross at 55hpf. Injection of *lamb1b* ATG MO + *tp53* MO into sibling embryos and *lamb1b*$^{\Delta 2}$ homozygous mutant embryos results in a significant reduction in heart looping ratio at 55hpf compared to injection controls of relevant genotype. **(B-C)** Quantification of atrial circularity of injection controls and *lamb1b* ATG + *tp53* MO injected embryos from a *lamb1b*$^{\Delta 2}$ (B) or *lamb1b*$^{\Delta 25}$ (C) heterozygous inX at 55hpf. Injection of *lamb1b* ATG MO + *tp53* MO into sibling embryos and *lamb1b* homozygous mutant embryos results in a significant reduction in atrial circularity ratio at 55hpf compared to injection controls of relevant phenotype. A: Median with interquartile range, Kruskal-Wallis, Dunn's multiple comparisons. B, C: Arithmetic mean with standard deviation, Tukey's multiple comparisons. ns: not significant, *: $p<0.05$, **: $p<0.01$, ***: $p<0.001$, ****: $p<0.0001$

4.1.5 Developing CRISPRi as a tool for targeted gene knockdown

The disparity between mutant and morphant phenotypes has driven development of the genetic toolkit in zebrafish to definitively uncover gene function during development. CRISPRi builds upon the exquisite targeting nature of CRISPR by modifying the Cas9 protein for knockdown of gene function rather than knockout. dCas9 is recruited by gRNAs to prevent either initiation or elongation of transcription (Larson et al., 2013; Qi et al., 2013) similar to how translation-targeting MOs result in knockdown (Bill et al., 2009) (Figure 1.2). Although originally developing in bacterial culture, CRISPRi has been successfully applied in zebrafish, where *egfl7* CRISPants recapitulate the *egfl7* MO phenotype (Rossi et al., 2015). More recently, an elegant study examining the role of *tmem33* in distinct aspects of zebrafish development utilised tissue-specific CRISPRi, placing the *dCas9* coding sequence under either endothelial or renal promoters, uncoupling the phenotypes observed using global knockdown by morpholino (Savage et al., 2019). Additionally, induction of *tp53* expression is reduced in CRISPant embryos compared to morphants, highlighting that CRISPRi is more specific and results in fewer off-target effects (Savage et al., 2019).

To continuing exploring the potential for genetic compensation to be active in *lamb1b* coding sequence mutants, a stable, globally-expressing dCas9 system was developed. The *dCas9* coding sequence (Savage et al., 2019) was placed under the control of the ubiquitously active promoter of *ubiquitin B* (*ubb*, *ubi*) (Mossiman 2011), in a Gateway vector containing the transgenesis marker *cryaa:CFP*, which results in CFP expression in the retina from 2dpf onwards (Savage et al., 2019) (Figure 4.14A). The *ubi:dCas9poly(A), cryaa:CFP* plasmid was injected together with *tol2* mRNA into the cell of 1-cell stage embryos and CFP-positive embryos were grown to adulthood. Two founders transmitting the *ubi:dCas9* construct through the germline were identified and outcrossed to generate two stable lines of *Tg(ubi:dCas9, cryaa:CFP).* To confirm segregation of *dCas9* transcript with the

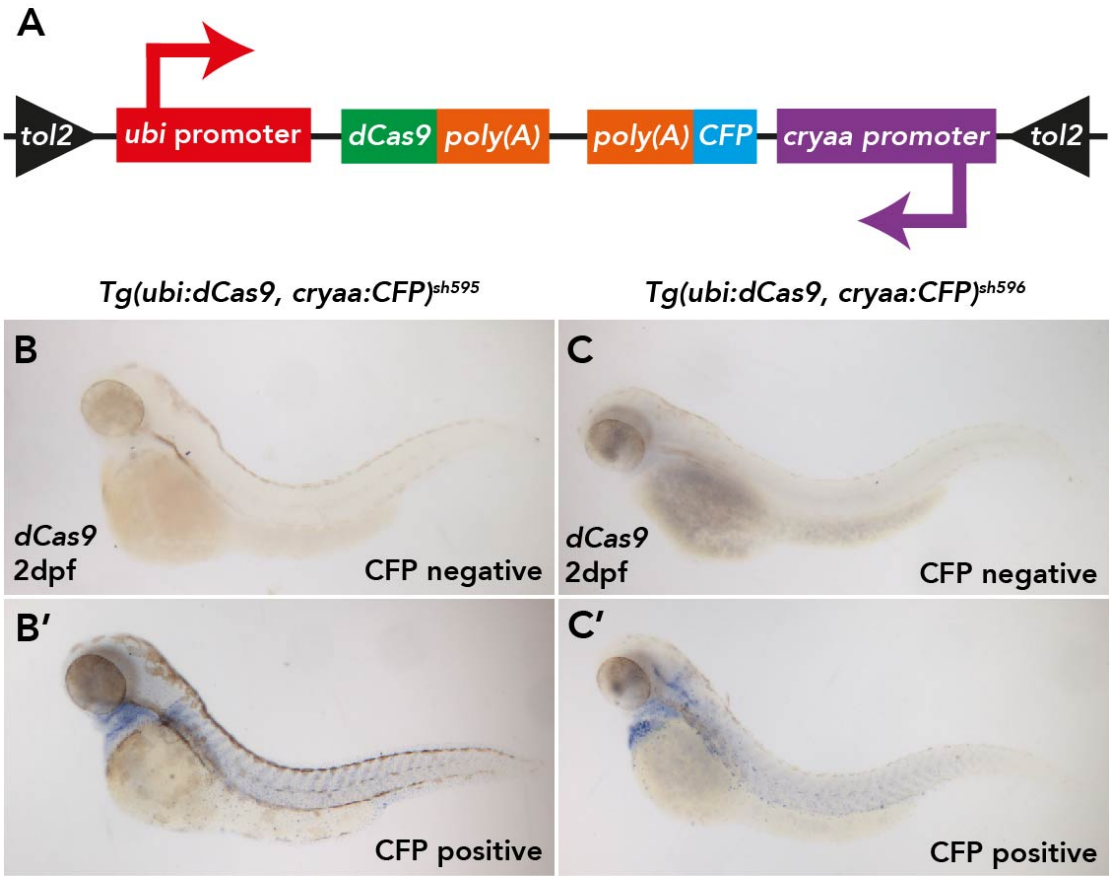

Figure 4.14. Generation of *Tg(ubi:dCas9, cryaaCFP)* for global CRISPRi.

(A) Schematic of *Tg(ubi:dCas9, cryaaCFP)* construct used to generate the transgenic zebrafish line. The *dCas9* coding sequence (green), together with the SV40 poly(A) antigen (orange) were placed downstream of the *ubi* promoter (red) to drive ubiquitous expression of *dCas9*. On the opposite strand, the *cryaa* promoter (purple) drives expression of Cerulean Fluorescent Protein (CFP, cyan) as a marker for transgenesis. **(B-C')** mRNA *in situ* hybridisation analysis of *dCas9* expression in progeny from two founders, screened for CFP transgenesis at 2dpf. *dCas9* expression segregates with CFP+ progeny as confirmed by *dCas9* expression (B', C'). No *dCas9* expression is observed in CFP- negative sibling embryos (B, C). The *sh595* allele (B') appears to drive slightly stronger expression than the *sh596* allele. B-C': lateral views, anterior left.

transgenesis marker, F1 offspring were screened for CFP expression at 2dpf. Subsequently, *dCas9* expression in CFP positive and CFP negative embryos was examined by ISH which confirmed *dCas9* expression only in embryos with the CFP marker (Figure 4.14B-C').

Having generated a ubiquitous *dCas9*-expressing transgenic line, two gRNAs targeting *lamb1b* were designed to prevent *lamb1b* transcription: gRNA 1 targeting the template strand upstream of the initiating ATG in exon 2, and gRNA 2 targeting the non-template strand of exon 3 (Figure 4.15A) in line with previously reported strand specificity for gene knockdown (Larson et al., 2013; Qi et al., 2013; Xu et al., 2015). The two gRNAs were injected into 1-cell stage embryos from an outcross of *Tg(ubi:dCas9, cryaa:CFP)*^{sh596}. Embryos were fixed at 24hpf, expression of *lamb1b* examined by ISH to confirm knockdown of the transcript, and carriers of the *ubi:dCas9* construct identified by PCR (as the *cryaa:CFP* marker is not visible at 24hpf). No change in *lamb1b* expression is observed in *Tg(ubi:dCas9, cryaa:CFP)*^{sh596} injected embryos when compared to uninjected controls (Figure 4.15B') or non-transgenic injected siblings (Figure 4.15B''), demonstrating unsuccessful knockdown of *lamb1b* transcription by CRISPRi, and suggesting that further development and optimisation of the CRISPRi system is required for routine use.

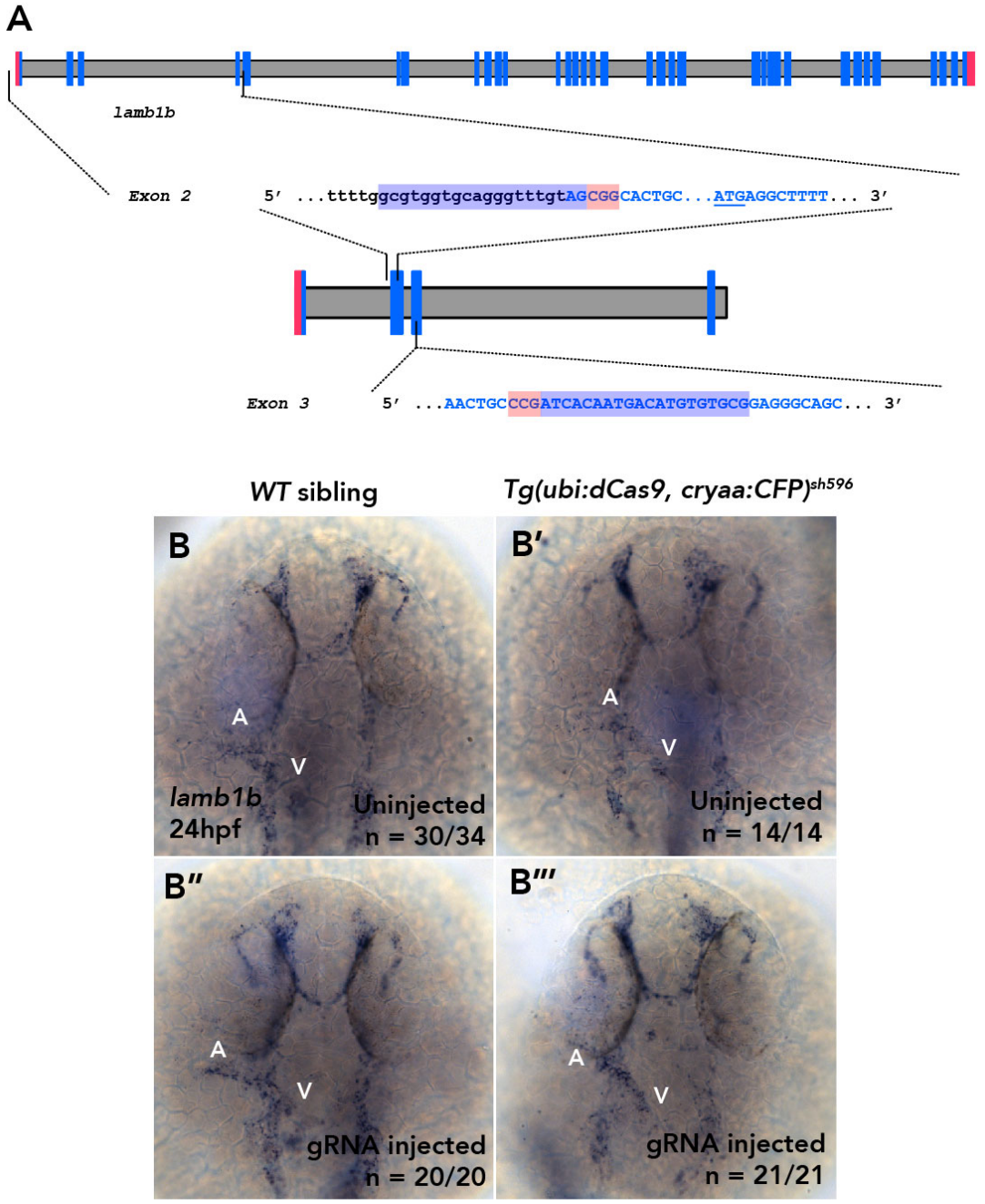

Figure 4.15. Knockdown of *lamb1b* is not observed using *Tg(ubi:dCas9, cryaaCFP)*.

(A) Schematic showing targeting location of the *lamb1b* CRISPRi gRNAs for *lamb1b* global CRISPRi. **(B-B‴)** mRNA *in situ* hybridisation analysis of *lamb1b* expression at 24hpf in WT sibling, uninjected (B), *Tg(ubi:dCas9, cryaaCFP)*^{sh596} uninjected (B′), WT sibling *lamb1b* gRNA injected (B″) and *Tg(ubi:dCas9, cryaaCFP)*^{sh596}, *lamb1b* gRNA injected (B‴). No knockdown of *lamb1b* transcript is observed in *Tg(ubi:dCas9, cryaaCFP)*^{sh596}, *lamb1b* gRNA injected embryos (B‴) compared to any control group. B-B‴: dorsal views. V: ventricle, A: atrium.

4.1.6 Generation and characterisation of *lamb1a* coding sequence mutants by CRISPR-Cas9 mutagenesis

Having identified that the *lamb1b* ATG morphant phenotype is due to off-target effects and that although a promising system, CRISPRi requires significant further investment, to examine whether *lamb1b* coding sequence mutants display genetic compensation, mutagenesis of the most likely compensating gene, *lamb1a*, was undertaken. A gRNA targeting exon 6 of *lamb1a* (Figure 4.16A) was injected into an outcross of *lamb1b*$^{\Delta 2}$ heterozygotes at the 1-cell stage (E. Noël) and F0 adults were screened for germline transmission. A single adult heterozygous for the *lamb1b*$^{\Delta 2}$ allele was identified transmitting two different deletions, and this founder was outcrossed to generate two stable lines: *lamb1a*$^{\Delta 19}$and *lamb1a*$^{\Delta 25}$. Both mutant alleles are predicted to result in premature termination codons in the Laminin N-terminal domain of the Lamb1a protein (Figure 4.16B-C). Both mutant alleles of *lamb1a* display a short body axis (Figure 4.17A', B') and abnormal asymmetric morphogenesis of the endoderm marked by *foxa1* (*forkhead box A1)* expression (Figure 4.17C-C''') consistent with defects previously described in *lamb1a* mutants (Hochgreb-Hägele et al., 2013; Stemple et al., 1996). Both phenotypes are present solely in *lamb1a* mutants, irrespective of *lamb1b* genotype (Figure 4.17C''').

To investigate whether *lamb1a* compensates for loss of *lamb1b* in heart looping morphogenesis, *lamb1a; lamb1b* heterozygous adults were incrossed, embryos fixed at 55hpf and using mRNA *in situ* hybridisation analysis of *myl7*, the heart looping ratio quantified at 55hpf (Figure 4.18). In line with previous studies, loss of *lamb1a* alone does not impact upon heart looping (4.18A', B ,C' ,D) (Hochgreb-Hägele et al., 2013), and furthermore in combination with loss of *lamb1b* function, no significant reduction in heart looping ratio is observed (4.18A''', B, C''', D). Together this suggests that neither *lamb1* gene is required to promote heart morphogenesis and that loss of *lamb1b* is not compensated for by *lamb1a* function.

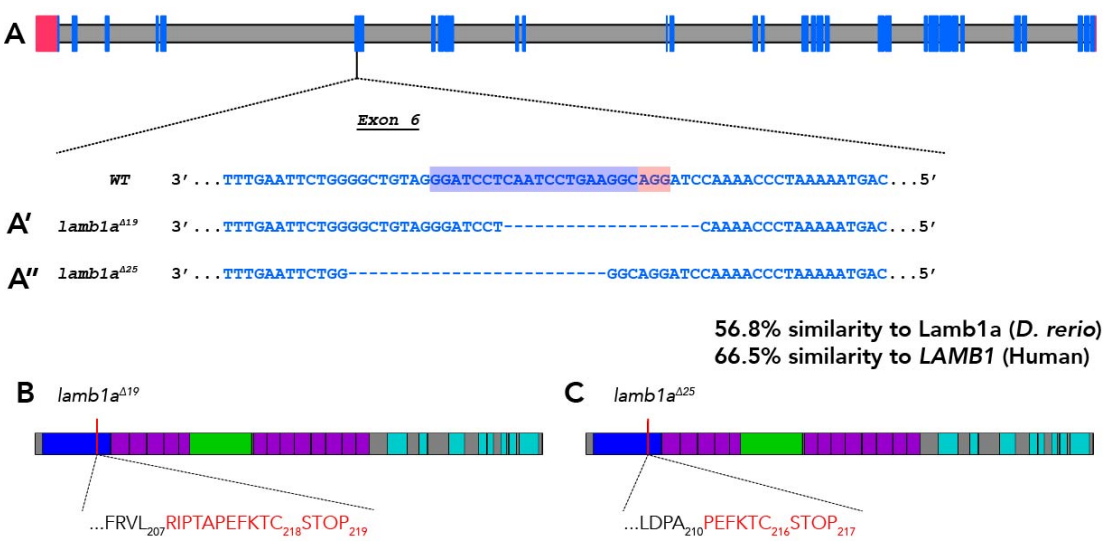

Figure 4.16. Generation of *lamb1a* coding sequence mutants by CRISPR-Cas9 mutagenesis.

Mutagenesis strategy and predicted impact on Lamb1a protein **(A)** Schematic of *lamb1a* genomic DNA based on danRer10/GRCz10 and UniProt accession number Q8JHV7, Red: non-coding DNA, Blue: coding DNA, Grey: intronic DNA. A single gRNA targeting Exon 6, spacer highlighted in blue, PAM highlighted in red, was injected and two mutations were identified. **(A')** The *lamb1a*$^{\Delta 19}$ allele results in a 19bp deletion. **(A'')** The *lamb1a*$^{\Delta 25}$ allele results in a 25bp deletion. **(B)** Predicted effect of the *lamb1a*$^{\Delta 19}$ allele. The initial 207 amino acids are unaffected, followed by 11 altered amino acids and a premature stop codon. **(C)** Predicted effect of the *lamb1a*$^{\Delta 25}$ allele. The initial 210 amino acids are unaffected, followed by 6 altered amino acids and a premature stop codon. Zebrafish Lamb1a protein shares 56.8% amino acid similarity to zebrafish Lamb1b and 66.5% amino acid similarity to Human LAMB1. Blue: Laminin N-terminal domain, Purple: Laminin EGF-repeat, Green: Laminin domain IV type, Cyan: Coiled-coil.

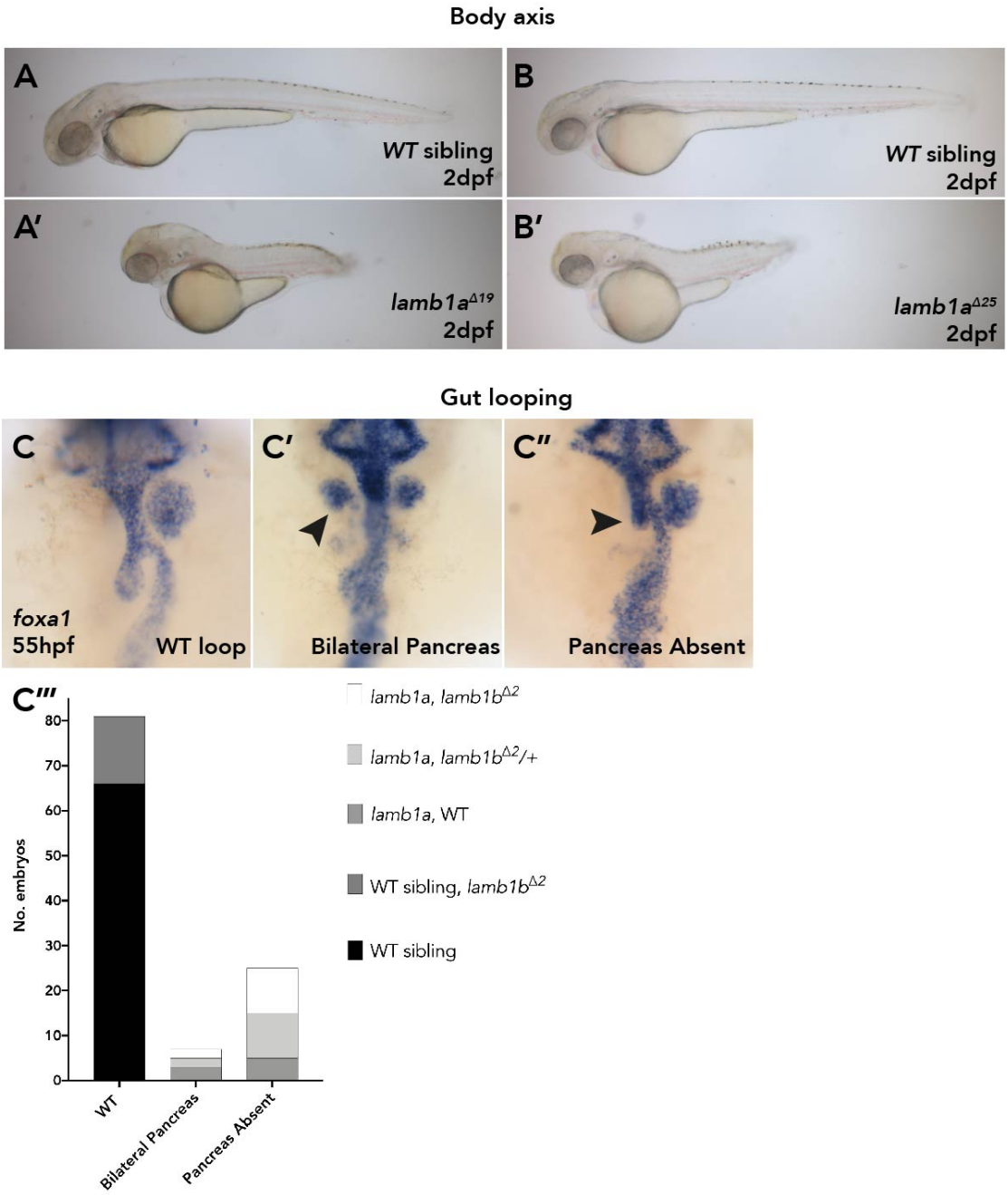

Figure 4.17. *lamb1a* coding sequence mutants recapitulate previously published *lamb1a* alleles.

(A-B') Representative brightfield images of sibling (A), *lamb1a*$^{\Delta 19}$ homozygous mutant (A'), sibling (B) and *lamb1a*$^{\Delta 25}$ homozygous mutant (B') at 2dpf. *lamb1a* mutants are shorter than sibling embryos. **(C-C''')** mRNA *in situ* hybridisation analysis of *foxa1* expression as a marker of endoderm morphology in WT, *lamb1b* homozygous mutants, *lamb1a* homozygous mutants, *lamb1a* homozygous; *lamb1b* heterozygous mutants and double *lamb1a; lamb1b* homozygous mutants at 55hpf.

Figure 4.17 continued.

Three classes of gut morphology are observed WT (C), bilateral pancreas (C', arrowhead) and absent pancreas (C'', arrowhead). Defective gut morphogenesis is only observed in *lamb1a* homozygous mutants (C'''). A-B': lateral views, anterior left. C-C'': ventral views.

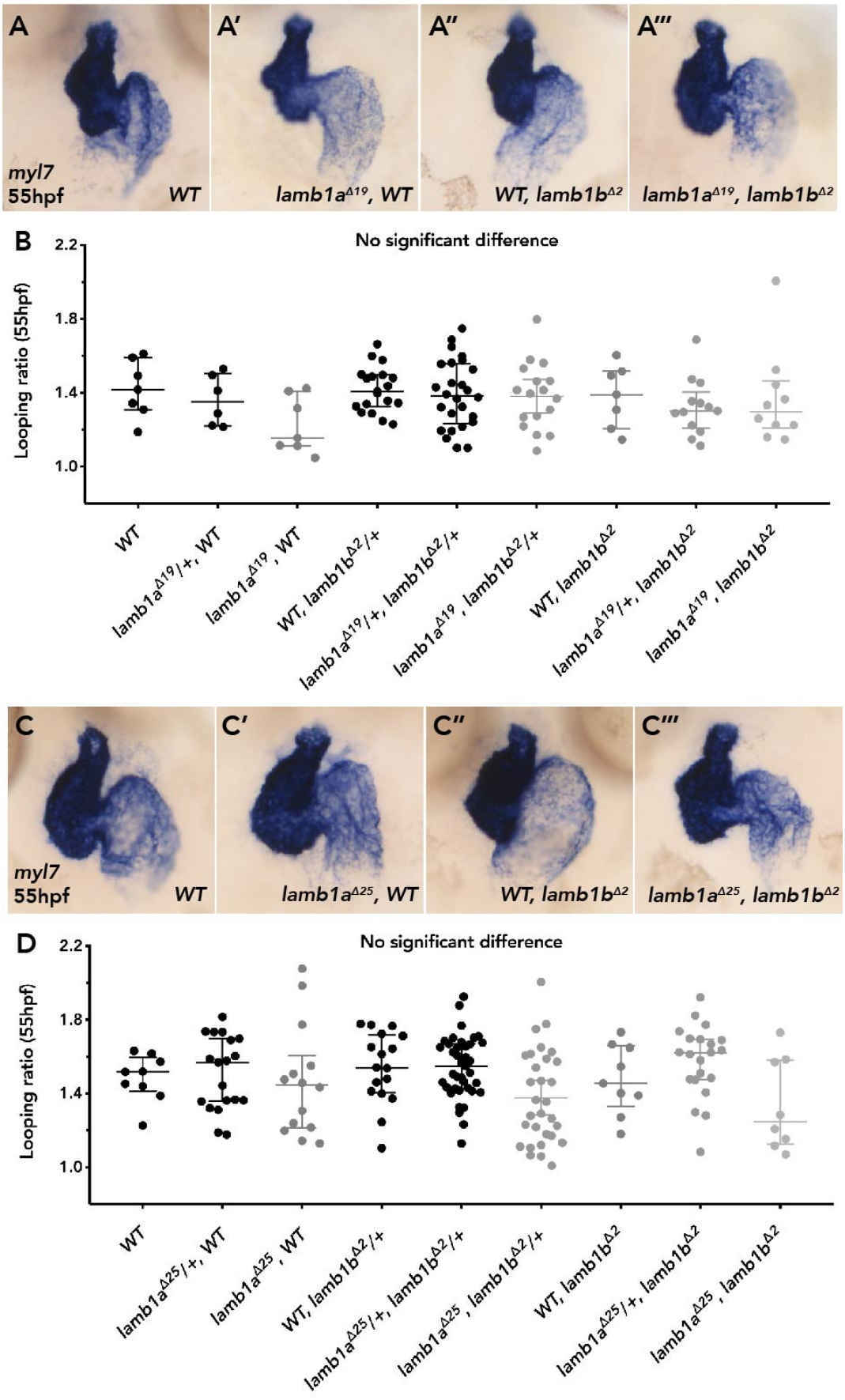
A
A′
A″
A‴
myl7
55hpf
WT
lamb1a^Δ19, WT
WT, lamb1b^Δ2
lamb1a^Δ19, lamb1b^Δ2
B
No significant difference
Looping ratio (55hpf)
2.2
1.8
1.4
1.0
WT
lamb1a^Δ19/+, WT
lamb1a^Δ19, WT
WT, lamb1b^Δ2/+
lamb1a^Δ19/+, lamb1b^Δ2/+
lamb1a^Δ19, lamb1b^Δ2/+
WT, lamb1b^Δ2
lamb1a^Δ19/+, lamb1b^Δ2
lamb1a^Δ19, lamb1b^Δ2
C
C′
C″
C‴
myl7
55hpf
WT
lamb1a^Δ25, WT
WT, lamb1b^Δ2
lamb1a^Δ25, lamb1b^Δ2
D
No significant difference
Looping ratio (55hpf)
2.2
1.8
1.4
1.0
WT
lamb1a^Δ25/+, WT
lamb1a^Δ25, WT
WT, lamb1b^Δ2/+
lamb1a^Δ25/+, lamb1b^Δ2/+
lamb1a^Δ25, lamb1b^Δ2/+
WT, lamb1b^Δ2
lamb1a^Δ25/+, lamb1b^Δ2
lamb1a^Δ25, lamb1b^Δ2

Figure 4.18. *lamb1a* does not compensate for loss of *lamb1b* during heart looping.
Quantitative analysis of heart looping in *lamb1a*; *lamb1b* mutants at 55hpf **(A-A'')** Representative images of mRNA *in situ* hybridisation analysis of *myl7* expression at 55hpf to examine heart morphology in WT (A), *lamb1a*$^{\Delta 19}$ homozygous mutants (A'), *lamb1b*$^{\Delta 2}$ homozygous mutants (A'') and double *lamb1a*$^{\Delta 19}$*; lamb1b*$^{\Delta 2}$ homozygous mutants. **(B)** Quantification of heart looping ratio of *lamb1a*$^{\Delta 19}$*; lamb1b*$^{\Delta 2}$ mutants and siblings at 55hpf, reveals no significant differences between genotypes. **(C-C'')** Representative images of mRNA *in situ* hybridisation analysis of *myl7* expression at 55hpf to examine heart morphology in WT (C), *lamb1a*$^{\Delta 25}$ homozygous mutants (C'), *lamb1b*$^{\Delta 2}$ homozygous mutants (C'') and double *lamb1a*$^{\Delta 25}$; *lamb1b*$^{\Delta 2}$ homozygous mutants. **(D)** Quantification of heart looping ratio of *lamb1a*$^{\Delta 25}$; *lamb1b*$^{\Delta 2}$ mutants and siblings at 55hpf reveals no significant differences between genotypes. Ventral views. B, D: Median with interquartile range, Kruskal-Wallis, Dunn's multiple comparisons.

4.1.7 Deletion of the *lamb1b* promoter demonstrates that *lamb1b* is dispensable for heart development

Evidence suggested that *lamb1b* is undergoing NMD which could activate genetic compensation (Figure 4.8) (El-Brolosy et al., 2019). However, neither a well-controlled or robust knockdown of *lamb1b* function by either MO or CRISPRi respectively could be achieved (Figure 4.13, 4.15) and having shown that *lamb1a* does not compensate for loss of *lamb1b* (Figure 4.18) a different approach to examine the role of *lamb1b* was required. To finally test the function of *lamb1b* and following current guidelines to overcome genetic compensation (El-Brolosy et al., 2019) targeted mutagenesis of the annotated *lamb1b* promoter (identified using the eukaryotic promoter database) (Dreos et al., 2016) using two gRNAs was undertaken (Figure 4.19A).

Three separate deletions removing different regions surrounding or partially surrounding the promoter were identified in the germline of F0 adults, and these founders were outcrossed to generate stable lines (Figure 4.19A). Successful deletion of the promoter was confirmed by ISH analysis of *lamb1b* expression in homozygous *lamb1b* promoter mutant embryos, where expression of *lamb1b* was completely abolished in mutant embryos compared to WT sibling embryos (Figure 4.19B-B''). Analysis of heart morphology using *myl7* expression revealed that none of three *lamb1b* promoter mutant alleles displayed a significant reduction in heart looping morphogenesis compared to either WT or heterozygous siblings (Figure 4.20), directly contradicting the *lamb1b* ATG morphant phenotype. As a secondary approach to confirm that loss of *lamb1b* does not recapitulate the morphant knockdown phenotype and has no effect on heart development, *notch1b* expression was examined in *lamb1b* promoter mutants. At 55hpf, *notch1b* expression is unchanged in *lamb1b* promoter mutants when compared to WT or heterozygous siblings (Figure 4.21) in contrast to the obvious expansion observed in *lamb1b* ATG morphants (Figure 4.12B-B'').

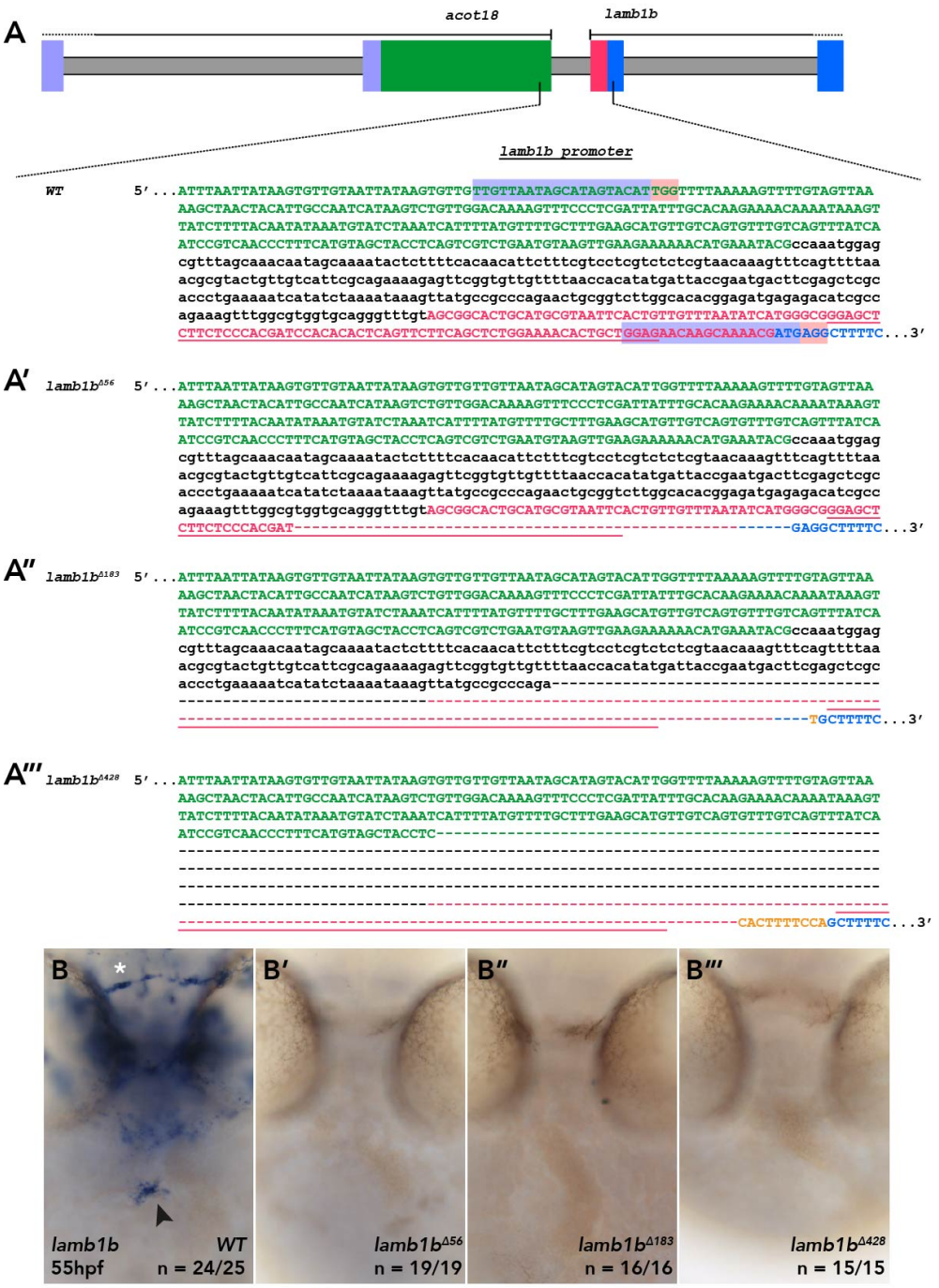

Figure 4.19. Targeted deletion of the *lamb1b* promoter by CRISPR-Cas9 results in complete loss of *lamb1b* transcript.

Mutagenesis strategy to delete the annotated *lamb1b* promoter. **(A)** Schematic of annotated *lamb1b* promoter based on Eukaryotic Promoter Database and upstream region based on danRer10/GRCz10, Red: non-coding *lamb1b* DNA (annotated *lamb1b* promoter underlined), Blue: coding *lamb1b* DNA, Lilac: coding *acot18* DNA, Green: non-coding *acot18* DNA Grey: intronic DNA. Two gRNAs targeting

Figure 4.19 continued.

around the *lamb1b* promoter spacer highlighted in blue, PAM highlighted in red, were injected and three mutations were identified. **(A')** The *lamb1b*$^{\Delta 56}$ allele results in a 56bp deletion, but leaves some of the *lamb1b* promoter intact. **(A'')** The *lamb1b*$^{\Delta 183}$ allele results in a 184bp deletion and a 1bp insertion (yellow), resulting in complete deletion of the annotated *lamb1b* promoter. **(A''')** The *lamb1b*$^{\Delta 428}$ allele results in a 428bp deletion and a 10bp insertion (yellow), resulting in complete deletion of the annotated *lamb1b* promoter and some non-coding 3' elements of the *acot18* transcript. **(B'-B''')** mRNA *in situ* hybridisation of *lamb1b* at 55hpf in WT sibling embryos (B), showing prominent expression at the atrioventricular canal (B, arrowhead) and head vasculature (B, asterisk). In all three *lamb1b* promoter deletion alleles *lamb1b*$^{\Delta 56}$ (B'), *lamb1b*$^{\Delta 183}$ (B'') and *lamb1b*$^{\Delta 428}$ (B'''), *lamb1b* expression is abolished. Ventral views.

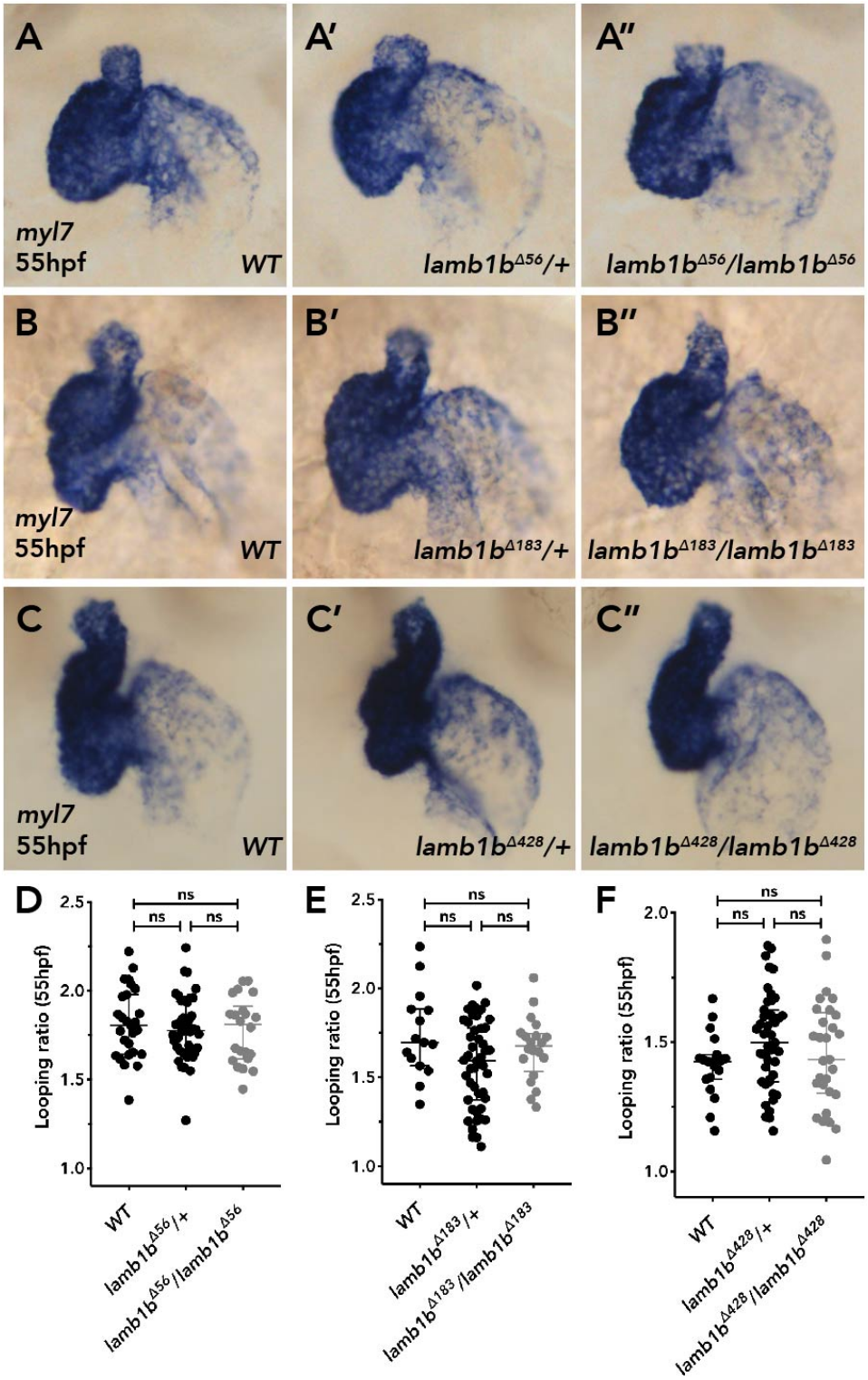

Figure 4.20 *lamb1b* promoter mutants do not phenocopy *lamb1b* ATG morphants. Quantitative analysis of heart looping in *lamb1b* promoter mutants at 55hpf. **(A-A'')** Representative images of mRNA *in situ* hybridisation analysis of *myl7* expression at 55hpf to examine heart morphology in WT (A), *lamb1b*$^{\Delta 56}$ heterozygotes (A') and *lamb1b*$^{\Delta 56}$ homozygous mutants (A''). **(B-B'')** Representative images of mRNA *in situ*

Figure 4.20 continued.

hybridisation analysis of *myl7* expression at 55hpf to examine heart morphology in WT (B), *lamb1b*$^{\Delta183}$ heterozygotes (B') and *lamb1b*$^{\Delta183}$ homozygous mutants (B''). **(C-C'')** Representative images of mRNA *in situ* hybridisation analysis of *myl7* at 55hpf to examine heart morphology in WT (C), *lamb1b*$^{\Delta428}$ heterozygotes (C') and *lamb1b*$^{\Delta428}$ homozygous mutants (C''). **(D-F)** Quantification of heart looping ratio of *lamb1b*$^{\Delta56}$ mutants and siblings (D) *lamb1b*$^{\Delta183}$ mutants and siblings (E) and *lamb1b*$^{\Delta428}$ mutants and siblings (F) at 55hpf reveals no significant differences in heart looping of mutants compared to siblings. Ventral views D-F: Median with interquartile range, Kruskal-Wallis, Dunn's multiple comparisons, ns: not significant.

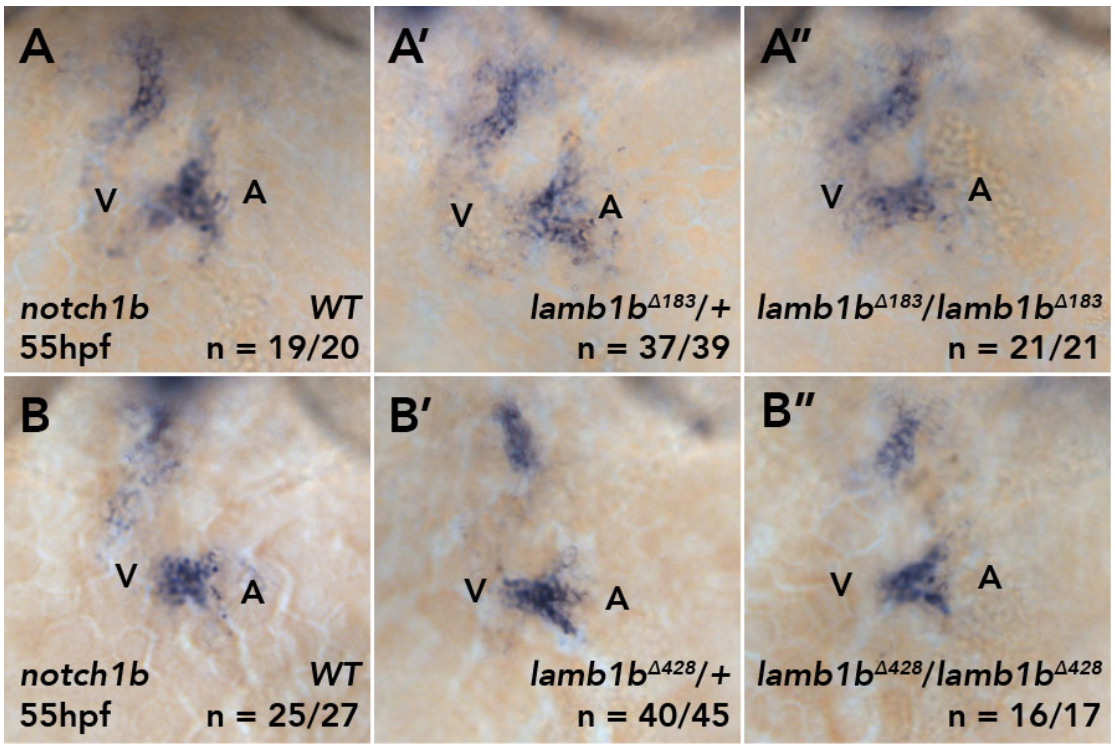

Figure 4.21. *lamb1b* promoter mutants do not recapitulate expansion of *notch1b* observed in *lamb1b* ATG morphants.

mRNA *in situ* hybridisation analysis *notch1b* expression in *lamb1b* promoter mutants at 55hpf. **(A-B'')** Expression of *notch1b* at the atriovenctricular canal and outflow tract in WT embryos (A, B) is unaffected in heterozygous embryos for *lamb1b*$^{\Delta 183}$ (A'), *lamb1b*$^{\Delta 428}$ (B') or homozygous mutant embryos for *lamb1b*$^{\Delta 183}$ (A''), *lamb1b*$^{\Delta 428}$ (B''). Ventral views. V: ventricle, A: atrium.

Together, the deletion of the *lamb1b* promoter results in a complete loss of *lamb1b* transcript in the embryo, evading the proposed mechanisms that would activate genetic compensation which could be functioning in *lamb1b* coding sequence mutants (Figure 4.19) (El-Brolosy et al., 2019; Rossi et al., 2015). As loss of *lamb1b* transcript does not result in any detectable effect on heart looping morphogenesis (Figure 4.20), or *notch1b* expression at the valve (Figure 4.21) this further confirms that the *lamb1b* ATG morphant phenotype is due to either off-target effects or a generalised delay of embryogenesis and demonstrates that *lamb1b* is dispensable for embryonic development.

4.2 Discussion

In Chapter 3 I demonstrated that mutagenesis of *lamc1* identified a role for Laminins in heart looping morphogenesis. *lamb1a* and *lamb2* are expressed in the heart at the same time as *lamc1*, yet mutants have previously been described with no associated impact on heart development (Hochgreb-Hägele et al., 2013; Jacoby et al., 2009). Thus to further identify the components of the Lamc1-containing isoform which are required for heart looping, I characterised the third Laminin beta subunit expressed in the heart: *lamb1b*. *lamb1b* expression is highly dynamic during heart morphogenesis and expression is highly specific to the heart and vasculature during zebrafish development, making it an excellent candidate for promoting heart looping morphogenesis together with *lamc1*. However, using CRISPR-Cas9 mutagenesis of first the coding sequence, and subsequently the promoter of *lamb1b*, I have demonstrated that *lamb1b* function is not required to promote heart development.

The disparity between phenotypes observed in morpholino-mediated knockdowns when compared to genetic mutants is well described within the zebrafish community, particularly highlighted by one study which aimed to generate and characterise zebrafish mutants of genes for which knockdown by MO had resulted in severe phenotypes (Kok et al., 2015). Only 3 of the 24 mutants recapitulated the MO phenotype and the remaining lines were indistinguishable from wild-type (Kok et al., 2015). Importantly, this phenomenon is not restricted to zebrafish, nor the animal kingdom, with discrepancies occurring in *Arabidopsis thaliana*, mice and human cell culture (Braun et al., 2008; El-Brolosy et al., 2019; El-Brolosy and Stainier, 2017; Gao et al., 2015; Lin et al., 2017, 2007; Rossi et al., 2015; Savage et al., 2019; Williams et al., 2015). Whilst the differing results in techniques to assess gene function may appear concerning, there are many cases in the human population where seemingly healthy individuals have deleterious mutations in genes predicted to cause disease (D.-H. Chen et al., 2016; Narasimhan et al., 2016; Sulem et al., 2015). These findings demonstrate the weight given to conclusions developed from

the use of one method to assess gene function should be carefully considered, particularly when using the literature to inform the design of models for biological processes.

Increasingly apparent, the choice of technique is an important consideration in relation to the question being asked: the specific role of a gene/protein in a developmental process is a different question to that of the impact of mutation of the gene on an organism. Whilst the former be can identified through knockdown or deletion of the entire gene/promoter (El-Brolosy et al., 2019), the effect of a mutation associated with milder or less penetrant phenotypes, which may be associated with syndromes is more challenging. These considerations are exemplified in the penetrance of different phenotypes presented by patients with syndromes such as Dandy-Walker or Adams-Oliver (AOS). All DWS patients are characterised with brain abnormalities, but only around a third possess CHDs, and thus it is likely that the interactions between known causative genes and normally non-pathogenic mutations in other genes results in diverse presentation of other defects. Similar to DWS, AOS have a classical defining abnormality of the scalp (cutis aplasia congenita) and transverse limb defects, but only 20% of sufferers have CHDs (Hassed et al., 2017). Acute knockdown of *DOCK6* in cell culture, a gene linked to AOS, results in defects in actin organisation, whilst two independent *DOCK6* CRISPR KO cell lines do not show similar severe defects (Cerikan et al., 2016). Prolonged knockdown of *DOCK6* was shown to later recover, through induction of a separate mechanism, independent of *DOCK6* function (Cerikan et al., 2016). The severity of the acute loss of *DOCK6* function would clearly be incompatible with embryonic development, suggesting that whilst *DOCK6* mutations are causative for AOS, mutations in compensatory pathways (which under WT *DOCK6* conditions are not pathogenic) may act in concert with *DOCK6* mutations to cause AOS. This concept is not as striking as is first apparent, and simply builds on multiple discussions of the two-hit hypothesis or the transformation of cells necessary to result in cancer, where loss of multiple tumour suppressors or activation of oncogenes is required

(Knudson, 1971). Ultimately, this means that a better understanding of the mechanisms underlying genetic robustness which allow organisms to recover from potentially damaging mutations is important to be able to choose the best genetic model based on the biological question, and thus to confidently assign gene function during development.

In the last five years, the field examining the mechanisms of genetic robustness, in particular genetic compensation in zebrafish has advanced rapidly. Basing conclusions on the differences between the *lamb1b* CDS mutant and *lamb1b* ATG morphant phenotype, would have defined a role for *lamb1b* in restricting the valve programme. However, the guidelines for interpretation of morphant phenotypes (confirmation of by injecting morpholino into mutants) and the mechanism by which genetic compensation can be avoided (targeted promoter deletion), identify that *lamb1b* does not have a role in heart development. Furthermore, I developed additional tools to attempt to systematically define *lamb1b* gene function in zebrafish (Figure 4.14) and below I discuss the considerations for overcoming these mechanisms.

One possible compensatory mechanism identified in zebrafish is that in some cases exon skipping is able to recover the frame of a mutant transcript (Anderson et al., 2017). I carried out a similar analysis by Anderson et al. and found no evidence for this mechanism functioning in the two *lamb1b* coding sequence mutant alleles (Figure 4.7).

Emerging evidence suggests that the site of mutagenesis targeting and the resulting lesion are important points for consideration when designing a mutagenesis strategy. In zebrafish, two mutant alleles of *mt2*, generating early PTCs with similar lengths of truncated protein show differing severities of phenotypes in maternal-zygotic embryos. The mild *mt2* allele shows almost complete loss of *mt2* transcript, while more *mt2* transcript was observed in the severe allele, suggesting inverse

correlation between levels of transcript degradation with phenotypic severity. Knockdown of the NMD pathway in the strongest *mt2* allele resulted in greater penetrance of the *mt2* phenotype (Schuermann et al., 2015). This initial consideration of severity of allele linked to level of degradation of mutant transcript supports the recently proposed model of genetic compensation activated by NMD of the mutant transcript (El-Brolosy et al., 2019). This suggests that currently to investigate gene function by generation of a complete loss-of-function phenotype, , mutagenesis strategies should be designed to abrogate transcription rather than disrupt protein translation. Importantly, this does not appear to be a zebrafish-specific consideration: genetic compensation has been reported in mouse and human cell and tissue lines (Dawlaty et al., 2011; Freudenberg et al., 2011; Jackson and Pereira-Smith, 2006; Mulligan et al., 1998).

To overcome potential genetic compensation for the loss of *lamb1b*, I was able to successfully identify and delete the annotated promoter of *lamb1b* and could confirm loss of *lamb1b* transcript. This is one of the first documented mutagenesis approaches where a loss-of-function zebrafish mutant is generated by removing the promoter. However, for many genes, promoter identification may not be possible, or alternatively a promoter may be too large to remove or mutate with complete confidence in abolishing transcription. Furthermore, our complete understanding of transcriptional control is limited to a very small number of genes. Therefore, a more nuanced approach for mutagenesis of some genes may be required, such as targeting of conserved motifs or residues known to be required for protein function to generate in-frame deletions, thus preventing NMD of transcripts and genetic compensation. Added to this, and highlighting the advantages offered by zebrafish, introduction of patient-specific mutations using CRISPR knock-in protocols (Tessadori et al., 2018), are also likely to become commonplace. Again, selection of promoter deletion as a mutagenesis strategy is important within the context of whether the study wishes understand the function of a gene or characterise the effect of patient-specific mutations on development.

Targeting the promoter also comes with the important consideration as there is the possibility for generation of alternative transcripts from the same locus, utilising a different, and potentially not annotated promoter. Design of multiple different mRNA probes that bind along the whole gene would be sufficient to confirm that all transcription of the target gene is abolished. It is possible that this could be the case for *lamb1b*, as the mRNA probe used in this study binds in the first 1.5kbp of the 5.6kbp fragment, however, no other transcript is annotated for *lamb1b* and given the highly conserved, modular structure of Laminin subunits, it seems unlikely that alternative and likely shorter transcripts would be sufficient to function.

The use of morpholinos remains commonplace in developmental biology, despite the caveats of off-target effects and developmental delay observed here with the use of the *lamb1b* morpholino. Yet, many morpholinos do recapitulate the phenotypes observed in stable mutant lines and have often been used to confirm mapping of mutations to specific genes following genetic screens, such as *tnnt2a*, *jekyll* or *southpaw* (Noël et al., 2013; Sehnert et al., 2002; Walsh and Stainier, 2001). How and why one morpholino may produce such varied, non-specific phenotypes, often at concentrations when other morpholinos display highly specific and reproducible effects remains elusive. One well described effect of morpholino injection is the up-regulation of *tp53* (Robu et al., 2007), and recently mis-splicing and induction of immune response genes have been reported upon injection of morpholinos (Lai et al., 2019, references therein). This reinforces the need for robust controls and careful examination of data exclusively obtained from morpholino usage such as injection of MO in mutants to examine for protection from MO phenotype (Stainier et al., 2017).

Whilst I generated a novel transgenic line to stably and ubiquitously express dCas9 in the zebrafish to perform global CRISPRi, I was unable to achieve knockdown of the *lamb1b* transcript. However, the development of global and tissue-specific

CRISPRi has the potential to overtake morpholino usage as the preferred technique for gene knockdown, particularly as it appears that induction of *tp53* expression is less in CRISPants compared to morphants (Savage et al., 2019). Development of tissue-specific CRISPRi would provide a powerful method to investigate gene function in zebrafish in a tissue-specific manner, similar to the Cre-lox system in mice (Gilbert et al., 2014, 2013). This approach is not possible with morpholino or mutant analyses and will be an invaluable tool for which the zebrafish community has a widespread need. However, the CRISPRi technique was developed using *E.coli* and knockdown by this system is strongly dependent on specific aspects of gRNA targeting. Inhibition of transcriptional initiation is not strand specific: gRNAs can target either strand, but repression is inversely correlated with gRNA target distance from the transcriptional start site (Qi et al., 2013). Conversely, CRISPRi-mediated inhibition of transcriptional elongation is strand specific: only gRNAs which bind to the non-template strand show effective repression (Larson et al., 2013; Qi et al., 2013). During gRNA design for targeting of *lamb1b*, these guidelines were followed, however, no knockdown of *lamb1b* was observed suggesting that other factors may play a role in the efficacy of this technique.

However, whilst the initial use of CRISPRi in zebrafish is promising (Rossi et al., 2015; Savage et al., 2019; Zhu et al., 2017), there are more factors that need consideration. In mammalian cells, CRISPRi was less efficient at gene knockdown when compared to *E. coli* and the authors suggest that the local chromatin environment is an important factor for CRISPRi in eukaryotic cells (Larson et al., 2013; Qi et al., 2013). This has been examined in zebrafish, where gRNAs were significantly more effective at targeting and inducing mutations in open chromatin regions (Chen et al., 2017). In addition to chromatin accessibility, the sequence of the gRNA targeting Cas9 or dCas9 is another important factor. Using data from previous studies, logo maps for successful gRNAs which recruit Cas9 were shown to have key features which are distinct from gRNAs used in CRISPRi (Xu et al., 2015). Additionally, concentration of gRNA and the efficiency of the promoter in driving

tissue specific dCas9 expression are factors yet to be fully optimised. A caveat of both CRISPRi and morpholino usage is the transient nature of the knockdown, morpholinos are anecdotally functional until approximately 3dpf and gRNA remains stable until 2dpf (A. Savage, personal communication). Therefore, functional analyses during only very early development would be feasible using these techniques. To overcome these limitations, stable gRNAs could be ubiquitously expressed in the zebrafish together with a tissue-specific dCas9 cassette, although again this would require a substantial level of optimisation, potentially on a gene-by-gene basis.

In the last decade, the identification and development of CRISPR-Cas9-mediated genome engineering has revolutionised developmental biology, and within the last five years, initial discovery and characterisation of mechanisms of genetic compensation across *Eukarya* has driven a more refined and tailored approach to mutagenesis (El-Brolosy et al., 2019). Understanding the mechanisms by which genetic compensation is achieved is important for the correct selection and analysis of genetic models in order to be able to reliably ascribe function to a gene during development. Therefore, in line with current models, the generation of the promoter-less *lamb1b* mutants which have no embryonic phenotype demonstrates that *lamb1b* does not play a role in heart development and is likely dispensable for development in general, although alternative transcription sites cannot be ruled out. I have also identified that loss of *lamb1a* also does not appear to result in a heart looping phenotype, however I did not investigate whether genetic compensation is active in the generated alleles of *lamb1a*. Together, this strongly suggests that the Laminin isoform promoting heart looping, which contains Lamc1, also contains either Lamb2 which plays an unappreciated role in heart development, or Lamb1a, where the absence of a heart looping phenotype may be due to genetic compensation.

5. Laminins are required to limit heart size

Having established that *lamb1b* is not required for heart development, I have investigated the role of the two remaining Laminin beta chains expressed in the heart during early morphogenesis: *lamb1a* and *lamb2*. Using a simple, quantitative analysis I have identified a previously undescribed cardiac phenotype associated with the loss of *lamb1a*. As previously described, *lamb1a* mutant hearts undergo early looping morphogenesis relatively normally, however heart size in significantly increased by 3dpf compared to siblings. I further reveal that as well as promoting heart looping, *lamc1* is also required to limit heart size.

Examining early cardiac development reveals that *lamb1a* mutants up-regulate flow-responsive genes. However, under no-flow conditions this up-regulation persists, suggesting that the enlarged heart in *lamb1a* mutants is likely due to mis-regulation of pathways upstream of flow sensing. Together, this work begins to define two novel roles for Laminin genes during heart looping morphogenesis.

5.1 Results

5.1.1 *lamb1a* coding sequence mutants display hallmarks of genetic compensation and up-regulate *lamb1b*

Extensive study of the *lamb1b* mutant lines generated establish that *lamb1b* does not play a role in heart looping or more broadly in embryonic development. However, having identified a role for Laminins in heart looping through mutagenesis of *lamc1*, it is therefore likely that either *lamb1a* or *lamb2* or both functions together with *lamc1* to promote heart looping. Although the *lamb1a* mutants generated in Chapter 4 display axis and endodermal phenotypes consistent with previously-described mutants, since the novel *lamb1a* mutants harbour lesions in the coding

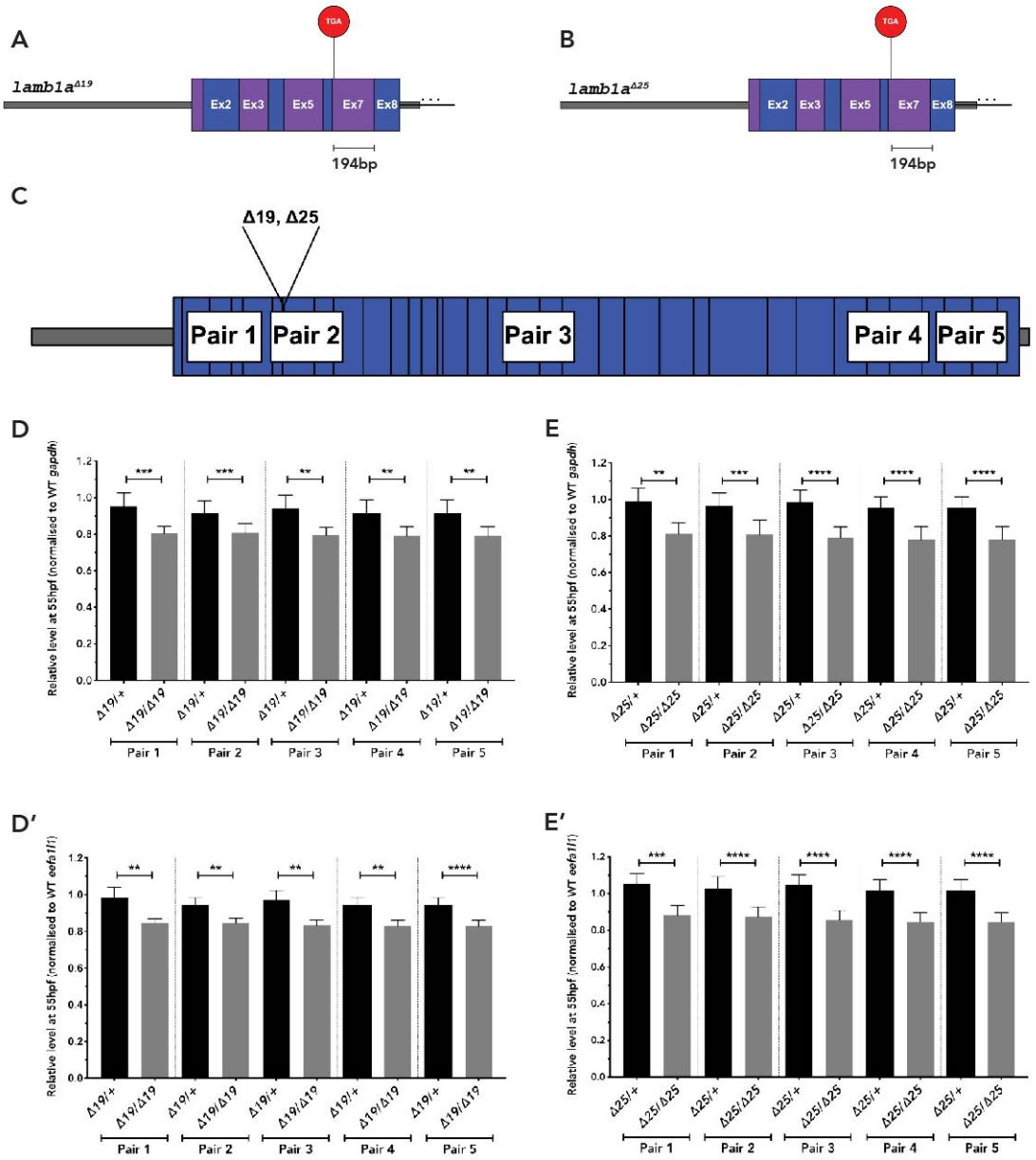

Figure 5.1 *lamb1a* mutant transcripts are subject to RNA decay.

Semi-quantitative analysis of levels of *lamb1a* mRNA mutant transcript. **(A-B)** Schematic of *lamb1a* mRNA, demonstrating that both mutant alleles have a premature stop codon (Red, TGA) greater than 50-55bp upstream of the exon7-exon8 junction. **(C)** Schematic of *lamb1a* mRNA (blue: translated, grey: non-translated), showing region amplified by primers used for semi-qPCR. Pair2 cover the two mutation sites. **(D-D')** Quantification of levels of transcript in *lamb1a*$^{\Delta 19}$ sibling and homozygous mutants, normalised to WT *gapdh* (D) or *eefa1l1* (D') loading control. All regions show significant reduction in *lamb1a* mutants compared

sequence (Figure 4.16), it is still possible that genetic compensation could be functioning in the *lamb1a* mutants masking, a role for *lamb1a* in heart looping.

Both *lamb1a* coding sequence mutants are predicted to have premature termination codons 194bp upstream of the exon 7, exon 8 boundary which could activate NMD of the mutant transcript (Figure 5.1A, B) (Maquat, 2005; Wittkopp et al., 2009). Comparative analysis of *lamb1a* transcript levels by semi-qPCR analysis of five different regions of the *lamb1a* transcript (Figure 5.1C) reveals a significant reduction of *lamb1a* mutant transcript when compared to WT siblings of either allele (Figure 5.1D-E'). These data could suggest that the *lamb1a* phenotype may not be fully penetrant and that genetic compensation activated by decay of the mutant transcript could allow heart development to proceed normally, whilst other aspects of development, such as gut morphogenesis and convergent extension are defective (Hochgreb-Hägele et al., 2013; Stemple et al., 1996) (Figure 4.17).

lamb1a mutants display the hallmarks of NMD which could activate genetic compensation. Despite the fact that *lamb1b* is not required for heart development in WT embryos, *lamb1b* still represents the most closely related Laminin beta subunit to *lamb1a* (Sztal et al., 2011), and could be functional in a *lamb1a* mutant embryo. Therefore, *lamb1b* remains the most likely candidate to be up-regulated to compensate for loss of *lamb1a*. To investigate this, *lamb1b* expression was analysed in an incross of *lamb1a*;*lamb1b* heterozygotes by ISH. At 30hpf, *lamb1b* is

Figure 5.1 continued.

to siblings. **(E-E')** Quantification of levels of transcript in *lamb1a*$^{\Delta 25}$ sibling and homozygous mutants, normalised to WT *gapdh* (E) or *eefa1l1* (E') loading control. All regions show significant reduction in lamb1a mutants compared to siblings. D-E': Arithmetic mean with standard deviation, One-way ANOVA, **: $p<0.01$, ***: $p<0.001$, ****: $p<0.0001$.

expressed predominantly in the ventricular endocardium in WT embryos, with weak expression in the atrial endocardium (Figure 5.2A, B). However, in *lamb1a* mutants, *lamb1b* expression is up-regulated in the endocardium compared to WT siblings and is also expanded into the atrium (Figure 5.2A', B'). Following heart looping, *lamb1b* is restricted to the AVC in WT embryos, (Figure 5.2C, D), however in *lamb1a*$^{\Delta 19}$ homozygous mutants, mild expression of *lamb1b* persists in the ventricular endocardium (Figure 5.2C'). More strikingly, *lamb1b* remains expressed throughout the entire endocardium in *lamb1a*$^{\Delta 25}$ homozygous mutants at 55hpf (Figure 5.2D'), highlighting potential differences in the severity of the *lamb1a* alleles generated. Together, *lamb1a* mutants display key characteristics of NMD-activated genetic compensation: a reduction in levels of mutant transcript and up-regulation of a related gene which could functionally compensate for loss of *lamb1a*. These data also suggest that, whilst *lamb1b* is not required for development, it could act to function in the absence of *lamb1a*.

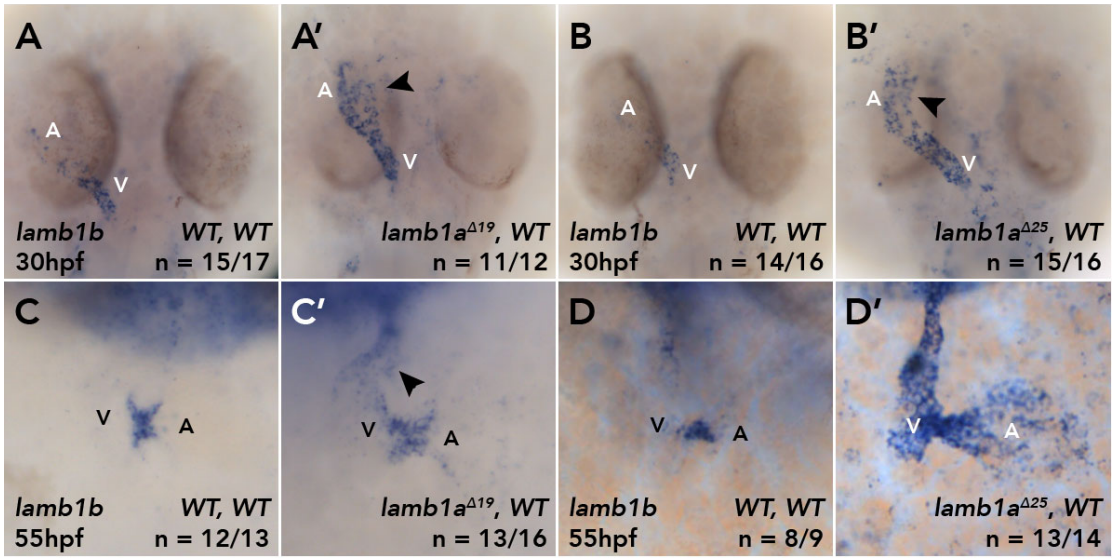

Figure 5.2. *lamb1b* is up-regulated in *lamb1a* coding sequence mutants with allele-specific persistence.

mRNA *in situ* hybridisation analysis of *lamb1b* expression in *lamb1a* siblings and homozygous mutants during heart development. **(A-B')** In WT embryos, *lamb1b* is expressed in the ventricular endocardium (A, B). Loss of *lamb1a* results in an up-regulation and expansion of *lamb1b* expression throughout the endocardium into the atrium (A', B, arrowheads). **(C-D')**. At 55hpf, *lamb1b* is expressed in the atrioventricular canal (C, D). In *lamb1a*$^{\Delta 19}$ homozygous mutants at 55hpf, *lamb1b* expression is observed in the outflow tract (C', arrowhead). In *lamb1a*$^{\Delta 25}$ homozygous mutants at 55hpf, *lamb1b* expression remains present throughout the endocardium (D'). A-B': dorsal views. C-D': ventral views. V: ventricle, A: atrium.

5.1.2 *lamb1b* does not compensate for loss of *lamb1a*

NMD machinery is highly conserved in zebrafish, where the core components are maternally deposited and are required for correct development of the embryo (Wittkopp et al., 2009). Attenuation of NMD in zebrafish has been shown to inhibit NMD-induced genetic compensation (El-Brolosy et al., 2019) and also increase the penetrance of mutant phenotypes (Schuermann et al., 2015). Knockdown of the NMD pathway components *smg1* (*SMG1 nonsense mediated mRNA decay associated PI3K related kinase*) and *upf1* (*UPF1 RNA helicase and ATPase*) have

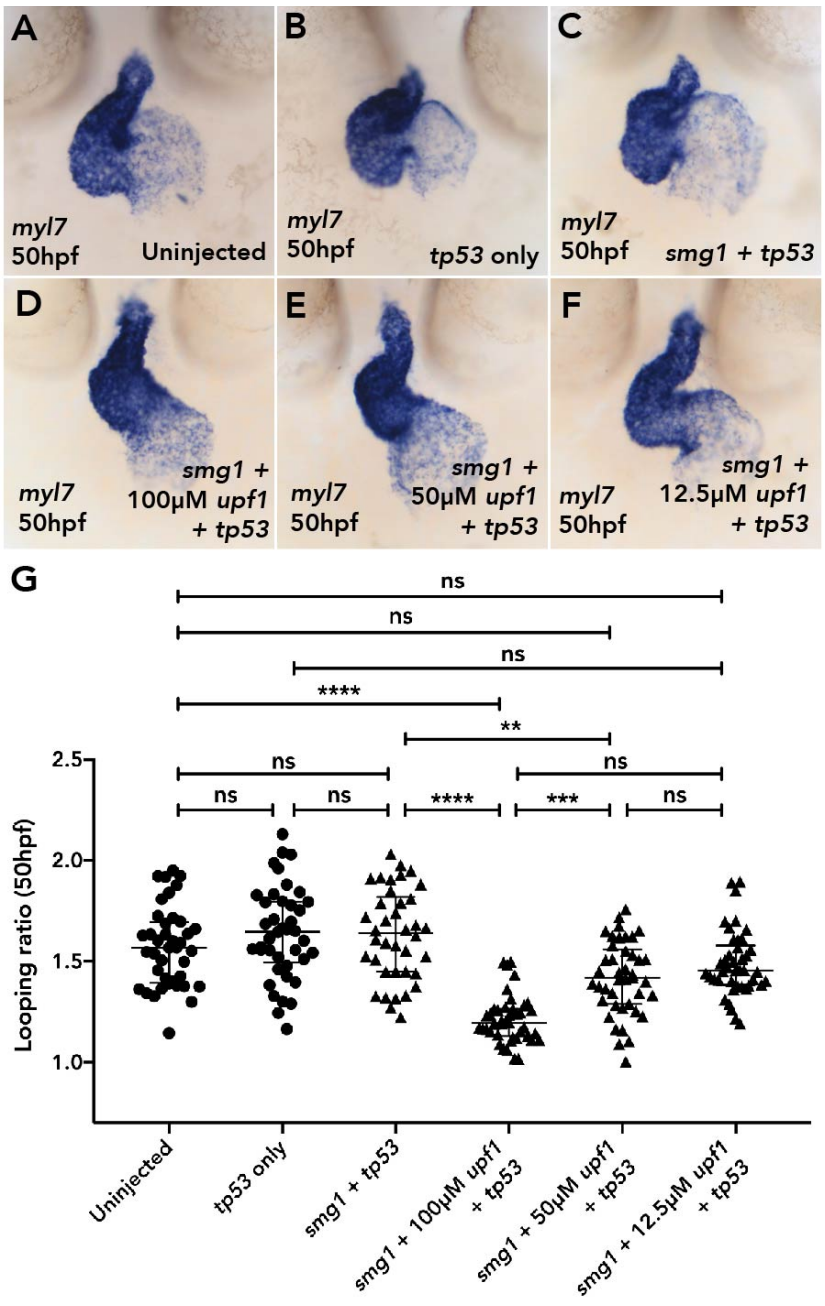

Figure 5.3 Titration of sub-phenotypic dosage of NMD blocking morpholino.

Quantitative analysis of heart looping using mRNA *in situ* hybridisation of *myl7* at 50hpf in embryos injected with differing concentrations of NMD-targeting morpholinos. **(A-C)** Heart looping appears normal in uninjected embryos (A), *tp53* MO only injected embryos (B) or *smg1* MO + *tp53* MO injected embryos (C). **(D)** *smg1* MO + 100μM *upf1* MO + *tp53* MO injected embryos have a severe heart looping phenotype at 50hpf. **(E)** *smg1* MO + 50μM *upf1* MO + *tp53* MO injected embryos have a clear heart looping phenotype at 50hpf, but is less severe than (D).

previously been used to inhibit decay of the mutant *mt2* transcript, leading to an increased penetrance of phenotype, consistent with morpholino-mediated knockdown of *mt2* (Schuermann et al., 2015).

Previously published concentrations of the morpholino used to perform *upf1* knockdown in zebrafish results in severe morphological defects that would impact on heart looping morphogenesis independent of the genetic background of the embryo (Wittkopp et al., 2009). Therefore, to negate any general effects related to the impact of loss of NMD pathway function on heart looping morphogenesis, concentrations of *smg1* and *upf1* were titrated in an attempt to determine a sub-phenotypic dosage that did not impact on heart morphogenesis (Figure 5.3). Depletion of *smg1* alone does not affect heart looping ratio (Figure 5.3C ,G), but together with the *upf1* MO at 100µM or 50µM results in a significant reduction in heart looping morphogenesis, associated with a failure of constriction at the AVC and loss of atrial ballooning (Figure 5.3D, E ,G), whilst coinjection of 12.5µM *upf1* MO together with *smg1* MO results in a non-significant reduction in heart looping and abnormal AVC morphology (Figure 5.3F, G), demonstrating that heart development may be highly sensitive to levels of Upf1.

Figure 5.3 continued.

(F) *smg1* MO + 12.5µM *upf1* MO + *tp53* MO injected embryos have a mild heart looping phenotype at 50hpf, but is less severe than (E). **(G)** Quantification of heart looping ratio of all injection groups at 50hpf. Injection of *smg1* MO has no impact on heart morphogenesis, while coinjection of 100µM or 50µM *upf1* MO results in a significant reduction in heart looping. Coinjection of 12.5µM *upf1* MO together with *smg1* MO results in a mild, non-significant reduction heart looping. Ventral views. G: Median with interquartile range, Kruskal-Wallis, Dunn's multiple comparisons. ns: not significant, **: $p<0.01$, ***: $p<0.001$, ****: $p<0.0001$.

Having established an upper limit for *upf1* MO concentration at 12.5μM where heart morphology is still mildly impacted (Figure 5.3F), a sub-phenotypic dosage of NMD-targeting MOs (NMD KD: 0.5mM *smg1*, 10μM *upf1*) not expected to negatively impact on heart morphogenesis in WT embryos was injected into an incross of *lamb1a*$^{\Delta 25}$ heterozygotes. At 50hpf, embryos were fixed and heart looping ratio was quantified through *in situ* hybridisation analysis of *myl7* expression (Figure 5.4). Injection of NMD-targeting MOs does not significantly impact heart looping ratio and hearts appear morphologically normal when compared to uninjected or *tp53* MO-injected controls, in either *lamb1a* mutants or siblings (Figure 5.4D). However, morpholino-mediated knockdown of NMD pathway components does not result in recovery of *lamb1a* transcript levels when examined by ISH (compare Figure 4A'', B'', C'') suggesting that NMD machinery is still active. Whilst knockdown of *upf1* could be increased sufficiently to inhibit NMD, it is likely that the resulting heart looping phenotype would be the result of mechanisms independent of *lamb1a* function (Figure 5.3G).

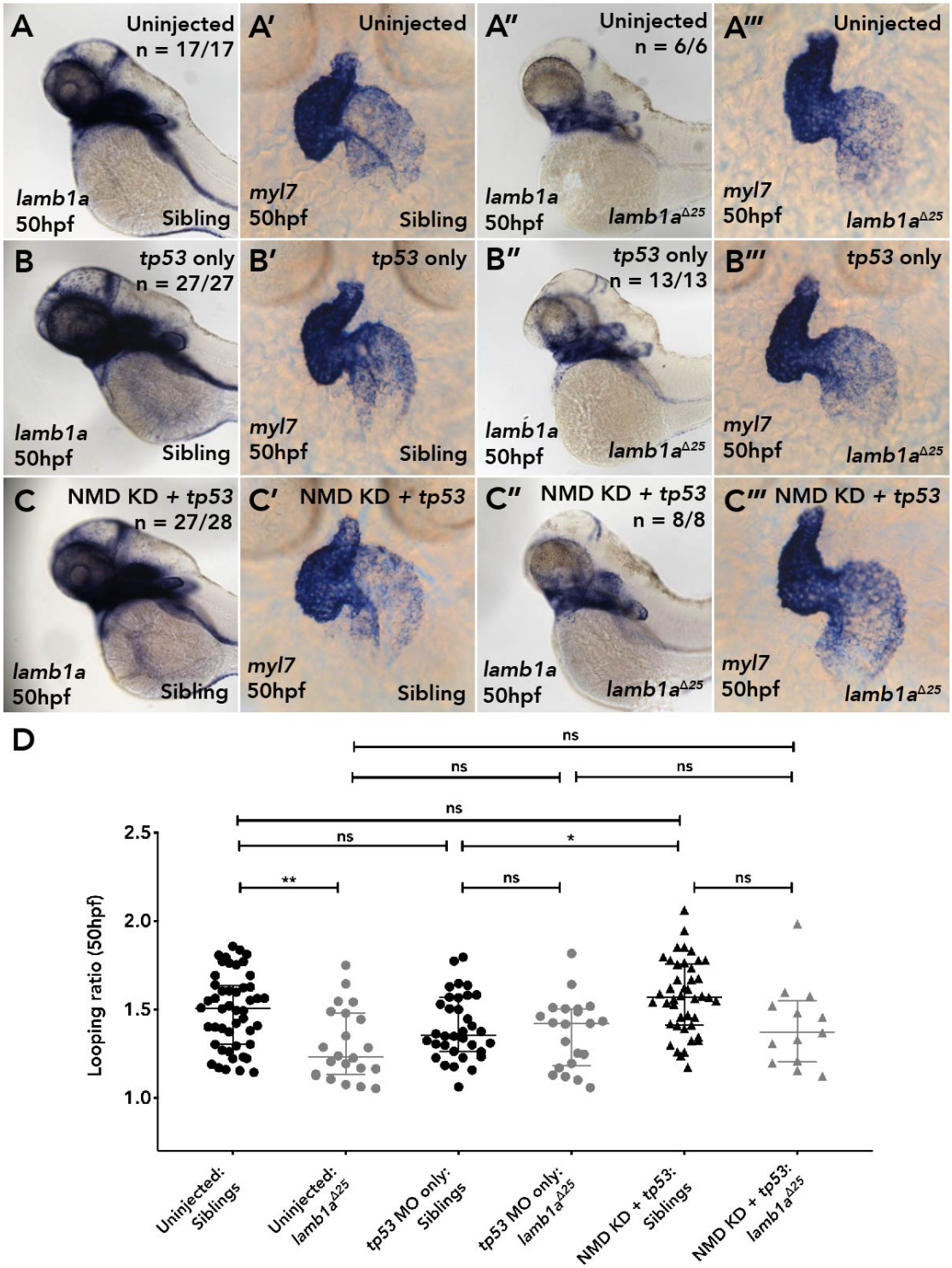
A
Uninjected
n = 17/17
lamb1a
50hpf
Sibling
A′
Uninjected
myl7
50hpf
Sibling
A″
Uninjected
n = 6/6
lamb1a
50hpf
lamb1a^Δ25
A‴
Uninjected
myl7
50hpf
lamb1a^Δ25
B
tp53 only
n = 27/27
lamb1a
50hpf
Sibling
B′
tp53 only
myl7
50hpf
Sibling
B″
tp53 only
n = 13/13
lamb1a
50hpf
lamb1a^Δ25
B‴
tp53 only
myl7
50hpf
lamb1a^Δ25
C
NMD KD + tp53
n = 27/28
lamb1a
50hpf
Sibling
C′
NMD KD + tp53
myl7
50hpf
Sibling
C″
NMD KD + tp53
n = 8/8
lamb1a
50hpf
lamb1a^Δ25
C‴
NMD KD + tp53
myl7
50hpf
lamb1a^Δ25
D
Looping ratio (50hpf)
2.5
2.0
1.5
1.0
ns
ns
ns
ns
ns
*
**
ns
ns
Uninjected: Siblings
Uninjected: lamb1a^Δ25
tp53 MO only: Siblings
tp53 MO only: lamb1a^Δ25
NMD KD + tp53: Siblings
NMD KD + tp53: lamb1a^Δ25

Figure 5.4 Morpholino-mediated knockdown of nonsense-mediated decay machinery does not recover *lamb1a* transcript or impact heart looping morphogenesis.

mRNA *in situ* hybridisation analysis of *lamb1a* expression in *lamb1a* homozygous mutants following injection of a sub-phenotypic dose of NMD targeting morpholino (NMD KD) and quantitative analysis of NMD knockdown on heart looping morphology, analysed by *myl7* expression at 50hpf. **(A-A'''')** In uninjected controls, *lamb1a* is highly expressed in sibling embryos (A) and heart morphology is normal (A'). *lamb1a* expression is reduced in uninjected *lamb1a* homozygous mutants (A'') and heart morphology appears normal (A'''). **(B-B'''')** In *tp53* MO injected controls, *lamb1a* is highly expressed in sibling embryos (B) and heart morphology appears normal (B'). *lamb1a* expression is reduced in *tp53* MO injected *lamb1a* homozygous mutants (B'') and heart morphology appears comparable to sibling and uninjected controls (B'''). **(C-C'''')** In NMD knockdown embryos, *lamb1a* is highly expressed in sibling embryos (C) and heart morphology appears normal compared to controls (C'). *lamb1a* expression in NMD knockdown *lamb1a* homozygous mutants (C'') is comparable to injection controls (A'', B'') and heart morphology appears normal (C'''). **(D)** Quantification of heart looping ratio of all injection groups in *lamb1a* sibling and mutants at 50hpf. A mild, yet significant reducing in heart looping ratio is observed between uninjected siblings and uninjected *lamb1a* homozygous mutants. An increase in heart looping ratio is observed in NMD KD siblings compared to *tp53* MO only siblings. No significant difference is observed between siblings and *lamb1a* mutants subjected to NMD KD injection. A, A'', B, B'', C, C'': lateral views, anterior left. A', A''', B', B''', C', C''': dorsal views. D: Median with interquartile range, Kruskal-Wallis, Dunn's multiple comparisons, ns: not significant, *: $p<0.05$, **: $p<0.01$

As use of NMD-targeting MOs could not recover *lamb1a* mutant transcript levels, it was unclear whether NMD was not successfully blocked, or whether the reduction in *lamb1a* transcript is due to an alternative mechanism of degradation (Schoenberg 2012). To investigate the former, a secondary method to block NMD was performed, using the published NMD inhibitor (ethyl 2-{[(6,7 —dimethyl—3-oxo-1,2,3,4-tetrahydro-2-quinoxalinyl)acetyl]amino}-4,5-dimethyl-3-thiophenecarboxylate, NMDI14, NMDi) which functions by blocking the interaction between SMG7 and UPF1 (Martin et al., 2014). NMDi has previously been used in zebrafish to successfully inhibit NMD between 3dpf and 6dpf, preventing up-regulation of compensating genes (El-Brolosy et al., 2019). However, as the *lamc1* phenotype is apparent at 2dpf and up-regulation of *lamb1b* is observed in *lamb1a* mutants at 1dpf, the time window when an increase in penetrance of the *lamb1a* phenotype would result in a clear looping phenotype similar to loss of *lamc1* would be prior to 3dpf, thus requiring an earlier NMDi treatment window.

Embryos obtained from an incross of *lamb1a*$^{\Delta 25}$ heterozygous adults were incubated in either 10μM or 20μM NMDi (consistent with previously published concentrations) from 8hpf to 55hpf, alongside untreated and 1% DMSO controls. At 55hpf, embryos were fixed, heart morphology assessed by *in situ* hybridisation analysis of *myl7* expression, and heart looping ratio was quantified (Figure 5.5). Incubation with either 10μM or 20μM NMDi between 8hpf and 55hpf had no significant effect on heart looping morphogenesis at 55hpf in either WT siblings or *lamb1a*$^{\Delta 25}$ mutants (Figure 5.5E) compared to control embryos. In addition, similar to injection of NMD-pathway MOs, no obvious recovery of *lamb1a* expression was observed in NMDi-treated embryos when compared to control groups (compare Figure 5.5A'', B'', C'', D'').

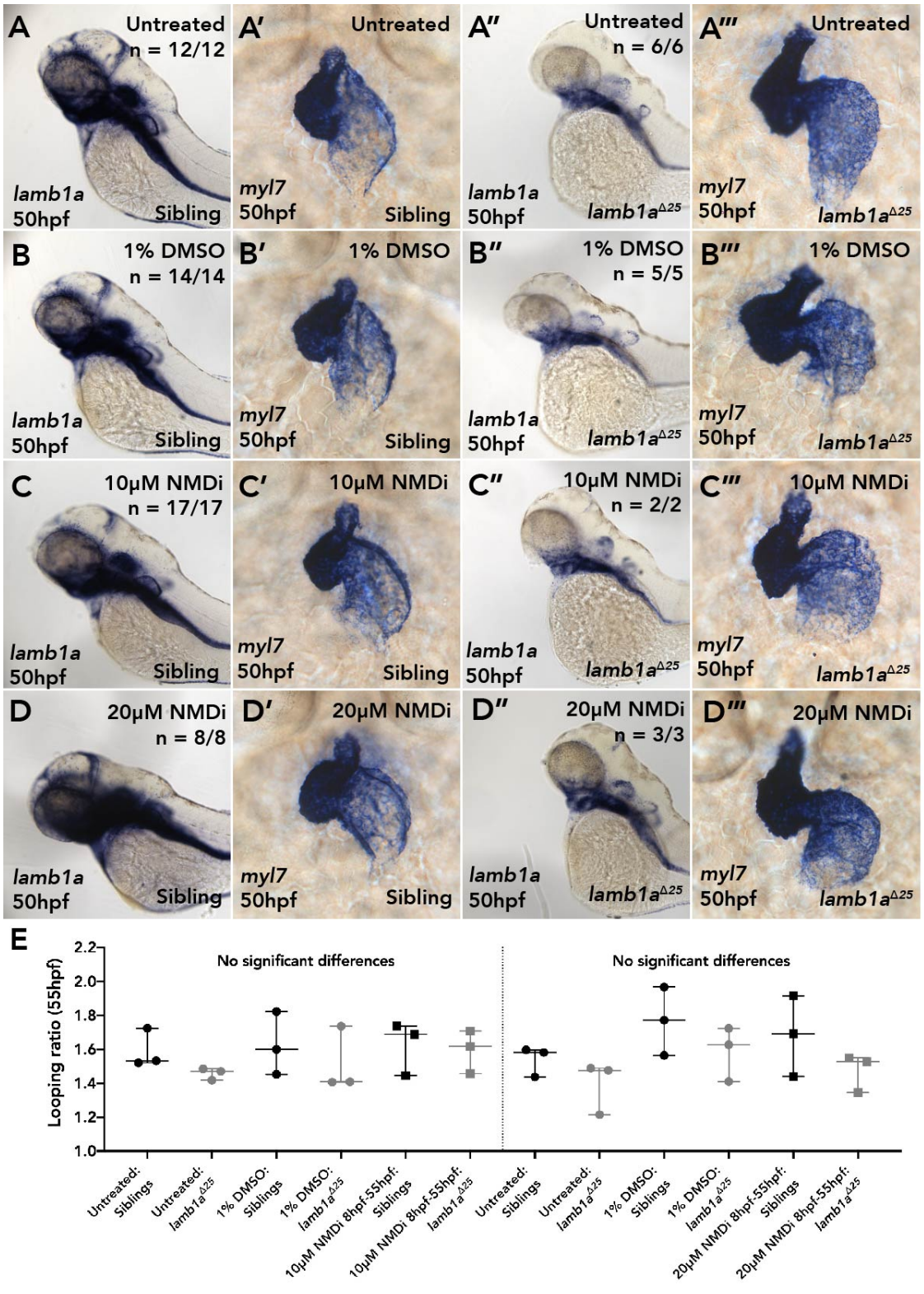
A
Untreated
n = 12/12
lamb1a
50hpf
Sibling
A′
Untreated
myl7
50hpf
Sibling
A″
Untreated
n = 6/6
lamb1a
50hpf
lamb1a^Δ25
A‴
Untreated
myl7
50hpf
lamb1a^Δ25
B
1% DMSO
n = 14/14
lamb1a
50hpf
Sibling
B′
1% DMSO
myl7
50hpf
Sibling
B″
1% DMSO
n = 5/5
lamb1a
50hpf
lamb1a^Δ25
B‴
1% DMSO
myl7
50hpf
lamb1a^Δ25
C
10μM NMDi
n = 17/17
lamb1a
50hpf
Sibling
C′
10μM NMDi
myl7
50hpf
Sibling
C″
10μM NMDi
n = 2/2
lamb1a
50hpf
lamb1a^Δ25
C‴
10μM NMDi
myl7
50hpf
lamb1a^Δ25
D
20μM NMDi
n = 8/8
lamb1a
50hpf
Sibling
D′
20μM NMDi
myl7
50hpf
Sibling
D″
20μM NMDi
n = 3/3
lamb1a
50hpf
lamb1a^Δ25
D‴
20μM NMDi
myl7
50hpf
lamb1a^Δ25
E
Looping ratio (55hpf)
2.2
2.0
1.8
1.6
1.4
1.2
1.0
No significant differences
No significant differences
Untreated: Siblings
Untreated: lamb1a^Δ25
1% DMSO: Siblings
1% DMSO: lamb1a^Δ25
10μM NMDi 8hpf-55hpf: Siblings
10μM NMDi 8hpf-55hpf: lamb1a^Δ25
Untreated: Siblings
Untreated: lamb1a^Δ25
1% DMSO: Siblings
1% DMSO: lamb1a^Δ25
20μM NMDi 8hpf-55hpf: Siblings
20μM NMDi 8hpf-55hpf: lamb1a^Δ25

Together, neither published technique for blocking NMD impacted heart morphology of *lamb1a* mutants, however neither approach was able to recover the expression of *lamb1a* in *lamb1a* mutant embryos to wild type levels (Figure 5.4, 5.5). This suggests that either more nuanced techniques would be required to abolish NMD in *lamb1a* mutants, such as mutagenesis of *upf1* (El-Brolosy et al., 2019), or that the *lamb1a* transcript is not subjected to NMD, and may be degraded by

---

Figure 5.5 Pharmacological inhibition of nonsense-mediated decay does not recover *lamb1a* transcript levels or impact heart looping morphogenesis.

mRNA *in situ* hybridisation analysis of *lamb1a* expression in *lamb1a* homozygous mutants following treatment with two concentrations of the NMD inhibitor (NMDi) between 8hpf-55hpf, and subsequent quantitative analysis of treatment on heart looping analysed by *myl7* expression at 55hpf. **(A-A'''')** In untreated controls, *lamb1a* is highly expressed in sibling embryos (A) and heart morphology appears normal (A'). *lamb1a* expression is reduced in untreated *lamb1a* homozygous mutants (A'') and heart morphology is comparable with wild type siblings (A'''). **(B-B'''')** In vehicle controls (1% DMSO), *lamb1a* is highly expressed in sibling embryos (B) and heart morphology appears comparable with untreated controls (B'). *lamb1a* expression is reduced in 1% DMSO treated *lamb1a* homozygous mutants (B'') and heart morphology appears normal (B'''). **(C-D'''')** In embryos treated with either 10μM or 20μM NMDi from 8hpf-55hpf, *lamb1a* is highly expressed in sibling embryos (C,D) and heart morphology appears comparable to controls (C',D'). *lamb1a* expression in 10μM or 20μM NMDi treated *lamb1a* homozygous mutant embryos (C'',D'') is comparable to controls (A'', B'') and heart morphology appears normal (C''',D'''). **(E)** Quantification of heart looping ratio of all treated groups in lamb1a sibling and mutants at 55hpf. 10μM and 20μM treatments were run in parallel, but analysed separately. No significant differences are observed in heart looping morphogenesis in either treatment between any groups. A, A'', B, B'', C, C'', D, D'': lateral views, anterior left. A', A''', B', B''', C', C''', D', D''': dorsal views. E: Median with interquartile range, Kruskal-Wallis, Dunn's multiple comparisons.

another RNA surveillance mechanism (Schoenberg and Maquat, 2012), or finally that Lamb1a regulates the expression of genes which are required to maintain its own expression.

Despite clear down-regulation of *lamb1a* expression and location of PTC permissive for NMD of the *lamb1a* transcript (Figure 5.1), it was not possible to define whether *lamb1a* mutant transcripts are subject to NMD. However, as *lamb1b* exhibits clear up regulation in both mutant alleles of *lamb1a*, *lamb1b* represents a suitable candidate which could be compensating for the loss of *lamb1a* in regulation of heart looping morphogenesis and that *lamb1a* may be required to interact with *lamc1* to regulate looping morphogenesis. To examine whether up-regulation of *lamb1b* is functionally compensating for loss of *lamb1a*, *lamb1a*$^{\Delta 25}$ mutants were crossed into *lamb1b*$^{\Delta 183}$ or *lamb1b*$^{\Delta 428}$ background (promoter mutants lacking *lamb1b* transcript, Figure 4.19) to generate double *lamb1* heterozygous adults. Analysis of *lamb1b* expression in embryos derived from an incross of double heterozygotes was carried out to confirm complete loss of *lamb1b* transcript in *lamb1a*; *lamb1b* double mutants (Figure 5.6). As previously described, *lamb1a* mutants up-regulate *lamb1b* at 30hpf (Figure 5.6A', B') and the deletion of the *lamb1b* promoter results in complete abolishment of *lamb1b* transcript in both wild type and *lamb1a* mutants (Figure 5.6A''-A''', B''-B'''), removing the capacity for *lamb1b* to functionally compensate for loss of *lamb1a*.

To determine whether up-regulation of *lamb1b* in *lamb1a* mutants functions to protect *lamb1a* mutants from heart looping defects, heart morphology at 55hpf was analysed by *myl7* expression. At 55hpf, *lamb1a*; *lamb1b* double mutants do not display any significant reduction in heart looping ratio when compared to WT or single *lamb1a* or *lamb1b* mutants (Figure 5.7C, D). Therefore taking all mutant data for *lamb1a* and *lamb1b* into account, the absence of any heart looping phenotype shows that Lamb1a- or Lamb1b-containing Laminin trimers are not required to promote early heart looping morphogenesis.

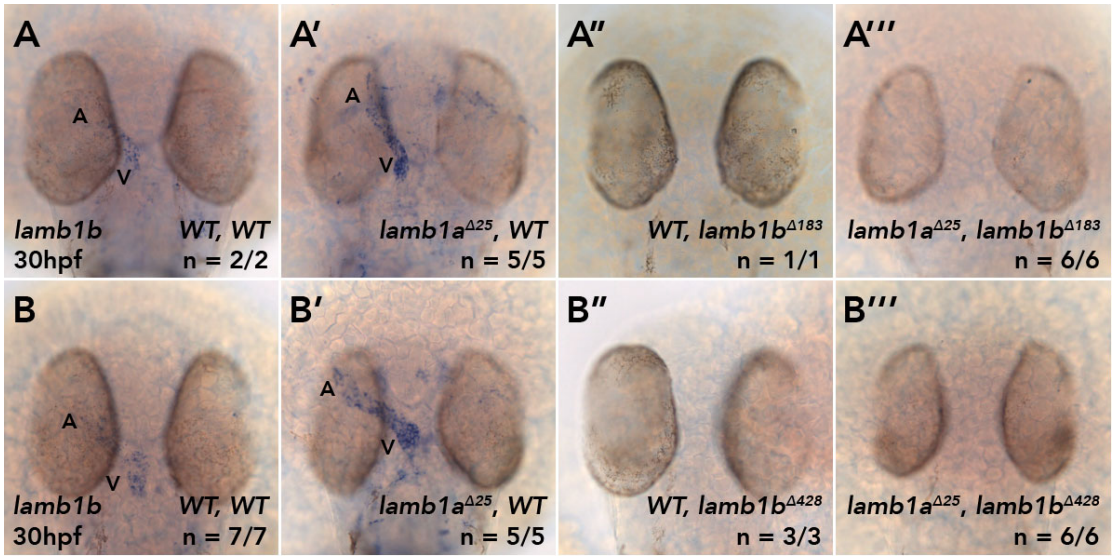

Figure 5.6. *lamb1b* expression is abolished in *lamb1a*; *lamb1b* promoter double mutants.

mRNA *in situ* hybridisation analysis of *lamb1b* expression in *lamb1a*$^{\Delta 25}$; *lamb1b*$^{\Delta 183}$ heterozygous incross and *lamb1a*$^{\Delta 25}$; *lamb1b*$^{\Delta 428}$ heterozygous incross at 30hpf. **(A-A‴)** At 30hpf in WT embryos (A), *lamb1b* is expressed in the ventricular endocardium. *lamb1a*$^{\Delta 25}$ mutants show misexpression of *lamb1b* throughout the endocardium at 30hpf (A′). *lamb1b* expression is *completely* absent from the heart in *lamb1b*$^{\Delta 183}$ homozygous mutants (A″) and double *lamb1a*$^{\Delta 25}$; *lamb1b*$^{\Delta 183}$ homozygous mutants (A‴). **(B-B‴)** The same result is observed in the *lamb1b*$^{\Delta 428}$ allele. Dorsal views. V: ventricle, A: atrium.

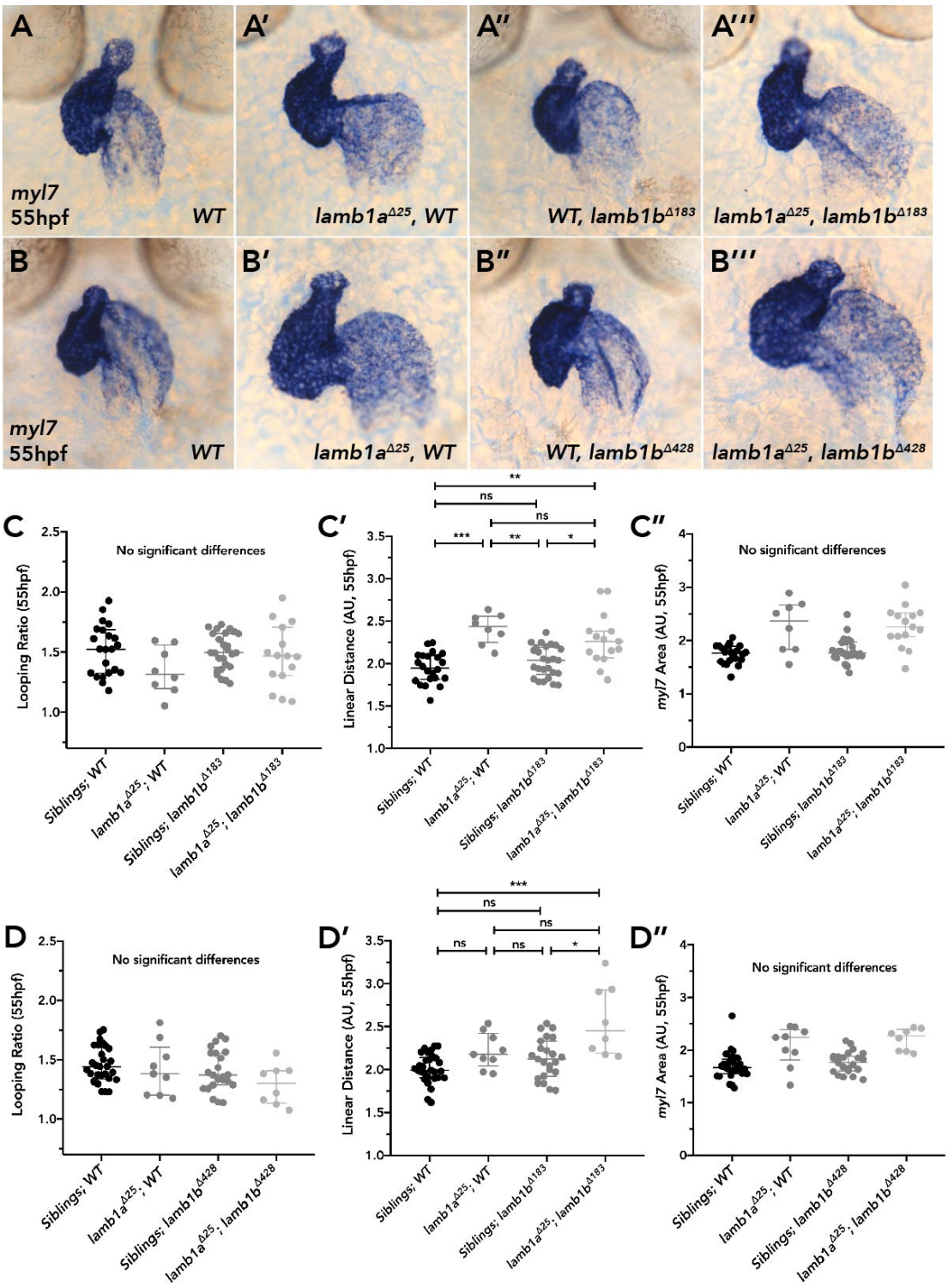

Figure 5.7. *lamb1* subunits are dispensable for heart looping morphogenesis.

Quantitative analysis of heart morphology in WT, *lamb1a*, *lamb1b* and double *lamb1a*; *lamb1b* mutants at 55hpf by analysis of *myl7* expression. **(A-A‴)** Representative images of WT (A), *lamb1a*$^{\Delta 25}$ homozygous mutant (A′), *lamb1b*$^{\Delta 183}$ homozygous mutants and *lamb1a*$^{\Delta 25}$; *lamb1b*$^{\Delta 183}$ double homozygous mutants (A‴)

5.1.3 *lamb1a* is required to limit heart size, but is dispensable for heart looping morphogenesis

Although *lamb1a* mutants do not exhibit clear abnormalities in heart looping morphogenesis when measured by looping ratio, upon closer examination *lamb1a* homozygous mutant hearts do not appear as compacted as their WT or *lamb1b* single mutant siblings (compare Figure 5.7A' with A or A'', and Figure 5.7B' with B or B''). Measuring the linear distance from the arterial pole to the venous pole at 55hpf as a readout of heart compaction reveals an increase in pole-pole distance in the heart of *lamb1a* mutants compared to WT siblings, suggesting that while

Figure 5.7 continued.

at 55hpf. **(B-B''')** Representative images of WT (B), *lamb1a*$^{\Delta 25}$ homozygous mutant (B'), *lamb1b*$^{\Delta 428}$ homozygous mutants and *lamb1a*$^{\Delta 25}$; *lamb1b*$^{\Delta 428}$ double homozygous mutants (B''') at 55hpf. **(C-C'')** Quantification of heart morphology in embryos derived from *lamb1a*$^{\Delta 25}$; *lamb1b*$^{\Delta 183}$ heterozygous incross. No combination of *lamb1* mutations have a significant effect on heart looping ratio (C). Loss of *lamb1a* significantly increases linear distance, not observed in single *lamb1b*$^{\Delta 183}$ homozygous mutants and loss of *lamb1b* function does not increase the severity of the phenotype (C'). No significant differences are measured in heart area for any genotype at 55hpf, although *lamb1a*$^{\Delta 25}$and *lamb1a*$^{\Delta 25}$; *lamb1b*$^{\Delta 183}$ homozygous mutants show a trend towards increased *myl7* area. **(D-D'')** Quantification of heart morphology in embryos derived from a *lamb1a*$^{\Delta 25}$; *lamb1b*$^{\Delta 428}$ heterozygous incross. No combination of mutations has a significant effect on heart looping ratio (D). Loss of *lamb1a* mildly increases linear distance, whilst loss of *lamb1b* function increases the severity of the phenotype (D'). No significant differences are measured in heart area for any genotype at 55hpf, although *lamb1a*$^{\Delta 25}$and *lamb1a*$^{\Delta 25}$; *lamb1b*$^{\Delta 428}$ homozygous mutants show a trend towards increased *myl7* area (D''). Ventral views. C-D'': Median with interquartile range, Kruskal-Wallis, Dunn's multiple comparisons ns: not significant, *: p<0.05, **: p<0.01, ***: p<0.001.

looping proceeds normally in *lamb1a* mutants, heart size could be affected (Figure 5.7C', D'). As looping ratio is not significantly altered in *lamb1a* mutants, this implies that in *lamb1a* mutants the looped distance is also greater, and would suggest that whilst *lamb1a* mutants do not have a reduction in heart looping, they may have an increase in heart size. To further characterise the morphology of *lamb1a* mutant hearts, the area of *myl7* staining across the four genotypes was quantified as a proxy for heart size, revealing a trend towards increased heart size at 55hpf (5.7C'', D''). This analysis suggests that independent of heart looping, *lamb1a* may be required to restrict heart size during cardiac morphogenesis.

To examine whether the mild increase in heart size in *lamb1a* mutants progresses past 2dpf, heart morphology at 72hpf was analysed by *myl7* expression in embryos derived from a *lamb1a*; *lamb1b* heterozygote incross. By 72dpf, *lamb1a* mutant hearts are almost twice the size of either WT or *lamb1b* mutant hearts whilst overall heart morphology appears normal. Furthermore, loss of *lamb1b* does not further increase heart size (Figure 5.8C', D') demonstrating that *lamb1a* is required to limit heart size independent of *lamb1b* function.

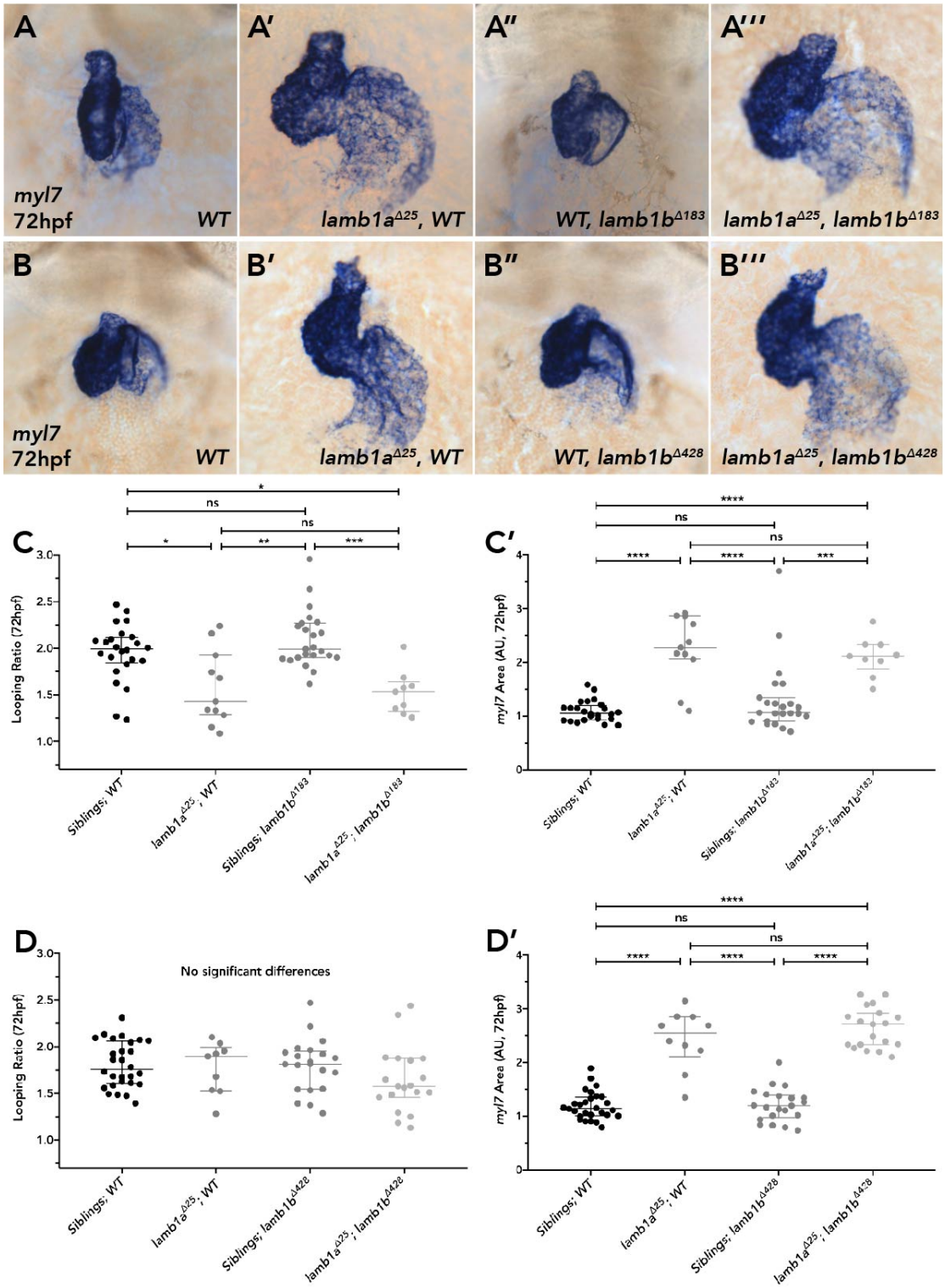

Figure 5.8. *lamb1a* is required to restrict heart size independent of *lamb1b*

Quantitative analysis of heart morphology in WT, *lamb1a*, *lamb1b* and double *lamb1a*; *lamb1b* mutants at 72hpf by analysis in situ hybridisation analysis of *myl7* expression. **(A-A‴)** Representative images of WT (A), *lamb1a*$^{\Delta 25}$ homozygous mutant (A′), *lamb1b*$^{\Delta 183}$ homozygous mutants and *lamb1a*$^{\Delta 25}$; *lamb1b*$^{\Delta 183}$ double

Previous studies suggesting that *lamb1a* is dispensable for cardiac development focussed on heart laterality and morphogenesis at relatively early stages, prior to 2dpf, in an ENU (N-ethyl-N-nitrosourea) mutant identified in forward genetic screen (Eeden et al., 1996; Hochgreb-Hägele et al., 2013; Karlstrom et al., 1996; Odenthal et al., 1996; Stemple et al., 1996). To confirm that the enlarged hearts found in the CRISPR-Cas9-generated *lamb1a* mutant alleles are related to the loss of *lamb1a*, and not an off-target effect of the mutagenesis, cardiac morphology was examined in an additional, previously-characterised *lamb1a* mutant allele *gup*^{tj299a}, generated by random ENU mutagenesis (Eeden et al., 1996; Karlstrom et al., 1996; Odenthal et al., 1996; Stemple et al., 1996), thought to disrupt splicing of the lamb1a transcript (A. Grierson, personal communication) (Figure 5.9). *gup*^{tj299a} mutants also display no significant reduction in heart looping ratio at 55hpf or 72hpf (Figure 5.9A-B', D, E), but have significantly larger hearts at 55hpf and 72hpf when compared to siblings (Figure 5.9C, C', E). In addition, similar to both novel *lamb1a* CDS alleles,

Figure 5.8 continued.

homozygous mutants (A''') at 72hpf. **(B-B''')** Representative images of WT (B), *lamb1a*$^{\Delta 25}$ homozygous mutant (B'), *lamb1b*$^{\Delta 428}$ homozygous mutants and *lamb1a*$^{\Delta 25}$; *lamb1b*$^{\Delta 428}$ double homozygous mutants (B''') at 72hpf. *lamb1a*$^{\Delta 25}$ hearts appear much larger than WT or *lamb1b* homozygous mutant hearts. **(C-C'')** Quantification of heart morphology in embryos from a *lamb1a*$^{\Delta 25}$; *lamb1b*$^{\Delta 183}$ heterozygous incross (C). Loss of *lamb1a*, independent of *lamb1b* function results in a significant increase in *myl7* area at 72hpf. No increase in heart size is observed in single *lamb1b*$^{\Delta 183}$ homozygous mutants (C'). **(D-D')** Quantification of heart morphology in embryos from *lamb1a*$^{\Delta 25}$; *lamb1b*$^{\Delta 428}$ heterozygous incross. No combination of mutations has a significant impact on heart looping ratio (D). Loss of *lamb1a*, independent of *lamb1b* function results in a significant increase in *myl7* area at 72hpf. No increase in heart size is observed in single *lamb1b*$^{\Delta 428}$ homozygous mutants (D'). Ventral views. C-D': Median with interquartile range, Kruskal-Wallis, Dunn's multiple comparisons, ns: not significant, *: p<0.05, **: p<0.01, ***: p<0.001, ****: p<0.0001.

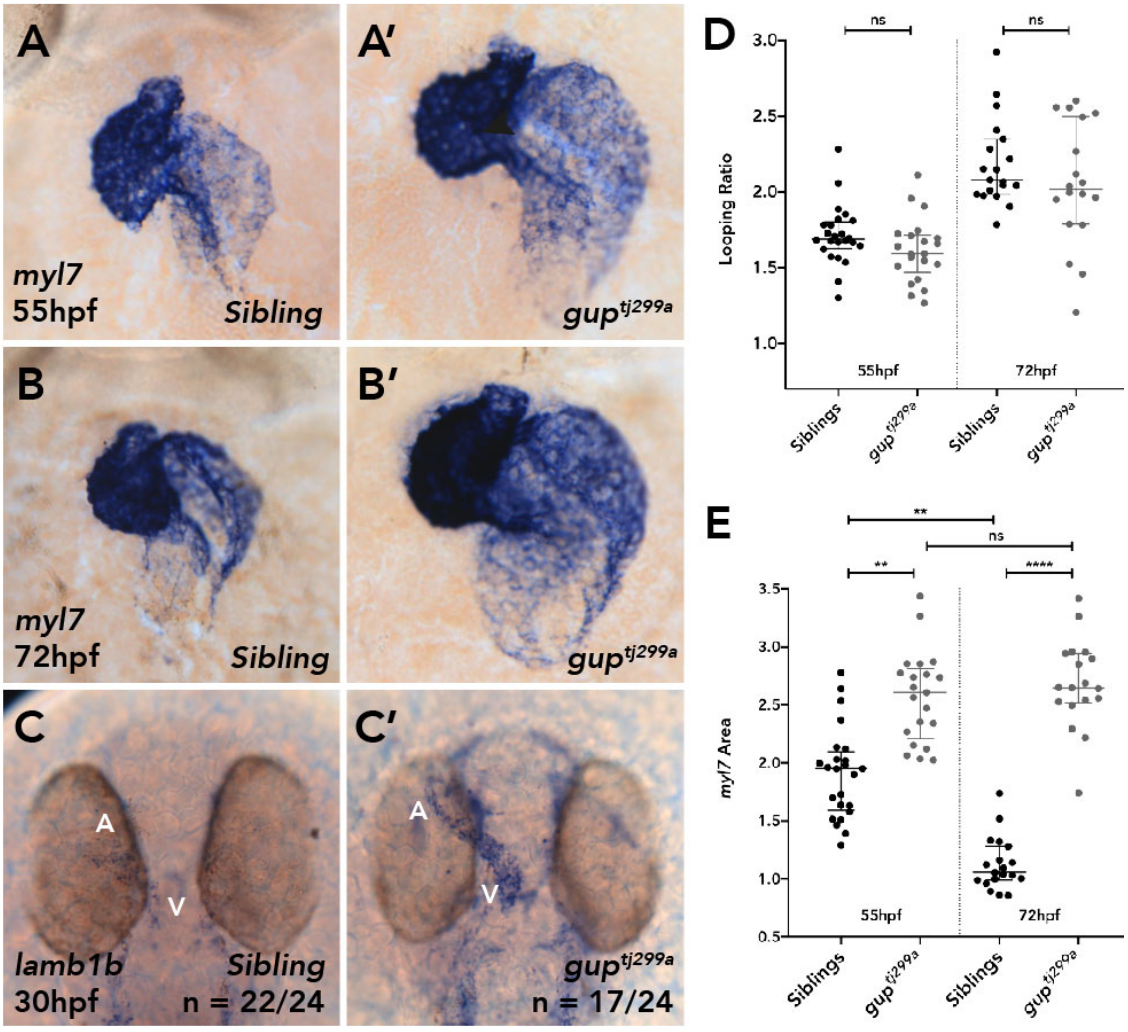

Figure 5.9. *guptj299a* mutants have larger hearts and up-regulate *lamb1b*.

Characterisation of heart morphology and *lamb1b* expression by mRNA *in situ* hybridisation in the *lamb1a* allele *gup*^{tj299a}. **(A-B')** Representative images of sibling (A) and *gup*^{tj299a} (A') *myl7* expression at 55hpf and 72hpf (B, B' respectively). *gup*^{tj299a} hearts have increased size compared to siblings. **(C-C')** At 30hpf, *lamb1b* expression in *gup*^{tj299a} siblings is restricted to the ventricular endocardium of the heart (C). In *gup*^{tj299a} mutants, *lamb1b* is expressed throughout the endocardium (C'). **(D-E)** Quantification of heart morphology comparing siblings and *gup*^{tj299a} mutants at 55hpf and 72hpf. *gup*^{tj299a} mutants do not display a significant reduction in heart looping ratio (D). *gup*^{tj299a} mutants exhibit significantly larger hearts at 55hpf and 72hpf (E). A-B': ventral views, C-C': dorsal views. V: ventricle, A: atrium. D-E: Median with interquartile range, Kruskal-Wallis, Dunn's multiple comparisons, ns: not significant, **: p<0.01, ****: p<0.0001.

gup^{tj299a} mutants display an up-regulation of *lamb1b* expression at 30hpf compared to siblings (Figure 5.9C, C'). Together these data support a novel role for Laminins in regulating cardiac size/restricting cardiac growth during development .

To investigate the temporal requirement for *lamb1a* in restricting heart size, single *lamb1a* mutant heterozygous adults were incrossed and embryos fixed at 30hpf, 55hpf, 63hpf and 72hpf to analyse heart looping ratio and heart area using *in situ* hybridisation analysis of *myl7* expression, (Figure 5.10). At 30hpf, no significant difference in heart size or morphology is apparent between *lamb1a* mutants and WT siblings (Figure 5.10A, A', G, G'), however by 55hpf *lamb1a* mutants have larger hearts than WT siblings, with a more pronounced phenotype in the *lamb1a*$^{\Delta 19}$ allele (Figure 5.10B, B', H, H'). At 55hpf, both *lamb1a* mutants display a mild reduction in heart looping ratio, which recovers by 63hpf (Figure 5.10E, K). Additionally, between 55hpf and 72hpf, whilst sibling heart area is significantly reduced due to changes in morphology, *lamb1a* mutant hearts, whilst remaining significantly larger than their siblings do not significantly change in size. This suggests that whilst by 55hpf *lamb1a* mutants have larger hearts, loss of *lamb1a* does not continue to increase heart size, implying the critical window of *lamb1a* activity during heart looping is between 30hpf and 55hpf. A similar non-significant increase in heart area between 55hpf and 72hpf is observed in the *gup*^{tj299a} allele. (Figure 5.10D, D', J, J', Figure 5.9E).

As a secondary method to confirm that *lamb1a* regulates size of the heart, the size of individual chambers was measured at 30hpf and 55hpf, using *in situ* hybridisation expression analysis of *myh7l* and *myh6* to quantify size of the ventricle and atrium respectively (Figure 5.11). At 30hpf, no significant difference in chamber size is observed for either the atrium or ventricle (Figure 5.11A-A', D-D', C, F, G-G', J-J', I, L), however by 55hpf, both chambers in both alleles are significantly larger than their siblings (Figure 5.11B-B' E-E', C, F, H-H', K-K', I, L).

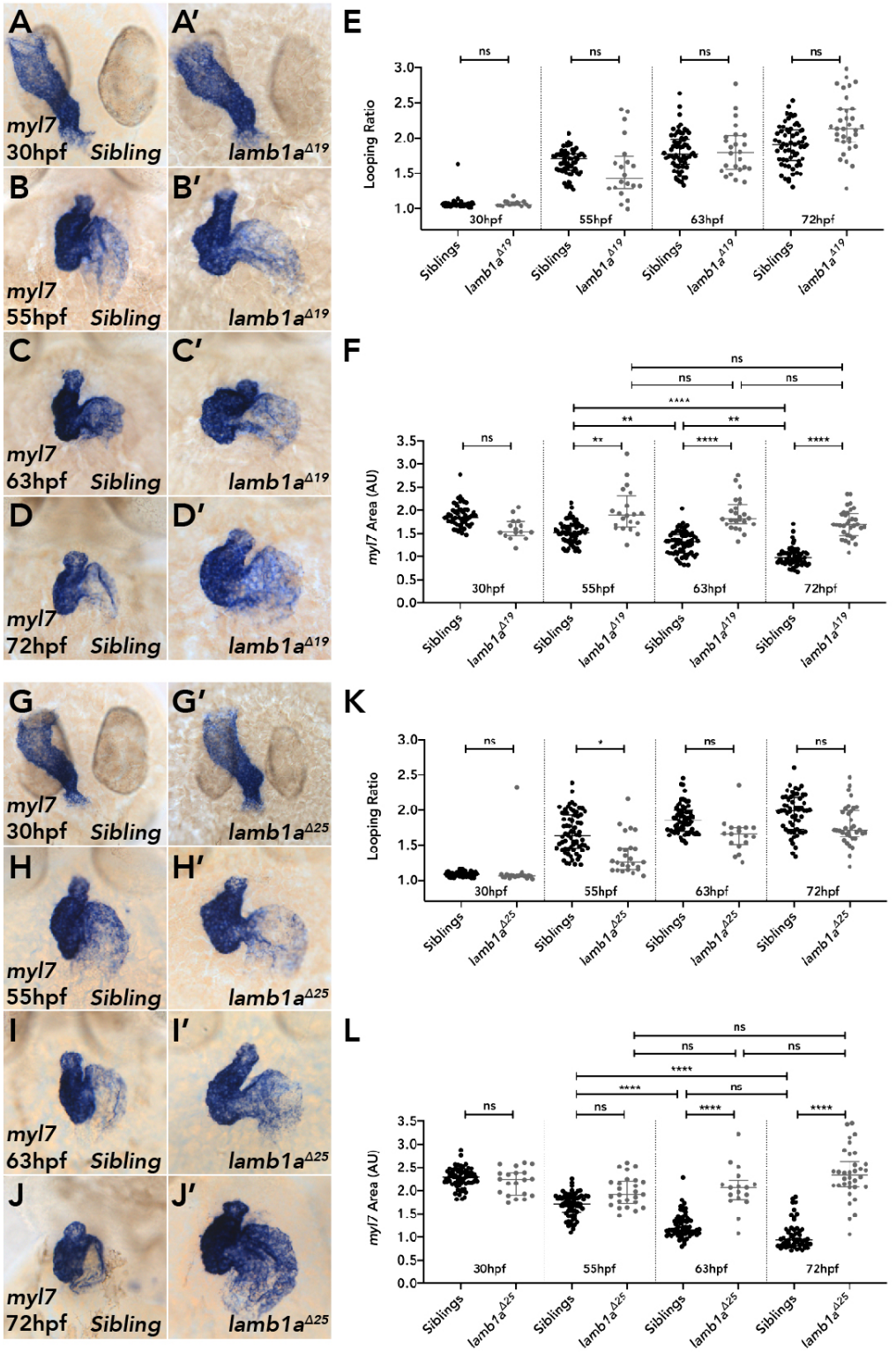

Figure 5.10. *lamb1a* is dispensable for heart looping morphogenesis, but is required to limit heart size.

(A-D′) Representative images for time-course analysis of *myl7* expression in *lamb1a*$^{\Delta 19}$ heterozygous incross at 30hpf (A-A′), 55hpf (B-B′), 63hpf (C-C′) and 72hpf

Figure 5.10 continued.

(D-D'). By 72hpf a clear increase in heart size is apparent. **(E-F)** Quantification of heart morphology in *lamb1a*$^{\Delta 19}$ mutants and siblings. No significant reduction in heart looping ratio is observed between 30hpf to 72hpf between siblings and *lamb1a*$^{\Delta 19}$ homozygous mutants, although a mild reduction in looping ratio in mutants is observed at 55hpf (E). By 55hpf a significant increase in *myl7* area is present. No increase in *lamb1a*$^{\Delta 19}$ mutant heart size is observed between 55hpf and 63hpf, whilst sibling hearts are observed to become smaller (F). **(G-J')** Representative images for time-course analysis of *myl7* expression in *lamb1a*$^{\Delta 25}$ heterozygous incross at 30hpf (G-G'), 55hpf (H-H'), 63hpf (I-I') and 72hpf (J-J'). By 72hpf a clear increase in heart size is apparent. **(K-L)** Quantification of heart morphology in *lamb1a*$^{\Delta 25}$ mutants and siblings. A significant reduction in heart looping ratio is observed at 55hpf between siblings and *lamb1a*$^{\Delta 25}$ homozygous mutants, although this has recovered by 63hpf (K). By 63hpf a significant increase in *myl7* area is present, with a non-significant increase apparent at 55hpf. No increase in *lamb1a*$^{\Delta 25}$ mutant heart size is observed between 55hpf and 63hpf, whilst sibling hearts appear to reduce in size as the heart compacts (L). A, A', G, G': dorsal views. B-D', H-J': ventral views. E, F, K, L: Median with interquartile range, Kruskal-Wallis, Dunn's multiple comparisons, ns: not significant, *: $p<0.05$, **: $p<0.01$, ****: $p<0.0001$.

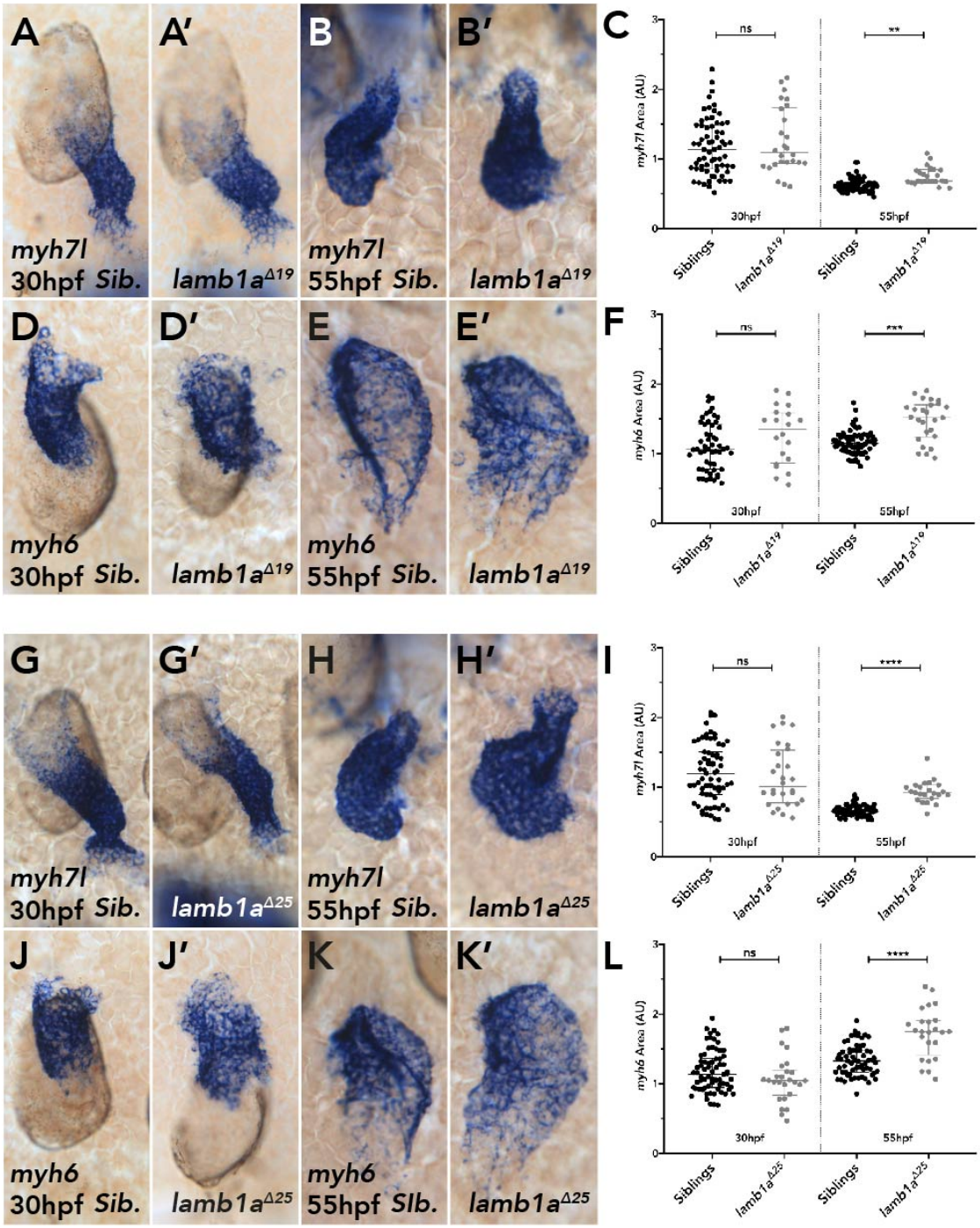

Figure 5.11. *lamb1a* is required to limit chamber size.

(A-B') Representative images for time-course analysis of *myh7l* expression in *lamb1a*$^{\Delta 19}$ heterozygous incross at 30hpf (A-A'), 55hpf (B-B'). **(C)** Quantification of ventricular size demonstrates a subtle but significant increase in *lamb1a*$^{\Delta 19}$ homozygous mutants at 55hpf. **(D-E')** Representative images for time-course analysis of *myh6* expression in *lamb1a*$^{\Delta 19}$ heterozygous incross at 30hpf (D-D'), 55hpf (E-E'). **(F)** Quantification of atrial size demonstrates a subtle but significant increase

Collectively these data highlight a novel role for *lamb1a* in limiting the size of the developing heart, but demonstrate it is dispensable for early heart looping morphogenesis. Careful time course analysis suggests that the critical window for *lamb1a* function is between 30hpf and 55hpf, identical to that of the role for *lamc1* in promoting heart looping (Figure 3.11, 3.12). Additionally, while *lamb1b* is up-regulated in the hearts of *lamb1a* mutants, *lamb1b* does not play a role in mediating the *lamb1a* mutant phenotype.

5.1.4 Lamb1a-Lamc1 containing Laminin isoforms are required to limit heart size

As *lamc1* is the sole identified Laminin gamma subunit expressed in the heart during early cardiac morphogenesis, loss of *lamc1* is predicted to prevent the formation of all *lamb1a* containing isoforms (Libby et al., 2000; Yurchenco et al., 1997). If this hypothesis is correct, *lamc1* F0 mutants would also display the increased heart size phenotype exhibited in *lamb1a* mutants. In agreement with this, while at 72hpf *lamc1* F0 mutants continue to display a significant reduction in heart looping ratio compared to injection controls (Figure 5.12B), they also exhibit as a significant increase in heart size (Figure 5.12C), similar to that observed in *lamb1a* mutants.

Figure 5.11 continued.

in *lamb1a*$^{\Delta 19}$ homozygous mutants at 55hpf. **(G-H')** Representative images for time-course analysis of *myh7l* expression in *lamb1a*$^{\Delta 25}$ heterozygous incross at 30hpf (G-G'), 55hpf (H-H'). **(I)** Quantification of ventricular size demonstrates a subtle but significant increase in *lamb1a*$^{\Delta 25}$ homozygous mutants at 55hpf. **(J-K')** Representative images for time-course analysis of *myh6* expression in *lamb1a*$^{\Delta 25}$ heterozygous incross at 30hpf (J-J'), 5hpf (K-K'). **(L)** Quantification of atrial size demonstrates a subtle but significant increase in *lamb1a*$^{\Delta 25}$ homozygous mutants at 55hpf. A, A', D, D', G, G', J, J': dorsal views. B, B', E, E', H, H', K, K': ventral views. C, F, I, L: Median with interquartile range, Kruskal-Wallis, Dunn's multiple comparisons, ns: not significant, *: $p<0.05$, **: $p<0.01$, ***: $p<0.001$.

Characterisation of heart area at 30hpf and 55hpf (Figure 5.13D) reveals that *lamc1* may be required for heart size at 30hpf but not at 55hpf and may suggest a possible underlying mechanism for the looping phenotype observed (See Chapter 8).

It is possible that *lamb1a* and *lamc1* may function independently to limit heart size during development, and as such loss of both *lamb1a* and *lamc1* would result in hearts larger than single mutants. However, if *lamb1a* and *lamc1* interact together in the same complex, heart area should be indistinguishable between either single mutant or the double mutant. To examine this, *lamc1* F0 mutants were generated in the *lamb1a*$^{\Delta 25}$ background and the resulting cardiac phenotypes characterised at 55hpf and 72hpf using *myl7* expression to analyse heart looping ratio and heart area. At both 55hpf and 72hpf, independent of *lamb1a* genotype, *lamc1* F0 mutants display a reduction in heart looping ratio (Figure 5.13D-D', E, Figure 5.14D-D', E). As previously described, *lamb1a* mutants either injected with guides targeting *lamc1* or uninjected controls have a mild non-significant reduction in heart looping ratio at 55hpf (Figure 5.13E), which recovers by 72hpf (Figure 5.14E). However, both *lamb1a*$^{\Delta 25}$ and *lamc1* F0 mutants have significantly increased heart size by 72hpf (Figure 5.14F), not observed at 55hpf (Figure 5.13F). Of note is no additive effect of loss of *lamc1* and *lamb1a* at 72hpf with regards to heart size (Figure 5.14F), suggesting that Lamb1a and Lamc1 function in the same Laminin isoform to restrict heart size. Whilst *lamc1* F0 mutants and *lamb1a* mutants are indistinguishable with respect to heart area at 72hpf (Figure 5.12C, 5.14D-D', F), *lamb1a* mutants do not display a significant reduction in heart looping ratio compared to sibling controls at 72hpf as observed in *lamc1* F0 mutants (Figure 5.14E). Together this suggests that heart looping and control of heart size are regulated by distinct Laminin isoforms and that a separate beta chain is functioning together with Lamc1 to promote looping morphogenesis.

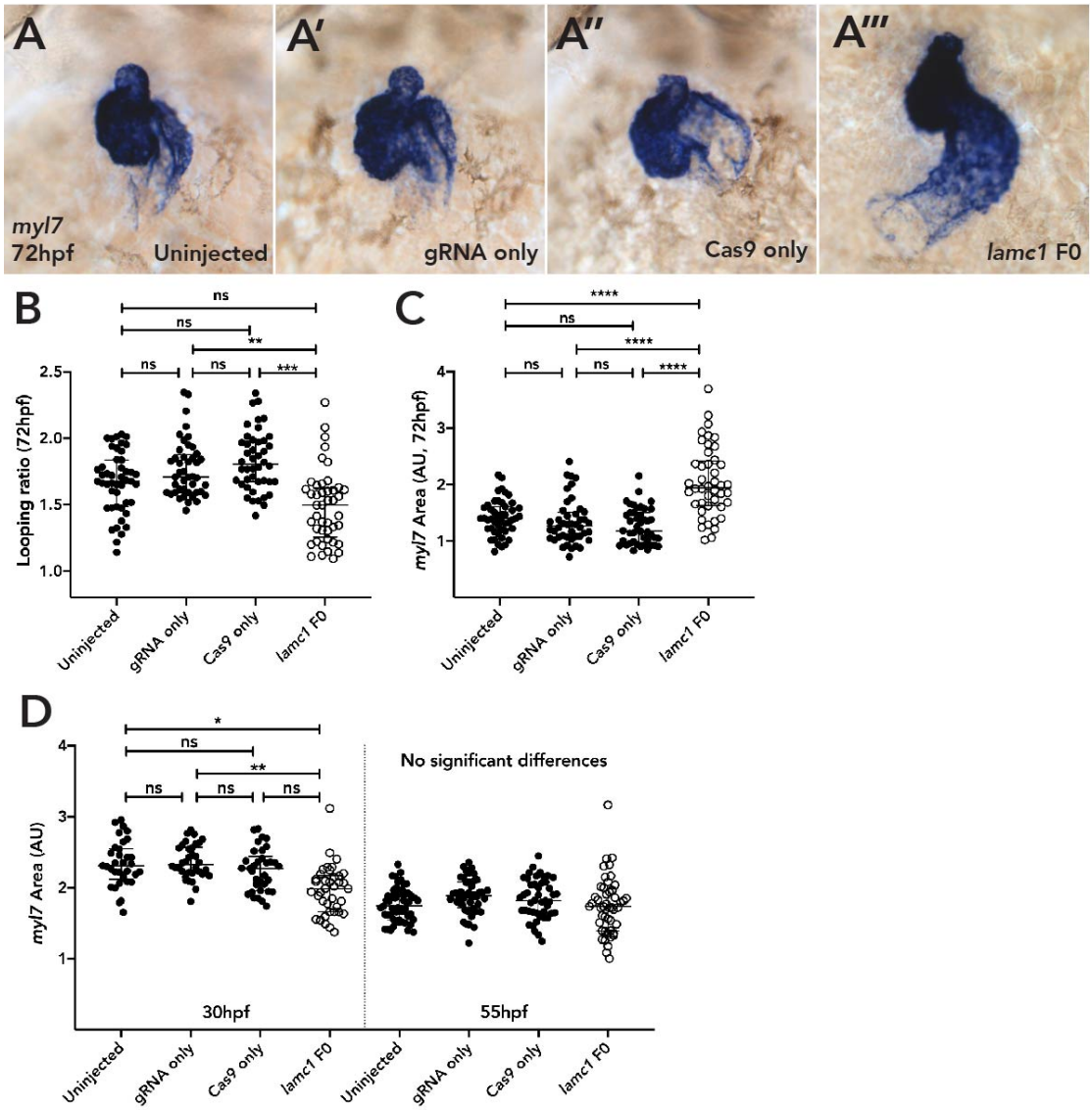

Figure 5.12. *lamc1* is required to restrict heart size and promote heart morphogenesis.

Quantitative analysis of heart looping at 72hpf and heart area at 30hpf, 55hpf, and 72hpf in *lamc1* F0 mutants. **(A-A'''')** Representative images of mRNA *in situ* hybridisation analysis of *myl7* at 72hpf to examine heart morphology in uninjected (A), *lamc1* targeting gRNA only (A'), Cas9 only (A'') and *lamc1* F0 mutants (A'''). *lamc1* F0 mutants at 72hpf display a severe heart looping phenotype but are also clearly larger than injection controls (A'''). **(B)** Quantification of heart looping ratio in *lamc1* F0 mutants and control groups at 72hpf; *lamc1* F0 mutants have a significant reduction in heart looping ratio compared to gRNA only or Cas9 only injection controls. **(C)** Quantification of *myl7* area in *lamc1* F0 mutants and control groups at

Figure 5.12 continued.

72hpf. *lamc1* F0 mutants have significantly larger hearts than any control group. **(D)** Quantification of *myl7* area in *lamc1* F0 mutants and control groups at 30hpf and 55hpf. At 30hpf, *lamc1* F0 mutants have significantly smaller hearts compared to uninjected controls and gRNA only injected controls, which has recovered by 55hpf. No significant differences are observed between uninjected, *lamc1* targeting gRNA or Cas9 only controls, however *lamc1* F0 mutants have a significant reduction in heart looping ratio at 55hpf when compared to any control group. A-A''': dorsal views. B-D: Median with interquartile range, Kruskal-Wallis, Dunn's multiple comparisons, ns: not significant, *: $p<0.05$, **: $p<0.01$, ***: $p<0.001$, ****: $p<0.0001$.

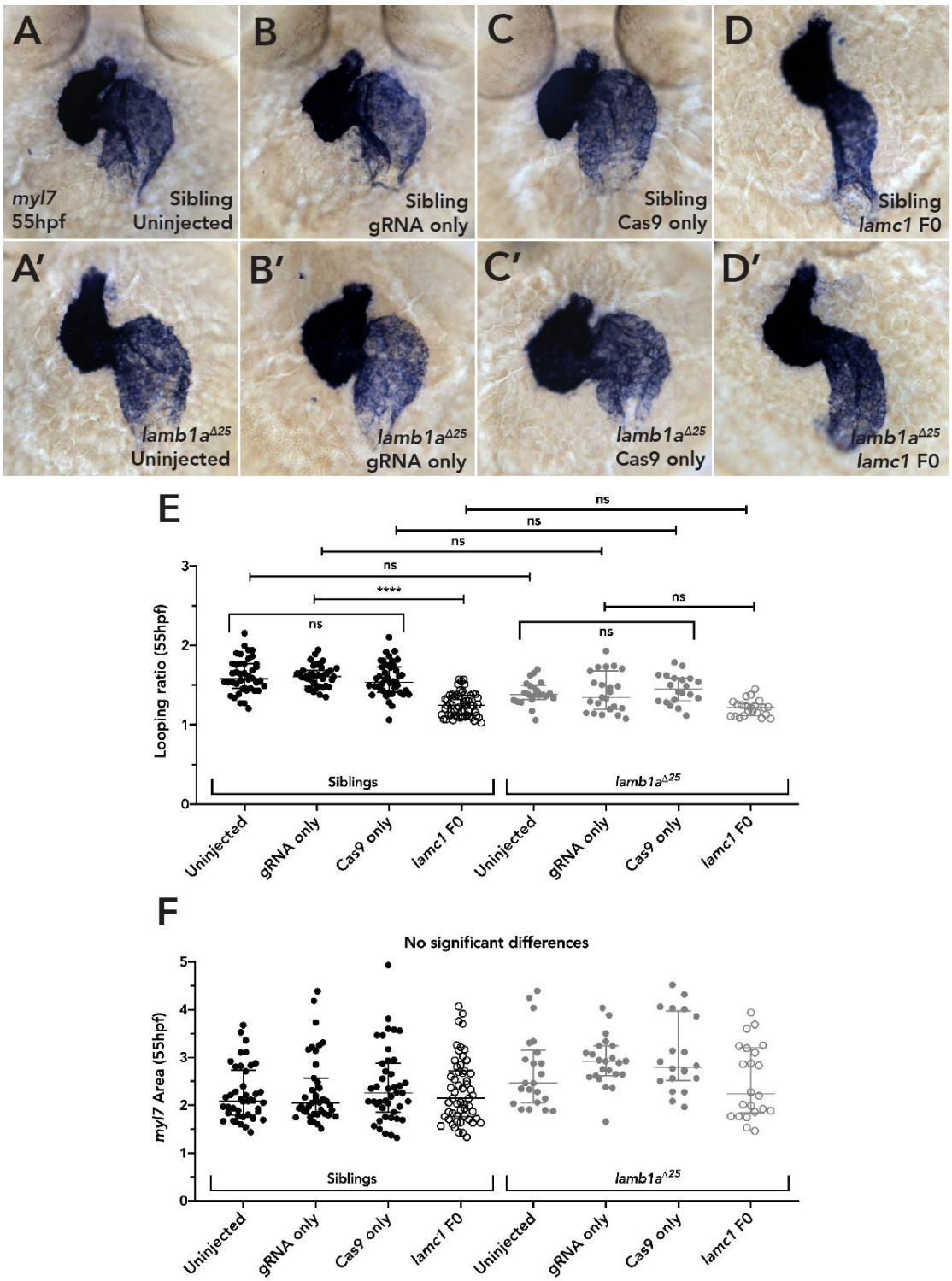

Figure 5.13. The *lamc1* cardiac phenotype is epistatic to *lamb1a*.

mRNA *in situ* hybridisation analysis of *myl7* expression at 55hpf in *lamb1a*, *lamc1* F0 mutants and controls. **(A-D')** Representative images of mRNA *in situ* hybridisation analysis of *myl7* at 55hpf to examine heart morphology in uninjected sibling (A), uninjected *lamb1a*$^{\Delta 25}$ mutants (A'), gRNA only sibling (B), gRNA only *lamb1a*$^{\Delta 25}$

Figure 5.13 continued.

mutants (B'), Cas9 only sibling (C), Cas9 only *lamb1a*$^{\Delta 25}$ mutants (C'), *lamc1* F0 mutants (D) and *lamb1a*$^{\Delta 25}$; *lamc1* F0 mutants (D'). **(E)** Quantification of looping ratio at 55hpf in *lamb1a*; *lamc1* F0 mutants and controls. *lamc1* F0 have a significant reduction in heart looping ratio compared to injection controls in *lamb1a* siblings. *lamb1a*$^{\Delta 25}$; *lamc1* F0 double mutants have a non-significant reduction in heart looping compared to *lamb1a*$^{\Delta 25}$ injection controls. **(F)** Quantification of *myl7* area at 55hpf in *lamb1a*; *lamc1* F0 mutants and controls, no significant differences are observed. A-D': ventral views. E, F: Median with interquartile range, Kruskal-Wallis, Dunn's multiple comparisons, ns: not significant, ****: $p<0.0001$.

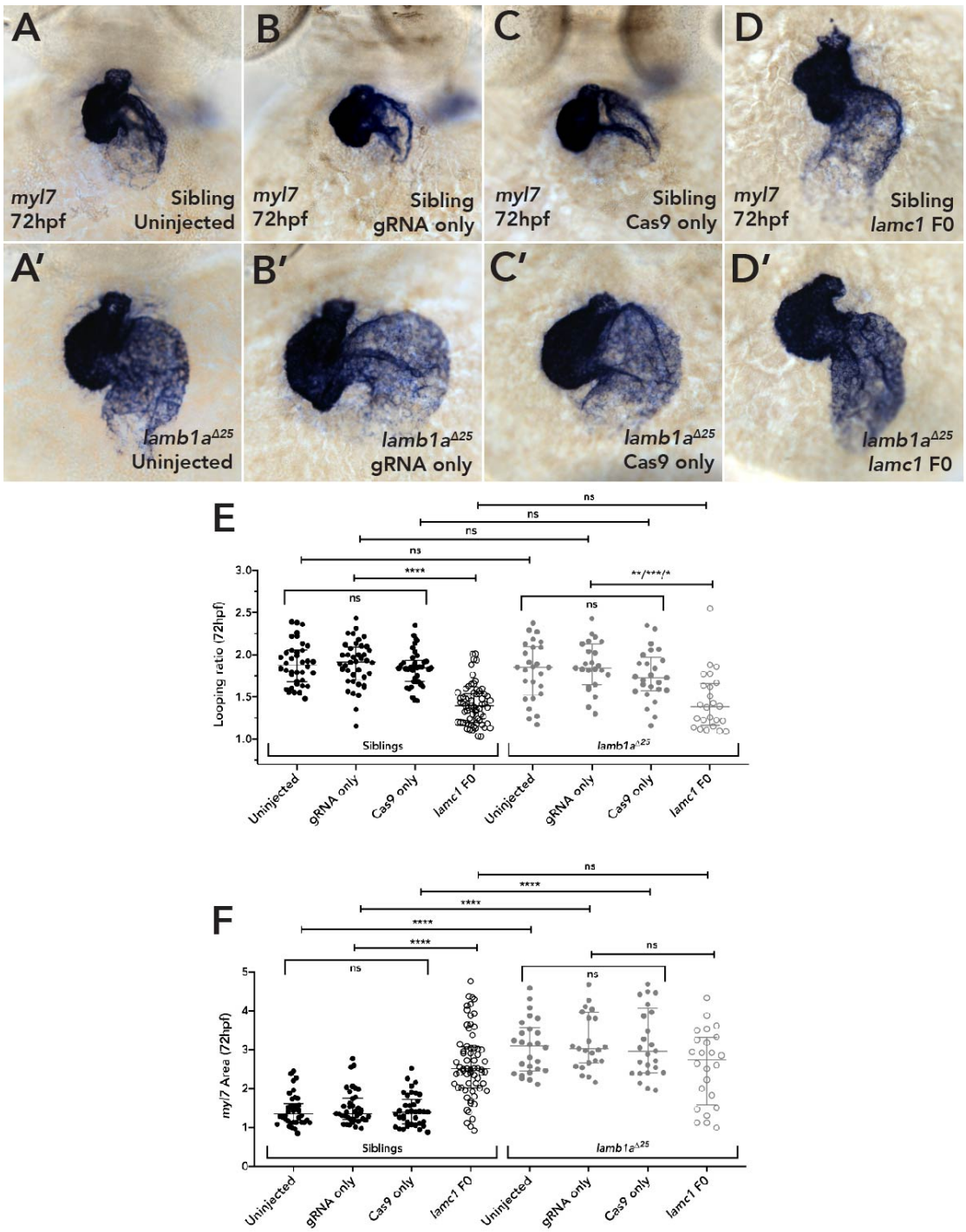

Figure 5.14. Laminins perform distinct roles during heart development.

mRNA *in situ* hybridisation for *myl7* at 72hpf in *lamb1a*, *lamc1* F0 mutants and controls. **(A-D')** Representative images of mRNA *in situ* hybridisation analysis of *myl7* expression at 72hpf to examine heart morphology in uninjected sibling (A), uninjected *lamb1a*$^{\Delta 25}$ mutants (A'), gRNA only sibling (B), gRNA only *lamb1a*$^{\Delta 25}$ mutants (B'), Cas9 only sibling (C), Cas9 only *lamb1a*$^{\Delta 25}$ mutants (C'), *lamc1* F0

The only remaining Laminin beta subunit expressed in the heart during early looping morphogenesis is *lamb2* (Figure 3.2, 3.3, 3.12), the expression of which is unchanged following loss of *lamb1a*; *lamb1b* or both *lamb1* subunits (Figure 4.19, 5.15), suggesting an NMD-induced compensation mechanism may not be acting, but that endogenous *lamb2* could act together with *lamc1*, Furthermore, as Lamb1a-containing trimers are only required to limit heart size, this supports a role for *lamb2* function in acting together with *lamc1* to promote heart looping. This would suggest that loss of *lamb1a* and *lamb2* would recapitulate the *lamc1* F0 phenotype. To investigate this possible role for *lamb2* in heart development, CRISPR F0 mutagenesis (Burger et al., 2016; Wu et al., 2018) was undertaken, a similar approach used to generate *lamc1* F0 mutants (Figure 5.16A). Four gRNAs targeting *lamb2* were injected together with active Cas9 protein into an incross of *lamb1a*$^{\Delta 25}$ heterozygous carriers and embryos were fixed at 55hpf and 72hpf. Heart looping ratio and heart area was subsequently quantified using *in situ* hybridisation analysis of *myl7* expression (Figure 5.16, 5.17). *lamb2* stable mutants have no clear morphological defects, (Jacoby et al., 2009) therefore to confirm successful mutagenesis of the *lamb2* gene, gel electrophoresis of PCR-amplified mutagenesis target regions was used to identify *lamb2* F0 mutants, as described in Chapter 3

Figure 5.14 continued.

mutants (D) and *lamb1a*$^{\Delta 25}$; *lamc1* F0 mutants (D'). **(E)** Quantification of looping ratio at 72hpf in *lamb1a* ;*lamc1* F0 mutants and controls. *lamc1* F0 have a significant reduction in heart looping ratio compared to injection controls. Loss of *lamc1* results a phenotype independent of *lamb1a* genotype. **(F)** Quantification of *myl7* area at 72hpf in *lamb1a*; *lamc1* F0 mutants and controls. No significant differences are present between the *myl7* area of *lamb1a*, *lamc1* and *lamb1a*; *lamc1* F0 double mutants and are significantly larger than *lamb1a* siblings or injection controls. E, F: Median with interquartile range, Kruskal-Wallis, Dunn's multiple comparisons. Ventral views ns: not significant, *: $p<0.05$, **: $p<0.01$, ***: $p<0.001$, ****: $p<0.0001$.

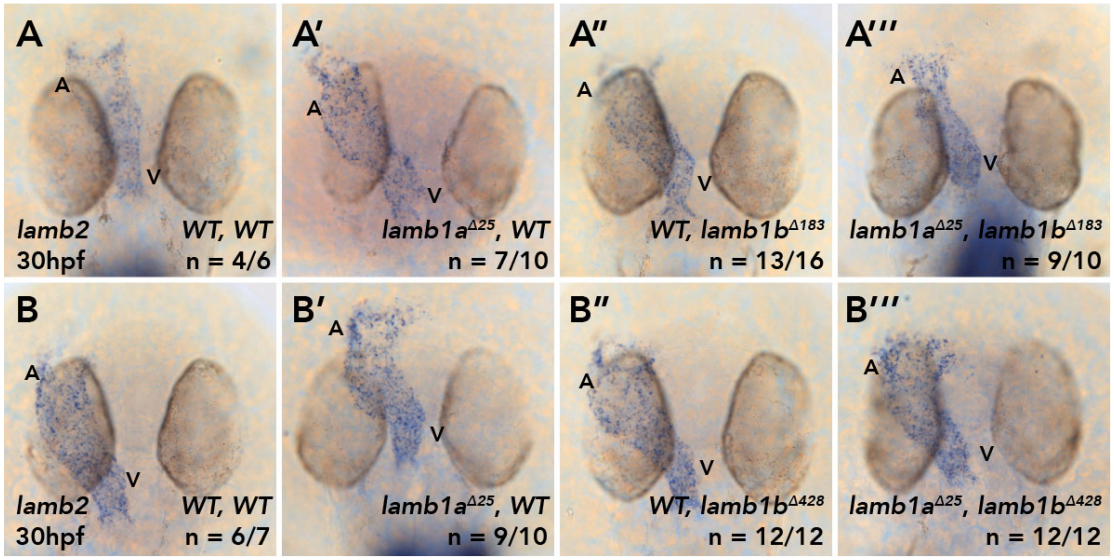

Figure 5.15. *lamb2* expression is unchanged by loss of *lamb1a* and/or *lamb1b*.

mRNA *in situ* hybridisation analysis of *lamb2* expression at 30hpf in single or double *lamb1a*; *lamb1b* mutants. **(A-A‴)** *lamb2* is expressed throughout the myocardium in WT embryos (A), and expression is unchanged in *lamb1a*$^{\Delta 25}$ homozygous mutants (A′), *lamb1b*$^{\Delta 183}$ homozygous mutants (A″) or *lamb1a*$^{\Delta 25}$; *lamb1b*$^{\Delta 183}$ double homozygous mutants (A‴). **(B-B‴)** The same result is observed in the *lamb1b*^{428} allele. Dorsal views. V: ventricle, A: atrium.

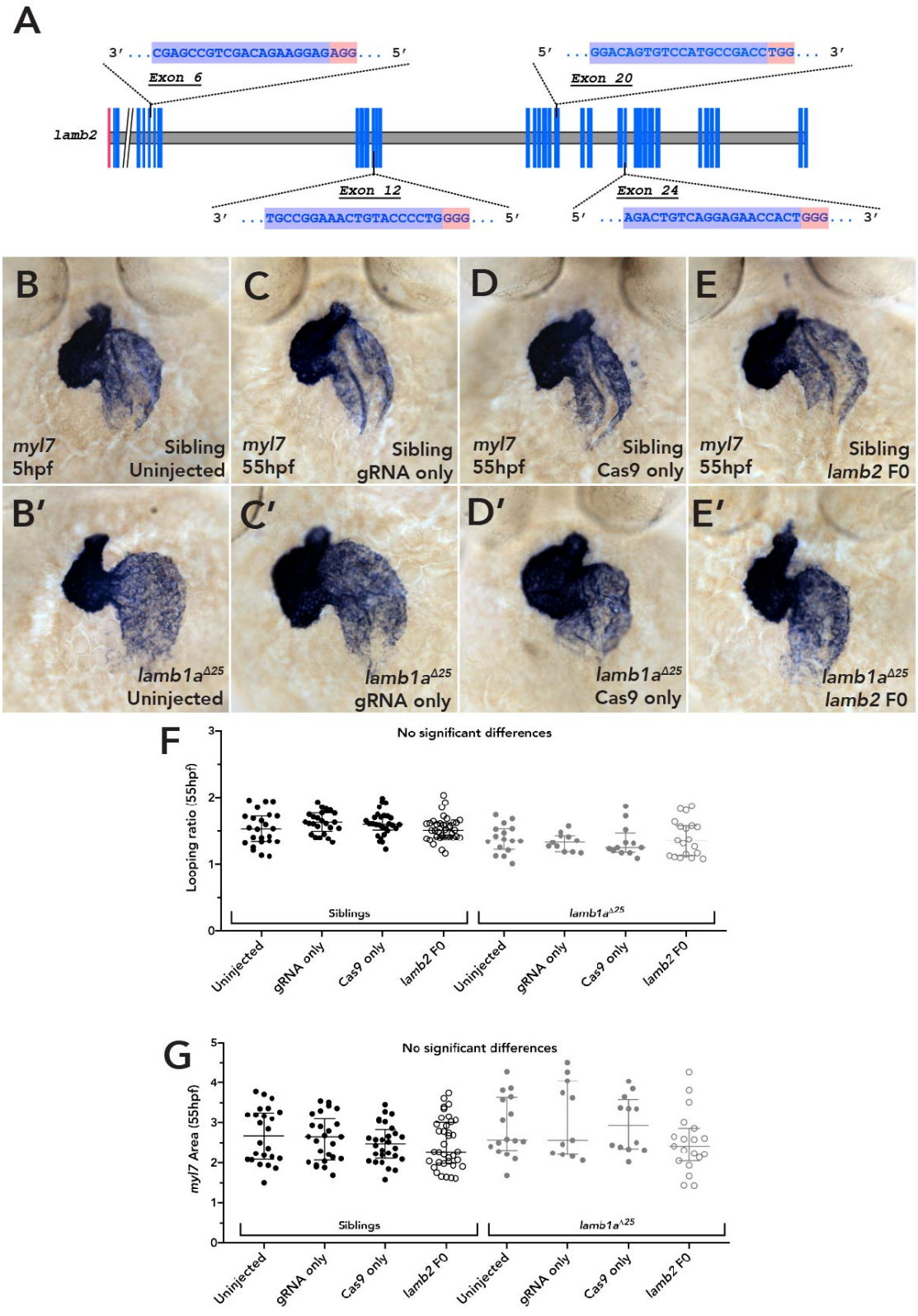

Figure 5.16. *lamb2* is dispensable for heart looping at 55hpf.

Generation of *lamb2* F0 mutants by CRISPR-Cas9 genome editing, and characterisation by mRNA *in situ* hybridisation analysis of *myl7* expression at 55hpf

(data not shown). Contrary to expectations, at both 55hpf (Figure 5.16) and 72hpf (Figure 5.17), *lamb2* F0 mutants display no clear defects in heart morphology or significant reduction in heart looping ratio (Figure 5.16F, Figure 5.17E). As expected, loss of *lamb2* does not impact heart size at 55hpf or 72hpf in either wild type or *lamb1a* mutants (Figure 5.16G, Figure 5.17F). Together, this demonstrates that while *lamb1a* and *lamc1* interact during development to limit heart size, neither *lamb1a* or *lamb2* interact with *lamc1* to promote looping morphogenesis, suggesting an as-yet unidentified Laminin beta subunit regulates this aspect of cardiac morphogenesis.

Figure 5.16 continued.

in *lamb1a*, *lamb2* F0 mutants and controls. **(A)** Schematic showing *lamb2* genomic DNA, coding exons in blue, non-coding exons in red, based on danRer10/GRCz10 (oblique cut line represents 25kbp). Four gRNAs (spacer highlighted in blue, PAM highlighted in red) targeting the exons 6, 12, 20 and 24 were injected to generate *lamb2* F0 mutants. **(B-E')** Representative images of mRNA *in situ* hybridisation analysis of *myl7* at 55hpf to examine heart morphology in uninjected sibling (B), uninjected *lamb1a*$^{\Delta 25}$ mutants (B'), gRNA only sibling (C), gRNA only *lamb1a*$^{\Delta 25}$ mutants (C'), Cas9 only sibling (D), Cas9 only *lamb1a*$^{\Delta 25}$ mutants (D'), *lamb2* F0 mutants (E) and *lamb1a*$^{\Delta 25}$; *lamb2* F0 mutants (E'). **(F)** Quantification of looping ratio at 55hpf in *lamb1a*; *lamb2* F0 mutants and controls. No significant differences are observed. **(G)** Quantification of *myl7* area at 55hpf in *lamb1a*; *lamb2* F0 mutants and controls, no significant differences are observed. B-E': ventral views. F, G: Median with interquartile range, Kruskal-Wallis, Dunn's multiple comparisons.

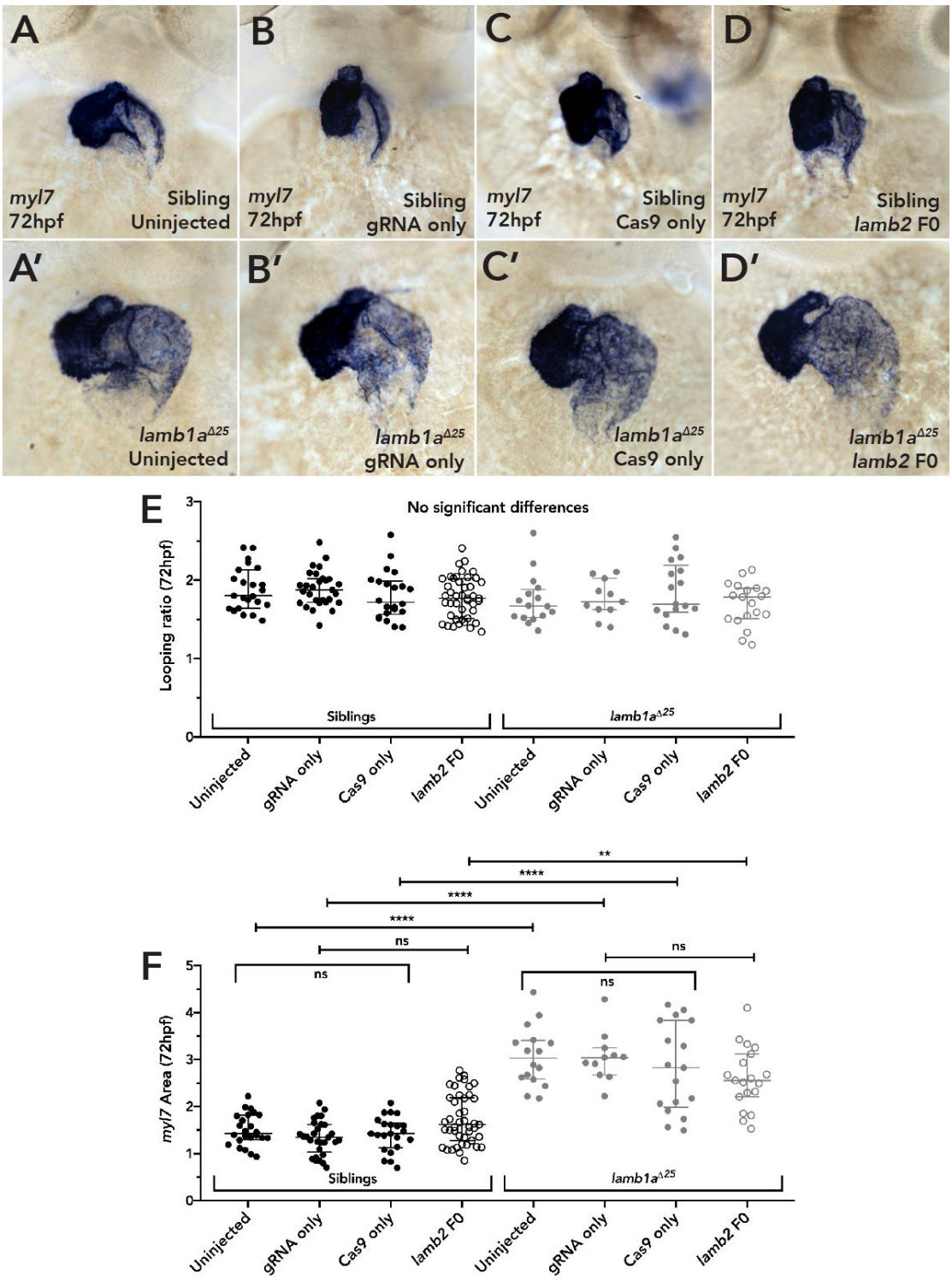

Figure 5.17. *lamb2* is dispensable for early heart morphogenesis.

mRNA *in situ* hybridisation analysis of *myl7* at 72hpf in *lamb1a*;*lamb2* F0 mutants and controls. **(A-D')** Representative images of mRNA *in situ* hybridisation analysis of *myl7* at 72hpf to examine heart morphology in uninjected sibling (A), uninjected *lamb1a*$^{\Delta 25}$ mutants (A'), gRNA only sibling (B), gRNA only *lamb1a*$^{\Delta 25}$ mutants (B'),

5.1.5 *lamb1a* mutants display mis-regulation of flow responsive genes

Having defined a requirement for a Lamb1a-Lamc1 containing Laminin isoform in restricting heart size during heart looping morphogenesis, the mechanisms underlying the *lamb1a* mutant phenotype were investigated. A failure to restrict heart size may result from improper patterning of the heart which may impact on heart function and lead to increased heart size. *nppa* is a marker of the outer curvature of the ballooning chambers, expressed in the working myocardium at 55hpf (Figure 5.18 A, B) (Auman et al., 2007; Grassini et al., 2018). In both *lamb1a* mutant alleles, expression of *nppa* is unchanged, demonstrating that the chambers are undergoing ballooning correctly and suggesting that heart function is not altered in *lamb1a* mutants, as *nppa* expression is sensitive to heart contractility (Auman et al., 2007). *nppa* and the related gene *nppb* are part of an inhibitory feedback loop with *bmp4* which is required to restrict the valve program to the AVC in the zebrafish heart (Grassini et al., 2018). Whilst *nppa* marks working myocardium, *bmp4* is expressed in the non-working myocardium where it is normally expressed in small rings of cells at the inflow tract, outflow tract and atrioventricular canal (Figure 5.18C, D). However, in *lamb1a* mutants, *bmp4* expression appears up-regulated in the ventricle of just over half of *lamb1a* mutants compared to siblings. Additionally, *bmp4* expression is observed in *lamb1a* mutants to be expanded at the inflow tract

Figure 5.17 continued.

Cas9 only sibling (C), Cas9 only *lamb1a*$^{\Delta 25}$ mutants (C'), *lamb2* F0 mutants (D) and *lamb1a*$^{\Delta 25}$; *lamb2* F0 mutants (D'). **(E)** Quantification of looping ratio at 72hpf in *lamb1a*; *lamb2* F0 mutants and controls. No significant differences are observed. **(F)** Quantification of *myl7* area at 72hpf in *lamb1a*; *lamb2* F0 mutants and controls, no significant differences are observed. A-D': ventral views. E, F: Median with interquartile range, Kruskal-Wallis, Dunn's multiple comparisons, ns: not significant, **: p<0.01, ****: p<0.0001.

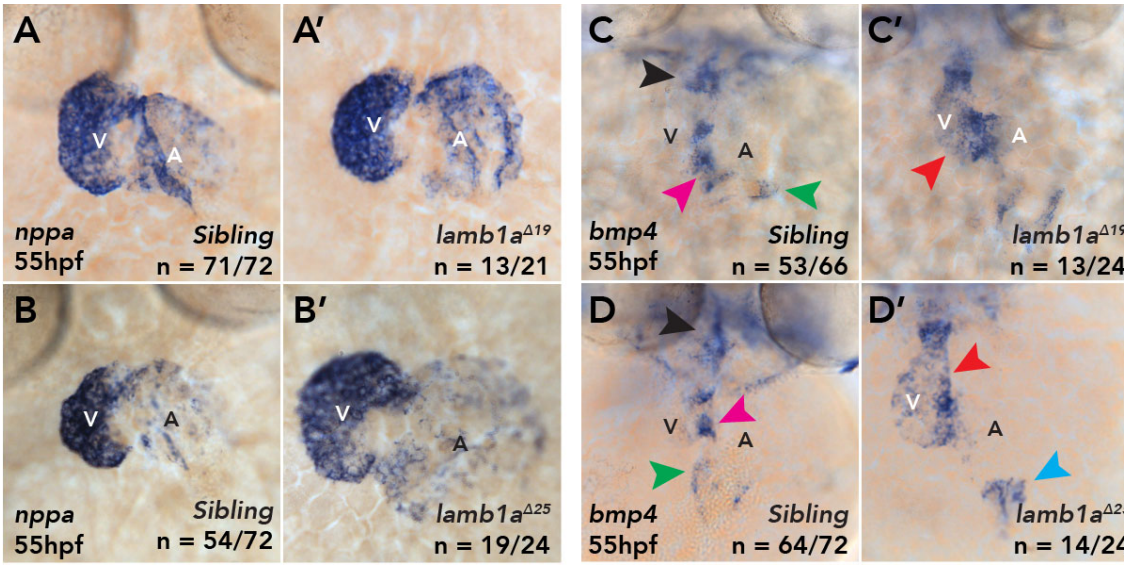

Figure 5.18. *lamb1a* mutants display mild cardiac patterning defects.

mRNA *in situ* hybridisation expression analysis of cardiac patterning markers *bmp4* and *nppa* in *lamb1a* mutants. **(A-B′)** In siblings at 55hpf, *nppa* is expressed in the working myocardium and excluded from the atrioventricular canal (A, B). Expression of *nppa* is unchanged in *lamb1a*$^{\Delta 19}$ (A′) or *lamb1a*$^{\Delta 25}$ homozygous mutants (B′). **(C-D′)** In siblings at 55hpf, *bmp4* is expressed in the non-working myocardium: outflow tract (C, D, black arrowhead), atrioventricular canal (C, D, magenta arrowhead) and inflow tract (C, D, green arrowhead). Expression of *bmp4* is expanded into the ventricle in *lamb1a* mutants (C′, D′, red arrowhead). In a subset of *lamb1a*$^{\Delta 25}$ mutants, *bmp4* expression is expanded at the inflow tract (D′, blue arrowhead) embryos. Ventral views. V: ventricle, A: atrium.

of the heart (Figure 5.18C-D′). This suggests that the patterning of *lamb1a* mutant hearts is only mildly affected and that this is unlikely to be the basis for the increase in heart size in the *lamb1a* mutants.

The increase in size of *lamb1a* mutant hearts is reminiscent of the enlarged heart phenotype observed in mutations affecting the Cerebral Cavernous Malformation (CCM) pathway (Mably et al., 2006, 2003). *ccm* mutants exhibit an up-regulation of the mechanotransductive transcription factor *klf2a* through blood-flow independent mechanisms, the exact mechanism by which heart size is then affected is unclear,

although evidence suggests modulation of the ROCK cytoskeletal effector (Lisowska et al., 2018). Classically, *klf2a* is regulated by blood-flow, where it is required to regulate endocardial ballooning and initiation of the valve programme at the AVC (Dietrich et al., 2014; Heckel et al., 2015; Vermot et al., 2009). Furthermore, *lamb1b*, a flow-dependent gene (Chapter 3) is up-regulated in *lamb1a* mutants, again suggesting a similarity between *lamb1a* mutants and *ccm* mutants.

To examine whether the mechanism acting in *lamb1a* mutant hearts is similar to that underlying the cardiac defects in *ccm* mutants, embryos from a *lamb1a* heterozygous incross were injected with a *tnnt2a* morpholino to block heart contractility, thus abolishing blood flow (Sehnert et al., 2002). Expression of *klf2a* and *lamb1b* were then characterised at 30hpf by mRNA *in situ* hybridisation (Figure 5.19).

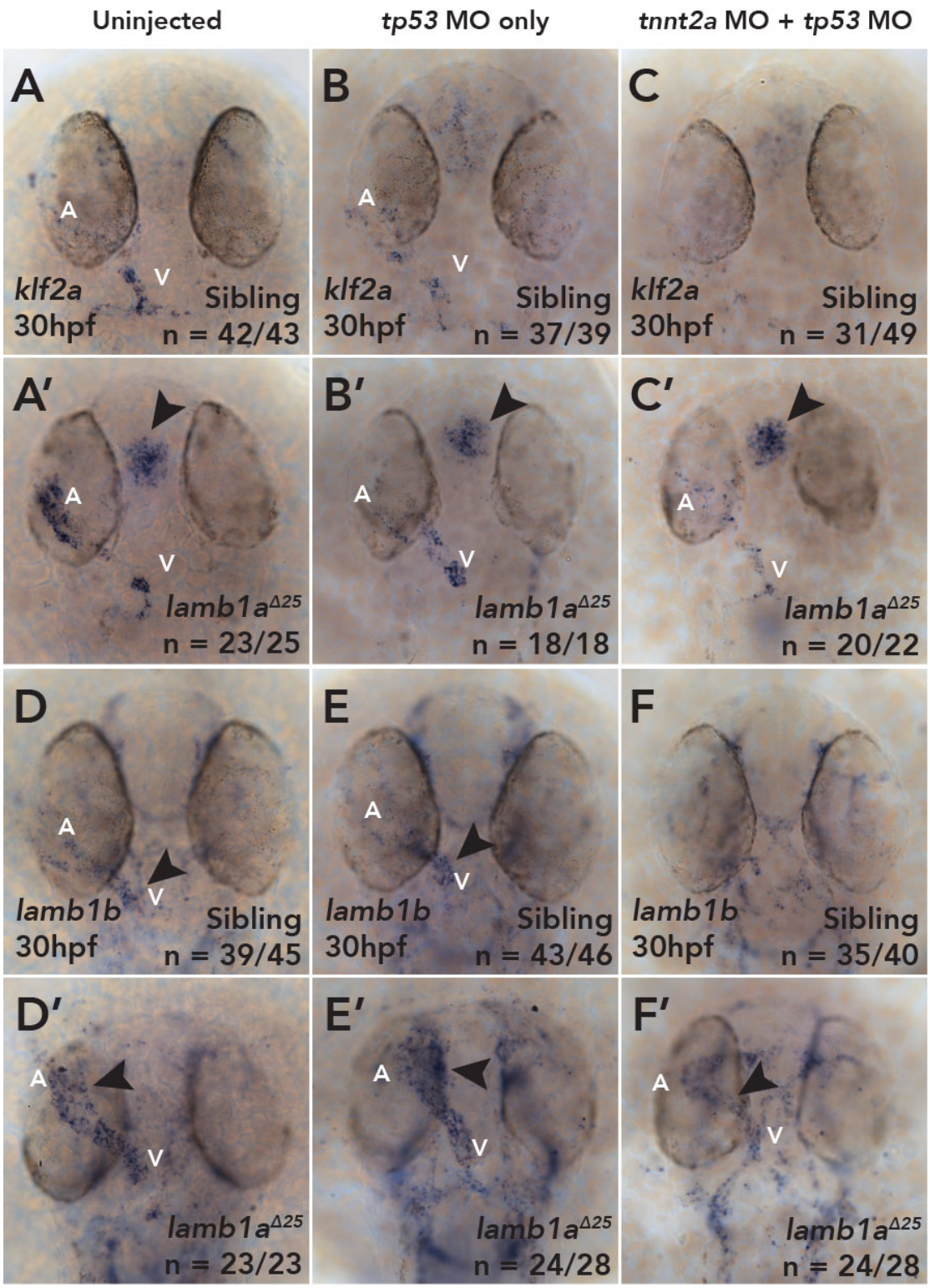

Figure 5.19 *lamb1a* mutants display flow-independent expression of flow-dependent genes.

mRNA *in situ* hybridisation analysis of the flow dependent genes *klf2a* and *lamb1b* under no flow conditions in *lamb1a* mutants. **(A-A')** *klf2a* is expressed predominantly

In sibling uninjected embryos, *klf2a* expression is localised to predominantly the arterial pole endocardium (Figure 5.19A), whereas uninjected *lamb1a* mutants misexpress *klf2a* more broadly throughout the heart and also have prominent expression of *klf2a* in the head (Figure 5.19A'). Morpholino-mediated knockdown of *tnnt2a* in sibling embryos results in almost total loss of *klf2a* expression in the endocardium (Figure 5.19C). Loss of heart contractility in *lamb1a* mutants results in reduced endocardial expression of *klf2a* compared *tp53* MO injected *lamb1a* mutant controls however, *klf2a* is still expressed at higher levels in *lamb1a* mutant *tnnt2a* morphants compared to *tnnt2a* morphant siblings. Intriguingly, loss of heart contractility does not affect *klf2a* expression in the head of *lamb1a* mutants (Figure 5.19C'). Together, upon loss of heart contractility, *klf2a* is absent in sibling embryos but some residual expression is retained specifically in *lamb1a* mutants, suggesting that misexpression of *klf2a* in the mutants is independent of heart function and probably blood flow.

Figure 5.19 continued.

at the arterial pole in sibling embryos (A), but is misexpressed in the endocardium of *lamb1a*$^{\Delta 25}$ mutants and also prominently up-regulated in the head (A', arrowhead). **(B-B')** Expression of *klf2a* is unchanged in sibling (B) or *lamb1a*$^{\Delta 25}$ mutants injected with *tp53* MO (B'). **(C-C')** *klf2a* expression is almost completely absent in sibling embryos injected with *tnnt2a* MO (C). However, *klf2a* expression in the heart is still present in *lamb1a*$^{\Delta 25}$ mutants, although to a lesser degree than control injected embryos (C'), and the up-regulated expression in the head is retained (A', B',C'). **(D-D')** *lamb1b* is expressed in the ventricular endocardium in sibling embryos (D, arrowhead), but is misexpressed throughout in the endocardium of *lamb1a*$^{\Delta 25}$ mutants (D', arrowhead). **(E-E')** Expression of *lamb1b* is unchanged in sibling (E) or *lamb1a*$^{\Delta 25}$ mutants injected with *tp53* MO (E'). **(F-F')** *lamb1b* expression is almost completely absent in sibling embryos injected with *tnnt2a* MO (F), whilst *lamb1b* expression is still present in *lamb1a*$^{\Delta 25}$ mutants (F'), although to a lesser degree than control injected embryos. Dorsal views. V: ventricle, A: atrium.

To determine whether loss of *lamb1a* specifically affects expression of *klf2a* through blood-low independent mechanisms or whether a common mechanism of blood flow sensation is altered upon loss of *lamb1a*, expression of *lamb1b* was examined following *tnnt2a* knockdown in *lamb1a* mutants. Similar to *klf2a*, *lamb1b* expression in the endocardium is maintained in *lamb1a* mutants injected with *tnnt2a*-targeting morpholino (Figure 5.19F'), albeit at lower levels when compared with *lamb1a* mutant embryos injected with control morpholino (Figure 5.19E'). This is in contrast to the loss of *lamb1b* expression in sibling embryos injected with *tnnt2a* morpholino (Figure 5.19D-F). Together these data demonstrate that the misexpression of two flow-dependent genes, *klf2a* and *lamb1b* in *lamb1a* mutants is flow-independent, suggesting that misregulation of flow sensing pathways or the improper response to blood flow sensation may result in larger hearts.

To investigate whether increased shear stress is responsible for the *lamb1a* phenotype, blood viscosity was lowered through morpholino-mediated knockdown of the transcription factor *gata1a* (Hsu et al., 2019), a master regulator of erythropoiesis (Brownlie and Zon, 1999). Control and *gata1a* injected embryos were fixed at 55hpf to examine the expression of the haemoglobin subunit *hbbe1.1 (hemoglobin beta embryonic-1.1*) (Paffett-Lugassy et al., 2007; Quinkertz and Campos-Ortega, 1999) by mRNA *in situ* hybridisation to confirm efficiency of *gata1a* knockdown. *gata1a* knockdown in *lamb1a* sibling embryos results in almost complete loss of expression of *hbbe1.1* when compared to uninjected or *tp53* injection controls at 55hpf (Figure 5.20A-C, one experimental repeat). Control and *gata1a* injected embryos were also fixed at 72hpf to examine the heart morphology by mRNA *in situ* hybridisation of *myl7*. Preliminary analysis suggests that loss of Gata1a function and reduction in blood viscosity does not significantly impact on heart looping morphogenesis at 72hpf (Figure 5.20D) and does not rescue *lamb1a* mutant heart size to wild type (Figure 5.20E). This supports the notion that changes to up-regulation of *klf2a* in *lamb1a* mutants is unlikely to be due to increased shear stress, although *klf2a* expression was not examined in *gata1a* morphants.

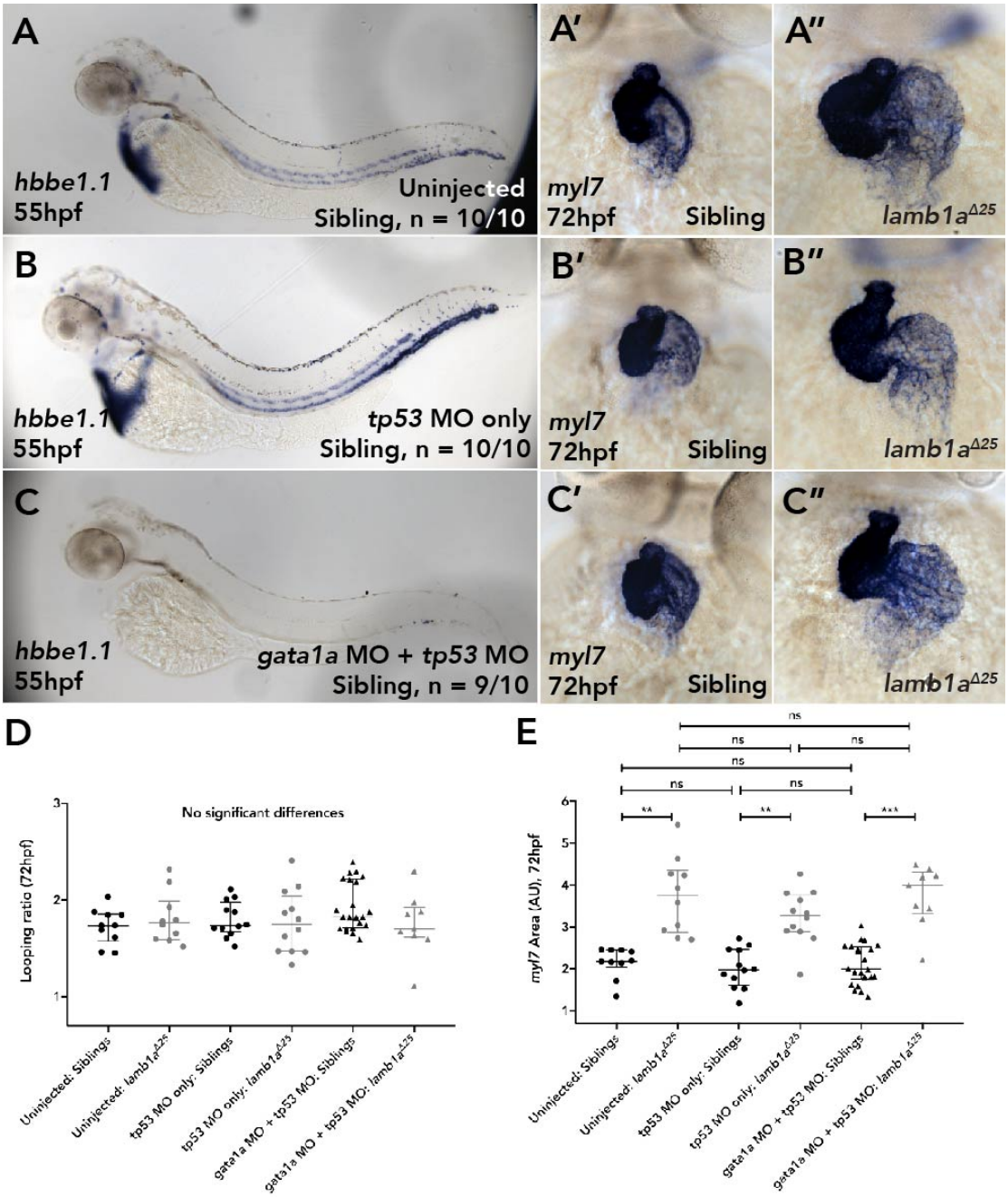

Figure 5.20. Knockdown of *gata1a* does not rescue heart size in *lamb1a* mutants.

mRNA *in situ* hybridisation analysis of the effect of *gata1a* knockdown on *lamb1a* cardiac morphology. **(A-A'')** Representative images of *hbbe1.1* expression in uninjected sibling embryos at 55hpf (A). Representative images of *myl7* expression in uninjected sibling (A') and *lamb1a*$^{\Delta 25}$ mutants (A'') at 72hpf. **(B-B'')** Representative images of *hbbe1.1* expression in *tp53* MO injected sibling embryos at 55hpf (B). Representative images of *myl7* expression in *tp53* MO injected sibling (B') and *lamb1a*$^{\Delta 25}$ mutants (B'') at 72hpf. **(C-C'')** In *gata1a* MO injected embryos, *hbbe1.1*

As a separate method to test the links between blood flow sensation and increased heart size, blood viscosity was increased through *erythropoietin a* (*epoa*) mRNA injection at the 1-cell stage. Epoa acts through the conserved Epo receptor (Paffett-Lugassy et al., 2007) stimulating a JAK-STAT axis, promoting erythropoeisis and resulting in an increase in erythrocyte number and blood viscosity (Koury and Bondurant, 1991). As *klf2a* expression is sensitive to increased shear stress, increasing blood viscosity through *epoa* mRNA injection (Hsu et al., 2019) would be predicted to increase *klf2a* expression. Similarly, if increased *klf2a* expression is the basis for the enlarged hearts observed in *lamb1a* mutants, *epoa* mRNA-injected embryos would be predicted to have enlarged hearts by 72hpf, phenocopying the *lamb1a* mutant. To examine whether increased blood content could be sufficient to drive an increase in heart size, *lamb1a* heterozygotes were outcrossed to WT and embryos injected with *epoa* mRNA or water (sham). *lamb1a* heterozygous embryos were included in the analysis alongside WT since examining whether *lamb1a* heterozygotes are sensitised to increased blood viscosity may provide a stronger link between the role of blood flow and increased heart size in *lamb1a* mutants.

Figure 5.20 continued.

expression is absent (C). Representative images of *myl7* expression in *gata1a* knockdown sibling (C') and *lamb1a*$^{\Delta 25}$ mutants (C'') at 72hpf. **(D)** Quantification of heart looping ratio in sibling and *lamb1a*$^{\Delta 25}$ mutants at 72hpf across all injection groups. No significant differences are observed. **(E)** Quantification of *myl7* area in sibling and *lamb1a*$^{\Delta 25}$ mutants at 72hpf across all injection groups. *lamb1a*$^{\Delta 25}$ mutants subject to knockdown still display a significant increase in heart area compared to siblings. A, B, C: lateral views, anterior left. A', A'', B', B'', C', C'': ventral views. D, E: Median with interquartile range, Kruskal-Wallis, Dunn's multiple comparisons. One experimental repeat, ns: not significant, **: $p<0.01$, ***: $p<0.001$

To first demonstrate that *epoa* mRNA injection increases erythropoiesis, *hbbe1.1* expression was analysed in injected embryos. Both WT and *lamb1a* heterozygous embryos injected with *epoa* mRNA at the 1-cell stage display greatly increased expression of *hbbe1.1* expression at 55hpf (compare Figure 5.21A, A'' to B, B'' and C, C''). Having confirmed that *epoa* mRNA increases erythrocyte number, the impact of this on heart morphology at 72hpf was analysed by *myl7* expression (Figure 5.21 A-C, A'''-C'''). Increase in blood viscosity has no significant impact on heart looping at 72hpf in either WT embryos or *lamb1a* heterozygotes (Figure 5.21D). However, compared to sham injections *lamb1a* heterozygotes display a mild, yet significant increase in *myl7* area, not observed in WT embryos (Figure 5.21E), suggesting that *lamb1a* heterozygotes may be sensitised to increased blood flow. As manipulation of blood viscosity is not sufficient to increase heart size sufficiently to recapitulate the mutant phenotype and *klf2a* and *lamb1b* display blood flow-independent regulation in *lamb1a* mutants, these data suggest that increased shear stress is not responsible for increased heart size in *lamb1a* mutants.

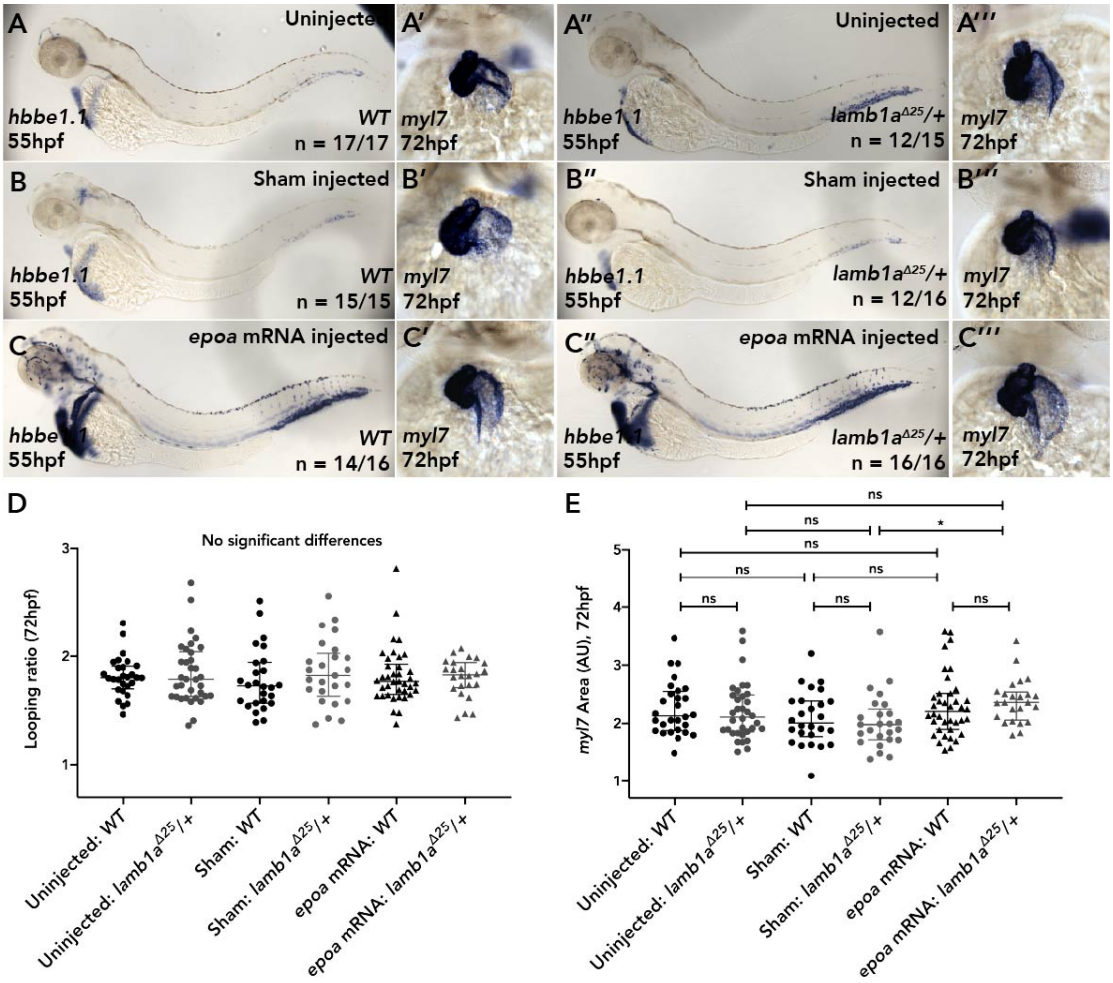

Figure 5.21. Increasing blood flow is not sufficient to increase heart size.

mRNA *in situ* hybridisation analysis of the impact of increased blood flow. **(A-A''')** Representative images of *hbbe1.1* expression in uninjected WT (A) and *lamb1a*$^{\Delta 25}$ heterozyogtes at 55hpf (A''). Representative images of *myl7* in uninjected WT (A') and *lamb1a*$^{\Delta 25}$ heterozyogtes at 72hpf (A'''). **(B-B''')** Representative images of *hbbe1.1* expression in sham injected WT (B) and *lamb1a*$^{\Delta 25}$ heterozyogtes at 55hpf (B''). Representative images of *myl7* in sham injected WT (B') and *lamb1a*$^{\Delta 25}$ heterozygotes at 72hpf (B'''). **(C-C'')** In *epoa* mRNA-injected embryos, *hbbe1.1* expression is up-regulated (C, C''). Representative images of *myl7* expression in *epoa* mRNA-injected WT (C') and *lamb1a*$^{\Delta 25}$ heterozygotes (C''') at 72hpf. **(D)** Quantification of heart looping ratio in WT and *lamb1a* heterozygotes at 72hpf across all injection groups. No significant differences are observed. **(E)** Quantification of *myl7* area in sibling and *lamb1a* heterozygotes at 72hpf across all

Blood-flow-independent misexpression of *klf2a* in *lamb1a* mutants is similar to the cardiac phenotype described in *ccm* mutants, in which *KLF2* expression is regulated through the MEKK3-MEK5-ERK5 axis (Otten et al., 2018; Zhou et al., 2016, 2015). To investigate whether *lamb1a* mutants have increased activity of the MEK5-ERK5 axis, phosphoERK (pERK) levels, a marker of ERK activity, were analysed in *lamb1a* mutants by immunohistochemistry (E. Noël Figure 5.22).

At 30hpf, only a small number of pERK positive cells are found in the heart tube (visualised with the membrane maker Alcama) and the surrounding tissue (Figure 5.22 A-A'', E. Noël). *lamb1a* mutants display an increase in pERK staining when compared to siblings, both within the heart) and in the surrounding tissue (Figure 5.22 B-B'', E. Noël), which may represent the second heart field. This suggests that an increase in ERK activity may underly the flow-independent up regulation of *klf2a* in the *lamb1a* mutants, further supporting this may drive an increase in heart size. Having established that *lamb1a* mutants display increased in pERK staining and blood flow independent regulation of *klf2a*, a likely candidate for driving increase in heart size is ERK5 (Otten et al., 2018; Zhou et al., 2016, 2015).

To test whether ERK5 activity is responsible for the *lamb1a* mutant cardiac phenotype, *lamb1a* embryos were treated with the ERK5 inhibitor XMD17-109 (ERK5i) (Elkins et al., 2013; Gilbert et al., 2017) between 24hpf and 55hpf, the most likely critical window of function for *lamb1a* in heart morphogenesis. At 55hpf the compound was removed from the embryos, which were thoroughly washed and

Figure 5.21 continued.

injection groups. A mild, but significant increase in *myl7* area is observed between *epoa* mRNA-injected *lamb1a* heterozygotes and sham injected *lamb1a* heterozygotes A, A'', B, B'', C, C'': lateral views, anterior left. A', A''', B', B''', C', C''': ventral views. D, E: Median with interquartile range, Kruskal-Wallis, Dunn's multiple comparisons, ns: not significant, *: $p<0.05$.

allowed to develop until 72hpf when cardiac morphology was analysed by *myl7* expression (Figure 5.23A-C'). Preliminary analysis suggests that inhibition of ERK5 during early heart looping morphogenesis does not impact on heart looping ratio (Figure 5.23D) or rescue heart size to wild type in *lamb1a* mutants (Figure 5.23E), suggesting that a separate ERK could be driving increase in heart size in *lamb1a* mutants, distinct from ERK5 (McCain, 2013).

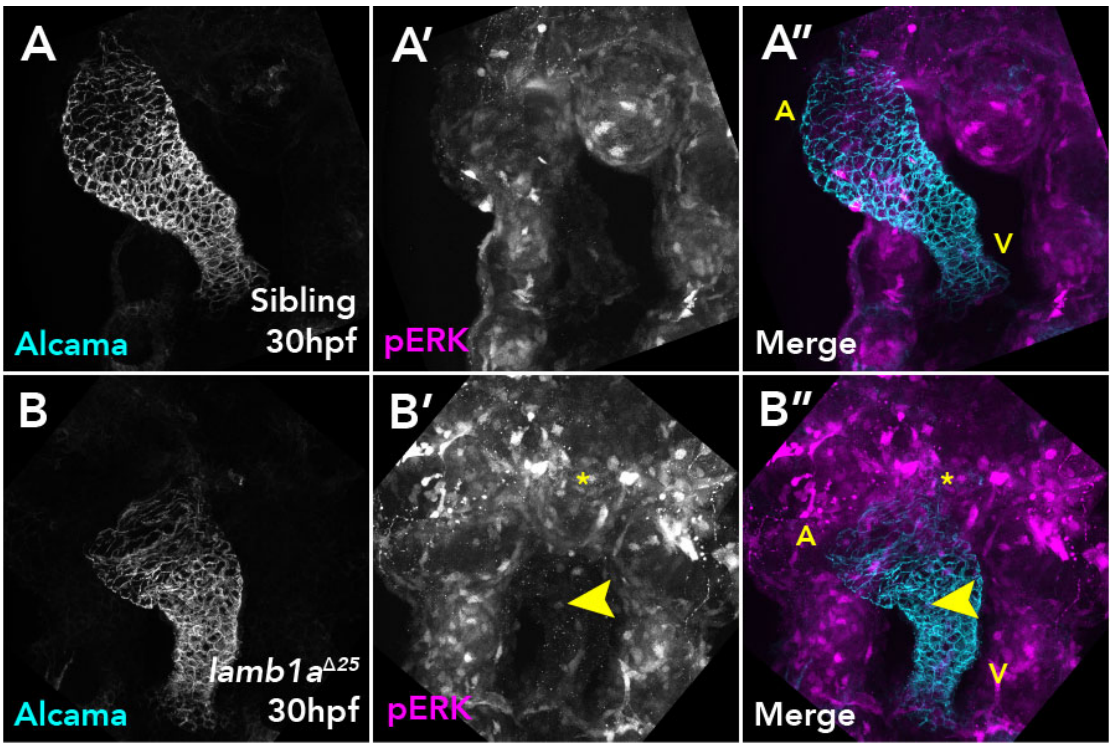

Figure 5.22. *lamb1a* mutants display an increase in pERK at 30hpf.

(A-A'') Representative maximum intensity projection confocal images of sibling heart using immunohistochemistry for the cell membrane marker Alcama (A) to mark the myocardium of the heart. pERK staining (A') is present throughout the embryo. The majority of pERK is mainly observed outside the heart tube (A''). **(B-B'')** Representative maximum intensity projection confocal images of a *lamb1a* homozygous mutant heart using the cell membrane marker Alcama (B) to mark the myocardium of the heart. pERK staining (B') is increased relative to siblings both in the heart (arrowhead) and in the tissue surrounding the heart (asterisk). The majority of pERK is mainly observed outside the heart tube, with elevated expression at the venous pole (B''). Dorsal views. V: ventricle, A: atrium. Immunohistochemistry performed by E. Noël.

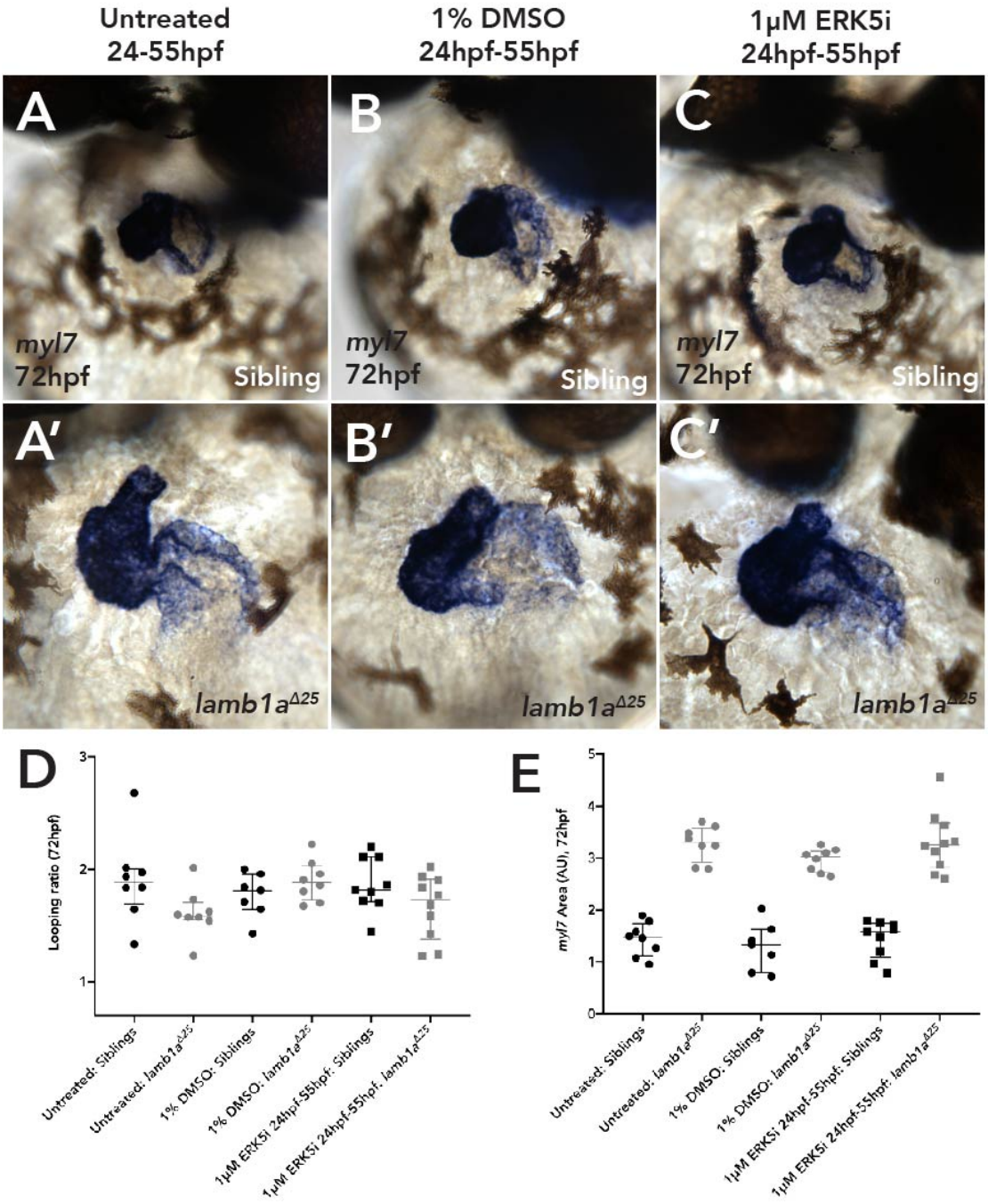

Figure 5.23. Inhibition of ERK5 activity does not rescue the *lamb1a* phenotype.

mRNA *in situ* hybridisation analysis of the effect of ERK5i treatment on heart morphology in siblings and homozygous *lamb1a* mutants. **(A-A')** Representative images of *myl7* expression in untreated sibling embryos (A) or untreated *lamb1a* homozygous mutants (A'). **(B-B')** In vehicle control treated embryos (1% DMSO) heart morphology in sibling embryos (B) or *lamb1a* homozygous mutants (B') is unaffected. **(C-C')** Inhibition of ERK5i activity between 24hpf-55hpf does not appear

In conclusion, I have defined distinct roles for Laminin complexes during heart morphogenesis (Figure 5.24). Loss of *lamb1a* does not impact on heart looping morphogenesis, but is required together with *lamc1* to limit the size of the heart. *lamb1a* mutants display a mis-regulation of flow-sensing pathways, and also display an increase in ERK activity, which provide insight as to the possible developmental mechanisms which Laminins act through during cardiac development.

5.2 Discussion

I have demonstrated for the first time that Lamb1a/Lamc1-containing Laminin trimers are required to regulate heart size during cardiac looping. While mutations in *lamb1a* have previously been isolated in forward genetic screens identifying roles in gut looping, notochord vacuolation, lens and neuronal development (Eeden et al., 1996; Hochgreb-Hägele et al., 2013; Karlstrom et al., 1996; Odenthal et al., 1996; Parsons et al., 2002; Pollard et al., 2006; Stemple et al., 1996), this is the first description of a developmental cardiac phenotype upon loss of specific Laminin subunits.

Figure 5.23 continued.

to affect heart morphology in sibling embryos (C) or *lamb1a* homozygous mutants (C'). **(D)** Quantification of heart looping ratio in sibling and *lamb1a* homozygous mutants across all treatment groups. **(E)** Quantification of *myl7* area in sibling and *lamb1a* homozygous mutants across all treatment groups. A-C': ventral views. D, E: no statistical tests performed. One experimental repeat.

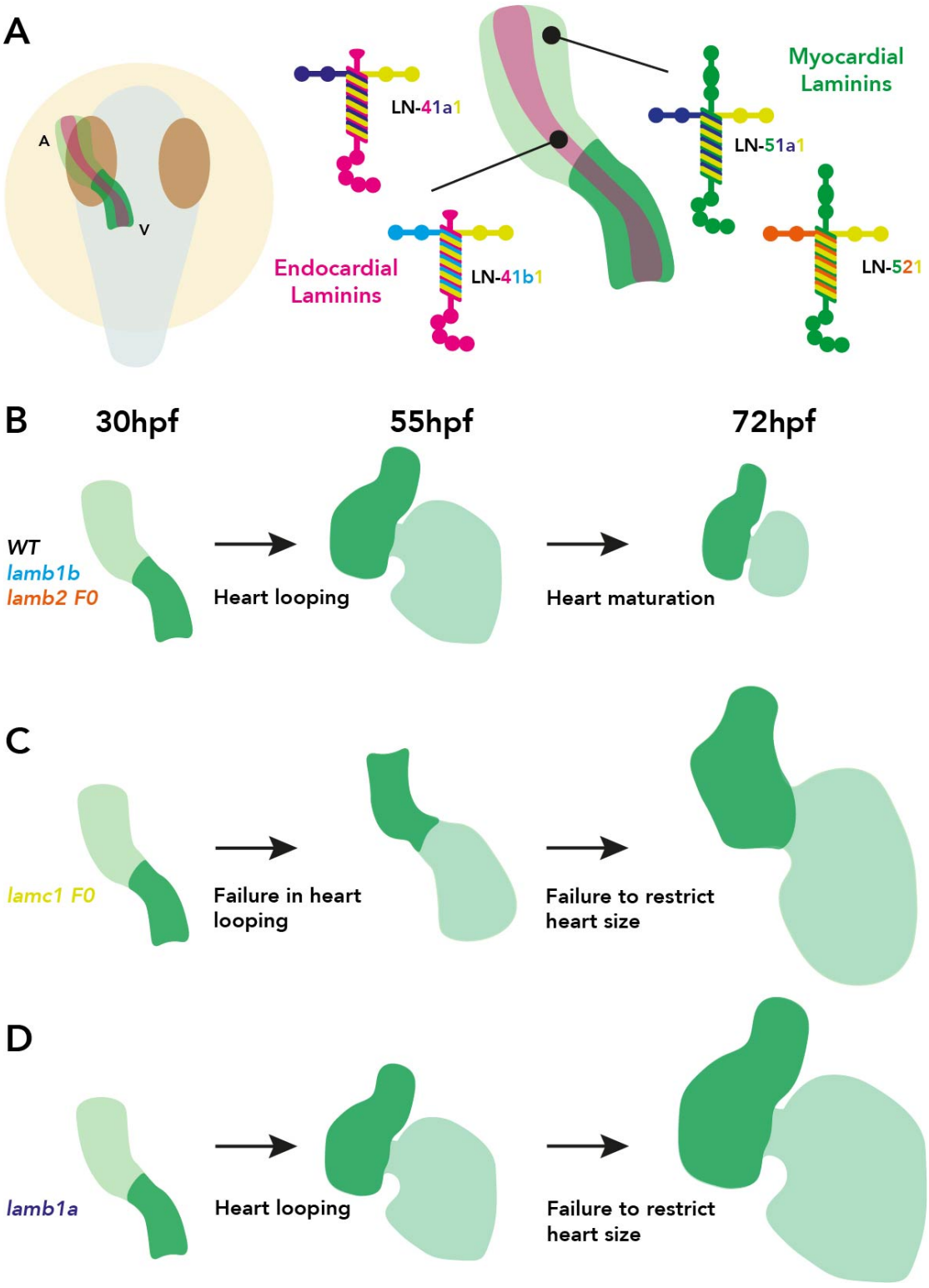

Figure 5.24. Laminins perform distinct functions during heart development.

(A) At 30hpf, six Laminin subunit genes are expressed in the zebrafish heart, suggesting that four distinct isoforms (two endocardial, magenta, two myocardial, green) may be functioning to promote heart morphogenesis. **(B)** In WT embryos,

The increase in cardiac size observed in *lamb1a* and *lamc1* mutants could result from perturbation of any one or more of the developmental mechanisms regulating heart morphogenesis. Two straightforward mechanisms underlying the enlarged heart phenotype could be increased cell size or cell proliferation in the mutants, or an additive effect of the two. This could be examined through quantification of myocardial cell number and cell size using a nuclear reporter such as *Tg(myl7:dsRed)* (Mably et al., 2003; Pater et al., 2009) and outlining cell membranes using antibodies against membrane-localised proteins such as Alcama (above). Recently cross-talk between the myocardial and endocardial tissue layers of the heart has been shown to co-ordinate myocardial chamber ballooning with endocardial proliferation through biomechanical signalling at cadherin junctions (Bornhorst et al., 2019).This suggests that examining both myocardial and endocardial cell number together with characterising the proliferative index of each tissue will help to uncover which tissue is driving the changes observed in the *lamb1a* mutant hearts. Two models could be proposed: one where the endocardium is primarily affected, resulting in increased endocardial proliferation, causing the myocardium to change shape; alternatively, myocardial proliferation is increased, with no impact on endocardial parameters. How the loss of Laminins would result in these processes

Figure 5.24 continued.

between 30hpf and 55hpf, the heart undergoes a robust, asymmetric dextral looping morphogenesis, and between 55hpf and 72hpf the heart appears to compact as it undergoes maturation. Loss of *lamb1b* or mutagenesis of *lamb2* does not affect heart development, suggesting they are dispensable. **(C)** In *lamc1* F0 mutants, heart morphology appears normal at 30hpf, whilst by 55hpf. The heart has failed to loop, and the chambers have not started ballooning. At 72hpf, heart size has not been restricted and the heart does not compact. **(D)** In *lamb1a* mutants, heart looping proceeds normally between 30hpf and 55hpf, however by 72hpf, *lamb1a* mutant hearts have significantly larger hearts than WT. A: atrium, V: ventricle.

could be either through a role for Laminins in regulating the cross-talk between the tissue layers of the heart, or through having tissue-specific roles in the development of either tissue, independent of the other. As the key time window of requirement for *lamb1a* and *lamc1* appears to be between 30hpf and 55hpf, when regionalised changes in cell shape in the chambers are observed (Auman et al., 2007; Dietrich et al., 2014), characterisation of these processes would be a suitable starting point.

lamb1a mutants exhibit an up-regulation of the flow-responsive genes *lamb1b* and *klf2a*. This suggests that alterations to blood flow sensing may underly the *lamb1a* phenotype as blood flow sensation regulates regional endocardial cell shape changes (Dietrich et al., 2014). In cultured mice endothelial cells, cadherin junctions are stabilised through integrin β1 binding to LN-511 (Russo et al., 2016). In *Lama5* mutant mouse *ex vivo* artery culture, endothelial cells fail to respond appropriately to blood flow-generated shear stress (Russo et al., 2016), resulting in a significant reduction in adhesion complexes and cortical stiffness. Interestingly, loss of *Lama4* appears to have opposing effects (Russo et al., 2016). Together with a recently identified role for cadherin tension in the regulation of cardiac ballooning (Bornhorst et al., 2019), this could suggest that loss of *lamb1a* alters the ability of endocardial cells to responds to blood flow and potentially disrupts cardiac development.

These models would predict that alterations to blood flow sensing in *lamb1a* mutants, (confirmed by blood-flow independent expression of the flow-responsive transcription factor *klf2a*) drive the increase in heart size. Yet, reduction in blood viscosity by *gata1a* knockdown does not appear to rescue heart size in *lamb1a* mutants. However, the effect of *gata1a* knockdown on *klf2a* expression in *lamb1a* mutants was not examined and although *gata1a* knockdown results in almost a total reduction in blood viscosity (Brownlie and Zon, 1999, Figure 5.20) and shear stress (Hsu et al. 2019), the effect on *klf2a* expression is reported to be less severe than knockdown of *gata2*, due to the more dramatic reduction in reversing blood flow fraction (Vermot et al., 2009). Examining the impact of this more profound alteration

to flow dynamics upon knock down of *gata2* in *lamb1a* mutants would reinforce the role of blood flow in the basis of the *lamb1a* cardiac phenotype.

Furthermore, biomechanical signals may be derived from the active pumping of the heart, independent of the sensation of blood flow as exemplified by the requirement for functional *myh7* to drive regionalised cell shape changes (Auman et al., 2007). Whilst I tested the role of heart contractility on the expression of *klf2a*, I did not quantify the effect on heart morphology. Examining the *lamb1a* cardiac phenotype at 72hpf in embryos where heart contraction is prevented (for example through injection of *tnnt2a* morpholino), although impacting on heart looping (Lombardo et al., 2019), should not affect heart size if the increase is totally independent of blood flow and other mechanical cues. Interestingly, whilst increasing blood viscosity by *epoa* mRNA injection was not able to drive an increase in heart size similar to that observed in *lamb1a* mutants, *lamb1a* heterozygotes may be sensitised to increased blood viscosity, however as *epoa* mRNA injection has been shown to lead to a mild reduction in heart rate (Hsu et al., 2019), influences of mechanical stimuli cannot be ruled out. Whether increasing blood viscosity in *lamb1a* mutants is able to further increase heart size may help to understand whether increased flow sensitivity is causative of the *lamb1a* mutant phenotype or rather a non-consequential effect of loss of *lamb1a*. In addition, loss of *lamb1a* may result in an increase in blood viscosity, resulting in an increase in heart size and thus knockdown of *gata1a* in *lamb1a* mutants may not be penetrant enough to rescue the phenotype. Therefore, it is important that blood flow and blood viscosity should be characterised in *lamb1a* mutants. However, if blood content were increased in *lamb1a* mutants, this may suggest that as increased blood content in a WT setting is not sufficient to fully recapitulate the increased heart size, Laminin deposition could limit the responsiveness to blood flow (Russo et al., 2016), a possibility raised by the mild increase in heart size in *epoa* mRNA-injected *lamb1a* heterozygotes.

A promising avenue of investigation downstream of integrins and suggested by blood flow-independent *klf2a* expression is the well characterised MEKK3-MEK5-ERK5 pathway, shown to be hyperactive in the family of mutants affecting the Ccm proteins (Otten et al., 2018; Zhou et al., 2016, 2015). Similar to *lamb1a* mutants, *ccm* mutants also display enlarged hearts (Mably et al., 2006, 2003; Otten et al., 2018; Zhou et al., 2016, 2015) due to failure of restriction of MEKK3 activity. Independent studies in both zebrafish and mice have demonstrated that inhibition of MEK5 (Zhou et al., 2015) or ERK5 (Otten et al., 2018) can partially alleviate the *CCM* mutant phenotype. *lamb1a* mutants display an increase in pERK staining at 30hpf (Figure 5.22), however preliminary results suggest that inhibition of ERK5 between 24hpf and 55hpf is unable to rescue the *lamb1a* cardiac phenotype. Whilst action of the drug was not confirmed, this suggests that either the timing of increased ERK5 activity driving heart growth in *lamb1a* mutants is outside of the treatment window used here or that ERK5 activity is not responsible for the enlarged hearts and that this pathway of *klf2a* flow independent up-regulation is not functioning in *lamb1a* mutants.

Including ERK5, at least 4 classes of ERK pathways have been described (McCain, 2013) and previous analysis of heart development in mouse mutants for *Fibronectin* (*FN*) and its receptor *Itga5* have identified a link between ERK signalling and the extracellular matrix (Mittal et al., 2013). Both *FN* and *Itga5* mutants exhibit a reduction in second heart field addition (Mittal et al., 2013) due to a failure in sensitisation of cells to FGF8 signalling, a ligand with a highly conserved role in promoting second heat field addition in mice, fish and chick (Hami et al., 2011; Ilagan et al., 2006; Lazic and Scott, 2011; Park et al., 2008; Pater et al., 2009; Reifers et al., 2000). *lamb1a* mutants display increased levels of phospho-ERK staining both within the heart and surrounding the heart tube where the second heart field resides. Therefore, another possible mechanism underlying the increased cardiac size in *lamb1a* mutants may be an increase in sensitivity to pro-additive signals such as FGF8, resulting in increased pERK, increased addition from the second heart field

and enlarged hearts. Examining markers of second heart progenitors such as *ltbp3* (Zhou et al., 2011) and downstream readouts of FGF signalling such as *sprouty homolog 4 (Drosophila) (sprouty4)* (Pater et al., 2009) should be carried out at classical timepoints of SHF addition as well as within the critical window of 55hpf to 72hpf. Together with developmental timing assays to quantify differences in SHF addition (Pater et al., 2009) together this would help define whether this mechanism could be responsible for increased heart size in *lamb1a* mutants, and would support a role for Laminins in regulation SHF addition (See Chapter 8).

In addition to the increase in heart size identical to *lamb1a*, mutations in *lamc1* result in a significant reduction in heart looping morphogenesis not found in *lamb1a* mutants (Figure 5.24C), suggesting that specific Laminin isoforms regulate distinct processes of heart development. Since *lamb2* is the only beta subunit I have identified to be expressed in the heart during looping morphogenesis (Figure 3.2, 3.3, 5.24A), the absence of a heart looping phenotype in *lamb1a* mutants strongly suggested that Lamb2-Lamc1 containing trimers function to promote heart looping morphogenesis. However, *lamb2* F0 mutants do not recapitulate the looping phenotype observed in *lamc1* F0 mutants, (Figure 5.16, 5.17) suggesting that a different Laminin beta subunit functions together with Lamc1. Supporting the notion of no role for *lamb2* in heart development upto 72hpf is the absence of any described heart phenotype in the *softy* (*lamb2*) mutant (Jacoby et al., 2009), however as the heart phenotypes described here have previously been overlooked, a more detailed description of the *lamb2* cardiac phenotype may be required. As none of the beta subunit knockouts generated here recapitulate the *lamc1* heart looping defect, this suggests that an alternative beta subunit may promote heart looping morphogenesis. However, I have not identified another beta subunit expressed in the heart (and at earlier developmental stages no additional beta subunits have been found to be expressed in the heart disc itself, Farah Hussein, personal communication).

The absence of a *lamb2* F0 cardiac phenotype could suggest that the function of *lamc1* in promoting looping morphogenesis may be non-autonomous to heart tube. Supporting this hypothesis, expression of both *lamb1a* and *lamc1* are very broad at 30hpf, and their expression overlaps in the region of the embryo where the SHF is located (Figure 3.2). This may suggest that *lamc1* is required to regulate the environment surrounding the heart as it undergoes morphogenesis. Multiple approaches could be taken to test this hypothesis for example using tissue-specific constructs driving *lamc1* expression either under the *myl7* (myocardial) or *fli1a* (endocardial) promoter to determine whether reinstating *lamc1* in the heart tube myocardium or endocardium of *lamc1* mutants can rescue heart looping morphogenesis. However, this would need to be performed in stable *lamc1* mutants (Kettleborough et al., 2013; Parsons et al., 2002; Stemple et al., 1996) to avoid targeting of the rescue construct by *lamc1* gRNAs. Another approach would be tissue-specific CRISPRi of *lamc1*, using *myl7* or *fli1a* promoters to drive dCas9 expression, knocking down *lamc1* expression only in the heart tube or endothelium respectively, and analysing whether this can recapitulate the *lamc1* F0 heart looping defects. However, as discussed in Chapter 4, significant optimisation of the gRNA sequence may be required, although the high level of efficiency displayed by the *lamc1* gRNAs reflects a promising starting point.

In order to better understand the mechanisms by which Laminins drive heart looping morphogenesis and restrict growth of the heart, it will be important to define which tissue the Lamb1a-Lamc1 containing trimers are secreted from, as both *lamb1a* and *lamc1* are expressed in the myocardium and endocardium. While *lamb1a* and *lamc1* are expressed in both the myocardium and endocardium, *lama5* and *lama4* display tissue-restricted expression in the myocardium and endocardium respectively, suggesting that either Laminin-511 or Laminin-411 is required to limit heart size, or possibly both isoforms are necessary. Mutagenesis of *lama4* or *lama5* will be invaluable in dissecting the exact Laminin isoform restricting heart size.

Although no role for Laminins in has previously been identified in the regulating size and shape of the vertebrate heart, Laminins have been shown to play an important role in cardiac function. *Lama4* mutant mice have been characterised to survive post-partum but have enlarged hearts, linked to hypoxia-related cardiomyopathy at 16-20 weeks (Wang et al., 2005). Cardiomyopathy is also observed in *lama4* morphant zebrafish and human patients with *LAMA4* mutations (Knoll et al., 2007). Whilst these phenotypes are highly comparable, for both humans and mice, they are late onset. However, subtly affecting heart size during early development may be sufficient to result in pathogenic changes due to increased pre-load or afterload due to increased heart size (Auman et al., 2007).

Zebrafish *lama5* mutants have been isolated from genetic screens for genes implicated in fin bud formation (Carney et al., 2010) but no heart phenotype has been described, however mutations in human *LAMA5* have been reported to result in mitral valve defects (Sampaolo et al., 2017). Together this demonstrates potentially conserved roles for multiple Laminins in distinct aspects of heart form and function. Whilst these roles are mostly related to cardiac function, it is interesting to speculate that these functional defects may be due to subtle changes in the morphology of the developing heart such as increases in size and/or abnormal looping morphogenesis. This highlights the need for a better understanding of the effect Laminin knockouts on heart morphology and function. Zebrafish are the ideal model to investigate these questions as experiments can achieved *in vivo* to make links between form, function and the role that Laminin plays in promoting heart development.

In summary, I have identified a novel, previously uncharacterised phenotype associated with the loss of *lamb1a* during heart morphogenesis. Together with data highlighting the need for *lamc1* to promote heart morphogenesis I have defined two distinct roles for Laminins during heart development in zebrafish: promoting robust morphogenesis of the linear heart tube and restriction of cardiac size.

6. The cardiac jelly displays regional asymmetry during heart development

Heart looping morphogenesis is an asymmetric, tissue intrinsic process, occurring independently of the extrinsic laterality cues of the embryo. The cardiac jelly is a reservoir of signalling molecules and structural proteins, loss of which results in failure in this asymmetric morphogenesis. However, these ECM components are broadly considered to be uniformly expressed, and therefore how a seemingly homogeneous ECM could promote an asymmetric process is unclear. As the ECM represents a key intrinsic factor in promoting heart development, I set out to examine whether the cardiac jelly shows regional differences during heart development and whether this regionalisation is a contributing factor in promoting asymmetric heart morphogenesis.

Using live *in vivo* imaging of the embryonic heart tube in the zebrafish I identify a previously uncharacterised asymmetric expansion of the ECM at the onset of heart looping. I show that the cardiac jelly contains Hyaluronic Acid (HA) and describe expression patterns of known interacting partners of HA. However, none of these previously implicated genes have expression which correlates with the observed ECM asymmetry. Subsequently, I describe the identification of *hyaluronan and proteoglycan link protein 1a* (*hapln1a*), a candidate gene for regulating asymmetric cardiac jelly expansion. I show that *hapln1a* expression overlaps with cardiac ECM expansion and that the regionalisation of *hapln1a* is important for promoting heart looping morphogenesis. Finally, I show that *hapln1a* expression is independent of extrinsic laterality cues, and propose that ECM expansion is part of the tissue intrinsic mechanism which drives heart tube morphogenesis.

6.1 Results

6.1.1 Light sheet microscopy identifies regional differences in ECM thickness in the developing heart

The advancement of microscopy to facilitate live imaging not only allows for preservation of morphology of cell shape, but also the ECM. To enable visualisation of the cardiac jelly in the zebrafish heart, the hearts of double transgenic embryos harbouring the myocardial marker *Tg(myl7:lifeActGFP)* and endothelial marker *Tg(fli1a:AC-TagRFP)* were imaged using live light-sheet microscopy. Since the cardiac jelly lies between the myocardium and endocardium of the developing heart, the absence of fluorescent signal between the two transgenes denotes the cardiac ECM. An optical cross-section through the ventricle at 50hpf (Figure 6.1A) highlights the two tissue layers are in close proximity, with little or no ECM visible (Figure 6.1B'', C'').

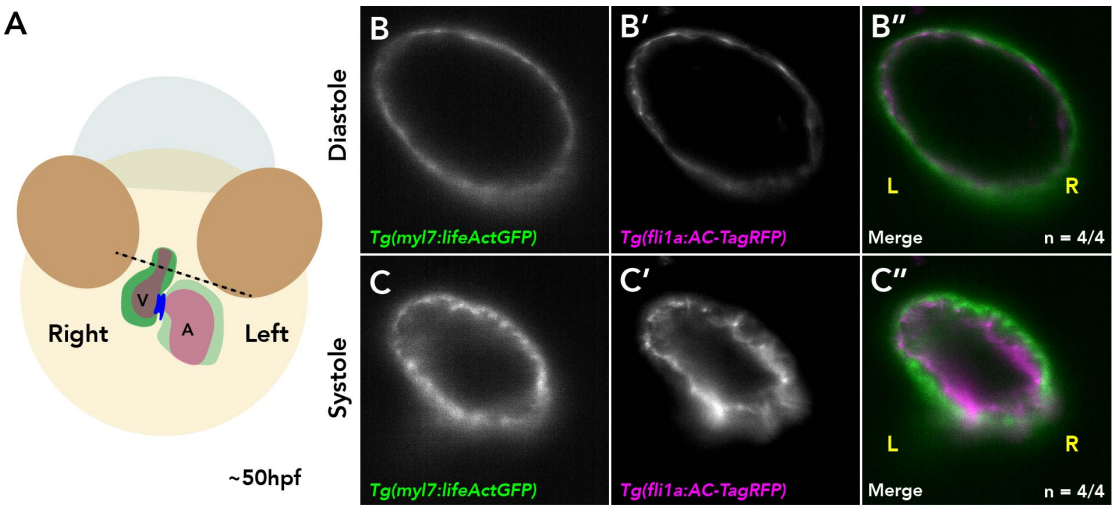

Figure 6.1. Ventricular ECM is thin and uniformly distributed in the looped heart.

(A) Schematic of 50hpf zebrafish embryo, dotted line denotes approximate transverse section taken for imaging the ventricle. **(B,C)** *Tg(myl7:lifeActGFP)* marks the myocardium. **(B′,C′)** *Tg(fli1a:AC-TagRFP)* marks the endocardium. **(B′′)** Merge of (B-B′) highlight the two tissue layers of the ventricle in diastole. **(C′′)** Merge of (C-C′) highlights the two tissue layers of the ventricle in systole. The absence of fluorescent signal between the two tissue layers denotes the cardiac jelly. A: ventral view. B-C′′: cranial view. L: left. R: right.

To aid orientation of the heart during imaging of atrial tissue, two additional transgenic constructs labelling *lefty2* (*lft2*)-positive cells - *Tg(lft2BAC:GalFF; UAS:RFP)* (Derrick et al., 2019) - were used to mark the dorsal myocardium which is derived from the left side of the heart disc (Smith et al., 2008). Imaging optical cross-sections of the atrium at 50hpf (Figure 6.2A) reveals that the atrial ECM is generally thicker than that of the ventricle, and in addition there is a difference in ECM thickness between the left and right sides of the atrium during both diastole (Figure 6.2B′′) and systole (Figure 6.2C′′). To quantify differences in ECM thickness the expression profile of *lft2* was used to orient the dorsal-ventral and thus left-right axis of the heart, and the thickness of the cardiac jelly was then measured on both left and right sides of the atrium at five different systoles and diastoles for a single

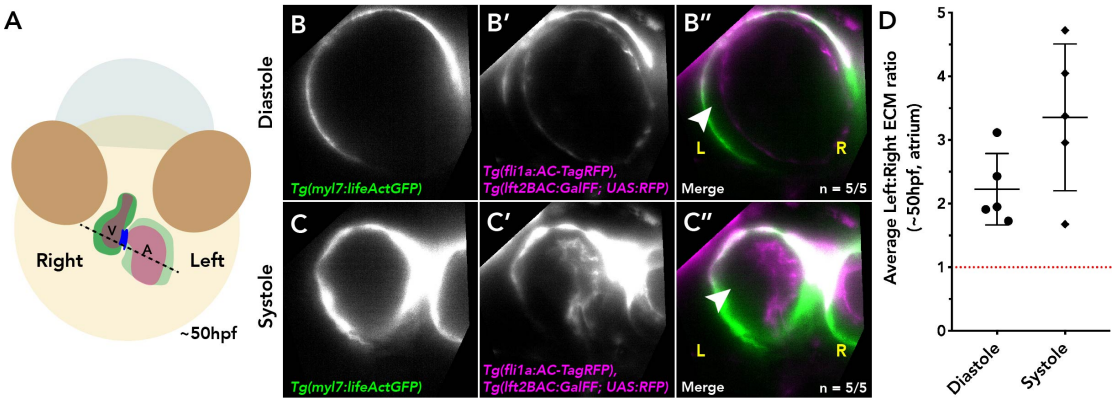

Figure 6.2. The atrium displays regional differences in cardiac jelly thickness following heart looping morphogenesis.

(A) Schematic of 50hpf zebrafish embryo, dotted line denotes approximate transverse section taken for imaging the atrium. **(B,C)** *Tg(myl7:lifeActGFP)* marks the myocardium. **(B′,C′)** *Tg(fli1a:AC-TagRFP)* marks the endocardium (inner signal), *Tg(lft2BAC:GalFF; UAS:RFP)* marks the dorsal myocardium (outer, brighter signal). **(B′′)** Merge of (B-B′) highlight the two tissue layers of the atrium in diastole Arrowhead marks the left-sided expansion of the non-fluorescent space, marking the cardiac jelly. **(C′′)** Merge of (C-C′) highlights the two tissue layers of the atrial in systole. Arrowhead marks the left-sided expansion of the non-fluorescent space, marking the cardiac jelly. **(D)** Quantification of the average Left:Right ECM ratio in the atrium at 50hpf in both diastole and systole. A value great than one (red line) denotes a left-sided expansion of the atrial cardiac jelly. Each data point represents the average of five separate contraction cycles from one embryo. A: ventral view. B-C′′: cranial view. D: Arithmetic Mean with standard deviation. L: left. R: right.

embryo. A ratio of left/right ECM thickness was calculated at each time point and averaged for a single embryo, where a ratio greater than 1 (Figure 6.2D, red line) represents a left-sided thickening of the ECM. This method objectively confirms a left-sided expansion of the ECM in the atrium in the looped heart, with a greater difference apparent during atrial systole (Figure 6.2C′′).

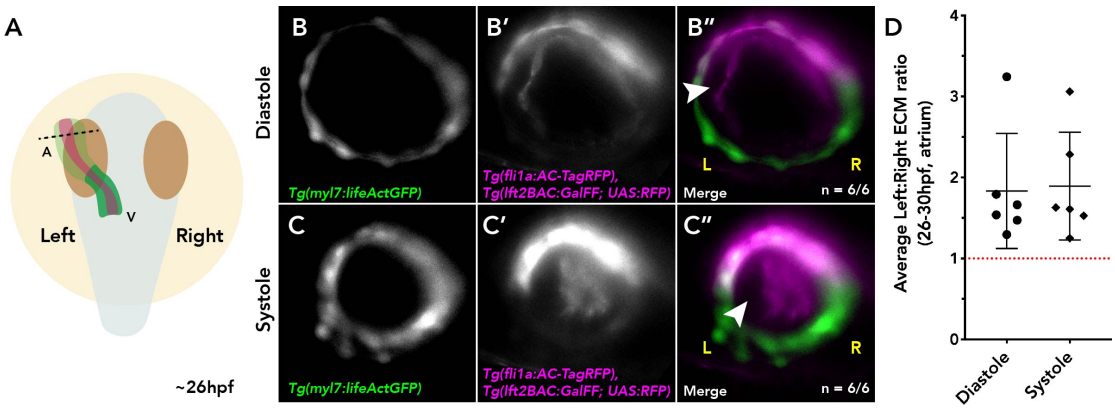

Figure 6.3. The cardiac jelly is asymmetrically expanded at the venous pole prior to heart looping morphogenesis.

(A) Schematic of 26hpf zebrafish embryo, dotted line denotes approximate position of the transverse section used for imaging the atrium. **(B,C)** *Tg(myl7:lifeActGFP)* marks the myocardium. **(B′,C′)** *Tg(fli1a:AC-TagRFP)* marks the endocardium (inner signal), *Tg(lft2BAC:GalFF; UAS:RFP)* marks the dorsal myocardium (outer, brighter signal). **(B′′)** Merge of (B-B′), highlighting two tissue layers with of the atrium in diastole, dorsal myocardium top. **(C′′)** Merge of (C-C′), highlighting two tissue layers with of the atrium in systole, dorsal myocardium top, arrowhead marks the left-sided expansion of the non-fluorescent space, marking the cardiac jelly. **(D)** Quantification of the average Left:Right ECM ratio in the atrium at 26hpf in both diastole and systole. A value great than one (red line) denotes a left-sided expansion of the atrial cardiac jelly. Each data point represents the average of five separate contraction cycles from one embryo. A: dorsal view. B-C′′: cranial view. D: Arithmetic Mean with standard deviation. L: left. R: right.

To establish whether ECM asymmetry is present prior to heart morphogenesis, the venous pole/atrium of the heart tube in *Tg(myl7:lifeActGFP)*; *Tg(fli1a:AC-TagRFP)*; *Tg(lft2BAC:GalFF; UAS:RFP)* quadruple transgenic embryos was imaged at 26hpf (Figure 6.3A). A noticeably thicker ECM appeared to be present on the left side of the heart tube when compared to the right at 26hpf (Figure 6.3B-C′′), which was confirmed by quantification of left/right ECM ratio (Figure 6.3D).

Together, live, *in vivo*, light-sheet imaging of the zebrafish heart at 50hpf identifies different thicknesses of the cardiac jelly between the ventricle and atrium. Interestingly, this left-right ECM asymmetry is established prior to the onset of looping morphogenesis, suggesting it may help to promote cardiac morphology during development.

6.1.2 The cardiac jelly is rich in the glycosaminoglycan Hyaluronan

Whilst multiple studies have examined the composition of the cardiac jelly in adult hearts, particularly focussing on regeneration studies, a relatively limited description of the composition of the embryonic ECM exists. However, one key molecule present in the embryonic cardiac jelly is the glycosaminoglycan Hyaluronic Acid (Hyaluronan, Hyaluronate, HA) (Camenisch et al., 2000; Grassini et al., 2018; Lagendijk et al., 2011). Loss of HA results in a uniformly thin cardiac jelly in the mouse (Camenisch et al., 2000), suggesting that HA and its interacting partners represent suitable candidates which could be responsible for the regionalisation of the cardiac ECM.

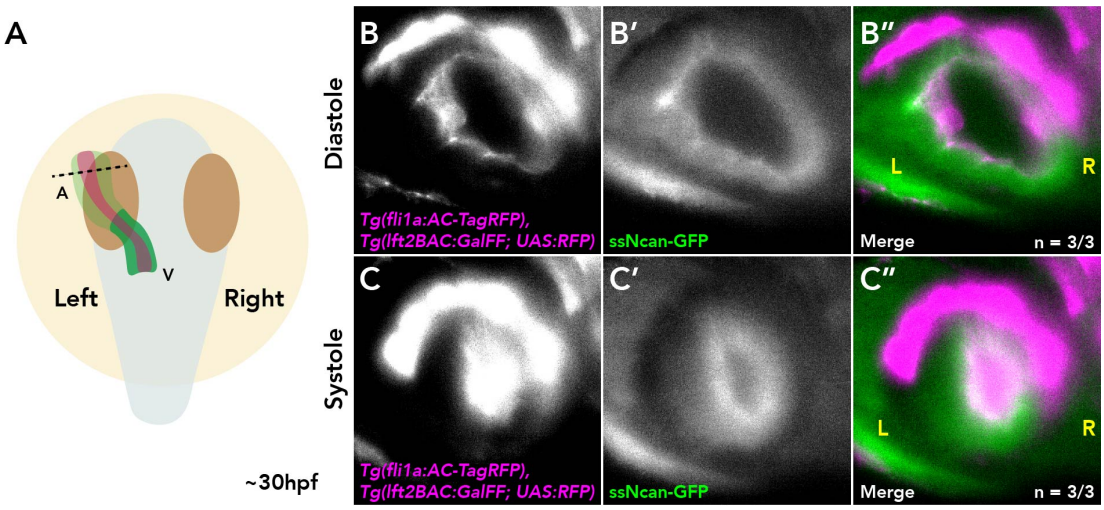

Figure 6.4. Hyaluronic Acid is not asymmetrically deposited into the cardiac jelly.

(A) Schematic of 26hpf zebrafish embryo, dotted line denotes approximate transverse section taken for imaging the atrium. **(B,C)** *Tg(fli1a:AC-TagRFP)* marks the endocardium (inner signal), *Tg(lft2BAC:GalFF; UAS:RFP)* marks the dorsal myocardium (outer, brighter signal). **(B',C')** ssNcan-GFP, a biosensor for Hyaluronic Acid. **(B'')** Merge of (B-B') shows that ssNcan-GFP reported displays uniform intensity throughout the cardiac jelly, with increased signal in the endocardium in atrial diastole. **(C'')** Merge of (C-C') shows that ssNcan-GFP reported displays uniform intensity throughout the cardiac jelly, with increased signal in the endocardium in atrial systole. A: dorsal view. B-C'': cranial view.

To investigate whether the ECM of the linear heart tube contains regionalised HA, mRNA encoding the HA biosensor *ssNcan-GFP*, comprising the HA-binding domain of mouse Neurocan (Ncan) fused to GFP and tagged with a secretion signal (Grassini et al., 2018), was injected into 1-cell stage embryos expressing *Tg(fli1a:AC-TagRFP); Tg(lft2BAC:GALFF; UAS:RFP)* transgenes (Figure 6.4). The hearts of *ssNcan-GFP* mRNA-injected embryos were live-imaged at 28hpf using light sheet microscopy and optical cross-sections of the atrium demonstrated for the first time that prior to heart looping the cardiac jelly is rich in HA (Figure 6.4B-C''). Furthermore, levels of the HA sensor do not appear to exhibit left-right differences in the heart tube (Figure 6.4B'', C''), suggesting that the cardiac ECM has a uniform distribution of HA and that asymmetric deposition of HA is unlikely to be responsible for regionalised

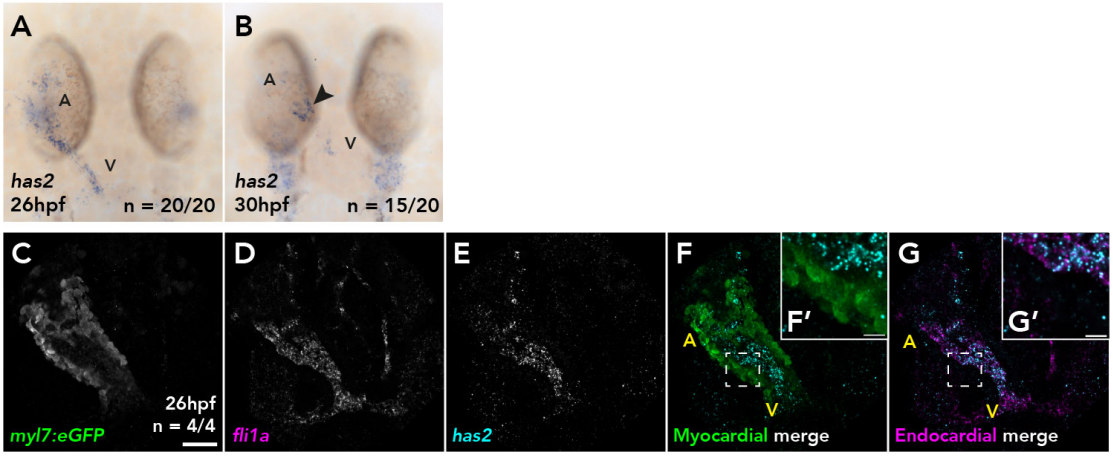

Figure 6.5. Endocardial *has2* is not asymmetrically expressed the heart tube.

mRNA *in situ* hybridisation and immunohistochemistry to identify domain and tissue of expression of *has2* at 26hpf and 30hpf. **(A)** At 26hpf, *has2* expression is uniform throughout the linear heart tube. **(B)** *has2* expression is restricted to the presumptive atrioventricular canal by 30hpf (arrowhead), expression is also apparent in the bilaterally located otic vesicles. **(C)** Anti-GFP antibody marking the myocardial transgene *Tg(myl7:eGFP)*. **(D)** mRNA *in situ* hybridisation of the endothelial marker *fli1a*. **(D)** mRNA in situ hybridisation of *has2*. **(F-F')** Merge of myocardium (green) and *has2* (cyan) expression demonstrating that *has2* and *myl7* expression do not co-localise (inset, E'). **(G-G')** Merge of endocardium (magenta) and *has2* (cyan) expression demonstrating that *has2* and *fli1a* expression overlap (inset, F'). Dorsal views. V: ventricle. A: atrium. Scale bars C: 50μm. F', G': 10μm.

ECM expansion.

6.1.3 Previously identified proteoglycan-related genes not exhibit left-right asymmetric expression in the heart tube

The use of the HA sensor demonstrates that the cardiac jelly contains HA (Figure 6.4) and suggests that it is not asymmetric HA synthesis that drives the asymmetry. ISH analysis of the major cardiac HA synthesising enzyme *has2* shows that *has2* is not asymmetrically expressed in the endocardium at 26hpf (Figure 6.5A, C-G') and that by 30hpf expression is restricted to the forming atrioventricular canal (Figure

6.5B), suggesting that by 30hpf the role of *has2* is to generate the ECM necessary for valvulogenesis. Together this further supports the hypothesis that asymmetric HA synthesis in the heart tube is unlikely to play a role in generating the left-sided ECM expansion.

Following synthesis and secretion, HA can interact with a variety of Proteoglycan units containing different core proteins and Glycosaminoglycans such as Chondroitin Sulfate or Heparan Sulfate (Pomin and Mulloy, 2018). Asymmetric expression of these genes could promote ECM regionalisation during and to examine this, expression patterns in the heart tube were analysed by mRNA *in situ* hybridisation. Chondroitin Sulfate, synthesised by *chsy1* has been shown to be present in the cardiac jelly where it is thought to be required for valve development (Peal et al., 2009). However, little or no expression of *chsy1* is observed specifically in the heart at 26hpf or 30hpf (Figure 6.6A-A'), suggesting asymmetric deposition of CS is not responsible for asymmetric ECM expansion.

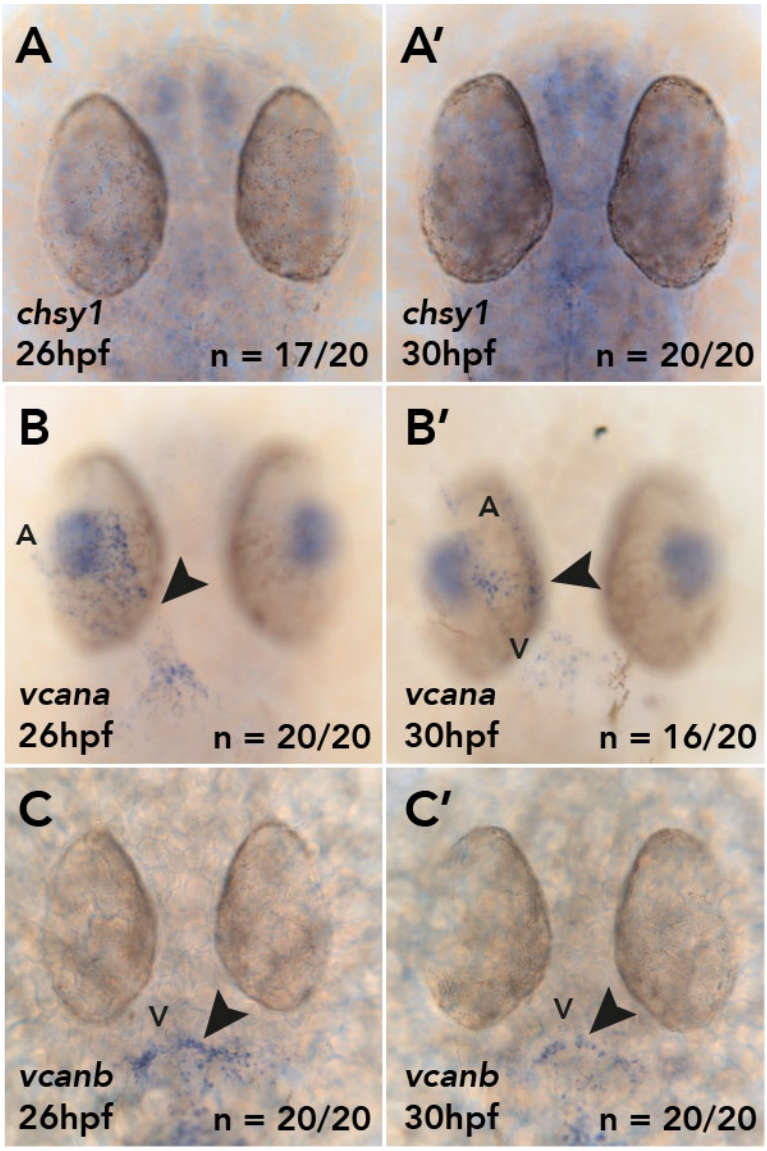

Figure 6.6. Chondroitin Sulfate Proteoglycans exhibit dynamic and complementary expression patterns during early heart morphogenesis.

mRNA *in situ* hybridisation analysis of *chsy1*, *vcana* and *vcanb* at 26hpf and 30hpf. **(A-A')** *chsy1* expression shows no spatial restriction at either 26hpf (A), or 30hpf (A'). **(B)** At 26hpf *vcana* is expressed throughout the heart tube but is excluded at the presumptive atrioventricular canal (arrowhead). **(B')** At 30hpf, *vcana* expression is reduced, but with a low level of expression at the presumptive atrioventricular canal (arrowhead). No lateralised expression is observed at either 26hpf (B) or 30hpf (B'). **(C-C')** Between 26hpf and 30hpf *vcanb* expression is excluded from the heart tube, but is present at the arterial pole of the heart (C-C' arrowhead). Expression is slightly down-regulated by 30hpf (C'). Dorsal views. V: ventricle, A: atrium.

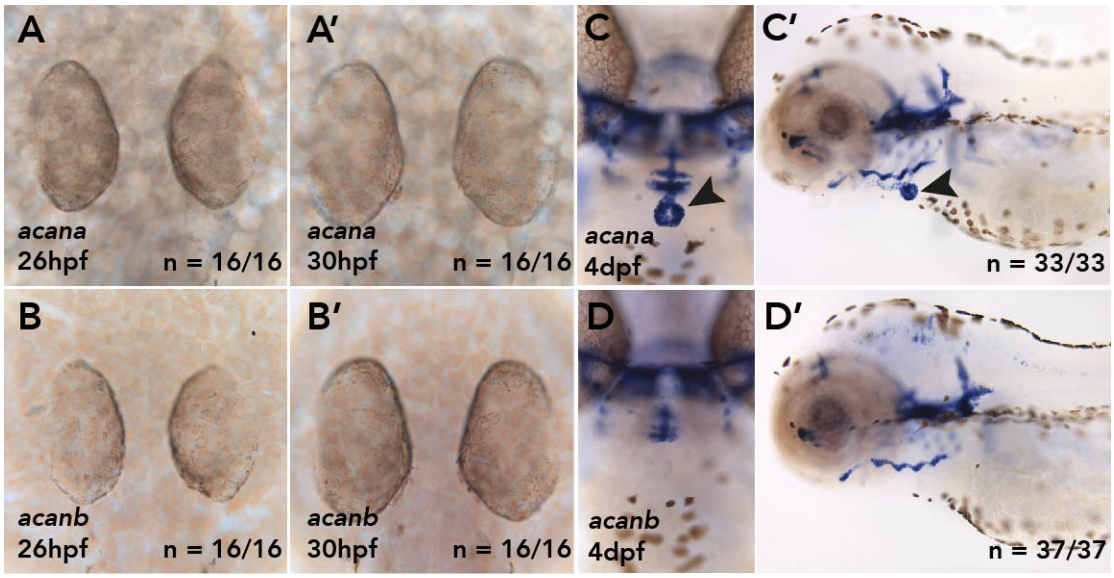

Figure 6.7. *acana* and *acanb* are expressed in the heart post-looping.

mRNA *in situ* hybridisation analysis of *acana* and *acanb* at 26hpf, 30hpf and 4dpf. **(A-B')** *acana* and *acanb* expression is absent from the linear heart at 26hpf (A, B) and 30hpf (A', B'). **(C-C')** At 4dpf, *acana* is expressed in the aortic arches and other structures inducing the presumptive bulbous arteriosus (arrowhead). **(D-D')** At 4dpf, *acanb* is expressed in a similar domain to *acana* (C-C') but expression is absent from the heart. A-B': dorsal views. C, D: ventral views. C', D': lateral views.

Versican (a Chondroitin Sulfate Proteoglycan) has been previously implicated in heart development, although primarily at later stages in valve development in zebrafish, but more recently for both heart looping and SHF addition in medaka (Mittal et al., 2019; Patra et al., 2011). Zebrafish have two paralogous *versican* genes, predicted to have divided the labour of the single human and mouse *Versican* gene (Kang et al., 2004). At 26hpf, *vcana* (*versican a*) is expressed in the heart tube, but is not lateralised, and appears to be excluded from the developing AVC (Figure 6.6B). By 30hpf *vcana* expression is lost from working myocardium but is weakly expressed at the future AVC (Figure 6.6B'), in a domain hypothesised to overlap with *has2* expression (Figure 6.5B). *vcanb* (*versican b*) is not expressed in the heart tube at either 26hpf or 30hpf (Figure 6.6C-C'), however a robust and persistent

expression is present at the arterial pole (Figure 6.6C, C') where cardiomyocytes are migrating into the heart from the second heart field (Pater et al., 2009).

Another core protein Aggrecan is commonly associated with cartilage (Aspberg, 2012; Roughley and Mort, 2014), however an early study identified Aggrecan expression in the chick heart during maturation (Zanin et al., 1999) and more recently work investigating the function of zebrafish *aggrecan a* has implicated Aggrecan in the disease pathology of Bicuspid Aortic Valve (Rambeau et al., 2017). *in situ* hybridisation expression analysis of the zebrafish *aggrecan* genes *acana* and *acanb* show no detectable expression in the heart at 26hpf or 30hpf (Figure 6.7A-B'). However, both *aggrecan* genes are expressed at 4dpf, particularly in the developing aortic arches (Figure 6.7C', D'), and *acana* is strongly expressed in the bulbus arterious (Figure 6.7C, C') as previously reported (Rambeau et al., 2017). Together, these data show that core proteins and Proteoglycan components previously implicated in heart development do not exhibit expression which overlaps with the observed asymmetric expansion of the cardiac jelly prior to heart looping. This supports the theory that asymmetric synthesis of any previously identified ECM components does not drive cardiac ECM asymmetry.

6.1.4 Expression of *hyaluronan and proteoglycan link protein 1a* (*hapln1a*) overlaps with observed ECM expansion

Having identified no asymmetric expression of previously implicated ECM components during heart looping, to identify candidate genes which could drive ECM expansion during early heart development, the Tomo-Seq dataset was examined for atrial-enriched genes (where the ECM expansion is observed) annotated as ECM synthesis, degradation or interacting proteins (Derrick et al., 2019). This approach identified *hyaluronan and proteoglycan link protein 1a* (*hapln1a*) as a candidate gene for ECM expansion. Hapln1a is a member of the link protein family, functioning to link HA with Proteoglycans such as Versican (Aspberg,

2012; Spicer et al., 2003), and the mouse homolog, *Hapln1* (formerly *Crtl1*) has previously been implicated in heart development (Wirrig et al., 2007). Together this suggested *hapln1a* as a candidate gene for ECM expansion.

mRNA *in situ* hybridisation analysis at 26hpf revealed *hapln1a* expression is highly regionalised in the heart, and overlaps with the domains of regionalised ECM expansion. At 26hpf, *hapln1a* expression is elevated with a broader domain of expression on the left side of the heart tube compared to the right. Futhermore, *hapln1a* is expressed in the atrium, with no observable signal in the ventricle (Figure 6.8A). *hapln1a* expression in the heart tube appears to be transient, as whilst the left-sided, atrial elevated expression is maintained, overall levels of expression are reduced at 30hpf (Figure 6.8A'). Together, the expression pattern of *hapln1a* strongly suggests that Hapln1a is responsible for the cardiac ECM asymmetry.

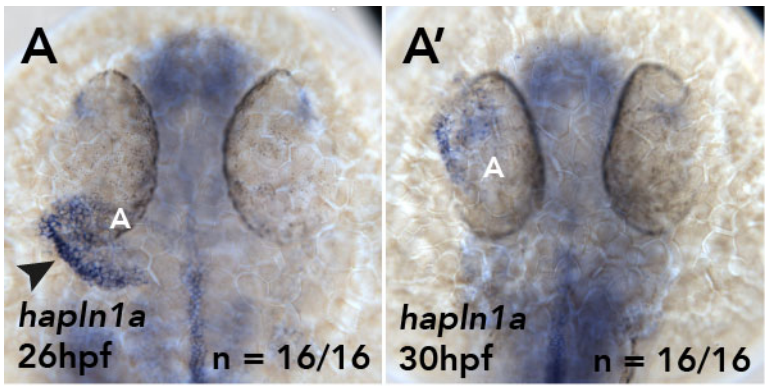

Figure 6.8. *hapln1a* expression overlaps observed ECM expansion prior to heart looping.

mRNA *in situ* hybridisation analysis of *hapln1a* at 26hpf and 30hpf. **(A)** At 26hpf, *hapln1a* expression is elevated on the left of the heart tube, with a broader domain of expression than the right (arrowhead). Expression is restricted mainly to atrial tissue. **(A')** Expression of *hapln1a* at 30hpf is reduced in the heart. Left sided up-regulation, together with a broader domain of expression than the right, is observed in the atrium, with little or no expression in the ventricle. Dorsal views. A: atrium.

The expression patterns of *has2* and *vcana* are highly dynamic during heart looping, in particular the restriction of *has2* expression between 26hpf and 30hpf suggests that at this stage HA synthesis is required for valve formation and not looping morphogenesis. As a result, ECM synthesis, asymmetric expression of *hapln1a*, and its interaction with other Proteoglycans may be required prior to heart tube morphogenesis for subsequent heart looping. Furthermore, as cells positioned on the left side of the heart arise from the posterior compartment of the cardiac disc during heart tube formation (Guerra et al., 2018; Smith et al., 2008), the expression pattern of *hapln1a* suggested that cardiac proteoglycan genes (which represent candidate interacting partners for Hapln1a) were also likely to be expressed prior to tube formation.

ISH analysis at 21hpf confirms previously identified *has2* expression in the cardiac cone (Figure 6.9A) (Smith et al., 2008; Veerkamp et al., 2013) and identifies that *chsy1* expression in the heart is highly dynamic, with clear expression only observable prior to tube formation (Figure 6.9B). Both *versican* genes are expressed in the heart cone; *vcana* is expressed in the myocardium (Figure 6.9C) and more broadly than *vcanb* (Figure 6.9C). In line with absence of expression in the heart tube and confirming a later role in heart development for *acana*, no expression of either *aggrecan* gene is observed in the cardiac cone at 21hpf (Figure 6.9E, F). Similar to expression of *meis2b* (*Meis homeobox 2b*) (Guerra et al., 2018), *hapln1a* is primarily expressed in the posterior of the cardiac cone (Figure 6.9G, black arrowhead), with some expression in the anterior cone (Figure 6.9G, green arrowhead). Together, this suggests that regionalised *hapln1a* expression is initiated from at least 21hpf in the posterior cardiac disc, becomes repositioned on the left-side of the heart tube, and may interact with VersicanA Proteoglycan and HA to generate an expanded cardiac jelly in the heart tube.

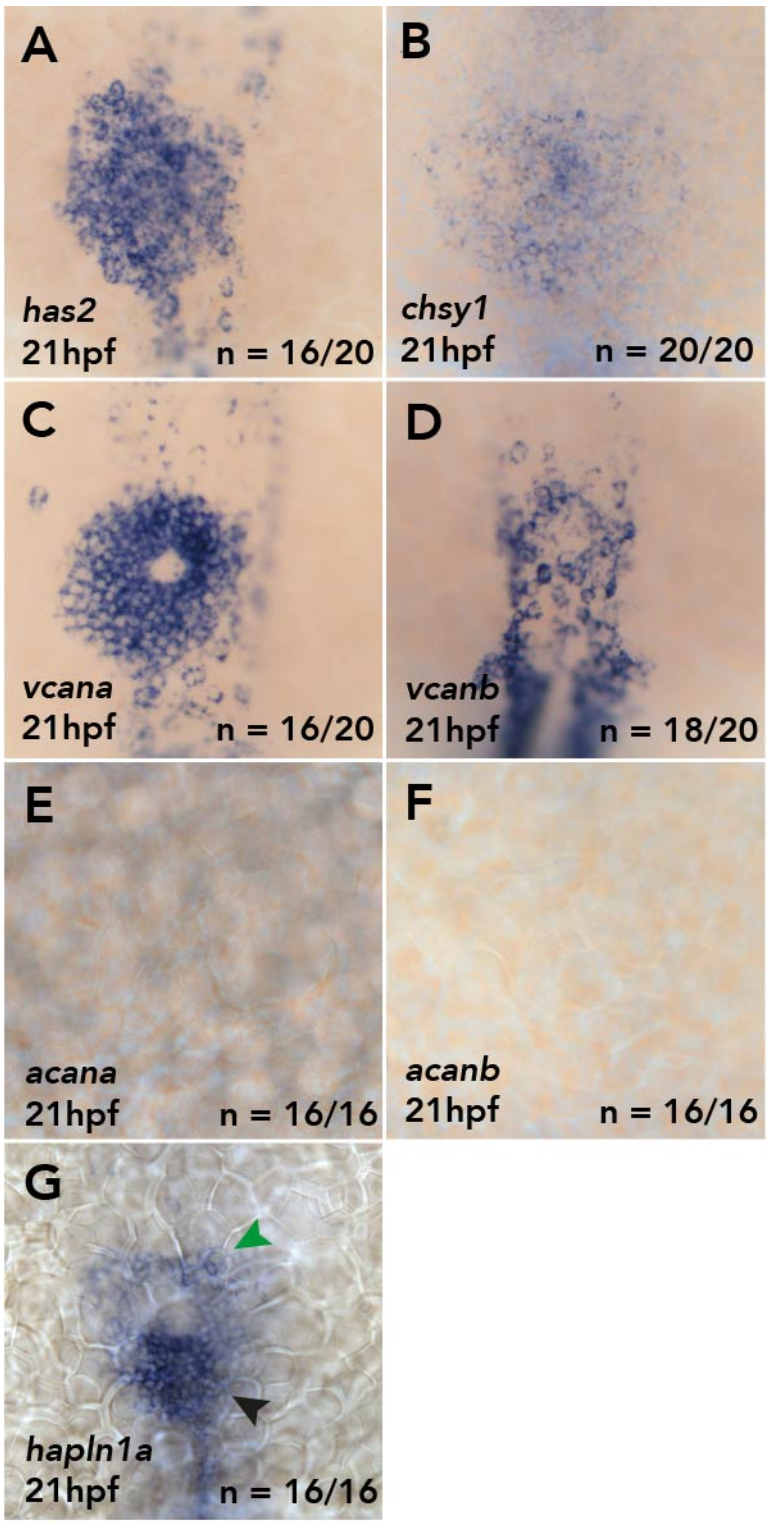

Figure 6.9 Proteoglycan components display distinct expression patterns in the cardiac cone.

mRNA *in situ* hybridisation analysis of proteogylcan genes in the cardiac cone at 21hpf. **(A)** *has2* is predominantly expressed on the left side of the cardiac cone. **(B)**

6.1.5 Regionalised expression of *hapln1a* is required for correct cardiac morphogenesis

Asymmetric regionalisation of the cardiac ECM represents an intrinsic mechanism which could be driving heart looping morphogenesis. As the regionalisation of the cardiac ECM overlaps with *hapln1a* expression, one hypothesis is that asymmetric expression of *hapln1a* is required to promote heart looping. To test whether the regionalisation of *hapln1a* expression in the heart tube is required for heart looping, an overexpression construct containing the *hapln1a* coding sequence under the control of the pan-myocardial *myl7* promoter, flanked by Tol2 transposon sites was created (Figure 6.10A) (Kwan et al., 2007). The resulting *myl7:hapln1a* construct was injected together with *tol2* mRNA into the cell at the 1-cell stage to facilitate integration of the construct into the genome and result in mosaic misexpression of *hapln1a* in the myocardium (Figure 6.10B-B''). ISH analysis of *hapln1a* at 55hpf in embryos injected with *myl7:hapln1a* demonstrates varying levels of *hapln1a* misexpression in the myocardium (Figure 6.10B'-B''), distinct from uninjected embryos where *hapln1a* is restricted to the atrioventricular canal (Figure 6.10B).

To examine the effect of loss of *hapln1a* regionalisation, two colour ISH was performed at 55hpf to identify *hapln1a* expressing cells (Figure 6.10C-C'', blue) and outline heart morphology using *myl7* expression (Figure 6.10C-C'', red). In WT

Figure 6.9 continued.

chsy1 expression is elevated in the heart, but with no lateralised expression. **(C)** *vcana* is strongly and uniformly expressed in the heart. **(D)** *vcanb* is expressed in the cardiac cone, with no clear localisation to any specific quadrant. **(E-F)** Neither *acana* nor *acanb* are expressed in the heart at 21hpf. **(G)** *hapln1a* expression is elevated in the posterior cardiac cone (black arrowhead), with lower levels and a smaller domain of expression in the anterior of the cone (green arrowhead). Dorsal views.

embryos at 26hpf, *hapln1a* expression is predominantly atrial (Figure 6.8A), with elevated expression on the left suggesting *hapln1a* misexpression may have different impacts on heart looping morphogenesis depending on its chamber of expression. Therefore, the percentage coverage of *hapln1a* in either chamber was quantified and plotted against looping ratio (Figure 6.10D-E). Interestingly, whilst frequent misexpression of *hapln1a* in the ventricle was observed in injected embryos (Figure 6.10D), very few embryos were recovered displaying misexpression of *hapln1a* in the atrium (Figure 6.10E). Overexpression of *hapln1a* in the ventricle upto 35% does significantly impact on heart looping, although in embryos with greater than 35% expression of *hapln1a* in the ventricle, a non-significant reduction is apparent (Figure 6.10D). However, in the atrium, misexpression greater than 10% is sufficient to result in a significant reduction in heart looping (Figure 6.10E). Together, this suggests that heart morphogenesis displays a greater sensitivity to over-expression of *hapln1a* in the atrium and therefore the regional restriction of *hapln1a* in the atrium may be required to promote proper heart looping.

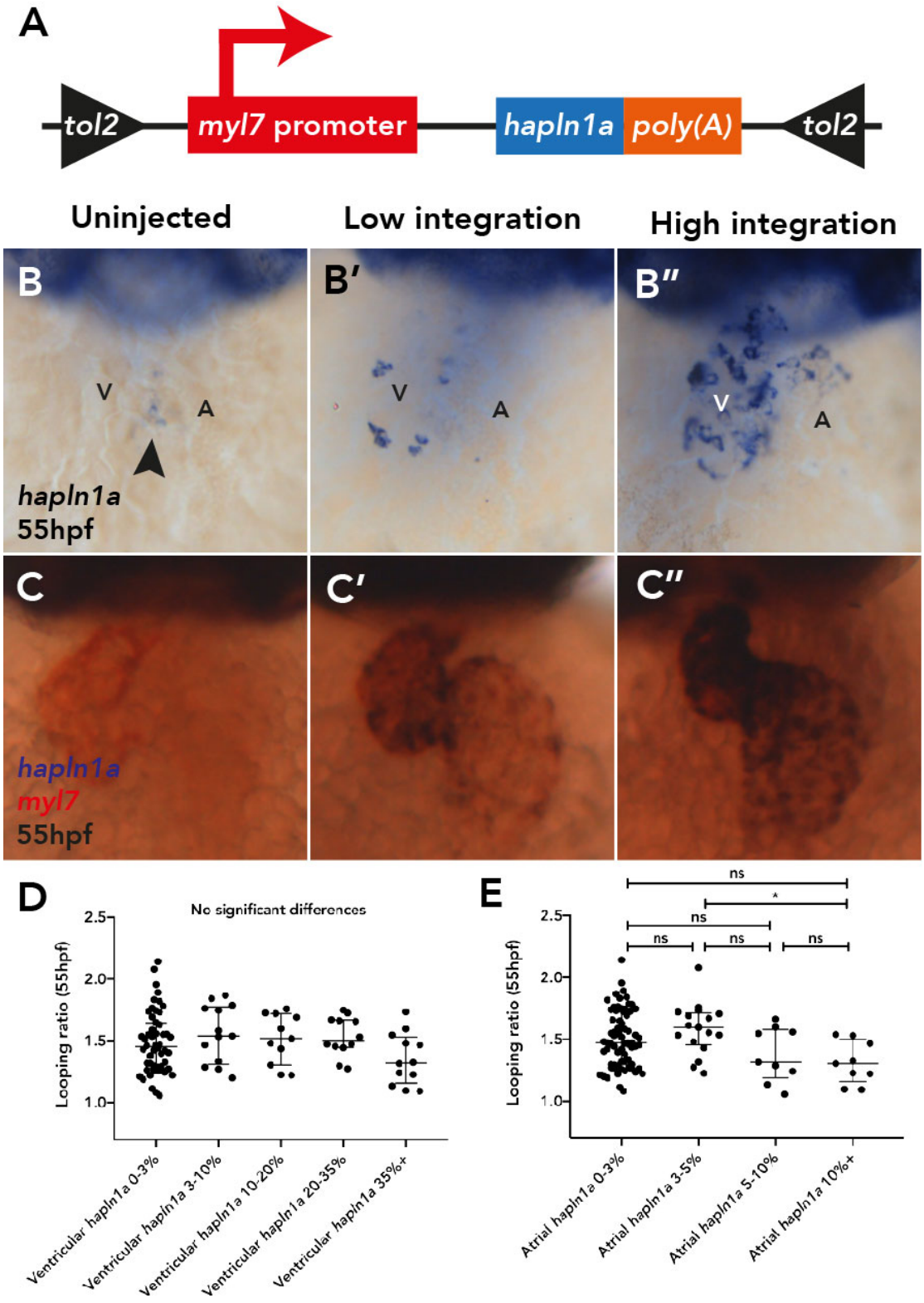

Figure 6.10. Regionalised *hapln1a* expression is required to promote proper heart morphogenesis.

(A) Schematic of *myl7:hapln1a* misexpression construct. The *hapln1a* coding sequence (blue), together with an SV40 antigen poly(A) tail (orange) are placed

under the promoter of the pan cardiac gene *myl7* (red). This is flanked by *tol2* transposon sites (black) for Tol2-mediated transgenesis through injection into the

Figure 6.10 continued.

cell at the 1-cell stage together with *tol2* mRNA. **(B-B'')** Confirmation of *myl7:hapln1a* construct efficacy by mRNA in situ hybridisation of *hapln1a* in uninjected (B) or injected embryos at 55hpf (B'-B''). In uninjected embryos at 2dpf, *hapln1a* expression is restricted to the atrioventricular canal (B, arrowhead). Embryos injected with the *myl7:hapln1a* construct display a range of levels of *hapln1a* misexpression in the working myocardium (B'-B''). **(C-C'')** Representative images of mRNA *in situ* hybridisation analysis at 55hpf of *hapln1a* (blue) to examine percentage coverage of misexpression of *hapln1a* using the *myl7:hapln1a* contract, and *myl7* (red) to characterise the morphology of the heart. Uninjected embryos have little or no *hapln1a* expression in the heart (C), whilst varying levels or *hapln1a* mis expression are observed in embryos injected with the *myl7:hapln1a* plasmid (C'-C''). **(D)** Quantification of the impact of increased ventricular expression of *hapln1a* on heart looping ratio at 55hpf. Misexpression of *hapln1a* in the ventricular myocardium has no significant effect on heart looping ratio. **(E)** Quantification of the impact of increased atrial expression of *hapln1a* on heart looping ratio at 55hpf. Misexpression of *hapln1a* in the atrial myocardium above 10% results ins a significant reduction on heart looping. B-C'': ventral views. V: ventricle, A: atrium. D, E: Median with interquartile range, Kruskal-Wallis, Dunn's multiple comparisons, ns: not significant, *: $p<0.05$.

6.1.6 *hapln1a* expression is independent of embryonic left-right asymmetry

hapln1a is expressed in the posterior half of the cardiac disc (Figure 6.9G), which following heart jogging becomes re-organised to the left-side of the tube (Figure 1.4 and 6.8A) (Guerra et al., 2018), and this regionalisation of *hapln1a* is required to promote heart morphogenesis (Figure 6.10). *hapln1a* represents a candidate gene which may contribute to the tissue intrinsic nature of heart looping morphogenesis in fish and chick (Manning and McLachlan, 1990; Noël et al., 2013). Under this model, regionalised *hapln1a* expression would be independent of embryonic left-right laterality cues as heart looping in zebrafish is independent of Nodal signalling (Noël et al., 2013). To examine the interaction between *hapln1a* expression and laterality, *hapln1a* expression was characterised in *spaw* mutants, which lack left-right asymmetry (Noël et al., 2013). At 19hpf, *hapln1a* is expressed in the posterior compartment of the cardiac disc (Figure 6.11A, 6.9 G), and in *spaw* mutant embryos at the same stage, posterior up-regulation of *hapln1a* expression in the cardiac disc is unaffected (Figure 6.11A), demonstrating that asymmetric *hapln1a* expression is independent of embryonic left-right asymmetry.

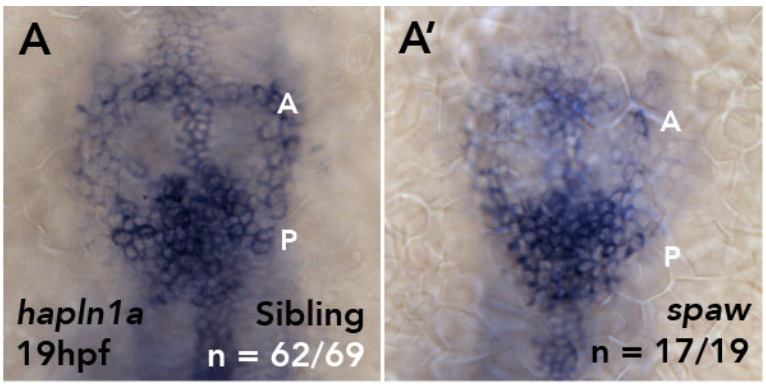

Figure 6.11. Expression of *hapln1a* is independent of embryonic left-right laterality. mRNA *in situ* hybridisation analysis of *hapln1a* expression in the heart disc of WT and *southpaw* mutants at 19hpf. **(A)** *hapln1a* is expressed in the posterior half of the cardiac disc at 19hpf. **(A')** In *spaw* mutants, expression of *hapln1a* is unaffected. Dorsal views. A: anterior, P: posterior.

Together with previous work, the regionalised expression of HA-proteoglycan complex components in the heart disc and subsequently in the heart tube suggest a number of roles for distinct proteoglycan complexes in promoting vertebrate development (Figure 6.12). In the heart disc (Figure 6.12A), laterality-dependent *has2* expression (yellow) on the left side of the disc dampens BMP activity, resulting in increased cell migration speed on the left (Smith et al., 2008; Veerkamp et al., 2013), whilst *hapln1a* is expressed in a laterality-independent manner in the posterior heart disc (blue), which correlates with faster cell speed, and the differences in cell speed, together with rotation drive heart jogging. By 26hpf (Figure 6.12B) heart jogging has repositioned posterior cells of the disc expressing *hapln1a* to the left-side of the heart tube and myocardial *has2* expression has been turned off and replaced with prominent endocardial expression. *vcana* expression is almost uniformly expressed in the myocardium, whilst *vcanb* (orange) expression is only observed at the arterial pole, overlapping the main region of cell addition during heart looping in zebrafish. The expression of *hapln1a* in the heart tube overlaps with an expanded cardiac ECM at 26hpf at the venous pole (Figure 6.12C) and regionalised *hapln1a* expression is required to promote heart morphogenesis.

6.2 Discussion

Using live, *in vivo* light sheet imaging, I have identified and begun to characterise an asymmetric expansion of the cardiac jelly prior to and following heart looping morphogenesis (Figures 6.1, 6.2 and 6.3). In line with previous studies, I have shown the cardiac jelly is rich in HA and established that HA is present in the cardiac ECM from the linear heart tube stage (Figure 6.4). Multiple studies both in zebrafish have suggested that HA is a major component of the cardiac ECM, and *has2* mutant mice, which exhibit severe widespread morphological phenotypes, exhibit an almost total lack of cardiac jelly and a failure to undergo heart looping morphogenesis (Camenisch et al., 2000). However, the mechanisms by which HA promotes the asymmetric morphogenesis underlying cardiac looping remain unclear.

I have identified that prior to heart looping, the cardiac ECM of the heart tube is asymmetrically expanded and have identified that regionalised expression of a candidate gene, *hapln1a*, is required for heart morphogenesis to occur correctly (Figure 6.8, 6.10). Morpholino-mediated knockdown of *hapln1a* results in a loss of left-sided ECM expansion at 26hpf and *hapln1a* promoter mutants display a thinner cardiac jelly at 50hpf and 72hpf, together with abnormal heart morphology, demonstrating that Hapln1a is required for ECM expansion (Derrick et al., 2019). Further supporting a role for *hapln1a* in heart development, Hapln1 mutant mice display a number of heart valve phenotypes and cardiac abnormalities (Wirrig et al., 2007), however, as the onset of phenotype was not characterised earlier in development, it is possible that valve defects may be associated with a failure in the early morphogenesis of the heart tube.

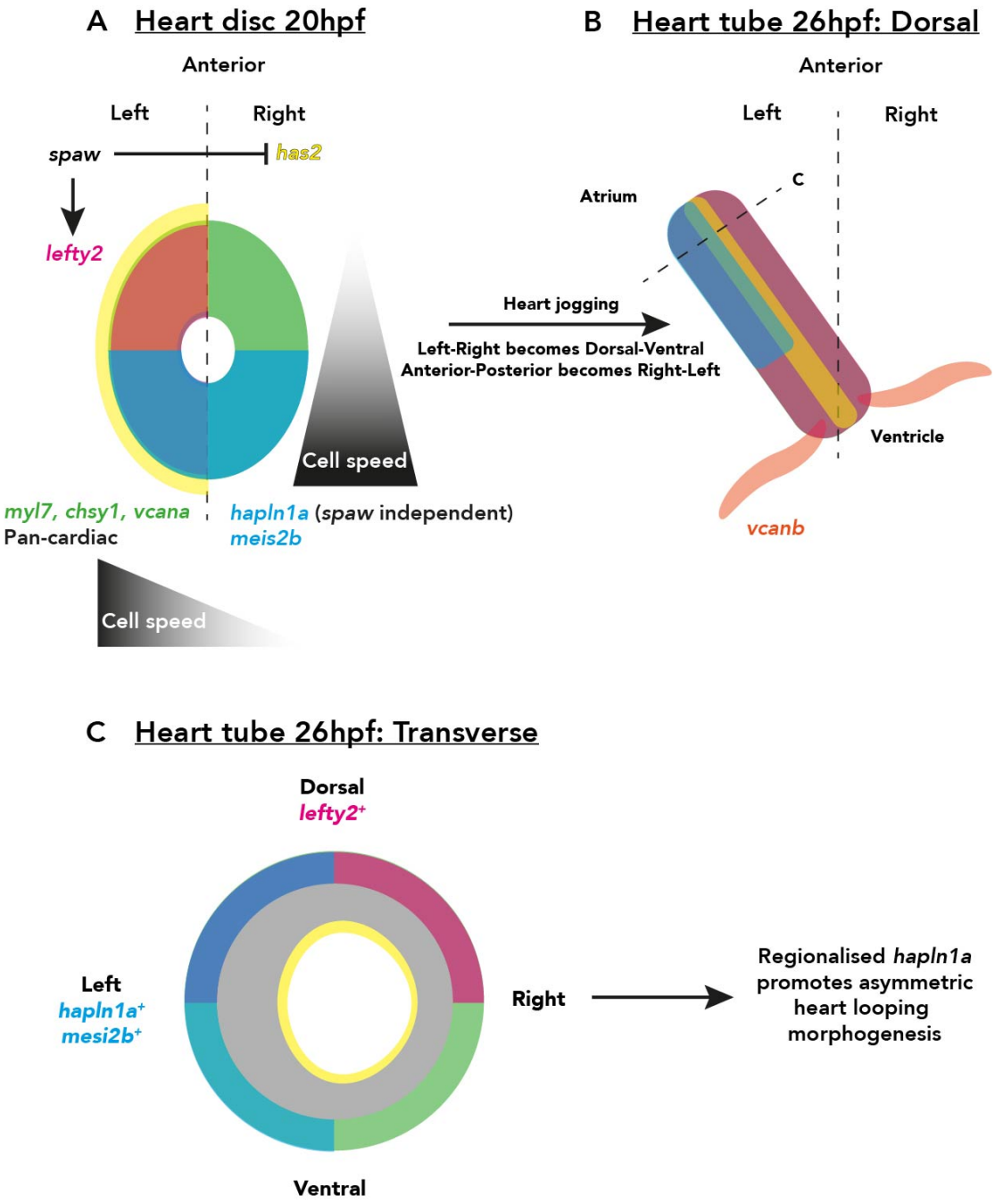

Figure 6.12. Model for regionalised gene expression during zebrafish heart development.

(A) At 20hpf, the heart disc (green) is patterned across the left-right and anterior-posterior axis. Nodal signalling (*spaw*) acts to promote *lefty2* (magenta) and restrict *has2* (yellow) expression to the left-side of the disc. A *spaw*-independent mechanism results in *hapln1a* (blue) expression in the posterior cardiac disc, where it overlaps with *meis2b* and significantly faster cell migration speeds. *vcana* and *chsy1* (green)

Prior to tube formation, *hapln1a* is expressed in the posterior of the cardiac disc and following heart jogging is repositioned on the left side of the heart tube (Figure 6.12) (Guerra et al., 2018). *hapln1a* expression in the heart overlaps with the transcription factor *meis2b*, suggesting that the generation of left-right asymmetry in the cardiac jelly may be set-up as early as 12hpf when *meis2b*-positive cardiomyocytes are first identified (Guerra et al., 2018). Examining expression of *hapln1a* in *meis2b* mutant hearts may provide the first step in understanding the transcriptional network required to generate lateralised cardiac ECM asymmetry (See Chapter 8).

hapln1a expression is highly dynamic during heart development, with eventual restriction to the atrioventricular canal (Figure 6.10). This restriction of *hapln1a* to the AVC appears necessary to promote cardiac looping as even a low level of misexpression of *hapln1a* in the atrial myocardium results in a reduction in heart looping (Figure 6.10), (Derrick et al., 2019). What is unclear is why a much greater

Figure 6.12 continued.

are expressed throughout the cardiac disc. Differences in cell migration speed in the cardiac disc result in a reorganisation of left-right and anterior-posterior patterning as the disc forms the tube during heart jogging. **(B)** At 26hpf, *lefty2* is expressed in the dorsal myocardium, and *has2* expression is now restricted to the endocardium. *chsy1* expression is no longer observed in the heart, suggesting that Chondoitin Sulfate synthesis is only required at the disc stage. *vcana* is expressed almost ubiquitously throughout the myocardium at low levels, which may represent a loss of expression as its role it re-assigned to valvulogenesis together with *has2*. *vcanb* (orange) is expressed at the arterial pole of the heart where it may regulate addition of the second heart field. *hapln1a* is expressed predominantly on the left side of the atrium, overlapping with the expanded cardiac jelly **(C)** and regionalised *hapln1a* promotes heart looping morphogenesis.

number of embryos with considerable misexpression in the ventricle compared to the atrium was achieved by the *myl7:hapln1a* mosaic study. This could suggest that atrial cells which express *hapln1a* are actively excluded from the chamber, or perhaps that sufficient over-expression of *hapln1a* from as early as 14ss when the *myl7* promoter is active (Yelon et al., 1999) results in a fate switch from atrial to ventricular. This hurdle of achieving significant overexpression in the atrium resulted in comparatively few embryos being analysed. To strengthen the conclusion that *hapln1a* must be spatially restricted in the atrium to promote morphogenesis, an atrial-specific driver such as the *myh6* promoter (Zhang et al., 2013) could be used in conjunction with the GAL4/UAS system together with a stably expressed *UAS:hapln1a* to stably misexpress *hapln1a* throughout the atrium. This approach would also allow for misexpression of *hapln1a* in other domains of the heart, such as under the lft:BAC:GALFF to examine the effect of misexpression of *hapln1a* in the left cardiac disc altering the axis of ECM asymmetry within the heart tube. Finally, whilst misexpression of *hapln1a* mRNA is clearly observed, it will be important to confirm that Hapln1a protein is also mislocalised in the cardiac jelly. Further work with these and similar tools can be used to investigate the mechanisms by which differences in ECM regionalisation promote heart morphogenesis.

In E9.5 mouse embryos *Has2* and *Versican* have highly similar expression patterns in the heart, and the cardiac jelly is rich in both HA and Versican (Camenisch et. al. 2000). Furthermore, *Versican* mutant mice exhibit heart defects, including a uniformly thin ECM similar to *Has2* mutants (Mjaatvedt et al., 1998; Yamamura et al., 1997) suggesting Versican is the core protein in the cardiac jelly, where it interacts with HA. In *Hapln1* mutant mice, levels of Versican protein are reduced, suggesting that Hapln binding to Versican may protect the protein from turnover or proteolytic cleavage (Wirrig et al., 2007). Together this suggests that HA, Versican and Hapln1 act together to promote heart development.

Supporting this, ISH analysis of the two *versican* genes in zebrafish (Figure 6.6) suggests multiple roles for Versican Proteoglycans in heart development (Figure 6.12). *vcana* expression is solely myocardial at 21hpf and following heart tube formation expression is greatly reduced, displaying eventual restriction to the atrioventricular valve by 30hpf. This supports previous studies implicating *vcana*, together with *has2* in the development of the atrioventricular valve in zebrafish (Patra et al., 2011). *vcanb* expression is excluded from the linear heart tube but expression at the arterial pole suggests a distinct role in promoting addition of the SHF (Pater et al., 2009). In humans and mice, *Versican* pre-mRNA is reported to undergo differential splicing events to generate at least four distinct isoforms, all capable of interacting with HA but with differing biological roles, including cell proliferation and opposing roles in cell migration including during SHF addition (Kern et al., 2007; Nandadasa et al., 2014). Supporting multiple roles for Versican in heart development, a reverse genetic screen in Medaka isolated a *versican* mutant in which the heart fails to loop, cardiac jelly is absent and addition from the SHF is compromised (Mittal et al., 2019). Together with the non-overlapping expression domains of zebrafish *vcana* and *vcanb*, this would suggest that in zebrafish distinct Versican functions in heart development have been split between the two paralogs, and supporting a model where Vcana interacts with Hapln1a and HA to promotes heart looping, whilst Vcanb is required for SHF addition to the heart.

Versican is typically covalently linked to Chondroitin Sulfate (Pomin and Mulloy, 2018), and in zebrafish, the cardiac jelly has been shown to contain CS, where it is enriched at the atrioventricular canal from 36hpf (Peal et al., 2009) and in Medaka at 3dpf (Mittal et al., 2019). A combination of pharmacological inhibition of CS synthesis and morpholino-mediated knockdown of *chsy1* supported a role for CS in valve development (Peal et al., 2009). However, examination of *chsy1* expression at tube stages does not identify clear expression of *chsy1* in the heart tube (Figure 6.5). instead, *chsy1* expression is observed prior to tube formation (Figure 6.9),

suggesting that, similar to HA, the production of CS required for heart morphogenesis occurs before the heart tube forms.

HA plays multiple roles during heart development: formation of the linear heart tube (Smith et al., 2008), looping morphogenesis (Camenisch et al., 2000; Derrick et al., 2019), formation of the atrioventricular valve (Camenisch et al., 2002; Lagendijk et al., 2013) and trabeculation (Monte-Nieto et al., 2018). Prior to heart tube formation, *has2* is expressed in the myocardium (Smith et al., 2008; Veerkamp et al., 2013) and analysis of *has2* expression during disc to tube transition identifies a switch in the tissue of expression from myocardium to endocardium. This switch may reflect a change in the role of HA in specific aspects of heart development during these timepoints (Figures 6.5, 6.9, 6.12): HA derived from the myocardium is required to form the tube and position it in the correct place (Derrick et al., 2019; Smith et al., 2008), whilst endocardially-derived HA is necessary for valvulogenesis (Camenisch et al., 2002, 2000) Supporting a model where HA plays multiple and distinct roles in heart development, is the use of timed pharmacological inhibition of HA synthesis, where inhibition of synthesis prior to tube stage (during myocardial expression of *has2*) results in a failure of heart looping, yet inhibition following tube formation when *has2* is endocardially expressed does not impact on heart looping (Derrick et al., 2019) (Noël, unpublished). Thus, the synthesis of the HA-containing ECM required for morphogenesis of the heart tube occurs as the tube is being formed (Derrick et al., 2019) and following heart tube formation, the role of ECM synthesis is likely directed to generate the atrioventricular valve. Together, the zebrafish represents an excellent model in which these multiple, spatiotemporal roles for HA during heart development can be elucidated. This will be discussed further in Chapter 8.

Live light sheet imaging of the heart at 2dpf revealed that the ECM asymmetry present at 1dpf in the atrium persists after the heart tube has begun to undergo looping and ballooning morphogenesis. This continued ECM asymmetry correlates

with persistent Hapln1a protein in the 2dpf heart (Derrick et al., 2019), despite restriction of *hapln1a* mRNA expression to the valve at this stage. In the ventricle, the ECM is uniformly thin, likely at least in part due to the absence of Hapln1a protein (Derrick et al., 2019). This may reflect the differences in ECM organisation which facilitate trabeculation in later stages of heart development, where myocardial cells proliferate into the cardiac lumen inside a localised ECM bubble, which is then remodelled to form the mature trabeculae (Monte-Nieto et al., 2018; Passer et al., 2016). Therefore, whilst expression of *hapln1a* in the left atrial myocardium may be responsible for generating the correct shape of the heart during looping and ballooning morphogenesis, exclusion of Hapln1a from ventricular ECM may be required to facilitate close contact of the two tissue layers to promote maturation of the heart (See chapter 8). Characterisation of trabeculation in *myl7:hapln1a* injected embryos with ventricular misexpression at 3dpf, which at 2dpf do not possess heart looping defects (Figure 6.10) (Derrick et al., 2019) would help identify whether the atrial-ventricular differences in ECM composition are required to promote distinct aspects of maturation such as trabeculation, and will further define the role of early patterning of the heart disc and tube to regionalise the cardiac jelly and promote heart morphogenesis.

There are several mechanisms through which ECM crosslinking could drive asymmetric heart morphogenesis. One is that ECM expansion is likely to result in differences in ECM stiffness (Nagy et al., 2017). These differences could be read by cellular tension sensors such as the Hippo pathway, a well characterised mechanosensitive pathway which can act as a modulator of the actomyosin cytoskeleton or to regulate growth through regionalised differences in proliferation (Low et al., 2014). Another potential mechanism may be through limiting the bioavailability of ligands such as BMP. *lamc1* mutants have reduced HSPGs and ectopic BMP signalling, which impacts on myotome development (Dolez et al., 2010). Supporting a role for BMP signalling in the directionality of heart looping, up-regulated expression of *bmp4* in the jogged heart appears to correlate with

sidedness of jogging (Chen et al., 1997). However, careful dissection of the role for BMP signalling specifically in asymmetric morphogenesis will be necessary due to the role of HA in dampening BMP signalling to promote proper rotation and involution of the cardiac disc during tube formation (Smith et al., 2008; Veerkamp et al., 2013). Furthermore, posterior expression of *hapln1a* in the cardiac disc, overlaps quadrants I and IV which encompass the two fastest migrating populations of cells during heart jogging (Campos-Baptista et al., 2008). This suggests a potential role for *hapln1a* even earlier heart development in regulating cardiomyocyte migration speed, necessary to generate the correctly positioned heart tube (Noël et al., 2013; Smith et al., 2008). Imaging of the migration of the heart disc in *hapln1a* mutants, or quantification of the angle of heart jogging would be sufficient to confirm this.

The role that asymmetric expansion of the cardiac jelly, mediated by Hapln1a, plays in cardiac morphogenesis remains unknown, however the Nodal-independent expression of *hapln1a* in the posterior of cardiac disc (Figure 6.11) suggests that ECM expansion could be sufficient to direct asymmetric looping and ballooning morphogenesis of the heart tube. Indeed, in *pkd2 (polycystic kidney disease 2)* mutants in which laterality is randomised (Bataille et al., 2011; Schottenfeld et al., 2007), *hapln1a*-expressing cells are positioned on the right side of the tube in right-jogged hearts, potentially explaining why direction of jogging is an accurate predictor of heart looping directionality (Chen et al., 1997; Derrick et al., 2019; Grimes et al., 2019; Noël et al., 2013). Importantly, whilst *spaw* mutant embryos exhibit midline hearts, there is a mild rotation in the heart disc during tube formation which is correlated with looping direction (Noël et al., 2013), suggesting that even subtle lateralisation of the ECM by Hapln1a could dictate the direction of looping in the absence of laterality cues. However, *hapln1a* mutants (Derrick et al., 2019) and morphants (Noël, unpublished) do undergo looping morphogenesis, although the morphology of mutant hearts is abnormal (Derrick et al., 2019) suggesting that ECM asymmetry is a contributing factor to intrinsic heart looping and that embryonic laterality cues are required to position the asymmetry to promote morphogenesis.

Examining the effect of loss of *hapln1a* in *spaw* mutants will be invaluable in examining this interaction between intrinsic heart patterning and extrinsic left-right cues in promoting heart morphogenesis.

Similar to the cardiac jelly, the right ECM of the chick midgut is expanded, but *Has2* is not differentially expressed (Sivakumar et al., 2018). Rather, *Tsg6 (tumor necrosis factor-α-stimulated gene 6)* a modifier of HA is restricted to the right side of the endodermal ECM and loss of Tsg6 function results in loss of lateralised ECM expansion and a failure of gut rotation (Sivakumar et al., 2018). This asymmetric expansion mediated by Tsg6 is required for exclusion of vasculature from the right ECM through inhibition of *Cxcl12* (*Chemokine (C-X-C motif) ligand 12*) expression (Sivakumar et al., 2018), demonstrating that asymmetric ECM components can indirectly regulate gene expression and tissue morphogenesis. This suggests regional modulation of HA dynamics may be a conserved mechanism in promoting asymmetric morphogenesis of tubular organs (Sivakumar et al., 2018).

In summary, I have identified and begun to characterise an asymmetric, left-sided expansion of the embryonic cardiac jelly which is established prior to looping morphogenesis, independent of left-right asymmetry. Misexpression of *hapln1a*, the candidate gene for asymmetric ECM expansion results in abnormal cardiac morphogenesis, demonstrating that tight spatiotemporal control of ECM components is required for proper heart development. This will be discussed further in Chapter 8.

7. *rhoca* and *rhocb* are dispensable for early cardiac development

I have identified a role for Lamb1a-Lamc1 containing Laminins in restriction of heart size and determined the specific Laminin-binding integrins, which are present in the heart during early morphogenesis. To begin to define the signalling axis which promotes heart looping and limits heart size, I have examined the role of two small Rho GTPases, which could represent a node of the Laminin-Integrin pathway. The family of small Rho GTPases are classical intracellular transducers of external signals, often located at the cell membrane where they regulate the dynamics of the actomyosin cytoskeleton. Different Rho GTPases are able to generate functionally distinct arrangements of actin, facilitating changes in cell motility, cell shape and programmed cell death.

Here I characterise the expression and function of the two paralogs of the human *RHOC* gene during heart looping morphogenesis in zebrafish. Loss of either *rhoca* or *rhocb*, or both, does not impact embryonic heart development significantly, suggesting that both genes are dispensable for development.

7.1 Results

7.1.1 *rhoca* is expressed in the heart during looping morphogenesis

A candidate gene identified within the Tomo-Seq dataset which may provide a functional link between extracellular matrix signalling and cellular responses in the heart was *ras homolog family member Ca* (*rhoca*, formerly *rhoae)* (Figure 7.1A). *rhoca* is over 90% similar in amino acid composition to human *RHOC*, a member of the Rho subfamily of small GTPases (Salas-Vidal et al., 2005).

Rho GTPases switch between an active, GTP bound state and an inactive GDP bound state, and the interaction between cytosolic effectors which regulate actomyosin dynamics in their GTP bound form results in changes to the cell shape and attachment in response to external cues. The cycling of the GTP- and GDP-bound states of Rho GTPases is regulated by three classes of proteins. GEFs (Guanine Exhange Factors) facilitate release of GDP and binding of GTP, activating GTPases. GAPs (GTPase Activating Proteins), inactivate Rho GTPases through stimulation of GTPase activity whilst GDIs (Guanine nucleotide Dissociation Inhibitors) sequester Rho GTPases to the cytosol away from their interacting partners. In the active, GTP-bound state, Rho GTPases can interact with multiple effectors including protein kinases and actin-binding proteins, resulting in changes in gene expression and the organisation of the actin network of the cell (Heasman and Ridley, 2008).

RhoC promotes proliferation and inhibits migration in cell culture, acting through VEGFR2 (Vascular endothelial growth factor receptor 2) (Hoeppner et al., 2015). In zebrafish, morpholino-mediated knockdown of *rhoca* and its paralog *ras homolog family member Cb* (*rhocb*, formerly *rhoad*) results in increased vascular permeability (Hoeppner et al., 2015), although heart morphogenesis in these models is not described.

To begin to define the role of *rhoca* in heart development, mRNA *in situ* hybridisation was performed at 24, 30 and 55hpf in WT embryos to characterise *rhoca* expression dynamics during heart morphogenesis (Figure 7.1B-D). During early heart tube stages *rhoca* is expressed throughout the heart (Figure 7.1B-C), however following heart looping, *rhoca* expression is restricted to ventricular tissue and the atrioventricular canal by 55hpf (7.1D), closely following many of the Laminin and integrin subunits described in Chapter 3 (Figure 3.1).

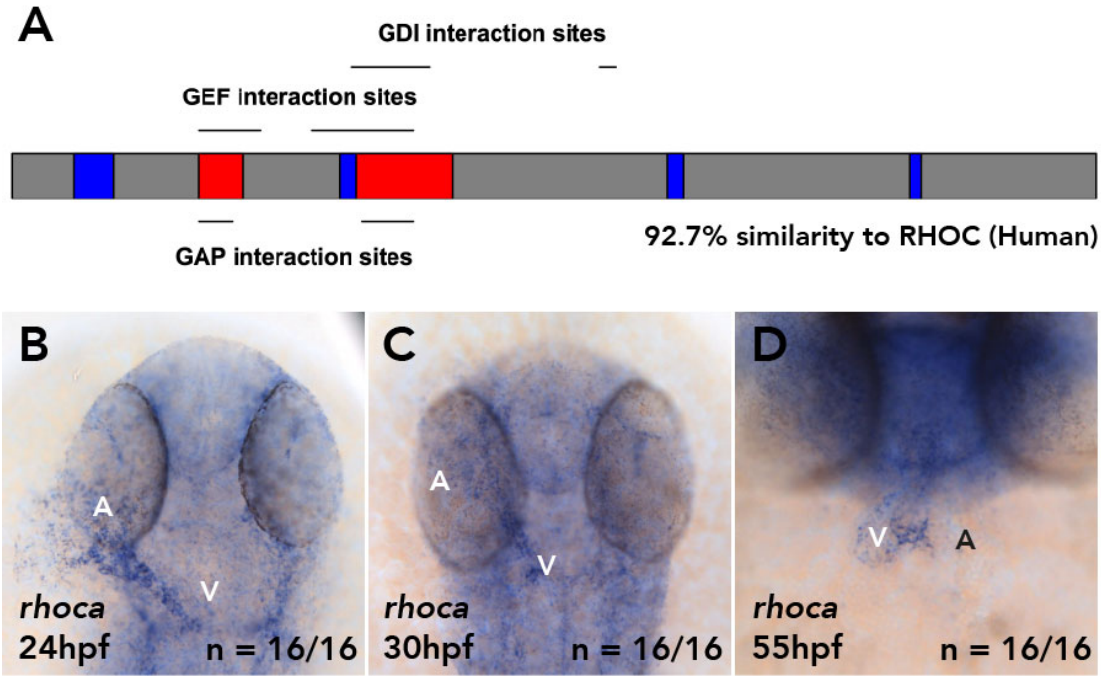

Figure 7.1. *rhoca* is expressed in the heart during early morphogenesis.

Characterisation of *rhoca* expression during heart looping morphogenesis by mRNA *in situ* hybridisation. **(A)** Schematic of *rhoca* structure based on UniProt accession number Q7T399. Zebrafish Rhoca protein shares 92.7% amino acid similarity to Human RHOC. Blue: G boxes, Red: Switch regions. **(B-C)** *rhoca* is expressed throughout the linear heart tube between 24hpf and 30hpf. **(D)** At 55hpf, *rhoca* is expression is restricted to the ventricle and atrioventricular canal. B-C, dorsal views. D: ventral views. V: ventricle, A: atrium.

7.1.2 Generation and characterisation of *rhoca* CDS mutants

To investigate the role of *rhoca* in heart morphogenesis, CRISPR-Cas9 mediated mutagenesis was used to target the CDS of *rhoca* (Figure 7.2). Two mutations were isolated: *rhoca*^{ins10} (a 2bp deletion and 12bp insertion, Figure 7.2A', B) leading to a frameshift and premature termination codon, and *rhoca*$^{\Delta ATG}$ (a 99bp deletion and 384bp deletion), resulting in a loss of the translational start site due to a skipping of exon 2 (Figure 7.2A'', C), which contains the initiating ATG codon. This suggests that no functional protein is translated in *rhoca*$^{\Delta ATG}$ mutants, however translation

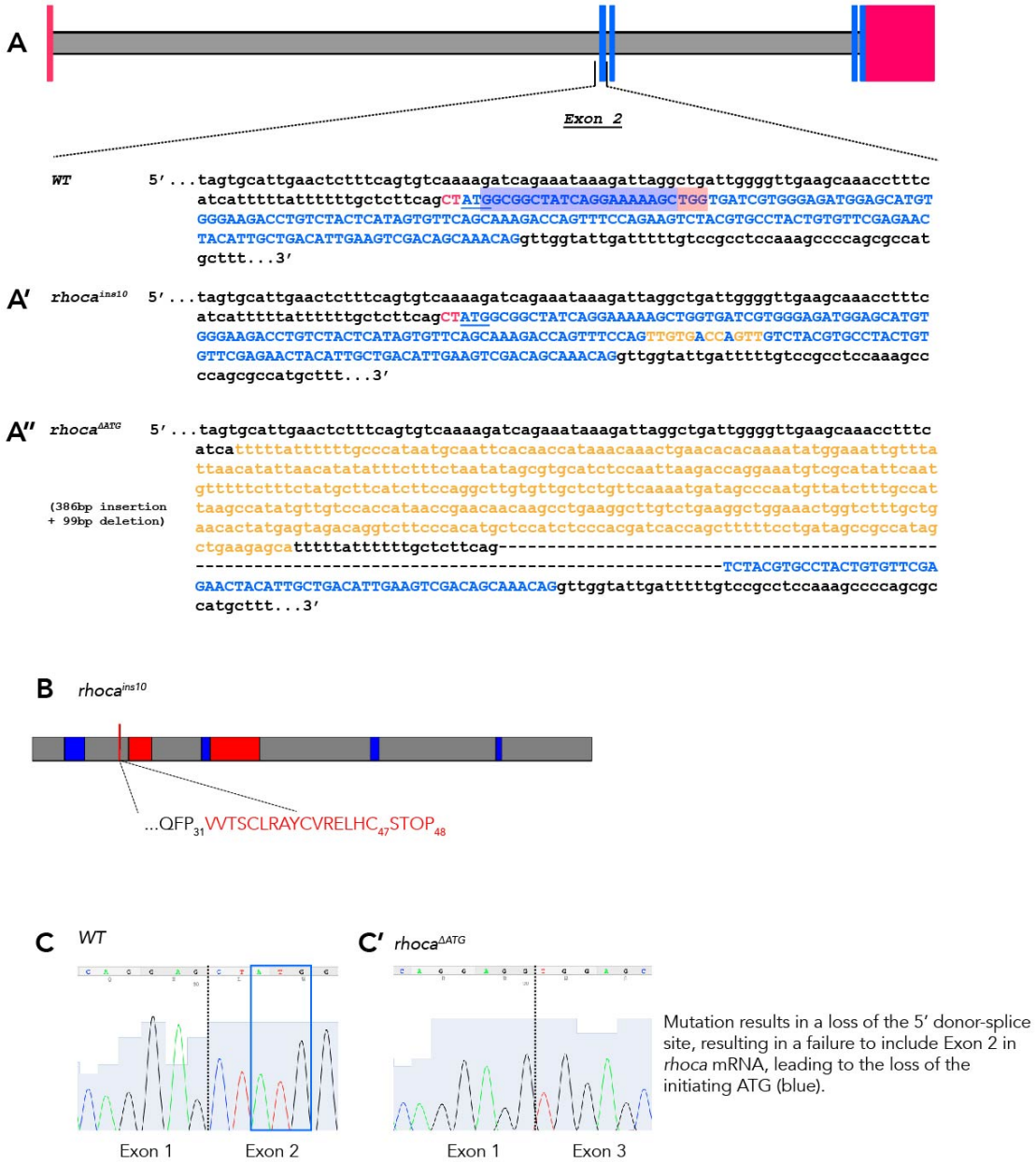

Figure 7.2. Generation of *rhoca* coding sequence mutants by CRISPR-Cas9 mutagenesis.

Mutagenesis strategy and predicted impact on Rhoca protein **(A)** Schematic of *rhoca* genomic DNA based on danRer10/GRCz10, Red: non-coding DNA, Blue: coding DNA, Grey: intronic DNA. A single gRNA targeting Exon 2, downstream of the annotated initiating ATG (blue, underlined), spacer highlighted in blue, PAM highlighted in red, was injected and two mutations were identified. **(A')** The *rhoca*^{ins10} allele results from a 2bp deletion and 12bp insertion (yellow). (A'') The *rhoca*^{ins10} allele deletes 99bp (dashed lines) and a 386bp insertion (yellow). **(B)**

initiating from a downstream codon cannot be ruled out. Both mutant alleles were established as stable lines at F2.

Having generated two mutations predicted to have different mechanisms of abolishing Rhoca function, the effect of both mutations on heart looping was analysed by mRNA *in situ* hybridisation analysis of *myl7* expression in homozygous mutant embryos for each allele at 55hpf, and in *rhoca*^{ins10} mutant embryos at 72hpf (Figure 7.3). (The *rhoca*$^{\Delta ATG}$ allele could not be analysed at 72hpf due to husbandry issues, however see 7.1.4 for further analysis). Loss of *rhoca* does not impact upon looping morphogenesis or heart size in either mutant allele at 55hpf, or at 72hpf in *rhoca*^{ins10} mutants (Figure 7.3A-D). Furthermore, *rhoca* mutants are adult viable and fertile, therefore I could investigate whether maternally-deposited *rhoca* masks any phenotypes in zygotic *rhoca* mutants. MPZ *rhoca* mutants do not display cardiac looping phenotypes at 55hpf (Figure 7.4B, E. WT and zygotic mutant data reproduced from Figure 7.3). However, when compared to WT, *rhoca*$^{\Delta ATG}$ MPZ mutants display a significant reduction in heart area at 55hpf, consistent with a trend towards smaller hearts observed between WT and zygotic mutants (Figure 7.4F). A similar, but non-significant trend is observed for the *rhoca*^{ins10} allele (Figure 7.4C). Together this suggests that *rhoca* is dispensable for cardiac morphogenesis in the embryo, but may play a minor role in regulation of cardiac size.

Figure 7.2 continued.

Predicted effect of the *rhoca*^{ins10} allele. The initial 31 amino acids are unaffected, followed by 16 amino acids of missense and a premature stop codon. **(C-C')** Effect of the *rhoca*$^{\Delta ATG}$ mutation on the splicing of *rhoca* mRNA. In WT embryos (C), correctly spliced mRNA includes the annotated initiating ATG of Exon 2 (blue box). *rhoca*$^{\Delta ATG}$ mutation (C') results in loss of Exon 2 from the mRNA, leading to loss of the initiating ATG.

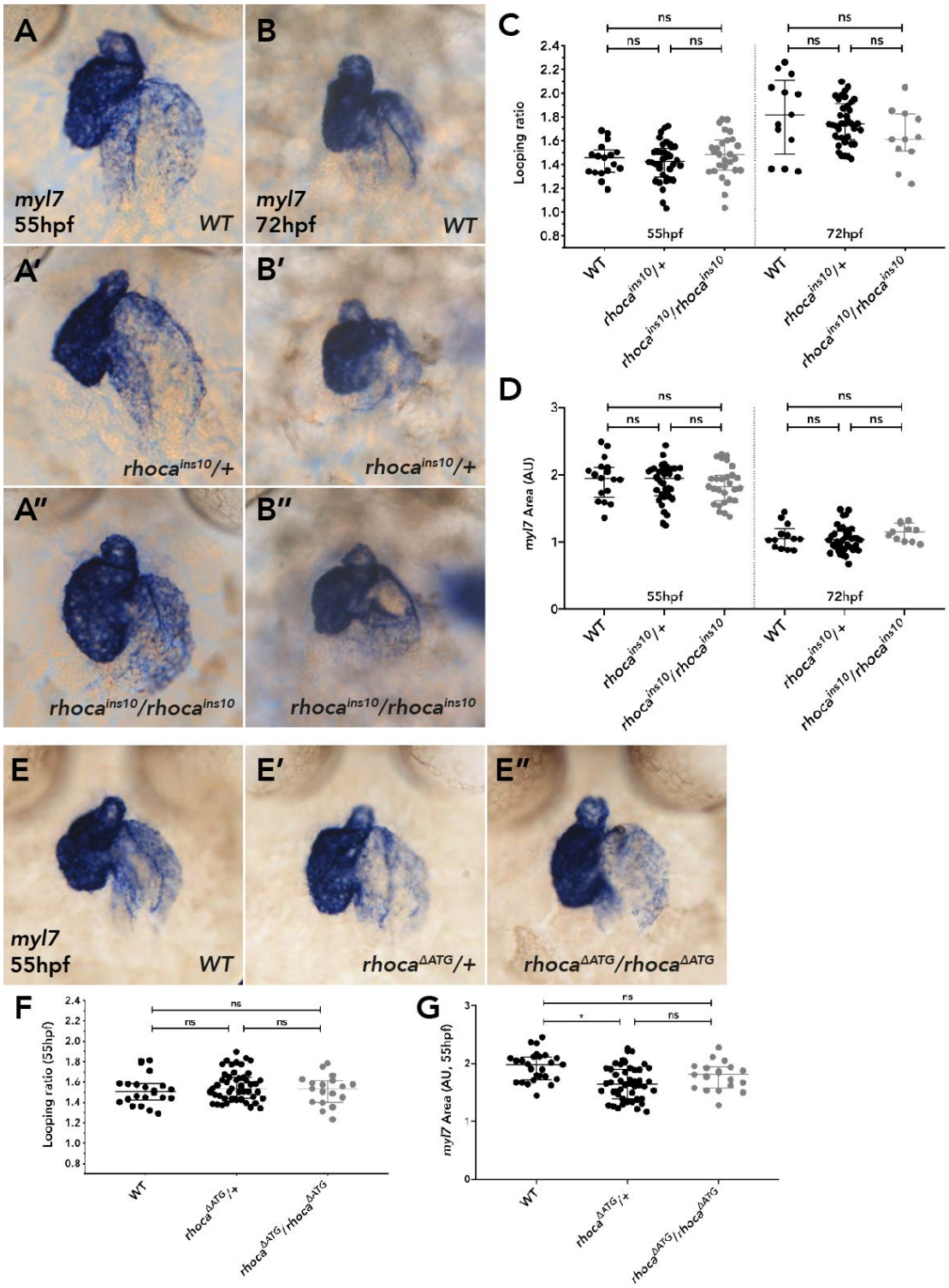

Figure 7.3. *rhoca* Zygotic mutants do not exhibit cardiac phenotypes.

Quantitative analysis of heart looping and heart size in *rhoca* mutants at 55hpf and 72hpf. **(A-A'')** Representative images of mRNA *in situ* hybridisation analysis of *myl7* at 55hpf to examine heart morphology in WT (A), *rhoca*^{ins10} heterozygotes (A') and *rhoca*^{ins10} homozygous mutants (A''). **(B-B'')** Representative images of mRNA *in situ*

Figure 7.3 continued.

hybridisation analysis of *myl7* at 72hpf to examine heart morphology in WT (B), *rhoca*^{ins10} heterozygotes (B') and *rhoca*^{ins10} homozygous mutants (B''). **(C)** Quantification of heart looping ratio of *rhoca*^{ins10} mutants and siblings at 55hpf and 72hpf, no significant differences are measured. **(D)** Quantification of heart area in *rhoca*^{ins10} mutants and siblings at 55hpf and 72hpf, no significant differences are measured. **(E-E'')** Representative images of mRNA *in situ* hybridisation analysis of myl7 at 55hpf to examine heart morphology in WT (E), *rhoca*$^{\Delta ATG}$ heterozygotes (E') and *rhoca*$^{\Delta ATG}$ homozygous mutants (E''). **(F)** Quantification of heart looping ratio of *rhoca*$^{\Delta ATG}$ mutants and siblings at 55hpf, no significant differences are measured. **(G)** Quantification of heart area in *rhoca*$^{\Delta ATG}$ mutants and siblings at 55hpf, *rhoca*$^{\Delta ATG}$ heterozygotes display a mild, yet significant reduction in heart size compared to WT siblings. Ventral views. C, D, F, G: Median with interquartile range, Kruskal-Wallis, Dunn's multiple comparisons, ns: not significant, *: $p<0.05$.

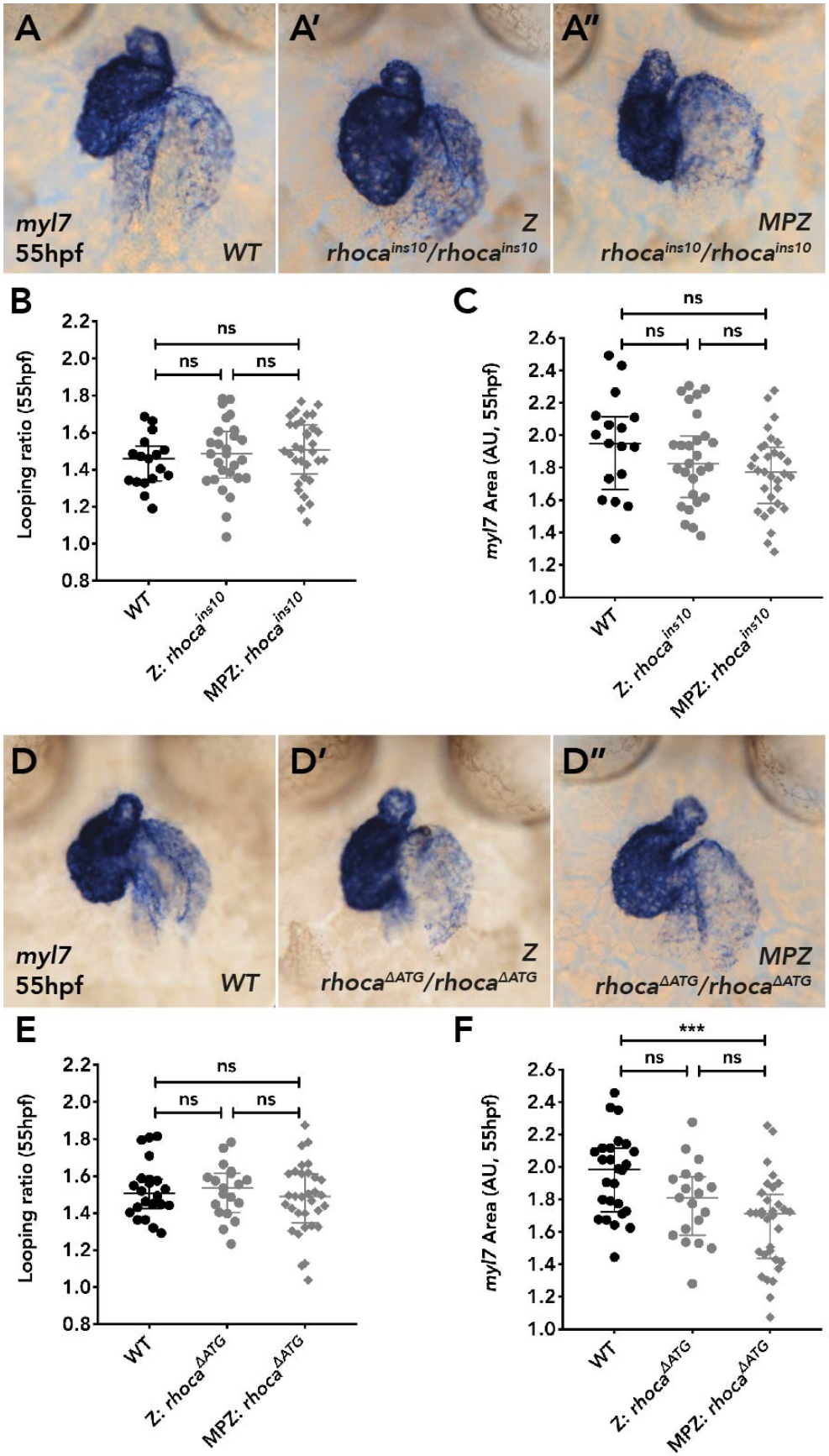
A
myl7
55hpf
WT
A'
Z
rhoca^ins10/rhoca^ins10
A''
MPZ
rhoca^ins10/rhoca^ins10
B
Looping ratio (55hpf)
ns
ns
ns
WT
Z: rhoca^ins10
MPZ: rhoca^ins10
C
myl7 Area (AU, 55hpf)
ns
ns
ns
WT
Z: rhoca^ins10
MPZ: rhoca^ins10
D
myl7
55hpf
WT
D'
Z
rhoca^ΔATG/rhoca^ΔATG
D''
MPZ
rhoca^ΔATG/rhoca^ΔATG
E
Looping ratio (55hpf)
ns
ns
ns
WT
Z: rhoca^ΔATG
MPZ: rhoca^ΔATG
F
myl7 Area (AU, 55hpf)
***
ns
ns
WT
Z: rhoca^ΔATG
MPZ: rhoca^ΔATG

Figure 7.4. *rhoca* Maternal-Paternal-Zygotic mutants do not have significant morphological defects.

Quantitative comparison of heart looping and heart size in *rhoca* Zygotic (Z) and *rhoca* Maternal-Paternal-Zygotic (MPZ) mutants at 55hpf **(A-A'')** Representative images of mRNA *in situ* hybridisation analysis of *myl7* expression at 55hpf to examine heart morphology in WT (A), *rhoca* Zygotic mutants (A') and *rhoca* Maternal-Paternal-Zygotic mutants (A''). **(B)** Quantification of heart looping ratio of WT, zygotic and maternal-paternal-zygotic *rhoca*^{ins10} mutants at 55hpf reveals no significant differences. **(C)** Quantification of heart size in WT, zygotic and maternal-paternal-zygotic *rhoca*^{ins10} mutants at 55hpf reveals no significant differences measured. **(D-D'')** Representative images of mRNA *in situ* hybridisation analysis of *myl7* expression at 55hpf to examine heart morphology in WT (D), *rhoca* Zygotic mutants (D') and *rhoca* Maternal-Paternal-Zygotic mutants (D''). **(E)** Quantification of heart looping ratio of WT, zygotic and maternal-paternal-zygotic *rhoca*$^{\Delta ATG}$ mutants at 55hpf no significant differences are measured. **(F)** Quantification of heart size in WT, zygotic and maternal-paternal-zygotic *rhoca*$^{\Delta ATG}$ mutants at 55hpf, MPZ *rhoca*$^{\Delta ATG}$ mutants have a significant reduction in heart area compared to WT. Ventral views. B, C, E, F: Median with interquartile range, Kruskal-Wallis, Dunn's multiple comparisons, ns: not significant, ***: $p<0.001$.

7.1.3 Loss of *rhoca* does not affect *rhocb* expression

Whilst both *rhoca* alleles are predicted to result in loss of functional Rhoca protein (Figure 7.2B, C) it is possible that *rhocb*, the paralog of *rhoca* (Salas-Vidal et al., 2005), may functionally compensate for loss of *rhoca*. NMD-induced genetic compensation (El-Brolosy et al., 2019) may be functioning in the *rhoca*^{ins10} allele, which could explain the less severe reduction in heart size in *rhoca*^{ins10} MPZ mutants compared to *rhoca*$^{\Delta ATG}$ MPZ mutants as the *rhoca*$^{\Delta ATG}$ allele is not predicted to activate genetic compensation (Figure 7.4C). Alternatively, coincident expression of *rhocb* with *rhoca* in the heart may be sufficient to partially rescue the heart size phenotype. Supporting this, Rhoca and Rhocb proteins are highly similar (Figure 7.5A) suggesting functional redundancy could be likely.

Although *rhocb* is expressed more ubiquitously throughout the embryo than *rhoca*, similar to *rhoca, rhocb* is expressed throughout the heart at 24hpf (Figure 7.5B, arrowheads) and becomes restricted to ventricular and atrioventricular canal tissue by 55hpf (Figure 7.5C). *rhocb* expression is unchanged in *rhoca* mutants at 55hpf (Figure 5D-E''), however expression of *rhocb* in the same domain in the heart as *rhoca* could explain the absence of a more severe phenotype in *rhoca* mutants.

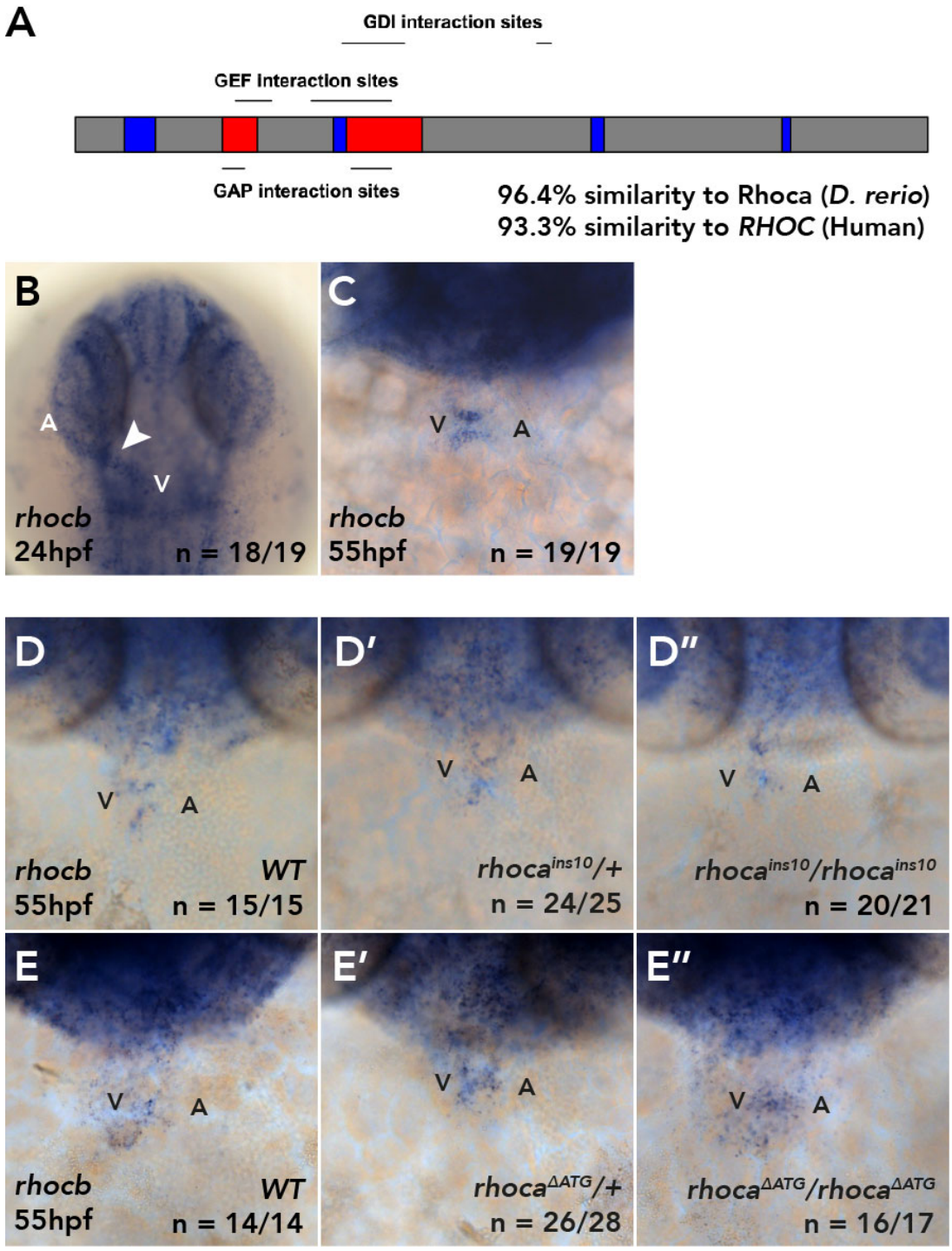

Figure 7.5. *rhocb* is expressed in the heart and expression is not altered by loss of *rhoca*.

Characterisation of *rhocb* expression pattern during heart looping morphogenesis and in rhoca mutants by mRNA *in situ* hybridisation. **(A)** Schematic of *rhocb* structure based on UniProt accession number Q6DHE8. Zebrafish Rhocb protein shares 93.4% amino acid similarity to Human RHOC and 96.4% amino acid similarly

7.1.4 Generation and characterisation of *rhocb* CDS mutants

To test whether *rhocb* function is required for cardiac morphogenesis or compensates for the loss of *rhoca*, CRISPR-Cas9 mutagenesis of the *rhocb* locus was performed in a WT background (Figure 7.6A). Two alleles of *rhocb* were isolated: *rhocb*$^{\Delta 20}$ (Figure 7.6B) and *rhocb*$^{\Delta 38}$, both of which are predicted to remove a splice acceptor site and cause the incorrect splicing of the second intron from the *rhocb* pre-mRNA, resulting in intron inclusion and a subsequent frameshift (Figure 7.6B). Founders transmitting the mutations were outcrossed to *rhoca*$^{\Delta ATG}$ heterozygous adults (predicted to be the more severe *rhoca* allele based upon the MPZ cardiac size phenotype (Figure 7.4F)), to generate double *rhoca*; *rhocb* heterozygous carriers.

To determine whether *rhocb* functionally compensates for loss of *rhoca*, *rhoca*; *rhocb* double heterozygous carriers were incrossed and heart morphology in the resulting embryos characterised at 55hpf and 72hpf by *myl7* expression (Figure 7.7). As described previously, loss of *rhoca* alone does not affect cardiac looping (Figure 7.3C, F) and additionally, loss of *rhocb* function either alone or in combination with loss of *rhoca* does not impact upon heart looping at either 55hpf or 72hpf (Figure 7.7I, J). Furthermore, no significant change is observed in *myl7* area at either 55hpf or 72hpf upon loss of either *rhocb* alone, or in combination with *rhoca* (Figure 7.7K,

Figure 7.5 continued.

to Zebrafish Rhoca. Blue: G boxes, Red: Switch domains. **(B-C)** *rhocb* is expressed throughout the linear heart tube at 24hpf (B, arrowhead) and at 55hpf *rhocb* is expression is restricted to atrioventricular canal. **(D-D'')** *rhocb* expression is unchanged between WT (D) and *rhoca*^{ins10} heterozygous (D') or *rhoca*^{ins10} homozygous mutants (D'') at 55hpf. **(E-E'')** *rhocb* expression is unchanged between WT (E) and *rhoca*$^{\Delta ATG}$ heterozygous (E') or *rhoca*$^{\Delta ATG}$ homozygous mutants (E'') at 55hpf. B: dorsal view. C-E'': ventral views. V: ventricle, A: atrium.

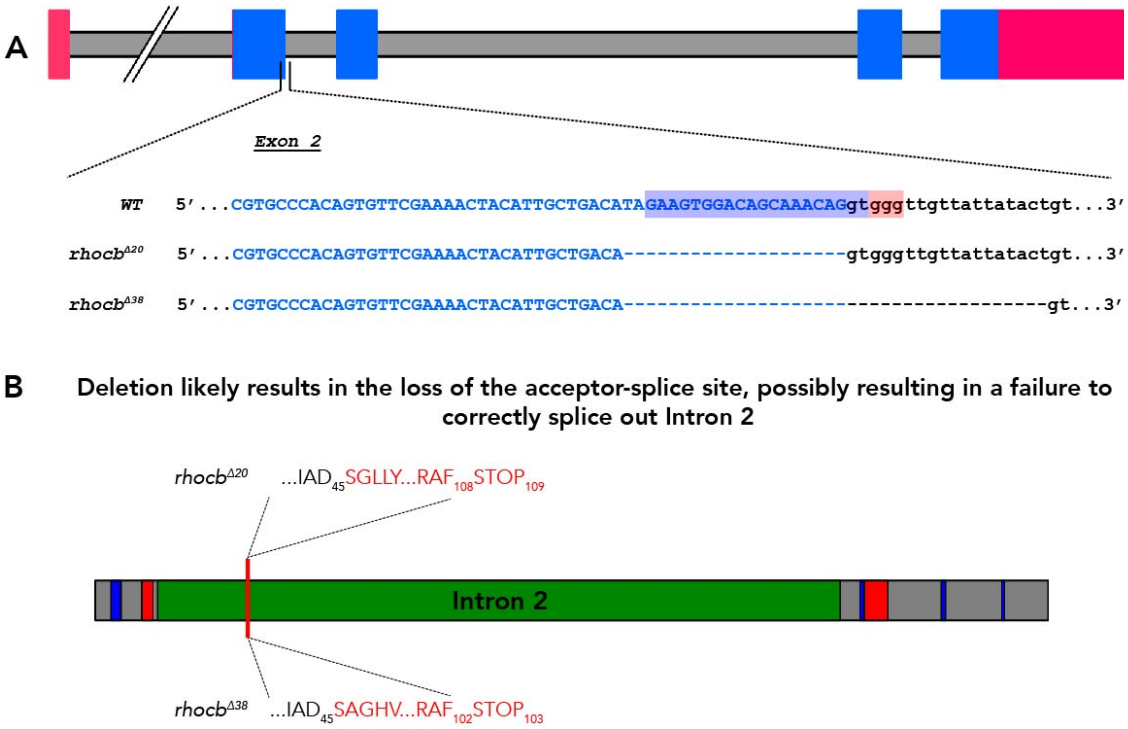

Figure 7.6. Generation of *rhocb* coding sequence mutants by CRISPR-Cas9 mutagenesis.

Mutagenesis strategy and predicted impact on Rhocb protein **(A)** Schematic of *rhocb* genomic DNA based on danRer10/GRCz10, Oblique cut-line: 50kbp, Red: non-coding DNA, Blue: coding DNA, Grey: intronic DNA. A single gRNA targeting Exon 2, spacer highlighted in blue, PAM highlighted in red was injected and two mutations were identified. **(A')** *rhocb*$^{\Delta 20}$ mutation results in loss of the last 20bp of Exon 2. **(A'')** *rhocb*$^{\Delta 38}$ deletes last 20bp of Exon 2 and the first 18bp of Intron 2. (B) Predicted impact of each *rhocb* allele on the Rhocb protein (UniProt Q6DHE8). The deletion in both alleles likely results in the loss of the acceptor-splice site, possible resulting in a failure to correctly splice out Intron 2 (green). This results in the first 45 amino acids of the Rhocb protein being unaffected, followed by an altered amino acid sequence and a premature termination codon at amino acid 109 for *rhocb*$^{\Delta 20}$ and amino acid 103 for *rhocb*$^{\Delta 38}$.

L). Taken together, the absence of embryonic heart morphology defects in either single or double *rhoca*; *rhocb* mutants or *rhoca* MPZ mutants suggests that *rhoca* and *rhocb* are not required for heart morphogenesis.

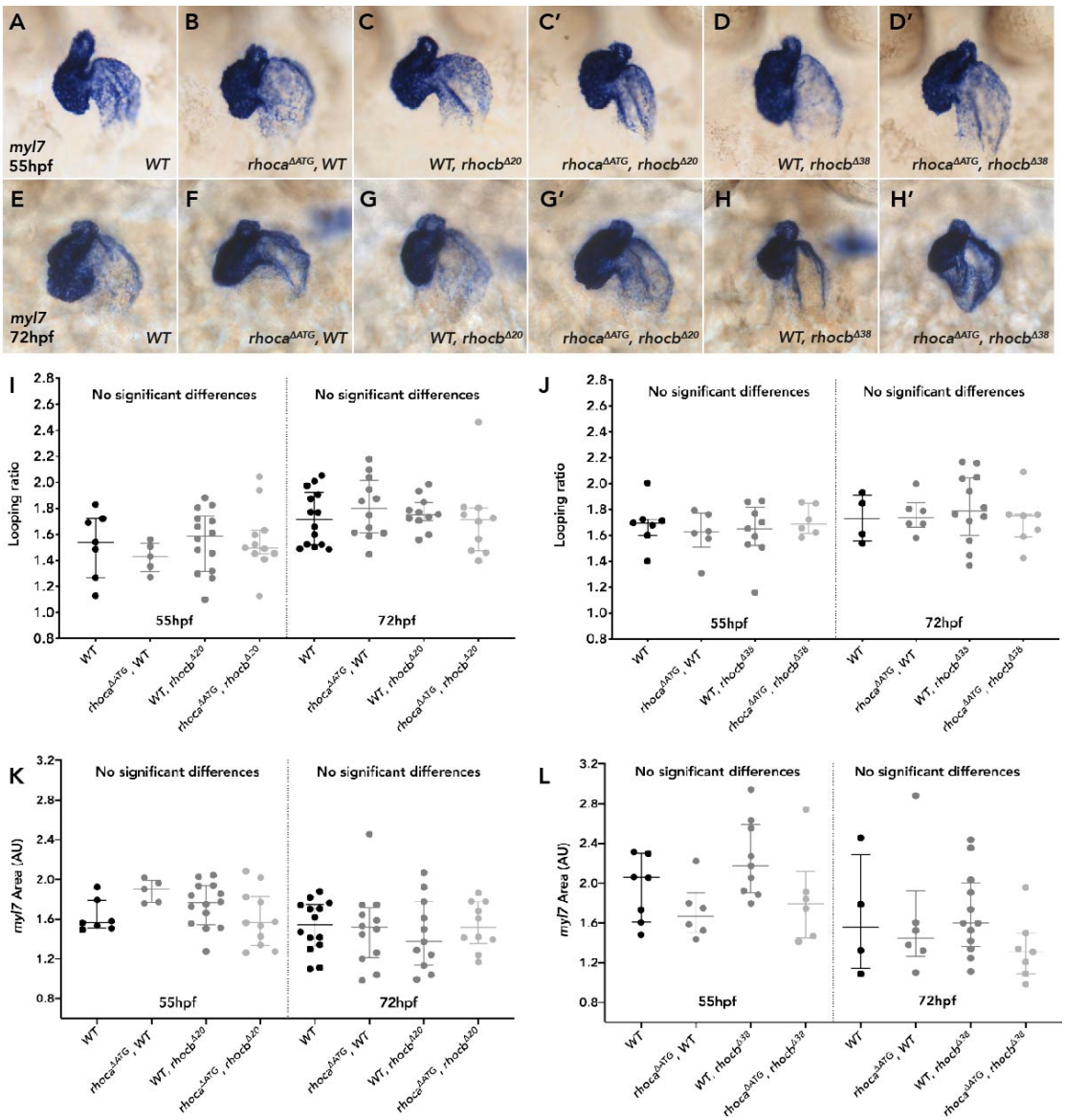

Figure 7.7. *rhoca* and *rhocb* are dispensable for early heart morphogenesis.

Quantitative analysis of heart looping and heart size in single and double *rhoca*; *rhocb* mutants at 55hpf and 72hpf. **(A-D')** Representative images of *mRNA in situ* hybridisation analysis of *myl7* at 55hpf to examine heart morphology in WT (A), *rhoca*$^{\Delta ATG}$ homozygous mutants (B), *rhocb*$^{\Delta 20}$ homozygous mutants (C), *rhoca*$^{\Delta ATG}$; *rhocb*$^{\Delta 20}$ double homozygous mutants (C'), *rhocb*$^{\Delta 38}$ homozygous mutants (D), *rhoca*$^{\Delta ATG}$; *rhocb*$^{\Delta 38}$ double homozygous mutants (D'). **(E-H')** Representative images of mRNA *in situ* hybridisation analysis of *myl7* at 72hpf to examine heart morphology in WT (E), *rhoca*$^{\Delta ATG}$ homozygous mutants (F), *rhocb*$^{\Delta 20}$ homozygous mutants (G), *rhoca*$^{\Delta ATG}$; *rhocb*$^{\Delta 20}$ double homozygous mutants (G'), *rhocb*$^{\Delta 38}$

7.1.5 Loss of *rhoca* does not affect cardiac size in adults

Whilst *rhoca* is non-essential for embryonic development (Figure 7.3, 7.4, 7.7) it is possible that *rhoca* function may be necessary later in development and that adult *rhoca* mutants, although viable, may present with cardiac abnormalities, particularly in size, given the potential role in regulating embryonic heart size. Hearts were dissected from adult fish either heterozygous or homozygous for *rhoca*^{ins10} or *rhoca*$^{\Delta ATG}$ and the ratio of heart mass to body mass calculated (Figure 7.8). At 2 years old the hearts of *rhoca* mutants looked grossly normal, and no significant difference were observed in heart mass to body mass ratio between homozygous mutants and heterozygous siblings (Figure 7.8), suggesting that *rhoca* is not required in the embryo or adult zebrafish for heart form.

Figure 7.7 continued.

homozygous mutants (H), *rhoca*$^{\Delta ATG}$; *rhocb*$^{\Delta 38}$ double homozygous mutants (H'). **(I, K)** Quantification of heart looping ratio (I) and heart area (K) in embryos obtained from *rhoca*$^{\Delta ATG}$; *rhocb*$^{\Delta 20}$ double heterozygous incross at 55hpf and 72hpf. No significant differences in looping ratio or heart area are observed. **(J)** Quantification of heart looping ratio and heart area (L) in embryos obtained from *rhoca*$^{\Delta ATG}$; *rhocb*$^{\Delta 38}$ double heterozygous incross at 55hpf and 72hpf. No significant differences are observed. A-H': ventral views. I-L: Median with interquartile range, Kruskal-Wallis, Dunn's multiple comparisons.

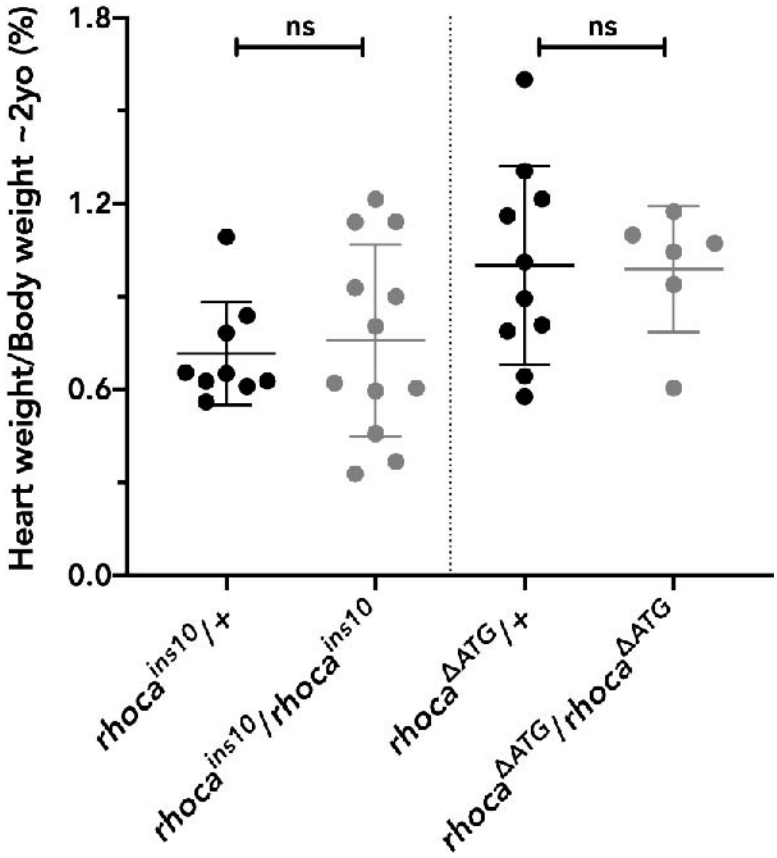

Figure 7.8. Loss of *rhoca* does not impact adult heart size.

Comparison of heart weight expressed as a percentage of body weight in adult *rhoca* heterozygous and homozygous mutants, both obtained from a *rhoca* heterozygous incross. No significant differences are present between homozygous mutants and their respective heterozygous siblings. Arithmetic Mean with Standard Deviation, Brown-Forsythe and Welch ANOVA, ns: not significant.

7.2 Discussion

The family of small Rho GTPases have multiple roles within the cell, with the most well-defined being the regulation of actin cytoskeleton organisation during cell migration, a process requiring correct intracellular responses to the extracellular environment (Heasman and Ridley, 2008; Sit and Manser, 2011). Using a reverse genetic screen approach based on spatial transcriptomics, *rhoca* was identified as a candidate Rho GTPase expressed in the heart during early heart tube morphogenesis.

Subsequent ISH expression analysis validated *rhoca* as a candidate gene exhibiting similar spatiotemporal expression dynamics to the Laminin and integrin subunits identified in Chapter 3. *rhoca* is initially expressed throughout the linear heart tube and expression is gradually restricted to ventricular and atrioventricular tissue (Figure 7.1). Loss of *rhoca* and/or *rhocb* does not impact cardiac morphogenesis, supporting a previous observation that whilst *rhoca* and *rhocb* are required for vascular integrity in the trunk (Hoeppner et al., 2015), they are not required for development of the heart. Further supporting that *rhoca* and *rhocb* are not required for development is the absence of a developmental phenotype following deletion of *RhoC* in mice (Hakem et al., 2005). However, in a murine model of breast cancer, although initial tumourogenesis was not affected, loss of *RhoC* resulted in a dramatic reduction in the number of secondary metastases present in the lungs (Hakem et al., 2005). Similarly, loss of *RhoB* in mice does not affect development, but leads to an increase in tumourogenesis under an inducible skin cancer model (Liu et al., 2001).

However, studies in mice models have proposed that RhoGTPase activity is important for heart development. Cardiac over-expression of Rho GDIα, an inhibitor of RhoGTPase function, abolishes heart looping and trabeculation by inhibiting cell proliferation through up-regulation of the cell cycle inhibitor *p21* (Wei et al., 2002). In cell culture, *RhoC* function has been shown to have a similar, but distinct effect on

cell cycle progression, independent of *p21*, whereby activation of RhoC by VEGFR2 results in increase of *CyclinD1* transcription, likely through increased nuclear translocation of β-Catenin (Hoeppner et al., 2015). This mechanism could provide a potential explanation for the reduction in heart size in *rhoca*$^{\Delta ATG}$ MPZ mutants. However, further characterisation as to whether overall heart size or a specific chamber is affected in *rhoca*$^{\Delta ATG}$ MPZ mutants is needed., This could be investigated through chamber specific quantification as carried out in Chapter 5.

More generally, it is tempting to speculate that loss of Rho GTPase function in the zebrafish may result in a change in the cell cycle during looping morphogenesis. This potential reduction in proliferative state would likely be attributed to the endocardium (Dietrich et al., 2014) the likely tissue of *rhoca* expression (Figure 7.1), however, the myocardium could also be affected, despite little or no proliferation observed in the myocardium during looping (Boer et al., 2012; Pater et al., 2009).

Importantly, the cardiac phenotype associated with over-expression of Rho-GDI is unlikely to be associated with the disruption of the function of a single RhoGTPase and as such is likely to be due to a broad spectrum of defects arising due to inhibition of multiple different Rho GTPases, and two studies in zebrafish suggest Rho GTPases play multiple roles during heart development. Zebrafish *rhoua*, part of the Cdc42 family of small GTPases (Salas-Vidal 2005), is required for heart looping morphogenesis, regulating the localisation of cell adhesion molecules at the atrioventricular canal (Dickover et al., 2014). Furthermore, morpholino knockdown of zebrafish *rhoab* (homolog of human *RHOA*) results in cardiac oedema, as well as a failure in convergent extension (Zhu et al., 2006). As both *lamb1a* and *lamc1* mutant also display defects in convergent extension (Parsons et al., 2002; Stemple et al., 1996), it is possible that the *rhoab* is the predominant Rho GTPase functioning during heart development which could transduce signals between the cells of the heart and the Lamb1a-Lamc1 containing Laminins in the cardiac jelly.

The data presented here demonstrates that *rhoca* and *rhocb* are not required for cardiac development and mouse models for *RhoB* or *RhoC* mutants also display no developmental phenotype. Yet interestingly, *RhoB* or *RhoC* mutant mouse embryonic fibroblasts display defects in cell motility or stress fibre formation respectively and these could be associated with the cellular stress associated with cell culture experiments (Hakem et al., 2005; Liu et al., 2001). It is possible that the loss of these genes is compensated for by a distinct, (non-paralogous, in the case of zebrafish) Rho GTPase. Based on current literature, an obvious candidate to examine in would be *RhoA*, for which no mouse or zebrafish stable mutant lines currently exist. In parallel, a number of potential approaches would begin to definitively assign no function to *RhoB* and *RhoC* in both mice and fish such as targeted promoter deletion (El-Brolosy et al., 2019) or in-frame deletions that target the active site of the protein, to abolish function but not result in degradation of the mutant allele mRNA. However, absence of a reported cardiac phenotype in zebrafish double morphants, supports the conclusion that *rhoca* and *rhocb* are dispensable for early cardiac development, and more broadly embryogenesis.

8. Discussion

Despite the focus of much investigation since its first description in the chick by Patten in 1922, heart looping has remained a complex morphogenetic process that remains poorly understood relative to other aspects of vertebrate heart development. In particular, the role of the ECM/cardiac jelly which influences multiple aspects of the development has been under-investigated in how this promotes heart looping morphogenesis, despite early studies suggesting a requirement (Barry, 1948; Davis, 1924; Nakamura and Manasek, 1981). I have defined a number of novel roles for multiple ECM components in distinct aspects of heart development, establishing the cardiac jelly as a central controller of vertebrate heart development. Below I discuss my work in the wide context of ECM biology and the next steps in investigating how the cardiac jelly promotes heart development.

8.1 Cell-ECM signalling

The ECM provides structural cues and plays roles in signalling to tissues undergoing morphogenesis during development, including the heart. Defining the interactions between cells and their environment and subsequent outcomes at both the cellular and tissue level is important in understanding how heart looping morphogenesis is achieved. I have shown that Lamb1a-Lamc1-containing Laminin isoforms are required to limit heart size during heart development and that Lamc1-containing Laminins are necessary for heart looping to occur (Chapters 3, 5). I have also identified a number of Laminin-binding integrins expressed in the heart during the same time frame as Laminin subunit expression. Previous work in zebrafish has identified that Laminins and *integrin linked kinase* (a downstream effector of integrin signalling) function together/genetically interact in heart development (Knoll et al., 2007) suggesting that the integrins I have identified could bind these Lamc1-

containing Laminin isoforms and transduce the signal to bring about correct cardiac morphogenesis.

The spatiotemporal dynamics of integrin expression during heart looping may help shed light on the tissue layer which responds to the Laminin as well as the time at which Laminin-integrin signalling may be playing its role. At 30hpf, *itga3b* and *itga7* are clearly expressed in the heart, whilst at 55hpf *itga7* expression is absent, but *itga3b* and *itgb1a* persist. Similar temporal shifts in integrin expression are observed in mice, although at later stages where at E13.6, *Itga5* and *Itga6* are expressed in ventricular and atrial cardiomyocytes respectively (Wiencierz et al., 2015), while at E15 all cells of the mouse heart express *Itgb1* and *Itga7*, alongside *Itga6* in the atrium, *Itga3* expression appears to be absent (Hierck et al., 1996). The highly dynamic expression of these genes suggest different Laminin-binding integrin complexes may play distinct roles in the maturation of the heart. Although the stages examined are not directly comparable to looping morphogenesis I characterised in Chapter 3, the combination of work in both zebrafish and mice suggest that both the composition of the ECM and the receptors which bind it are highly dynamic during heart morphogenesis. Furthermore, *lamb1a* mutants have enlarged atria at the time when Laminin and integrin expression appears to be broadly absent from the atrium, suggesting that these genes play an early role in setting up necessary processes which have impacts later in heart development.

The changes in integrin expression during heart looping, together with the different windows in which *lamb1a* and *lamc1* are required for proper cardiac development may provide insights into the specific interactions between complexes. For example, during early morphogenesis of the tube, the activity of Itga7 may be required to promote heart looping through binding of Lamc1-containing trimers, and as heart morphogenesis proceeds, a shift to Lamc1-Itga3b binding may be required to limit heart size, possibly by regulating ERK signalling (Manohar et al., 2004; Missan et al., 2015). There is some support for distinct temporal roles for specific integrins during

heart development in the literature. In rat cardiomyocytes isolated at the foetal-to-neonatal transition, changes in integrin subunit expression appears to follow/occur when cells actively withdraw from the cell cycle (Maitra et al., 2000). Spatial restriction in expression of integrin α subunits could represent the need to direct changes in proliferative capacity during heart morphogenesis. During heart looping, little or no myocardial proliferation occurs (Boer et al., 2012; Pater et al., 2009), however when trabeculation begins at E9.5 in the mouse, cell proliferation is increased specifically in the ventricles (Boer et al., 2012) which could be orchestrated through changing Laminin-integrin interactions

Another, well characterised Laminin-receptor interaction is with the Dystroglycan complex which can regulate ERK signalling in the heart (Bassat et al., 2017) suggesting another possible mechanism of increased heart size in *lamb1a* mutants. In this context, the YAP/TAZ signalling pathway is downstream of Dystroglycan activation (Bassat et al., 2017). The recently proposed biomechanical cross talk between the endocardium and myocardium during chamber ballooning involving YAP will likely involve the force transmission through ECM receptors (Bornhorst et al., 2019). Thus, increased size of Lamb1a-Lamc1 hearts could suggest that Laminins or their interacting partners are involved in this mechanism, possibly through regulation of YAP (Bornhorst et. al. 2019).

Alternatively, a careful balance between different integrin signals mediated through binding multiple ECM components may promote heart morphogenesis and/or restrict heart size, such as a balance of signalling through Laminin and Fibronectin-binding integrins converging to regulate levels of ERK signalling. Further work examining the expression of *itga3b* (and its paralog *itga3a*), *itga6a* and *itga7* throughout cardiac looping and trabeculation stages, in combination with analysis of proliferation dynamics may provide some insights into the requirement for dynamic integrin switching. Combining this characterisation with phenotypic analysis of heart development in the relevant mutants/published morphants of these genes and

comparing cardiac phenotypes with those observed upon loss of *lamb1a* and *lamc1* will also help to define the Laminin-Integrin signalling axis which regulates heart shape and size.

In addition to the proposed biomechanical role for HA and its interactions with the cells of the heart (Chapter 6), HA also has the ability to signal through membrane-localised receptors. In particular an HA signalling axis is necessary for valve development, where binding of HA to CD44 together with Erbb2 activates the small GTPase Ras, which is required for EndoMT (Camenisch et al., 2000). CD44 mouse mutants have been reported to have no obvious phenotypes (Protin et al., 1999), however a number of other HA receptors are encoded for, such as RHAMM, and whether genetic compensation occurs in the CD44 mutants or functional redundancy exists between receptors was not examined. Whether Hapln1a functions to regionally sequester HA in the ECM and prevent activation of HA-signalling receptors remains unclear and warrants further investigation. However, a more physical role for regionalised ECM expansion in driving asymmetric cardiac morphogenesis may be predicted based on similar roles in the developing chick gut (Sivakumar et al., 2018).

8.2 ECM and biochemical interactions

Signalling between the myocardium, endocardium and surrounding mesoderm is crucial for the co-ordination of heart development. The increased heart size *lamb1a* and *lamc1* mutants suggests that defects in this signalling could result in increased addition from the second heart field. One class of signalling molecule involved in SHF addition that has the potential to be highly mislocalised by changes to the constituents of the ECM is the Latent TGF-β Binding Protein (LTBP) family.

LTBPs are processed together with the TGF-β ligand forming a large latent complex (LLC) which when secreted is able to associate with other ECM molecules, most

commonly Fibronectin or Fibrillin through non-covalent interactions, sequestering the TGF-β ligand (Robertson et al., 2015). Upon cleavage of the LTBP, the TGF-β signal is then able to be received by cells, thus LTBPs uncouple ligand secretion and ligand action. Multiple LTBPs are expressed in the human heart (Davis et al., 2014), and the family member with the best characterised role in heart development in zebrafish is *ltbp3*. *ltbp3* is expressed at the onset of heart looping morphogenesis in the SHF at the arterial pole, and loss of *ltbp3* or TGF-β function during SHF addition results in a loss of arterial structures (Zhou et al., 2011). Changes in organisation to the ECM through loss of Laminin isoforms may indirectly affect organisation of the ECM and thus the ability of LTBPs to correctly partition the TGF-β signal. This may result in alterations to the temporal activity of the ligand either by premature activation, or delay in receipt of the signal due to inaccessibility of the LTBP for cleavage. As such, examining whether the activity or localisation of LTBPs is altered, leading to increased TGF-β signalling in *lamb1a* and *lamc1* mutants, may help to examine the molecular basis for increased heart size in these mutants.

SHF addition requires a highly conserved Fgf8 signalling axis and FGF signalling is sensitive to ECM composition, particularly to changes in Heparan Sulfate Proteoglycan (HSPG) content (Lin, 2004; Zhang et al. 2015). HSPGs are required for collective cell migration in the zebrafish lateral line, as loss of HS synthesis or inhibition of sulfation leads to loss of FGF signalling, increased Wnt responsiveness and a failure in the correct formation of the neuromasts (Venero Galanternik et al., 2015). Similarly, in *Drosophila*, loss of the enzyme required for HS synthesis results in a loss of tracheal cell migration, phenocopying loss of the FGF chemokine (Lin et al., 1999). Loss of *Ext1 (Exostosin glycosyltransferase 1)*, a major HS synthesising enzyme disrupts FGF signalling and cell proliferation in the SHF in mice (Zhang et al., 2015). *glypican4* (a class of cell membrane-localised HSPG) mutant zebrafish have a reduction in cell number in the heart at 2dpf, due to a failure of SHF addition where both BMP and Wnt signalling are altered (Strate et al., 2015). Although FGF signalling was not examined and the SHF appeared correctly specified, it seems

likely that the interaction between FGF signalling in deploying the SHF was also affected by loss of *glypican4* (Strate et al., 2015; Superina et al., 2014; Venero Galanternik et al., 2015).

Loss of *lamb1a* or *lamc1* could result in a mis-regulation of HSPG localisation or activity, which could impact on FGF signalling and result in an increase in heart size. *Lamb1* and HSPGs interact in the ECM, where they are minimally required in cell culture, interacting together to polarise epithelial cells and drive lumen formation in embryonic lung cells (Schuger et al., 1996). *lamc1* also regulates HSPG function, where it appears to pattern the HSPGs to regulate BMP signalling (Dolez et al., 2010). Loss of *lamc1* in zebrafish results in an almost total loss of HSPGs and is associated with an increase in BMP responsiveness resulting in changes to development of the myotome (Dolez et. al. 2010).

Together these studies demonstrate the high degree of interconnectivity between signalling ligands and ECM components during development. This suggests that expansion of BMP or FGF signalling though perturbation to the HSPG in the cardiac jelly may underlie the increased heart size in Laminin mutants, possibly through increased SHF addition.

8.3 Cardiac function and ECM

As well as biochemical interactions between the two tissue layers of the heart, there are also biomechanical interactions that are necessary for heart looping morphogenesis. Unique to the development of the heart is that form and function are interdependent and the sensation of blood flow is critical for correct cardiovascular development (Heckel et al., 2015; Hiermeier and Männer, 2017; Samsa et al., 2015; Vermot et al., 2009). In particular, the zebrafish model system has been invaluable for investigating how blood flow regulates the developmental mechanisms required for valve development and this has been informative in

investigating how expression of some ECM genes can be regulated by cardiac function.

Blood flow sensation through activation of *klf2a* expression at the atrioventricular canal correlates with *fn1b* expression between 48hpf-56hpf (Steed et al., 2016). Loss of *klf2a* function leads to absence of *fn1b* expression in the valve, and mutations in *fn1b* results in abnormal valve development through loss of EndoMT (Steed et. al. 2016). This highlights the coupling of blood flow to the specialisation of the valve ECM. I have also identified a role for blood flow in promoting the expression of ECM genes in the heart; *lamb1b* and *lama4* expression in the endocardium is blood flow-dependent, whilst endocardial expression of *lamb1a* and *lamc1* also appear to be regulated by blood flow (Chapter 3). Since *lamb1b* expression is highly reminiscent of *fn1b* at the valve, and *lamb1b* expression is also Notch-dependent, this together would suggest that a blood flow-Klf2a-Notch signalling axis promotes localised ECM synthesis at the valve. This could represent a potential intrinsic mechanism of how the cardiac ECM is patterned to generate regionalised changes in cell shape and size as heart looping proceeds. Whilst the specific integrin receptor subunit for Fibronectin, *itga5*, is initially expressed throughout the heart at 30hpf, its expression becomes predominantly localised to the ventricle and AVC at 55hpf (Chapter 3). However, as *fn1b* is only expressed at the AVC (Steed et. al. 2016), this localised ECM specialisation likely limits the action of Itga5 to the AVC, where through focal adhesions it drives endocardial cell migration during valve formation (Gunawan et al., 2019).

Another biomechanical role for the ECM in cardiac morphogenesis could lie in regulating the response of the endocardium to blood flow, as heart size in *lamb1a* heterozygous mutant embryos appear to be sensitised to increased blood viscosity (Chapter 5). One mechanism driving this could be that loss of Laminin function results in an increased sensitivity to shear stress. This model is supported by studies using artery explants, which demonstrates that loss of LN-511 in endothelial cells

leads to a hypersensitive response to increasing shear stress (Russo et al., 2016). Together this shows how important considerations of both form and function are in relation to patterning of the ECM and more broadly heart development.

8.4 Regulation of ECM synthesis

Tightly-coordinated spatiotemporal control of ECM-related genes is evident during cardiac development both in the work presented here and other studies (Chew and Lennon, 2018; Mouw et al., 2014; Schéele et al., 2007). Highlighted by FGF and HSPGs, signalling molecules and ECM synthesis are interdependent on one another (Galaneetrik 2015), making the dissection of pathways which directly regulate ECM genes more challenging.

I have demonstrated differential regulation of specific Laminin subunit expression during heart development. Expression of myocardial Laminins such as *lama5* are blood flow and Notch independent, whilst expression of *lama4* and endocardial expression of *lamb1a* and *lamc1* appear to be blood flow-dependent but Notch independent, which should be confirmed through fluorescent *in situ* hybridisation following *tnnt2a* knockdown. If a blood-flow dependent, Notch-independent mechanism regulating Laminin expression is active in the heart, the most obvious candidate pathway would be BMP signalling as links between blood flow and BMP signalling have been established in zebrafish, with myocardial expression of BMP ligands proposed to be received by the endocardium where they regulate endocardial ballooning and proliferation (Dietrich et al, 2014). In the fin fold of the zebrafish, *lama5* expression is required for basement membrane assembly and together with *lamb1a* and *lamc1* is regulated by canonical Wnt signalling (Nagendran et al., 2014; Webb et al., 2007). Wnt signalling is active during heart development, where it is required upstream of BMP signalling to regulate development of the atrioventricular valve (Goddard et al., 2017; Verhoeven et al., 2011). Treatment with BMP inhibitors or other chemical inhibitors such as for Wnt

will help to identify the necessary signals which regulate expression of the Laminin genes.

Thus, for many of these Laminin components it is unclear how their expression in the heart is regulated, both in terms of how it is induced, but also how expression subsequently becomes spatially restricted as the heart undergoes morphogenesis. Equally important as the initiation of Laminin expression in the heart is the restriction of expression from the atrium (and also ventricle for *lamb1b*) during heart looping. There is very little data from which potential mechanisms could be suggested as to how expression of Laminins is altered during heart looping, however insights from examining regulation of *lamb1b* provide some. *lamb1b* expression is dependent on flow and downstream of this Canonical Notch signalling (Samsa et al., 2015; Vermot et al., 2009) (Chapter 3). Importantly, the expression domain of *lamb1b* is not expanded upon loss of Notch activity, suggesting that Notch activity is not required to restrict *lamb1b* expression to the AVC, but is needed to maintain expression. This could suggest that broadly, restriction of Laminin expression may be guided by the activity of chamber specific signalling. The most obvious candidate pathway for ventricular-specific expression is Neuregulin-Erbb signalling which is required from 2dpf for trabeculation (Liu et al., 2010). This could suggest that, as the heart begins to take shape, the early role of Laminin to promote heart looping morphogenesis and restrict heart size is switched to regulate trabeculation. Separately, *lamb1b* is regulated by a distinct pathway which may have evolved following genome duplication, suggesting why *lamb1b* is dispensable for development.

I have demonstrated that the expression of *hapln1a* in the posterior of the heart disc is independent of laterality cues (Chapter 6), further adding to the intrinsic model of heart looping morphogenesis (Derrick et al., 2019; Grimes et al., 2019; Lombardo et al., 2019; Manning and McLachlan, 1990; Noël et al., 2013). One candidate transcription factor that may regulate the expression of *hapln1a* in the cardiac disc is *meis2b*, which overlaps with *hapln1a* (Guerra et al., 2018). Examining the expression

of *hapln1a* in *meis2b* mutants at disc stage may provide a link between these two genes, although how the asymmetric expression of *meis2b* is established in the heart disc remains unclear. Antero-posterior patterning of tissues during development is commonplace, the archetypical mechanism being through opposing gradients of FGF and Retinoic Acid (RA) signalling, exemplified by somitogenesis (Aulehla and Pourquié, 2010; Bertrand et al., 2015) and in the otic vesicle (Maier and Whitfield, 2014). Both RA and FGF signalling are utilised in distinct aspects of heart development, with one of the earliest roles for RA being the restriction of the size of the pool of cardiac progenitors (Keegan et al., 2005). During formation, the heart disc is located close to the developing otic vesicle and rhombomere 4 which are sources of FGF and RA ligands (Grandel et al., 2002; McCarroll and Nechiporuk, 2013; Nechiporuk et al., 2006), suggesting that these pathways may be able to influence cardiac patterning in addition to otic patterning. Pharmacological inhibition of FGF or RA signalling pathways following progenitor specification but before heart disc formation would begin to investigate the mechanism by which anterior posterior asymmetry in the heart disc is established.

I have shown that during heart development, expression of the HA synthase *has2* is highly dynamic between 21hpf and 30hpf, with initially myocardial expression in the disc and subsequently endocardial expression in the heart tube which is then restricted to the developing atrioventricular valve (Chapter 6). In mice at E8.5 *Has2* expression is present in the myocardium and endocardium of the heart, but just a day later, *Has2* expression is reduced in the myocardium, remaining only at the AVC myocardium, whilst *Versican* expression is retained in the myocardium throughout early looping (Camenisch 2000). These expression patterns could suggest a level of conservation in the regulation and restriction of *has2* expression during cardiac development between zebrafish and mice.

Valve development and specification is a highly complex series of genetic interactions best characterised in mouse. BMP signalling at regions specified to

become non-working myocardium results in *Tbx2* expression at the IFT, AVC, inner curvature and OFT which then out-competes the pan-cardiac expressed *Tbx5*, to form a complex with Nkx2.5 (Habets et al., 2002). Ultimately, this defines regions of the heart that are immature (future valve), or mature (marked by *nppa*/*ANF*) myocardium. A reciprocal interaction between *nppa* and *tbx2b* has been identified in zebrafish through deletion of the *nppa*/*nppb* gene cluster, leading to an expansion of *tbx2b* and *has2* into the atrium, associated with expansion of atrial cardiac jelly at 2dpf (Grassini et. al. 2018). This expansion can be rescued by morpholino-mediated knockdown of *bmp4*, suggesting that Nppa and Nppb act to restrict the valve programme through BMP4 signalling to confine *tbx2b* and *has2* expression to the AVC (Grassini et. al. 2018). Together this might suggest that *tbx2b* directly drives expression of *has2* during heart development, a hypothesis supported by one study where misexpression of *Tbx2* in mouse using a *Myh6* promoter correlated with a strong up-regulation of *Has2* (Shirai et al., 2009). However, *tbx2b* is expressed in the myocardium whilst in zebrafish, *has2* is expressed in the endocardium, how then could *Tbx2b* activity in the myocardium bind the *has2* promoter in the endocardium?

It is possible that early expression of *Tbx2* in the cardiac crescent (Harrelson et al., 2004) and potentially *tbx2b* the heart tube in zebrafish prior to looping (Sedletcaia and Evans, 2011) may promote myocardial *has2* expression driving HA deposition prior to heart looping, and that later the spatial disconnection of endocardial *has2* and myocardial *tbx2* expression results from a distinct genetic programme. Alternatively, zebrafish may also exhibit *tbx2b*-dependent myocardial expression of *has2* at 30hpf (although this seems unlikely to occur), or that mice and zebrafish have distinct mechanisms of *has2* regulation during embryogenesis. *has2* is also regulated post-transcriptionally by *miR-23* a miRNA with highly specific restriction at the atrioventricular canal during valvulogenesis (Lagendijk et. al., 2011). Loss of *miR-23* results in an up-regulation of *has2* and marked increase in deposition of HA (Lagendijk et. al., 2011).

Separately, a number of studies have reported that failure to restrict *has2* expression and associated expansion of the cardiac ECM result in looping defects (Grassini et al., 2018; Lagendijk et al., 2013, 2011; Patra et al., 2011; Shirai et al., 2009), suggesting that whilst restriction of these genes to the AVC is required for its development, restriction away from the chambers is also important to promote looping. Together, this supports that tight spatiotemporal control of ECM composition during heart development is critical in facilitating specialisation of different regions of the heart as they take on more distinct roles. This would therefore suggest that as heart development proceeds, the ECM must undergo continuous, dynamic remodeling achieved through temporal and tissue-specific expression patterns of these genes.

8.5 The dynamic ECM as a driver of heart development

Whilst this work has focused on components of the ECM and some enzymes required for synthesis of specific ECM constituents, co-ordination of ECM degradation is also necessary during development. Three independent forward genetic screens in zebrafish have identified the cell surface hyaluronidase *cemip2 (cell migration inducing hyaluronidase 2,* formerly *tmem2*) as a key regulator of cardiovascular development (Angelis et al., 2017; Smith et al., 2011; Totong et al., 2011). Loss of *cemip2* results in a dramatic loss of ISVs and a reduction in pERK-positive endothelial cells (Angelis et al., 2017). This phenotype can be recovered through injection of Hyaluronidase (HA'se) or shorter HA fragments into *cemip2* mutants suggesting that degradation of HA acts via ERK signalling to drive angiogenesis (Angelis et al., 2017).

Heart looping is profoundly affected in *cemip2* mutants, characterised by almost linear heart tubes with an absence of constriction at the atrioventricular canal (Totong et. al. 2011, Smith et al., 2011). Multiple genes involved in the development

of the AV valve show a dramatic expansion in *cemip2* mutants, including *bmp4, has2,* and *notch1b* as well as Notch downstream genes and expanded Wnt activity (Hernandez et al., 2019; Smith et al., 2011; Totong et al., 2011). In line with its role in HA degradation, loss of *cemip2* results in an expanded ECM on both sides of the myocardium (Hernandez et al., 2019), an increase in HA and also CS staining (Hernandez et al., 2019). However, increase in HA could be due to the expansion of endocardial *has2* in *cemip2* mutants (Smith et al., 2011), making a direct link between loss of hyaluronidase activity in the heart, increased cardiac jelly, and abnormal looping morphology difficult to directly link.

As in the ISV model, although not as successfully, hyaluronidase treatment is able to recover the *cemip2* phenotype, suggesting that degradation of the HA-containing ECM is required for aspects of heart looping morphogenesis (Hernandez et al., 2019). Most interestingly, HA'se treatment could rescue the expansion of Wnt activity to levels comparable to siblings, further demonstrating the relationship between the ECM and signalling pathways (Hernandez et al., 2019). Wnt activity lies upstream of BMP in specification of the AVC in both mice and fish (Hurlstone et al. 2003; Wang et al. 2013; Verhoeven et al., 2011), and *has2* expansion in *cemip2* mutants is recovered by knockdown of *bmp4* (Smith et al., 2011). Together these data suggest a model whereby HA degradation by Cemip2 in the chambers limits Wnt and BMP activity to the AVC resulting in restriction of *has2* expression to the AVC.

How the activity of Wnt could be limited remains unclear, one suggestion is through restriction of expression of the Wnt ligand to the valve, similar to expression of *wnt9b* in mice and zebrafish (Goddard et al., 2017). This also suggests that the enrichment of CS at the valve precursor (Peal et al., 2009) despite an absence of *chsy1* expression at 30hpf in the heart tube (Chapter 6) results from localised degradation by *cemip2*, rather than increased deposition as recently proposed (Hernandez et al., 2019).

This builds upon the model for the spatiotemporal role of PGs during heart development suggested by the time course of expression patterns in Chapter 6. Initially HA together with the expression of *hapln1a* in the posterior of the disc and asymmetric BMP activity across the left-right axis of the disc is required to drive heart jogging. At this stage, the HA laid down is required for heart looping, as inhibition of HA synthesis between 18-22hpf results in linear hearts at 48hpf (Derrick et al., 2019), and together with expression of *chsy1* and *vcana* at disc stage, would suggest that VersicanA-CS, linked to HA may be required for heart looping morphogenesis, in agreement with the *Has2* and *Versican* mutant mice (Camenisch et al., 2000;, Mjaatvedt et al., 1998) and also *Versican* mutant medaka (Mittal et al., 2019).

Following the initial stages of heart looping, the ECM subsequently undergoes regional remodelling, partially or wholly through the action of *cemip2*. This degradation of HA is required for proper restriction of Wnt, BMP and Notch signalling at the valve (Smith et al., 2011; Hernadez et al., 2019; Totong et al., 2011), which together with blood flow and *klf2a* activity promotes localised ECM synthesis at the AVC (Steed et al., 2016). Similarly, *has2* expression is restricted to AVC by *cemip2* (Smith et al., 2011) action where HA deposition is required for the development of the atrioventricular cushions (Camneisch et al. 2000), together with Vcana (Mjaatvedt et al., 1998; Yamamura et al., 1997) and potentially Hapln1a (Wirrig et al., 2007).

Whilst there appears to be a spatiotemporal disconnection between the role of HA synthesis during heart development (*has2* function required in the disc for the tube to loop) (Derrick et al., 2019), evidence shows that *cemip2* function is required to facilitate formation of the heart tube (Totong et al., 2011), although no expression analysis of *cemip2* at this timepoint has been carried out. Therefore, both *has2* and *cemip2* function during heart tube formation, which would suggest that HA

synthesised by *has2* is actively being degraded by *cemip2* during heart jogging. A number of theories could be possible to explain how these two opposing pathways could act to regulate heart tube formation. As *cemip2* activity is required to generate short fragments of HA (o-HA) which are required for ERK signaling (Angelis et al., 2017), degradation of HA may result in the activation of signal transduction pathways necessary to generate asymmetric movements in the disc. More generally, this mechanism of HA action makes the two separate functions of HA in the ECM (physical support and signalling) hard to uncouple. Secondly, the relative activities of *has2* and *cemip2* may be very different during tube formation compared to heart looping. It would therefore be expected that inhibition of HA synthesis allows HA degradation by *cemip2* to become the dominant factor and prevent heart looping morphogenesis. Finally, the pan-cardiac expression of *vcana* and posterior expression of *hapln1a* in the heart disc suggests that HA synthesised by Has2 is associated with Vcana and stabilised by Hapln1a and that this could prevent degradation of the posterior, future-left sided HA-ECM resulting in the expansion, supported by the reduction in Versican protein in Hapln1 mutant mice (Wirrig et al., 2007). This would place *hapln1a*, as the factor required to limit *cemip2* activity in the posterior of the heart disc, allowing the ECM expansion to occur which is then required to promote heart development. In fact, this may go so far to even suggest that left-sided expansion of the heart tube is not required for asymmetric morphogenesis, but the posterior expression of *hapln1a* prior to formation of the heart tube is the key event that drives heart looping morphogenesis, highlighting the importance of understanding the very early morphogenetic processes of heart development.

The exclusion of *vcanb* expression from the heart tube, but strong and specific expression at the arterial pole suggests that as in Medaka (Mittal et al., 2019) and mice (Kern et al., 2007; Mjaatvedt et al., 1998; Yamamura et al, 1997), Versican plays multiple roles during heart development. It would appear likely that following the teleost specific genome duplication, the roles of the ancestral single *Versican* gene

were divided between *vcana* (jogging, looping and valvulogenesis) and *vcanb* (SHF addition). Supporting a role for HA and its interaction with *Vcanb*, inhibition of HA synthesis during SHF addition results in a SHF addition defect (Noël, unpublished). These initial observations present an exciting avenue for further examining the role that the ECM plays in guiding cell migration during development.

Whilst many studies have focussed on the core protein, little work has examined the specific GAG attached to these and what role they play in heart development. Classically, CS is covalently linked to Versican proteins and the only study which has described a role for CS synthesis in heart development has been in zebrafish (Peal et al., 2009). Use of timed drug treatments ascribed the role of CS synthesis specifically to valvulogenesis based on loss of EndoMT markers (Peal et al., 2009). I have shown that *chsy1* expression is present in the cardiac cone at 21hpf but not the heart tube between 26-30hpf (Chapter 6) and suggest that early CS deposition is required for heart looping morphogenesis, which is later remodelled by *cemip2* during valve formation. Therefore, as the window of CS synthesis inhibition was very broad (between 7hpf and 48hpf) (Peal et al. 2009), it seems likely that this inhibition prevented the formation of the correct ECM environment at disc stage and therefore affected heart looping. This would then result in a secondary effect on the development of the valve, and loss of *vcana* and *tbx2b* expression in the hearts of embryos treated with the CS synthesis inhibitor (Peal et al., 2009) would support this idea. Together this supports that the interaction between valve specification and valve development is much more complex and is highly sensitive to the early events of heart development.

Rapid ECM remodelling is not only required for heart tube formation, looping morphogenesis and valve development. As maturation of the heart proceeds, the ventricular cardiac jelly undergoes a dynamic remodelling to build the trabeculae necessary for increased cardiac output in the adult (Liu et al., 2010, Monte-Nieto et al. 2018). As proposed in Chapter 6, the data from *myl7:hapln1a* injections

highlights potentially different spatiotemporal requirements for ECM in distinct processes of heart development. Whilst during early tube morphogenesis in zebrafish, the ECM of the ventricle is thin and uniform, as heart looping proceeds in mice the ventricular ECM undergoes localised expansion to form ECM bubbles during the sprouting and touchdown phases of trabeculation. The trabecular myocardium then invades the ECM bubbles as the trabeculae grow, and the ECM surrounding the trabecular myocardium eventually diminishes (Monte-Nieto et al., 2018). Interestingly during trabeculation, the production of the HA-rich ECM is dependent on Neuregulin signalling and limited by Notch signalling (Monte-Nieto et al., 2018). This is in contrast to the role of Notch signalling in ECM deposition during valve formation where loss of Notch results in a loss of cushion formation (Timmerman et al., 2004, Chi et al., 2007). This suggests that the signalling pathways regulating ECM synthesis are context dependent during heart development, most likely regulated by the effect of chamber (Tbx5) and non-chamber (Tbx2) transcription factors.

I have shown that during heart stages of heart morphogenesis, the atrium is more sensitive to perturbations in the composition of Proteoglycan-related ECM components, as over-expression of *hapln1a* in the atrium causes a more profound reduction in heart looping when compared to similar levels of ventricular over-expression (Chapter 6). As Hapln1a protein remains present in the atrial ECM until at least 55hpf, despite the loss of *hapln1a* mRNA expression from the atrium after 30hpf (Derrick et al., 2019), this would suggest that Hapln1a presence in the ventricular myocardium may cause premature and mislocalised expansion of the ECM which may impact on the building plan required for trabeculation, but not impact upon looping morphogenesis itself. However, light sheet imaging of the ventricle ECM compared to atrial ECM at 50hpf suggests that the constituents required for Hapln1a to bind and generate improper ECM expansion in the ventricle may not be present as the thin ventricular ECM may not contain sufficient HA to result in an expansion (Grassini et al., 2018). One could propose then, that spatial-

temporal restriction of ECM remodelling enzymes, in particular Hyaluronidases such as *cemip2*, which is expressed in the ventricle prior to the onset of trabeculation (Smith et al., 2011), is required to facilitate the close contact between the two ventricular tissue layers, which is later locally expanded, potentially by re-activation of *has2* in the trabecular myocardium (Monte-Nieto et al., 2018).

Whilst much focus is placed on the ECM of the ventricle during heart development, the role of the ECM in development of the atrium is remains understudied. Further characterisation of the atrial ECM at 72hpf using light-sheet imaging demonstrates that the left-sided expansion is maintained during heart maturation and this is dependent on *hapln1a* function (Derrick et al., 2019). A thin ventricular ECM can be reasoned as promoting close apposition of the cell layers to promote trabeculation (as discussed above), it could be possible that an expanded ECM may be required to prevent trabeculation from occurring in the atrium or that the later atrial webbing may require an ECM which is more capable of load bearing (Foglia et al., 2016). Examining cardiac function in *hapln1a* mutants, specifically the differences in the relative impacts on each chamber, together with overall morphology of the heart, may provide some clues as to the requirement for ECM regionalisation during heart development.

To answer some of these questions relating to the spatio-temporal role of the ECM, novel tools will be needed to identify how this is achieved. A promising technology is the tamoxifen-dependent Gal4-ERT transcription factor (Akerberg et al., 2014), which combines the spatial control of GAL4-UAS system from *Drosophila* together with the inducible nature of the Cre-ER system from mice, which could be applied to these questions. Together with a spatial promoter and a subtle UAS containing construct, genes such as a hyaluronidase (HYAL) could be placed under the control of the *hapln1a* promoter to generate *Tg(hapln1aBAC:Gal4-ERT), Tg(UAS:HYAL)* lines which would allow temporal expression of HYAL in the *hapln1a* domain to test the role for HA action at distinct points and regions of the heart during looping.

This technique could be further extended to examine the temporal requirement of a specific gene during development, when an earlier role may prevent later events being assayed independently, such as the role for *has2* in valve development or trabeculation. Under this mechanism, generation of a suitable BAC line that recapitulates endogenous expression of *has2* could be used to drive *has2* expression using the Gal4-ERT technique in *has2* mutant *(Tg(has2BAC:Gal4-ERT), Tg(UAS:has2)*). Induction of the *has2* phenotype would then be achieved by removal of the 4OHT (4-Hydroxytamoxifen) from the water at the necessary time point to examine the temporal role of the gene during the time period of interest.

Changes to the composition of the ECM during development of tissue is a common concept in tissue morphogenesis, best characterised in the glomerular basement membrane (GBM) of the kidney, where the Laminin composition changes from LN-111, to 511 and finally to 521 (John and Abrahamson, 2001; Miner and Sanes, 1994). Similar changes in the Collagen (IV) component of the GBM also occur (John and Abrahamson, 2001) Importantly, *Lamb2* mutant mice survive for a few months past-partum but die later due to proteinuria, and therefore an initial characterisation of the *lamb2* embryonic phenotype would have described a limited role for *Lamb2* in glomerular development. This suggests that the Laminin component of the cardiac jelly could also mature over time and that while I have only characterised the phenotype of *lamb2* F0 mutants up to 72hpf, *Lamb2* may be required later following the function of other Laminin isoforms. Relative to siblings, 64% of *lamb2* mutants survive to adulthood, (Jacoby et al., 2002) suggesting that there may be a relatively mild adult phenotype, therefore it would be interesting to examine heart rate and pacing in *lamb2* F0 mutants. Finally, as loss of *lamb2* in mice results in the failure of nueromuscular junctions to organise properly, where Schwann cells make excess contacts with the basal laminae and enter the synaptic cleft upon loss of *Lamb2* (Patton et al., 1998). This could suggest a role for *lamb2* in the innervation of the

heart, demonstrating how early ECM expression may be required for later developmental processes.

Laminins are also subject to degradation, and this is required for tissue morphogenesis (Mouw et al., 2014). The main class of proteases involved in ECM remodelling are the matrix metalloproteinases (MMPs) (Mouw et al., 2014), zymogens that are activated in the extracellular space where collectively, they are able to degrade all ECM proteins, although each member of the MMP family does have a level of component specificity (Mouw et al., 2014).

In zebrafish, Laminin at the interface between the gut and the LPM is asymmetrically degraded as the lateral plate mesoderm envelopes the developing gut, and this regional degradation is required for correct LPM migration (Yin et al., 2010). Commensurate with the role of MMPs in degrading ECM, pan-MMP inhibition results in a failure of LPM migration, specific knockdown of *mmp14a* results in an increased penetrance of a gut looping failure, suggesting that *mmp14a* activity degrades the Laminin isoforms in the LPM to promote asymmetric gut morphogenesis. Similar to the proposed role for regionalised degradation of HA in heart development, localised degradation of Laminin may be required for cardiac morphogenesis.

Although degradation of the ECM during heart looping to facilitate movement of the tissue is unlikely to be required in similar manner to gut looping, preliminary data suggests that the temporal requirement of Laminin is indeed in the window prior to 55hpf. Immunostaining using a supposed pan-Laminin antibody suggests Laminin is present throughout the heart at 30hpf, but absent in the atrium of the 55hpf heart (Noël, unpublished). However, this antibody does not sufficiently distinguish between different subunits (Parsons et al., 2002) and due to the complex tissue and temporal dynamics of Laminin subunit expression this makes interpretation of protein localisation and dynamics challenging.

The loss of expression of *lamb1a*, *lama4* and *lama5* from the atrium by 55hpf may suggest a similar role to localised Fibronectin synthesis with spatiotemporal requirements for Laminin deposition during heart development. However, this restriction seems at odds with the global roles of Laminins before 72hpf, as loss of *lamb1a* affects both atrial and ventricular size as early as 55hpf, despite expression of *lamb1a* being absent from the atrium this timepoint. This would suggest that Laminin deposition during early morphogenesis, similar to synthesis of HA during heart jogging is required for the morphogenesis of the tube and that Laminin deposition in the ventricle following heart looping may be required for other processes such as trabeculation. An interesting possibility is that cross-talk between Laminins and HA may be required for ventricular maturation, similar to roles identified for Laminins and HSPGs (Dolez et al., 2010). Examining localisation of HA (using the ssNcan-GFP sensor) and Hapln1a in *lamb1a* and *lamc1* mutants would begin to test this possibility.

Changes in composition of the cardiac basement membrane over heart development are observed for Laminin subunits, as young cardiac endothelial cells in mice (ECs, 12-15 weeks) predominantly express *Lamb2* chains, whilst in old cardiac ECs (18 months) *Lamb2* expression is reduced and *Lamb1* is the major beta chain expressed (Wagner et al., 2018). Differences in *Lamb1* and *Lamb2* expression correlate with the response to acute myocardial infarction (AMI) in young mice, where cardiac ischemia results in an increase in *Lamb1* and decrease in *Lamb2* expression (Wagner et al., 2018). These two different Laminins (LN-411, LN-421) have complementary effects in culture. Human Umbilical Vein Endothelial Cells plated on LN-411 had reduced adhesion, fewer branchpoints and reduced EC migration compared to LN-421 (Wagner et al., 2018). Furthermore, classical markers of EndoMT were clearly up-regulated in cells plated on LN-411 compared to plating on LN-421, which was shown to act through *ITGB1* (Wagner et al., 2018). LN-411 therefore appears to facilitate sensitisation towards a more mesenchymal state,

which may correlate with the increase in fibrosis and deposition of atheroma during ageing and also impact on the response to Myocardial Infarction (MI), suggesting that specific ECM composition may influence regenerative processes in the heart, and that the ECM is a potential therapeutic target for regenerative studies.

8.6 Therapeutic futures

Whilst zebrafish have remarkable regenerative capacity in multiple tissues in adulthood, including the heart, the ability of mice to regenerate cardiac tissue is only present at P1 (Notari et al., 2018). Removal of a small area of the left ventricle in P1 mice results in a clear injury at 3dpa (days post amputation) but the scar is resolved by 21dpa. However, if the same procedure is performed one day later, at P2, no regeneration of myocardial tissue is observed (Notari et al., 2018). Transcriptional profiling of P1 and P2 mice ventricular tissue identified almost 200 genes that altered transcriptional levels, the majority of which were related to the ECM (Notari et al., 2018). Between P1 and P2, levels of Elastin, Laminin, Collagen II and IV show a marked increase in the heart, correlating with an increase in tissue stiffness. A comparison of the zebrafish and mouse cardiac ECM has highlighted major differences in the composition of Collagen, Elastin and GAGs, where zebrafish ECM contained less Collagen and more Elastin and GAGs compared to the mouse (Chen et al., 2016), in line with the increased elastic modulus observed in P2 versus P1 mouse hearts (Notari et al., 2018). Reduction in tissue stiffness in P3 injured mice resulted in reduced myocardial fibrosis, suggesting the changes in tissue stiffness during the early neonatal period impacts on regenerative capacity, although no direct link between ECM composition and stiffness was proved (Notari et al., 2018).

In a separate study regenerative potential of the heart was shown to be contained within the ECM of zebrafish following heart injury (Chen et al., 2016). Injection of decelluarised, regenerating zebrafish ventricular ECM into mouse hearts post MI

induction resulted in a significant recovery of cardiac function, distinct from the injection of non-regenerating zebrafish ventricular ECM (Chen et al., 2016). Interestingly, inhibition of ErbB2 signalling appears to result in almost total loss of the therapeutic effect of regenerating zebrafish ECM, suggesting that the action of the regenerative capacity of zebrafish ECM acts through ErbB2 signalling, promoting cell proliferation (Chen et al., 2016).

Further implicating the PG components of the ECM in heart regeneration, removal of the HSPG proteoglycan Agrin from the cardiac mesoderm in mice, leads to compromised heart regeneration in the P1 mouse, with larger and more frequent scarring of the ventricle following resection (Bassat et al., 2017). As a potential therapeutic, injection of Agrin into the heart following experimental induction of MI, results in a reduction in scar size 14dpi (days post injury) and a recovery of heart function by 20dpi. In this context, Agrin is proposed to act through the Dystroglycan complex component *Dag1* to regulate ERK signalling, where Agrin treatment was able to increase ERK activation and nuclear YAP in P7 cardiomyocytes, facilitating increase in cell proliferation and subsequent regeneration (Bassat et al., 2017). The studies described here are by no means exhaustive, but highlight how altering ECM constituents can greatly impact on the regenerative potential of the heart and that understanding how these pathways act during embryonic heart development may inform therapies for the clinic.

The ECM is a vast, complex network of glycoproteins and fibrous proteins, which is highly specialised to the tissue which it encompasses and for role that the tissue plays in the multicellular organism. I have, for the first time identified asymmetries in the embryonic cardiac jelly, which are required to promote heart morphogenesis and defined the first functional roles for Laminins in multiple aspects of early cardiac development. The implications of this work propose that the ECM is a critical factor in the correct development of the vertebrate heart and that some of the earliest events during formation of the heart are essential for generating the final form of the

mature heart in later life. Furthermore, within the rapidly evolving field of regenerative biology, characterisation of the cell-environment interactions will be crucial in elucidating mechanisms which facilitate tissue regeneration. Finally, defining how cardiac development is achieved through interactions between cells and the extracellular matrix will begin to define potential therapeutic strategies to alleviate structural malformations of the heart caused by CHD.

9. References

Abrass, C.K., Berfield, A.K., Ryan, M.C., Carter, W.G., Hansen, K.M., 2006. Abnormal development of glomerular endothelial and mesangial cells in mice with targeted disruption of the lama3 gene. Kidney Int 70, 1062–1071. https://doi.org/10.1038/sj.ki.5001706

Abrass, C.K., Hansen, K.M., Patton, B.L., 2009. Laminin alpha4-null mutant mice develop chronic kidney disease with persistent overexpression of platelet-derived growth factor. Am J Pathology 176, 839–49. https://doi.org/10.2353/ajpath.2010.090570

Anderson, J.L., Mulligan, T.S., Shen, M.-C., Wang, H., Scahill, C.M., Tan, F.J., Du, S.J., Busch-Nentwich, E.M., Farber, S.A., 2017. mRNA processing in mutant zebrafish lines generated by chemical and CRISPR-mediated mutagenesis produces unexpected transcripts that escape nonsense-mediated decay. Plos Genet 13, e1007105. https://doi.org/10.1371/journal.pgen.1007105

Anderson, L.R., Owens, T.W., Naylor, M.J., 2013. Integrins in development and cancer. Biophysical Rev 6, 191–202. https://doi.org/10.1007/s12551-013-0123-1

Arrenberg, A.B., Stainier, D.Y.R., Baier, H., Huisken, J., 2010. Optogenetic control of cardiac function. Sci New York N Y 330, 971–4. https://doi.org/10.1126/science.1195929

Aspberg, A., 2012. The different roles of aggrecan interaction domains. J Histochem Cytochem Official J Histochem Soc 60, 987–96. https://doi.org/10.1369/0022155412464376

Aumailley, M., Bruckner-Tuderman, L., Carter, W.G., Deutzmann, R., Edgar, D., Ekblom, P., Engel, J., Engvall, E., Hohenester, E., Jones, J.C.R., Kleinman, H.K., Marinkovich, M.P., Martin, G.R., Mayer, U., Meneguzzi, G., Miner, J.H., Miyazaki, K., Patarroyo, M., Paulsson, M., Quaranta, V., Sanes, J.R., Sasaki, T., Sekiguchi, K., Sorokin, L.M., Talts, J.F., Tryggvason, K., Uitto, J., Virtanen, I., Mark, K. von der, Wewer, U.M., Yamada, Y., Yurchenco, P.D., 2005. A simplified Laminin nomenclature. Matrix Biol 24, 326–332. https://doi.org/10.1016/j.matbio.2005.05.006

Auman, H.J., Coleman, H., Riley, H.E., Olale, F., Tsai, H.-J., Yelon, D., 2007. Functional Modulation of Cardiac Form through Regionally Confined Cell Shape Changes. Plos Biol 5, e53. https://doi.org/10.1371/journal.pbio.0050053

Baker, K., Holtzman, N.G., Burdine, R.D., 2008. Direct and indirect roles for Nodal signaling in two axis conversions during asymmetric morphogenesis of the zebrafish heart. P Natl Acad Sci Usa 105, 13924–9. https://doi.org/10.1073/pnas.0802159105

Bakkers, J., 2011. Zebrafish as a model to study cardiac development and human cardiac disease. Cardiovasc Res 91, 279–88. https://doi.org/10.1093/cvr/cvr098

Baldini, A., Fulcoli, F.G., Illingworth, E., 2017. Current Topics in Developmental Biology. Curr Top Dev Biol 122, 223–243. https://doi.org/10.1016/bs.ctdb.2016.08.002

Barczyk, M., Carracedo, S., Gullberg, D., 2009. Integrins. Cell Tissue Res 339, 269–80. https://doi.org/10.1007/s00441-009-0834-6

Barry, A., 1948. The functional significance of the cardiac jelly in the tubular heart of the chick embryo. Anatomical Rec 102, 289–298. https://doi.org/10.1002/ar.1091020304

Bassat, E., Mutlak, Y.E., Genzelinakh, A., Shadrin, I.Y., Umansky, K.B., Yifa, O., Kain, D., Rajchman, D., Leach, J., Bassat, D.R., Udi, Y., Sarig, R., Sagi, I., Martin, J.F., Bursac, N., Cohen, S., Tzahor, E., 2017. The extracellular matrix protein agrin promotes heart regeneration in mice. Nature 547, 179–184. https://doi.org/10.1038/nature22978

Basson, C.T., Bachinsky, D.R., Lin, R.C., Levi, T., Elkins, J.A., Soults, J., Grayzel, D., Kroumpouzou, E., Traill, T.A., Leblanc-Straceski, J., Renault, B., Kucherlapati, R., J.G, S., Seidman, C.E., 1997. Mutations in human cause limb and cardiac malformation in Holt-Oram syndrome. Nat Genet 15, 30–35. https://doi.org/10.1038/ng0197-30

Beis, D., Bartman, T., Jin, S.-W., Scott, I.C., D'Amico, L.A., Ober, E.A., Verkade, H., Frantsve, J., Field, H.A., Wehman, A., Baier, H., Tallafuss, A., Bally-Cuif, L., Chen, J.-N., Stainier, D.Y.R., Jungblut, B., 2005. Genetic and cellular analyses of

zebrafish atrioventricular cushion and valve development. Development 132, 4193–4204. https://doi.org/10.1242/dev.01970

Berdougo, E., Coleman, H., Lee, D.H., Stainier, D.Y.R., Yelon, D., 2003. Mutation of weak atrium/atrial myosin heavy chain disrupts atrial function and influences ventricular morphogenesis in zebrafish. Development 130, 6121–6129. https://doi.org/10.1242/dev.00838

Bernier, P.-L., Stefanescu, A., Samoukovic, G., Tchervenkov, C.I., 2010. The Challenge of Congenital Heart Disease Worldwide: Epidemiologic and Demographic Facts.
Seminars Thorac Cardiovasc Surg Pediatric Cardiac Surg Annu 13, 26–34. https://doi.org/10.1053/j.pcsu.2010.02.005

Bill, B.R., Petzold, A.M., Clark, K.J., Schimmenti, L.A., Ekker, S.C., 2009. A primer for morpholino use in zebrafish. Zebrafish 6, 69–77. https://doi.org/10.1089/zeb.2008.0555

Bonnans, C., Chou, J., Werb, Z., 2014. Remodelling the extracellular matrix in development and disease. Nat Rev Mol Cell Biology 15, 786–801. https://doi.org/10.1038/nrm3904

Bornhorst, D., Xia, P., Nakajima, H., Dingare, C., Herzog, W., Lecaudey, V., Mochizuki, N., Heisenberg, C.-P., Yelon, D., Abdelilah-Seyfried, S., 2019. Biomechanical signaling within the developing zebrafish heart attunes endocardial growth to myocardial chamber dimensions. Nat Commun 10, 4113. https://doi.org/10.1038/s41467-019-12068-x

Boselli, F., Steed, E., Freund, J.B., Vermot, J., 2017. Anisotropic shear stress patterns predict the orientation of convergent tissue movements in the embryonic heart. Development 144, 4322–4327. https://doi.org/10.1242/dev.152124

Braun, N., Wyrzykowska, J., Muller, P., David, K., Couch, D., Perrot-Rechenmann, C., Fleming, A.J., 2008. Conditional repression of AUXIN BINDING PROTEIN1 reveals that it coordinates cell division and cell expansion during postembryonic

shoot development in Arabidopsis and tobacco. Plant Cell 20, 2746–62. https://doi.org/10.1105/tpc.108.059048

Bray, S.J., 2016. Notch signalling in context. Nat Rev Mol Cell Bio 17, 722–735. https://doi.org/10.1038/nrm.2016.94

Brennan, J., Norris, D.P., Robertson, E.J., 2002. Nodal activity in the node governs left-right asymmetry. Gene Dev 16, 2339–2344. https://doi.org/10.1101/gad.1016202

Brown, D., Samsa, L., Qian, L., Liu, J., 2016. Advances in the Study of Heart Development and Disease Using Zebrafish. J Cardiovasc Dev Dis 3, 13. https://doi.org/10.3390/jcdd3020013

BRUCH, M., LANDWEHR, R., ENGEL, J., 1989. Dissection of Laminin by cathepsin G into its long-arm and short-arm structures and localization of regions involved in calcium dependent stabilization and self-association. Eur J Biochem 185, 271–279. https://doi.org/10.1111/j.1432-1033.1989.tb15112.x

Bruneau, B.G., 2008. The developmental genetics of congenital heart disease. Nature 451, 943–948. https://doi.org/10.1038/nature06801

Bruneau, B.G., Logan, M., Davis, N., Levi, T., Tabin, C.J., Seidman, J.G., Seidman, C.E., 1999. Chamber-Specific Cardiac Expression of Tbx5 and Heart Defects in Holt–Oram Syndrome. Dev Biol 211, 100–108. https://doi.org/10.1006/dbio.1999.9298

Bruneau, B.G., Nemer, G., Schmitt, J.P., Charron, F., Robitaille, L., Caron, S., Conner, D.A., Gessler, M., Nemer, M., Seidman, C.E., Seidman, J.G., 2001. A Murine Model of Holt-Oram Syndrome Defines Roles of the T-Box Transcription Factor Tbx5 in Cardiogenesis and Disease. Cell 106, 709–721. https://doi.org/10.1016/s0092-8674(01)00493-7

Burdine, R.D., Schier, A.F., 2000. Conserved and divergent mechanisms in left-right axis formation. Gene Dev 14, 763–76.

Burger, A., Lindsay, H., Felker, A., Hess, C., Anders, C., Chiavacci, E., Zaugg, J., Weber, L.M., Catena, R., Jinek, M., Robinson, M.D., Mosimann, C., 2016. Maximizing mutagenesis with solubilized CRISPR-Cas9 ribonucleoprotein complexes. Development 143, 2025–2037. https://doi.org/10.1242/dev.134809

Burgeson, R.E., Chiquet, M., Deutzmann, R., Ekblom, P., Engel, J., Kleinman, H., Martin, G.R., Meneguzzi, G., Paulsson, M., Sanes, J., Timpl, R., Tryggvason, K., Yamada, Y., Yurchenco, P.D., 1994. A new nomenclature for the Laminins. Matrix Biol 14, 209–211. https://doi.org/10.1016/0945-053x(94)90184-8

Burkhard, S., Eif, V. van, Garric, L., Christoffels, V., Bakkers, J., 2017. On the Evolution of the Cardiac Pacemaker. J Cardiovasc Dev Dis 4, 4. https://doi.org/10.3390/jcdd4020004

Burkhard, S.B., Bakkers, J., 2018. Spatially resolved RNA-sequencing of the embryonic heart identifies a role for Wnt/β-catenin signaling in autonomic control of heart rate. Elife 7, e31515. https://doi.org/10.7554/elife.31515

Bussmann, J., Bakkers, J., Schulte-Merker, S., 2007. Early Endocardial Morphogenesis Requires Scl/Tal1. Plos Genet 3, e140. https://doi.org/10.1371/journal.pgen.0030140

Butcher, J.T., Markwald, R.R., 2007. Valvulogenesis: the moving target. Philosophical Transactions Royal Soc B Biological Sci 362, 1489–1503. https://doi.org/10.1098/rstb.2007.2130

Butler, Keith, J., 1952. An Experimental Analysis of Cardiac Loop Formation in the Chick.

Camenisch, T.D., Schroeder, J.A., Bradley, J., Klewer, S.E., McDonald, J.A., 2002. Heart-valve mesenchyme formation is dependent on hyaluronan-augmented activation of ErbB2–ErbB3 receptors. Nat Med 8, 850–855. https://doi.org/10.1038/nm742

Camenisch, T.D., Spicer, A.P., Brehm-Gibson, T., Biesterfeldt, J., Augustine, M.L., Calabro, A., Kubalak, S., Klewer, S.E., McDonald, J.A., 2000. Disruption of hyaluronan synthase-2 abrogates normal cardiac morphogenesis and hyaluronan-mediated transformation of epithelium to mesenchyme. J Clin Invest 106, 349–360. https://doi.org/10.1172/jci10272

Campbell, I.D., Humphries, M.J., 2011. Integrin structure, activation, and interactions. Csh Perspect Biol 3, a004994–a004994. https://doi.org/10.1101/cshperspect.a004994

Campos-Baptista, M.I.M. de, Holtzman, N.G., Yelon, D., Schier, A.F., 2008. Nodal signaling promotes the speed and directional movement of cardiomyocytes in zebrafish. Dev Dynam 237, 3624–3633. https://doi.org/10.1002/dvdy.21777

Castro-Quezada, A., Nadal-Ginard, B., Cruz, M.V.D.L., 1972. Experimental study of the formation of the bulboventricular loop in the chick. J Embryol Exp Morph 27, 623–37.

Charpentier, M.S., Christine, K.S., Amin, N.M., Dorr, K.M., Kushner, E.J., Bautch, V.L., Taylor, J.M., Conlon, F.L., 2013. CASZ1 Promotes Vascular Assembly and Morphogenesis through the Direct Regulation of an EGFL7/RhoA-Mediated Pathway. Dev Cell 25, 132–143. https://doi.org/10.1016/j.devcel.2013.03.003

Chen, D.-H., Below, J.E., Shimamura, A., Keel, S.B., Matsushita, M., Wolff, J., Sul, Y., Bonkowski, E., Castella, M., Taniguchi, T., Nickerson, D., Papayannopoulou, T., Bird, T.D., Raskind, W.H., 2016. Ataxia-Pancytopenia Syndrome Is Caused by Missense Mutations in SAMD9L. Am J Hum Genet 98, 1146–58. https://doi.org/10.1016/j.ajhg.2016.04.009

Chen, J.N., Eeden, F.J. van, Warren, K.S., Chin, A., Nüsslein-Volhard, C., Haffter, P., Fishman, M.C., 1997. Left-right pattern of cardiac BMP4 may drive asymmetry of the heart in zebrafish. Dev Camb Engl 124, 4373–82.

Chen, L., Fulcoli, F.G., Tang, S., Baldini, A., 2009. Tbx1 regulates proliferation and differentiation of multipotent heart progenitors. Circ Res 105, 842–51. https://doi.org/10.1161/circresaha.109.200295

Chen, W.C.W., Wang, Z., Missinato, M.A., Park, D.W., Long, D.W., Liu, H.-J., Zeng, X., Yates, N.A., Kim, K., Wang, Y., 2016. Decellularized zebrafish cardiac extracellular matrix induces mammalian heart regeneration. Sci Adv 2, e1600844. https://doi.org/10.1126/sciadv.1600844

Chen, Y., Zeng, S., Hu, R., Wang, X., Huang, W., Liu, J., Wang, L., Liu, G., Cao, Y., Zhang, Y., 2017. Using local chromatin structure to improve CRISPR/Cas9 efficiency in zebrafish. Plos One 12, e0182528. https://doi.org/10.1371/journal.pone.0182528

Chew, C., Lennon, R., 2018. Basement Membrane Defects in Genetic Kidney Diseases. Frontiers Pediatrics 6, 11. https://doi.org/10.3389/fped.2018.00011

Chi, N.C., Shaw, R.M., Val, S.D., Kang, G., Jan, L.Y., Black, B.L., Stainier, D.Y.R., 2008. Foxn4 directly regulates tbx2b expression and atrioventricular canal formation. Gene Dev 22, 734–9. https://doi.org/10.1101/gad.1629408

Chocron, S., Verhoeven, M.C., Rentzsch, F., Hammerschmidt, M., Bakkers, J., 2007. Zebrafish Bmp4 regulates left–right asymmetry at two distinct developmental time points. Dev Biol 305, 577–588. https://doi.org/10.1016/j.ydbio.2007.03.001

Chung, A.E., Jaffe, R., Freeman, I.L., Vergnes, J.-P., Braginski, J.E., Carlin, B., 1979. Properties of a basement membrane-related glycoprotein synthesized in culture by a mouse embryonal carcinoma-derived cell line. Cell 16, 277–287. https://doi.org/10.1016/0092-8674(79)90005-9

Cooper, A.R., MacQueen, H.A., 1983. Subunits of Laminin are differentially synthesized in mouse eggs and early embryos. Dev Biol 96, 467–471. https://doi.org/10.1016/0012-1606(83)90183-5

Cruz, M.V. de la, Gómez, C.S., Arteaga, M.M., Argüello, C., 1977. Experimental study of the development of the truncus and the conus in the chick embryo. J Anat 123, 661–86.

Darbro, B.W., Mahajan, V.B., Gakhar, L., Skeie, J.M., Campbell, E., Wu, S., Bing, X., Millen, K.J., Dobyns, W.B., Kessler, J.A., Jalali, A., Cremer, J., Segre, A., Manak, J.R., Aldinger, K.A., Suzuki, S., Natsume, N., Ono, M., Hai, H.D., Viet, L.T., Loddo, S., Valente, E.M., Bernardini, L., Ghonge, N., Ferguson, P.J., Bassuk, A.G., 2013. Mutations in Extracellular Matrix Genes NID1 and LAMC1 Cause Autosomal Dominant Dandy-Walker Malformation and Occipital Cephaloceles. Hum Mutat 34, 1075–1079. https://doi.org/10.1002/humu.22351

Davis, C.L., 1924. The cardiac jelly of the chick embryo. Anat Rec 27:201–202

Dawlaty, M.M., Ganz, K., Powell, B.E., Hu, Y.-C., Markoulaki, S., Cheng, A.W., Gao, Q., Kim, J., Choi, S.-W., Page, D.C., Jaenisch, R., 2011. Tet1 Is Dispensable for Maintaining Pluripotency and Its Loss Is Compatible with Embryonic and

Postnatal Development. Cell Stem Cell 9, 166–175. https://doi.org/10.1016/j.stem.2011.07.010

Derrick, C.J., Sánchez-Posada, J., Hussein, F., Tessadori, F., Pollitt, E.J., Savage, A.M., Wilkinson, R.N., Chico, T.J., Eeden, F.J. van, Bakkers, J., Noël, E.S., 2019. Asymmetric Hapln1a drives regionalised cardiac ECM expansion and promotes heart morphogenesis during zebrafish development. Biorxiv 838128. https://doi.org/10.1101/838128

Desgrange, A., Garrec, J.-F.L., Bernheim, S., Bonnelykke, T.H., Meilhac, S., 2019. Transient Nodal signalling in left precursors coordinates opposed asymmetries shaping the heart loop. Biorxiv 854463. https://doi.org/10.1101/854463

Desgrange, A., Garrec, J.-F.L., Meilhac, S.M., 2018. Left-right asymmetry in heart development and disease: forming the right loop. Development 145, dev162776. https://doi.org/10.1242/dev.162776

Dietrich, A.-C., Lombardo, V.A., Veerkamp, J., Priller, F., Abdelilah-Seyfried, S., 2014. Blood Flow and Bmp Signaling Control Endocardial Chamber Morphogenesis. Dev Cell 30, 367–377. https://doi.org/10.1016/j.devcel.2014.06.020

Dolez, M., Nicolas, J.-F., Hirsinger, E., 2010. Laminins, via heparan Sulfate Proteoglycans, participate in zebrafish myotome morphogenesis by modulating the pattern of Bmp responsiveness. Development 138, 97–106. https://doi.org/10.1242/dev.053975

Domogatskaya, A., Rodin, S., Tryggvason, K., 2012. Functional Diversity of Laminins. Annu Rev Cell Dev Bi 28, 523–553. https://doi.org/10.1146/annurev-cellbio-101011-155750

Dovey, H.F., John, V., Anderson, J.P., Chen, L.Z., Andrieu, P.D.S., Fang, L.Y., Freedman, S.B., Folmer, B., Goldbach, E., Holsztynska, E.J., Hu, K.L., Johnson-Wood, K.L., Kennedy, S.L., Kholodenko, D., Knops, J.E., Latimer, L.H., Lee, M., Liao, Z., Lieberburg, I.M., Motter, R.N., Mutter, L.C., Nietz, J., Quinn, K.P., Sacchi, K.L., Seubert, P.A., Shopp, G.M., Thorsett, E.D., Tung, J.S., Wu, J., Yang, S., Yin, C.T., Schenk, D.B., May, P.C., Altstiel, L.D., Bender, M.H., Boggs, L.N.,

Britton, T.C., Clemens, J.C., Czilli, D.L., Dieckman-McGinty, D.K., Droste, J.J., Fuson, K.S., Gitter, B.D., Hyslop, P.A., Johnstone, E.M., Li, W.-Y., Little, S.P., Mabry, T.E., Miller, F.D., Ni, B., Nissen, J.S., Porter, W.J., Potts, B.D., Reel, J.K., Stephenson, D., Su, Y., Shipley, L.A., Whitesitt, C.A., Yin, T., Audia, J.E., 2009. Functional gamma-secretase inhibitors reduce beta-amyloid peptide levels in brain: **γ**-secretase inhibitors reduce A**β** levels in PDAPP mouse brain. J Neurochem 76, 173–181. https://doi.org/10.1046/j.1471-4159.2001.00012.x

Dreos, R., Ambrosini, G., Groux, R., Cavin Périer, R., Bucher, P., 2016. The eukaryotic promoter database in its 30th year: focus on non-vertebrate organisms. Nucleic Acids Res 45, D51–D55. https://doi.org/10.1093/nar/gkw1069

Duchemin, A.-L., Vignes, H., Vermot, J., 2019. Mechanically activated piezo channels modulate outflow tract valve development through the Yap1 and Klf2-Notch signaling axis. Elife 8, e44706. https://doi.org/10.7554/elife.44706

Eeden, F.J. van, Granato, M., Schach, U., Brand, M., Furutani-Seiki, M., Haffter, P., Hammerschmidt, M., Heisenberg, C.P., Jiang, Y.J., Kane, D.A., Kelsh, R.N., Mullins, M.C., Odenthal, J., Warga, R.M., Allende, M.L., Weinberg, E.S., Nüsslein-Volhard, C., 1996. Mutations affecting somite formation and patterning in the zebrafish, Danio rerio. Dev Camb Engl 123, 153–64.

Eisen, J.S., Smith, J.C., 2008. Controlling morpholino experiments: don't stop making antisense. Development 135, 1735–1743. https://doi.org/10.1242/dev.001115

El-Brolosy, M.A., Kontarakis, Z., Rossi, A., Kuenne, C., Günther, S., Fukuda, N., Kikhi, K., Boezio, G.L.M., Takacs, C.M., Lai, S.-L., Fukuda, R., Gerri, C., Giraldez, A.J., Stainier, D.Y.R., 2019. Genetic compensation triggered by mutant mRNA degradation. Nature 568, 193–197. https://doi.org/10.1038/s41586-019-1064-z

El-Brolosy, M.A., Stainier, D.Y.R., 2017. Genetic compensation: A phenomenon in search of mechanisms. Plos Genet 13, e1006780. https://doi.org/10.1371/journal.pgen.1006780

Engel, J., Odermatt, E., Engel, A., Madri, J.A., Furthmayr, H., Rohde, H., Timpl, R., 1981. Shapes, domain organizations and flexibility of Laminin and fibronectin, two multifunctional proteins of the extracellular matrix. J Mol Biol 150, 97–120. https://doi.org/10.1016/0022-2836(81)90326-0

Esko., V.H. and J.D., 2017. Essentials of Glycobiology Chapter 16 Hyaluronan. https://doi.org/10.1101/glycobiology.3e.016

Faltz, L.L., Caputo, C.B., Kimura, J.H., Schrode, J., Hascall, V.C., 1979. Structure of the complex between hyaluronic acid, the hyaluronic acid-binding region, and the link protein of proteoglycan aggregates from the swarm rat Chondrosarcoma. J Biological Chem 254, 1381–7.

Felker, A., Prummel, K.D., Merks, A.M., Mickoleit, M., Brombacher, E.C., Huisken, J., Panáková, D., Mosimann, C., 2018. Continuous addition of progenitors forms the cardiac ventricle in zebrafish. Nat Commun 9, 2001. https://doi.org/10.1038/s41467-018-04402-6

Ferletta, M., Kikkawa, Y., Yu, H., Talts, J.F., Durbeej, M., Sonnenberg, A., Timpl, R., Campbell, K.P., Ekblom, P., Genersch, E., 2003. Opposing Roles of Integrin **α**6A**β**1 and Dystroglycan in Laminin-mediated Extracellular Signal-regulated Kinase Activation. Mol Biol Cell 14, 2088–2103. https://doi.org/10.1091/mbc.e03-01-0852

Fishman, M.C., Chien, K.R., 1997. Fashioning the vertebrate heart: earliest embryonic decisions. Dev Camb Engl 124, 2099–117.

Foglia, M.J., Cao, J., Tornini, V.A., Poss, K.D., 2016. Multicolor mapping of the cardiomyocyte proliferation dynamics that construct the atrium. Development 143, 1688–1696. https://doi.org/10.1242/dev.136606

Freudenberg, J.M., Ghosh, S., Lackford, B.L., Yellaboina, S., Zheng, X., Li, R., Cuddapah, S., Wade, P.A., Hu, G., Jothi, R., 2011. Acute depletion of Tet1-dependent 5-hydroxymethylcytosine levels impairs LIF/Stat3 signaling and results in loss of embryonic stem cell identity. Nucleic Acids Res 40, 3364–3377. https://doi.org/10.1093/nar/gkr1253

Frieser, M., Nockel, H., Pausch, F., Roder, C., Hahn, A., Deutzmann, R., Sorokin, L.M., 1997. Cloning of the Mouse Laminin alpha4 cDNA. Expression in a Subset of Endothelium. Eur J Biochem 246, 727–735. https://doi.org/10.1111/j.1432-1033.1997.t01-1-00727.x

Gaj, T., Gersbach, C.A., Barbas, C.F., 2013. ZFN, TALEN, and CRISPR/Cas-based methods for genome engineering. Trends Biotechnol 31, 397–405. https://doi.org/10.1016/j.tibtech.2013.04.004

Galloway, J.L., Wingert, R.A., Thisse, C., Thisse, B., Zon, L.I., 2005. Loss of Gata1 but Not Gata2 Converts Erythropoiesis to Myelopoiesis in Zebrafish Embryos. Dev Cell 8, 109–116. https://doi.org/10.1016/j.devcel.2004.12.001

Gao, Y., Zhang, Y., Zhang, D., Dai, X., Estelle, M., Zhao, Y., 2015. Auxin binding protein 1 (ABP1) is not required for either auxin signaling or Arabidopsis development. Proc National Acad Sci 112, 2275–2280. https://doi.org/10.1073/pnas.1500365112

Garrec, J.-F.L., Domínguez, J.N., Desgrange, A., Ivanovitch, K.D., Raphaël, E., Bangham, J.A., Torres, M., Coen, E., Mohun, T.J., Meilhac, S.M., 2017. A predictive model of asymmetric morphogenesis from 3D reconstructions of mouse heart looping dynamics. Elife 6, e28951. https://doi.org/10.7554/elife.28951

Garrity, D.M., Childs, S., Fishman, M.C., 2002. The heartstrings mutation in zebrafish causes heart/fin Tbx5 deficiency syndrome. Dev Camb Engl 129, 4635–45.

Gore, A.V., Monzo, K., Cha, Y.R., Pan, W., Weinstein, B.M., 2012. Vascular development in the zebrafish. Csh Perspect Med 2, a006684. https://doi.org/10.1101/cshperspect.a006684

Grassini, D.R., Lagendijk, A.K., Angelis, J.E.D., Silva, J.D., Jeanes, A., Zettler, N., Bower, N.I., Hogan, B.M., Smith, K.A., 2018. Nppa and Nppb act redundantly during zebrafish cardiac development to confine AVC marker expression and reduce cardiac jelly volume. Development 145, dev160739. https://doi.org/10.1242/dev.160739

Grimes, D.T., 2019. Making and breaking symmetry in development, growth and disease. Development 146, dev170985. https://doi.org/10.1242/dev.170985

Grimes, D.T., Burdine, R.D., 2017. Left–Right Patterning: Breaking Symmetry to Asymmetric Morphogenesis. Trends Genet 33, 616–628. https://doi.org/10.1016/j.tig.2017.06.004

Grimes, D.T., Patterson, V.L., Luna-Arvizu, G., Schottenfeld-Roames, J., Irons, Z.H., Burdine, R.D., 2019. Left-right asymmetric heart jogging increases the robustness of dextral heart looping in zebrafish. Dev Biol. https://doi.org/10.1016/j.ydbio.2019.11.012

Groenendijk, B.C.W., Hierck, B.P., Groot, A.C.G., Poelmann, R.E., 2004. Development-related changes in the expression of shear stress responsive genesKLF-2,ET-1, andNOS-3 in the developing cardiovascular system of chicken embryos. Dev Dynam 230, 57–68. https://doi.org/10.1002/dvdy.20029

Guerra, A., Germano, R.F., Stone, O., Arnaout, R., Guenther, S., Ahuja, S., Uribe, V., Vanhollebeke, B., Stainier, D.Y., Reischauer, S., 2018. Distinct myocardial lineages break atrial symmetry during cardiogenesis in zebrafish. Elife 7, e32833. https://doi.org/10.7554/elife.32833

Gunawan, F., Gentile, A., Fukuda, R., Tsedeke, A.T., Jiménez-Amilburu, V., Ramadass, R., Iida, A., Sehara-Fujisawa, A., Stainier, D.Y.R., 2019. Focal adhesions are essential to drive zebrafish heart valve morphogenesis. J Cell Biology 218, 1039–1054. https://doi.org/10.1083/jcb.201807175

Gupta, V., Poss, K.D., 2012. Clonally dominant cardiomyocytes direct heart morphogenesis. Nature 484, 479–484. https://doi.org/10.1038/nature11045

Habets, P.E.M.H., Moorman, A.F.M., Clout, D.E.W., Roon, M.A. van, Lingbeek, M., Lohuizen, M. van, Campione, M., Christoffels, V.M., 2002. Cooperative action of Tbx2 and Nkx2.5 inhibits ANF expression in the atrioventricular canal: implications for cardiac chamber formation. Gene Dev 16, 1234–1246. https://doi.org/10.1101/gad.222902

Haddadi, K., Zare, A., Asadian, L., 2018. Dandy-Walker Syndrome: A Review of New Diagnosis and Management in Children. J Pediatrics Rev 6. https://doi.org/10.5812/jpr.63486

Hallmann, R., Horn, N., Selg, M., Wendler, O., Pausch, F., Sorokin, L.M., 2005. Expression and Function of Laminins in the Embryonic and Mature Vasculature. Physiol Rev 85, 979–1000. https://doi.org/10.1152/physrev.00014.2004

Hami, D., Grimes, A.C., Tsai, H.-J., Kirby, M.L., 2011. Zebrafish cardiac development requires a conserved secondary heart field. Development 138, 2389–2398. https://doi.org/10.1242/dev.061473

HARDINGHAM, T., MUIR, H., 1972. The specific interaction of hyaluronic acid with cartilage Proteoglycans. Biochimica Et Biophysica Acta Bba - Gen Subj 279, 401–405. https://doi.org/10.1016/0304-4165(72)90160-2

Harvey, R.P., 2002. Patterning the vertebrate heart. Nat Rev Genet 3, 544–556. https://doi.org/10.1038/nrg843

Hassed, S., Li, S., Mulvihill, J., Aston, C., Palmer, S., 2017. Adams-Oliver syndrome review of the literature: Refining the diagnostic phenotype: Adams-Oliver Syndrome: Refining the Phenotype. Am J Med Genet A 173, 790–800. https://doi.org/10.1002/ajmg.a.37889

Heckel, E., Boselli, F., Roth, S., Krudewig, A., Belting, H.-G., Charvin, G., Vermot, J., 2015. Oscillatory Flow Modulates Mechanosensitive klf2a Expression through trpv4 and trpp2 during Heart Valve Development. Curr Biology Cb 25, 1354–61. https://doi.org/10.1016/j.cub.2015.03.038

Helbling-Leclerc, A., Zhang, X., Topaloglu, H., Cruaud, C., Tesson, F., Weissenbach, J., Tomé, F.M.S., Schwartz, K., Fardeau, M., Tryggvason, K., Guicheney, P., 1995. Mutations in the Laminin **α**2–chain gene (LAMA2) cause merosin–deficient congenital muscular dystrophy. Nat Genet 11, 216–218. https://doi.org/10.1038/ng1095-216

Hernandez, L., Ryckebüsch, L., Wang, C., Ling, R., Yelon, D., 2019. Tmem2 restricts atrioventricular canal differentiation by regulating degradation of hyaluronic acid. Dev Dynam 248, 1195–1210. https://doi.org/10.1002/dvdy.106

Hierck, B.P., Poelmann, R.E., Iperen, L. van, Brouwer, A., Groot, A.C.G., 1996. Differential expression of **α**6 and other subunits of Laminin binding integrins during development of the murine heart. Dev Dynam 206, 100–111. https://doi.org/10.1002/(sici)1097-0177(199605)206:1<100::aid-aja9>3.0.co;2-m

Hiermeier, F., Männer, J., 2017. Kinking and Torsion Can Significantly Improve the Efficiency of Valveless Pumping in Periodically Compressed Tubular Conduits. Implications for Understanding of the Form-Function Relationship of Embryonic Heart Tubes. J Cardiovasc Dev Dis 4, 19. https://doi.org/10.3390/jcdd4040019

Hochgreb-Hägele, T., Yin, C., Koo, D.E.S., Bronner, M.E., Stainier, D.Y.R., 2013. Laminin **β**1a controls distinct steps during the establishment of digestive organ laterality. Development 140, 2734–2745. https://doi.org/10.1242/dev.097618

Hoffman, J.I.E., Kaplan, S., 2002. The incidence of congenital heart disease. J Am Coll Cardiol 39, 1890–1900. https://doi.org/10.1016/s0735-1097(02)01886-7

Hogan, B.L.M., Cooper, A.R., Kurkinen, M., 1980. Incorporation into Reichert's membrane of Laminin-like extracellular proteins synthesized by parietal endoderm cells of the mouse embryo. Dev Biol 80, 289–300. https://doi.org/10.1016/0012-1606(80)90405-4

Holtzman, N.G., Schoenebeck, J.J., Tsai, H.-J., Yelon, D., 2007. Endocardium is necessary for cardiomyocyte movement during heart tube assembly. Development 134, 2379–2386. https://doi.org/10.1242/dev.02857

Honda, H., Abe, T., Fujimori, T., 2019. The Chiral Looping of the Embryonic Heart Is Formed by the Combination of Three Axial Asymmetries. Biophys J 118, 742–752. https://doi.org/10.1016/j.bpj.2019.11.3397

Hoog, T.G., Fredrickson, S.J., Hsu, C.-W., Senger, S.M., Dickinson, M.E., Udan, R.S., 2018. The effects of reduced hemodynamic loading on morphogenesis of the

mouse embryonic heart. Dev Biol 442, 127–137. https://doi.org/10.1016/j.ydbio.2018.07.007

Howe, C.C., Dietzschold, B., 1983. Structural analysis of three subunits of Laminin from teratocarcinoma-derived parietal endoderm cells. Dev Biol 98, 385–391. https://doi.org/10.1016/0012-1606(83)90367-6

Howe, K., Clark, M.D., Torroja, C.F., Torrance, J., Berthelot, C., Muffato, M., Collins, J.E., Humphray, S., McLaren, K., Matthews, L., McLaren, S., Sealy, I., Caccamo, M., Churcher, C., Scott, C., Barrett, J.C., Koch, R., Rauch, G.-J., White, S., Chow, W., Kilian, B., Quintais, L.T., Guerra-Assunção, J.A., Zhou, Y., Gu, Y., Yen, J., Vogel, J.-H., Eyre, T., Redmond, S., Banerjee, R., Chi, J., Fu, B., Langley, E., Maguire, S.F., Laird, G.K., Lloyd, D., Kenyon, E., Donaldson, S., Sehra, H., Almeida-King, J., Loveland, J., Trevanion, S., Jones, M., Quail, M., Willey, D., Hunt, A., Burton, J., Sims, S., McLay, K., Plumb, B., Davis, J., Clee, C., Oliver, K., Clark, R., Riddle, C., Elliot, D., Eliott, D., Threadgold, G., Harden, G., Ware, D., Begum, S., Mortimore, B., Mortimer, B., Kerry, G., Heath, P., Phillimore, B., Tracey, A., Corby, N., Dunn, M., Johnson, C., Wood, J., Clark, S., Pelan, S., Griffiths, G., Smith, M., Glithero, R., Howden, P., Barker, N., Lloyd, C., Stevens, C., Harley, J., Holt, K., Panagiotidis, G., Lovell, J., Beasley, H., Henderson, C., Gordon, D., Auger, K., Wright, D., Collins, J., Raisen, C., Dyer, L., Leung, K., Robertson, L., Ambridge, K., Leongamornlert, D., McGuire, S., Gilderthorp, R., Griffiths, C., Manthravadi, D., Nichol, S., Barker, G., Whitehead, S., Kay, M., Brown, J., Murnane, C., Gray, E., Humphries, M., Sycamore, N., Barker, D., Saunders, D., Wallis, J., Babbage, A., Hammond, S., Mashreghi-Mohammadi, M., Barr, L., Martin, S., Wray, P., Ellington, A., Matthews, N., Ellwood, M., Woodmansey, R., Clark, G., Cooper, J.D., Cooper, J., Tromans, A., Grafham, D., Skuce, C., Pandian, R., Andrews, R., Harrison, E., Kimberley, A., Garnett, J., Fosker, N., Hall, R., Garner, P., Kelly, D., Bird, C., Palmer, S., Gehring, I., Berger, A., Dooley, C.M., Ersan-Ürün, Z., Eser, C., Geiger, H., Geisler, M., Karotki, L., Kirn, A., Konantz, J., Konantz, M., Oberländer, M., Rudolph-Geiger, S., Teucke, M., Lanz, C., Raddatz, G., Osoegawa, K., Zhu, B., Rapp,

A., Widaa, S., Langford, C., Yang, F., Schuster, S.C., Carter, N.P., Harrow, J., Ning, Z., Herrero, J., Searle, S.M.J., Enright, A., Geisler, R., Plasterk, R.H.A., Lee, C., Westerfield, M., Jong, P.J. de, Zon, L.I., Postlethwait, J.H., Nüsslein-Volhard, C., Hubbard, T.J.P., Crollius, H.R., Rogers, J., Stemple, D.L., 2013. The zebrafish reference genome sequence and its relationship to the human genome. Nature 496, 498–503. https://doi.org/10.1038/nature12111

Hsu, J.J., Vedula, V., Baek, K.I., Chen, C., Chen, J., Chou, M.I., Lam, J., Subhedar, S., Wang, J., Ding, Y., Chang, C.-C., Lee, J., Demer, L.L., Tintut, Y., Marsden, A.L., Hsiai, T.K., 2019. Contractile and hemodynamic forces coordinate Notch1b-mediated outflow tract valve formation. Jci Insight 4. https://doi.org/10.1172/jci.insight.124460

Huang, C., Yuan, X., Li, Z., Tian, Z., Zhan, X., Zhang, J., Li, X., 2014. VE-statin/Egfl7 siRNA inhibits angiogenesis in malignant glioma in vitro. Int J Clin Exp Patho 7, 1077–84.

Huang, C.-J., Tu, C.-T., Hsiao, C.-D., Hsieh, F.-J., Tsai, H.-J., 2003. Germ-line transmission of a myocardium-specific GFP transgene reveals critical regulatory elements in the cardiac myosin light chain 2 promoter of zebrafish. Dev Dynam 228, 30–40. https://doi.org/10.1002/dvdy.10356

Hurlstone, A.F.L., Haramis, A.-P.G., Wienholds, E., Begthel, H., Korving, J., Eeden, F. van, Cuppen, E., Zivkovic, D., Plasterk, R.H.A., Clevers, H., 2003. The Wnt/**β**-catenin pathway regulates cardiac valve formation. Nature 425, 633–637. https://doi.org/10.1038/nature02028

Icardo, J.M., Ojeda, J.L., 1984. Effects of Colchicine on the Formation and Looping of the Tubular Heart of the Embryonic Chick. Cells Tissues Organs 119, 1–9. https://doi.org/10.1159/000145855

Iivanainen, A., Kortesmaa, J., Sahlberg, C., Morita, T., Bergmann, U., Thesleff, I., Tryggvason, K., 1997. Primary Structure, Developmental Expression, and Immunolocalization of the Murine Laminin **α**4 Chain. J Biol Chem 272, 27862–27868. https://doi.org/10.1074/jbc.272.44.27862

Jackson, J.G., Pereira-Smith, O.M., 2006. Primary and Compensatory Roles for RB Family Members at Cell Cycle Gene Promoters That Are Deacetylated and Down-regulated in Doxorubicin-Induced Senescence of Breast Cancer Cells. Mol Cell Biol 26, 2501–2510. https://doi.org/10.1128/mcb.26.7.2501-2510.2006

Jacoby, A.S., Busch-Nentwich, E., Bryson-Richardson, R.J., Hall, T.E., Berger, J., Berger, S., Sonntag, C., Sachs, C., Geisler, R., Stemple, D.L., Currie, P.D., 2009. The zebrafish dystrophic mutant softy maintains muscle fibre viability despite basement membrane rupture and muscle detachment. Development 136, 3367–3376. https://doi.org/10.1242/dev.034561

Jallerat, Q., Feinberg, A.W., 2020. Extracellular Matrix Structure and Composition in the Early Four-Chambered Embryonic Heart. Cells 9, 285. https://doi.org/10.3390/cells9020285

John, P.L.S., Abrahamson, D.R., 2001. Glomerular endothelial cells and podocytes jointly synthesize Laminin-1 and -11 chains. Kidney Int 60, 1037–1046. https://doi.org/10.1046/j.1523-1755.2001.0600031037.x

Junker, J.P., Noël, E.S., Guryev, V., Peterson, K.A., Shah, G., Huisken, J., McMahon, A.P., Berezikov, E., Bakkers, J., Oudenaarden, A. van, 2014. Genome-wide RNA Tomography in the zebrafish embryo. Cell 159, 662–75. https://doi.org/10.1016/j.cell.2014.09.038

Kang, J.S., Oohashi, T., Kawakami, Y., Bekku, Y., Belmonte, J.C.I., Ninomiya, Y., 2004. Characterization of dermacan, a novel zebrafish lectican gene, expressed in dermal bones. Mech Develop 121, 301–312. https://doi.org/10.1016/j.mod.2004.01.007

Karlstrom, R.O., Trowe, T., Klostermann, S., Baier, H., Brand, M., Crawford, A.D., Grunewald, B., Haffter, P., Hoffmann, H., Meyer, S.U., Müller, B.K., Richter, S., Eeden, F.J. van, Nüsslein-Volhard, C., Bonhoeffer, F., 1996. Zebrafish mutations affecting retinotectal axon pathfinding. Dev Camb Engl 123, 427–38.

Keeley, D.P., Hastie, E., Jayadev, R., Kelley, L.C., Chi, Q., Payne, S.G., Jeger, J.L., Hoffman, B.D., Sherwood, D.R., 2020. Comprehensive Endogenous Tagging of

Basement Membrane Components Reveals Dynamic Movement within the Matrix Scaffolding. Dev Cell. https://doi.org/10.1016/j.devcel.2020.05.022

Kelly, R.G., Brown, N.A., Buckingham, M.E., 2001. The Arterial Pole of the Mouse Heart Forms from Fgf10-Expressing Cells in Pharyngeal Mesoderm. Dev Cell 1, 435–440. https://doi.org/10.1016/s1534-5807(01)00040-5

Kelly, R.G., Buckingham, M.E., Moorman, A.F., 2014. Heart Fields and Cardiac Morphogenesis. Csh Perspect Med 4, a015750–a015750. https://doi.org/10.1101/cshperspect.a015750

Kern, C.B., Norris, R.A., Thompson, R.P., Argraves, W.S., Fairey, S.E., Reyes, L., Hoffman, S., Markwald, R.R., Mjaatvedt, C.H., 2007. Versican proteolysis mediates myocardial regression during outflow tract development. Dev Dynam 236, 671–683. https://doi.org/10.1002/dvdy.21059

Kettleborough, R.N.W., Busch-Nentwich, E.M., Harvey, S.A., Dooley, C.M., Bruijn, E. de, Eeden, F. van, Sealy, I., White, R.J., Herd, C., Nijman, I.J., Fényes, F., Mehroke, S., Scahill, C., Gibbons, R., Wali, N., Carruthers, S., Hall, A., Yen, J., Cuppen, E., Stemple, D.L., 2013. A systematic genome-wide analysis of zebrafish protein-coding gene function. Nature 496, 494–497. https://doi.org/10.1038/nature11992

Keyte, A.L., Alonzo-Johnsen, M., Hutson, M.R., 2014. Evolutionary and developmental origins of the cardiac neural crest: Building a divided outflow tract. Birth Defects Res Part C Embryo Today Rev 102, 309–323. https://doi.org/10.1002/bdrc.21076

KIANI, C., CHEN, L., WU, Y.J., YEE, A.J., YANG, B.B., 2002. Structure and function of aggrecan. Cell Res 12, 19–32. https://doi.org/10.1038/sj.cr.7290106

Kikkawa, Y., Miner, J.H., 2006. Molecular dissection of Laminin **α**5 in vivo reveals separable domain-specific roles in embryonic development and kidney function. Dev Biol 296, 265–277. https://doi.org/10.1016/j.ydbio.2006.04.463

Kim, S.-J., 2011. Heterotaxy syndrome. Korean Circ J 41, 227–32. https://doi.org/10.4070/kcj.2011.41.5.227

Kimmel, C.B., Ballard, W.W., Kimmel, S.R., Ullmann, B., Schilling, T.F., 1995. Stages of embryonic development of the zebrafish. Dev Dynam 203, 253–310. https://doi.org/10.1002/aja.1002030302

Knöll, R., Postel, R., Wang, J., Krätzner, R., Hennecke, G., Vacaru, A.M., Vakeel, P., Schubert, C., Murthy, K., Rana, B.K., Kube, D., Knöll, G., Schäfer, K., Hayashi, T., Holm, T., Kimura, A., Schork, N., Toliat, M.R., Nürnberg, P., Schultheiss, H.-P., Schaper, W., Schaper, J., Bos, E., Hertog, J.D., Eeden, F.J.M. van, Peters, P.J., Hasenfuss, G., Chien, K.R., Bakkers, J., 2007. Laminin-**α**4 and Integrin-Linked Kinase Mutations Cause Human Cardiomyopathy Via Simultaneous Defects in Cardiomyocytes and Endothelial Cells. Circulation 116, 515–525. https://doi.org/10.1161/circulationaha.107.689984

Kok, F.O., Shin, M., Ni, C.-W., Gupta, A., Grosse, A.S., van Impel, A., Kirchmaier, B.C., Peterson-Maduro, J., Kourkoulis, G., Male, I., DeSantis, D.F., Sheppard-Tindell, S., Ebarasi, L., Betsholtz, C., Schulte-Merker, S., Wolfe, S.A., Lawson, N.D., 2015. Reverse Genetic Screening Reveals Poor Correlation between Morpholino-Induced and Mutant Phenotypes in Zebrafish. Dev Cell 32, 97–108. https://doi.org/10.1016/j.devcel.2014.11.018

Kortesmaa, J., Yurchenco, P., Tryggvason, K., 2000. Recombinant Laminin-8 (**α** 4 **β** 1 **γ** 1). J Biol Chem 275, 14853–14859. https://doi.org/10.1074/jbc.275.20.14853

Kozak, M., 1987. At least six nucleotides preceding the AUG initiator codon enhance translation in mammalian cells. J Mol Biol 196, 947–950. https://doi.org/10.1016/0022-2836(87)90418-9

Kuhnert, F., Mancuso, M.R., Hampton, J., Stankunas, K., Asano, T., Chen, C.-Z., Kuo, C.J., 2008. Attribution of vascular phenotypes of the murine Egfl7 locus to the microRNA miR-126. Dev Camb Engl 135, 3989–93. https://doi.org/10.1242/dev.029736

Kwan, K.M., Fujimoto, E., Grabher, C., Mangum, B.D., Hardy, M.E., Campbell, D.S., Parant, J.M., Yost, H.J., Kanki, J.P., Chien, C.-B., 2007. The Tol2kit: A multisite gateway-based construction kit forTol2 transposon transgenesis constructs. Dev Dynam 236, 3088–3099. https://doi.org/10.1002/dvdy.21343

Labun, K., Montague, T.G., Gagnon, J.A., Thyme, S.B., Valen, E., 2016. CHOPCHOP v2: a web tool for the next generation of CRISPR genome engineering. Nucleic Acids Res 44, W272–W276. https://doi.org/10.1093/nar/gkw398

Lagendijk, A.K., Goumans, M.J., Burkhard, S.B., Bakkers, J., 2011. MicroRNA-23 restricts cardiac valve formation by inhibiting Has2 and extracellular hyaluronic acid production. Circ Res 109, 649–57. https://doi.org/10.1161/circresaha.111.247635

Lagendijk, A.K., Szabó, A., Merks, R.M.H., Bakkers, J., 2013. Hyaluronan: a critical regulator of endothelial-to-mesenchymal transition during cardiac valve formation. Trends Cardiovas Med 23, 135–42. https://doi.org/10.1016/j.tcm.2012.10.002

Lai, J.K.H., Gagalova, K.K., Kuenne, C., El-Brolosy, M.A., Stainier, D.Y.R., 2019. Induction of interferon-stimulated genes and cellular stress pathways by morpholinos in zebrafish. Dev Biol 454, 21–28. https://doi.org/10.1016/j.ydbio.2019.06.008

Langheinrich, U., Hennen, E., Stott, G., Vacun, G., 2002. Zebrafish as a Model Organism for the Identification and Characterization of Drugs and Genes Affecting p53 Signaling. Curr Biol 12, 2023–2028. https://doi.org/10.1016/s0960-9822(02)01319-2

Larson, M.H., Gilbert, L.A., Wang, X., Lim, W.A., Weissman, J.S., Qi, L.S., 2013. CRISPR interference (CRISPRi) for sequence-specific control of gene expression. Nat Protoc 8, 2180–96. https://doi.org/10.1038/nprot.2013.132

Lazic, S., Scott, I.C., 2011. Mef2cb regulates late myocardial cell addition from a second heart field-like population of progenitors in zebrafish. Dev Biol 354, 123–33. https://doi.org/10.1016/j.ydbio.2011.03.028

Lenhart, K.F., Holtzman, N.G., Williams, J.R., Burdine, R.D., 2013. Integration of Nodal and BMP Signals in the Heart Requires FoxH1 to Create Left–Right Differences in Cell Migration Rates That Direct Cardiac Asymmetry. Plos Genet 9, e1003109. https://doi.org/10.1371/journal.pgen.1003109

Levin, M., 2005. Left–right asymmetry in embryonic development: a comprehensive review. Mech Develop 122, 3–25. https://doi.org/10.1016/j.mod.2004.08.006

Li, L., Krantz, I.D., Deng, Y., Genin, A., Banta, A.B., Collins, C.C., Qi, M., Trask, B.J., Kuo, W.L., Cochran, J., Costa, T., Pierpont, M.E.M., Rand, E.B., Piccoli, D.A., Hood, L., Spinner, N.B., 1997. Alagille syndrome is caused by mutations in human Jagged1, which encodes a ligand for Notch1. Nat Genet 16, 243–251. https://doi.org/10.1038/ng0797-243

Libby, R.T., Champliaud, M.F., Claudepierre, T., Xu, Y., Gibbons, E.P., Koch, M., Burgeson, R.E., Hunter, D.D., Brunken, W.J., 2000. Laminin expression in adult and developing retinae: evidence of two novel CNS Laminins. J Neurosci Official J Soc Neurosci 20, 6517–28. https://doi.org/10.1523/jneurosci.20-17-06517.2000

Lin, A., Giuliano, C.J., Sayles, N.M., Sheltzer, J.M., 2017. CRISPR/Cas9 mutagenesis invalidates a putative cancer dependency targeted in on-going clinical trials. Elife 6, e24179. https://doi.org/10.7554/elife.24179

Lin, M.-L., Park, J.-H., Nishidate, T., Nakamura, Y., Katagiri, T., 2007. Involvement of maternal embryonic leucine zipper kinase (MELK) in mammary carcinogenesis through interaction with Bcl-G, a pro-apoptotic member of the Bcl-2 family. Breast Cancer Res 9, R17. https://doi.org/10.1186/bcr1650

Lin, X., Buff, E.M., Perrimon, N., Michelson, A.M., 1999. Heparan Sulfate Proteoglycans are essential for FGF receptor signaling during Drosophila embryonic development. Dev Camb Engl 126, 3715–23.

Lindahl, U., Couchman, J., Kimata, K., Esko., and J.D., 2017. Essentials of Glycobiology Chapter 17 Proteoglycans and Sulfated Glycosaminoglycans. https://doi.org/10.1101/glycobiology.3e.017

Linde, D. van der, Konings, E.E.M., Slager, M.A., Witsenburg, M., Helbing, W.A., Takkenberg, J.J.M., Roos-Hesselink, J.W., 2011. Birth prevalence of congenital heart disease worldwide: a systematic review and meta-analysis. J Am Coll Cardiol 58, 2241–7. https://doi.org/10.1016/j.jacc.2011.08.025

Lindsay, E.A., Vitelli, F., Su, H., Morishima, M., Huynh, T., Pramparo, T., Jurecic, V., Ogunrinu, G., Sutherland, H.F., Scambler, P.J., Bradley, A., Baldini, A., 2001. Tbx1 haploinsufficiency in the DiGeorge syndrome region causes aortic arch defects in mice. Nature 410, 97–101. https://doi.org/10.1038/35065105

Liu, W., Xie, Y., Ma, J., Luo, X., Nie, P., Zuo, Z., Lahrmann, U., Zhao, Q., Zheng, Y., Zhao, Y., Xue, Y., Ren, J., 2015. IBS: an illustrator for the presentation and visualization of biological sequences. Bioinform Oxf Engl 31, 3359–61. https://doi.org/10.1093/bioinformatics/btv362

Llorca, F.O., Gil, D.R., 1967. A causal analysis of the heart curvatures in the chicken embryo. Wilhelm Roux' Archiv F R Entwicklungsmechanik Der Org 158, 52–63. https://doi.org/10.1007/bf00713791

Lombardo, V.A., Heise, M., Moghtadaei, M., Bornhorst, D., Männer, J., Abdelilah-Seyfried, S., 2019. Morphogenetic control of zebrafish cardiac looping by Bmp signaling. Development 146, dev180091. https://doi.org/10.1242/dev.180091

Long, S., Ahmad, N., Rebagliati, M., 2003. The zebrafish nodal-related gene southpaw is required for visceral and diencephalic left-right asymmetry. Development 130, 2303–2316. https://doi.org/10.1242/dev.00436

Luxán, G., Casanova, J.C., Martínez-Poveda, B., Prados, B., D'Amato, G., MacGrogan, D., Gonzalez-Rajal, A., Dobarro, D., Torroja, C., Martinez, F., Izquierdo-García, J.L., Fernández-Friera, L., Sabater-Molina, M., Kong, Y.-Y., Pizarro, G., Ibañez, B., Medrano, C., García-Pavía, P., Gimeno, J.R., Monserrat, L., Jiménez-Borreguero, L.J., Pompa, J.L. de la, 2013. Mutations in the NOTCH pathway regulator MIB1 cause left ventricular noncompaction cardiomyopathy. Nat Med 19, 193–201. https://doi.org/10.1038/nm.3046

Mably, J.D., Burns, C.G., Chen, J.-N., Fishman, M.C., Mohideen, M.-A.P.K., 2003. heart of glass Regulates the Concentric Growth of the Heart in Zebrafish. Curr Biol 13, 2138–2147. https://doi.org/10.1016/j.cub.2003.12.055

Mably, J.D., Chuang, L.P., Serluca, F.C., Mohideen, M.-A.P.K., Chen, J.-N., Fishman, M.C., 2006. santa and valentine pattern concentric growth of cardiac

myocardium in the zebrafish. Development 133, 3139–3146. https://doi.org/10.1242/dev.02469

MacDonald, R.B., Pollack, J.N., Debiais-Thibaud, M., Heude, E., Talbot, J.C., Ekker, M., 2013. The ascl1a and dlx genes have a regulatory role in the development of GABAergic interneurons in the zebrafish diencephalon. Dev Biol 381, 276–85. https://doi.org/10.1016/j.ydbio.2013.05.025

MacGrogan, D., D'Amato, G., Travisano, S., Martinez-Poveda, B., Luxán, G., Monte-Nieto, G.D., Papoutsi, T., Sbroggio, M., Bou, V., Arco, P.G.-D., Gómez, M.J., Zhou, B., Redondo, J.M., Jiménez-Borreguero, L.J., Pompa, J.L. de la, 2016. Sequential Ligand-Dependent Notch Signaling Activation Regulates Valve Primordium Formation and Morphogenesis. Circ Res 118, 1480–97. https://doi.org/10.1161/circresaha.115.308077

Manasek, F.J., Monroe, R.G., 1972. Early cardiac morphogenesis is independent of function. Dev Biol 27, 584–588. https://doi.org/10.1016/0012-1606(72)90196-0

Männer, J., 2009. The anatomy of cardiac looping: A step towards the understanding of the morphogenesis of several forms of congenital cardiac malformations. Clin Anat 22, 21–35. https://doi.org/10.1002/ca.20652

Männer, J., 2004. On rotation, torsion, lateralization, and handedness of the embryonic heart loop: New insights from a simulation model for the heart loop of chick embryos. Anatomical Rec Part Discov Mol Cell Evol Biology 278A, 481–492. https://doi.org/10.1002/ar.a.20036

Manning, A., McLachlan, J.C., 1990. Looping of chick embryo hearts in vitro. J Anat 168, 257–63.

Maquat, L.E., 2005. Nonsense-mediated mRNA decay in mammals. J Cell Sci 118, 1773–1776. https://doi.org/10.1242/jcs.01701

Margadant, C., Charafeddine, R.A., Sonnenberg, A., 2010. Unique and redundant functions of integrins in the epidermis. Faseb J Official Publ Fed Am Soc Exp Biology 24, 4133–52. https://doi.org/10.1096/fj.09-151449

Martin, P., Ettinger, A., Sanes, 1995. A synaptic localization domain in the synaptic cleft protein laminin beta 2 (s-laminin). Science 269, 413–416. https://doi.org/10.1126/science.7618109

Matsubayashi, Y., Sánchez-Sánchez, B.J., Marcotti, S., Serna-Morales, E., Dragu, A., Díaz-de-la-Loza, M.-C., Vizcay-Barrena, G., Fleck, R.A., Stramer, B.M., 2020. Rapid Homeostatic Turnover of Embryonic ECM during Tissue Morphogenesis. Dev Cell. https://doi.org/10.1016/j.devcel.2020.06.005

McDaniell, R., Warthen, D.M., Sanchez-Lara, P.A., Pai, A., Krantz, I.D., Piccoli, D.A., Spinner, N.B., 2006. NOTCH2 Mutations Cause Alagille Syndrome, a Heterogeneous Disorder of the Notch Signaling Pathway. Am J Hum Genetics 79, 169–173. https://doi.org/10.1086/505332

Members, W.G., Roger, V.L., Go, A.S., Lloyd-Jones, D.M., Benjamin, E.J., Berry, J.D., Borden, W.B., Bravata, D.M., Dai, S., Ford, E.S., Fox, C.S., Fullerton, H.J., Gillespie, C., Hailpern, S.M., Heit, J.A., Howard, V.J., Kissela, B.M., Kittner, S.J., Lackland, D.T., Lichtman, J.H., Lisabeth, L.D., Makuc, D.M., Marcus, G.M., Marelli, A., Matchar, D.B., Moy, C.S., Mozaffarian, D., Mussolino, M.E., Nichol, G., Paynter, N.P., Soliman, E.Z., Sorlie, P.D., Sotoodehnia, N., Turan, T.N., Virani, S.S., Wong, N.D., Woo, D., Turner, M.B., 2012. Heart Disease and Stroke Statistics—2012 Update. Circulation 125, e2–e220. https://doi.org/10.1161/cir.0b013e31823ac046

Merscher, S., Funke, B., Epstein, J.A., Heyer, J., Puech, A., Lu, M.M., Xavier, R.J., Demay, M.B., Russell, R.G., Factor, S., Tokooya, K., Jore, B.St., Lopez, M., Pandita, R.K., Lia, M., Carrion, D., Xu, H., Schorle, H., Kobler, J.B., Scambler, P., Wynshaw-Boris, A., Skoultchi, A.I., Morrow, B.E., Kucherlapati, R., 2001. TBX1 Is Responsible for Cardiovascular Defects in Velo-Cardio-Facial/DiGeorge Syndrome. Cell 104, 619–629. https://doi.org/10.1016/s0092-8674(01)00247-1

Midgett, M., Chivukula, V.K., Dorn, C., Wallace, S., Rugonyi, S., 2015. Blood flow through the embryonic heart outflow tract during cardiac looping in HH13–HH18 chicken embryos. J Roy Soc Interface 12, 20150652. https://doi.org/10.1098/rsif.2015.0652

Miner, J.H., Cunningham, J., Sanes, J.R., 1998. Roles for Laminin in Embryogenesis: Exencephaly, Syndactyly, and Placentopathy in Mice Lacking the Laminin **α**5 Chain. J Cell Biology 143, 1713–1723. https://doi.org/10.1083/jcb.143.7.1713

Miner, J.H., Li, C., 2000. Defective Glomerulogenesis in the Absence of Laminin **α**5 Demonstrates a Developmental Role for the Kidney Glomerular Basement Membrane. Dev Biol 217, 278–289. https://doi.org/10.1006/dbio.1999.9546

Miner, J.H., Sanes, J.R., 1994. Collagen IV alpha 3, alpha 4, and alpha 5 chains in rodent basal laminae: sequence, distribution, association with Laminins, and developmental switches. J Cell Biology 127, 879–891. https://doi.org/10.1083/jcb.127.3.979

Miner, J.H., Yurchenco, P.D., 2004. LAMININ FUNCTIONS IN TISSUE MORPHOGENESIS. Cell Dev Biology 20, 255–284. https://doi.org/10.1146/annurev.cellbio.20.010403.094555

Mittal, A., Pulina, M., Hou, S.-Y., Astrof, S., 2013. Fibronectin and integrin alpha 5 play requisite roles in cardiac morphogenesis. Dev Biol 381, 73–82. https://doi.org/10.1016/j.ydbio.2013.06.010

Mittal, N., Yoon, S.H., Enomoto, H., Hiroshi, M., Shimizu, A., Kawakami, A., Fujita, M., Watanabe, H., Fukuda, K., Makino, S., 2019. Versican is crucial for the initiation of cardiovascular lumen development in medaka (Oryzias latipes). Sci Rep-uk 9, 9475. https://doi.org/10.1038/s41598-019-45851-3

Mjaatvedt, C.H., Yamamura, H., Capehart, A.A., Turner, D., Markwald, R.R., 1998. TheCspg2Gene, Disrupted in thehdfMutant, Is Required for Right Cardiac Chamber and Endocardial Cushion Formation. Dev Biol 202, 56–66. https://doi.org/10.1006/dbio.1998.9001

Mjaatvedt, C.H., Nakaoka, T., Moreno-Rodriguez, R., Norris, R.A., Kern, M.J., Eisenberg, C.A., Turner, D., Markwald, R.R., 2001. The Outflow Tract of the Heart Is Recruited from a Novel Heart-Forming Field. Dev Biol 238, 97–109. https://doi.org/10.1006/dbio.2001.0409

Monte-Nieto, G. del, Ramialison, M., Adam, A.A.S., Wu, B., Aharonov, A., D'Uva, G., Bourke, L.M., Pitulescu, M.E., Chen, H., Pompa, J.L. de la, Shou, W., Adams,

R.H., Harten, S.K., Tzahor, E., Zhou, B., Harvey, R.P., 2018. Control of cardiac jelly dynamics by NOTCH1 and NRG1 defines the building plan for trabeculation. Nature 557, 439–445. https://doi.org/10.1038/s41586-018-0110-6

Moon, A., 2008. Mouse models of congenital cardiovascular disease. Curr Top Dev Biol 84, 171–248. https://doi.org/10.1016/s0070-2153(08)00604-2

Moore, C.J., Winder, S.J., 2010. Dystroglycan versatility in cell adhesion: a tale of multiple motifs. Cell Commun Signal Ccs 8, 3. https://doi.org/10.1186/1478-811x-8-3

Mosimann, C., Kaufman, C.K., Li, P., Pugach, E.K., Tamplin, O.J., Zon, L.I., 2011. Ubiquitous transgene expression and Cre-based recombination driven by the ubiquitin promoter in zebrafish. Dev Camb Engl 138, 169–77. https://doi.org/10.1242/dev.059345

Mould, A.P., McLeish, J.A., Huxley-Jones, J., Goonesinghe, A.C., Hurlstone, A.F., Boot-Handford, R.P., Humphries, M.J., 2006. Identification of multiple integrin β1 homologs in zebrafish (Danio rerio). Bmc Cell Biol 7, 24. https://doi.org/10.1186/1471-2121-7-24

Mouw, J.K., Ou, G., Weaver, V.M., 2014. Extracellular matrix assembly: a multiscale deconstruction. Nat Rev Mol Cell Biology 15, 771–85. https://doi.org/10.1038/nrm3902

Mulligan, G.J., Wong, J., Jacks, T., 1998. p130 Is Dispensable in Peripheral T Lymphocytes: Evidence for Functional Compensation by p107 and pRB. Mol Cell Biol 18, 206–220. https://doi.org/10.1128/mcb.18.1.206

Muntean, I., Togănel, R., Benedek, T., 2016. Genetics of Congenital Heart Disease: Past and Present. Biochem Genet 55, 105–123. https://doi.org/10.1007/s10528-016-9780-7

MUTTERER, J., ZINCK, E., 2013. Quick-and-clean article figures with FigureJ: ARTICLE FIGURES WITH FigureJ. J Microsc-oxford 252, 89–91. https://doi.org/10.1111/jmi.12069

Nakamura, A., Manasek, F.J., 1981. An experimental study of the relation of cardiac jelly to the shape of the early chick embryonic heart. J Embryol Exp Morph 65, 235–56.

Nasevicius, A., Ekker, S.C., 2000. Effective targeted gene 'knockdown' in zebrafish. Nat Genet 26, 216–220. https://doi.org/10.1038/79951

Naylor, M.J., Li, N., Cheung, J., Lowe, E.T., Lambert, E., Marlow, R., Wang, P., Schatzmann, F., Wintermantel, T., Schüetz, G., Clarke, A.R., Mueller, U., Hynes, N.E., Streuli, C.H., 2005. Ablation of **β**1 integrin in mammary epithelium reveals a key role for integrin in glandular morphogenesis and differentiation. J Cell Biol 171, 717–728. https://doi.org/10.1083/jcb.200503144

Nevis, K., Obregon, P., Walsh, C., Guner-Ataman, B., Burns, C.G., Burns, C.E., 2013. Tbx1 is required for second heart field proliferation in zebrafish. Dev Dyn Official Publ Am Assoc Anatomists 242, 550–9. https://doi.org/10.1002/dvdy.23928

Nishiuchi, R., Takagi, J., Hayashi, M., Ido, H., Yagi, Y., Sanzen, N., Tsuji, T., Yamada, M., Sekiguchi, K., 2006. Ligand-binding specificities of Laminin-binding integrins: A comprehensive survey of Laminin–integrin interactions using recombinant **α**3**β**1, **α**6**β**1, **α**7**β**1 and **α**6**β**4 integrins. Matrix Biol 25, 189–197. https://doi.org/10.1016/j.matbio.2005.12.001

Noakes, P.G., Gautam, M., Mudd, J., Sanes, J.R., Merlie, J.P., 1995a. Aberrant differentiation of neuromuscular junctions in mice lacking s-Laminin/Laminin **β**2. Nature 374, 258–262. https://doi.org/10.1038/374258a0

Noakes, P.G., Miner, J.H., Gautam, M., Cunningham, J.M., Sanes, J.R., Merlie, J.P., 1995b. The renal glomerulus of mice lacking s–Laminin/Laminin **β**2: nephrosis despite molecular compensation by Laminin **β**1. Nat Genet 10, 400–406. https://doi.org/10.1038/ng0895-400

Noël, E.S., Verhoeven, M., Lagendijk, A.K., Tessadori, F., Smith, K., Choorapoikayil, S., Hertog, J. den, Bakkers, J., 2013. A Nodal-independent and tissue-intrinsic mechanism controls heart-looping chirality. Nat Commun 4, 2754. https://doi.org/10.1038/ncomms3754

Notari, M., Ventura-Rubio, A., Bedford-Guaus, S.J., Jorba, I., Mulero, L., Navajas, D., Martí, M., Raya, Á., 2018. The local microenvironment limits the regenerative potential of the mouse neonatal heart. Sci Adv 4, eaao5553. https://doi.org/10.1126/sciadv.aao5553

Novodvorsky, P., Watson, O., Gray, C., Wilkinson, R.N., Reeve, S., Smythe, C., Beniston, R., Plant, K., Maguire, R., Rothman, A.M.K., Elworthy, S., Eeden, F.J.M. van, Chico, T.J.A., 2015. klf2ash317 Mutant Zebrafish Do Not Recapitulate Morpholino-Induced Vascular and Haematopoietic Phenotypes. Plos One 10, e0141611. https://doi.org/10.1371/journal.pone.0141611

O'Brien, L.E., Jou, T.-S., Pollack, A.L., Zhang, Q., Hansen, S.H., Yurchenco, P., Mostov, K.E., 2001. Rac1 orientates epithelial apical polarity through effects on basolateral Laminin assembly. Nat Cell Biol 3, 831–838. https://doi.org/10.1038/ncb0901-831

Odenthal, J., Haffter, P., Vogelsang, E., Brand, M., Eeden, F.J. van, Furutani-Seiki, M., Granato, M., Hammerschmidt, M., Heisenberg, C.P., Jiang, Y.J., Kane, D.A., Kelsh, R.N., Mullins, M.C., Warga, R.M., Allende, M.L., Weinberg, E.S., Nüsslein-Volhard, C., 1996. Mutations affecting the formation of the notochord in the zebrafish, Danio rerio. Dev Camb Engl 123, 103–15.

Otten, C., Knox, J., Boulday, G., Eymery, M., Haniszewski, M., Neuenschwander, M., Radetzki, S., Vogt, I., Hähn, K., Luca, C.D., Cardoso, C., Hamad, S., Gil, C.I., Roy, P., Albiges-Rizo, C., Faurobert, E., Kries, J.P., Campillos, M., Tournier-Lasserve, E., Derry, W.B., Abdelilah-Seyfried, S., 2018. Systematic pharmacological screens uncover novel pathways involved in cerebral cavernous malformations. Embo Mol Med 10. https://doi.org/10.15252/emmm.201809155

Paffett-Lugassy, N., Hsia, N., Fraenkel, P.G., Paw, B., Leshinsky, I., Barut, B., Bahary, N., Caro, J., Handin, R., Zon, L.I., 2007. Functional conservation of erythropoietin signaling in zebrafish. Blood 110, 2718–2726. https://doi.org/10.1182/blood-2006-04-016535

Paine-Saunders, S., Viviano, B.L., Economides, A.N., Saunders, S., 2001. Heparan Sulfate Proteoglycans Retain Noggin at the Cell Surface. J Biol Chem 277, 2089–2096. https://doi.org/10.1074/jbc.m109151200

Palencia-Desai, S., Rost, M.S., Schumacher, J.A., Ton, Q.V., Craig, M.P., Baltrunaite, K., Koenig, A.L., Wang, J., Poss, K.D., Chi, N.C., Stainier, D.Y.R., Sumanas, S., 2015. Myocardium and BMP signaling are required for endocardial differentiation. Development 142, 2304–2315. https://doi.org/10.1242/dev.118687

Parker, L.H., Schmidt, M., Jin, S.-W., Gray, A.M., Beis, D., Pham, T., Frantz, G., Palmieri, S., Hillan, K., Stainier, D.Y.R., Sauvage, F.J. de, Ye, W., 2004. The endothelial-cell-derived secreted factor Egfl7 regulates vascular tube formation. Nature 428, 754–758. https://doi.org/10.1038/nature02416

Parsons, M.J., Pollard, S.M., Saúde, L., Feldman, B., Coutinho, P., Hirst, E.M.A., Stemple, D.L., 2002. Zebrafish mutants identify an essential role for Laminins in notochord formation. Dev Camb Engl 129, 3137–46.

Passer, D., Vrugt, A. van de, Atmanli, A., Domian, I.J., 2016. Atypical Protein Kinase C-Dependent Polarized Cell Division Is Required for Myocardial Trabeculation. Cell Reports 14, 1662–1672. https://doi.org/10.1016/j.celrep.2016.01.030

Pater, E. de, Clijsters, L., Marques, S.R., Lin, Y.-F., Garavito-Aguilar, Z.V., Yelon, D., Bakkers, J., 2009. Distinct phases of cardiomyocyte differentiation regulate growth of the zebrafish heart. Development 136, 1633–1641. https://doi.org/10.1242/dev.030924

Patra, C., Diehl, F., Ferrazzi, F., Amerongen, M.J. van, Novoyatleva, T., Schaefer, L., Mühlfeld, C., Jungblut, B., Engel, F.B., 2011. Nephronectin regulates atrioventricular canal differentiation via Bmp4-Has2 signaling in zebrafish. Dev Camb Engl 138, 4499–509. https://doi.org/10.1242/dev.067454

Patten, B.M., 1922. The formation of the cardiac loop in the chick. Am J Anat 30, 373–397. https://doi.org/10.1002/aja.1000300304

Patton, B.L., Chiu, A.Y., Sanes, J.R., 1998. Synaptic Laminin prevents glial entry into the synaptic cleft. Nature 393, 698–701. https://doi.org/10.1038/31502

Peal, D.S., Burns, C.G., Macrae, C.A., Milan, D., 2009. Chondroitin Sulfate expression is required for cardiac atrioventricular canal formation. Dev Dynam 238, 3103–3110. https://doi.org/10.1002/dvdy.22154

Peal, D.S., Lynch, S.N., Milan, D.J., 2011. Patterning and development of the atrioventricular canal in zebrafish. J Cardiovasc Transl 4, 720–6. https://doi.org/10.1007/s12265-011-9313-z

Peralta, M., Steed, E., Harlepp, S., González-Rosa, J.M., Monduc, F., Ariza-Cosano, A., Cortés, A., Rayón, T., Gómez-Skarmeta, J.-L., Zapata, A., Vermot, J., Mercader, N., 2013. Heartbeat-Driven Pericardiac Fluid Forces Contribute to Epicardium Morphogenesis. Curr Biol 23, 1726–1735. https://doi.org/10.1016/j.cub.2013.07.005

Perissinotto, D., Iacopetti, P., Bellina, I., Doliana, R., Colombatti, A., Pettway, Z., Bronner-Fraser, M., Shinomura, T., Kimata, K., Mörgelin, M., Löfberg, J., Perris, R., 2000. Avian neural crest cell migration is diversely regulated by the two major hyaluronan-binding Proteoglycans PG-M/versican and aggrecan. Dev Camb Engl 127, 2823–42.

Pestel, J., Ramadass, R., Gauvrit, S., Helker, C., Herzog, W., Stainier, D.Y.R., 2016. Real-time 3D visualization of cellular rearrangements during cardiac valve formation. Dev Camb Engl 143, 2217–27. https://doi.org/10.1242/dev.133272

Pickar-Oliver, A., Gersbach, C.A., 2019. The next generation of CRISPR–Cas technologies and applications. Nat Rev Mol Cell Bio 20, 490–507. https://doi.org/10.1038/s41580-019-0131-5

Pierpont, M.E.M., Markwald, R.R., Lin, A.E., 2000. Genetic aspects of atrioventricular septal defects. Am J Med Genet 97, 289–296. https://doi.org/10.1002/1096-8628(200024)97:4<289::aid-ajmg1279>3.0.co;2-u

Plageman, T.F., Yutzey, K.E., 2004. T-box genes and heart development: Putting the ?T? in heart. Dev Dynam 232, 11–20. https://doi.org/10.1002/dvdy.20201

Pollard, S.M., Parsons, M.J., Kamei, M., Kettleborough, R.N.W., Thomas, K.A., Pham, V.N., Bae, M.-K., Scott, A., Weinstein, B.M., Stemple, D.L., 2006. Essential

and overlapping roles for Laminin **α** chains in notochord and blood vessel formation. Dev Biol 289, 64–76. https://doi.org/10.1016/j.ydbio.2005.10.006

Pomin, V., Mulloy, B., 2018. Glycosaminoglycans and Proteoglycans. Pharm 11, 27. https://doi.org/10.3390/ph11010027

Pompa, J.L. de la, Timmerman, L.A., Takimoto, H., Yoshida, H., Elia, A.J., Samper, E., Potter, J., Wakeham, A., Marengere, L., Langille, B.L., Crabtree, G.R., Mak, T.W., 1998. Role of the NF-ATc transcription factor in morphogenesis of cardiac valves and septum. Nature 392, 182–186. https://doi.org/10.1038/32419

Popp, M.W., Maquat, L.E., 2016. Leveraging Rules of Nonsense-Mediated mRNA Decay for Genome Engineering and Personalized Medicine. Cell 165, 1319–22. https://doi.org/10.1016/j.cell.2016.05.053

Poulain, F.E., Yost, H.J., 2015. Heparan Sulfate Proteoglycans: a sugar code for vertebrate development? Development 142, 3456–3467. https://doi.org/10.1242/dev.098178

Qi, L.S., Larson, M.H., Gilbert, L.A., Doudna, J.A., Weissman, J.S., Arkin, A.P., Lim, W.A., 2013. Repurposing CRISPR as an RNA-guided platform for sequence-specific control of gene expression. Cell 152, 1173–83. https://doi.org/10.1016/j.cell.2013.02.022

Quinkertz, A., Campos-Ortega, J.A., 1999. A new **β**-globin gene from the zebrafish, **β** E1 , and its pattern of transcription during embryogenesis. Dev Genes Evol 209, 126–131. https://doi.org/10.1007/s004270050235

Rambeau, P., Faure, E., Théron, A., Avierinos, J.-F., Jopling, C., Zaffran, S., Faucherre, A., 2017. Reduced aggrecan expression affects cardiac outflow tract development in zebrafish and is associated with bicuspid aortic valve disease in humans. Int J Cardiol 249, 340–343. https://doi.org/10.1016/j.ijcard.2017.09.174

Raj, A., Rifkin, S.A., Andersen, E., Oudenaarden, A. van, 2010. Variability in gene expression underlies incomplete penetrance. Nature 463, 913–918. https://doi.org/10.1038/nature08781

Reifers, F., Walsh, E.C., Léger, S., Stainier, D.Y., Brand, M., 2000. Induction and differentiation of the zebrafish heart requires fibroblast growth factor 8 (fgf8/acerebellar). Dev Camb Engl 127, 225–35.

Reischauer, S., Arnaout, R., Ramadass, R., Stainier, D.Y.R., 2014. Actin binding GFP allows 4D in vivo imaging of myofilament dynamics in the zebrafish heart and the identification of Erbb2 signaling as a remodeling factor of myofibril architecture. Circ Res 115, 845–56. https://doi.org/10.1161/circresaha.115.304356

Renz, M., Otten, C., Faurobert, E., Rudolph, F., Zhu, Y., Boulday, G., Duchene, J., Mickoleit, M., Dietrich, A.-C., Ramspacher, C., Steed, E., Manet-Dupé, S., Benz, A., Hassel, D., Vermot, J., Huisken, J., Tournier-Lasserve, E., Felbor, U., Sure, U., Albiges-Rizo, C., Abdelilah-Seyfried, S., 2015. Regulation of β1 Integrin-Klf2-Mediated Angiogenesis by CCM Proteins. Dev Cell 32, 181–190. https://doi.org/10.1016/j.devcel.2014.12.016

Robu, M.E., Larson, J.D., Nasevicius, A., Beiraghi, S., Brenner, C., Farber, S.A., Ekker, S.C., 2007. p53 Activation by Knockdown Technologies. Plos Genet 3, e78. https://doi.org/10.1371/journal.pgen.0030078

Roediger, M., Miosge, N., Gersdorff, N., 2010. Tissue distribution of the Laminin beta1 and beta2 chain during embryonic and fetal human development. J Mol Histol 41, 177–84. https://doi.org/10.1007/s10735-010-9275-5

Rohr, S., Otten, C., Abdelilah-Seyfried, S., 2008. Asymmetric Involution of the Myocardial Field Drives Heart Tube Formation in Zebrafish. Circ Res 102, e12–e19. https://doi.org/10.1161/circresaha.107.165241

Rossi, A., Kontarakis, Z., Gerri, C., Nolte, H., Hölper, S., Krüger, M., Stainier, D.Y.R., 2015. Genetic compensation induced by deleterious mutations but not gene knockdowns. Nature 524, 230–3. https://doi.org/10.1038/nature14580

Roughley, P.J., Mort, J.S., 2014. The role of aggrecan in normal and osteoarthritic cartilage. J Exp Orthop 1, 8. https://doi.org/10.1186/s40634-014-0008-7

Rozario, T., DeSimone, D.W., 2009. The extracellular matrix in development and morphogenesis: a dynamic view. Dev Biol 341, 126–40. https://doi.org/10.1016/j.ydbio.2009.10.026

Ruiz-Villalba, A., Pérez-Pomares, J.M., 2012. The expanding role of the epicardium and epicardial-derived cells in cardiac development and disease. Curr Opin Pediatr 24, 569–76. https://doi.org/10.1097/mop.0b013e328357a532

Russo, J.D., Luik, A.-L., Yousif, L., Budny, S., Oberleithner, H., Hofschröer, V., Klingauf, J., Bavel, E. van, Bakker, E.N., Hellstrand, P., Bhattachariya, A., Albinsson, S., Pincet, F., Hallmann, R., Sorokin, L.M., 2016. Endothelial basement membrane Laminin 511 is essential for shear stress response. Embo J 36, 183–201. https://doi.org/10.15252/embj.201694756

Saha, P., Potiny, P., Rigdon, J., Morello, M., Tcheandjieu, C., Romfh, A., Fernandes, S.M., McElhinney, D.B., Bernstein, D., Lui, G.K., Shaw, G.M., Ingelsson, E., Priest, J.R., 2019. Substantial Cardiovascular Morbidity in Adults with Lower-Complexity Congenital Heart Disease. Circulation 139, 1889–1899. https://doi.org/10.1161/circulationaha.118.037064

Samsa, L.A., Givens, C., Tzima, E., Stainier, D.Y.R., Qian, L., Liu, J., 2015. Cardiac contraction activates endocardial Notch signaling to modulate chamber maturation in zebrafish. Dev Camb Engl 142, 4080–91. https://doi.org/10.1242/dev.125724

Samsa, L.A., Yang, B., Liu, J., 2013. Embryonic cardiac chamber maturation: Trabeculation, conduction, and cardiomyocyte proliferation. Am J Medical Genetics Part C Seminars Medical Genetics 163C, 157–68. https://doi.org/10.1002/ajmg.c.31366

Savage, A.M., Kurusamy, S., Chen, Y., Jiang, Z., Chhabria, K., MacDonald, R.B., Kim, H.R., Wilson, H.L., Eeden, F.J.M. van, Armesilla, A.L., Chico, T.J.A., Wilkinson, R.N., 2019. tmem33 is essential for VEGF-mediated endothelial calcium oscillations and angiogenesis. Nat Commun 10, 732. https://doi.org/10.1038/s41467-019-08590-7

Scherz, P.J., Huisken, J., Sahai-Hernandez, P., Stainier, D.Y.R., 2008. High-speed imaging of developing heart valves reveals interplay of morphogenesis and function. Development 135, 1179–1187. https://doi.org/10.1242/dev.010694

Schier, A.F., Neuhauss, S.C., Harvey, M., Malicki, J., Solnica-Krezel, L., Stainier, D.Y., Zwartkruis, F., Abdelilah, S., Stemple, D.L., Rangini, Z., Yang, H., Driever, W., 1996. Mutations affecting the development of the embryonic zebrafish brain. Dev Camb Engl 123, 165–78.

Schmidt, M., Paes, K., Maziere, A.D., Smyczek, T., Yang, S., Gray, A., French, D., Kasman, I., Klumperman, J., Rice, D.S., Ye, W., 2007. EGFL7 regulates the collective migration of endothelial cells by restricting their spatial distribution. Development 134, 2913–2923. https://doi.org/10.1242/dev.002576

Schuermann, A., Helker, C.S.M., Herzog, W., 2015. Metallothionein 2 regulates endothelial cell migration through transcriptional regulation of vegfc expression. Angiogenesis 18, 463–75. https://doi.org/10.1007/s10456-015-9473-6

Schumacher, J.A., Bloomekatz, J., Garavito-Aguilar, Z.V., Yelon, D., 2013. tal1 Regulates the formation of intercellular junctions and the maintenance of identity in the endocardium. Dev Biol 383, 214–26. https://doi.org/10.1016/j.ydbio.2013.09.019

Sedletcaia, A., Evans, T., 2011. Heart chamber size in zebrafish is regulated redundantly by duplicated tbx2 genes. Dev Dyn Official Publ Am Assoc Anatomists 240, 1548–57. https://doi.org/10.1002/dvdy.22622

Sehnert, A.J., Huq, A., Weinstein, B.M., Walker, C., Fishman, M., Stainier, D.Y.R., 2002. Cardiac troponin T is essential in sarcomere assembly and cardiac contractility. Nat Genet 31, 106–110. https://doi.org/10.1038/ng875

Shannon, M.B., Patton, B.L., Harvey, S.J., Miner, J.H., 2006. A Hypomorphic Mutation in the Mouse Laminin α5 Gene Causes Polycystic Kidney Disease. J Am Soc Nephrol 17, 1913–1922. https://doi.org/10.1681/asn.2005121298

Sifrim, A., Hitz, M.-P., Wilsdon, A., Breckpot, J., Turki, S.H.A., Thienpont, B., McRae, J., Fitzgerald, T.W., Singh, T., Swaminathan, G.J., Prigmore, E., Rajan, D., Abdul-

Khaliq, H., Banka, S., Bauer, U.M.M., Bentham, J., Berger, F., Bhattacharya, S., Bu'Lock, F., Canham, N., Colgiu, I.-G., Cosgrove, C., Cox, H., Daehnert, I., Daly, A., Danesh, J., Fryer, A., Gewillig, M., Hobson, E., Hoff, K., Homfray, T., Study, I., Kahlert, A.-K., Ketley, A., Kramer, H.-H., Lachlan, K., Lampe, A.K., Louw, J.J., Manickara, A.K., Manase, D., McCarthy, K.P., Metcalfe, K., Moore, C., Newbury-Ecob, R., Omer, S.O., Ouwehand, W.H., Park, S.-M., Parker, M.J., Pickardt, T., Pollard, M.O., Robert, L., Roberts, D.J., Sambrook, J., Setchfield, K., Stiller, B., Thornborough, C., Toka, O., Watkins, H., Williams, D., Wright, M., Mital, S., Daubeney, P.E.F., Keavney, B., Goodship, J., Consortium, U., Abu-Sulaiman, R.M., Klaassen, S., Wright, C.F., Firth, H.V., Barrett, J.C., Devriendt, K., FitzPatrick, D.R., Brook, J.D., Study, D.D.D., Hurles, M.E., 2016. Distinct genetic architectures for syndromic and nonsyndromic congenital heart defects identified by exome sequencing. Nat Genet 48, 1060–1065. https://doi.org/10.1038/ng.3627

Silversides, C.K., Lionel, A.C., Costain, G., Merico, D., Migita, O., Liu, B., Yuen, T., Rickaby, J., Thiruvahindrapuram, B., Marshall, C.R., Scherer, S.W., Bassett, A.S., 2012. Rare Copy Number Variations in Adults with Tetralogy of Fallot Implicate Novel Risk Gene Pathways. Plos Genet 8, e1002843. https://doi.org/10.1371/journal.pgen.1002843

Singleman, C., Holtzman, N.G., 2012. Analysis of postembryonic heart development and maturation in the zebrafish, Danio rerio. Dev Dyn Official Publ Am Assoc Anatomists 241, 1993–2004. https://doi.org/10.1002/dvdy.23882

Smith, K.A., Chocron, S., Hardt, S. von der, Pater, E. de, Soufan, A., Bussmann, J., Schulte-Merker, S., Hammerschmidt, M., Bakkers, J., 2008. Rotation and Asymmetric Development of the Zebrafish Heart Requires Directed Migration of Cardiac Progenitor Cells. Dev Cell 14, 287–297. https://doi.org/10.1016/j.devcel.2007.11.015

Smith, K.A., Lagendijk, A.K., Courtney, A.D., Chen, H., Paterson, S., Hogan, B.M., Wicking, C., Bakkers, J., 2011. Transmembrane protein 2 (Tmem2) is required to regionally restrict atrioventricular canal boundary and endocardial cushion

development. Development 138, 4193–4198. https://doi.org/10.1242/dev.065375

Smyth, N., Vatansever, H.S., Murray, P., Meyer, M., Frie, C., Paulsson, M., Edgar, D., 1999. Absence of Basement Membranes after Targeting the LAMC1 Gene Results in Embryonic Lethality Due to Failure of Endoderm Differentiation. J Cell Biology 144, 151–160. https://doi.org/10.1083/jcb.144.1.151

Soemedi, R., Wilson, I.J., Bentham, J., Darlay, R., Töpf, A., Zelenika, D., Cosgrove, C., Setchfield, K., Thornborough, C., Granados-Riveron, J., Blue, G.M., Breckpot, J., Hellens, S., Zwolinkski, S., Glen, E., Mamasoula, C., Rahman, T.J., Hall, D., Rauch, A., Devriendt, K., Gewillig, M., O' Sullivan, J., Winlaw, D.S., Bu'Lock, F., Brook, J.D., Bhattacharya, S., Lathrop, M., Santibanez-Koref, M., Cordell, H.J., Goodship, J.A., Keavney, B.D., 2012. Contribution of Global Rare Copy-Number Variants to the Risk of Sporadic Congenital Heart Disease. Am J Hum Genetics 91, 489–501. https://doi.org/10.1016/j.ajhg.2012.08.003

Spicer, A.P., Joo, A., Bowling, R.A., 2003. A Hyaluronan Binding Link Protein Gene Family Whose Members Are Physically Linked Adjacent to Chrondroitin Sulfate Proteoglycan Core Protein Genes. J Biol Chem 278, 21083–21091. https://doi.org/10.1074/jbc.m213100200

Srivastava, D., Olson, E.N., 2000. A genetic blueprint for cardiac development. Nature 407, 221–226. https://doi.org/10.1038/35025190

Stainier, D.Y., Lee, R.K., Fishman, M.C., 1993. Cardiovascular development in the zebrafish. I. Myocardial fate map and heart tube formation. Dev Camb Engl 119, 31–40.

Stainier, D.Y.R., 2001. Zebrafish genetics and vertebrate heart formation. Nat Rev Genet 2, 39–48. https://doi.org/10.1038/35047564

Stainier, D.Y.R., Raz, E., Lawson, N.D., Ekker, S.C., Burdine, R.D., Eisen, J.S., Ingham, P.W., Schulte-Merker, S., Yelon, D., Weinstein, B.M., Mullins, M.C., Wilson, S.W., Ramakrishnan, L., Amacher, S.L., Neuhauss, S.C.F., Meng, A., Mochizuki, N., Panula, P., Moens, C.B., 2017. Guidelines for morpholino use in

zebrafish. Plos Genet 13, e1007000. https://doi.org/10.1371/journal.pgen.1007000

Steed, E., Faggianelli, N., Roth, S., Ramspacher, C., Concordet, J.-P., Vermot, J., 2016. klf2a couples mechanotransduction and zebrafish valve morphogenesis through fibronectin synthesis. Nat Commun 7, 11646. https://doi.org/10.1038/ncomms11646

Stemple, D.L., Solnica-Krezel, L., Zwartkruis, F., Neuhauss, S.C., Schier, A.F., Malicki, J., Stainier, D.Y., Abdelilah, S., Rangini, Z., Mountcastle-Shah, E., Driever, W., 1996. Mutations affecting development of the notochord in zebrafish. Dev Camb Engl 123, 117–28.

Stenzel, D., Franco, C.A., Estrach, S., Mettouchi, A., Sauvaget, D., Rosewell, I., Schertel, A., Armer, H., Domogatskaya, A., Rodin, S., Tryggvason, K., Collinson, L., Sorokin, L., Gerhardt, H., 2011. Endothelial basement membrane limits tip cell formation by inducing Dll4/Notch signalling in vivo. Embo Rep 12, 1135–43. https://doi.org/10.1038/embor.2011.194

Sztal, T., Berger, S., Currie, P.D., Hall, T.E., 2011. Characterization of the Laminin gene family and evolution in zebrafish. Dev Dyn Official Publ Am Assoc Anatomists 240, 422–31. https://doi.org/10.1002/dvdy.22537

Taddei, I., Deugnier, M.-A., Faraldo, M.M., Petit, V., Bouvard, D., Medina, D., Fässler, R., Thiery, J.P., Glukhova, M.A., 2008. Beta1 integrin deletion from the basal compartment of the mammary epithelium affects stem cells. Nat Cell Biol 10, 716–22. https://doi.org/10.1038/ncb1734

Taddei, I., Faraldo, M.M., Teulière, J., Deugnier, M.-A., Thiery, J.P., Glukhova, M.A., 2003. Integrins in Mammary Gland Development and Differentiation of Mammary Epithelium. J Mammary Gland Biol 8, 383–394. https://doi.org/10.1023/b:jomg.0000017426.74915.b9

Tessadori, F., Roessler, H.I., Savelberg, S.M.C., Chocron, S., Kamel, S.M., Duran, K.J., Haelst, M.M. van, Haaften, G. van, Bakkers, J., 2018. Effective CRISPR/Cas9-based nucleotide editing in zebrafish to model human genetic cardiovascular

disorders. Dis Model Mech 11, dmm035469. https://doi.org/10.1242/dmm.035469

Tessadori, F., Weerd, J.H. van, Burkhard, S.B., Verkerk, A.O., Pater, E. de, Boukens, B.J., Vink, A., Christoffels, V.M., Bakkers, J., 2012. Identification and functional characterization of cardiac pacemaker cells in zebrafish. Plos One 7, e47644. https://doi.org/10.1371/journal.pone.0047644

Thisse, C., Thisse, B., 2007. High-resolution in situ hybridization to whole-mount zebrafish embryos. Nat Protoc 3, 59–69. https://doi.org/10.1038/nprot.2007.514

Timmerman, L.A., Grego-Bessa, J., Raya, A., Bertrán, E., Pérez-Pomares, J.M., Díez, J., Aranda, S., Palomo, S., McCormick, F., Izpisúa-Belmonte, J.C., Pompa, J.L. de la, 2004. Notch promotes epithelial-mesenchymal transition during cardiac development and oncogenic transformation. Gene Dev 18, 99–115. https://doi.org/10.1101/gad.276304

TIMPL, R., 1989. Structure and biological activity of basement membrane proteins. Eur J Biochem 180, 487–502. https://doi.org/10.1111/j.1432-1033.1989.tb14673.x

Todorovic, V., Finnegan, E., Freyer, L., Zilberberg, L., Ota, M., Rifkin, D.B., 2011. Long form of latent TGF-β binding protein 1 (Ltbp1L) regulates cardiac valve development. Dev Dyn Official Publ Am Assoc Anatomists 240, 176–87. https://doi.org/10.1002/dvdy.22521

Todorovic, V., Frendewey, D., Gutstein, D.E., Chen, Y., Freyer, L., Finnegan, E., Liu, F., Murphy, A., Valenzuela, D., Yancopoulos, G., Rifkin, D.B., 2007. Long form of latent TGF- binding protein 1 (Ltbp1L) is essential for cardiac outflow tract septation and remodeling. Development 134, 3723–3732. https://doi.org/10.1242/dev.008599

Veerkamp, J., Rudolph, F., Cseresnyes, Z., Priller, F., Otten, C., Renz, M., Schaefer, L., Abdelilah-Seyfried, S., 2013. Unilateral Dampening of Bmp Activity by Nodal Generates Cardiac Left-Right Asymmetry. Dev Cell 24, 660–667. https://doi.org/10.1016/j.devcel.2013.01.026

Verhoeven, M.C., Haase, C., Christoffels, V.M., Weidinger, G., Bakkers, J., 2011. Wnt signaling regulates atrioventricular canal formation upstream of BMP and Tbx2. Birth Defects Res Part Clin Mol Teratol 91, 435–440. https://doi.org/10.1002/bdra.20804

Vermot, J., Forouhar, A.S., Liebling, M., Wu, D., Plummer, D., Gharib, M., Fraser, S.E., 2009. Reversing Blood Flows Act through klf2a to Ensure Normal Valvulogenesis in the Developing Heart. Plos Biol 7, e1000246. https://doi.org/10.1371/journal.pbio.1000246

Villefranc, J.A., Amigo, J., Lawson, N.D., 2007. Gateway compatible vectors for analysis of gene function in the zebrafish. Dev Dynam 236, 3077–3087. https://doi.org/10.1002/dvdy.21354

Wagner, J.U.G., Chavakis, E., Rogg, E.-M., Muhly-Reinholz, M., Glaser, S.F., Günther, S., John, D., Bonini, F., Zeiher, A.M., Schaefer, L., Hannocks, M.-J., Boon, R.A., Dimmeler, S., 2018. Switch in Laminin **β**2 to Laminin **β**1 Isoforms During Aging Controls Endothelial Cell Functions-Brief Report. Arteriosclerosis Thrombosis Vasc Biology 38, 1170–1177. https://doi.org/10.1161/atvbaha.117.310685

Waldo, K.L., Kumiski, D.H., Wallis, K.T., Stadt, H.A., Hutson, M.R., Platt, D.H., Kirby, M.L., 2001. Conotruncal myocardium arises from a secondary heart field. Dev Camb Engl 128, 3179–88.

Walsh, E.C., Stainier, D.Y.R., 2001. UDP-Glucose Dehydrogenase Required for Cardiac Valve Formation in Zebrafish. Science 293, 1670–1673. https://doi.org/10.1126/science.293.6535.1670

Wang, J., Hoshijima, M., Lam, J., Zhou, Z., Jokiel, A., Dalton, N.D., Hultenby, K., Ruiz-Lozano, P., Ross, J., Tryggvason, K., Chien, K.R., 2005. Cardiomyopathy Associated with Microcirculation Dysfunction in Laminin **α**4 Chain-deficient Mice. J Biol Chem 281, 213–220. https://doi.org/10.1074/jbc.m505061200

Wang, X., Li, L., Liu, D., 2014. Expression analysis of integrin **β**1 isoforms during zebrafish embryonic development. Gene Expr Patterns 16, 86–92. https://doi.org/10.1016/j.gep.2014.10.001

Wang, Y., Wu, B., Chamberlain, A.A., Lui, W., Koirala, P., Susztak, K., Klein, D., Taylor, V., Zhou, B., 2013. Endocardial to Myocardial Notch-Wnt-Bmp Axis Regulates Early Heart Valve Development. Plos One 8, e60244. https://doi.org/10.1371/journal.pone.0060244

Williams, J.A., Ni, H.-M., Haynes, A., Manley, S., Li, Y., Jaeschke, H., Ding, W.-X., 2015. Chronic Deletion and Acute Knockdown of Parkin Have Differential Responses to Acetaminophen-induced Mitophagy and Liver Injury in Mice. J Biol Chem 290, 10934–10946. https://doi.org/10.1074/jbc.m114.602284

Williamson, R.A., Henry, M.D., Daniels, K.J., Hrstka, R.F., Lee, J.C., Sunada, Y., Ibraghimov-Beskrovnaya, O., Campbell, K.P., 1997. Dystroglycan Is Essential for Early Embryonic Development: Disruption of Reichert's Membrane in Dag1-Null Mice. Hum Mol Genet 6, 831–841. https://doi.org/10.1093/hmg/6.6.831

Wirrig, E.E., Snarr, B.S., Chintalapudi, M.R., O'Neal, J.L., Phelps, A.L., Barth, J.L., Fresco, V.M., Kern, C.B., Mjaatvedt, C.H., Toole, B.P., Hoffman, S., Trusk, T.C., Argraves, W.S., Wessels, A., 2007. Cartilage link protein 1 (Crtl1), an extracellular matrix component playing an important role in heart development. Dev Biol 310, 291–303. https://doi.org/10.1016/j.ydbio.2007.07.041

Wittkopp, N., Huntzinger, E., Weiler, C., Sauliere, J., Schmidt, S., Sonawane, M., Izaurralde, E., 2009. Nonsense-Mediated mRNA Decay Effectors Are Essential for Zebrafish Embryonic Development and Survival. Mol Cell Biol 29, 3517–3528. https://doi.org/10.1128/mcb.00177-09

Wu, R.S., Lam, I.I., Clay, H., Duong, D.N., Deo, R.C., Coughlin, S.R., 2018. A Rapid Method for Directed Gene Knockout for Screening in G0 Zebrafish. Dev Cell 46, 112-125.e4. https://doi.org/10.1016/j.devcel.2018.06.003

Xu, H., Xiao, T., Chen, C.-H., Li, W., Meyer, C.A., Wu, Q., Wu, D., Cong, L., Zhang, F., Liu, J.S., Brown, M., Liu, X.S., 2015. Sequence determinants of improved CRISPR sgRNA design. Genome Res 25, 1147–57. https://doi.org/10.1101/gr.191452.115

Yamamura, H., Zhang, M., Markwald, R.R., Mjaatvedt, C.H., 1997. A heart segmental defect in the anterior-posterior axis of a transgenic mutant mouse. Dev Biol 186, 58–72. https://doi.org/10.1006/dbio.1997.8559

Yang, T., Arslanova, D., Gu, Y., Augelli-Szafran, C., Xia, W., 2008. Quantification of gamma-secretase modulation differentiates inhibitor compound selectivity between two substrates Notch and amyloid precursor protein. Mol Brain 1, 15. https://doi.org/10.1186/1756-6606-1-15

Yelon, D., Horne, S.A., Stainier, D.Y.R., 1999. Restricted Expression of Cardiac Myosin Genes Reveals Regulated Aspects of Heart Tube Assembly in Zebrafish. Dev Biol 214, 23–37. https://doi.org/10.1006/dbio.1999.9406

Yin, C., Kikuchi, K., Hochgreb, T., Poss, K.D., Stainier, D.Y.R., 2010. Hand2 Regulates Extracellular Matrix Remodeling Essential for Gut-Looping Morphogenesis in Zebrafish. Dev Cell 18, 973–984. https://doi.org/10.1016/j.devcel.2010.05.009

Yousif, L.F., Russo, J.D., Sorokin, L., 2012. Laminin isoforms in endothelial and perivascular basement membranes. Cell Adhes Migr 7, 101–110. https://doi.org/10.4161/cam.22680

Yurchenco, P.D., Cheng, Y.S., 1993. Self-assembly and calcium-binding sites in Laminin. A three-arm interaction model. J Biological Chem 268, 17286–99.

Yurchenco, P.D., Quan, Y., Colognato, H., Mathus, T., Harrison, D., Yamada, Y., O'Rear, J.J., 1997. The **α** chain of Laminin-1 is independently secreted and drives secretion of its **β**- and **γ**-chain partners. Proc National Acad Sci 94, 10189–10194. https://doi.org/10.1073/pnas.94.19.10189

Zanin, M.K.B., Bundy, J., Ernst, H., Wessels, A., Conway, S.J., Hoffman, S., 1999. Distinct spatial and temporal distributions of aggrecan and versican in the embryonic chick heart. Anatomical Rec 256, 366–380. https://doi.org/10.1002/(sici)1097-0185(19991201)256:4<366::aid-ar4>3.0.co;2-#

Zhang, R., Cao, P., Yang, Z., Wang, Z., Wu, J.-L., Chen, Y., Pan, Y., 2015. Heparan Sulfate Biosynthesis Enzyme, Ext1, Contributes to Outflow Tract

Development of Mouse Heart via Modulation of FGF Signaling. Plos One 10, e0136518. https://doi.org/10.1371/journal.pone.0136518

10. Appendix

Table 10.1 Primer sequences used to generate mRNA ISH probes

Probe target	Sequence	Fragment size (bp)	Short name
lamb1a-F	TCCACTTCACCCACCTCATC	~1000	EN145
lamb1a-R	GGTCACAGTTCCTTCCGGTA		EN146
has2-F	GTTCACGCAGACCTCATCAC	1050	CD47
has2-R	CATCCAATACCTCACGCTGC		CD48
rhocb-F	CGCCAAGCAAAATCGAAACC	919	CD81
rhocb-R	ACCAGAATCAAAAGAGACAGAGA		CD82
lamb2l-F	CAGTGTATGTGTCGGCATGG	1062	CD87
lamb2l-R	AAGCTCCGTCCTTACACACA		CD88
lamb4-F	CTCGCAGCTTCTTCAACCTG	1051	CD89
lamb4-R	TACAGGCATAAGGGTCGTCC		CD90
spp1-F	TTTAACACTCCTCGTCGCCA	1015	CD145
spp1-R	ATTTGTGCTCGGCTGTGTTT		CD146
tbx2b-F	ACGTTTTCCCTGAGACCGAT	955	CD147
tbx2b-R	TAGGTGTAGGGGTACGGGAA		CD148
itga6a-F	CCAGCCTCACGACAAAACAA	1000	CD155
itga6a-R	GTTCTCCACAGACAGACCGA		CD156
itga6b-F	AATGGAGATGGGTGGCAAGA	1284	CD157
itga6b-R	AGAAATTCCTCCCGTGCTCA		CD158
itgb4-F	GGAAATGCGATGAGTGTCCC	1162	CD161
itgb4-R	AGGTCTGCTGTGCTGTATGT		CD162
itga2b-F	TGGCCGGGACATATGCATAT	1081	CD163
itag2b-R	TGTTCCAGATCACCCATGCT		CD164
tbx5a-F	ACACCTTTCGGCTCCAAAAC	1061	CD171
tbx5a-R	CTGAGAGTAGCTTAGGGGCC		CD172
rhoca-F	GGACAGGAGGACTATGACCG	1168	CD181
rhoca-R	CACAGCTCAATCCACATGCA		CD182
itga10-F	GCACCCAGATTCAAGCACAA	988	CD185

itga10-R	TCTTGTGTGTTGTTGGCCAG		CD186
itga7-F	CTTCTCCGTGGCTCTACAC	479	CD189
itga7-R	CGAGCAGCAGGAAGTTG		CD190
acana-F	CGGATCAAGTGGAGTCTGGT	1067	CD215
acana-R	GAAGGGAGGACGTGGGAAAT		CD216
acanb-F	ATCAAGACAGCACCCTCAGT	1035	CD217
acanb-R	TTTCTGGAAATGGCGTGGTC		CD218
dCas9-F	TGATCAGTCCAAGAACGGCT	~1200	
dCas9-R	CTTTCACCAGCTCATCGACG		
chsy1-F	CACCATTCAGCTCCATCGTG	801	
chsy1_R	TCGGCTTTGGGGTACTTCAT		